OUT-OF-PLANE INSTABILITY OF RECTANGULAR REINFORCED CONCRETE WALLS UNDER IN-PLANE LOADING

A thesis submitted in partial fulfilment of the requirements for the degree of

Doctor of Philosophy in Structural Engineering

By

Farhad Dashti

Supervised by:
Prof. Rajesh Dhakal
Prof. Stefano Pampanin

DEPARTMENT OF CIVIL AND NATURAL RESOURCES ENGINEERING

UNIVERSITY OF CANTERBURY

CHRISTCHURCH, NEW ZEALAND

UC
UNIVERSITY OF CANTERBURY
Te Whare Wānanga o Waitaha
CHRISTCHURCH NEW ZEALAND

June 2017

ABSTRACT

Structural wall system has been one of the most common lateral load resisting elements in reinforced concrete structures. A relatively high stiffness is provided by a structural wall along its in-plane direction making it the main lateral force resisting system of the structure. Observations of wall damage in some modern buildings in several earthquakes that took place in the 2010s proved the fact that some of the wall failure modes, interacting with each other and occurring successively in some occasions, are not yet well understood. The research presented here seeks to address the out-of-plane instability of rectangular walls which was observed in some well-confined modern walls and raised concerns about the reliability of current design code provisions.

A numerical modeling approach is developed in this research which is the first numerical model successful in capturing the trigger and evolution of out-of-plane deformation and ultimate failure due to out-of-plane instability under perfectly concentric and cyclic in-plane loading and without introducing any artificial imperfections. Experimental results of cantilever wall specimens which failed in different failure modes including out-of-plane instability are used for verification of the adopted modeling and analysis approach. The mechanism of out-of-plane instability failure in rectangular structural walls under in-plane loading has been studied by scrutinizing the sequence of events resulting in this mode of failure and using the validated numerical model. The parameters controlling this mode of failure are identified to be the wall thickness as well as the parameters that influence the maximum tensile strain developed in the longitudinal reinforcement.

Although out-of-plane instability failure was observed in several wall experiments, its evolution and the controlling parameters have not been fully investigated. An experimental campaign has been undertaken as a part of this research to investigate the effects of different parameters on out-of-plane deformation of rectangular walls. The experimental program was designed based on a parametric study using the verified numerical model. Data analysis, presented here, has been done to provide an improved understanding of the mechanism of out-of-plane instability and the parameters influencing this mode of failure. The experimental findings regarding the evolution of this mode of failure and the influential parameters are in good agreement with the numerical predictions. The inherent and mostly unmeasurable eccentricities, which could be comprised of the material, geometry, and

loading imperfections and were not included in the model, are found to affect the initiation and rate of increase in out-of-plane displacement. Also, the experimental findings have been used to evaluate the assumptions made in the available analytical models used for prediction of wall instability failure.

Deputy Vice-Chancellor's Office
Postgraduate Office

UNIVERSITY OF CANTERBURY
Te Whare Wānanga o Waitaha
CHRISTCHURCH NEW ZEALAND

CO-AUTHORSHIP FORM

This form is to accompany the submission of any thesis that contains research reported in co-authored work that has been published, accepted for publication, or submitted for publication. A copy of this form should be included for each co-authored work that is included in the thesis. Completed forms should be included at the front (after the thesis abstract) of each copy of the thesis submitted for examination and library deposit.

Please indicate the chapter/section/pages of this thesis that are extracted from co-authored work and provide details of the publication or submission from the extract comes:

Chapter 2

Dashti, F., R.P. Dhakal, S. Pampanin (2014) "Comparative In-plane Pushover Response of a Typical RC Rectangular Wall Designed by Different Standards", Earthquakes and Structures (EAS), Vol. 7, No. 5 (2014) 667-68, DOI: http://dx.doi.org/10.12989/eas.2014.7.5.667

Dashti, F., R.P. Dhakal, S. Pampanin (2015) "Seismic Performance of Existing New Zealand Shear Wall Structures " *New Zealand Concrete Industry Conference 2015*, Rotorua, New Zealand

Chapter 3

Dashti, F., R.P. Dhakal, S. Pampanin (2017) "Numerical Modeling of Rectangular Reinforced Concrete Structural Walls" *Journal of Structural Engineering*, 143(6), DOI: 10.1061/(ASCE)ST.1943-541X.0001729

Dashti, F., R.P. Dhakal , S. Pampanin (2014) "Numerical Simulation of Shear Wall Failure Mechanisms" *The 2014 New Zealand Society for Earthquake Engineering Conference, NZSEE2014*, Auckland, New Zealand

Chapter 4

Dashti, F., R.P. Dhakal, S. Pampanin (2016) "Validation of a Numerical Model for Prediction of Out-of-plane Instability in Ductile Structural Walls under Concentric In-plane Cyclic Loading" *Journal of Structural Engineering*, Ms. No. STENG-5314R2 (Under Review)

Dashti, F., R.P. Dhakal, S. Pampanin (2015) "Development of Out-of-plane Instability in

Rectangular RC Structural Walls" *The 2015 New Zealand Society for Earthquake Engineering Conference, NZSEE2015*, Rotorua, New Zealand

Dashti, F., R.P. Dhakal, S. Pampanin (2014) "Simulation of Out-of-plane Instability in Rectangular RC Structural Walls" *Second European Conference on Earthquake Engineering and Seismology, 2ECESS, August, 2014*, Istanbul, Turkey

Chapter 5

Dashti, F., R.P. Dhakal, S. Pampanin (2016) "Blind Prediction of In-plane and Out-of-plane Responses for a Thin Singly Reinforced Concrete Flanged Wall Specimen" *Bulletin of Earthquake Engineering*, DOI 10.1007/s10518-017-0211-x

Chapter 6

Dashti, F., R.P. Dhakal, S. Pampanin (2017) "Tests on Slender Ductile Structural Walls Designed According to New Zealand Standard" *Bulletin of the New Zealand Society for Earthquake Engineering*, (Accepted for publication)

Dashti, F., R.P. Dhakal, S. Pampanin (2017) "An Experimental Study on Out-of-plane Deformations of Rectangular Structural Walls Subject to In-plane Loading" *16th world conference on earthquake engineering, 16WCEE, January, 2017*, Santiago, Chile.

Chapter 8

Dashti, F., R.P. Dhakal, S. Pampanin (2017) "Evolution of Out-of-plane Deformation and Subsequent Instability in Rectangular RC Walls under In-plane Cyclic Loading; Experimental Observation" *Earthquake Engineering & Structural Dynamics*, EQE-17-0078 (Under Review)

Dashti, F., R.P. Dhakal, S. Pampanin (2016) "Out-of-plane Instability of a Rectangular Wall Specimen Subject to In-plane Cyclic Loading" *New Zealand Concrete Industry Conference 2016*, Auckland, New Zealand

Please detail the nature and extent (%) of contribution by the candidate:

The candidate did all the work (100%) under our supervision.

Certification by Co-authors:

If there is more than one co-author then a single co-author can sign on behalf of all

The undersigned certifies that:

- The above statement correctly reflects the nature and extent of the PhD candidate's contribution to this co-authored work.
- In cases where the candidate was the lead author of the co-authored work he or she wrote the text.

Name: *Rajesh P. Dhakal* Signature: *Rajesh P. Dhakal* Date: *30/01/2017*

Table of Contents

List of Tables

List of Figures

ACKNOWLEDGMENTS

I wish to acknowledge the financial support provided by the UC Doctoral Scholarship, the Natural Hazard Research Platform (NHRP), the Ministry of Business, Innovation and Employment (MBIE) and the Quake Centre at the University of Canterbury.

I would like to express my sincere gratitude to my supervisors, Prof. Rajesh Dhakal and Prof. Stefano Pampanin for their invaluable guidance and support during my PhD studies. I could not have done this without their continuous supervision and encouragement.

Thanks are extended to Alan Thirlwell for his valuable help with strain gauge installation, test setup preparation, and specimen testing. I would also like to thank Peter Coursey for his assistance with the loading program and data acquisition.

Particular thanks would have to go to my special friends Karim Tarbali and Saleh Malekpour for their friendship, guidance, and encouragement. Thanks also go to Mohammad Soleymani Ashtiani for his assistance with DIANA finite element analysis program and to Giuseppe Loporcaro for his help with material testing. Continuous encouragement provided by my friends and fellow postgraduate students at the University of Canterbury, including Dr. Patricio Quintana Gallo, Amir Malek, Kaveh Andisheh, Royce Liu, Reza Sedgh and many others is also greatly appreciated.

Finally, I would like to thank my parents for their love and support throughout my life and special thanks are reserved for my lovely wife Samaneh Dashti for her unwavering understanding and support throughout my PhD studies.

1 INTRODUCTION

Structural walls, also known as shear walls, are one of the common lateral load resisting elements in reinforced concrete (RC) buildings in seismic regions. Unlike other structural elements, structural walls are considerably longer in one cross-sectional dimension compared to the other to provide shear and moment resisting capacities in the desired direction. A relatively high stiffness is consequently provided by a structural wall along its in-plane direction making it the main lateral force resisting system of the structure. As a result, this structural system needs to prevent damage to non-structural elements during minor earthquakes, limit structural damage in moderate earthquakes and prevent the collapse of the building during major seismic events. To achieve this level of reliability, a structural wall needs to respond to seismic actions with enough ductility and energy dissipation capacity. Hence, any mode of failure that is bound to interfere with its operation must be impeded until the desired performance level is achieved. To achieve this goal, the failure modes that different types of structural walls are likely to sustain should be identified.

In recent years, as the optimization issues have gained importance, slender rectangular walls which take less space and are believed to be more economical designs have become more common in many countries. Use of higher concrete strengths has also resulted in more slender profiles than have been previously tested in the laboratory or in real buildings under earthquakes. Rectangular walls with relatively low thickness are very common in New Zealand and Chile. The performance of these structural walls in the Chile (February 2010) and New Zealand (February 2011) earthquakes has exposed some problems with the existing design of RC structural walls. Out-of-plane instability is one of the failure patterns that were observed in these walls (CERC 2012). This failure pattern refers to buckling of a portion of a wall section out-of-plane (Figure 1.1) as a result of pure in-plane loading or a combination of in-plane and out-of-plane (i.e. bi-directional) loading. This buckling under in-plane loading is limited to an end region of the wall, where the axial strains from in-plane loading are greatest.

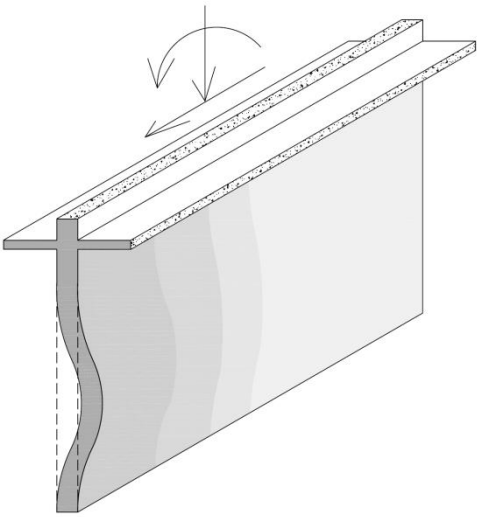

Figure 1.1: Out-of-plane instability of rectangular walls

1.1 OBJECTIVES

The structures with instability failure in walls are hardly repairable since a considerably abrupt loss of lateral load resistance can be induced in the building by this mode of failure, which can cause instability of the whole building. Paulay and Goodsir (1985) and Paulay and Priestley (1993) were the first to describe in detail the development of out-of-plane instability failure. As there were not many test results on this mode of failure, some assumptions such as the height of the wall involved in the formation of instability (buckling length) were made in these postulations. The current New Zealand design provisions for prevention of this mode of failure are based on the equations derived in these studies. The basic findings of these studies were confirmed by Chai and Elayer (1999), who investigated the out-of-plane instability of structural walls by testing concrete columns that represented boundary zones of rectangular walls. This method has become a common approach for investigating this mode of failure. However, many assumptions need to be made such as the wall region that undergoes the out-of-plane instability, the boundary conditions at the top, bottom and along the edge that joins boundary zone to panel as well as the height of the wall involved in the formation of out-of-plane instability. Also, despite being one of the observed failure patterns in the recent earthquakes in Chile and New Zealand, numerical simulation of out-of-plane instability has been seldom attempted. Researchers have tried to simulate this failure pattern by providing an initial imperfection (i.e. eccentricity). In such cases, however, the outcome cannot be generic as the prediction greatly depends on the arbitrary value of the initial imperfection input into the model.

Moreover, the mechanism of out-of-plane instability failure is not clearly understood so far, and consequently, the relevant design provisions are not backed up by strong research and clear understanding of the development of out-of-plane deformations in rectangular walls. Although this mode of failure has been observed in several wall tests, scrutinizing the failure mechanism and the governing parameters has not been the main objective of these researches. Therefore, the test setups did not include restraints at story levels to represent the unsupported height in a real building which is a crucial parameter for investigation of out-of-plane instability. Also, the measurements were not done to capture the initiation of out-of-plane deformation and its relationship with the local response of materials.

Given the facts noted above, to advance the knowledge of the out-of-plane deformation in rectangular RC structural walls and the subsequent instability failure, this PhD research tries to address the following issues.

- Proposing a numerical model for seismic performance assessment of RC walls including in-plane high localized strains as well as out-of-plane instability of slender walls
- Understanding the causes and consequences of out-of-plane instability failure mechanism of the RC structural walls under in-plane loading
- Collection and generation of experimental data to qualitatively and quantitatively understand the parameters affecting out-of-plane instability failure of rectangular walls

1.2 OUTLINE OF THE THESIS

Chapter 2 presents an overall literature review on different aspects of research on the seismic performance of walls and on the out-of-plane instability of rectangular walls. Earthquake damage to structural walls in two major earthquakes in the 2010s (2010 Chile and 2011 New Zealand) is reviewed. A brief state-of-the-art on different numerical models used for simulating the seismic response of reinforced concrete walls and the analytical models proposed for prediction of the out-of-plane instability in rectangular walls is presented. Previous experimental research on RC walls, including the parameters addressed in each research, as well as the tests conducted on the out-of-plane instability of rectangular walls is also summarized.

Chapter 3 explores numerical modeling of rectangular RC walls. It presents a comprehensive description and verification of a numerical modeling approach evaluated

using experimental results of walls with different shear-span ratios which failed in different modes. Details of the modeling approach, i.e. the element type, material models, and analysis features are discussed. The ability of the model to reliably predict the global and local responses of wall specimens designed to fail in different modes is verified and the key milestones of the wall response predicted by the model are compared with the experimental observations.

Chapter 4 verifies the model's ability to predict out-of-plane failure and the mechanisms leading to this mode of failure. It presents verification of the adopted modeling and analysis approach using experimental results of cantilever wall specimens which failed in out-of-plane mode. Development of the out-of-plane deformation in different regions of a wall section is comprehensively discussed using the detailed response of the reinforcement and concrete elements positioned along the wall thickness at different stages of the failure mode.

Chapter 5 presents details of a successful blind prediction carried out to simulate the response of a thin reinforced concrete wall tested under uni-directional (in-plane) quasi-static cyclic loading at the Structural Laboratory of the École Polytechnique Fédérale de Lausanne (EPFL). The prediction was done before the test results were available, and for completeness, the test results were added at a later stage, without any changes to the earlier prediction. The model prediction versus test observations, as well as a parametric study addressing the effects of shear-span ratio, reinforcement eccentricity and axial load ratio on the wall response, is discussed in this chapter.

Chapter 6 introduces the experimental phase of this research, which includes testing three half-scale rectangular wall specimens. It presents a brief review of the test program, including the test design, specimen construction, test setup, instrumentation, and loading protocol. The experimental observations are summarized in this chapter. The load-displacement response of the tested specimens and an overview of the progression of observed damage are presented, and a discussion on the local measurements and failure patterns of the specimens is included.

Chapter 7 presents comparison of the numerically predicted response of the test specimens with the experimental observations at global and local levels of the wall response scrutinizing the capabilities and shortcomings of the modeling approach.

Chapter 8 scrutinizes the development of out-of-plane instability in rectangular walls. It presents a comprehensive description of the sequence of events resulting in the formation of out-of-plane instability in one of the specimens, discussing the test measurements at different locations of the specimen. The proposed analytical models for prediction of this mode of failure are summarized and compared with the test observations.

Chapter 9 provides a summary of the thesis, including the research findings, and the areas needing further research.

1.3 REFERENCES

CERC (2012). "Canterbury Earthquakes Royal Commission Reports." *http://canterbury.royalcommission.govt.nz/Final-Report-Volume-Two-Contents*.

Chai, Y. H. and D. T. Elayer (1999). "Lateral stability of reinforced concrete columns under axial reversed cyclic tension and compression." *ACI Structural Journal* 96(5), 780-789.

Paulay, T. and W. Goodsir (1985). "The ductility of structural walls." *Bulletin of the New Zealand Society for Earthquake Engineering* 18(3), 250-269.

Paulay, T. and M. Priestley (1993). "Stability of ductile structural walls." *ACI Structural Journal* 90(4), 385-392.

2 LITERATURE REVIEW

This chapter presents a review of earthquake damage to structural walls in two major earthquakes in the 2010s (2010 Chile and 2011 New Zealand). A brief state-of-the-art on different types of the numerical models used for simulation of reinforced concrete walls is presented followed by a summary of the models proposed for prediction of out-of-plane instability. Previous experimental research on RC walls and the parameters addressed in each research are summarized. The past research conducted specifically on out-of-plane instability of rectangular walls is also addressed and the relevant design requirements of different seismic codes are outlined.

2.1 WALL DAMAGE OBSERVED DURING THE CHILE AND NEW ZEALAND EARTHQUAKES

2.1.1 FEBRUARY 27, 2010 CHILE EARTHQUAKE

The performance of modern buildings that utilize structural walls for the primary lateral-force-resisting system in the 2010 Chile earthquake showed that further research on design provisions of shear walls is required. In 1996, Chile adopted a new code based on ACI 318-95, resulting in more slender walls. The requirements were essentially similar to the US reinforced concrete code (ACI 318) provisions, except that boundary element confinement was not required. The 2010 Mw 8.8 earthquake caused serious damage to many of these walls, including crushing/spalling of concrete and buckling of vertical reinforcement, often over a large horizontal portion of the wall length (Figure 2.1). Some of the failures are attributable to lack of closely spaced transverse reinforcement at wall boundaries, which was not required by the Chilean code based on the good performance of buildings in the 1985 M7.8 earthquake. However, many of the failures observed in the 2010 Chile earthquake are not yet fully understood, and many suggest that there are deficiencies in the current US design provisions (Massone and Wallace 2011, Wallace 2011). In some cases, lateral instability (buckling) of a large portion of the wall section was observed (Figure 2.1

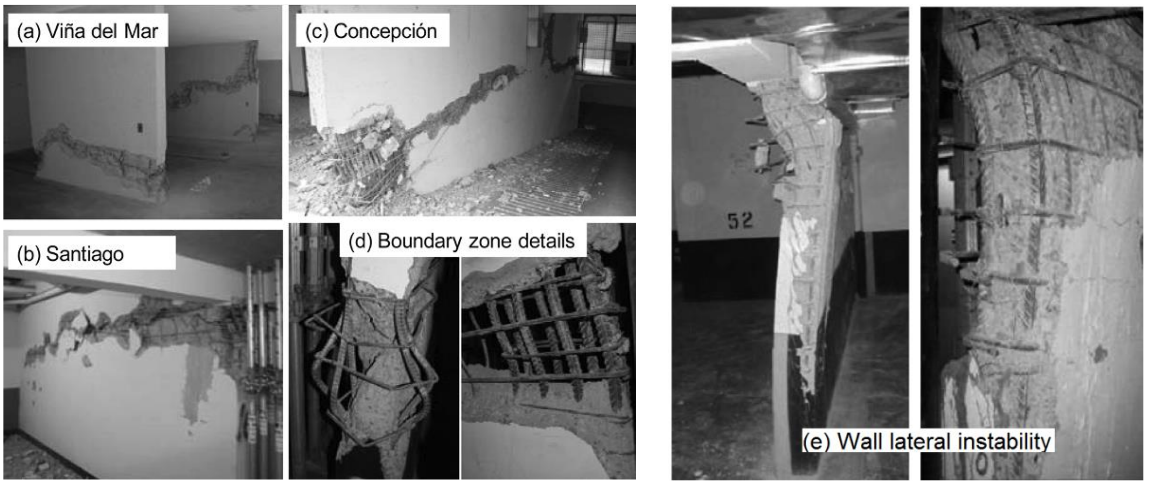

Figure 2.1: Typical wall damage in 2010 Chile earthquake (Wallace 2012)

2.1.2 FEBRUARY 22, 2011 CHRISTCHURCH EARTHQUAKE

The 2011 Christchurch earthquake showed many similar wall failures, suggesting the deficiencies observed in the 2010 Chile earthquake were not one-off. The RC buildings in New Zealand can be classified into two categories; namely Pre- 1970 buildings which were designed prior to the 1976 revision of the seismic loading standard NZS4203:1976 and 1974 version of the concrete structures standard NZS3152:1974, and modern buildings that were designed using the 1976 or a later version of the RC seismic design standard. Pre-1970s RC buildings generally have inadequate seismic capacity and are likely to experience brittle failure as they have deficiencies like lack of confinement in walls, joints and columns, inadequate reinforcing and anchorage details, poor material properties and use of plain reinforcing bars, no capacity design principles and irregular building configurations (Kam et al. 2011). According to the EERI special earthquake report on the M6.3 Christchurch, New Zealand, earthquake of February 22 (2011) and Canterbury Earthquakes Royal Commission Reports (2012), structural walls did not perform as anticipated. Boundary zone crushing and bar buckling were observed mostly in Pre-1970s RC walls which were generally lightly reinforced, were not detailed for ductility and had inadequate reinforcement to provide confinement to the concrete and buckling restraint to the longitudinal reinforcement.

On the other hand, modern (Post-1970s) RC wall buildings were observed to have experienced failure patterns like wall web buckling, boundary zone bar fracture and buckling failure of ducted splice. In a number of cases, compression failure occurred in the outstanding legs of T and L walls in addition to significant out-of-plane displacements,

thereby resulting in overall buckling of the wall. Figure 2.2 shows the overall buckling of one outstanding leg of a V-shaped wall. The building had two V-shaped concrete walls on either side of it. The wall on the south side of the building surrounded the elevator and stairs, while the wall on the north side had a direct connection to the diaphragm. It appears the north wall acted as an L-shaped section with a large tension flange contributing to buckling of the unsupported web.

In some cases, the transverse reinforcement did not meet the spacing requirement to prevent buckling of the longitudinal reinforcement, and bar buckling resulted in high localized strains. Buckling and fracture of bars were observed in lightly reinforced slender walls of a building which had numerous walls and did not require full ductile detailing as the number of walls made it possible to achieve the higher base shear demand required for a low ductility structural system (Figure 2.3(a)). Also, fracture of bars in boundary zones and shear-axial failure of slender walls were observed in the ground floor of an 8-sorey plus basement residential apartment building built in the 2000s (Figure 2.3(b)).

Also, one of the walls of the Grand Chancellor Hotel in Christchurch experienced a brittle in-plane shear-axial failure at its base together with out-of-plane instability. The failure plane initiated at the top of the lap splice in the web vertical reinforcement. The confinement hoops opened allowing boundary longitudinal bars to deform with the shortening of the wall. This wall was subjected to excessive amount of axial load and the combined axial load and bending exceeded the concrete crushing capacity given only a limited amount of tie reinforcement was provided at the base of the wall. Some out-of-plane deformation of the wall during the earthquake excitation and the plane of weakness created at the end of the splice of the web vertical reinforcement further contributed to the failure at the base of the wall.

Figure 2.2: Web buckling of well-confined wall (Elwood 2013)

(a) (b)

Figure 2.3: (a) Bar buckling and fracture in lightly reinforced slender RC shear wall; (b) slender wall shear-axial failure (Kam et al. 2011)

Figure 2.4: Failure of wall D5-6 of the Grand Chancellor Hotel (Kam et al. 2011)

2.1.2.1 RECOMMENDATIONS OF CANTERBURY EARTHQUAKES ROYAL COMMISSION

As a result of the performance of the shear walls in the canterbury earthquake sequence in New Zealand, the following issues have been identified to be further investigated (CERC 2012):

2.1.2.1.1 Reinforcement arrangement to ensure yielding beyond the vicinity of a primary crack

The reinforcement content and arrangement in a number of structural walls have been shown to be inadequate to ensure that yielding of reinforcement can extend beyond the immediate vicinity of a single primary crack. Improved ductility may be achieved by the use of higher minimum reinforcement contents, changes in the distribution of reinforcement in the wall; and de-bonding bars in critical zones. Where the de-bonding option is used the

potential negative implications of this action on shear and torsional behavior in T-shaped walls and in walls forming a shear core in a building should be identified.

Recommendation

Changes should be made to the Standard to ensure that yielding of reinforcement can extend beyond the immediate vicinity of a single primary crack, and that further research should be carried out to refine design requirements related to crack control in structural walls.

2.1.2.1.2 Confinement of boundary region, effect of bi-axial loading in design provisions

A number of structural walls did not perform in the earthquakes as well as anticipated. There are a number of possible reasons for this:

- The walls sustained greater axial forces than were anticipated in the design owing to the restraint that other structural elements provided against elongation when the wall developed a plastic hinge.
- Vertical reinforcement in a wall in the region between confined compression zones is subjected to compression when the bending moment decreases and reverses in direction. Under these conditions the longitudinal reinforcement may yield in compression, which can result in buckling.
- The majority of structural tests on walls that have been made to establish design criteria have been tested with in-plane loading only. The effect of bi-axial loading has received little attention, and this aspect needs further research.

Recommendation

The Standard should be modified to include requirements related to confinement of ductile walls.

For the ductile detailing length of ductile walls, transverse reinforcement shall be provided over the full length of the wall as follows:

Confinement of boundary regions shall be provided in accordance with NZS 3101:2006, clause 11.4.6[1], modified to provide confinement over the full length of the compression zone;

[1] Transverse reinforcement requirements of structural walls designed for ductility in earthquakes

Transverse reinforcement in the central portion of the wall shall satisfy the anti-buckling requirements of NZS 3101:2006, clause 11.4.6.3[2].

2.1.2.1.3 Provisions for buckling under moderate and high axial load ratios (Slenderness)

Suitable provisions to prevent buckling of walls subjected to moderate and high axial load ratios are currently not considered in the standard.

Recommendation

As a short-term measure, where there is a ductile detailing length in a wall and the axial load ratio equals or exceeds a value of 0.10, the ratio of the clear height between locations where the wall is laterally restrained to the wall thickness should not exceed the smaller of 10, or the value given by clause 11.4.2[3] in the Standard.

Research should also be carried out to establish more rational expressions for limiting the ratio of clear height to thickness, allowing for both the loading and the imposed deformations on walls.

2.1.3 SUMMARY

The observed structural wall performances following recent earthquakes strongly suggest that the observed problems are not isolated and that analysis and design provisions need to be reassessed. Figure 2.5 summarizes common 2D failure modes exhibited by structural walls (Paulay and Priestley 1992) as:

a) Free body diagram of a structural wall under lateral loading;
b) Flexural plastic hinge formed at the base of the wall;
c) Shear failure due to diagonal tension or compression failure;
d) Sliding shear failure along the foundation or construction joints;
e) Serviceability failure, due to excessive deflection under service loading.

[2] Transverse reinforcement for lateral restraint in plastic hinge regions

[3] Dimensional limitations of structural walls designed for ductility in earthquakes

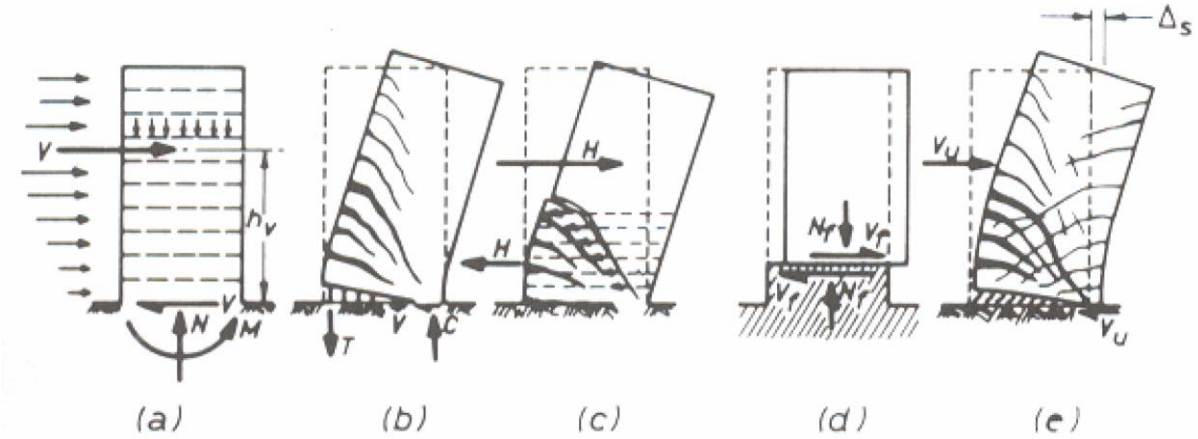

Figure 2.5: Common 2D failure modes exhibited in structural walls (Paulay and Priestley 1992)

As noted above, some unusual failure patterns were observed in the earthquakes occurred in Chile (2010) and New Zealand (2011) such as overall out-of-plane wall buckling which is considered as one of the major issues by the Canterbury Earthquakes Royal Commission, indicating a need to build on common 2D failure modes of walls, looking at 3D, different mechanical and geometric characteristics, etc.

2.2 NUMERICAL AND ANALYTICAL STUDIES

The procedures for numerical modeling of an RC shear wall can be classified into two broad groups, microscopic and macroscopic models. Microscopic models are based on a detailed interpretation of the local behavior to obtain a solution through the finite element approach, whereas phenomenological macroscopic models are based on capturing overall behavior with reasonable accuracy. Micro models can provide a detailed prediction of the local behavior, but due to complexities involved in developing the model and interpreting the results, their implementation is not common for nonlinear analyses of multi-story buildings with RC shear walls as it needs a large amount of time for preparing the structural model, computing the response, and interpreting the results. Considering all aspects of both procedures, especially practicality and efficiency, using macro models to predict the lateral load-displacement response of shear wall buildings has been typically preferred over spending much time on developing microscopic models.

In this section, a summary of the numerical modeling approaches proposed for simulation of reinforced concrete walls is provided and the previous research conducted on numerical as well as analytical prediction of out-of-plane instability is discussed.

2.2.1 MICRO MODELS

The elements used for finite element modeling of structural walls can be classified into i) solid (brick) elements, and ii) plane stress, plane strain, or shell elements. Although the two-dimensional plane stress elements, plate elements, and shell elements have been widely used in the finite element analysis of reinforced concrete, the use of three-dimensional solid element is very limited. This is due to the computational effort required in the analysis and to the lack of knowledge concerning the behaviour of concrete in a three-dimensional state of stress. Solid elements have been used by a number of researchers (Deshmukh et al. 2006, Moaveni et al. 2010). Using this approach, response of the wall elements along the length and thickness under bi-directional lateral loads can be investigated. However, a large number of solid elements may be required to model the concrete and reinforcement of a wall accurately, which may require significant computational time to run the analysis.

Plane stress, plane strain, and shell elements have also been used to simulate the response of structural walls in 2D. Studies conducted by Palermo and Vecchio (2002), and Kelly (2007) are good examples of this modeling approach. Telleen et al. (2012b) found some good agreement between results from sophisticated nonlinear finite element models and the failure mechanisms observed in certain buildings damaged during Chile earthquake. A preliminary study was conducted using a three-dimensional finite element model of a representative slice of a concrete wall building affected by the earthquake, using the model shown in Figure 2.6. The walls and floors of the building were represented by a detailed mesh of non-linear shell elements. Figure 2.6a and Figure 2.6b display the failure pattern of the building as well as the wall elements. Figure 2.6c shows a close-up of the lower stories of the wall at the initiation of collapse, with a concentration of vertical compression strain occurring at the first floor level. This preliminary analysis supports the hypothesis that compression failure in wall boundary elements can lead to collapse in certain cases. As shown in Figure 2.6d, the strain distribution along this section of the wall is not linear in the compression zone; compression strains increase sharply near the extreme fibre. This effect is due to the fact that plane sections are not enforced to remain plane in this type of model, allowing high localized strains to be captured. Moreover, stress and strain fields rather than force-resultant and deformation-resultant fields are represented by the model catering for the wall models with in-plane axial-flexure-shear interaction without empirical combination.

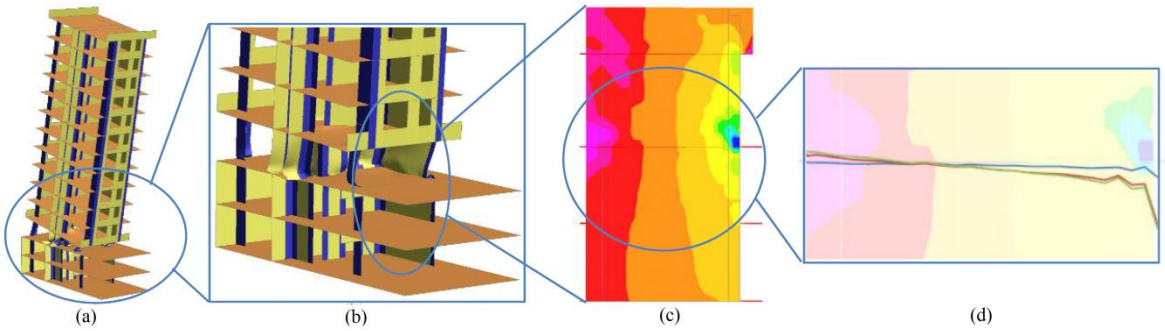

Figure 2.6: Analysis of wall with vertical discontinuity: (a) model deformed shape at failure; (b) close-up of lower stories; (c) vertical strain concentration at ground floor; (d) strain distribution on wall section (Telleen et al. 2012b)

2.2.1.1 REINFORCEMENT REPRESENTATION

Three major models of reinforcement have been used in the finite element analysis of reinforced concrete elements: 1) discrete steel model; 2) embedded steel model; 3) smeared steel model.

In a discrete model, a reinforcing bar is represented by a one-dimensional element. The element can be either simple truss elements or beam elements if the bending stiffness and the shear stiffness of the reinforcing bar are to be included. Although this model can include bond-slip relationships between concrete and steel by using interface elements, its mesh dependency, i.e. direction and location dependency of bar elements on the mesh layout, is the main drawback of this approach. Also, introducing more discrete elements in the model has its inherent complexity of more computation time and further convergence issues.

In an embedded model, reinforcing bars are embedded in structural elements, the so-called mother elements and do not have degrees of freedom of their own. Embedded reinforcements can be in forms of single bars or layers of reinforcement. The reinforcement stiffness is evaluated individually with an isoparametric shape function and the strains in the reinforcements are computed from the displacement field of the mother elements implying perfect bond between the reinforcement and the surrounding material. The model was proposed as a solution to the problem of mesh dependency allowing for generation of the finite element mesh without having to anticipate the location of reinforcements.

In a smeared model, reinforcing steel is assumed to be uniformly distributed over a concrete element in a particular direction. The amount of reinforcement is specified as a volume fraction, that is the volume of steel divided by the volume of concrete. The constitutive

matrix of reinforcing steel is superimposed on the one of concrete to obtain the total constitutive matrix of reinforced concrete (Sittipunt and Wood 1993).

2.2.2 MACRO MODELS

Various macroscopic models have been proposed to predict the nonlinear response of RC structural walls. Kabeyasawa et al. (1983) proposed a model in which axial springs at each end of the wall and a rotational spring at the center represented flexural behavior, while a horizontal spring modelled shear behaviour (TVLEM, Figure 2.7a). Vulcano and Bertero (1986) modified the model by using the two-axial-element-in-series model (AESM) to describe the axial hysteretic behavior of the elements constituting the wall model. Vulcano et al. (1988) proposed the multiple-vertical-line-element model (MVLEM, Figure 2.7b) which had more axial springs, the rotational spring in the center was removed in this model and a horizontal spring simulated the nonlinear shear response of the wall element. Linde (1993) suggested a simpler model having three axial springs and one horizontal spring and tried to develop a simple and clear kinematic formulation for the model (Figure 2.7c). The model has recently been investigated and used by Kim et al. (2005) to simulate the hysteretic behavior of different wall specimens. A modification to the original TVLEM was proposed by Milev (1996) in order to improve the prediction of the overall (shear and flexural) behavior of RC structural walls for both monotonic and reversed cyclic loading. The primary modification of the TVLEM involved substituting a two-dimensional nonlinear panel element for the vertical, horizontal, and rotational springs at the wall centerline (Figure 2.7d). Orakcal et al. (2004) used a multiple-vertical-line-element model similar to the one of Vulcano et al. (1988) and adopted hysteretic constitutive laws of concrete and steel for the springs. The tension stiffening effects were directly incorporated into the constitutive stress-strain relations implemented for concrete and steel. The model was calibrated, and validated against extensive experimental data at both local and global response levels by Orakcal and Wallace (2006). The multiple-vertical-line-element model provided an accurate prediction of experimentally observed flexural wall response at various response levels (wall load-displacement response, wall lateral load capacity at varying drift levels, wall displacement profile, average rotations and displacements over the region of inelastic deformations) for walls with rectangular cross sections. However, the model considered uncoupled shear and flexural responses. Massone et al. (2009) implemented and validated a more comprehensive modeling approach for squat structural

walls controlled by shear, which incorporates flexure-shear interaction, and improved the model by using test results.

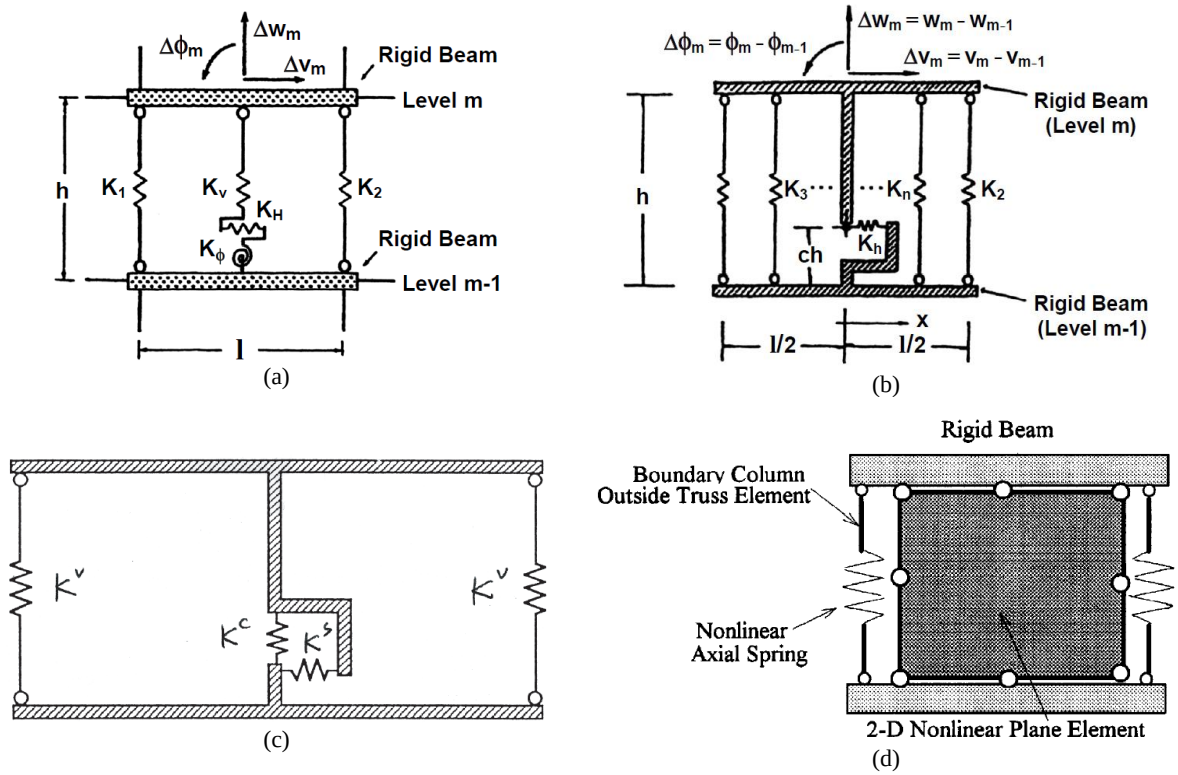

Figure 2.7: Macro models: (a)TVLEM (Kabeyasawa et al. 1983); (b) MVLEM (Vulcano et al. 1988); (c)Linde (1993); (d) Milev (1996)

The macro models described above require 'plane sections to remain plane' along the wall (clearly shown by the rigid elements along the element) and are not able to capture the nonlinear strain profile which is needed to simulate failure patterns coming from high localized strains. Also, shear-flexure interaction is an issue with most of these models and cannot be neglected if failure patterns are of more interest in an analysis. Fischinger et al. (2012) proposed a model base on the multiple-vertical-line-element to account for inelastic shear behavior and inelastic shear-flexural interaction. Kolozvari et al. (2015) developed a model that could incorporate RC panel behavior described with a constitutive fixed-strut-angle panel model into the multiple-vertical-line-element model. This model has been implemented in the computational platform OpenSees.

Beam-column elements with fiber sections have been used to simulate response of structural walls by a number of researchers (Grange et al. 2006, Martinelli and Filippou 2009). These models allow the user to specify uniaxial stress-strain behavior of longitudinal reinforcement as well as that of confined and unconfined concrete including the effects in the transverse direction. A large variety of models are available that can be used to

characterize the behavior of different materials in order to capture the section and member responses accurately. Since the model is based on the uniaxial stress-strain behavior of groups of fibers, the models are easier to build and understand. The disadvantage of fiber beam-column element is that the strain distribution at the section level is typically predefined. Additionally, some fiber based elements require the shear deformation to be handled separately. In this case, the beam-column element only considers the axial and bending deformations on the element, and no shear stiffness is included in the element stiffness. In order to include the effects of shear deformation, a separate material model must be used to define the global shear force-deformation relationship for the beam column element. The shear material model can be placed in parallel to the beam-column, thus including the shear stiffness in the global structural stiffness matrix.

2.2.3 PREDICTION OF OUT-OF-PLANE INSTABILITY

2.2.3.1 NUMERICAL

Simulating out-of-plane instability of RC walls through numerical models has been seldom attempted because of the challenges related to the nonlinear geometrical and material behaviour, as well as the lack of experimental data for comparison purposes. Dashti et al. (2014a, b) modelled the wall out-of-plane buckling using curved shell elements. Parra Torres (2016) used the same elements to study the stability of RC wall boundaries. However, an artificial eccentricity was introduced in the material properties across the wall thickness in this study to trigger this mode of failure.

2.2.3.2 ANALYTICAL

2.2.3.2.1 Paulay and Priestley (1993)

Paulay and Priestley (1993) scrutinized the mechanism of out-of-plane instability by idealization of the part of the wall height that has undergone out-of-plane deformation with a circular shape. By expressing the lateral displacement δ in terms of the wall thickness b, i.e., $\delta = \xi b$, and using expressions developed for estimation of the radius of curvature, the eccentricity ratio ξ was calculated as:

$$\xi = \frac{\varepsilon_{sm}}{8\beta}\left(\frac{l_o}{b}\right)^2 \qquad \textbf{2.1}$$

where

ε_{sm}= the maximum tensile strain (the relatively small elastic recovery was neglected and the residual strain was assumed to be of the order of ε_{sm})

l_o = the height along which out-of-plane instability develops and assumed to be equal to the theoretical length of the plastic hinge

βb = the distance from the layer of elastic reinforcement to the point of initial crack closure

In order to establish a stability criterion for the section undergoing out-of-plane deformations, the section equilibrium was used (Figure 2.8).

According to Paulay and Priestley (1993), out-of-plane instability of the section will occur if the lateral displacement exceeds half of the wall thickness. The equilibrium of the section shows that the compression force (C) applied with an eccentricity of $\delta = \xi b$ is sustained by the compressive actions of the reinforcement as well as some concrete compression force C_c within the crack closure area. It is assumed that all bars develop yield stress f_y at partial crack closure although the two layers of reinforcement would undergo different values of compressive strains. The equilibrium equations,

$$C = C_c + C_s \quad \textbf{2.2}$$

and

$$C_c = (\xi/\gamma)C \quad \textbf{2.3}$$

can be rearranged as

$$C = C_s/\left(1 - \frac{\xi}{\gamma}\right) \quad \textbf{2.4}$$

If C_s is replaced by its maximum value $C_s = \rho b f_y$:

$$C_c = \rho b f_y/(\gamma/\xi - 1) \quad \textbf{2.5}$$

Increasing reinforcement content in the end region of the wall section would increase both the total and the concrete compression force resulting in the lever arm γb being smaller and occurrence of instability at a lower eccentricity ξb.

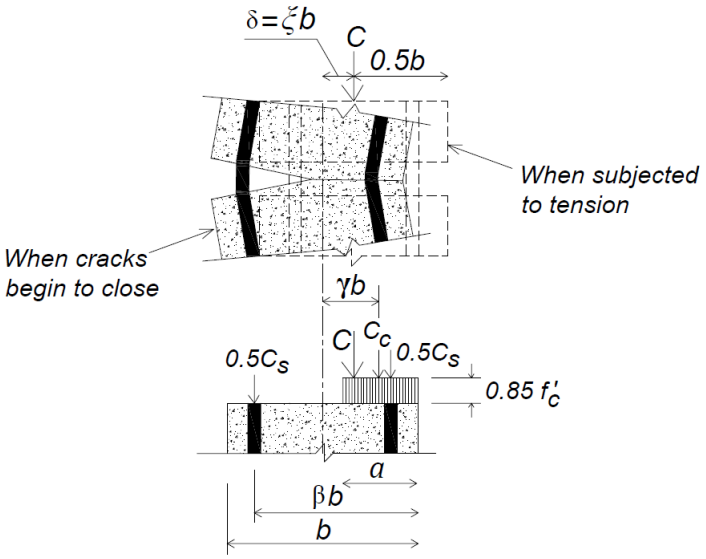

Figure 2.8: Relation of internal forces to eccentricity, modified after Paulay and Priestley (1993)

Considering the assumption of the equivalent rectangular compression stress block:

$$\gamma = \frac{1}{2}(1 - C_c/(0.85 f_c' b)) \quad \textbf{2.6}$$

And substituting from Equation 2.5 into Equation 2.6:

$$\gamma = \frac{1}{2}\left[(\xi + 0.5) - \sqrt{(\xi + 0.5)^2 - 2\xi(1 + 1.176m)}\right] \quad \textbf{2.7}$$

where $m = \rho f_y / f_c'$

As the term inside the square root sign needs to be nonnegative, the stability criterion of the wall section was derived as

$$\xi \leq 0.5(1 + 2.35m - \sqrt{5.53m^2 + 4.70m}) \quad \textbf{2.8}$$

Minimum wall thickness can be calculated as

$$b_c = l_o \sqrt{\frac{\varepsilon_{sm}}{8\beta\xi}} \quad \textbf{2.9}$$

2.2.3.2.2 Chai and Elayer (1999)

Chai and Elayer (1999) studied the out-of-plane instability of ductile RC walls by idealizing the end-region of the wall as an axially loaded RC column, as shown in Figure 2.9, and conducted an experimental study to examine the out-of-plane instability of several RC columns that were designed to represent the end-regions of a ductile planar RC wall under large amplitude reversed cyclic tension and compression.

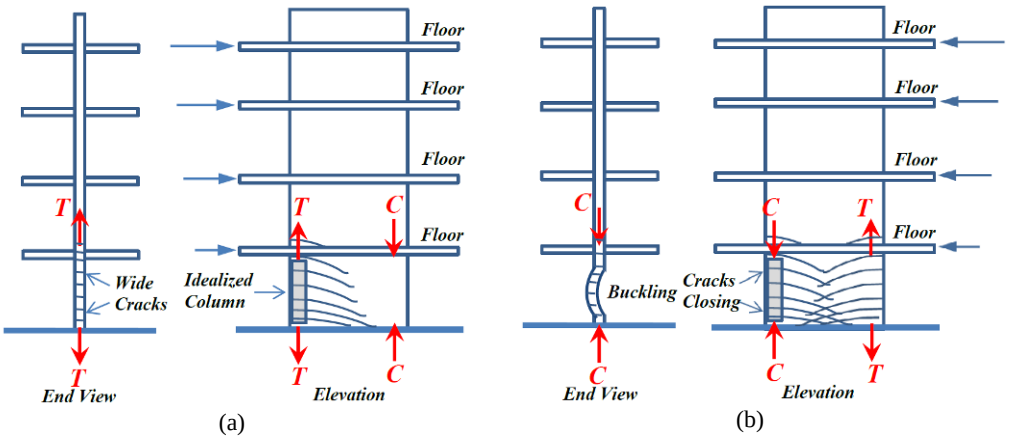

Figure 2.9: Idealization of reinforced concrete wall in end regions: (a) opening of cracks under tension cycle; and (b) closing of cracks under compression cycle, modified after Chai and Elayer (1999)

Based on this study, the critical influence of the maximum tensile strain on the lateral instability of slender rectangular walls was confirmed and the basic behaviour of the wall end-regions under an axial tension and compression cycle was described by axial strain versus out-of-plane displacement and axial strain versus axial force plots shown in Figure 2.10. Also, based on a kinematic relation between the axial strain and the out-of-plane displacement, and the axial force versus the axial strain response, a model was developed for the prediction of the maximum tensile strain. Points *a-f* display different stages of the idealized column response and are briefly described in Table 2.1.

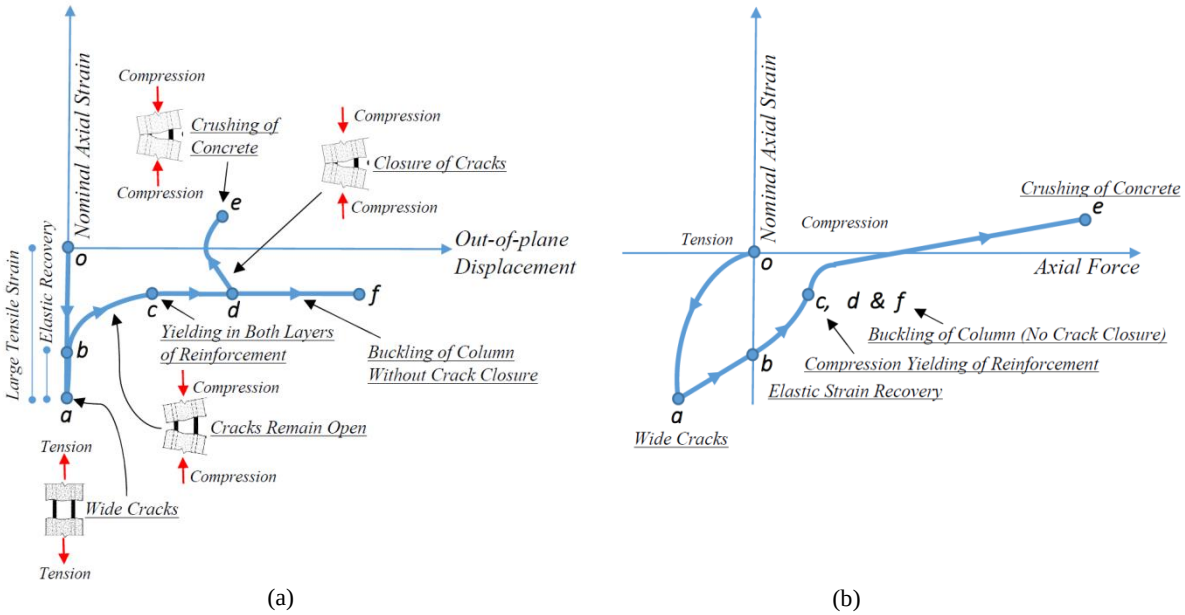

Figure 2.10: Axial reversed cyclic response of reinforced concrete column: (a) nominal axial strain versus out-of-plane displacement; and (b) nominal axial strain versus axial force, modified after Chai and Elayer (1999)

Table 2.1: Behavior of wall end-region under the loading cycle shown in Figure 2.10

	Path	
Loading	*o-a*	Large tensile strain
Unloading	*a-b*	Elastic strain recovery mainly in reinforcing steel
Reloading	*b-c*	Reloading in compression on the cracked concrete column accompanied by an out-of-plane displacement; yielding of the reinforcement closer to the applied axial force resulting in a reduced transverse stiffness of the column and an increased out-of-plane displacement.
	c-d	Compression yielding in the second layer of the reinforcement, and a rapid increase in the out-of-plane displacement
	d-e	Closure of cracks at Point d and decrease of out-of-plane displacement and increase of out-of-plane displacement after significant compressive strain is developed in the compressed concrete
	d-f	An excessive crack opening where subsequent compression would not result in the closure of the cracks but a continued increase in the out-of-plane displacement and eventual buckling of the column

As it can be seen in Figure 2.10, the idealized column was assumed to consist of the loading stage where a large tensile strain was applied to the specimen (Path *o-a*), the unloading branch (Path *a-b*) corresponding to the elastic strain recovery mainly in the reinforcement steel and the reloading in compression which can be either Path *b-c-d-e* or Path *b-c-d-f*. During Path *b-c*, when the axial compression is small, the compressive force in the column is resisted entirely by the reinforcement alone as the cracks are not closed, and a small out-of-plane displacement would occur due to inherent eccentricity of the axial force. The increase in axial compression would lead to yielding of the reinforcement on one side of the wall section; thereby resulting in a reduced transverse stiffness of the column and an increased out-of-plane displacement. Path *c-d* corresponds to compression yielding in the second layer of the reinforcement due to further increase in the axial compression which could rapidly increase the out-of-plane displacement. Response of the idealized column after Point *d* depends on the initial tensile strain. If the initial tensile strain is not excessive, the cracks could close at Point *d* resulting in decrease of out-of-plane displacement. However, the crack closure may cause significant compressive strain to develop in the compressed concrete after the out-of-plane displacement is decreased and lead to crushing of concrete and increase of out-of-plane displacement (Path *d-e*). In case of excessive crack opening, the following compression would not be able to close the cracks before the increase in the out-of-plane displacement results in eventual buckling failure of the column.

Chai and Elayer (1999) used the same stability criterion as Equation 2.8 and considered three components for ε_{sm} as:

$$\varepsilon_{sm} = \varepsilon_e + \varepsilon_r + \varepsilon_a^* \quad \textbf{2.10}$$

$$\varepsilon_{sm} = \eta_1 \varepsilon_y + \eta_2 \varepsilon_y + \varepsilon_a^* \quad \textbf{2.11}$$

1) ε_e= an elastic strain recovery for the unloading from a tensile excursion;

2) ε_r = a reloading strain associated with compression yielding of the reinforcement (and depends on the cyclic characteristic of the reinforcing steel since a reduced stiffness in the steel is expected due to the Bauchinger'strain effect)
3) ε_a^* = an axial strain at first closure of cracks

Based on experimental observations on response of axially loaded reinforced concrete columns that represented boundary regions of rectangular walls, η_1 was defined to be close to 1.5 and η_2 in the range of 3 to 5.

Based on the relationship of the transverse curvature at mid-height of the column with the mid-height out-of-plane displacement and axial strain corresponding to the first crack closure the following kinematic relation was derived:

$$\varepsilon_a^* = \left(\frac{1}{2c}\right)\left(\frac{b}{l_o}\right)^2 \xi_m \qquad \textbf{2.12}$$

Where, c depends on the transverse curvature distribution of the column and ξ_m is the out-of-plane displacement at mid-height of the column, as normalized by the wall thickness.

The following assumptions were made:

- The out-of-plane displacement for the crushing limit state (i.e., Point *e* in Figure 2.10) was assumed to be fairly close to the out-of-plane displacement at first crack closure i.e., Point *d* in Figure 2.10.
- The limit state for calculation of the out-of-plane displacement was concrete crushing. i.e. ξ_c is the out-of-plane displacement corresponding to the concrete crushing and the out-of-plane displacement should be limited to ξ_c.
- η_1 = 1.0, and η_2 = 2.0
- The curvature distribution was considered sinusoidal, i.e., coefficient $c = 1/\pi^2$

Based on these assumptions, the maximum tensile strain that may be imposed on the column was written as

$$\varepsilon_{sm} = \frac{\pi^2}{2}\left(\frac{b}{l_o}\right)^2 \xi_c + 3\varepsilon_y \qquad \textbf{2.13}$$

2.2.4 SUMMARY

Although various models have been proposed for numerical modeling of structural walls, the simulation of out-of-plane instability failure has seldom been attempted. An accurate prediction of the 3D response of structural walls can be provided using solid elements in a

finite element modeling approach. Mesh discretization along the wall thickness can represent the variation of material properties along the wall thickness due to the effect of confinement in the core region. However, the complexity of generating the model and conducting the analysis associated with this method, particularly with a decent mesh size, would put a limit on practicality of this approach. Models composed of nonlinear shell-type finite elements, which are less computationally demanding, are also able to capture the nonlinear strain profile along the wall length and axial-flexure-shear interaction, thereby enabling them to reliably predict different failure mechanisms of walls. If the mesh density is sufficient and the large deflection formulation is used, overall wall buckling can be captured by this modeling and analysis approach, as well (NEHRP 2014).

The out-of-plane instability of rectangular walls has generally been addressed using analytical approaches. As there are not many test results on initiation and development of this mode of failure, some assumptions such as the height of the wall involved in formation of the global buckling (buckling length) have been made in these postulations.

2.3 EXPERIMENTAL STUDIES

2.3.1 EXPERIMENTAL RESEARCH ON PERFORMANCE OF WALLS

This section summarizes previous experimental research investigating the performance of slender walls. The research programs are presented in chronological order (Table 2.2). The most important parameters investigated in each research clearly show what aspects of wall behavior have already been investigated by several researchers and which areas have received little attention.

Table 2.2: Experimental investigations on slender RC walls

	Researcher	Investigated Parameters
1	Cardenas and Magura (1972)	- Monotonic load histories - Axial load - Distribution of longitudinal reinforcement in boundary regions
2	Wang et al, (1975) EERC research Phase 1	- Hysteretic behavior of R/C framed-walls - Shape (framed walls (barbell cross-section) with spirally reinforced edge-columns) - Type of confinement - Shear stress - Loading history (Cyclic, Monotonic)
3	Vallenas et al, (1979) EERC research Phase 2	- Hysteretic behavior of reinforced concrete structural walls - Shape (Two framed walls (barbell cross-section),Two rectangular walls) - Type of confinement - Shear stress

		- Loading history (Cyclic, Monotonic)
4	PCA (Oesterle 1976, Oesterle 1979, Oesterle 1986)	- Shape (Rectangular, Barbell, H-shaped) - Loading (Monotonic+Cyclic) - Repair method - Longitudinal boundary region reinforcement ratio - Boundary region confining reinforcement ratio (ordinary column ties, rectangular hoops and cross-ties) - Horizontal reinforcement ratio - Concrete compressive strength - Axial load ratio
5	Iliya and Bertero, (1980) EERC research Phase 3	- Effects of amount and arrangement of wall-panel reinforcement on hysteretic behavior of reinforced concrete walls - Amount and arrangement of wall-panel reinforcement
6	Shiu et al (1981)	- The impact of openings on the seismic behavior of structural walls
7	Goodsir (1985)	- The design of coupled frame-wall structures for seismic actions - Behavior of wall sections with large concrete compression strains - Lateral instability - Boundary transverse reinforcement in T-walls
8	Morgan et al (1986)	- Test scale (Improve seismic safety by improving the understanding of the relationship between medium- and small-scale tests, component tests and analytical studies).
9	Lefas, Kotsovos, and Ambraseys (1990)	- Aspect ratio - Axial load - Concrete strength - Amount of shear reinforcement
10	Lefas and Kotsovos (1990)	- Repair methods
11	Ali and Wight (1990)	- The impact of the number and location of openings on the performance of walls
12	Wolschlag (1993)	- Response of H-shaped walls under both static (2 specimens) and dynamic loading (4 specimens)
13	Sittipunt and Wood (1993)	- Analytical and experimental study of C-shaped walls - The inelastic cyclic response and energy dissipation - The effective stiffness at various displacement levels - The influence of web reinforcement on the response of C-walls.
14	Pilakoutas and Elnashi (1995)	- Ductility and energy absorption of reinforced concrete walls
15	Thomsen and Wallace (1995)	- Verification of displacement based design approaches
16	Tupper (1999)	- Performance of walls with structural steel boundary elements
17	Tasnimi (2000)	- Evaluation of the Iranian seismic design code
18	Zhang and Wang (2000)	- Effect of high axial loads on rectangular walls
19	Mobeen (2002)	- Barbell walls - The impact of double-headed studs as a replacement for conventional cross-tie confinement
20	Oh, Han, and Lee (2002)	- Full scale walls designed for a Korean building, where wall area to floor area ratios and detailing requirements are similar to Chilean buildings - Shape - Confined versus unconfined boundary regions
21	Riva, Meda, and Giuriani (2003)	- Full-scale representation of rectangular walls

22	Paterson (2003)	- A proposed seismic retrofit method for existing rectangular walls
23	Liu (2004)	- The influence of high strength concrete on structural wall ductility
24	Khaliil and Ghobarah (2005)	- Failure methods and repair techniques for walls under earthquake loading
25	Ile and Reynouard (2005)	- U-shaped walls - The impact of load direction and bi-directional loading
26	Su and Wong (2007)	- Axial load ratio - Confining reinforcement ratios
27	Beyer, Dazio and Priestley (2008)	- U-shaped walls with different thicknesses - Bi-directional loading to provide experimental data on an infrequently tested wall configuration.
29	Dazio et al (2009)	- Rectangular walls - Vertical longitudinal reinforcement ratios, - Amount and detailing of confining reinforcement, - Ductility of reinforcement - Axial load ratio
30	Ghorbani-Renani (2009)	- The effect of scaling and loading in rectangular walls
31	Waugh (2009)	- T-shaped walls subjected to multi-directional displacements - Capabilities of OpenSees in capturing the wall response - Simulation improvements of OpenSees
32	Aaleti (2009)	- Behavior of rectangular concrete walls subjected to simulated seismic loading - Different approaches to anchor the wall into the foundation
33	Brueggen (2009)	- Performance of T-shaped walls subjected to multidirectional, cyclic loading. - Development of a simplified modeling approach to predict the load-deformation response of walls
34	Johnson (2010)	- Rectangular walls with un-symmetric reinforcement - Response of T-shaped walls - The impact of different splice methods on the performance of walls
35	Birely (2013)	- Seismic Performance of Slender Reinforced Concrete Structural Walls - Experimental testing of slender planar walls - Evaluation of performance-assessment tools for performance-based earthquake engineering. - Longitudinal reinforcement layout - Lateral load distribution and its impact on shear demand - Spliced longitudinal reinforcement at the base of the wall
36	Almeida et al. (2017)	- Influence of wall thickness on stability of singly-reinforced walls - Role of lap splices on damage distribution and displacement ductility - Effects of the simultaneous application of out-of-plane loading on the response of singly-reinforced walls

2.3.2 EXPERIMENTAL RESEARCH ON OUT-OF-PLANE INSTABILITY OF RECTANGULAR WALLS

The out-of-plane instability of rectangular reinforced concrete walls under in-plane loading has been mainly investigated by idealizing the boundary region of the wall as an axially loaded column. For this purpose, RC prism units were subjected to tension and compression cyclic loading.

This type of research on out-of-plane instability failure was first conducted by Goodsir (1985) and the main finding was the effect of the maximum tensile strain reached in the reinforcement on development of out-of-plane deformations. Chai and Elayer (1999) also conducted an experimental study to examine the out-of-plane instability of several RC columns that were designed to represent the end-regions of a ductile planar RC wall under large amplitude reversed cyclic tension and compression. Based on this study, the critical influence of the maximum tensile strain on the lateral instability of slender rectangular walls was confirmed and the basic behaviour of the wall end-regions under an axial tension and compression cycle was described by axial strain versus out-of-plane displacement and axial strain versus axial force plots. Also, based on a kinematic relation between the axial strain and the out-of-plane displacement, and the axial force versus the axial strain response, a model was developed for the prediction of the maximum tensile strain. The effect of the specimen thickness was studied in this research, as well. Creagh et al. (2010) and Chrysanidis and Tegos (2012) subjected concrete prisms to tension and then compression until failure. The results of these experiments confirmed the effect of maximum tensile strain developed during the tensile loading on out-of-plane instability of the specimen during unloading the compressive loading. In another test campaign by Shea et al. (2013), the influence of specimen thickness as well as the maximum tensile strain was investigated.

Investigation of the out-of-plane instability by doing experiments on idealized columns representing boundary zones of rectangular walls is a good assumption and may be an efficient approach for conducting parametric studies compared to testing a whole wall unit. However, the following features affecting this mode of failure are neglected in this approach (Rosso et al. 2015).

1. The wall region that undergoes out-of-plane instability is not limited to the end boundary region, and there is no clear definition of this region and its relationship with the longitudinal reinforcement layout.
2. The effect of boundary conditions (top and bottom connections as well as the connection of one side of the boundary region to the web region) and the strain variation along the wall height.
3. The assumption of plastic hinge length as the length involved in formation of out-of-plane deformation needs to be validated.

As can be seen in Table 2.2, the out-of-plane instability failure and the affecting parameters has not been the main research objective in the past experimental research. However, this mode of failure was observed and measured in several experiments. Rosso et al. (2015) summarized these experiments which were conducted by Oesterle (1976), Goodsir (1985), Thomsen IV and Wallace (1995), Johnson (2010) and Rosso et al. (2014). This data collection showed that the specimens affected by this mode of failure had a minimum shear span to thickness of 25 and were subjected to low axial load ratios ($\nu \leq 0.08$). These test units had some common features in their response such as reaching the same order of magnitude of maximum tensile strains and observation of the maximum out-of-plane displacement at approximately 0% in-plane drift. Almeida et al. (2017) investigated the out-of-plane failure mode of walls by analyzing the response of two singly reinforced T-shaped walls tested under cyclic loading. The specimens were identical but were subjected to two different in-plane and bi-directional loading patterns. However, no tests have been conducted on doubly reinforced walls to address the mechanism of out-of-plane instability failure in rectangular walls and the governing parameters.

2.3.3 SUMMARY

The researchers noted in Table 2.2 investigated the impact of different design parameters on slender walls. To further indicate the design parameters that have received little attention from the researchers, a summary of the main design parameters along with the tests carried out for each parameter are given in Table 2.3. As shown in this table, parametric investigation has been conducted on most of the issues related to design of slender rectangular walls except for wall geometrical parameters which are understandably connected with instability of rectangular walls.

The failure mechanism and the governing parameters of out-of-plane instability failure have generally been investigated by conducting experiments on concrete prisms representing boundary zones of rectangular walls. This approach requires further research on the assumptions generally made regarding the boundary conditions and the extent of the wall length and height involved in formation of the instability failure.

Table 2.3: Experimental work on the main design parameters of slender rectangular walls

	Parameter	Researcher
1	**Material Properties**	
	Concrete compressive strength	(Oesterle 1979, Lefas et al. 1990, Liu 2004)
	Steel ductility	(Dazio et al. 2009)
2	**Geometry**	
	Wall slenderness (h_s / t_w)	No Test
	Cross-section aspect ratio (l_w / t_w)	No Test
	Boundary element geometry Boundary element length ratio (l_b / l_w) Boundary element aspect ratio (l_b / t_w)	No Test
3	**Reinforcement Ratios**	
	Boundary element reinforcement	(Oesterle 1979, Lefas et al. 1990, Pilakoutas and Elnashai 1995, Dazio et al. 2009)
	Confining reinforcement	(Oesterle 1979, Thomsen IV and Wallace 2004)
	Web longitudinal reinforcement	(Dazio et al. 2009, Birely 2013)
	Horizontal reinforcement ratio	(Oesterle 1979, Pilakoutas and Elnashai 1995)
4	**Shear-Span Ratio**	(Lefas et al. 1990, Paterson and Mitchell 2003, Brueggen 2009, Dazio et al. 2009)
5	**Axial Load Ratio**	(Oesterle 1976, Oesterle 1979, Oesterle 1986, Lefas et al. 1990, Su and Wong 2007)
6	**Shear Demand and Capacity**	(Vallenas et al. 1979, Wood 1991, Pilakoutas and Elnashai 1995, Tasnimi 2000, Paterson and Mitchell 2003, Liu 2004, Birely 2013)

l_w = length of wall; h_s: unsupported height of the wall (typically, one story); t_w = web thickness;
l_b = boundary length; t_b = boundary thickness

2.4 CODE PROVISIONS FOR PREVENTION OF OUT-OF-PLANE INSTABILITY

The only requirements addressed in major seismic codes for buildings to avoid out-of-plane instability are related to minimum thickness provisions. The wall thickness requirements of different seismic codes summarized in fib-Bulletin-69 (2013) are presented in Table 2.4. As can be seen in this table, the ICBO 1997 (UBC 97) requires a boundary zone thickness greater than $l_u/16$, where l_u is the clear storey height (e refers to wall thickness in this table). The minimum thickness requirement of ACI is intended to apply to the walls designed according to an empirical method. No slenderness limits existed in ACI 318-11 for specially confined boundary zones, and a single curtain of web reinforcement was allowed as long as the shear stress did not exceed a specific value. ACI 318-14 requires a minimum thickness of $l_u/16$ at all specially confined boundary zones, and two curtains of web reinforcement are required in all walls having height to length ratios greater than or equal to 2.0 (Ghosh 2016).

In New Zealand, a minimum permissible thickness of 100 mm is required except for basements where the thickness may be increased to 250 mm. The out-of-plane buckling of slender walls is addressed in Section 11.4.2 (Dimensional Limitations) of the New Zealand standard (NZS3101 2006). For walls with axial force levels greater than $0.05f_c'A_g$ and for

ductile or limited ductile plastic region the thickness in the boundary region of the wall section, extending over the lesser of the plastic hinge length or the full height of the first storey, shall not be less than b_m (Table 2.4).

Table 2.4: Wall thickness requirements (fib-Bulletin-69 2013)

USA	$e > l_u/16$	*ICBO 1997*
	$e > l_u/25 \ or \ length/25$ $e > 4 \ in$	*ACI*
New Zealand	$100 \ mm < e < 250 \ mm$	Singly reinforced walls
	$b_m = \frac{\alpha_r k_m \beta (A_r + 2) L_w}{1700\sqrt{\xi}} \qquad \alpha_r = 1.0 - 1.25$ $\beta = 5 \ \ walls \ with \ limited \ ductile \ plastic \ regions$ $\beta = 7 \ \ walls \ with \ ductile \ plastic \ regions$ $\xi = 0.3 - \frac{\rho_l f_y}{2.5 f_c'} \geq 0.1$ $k_m = \frac{L_n}{(0.25 + 0.055 A_r) L_w} \leq 1.0$	Doubly reinforced walls
Canada	$l_u/14 < e < l_u/10$	Ductile walls
	$l_u/20 < e < l_u/14$	Moderately ductile walls
Japan	$e > 150 \ mm, e > h_u/20$	Structural walls
Europe	$b_{wo} \geq \max(0.15m, h_s/20)$ $b_w \geq h_s/15 \ or \ \ h_s/10^* \geq 200mm$ *depending on the length of the confined edge $b_{wo} \ is \ the \ thickness \ of \ the \ web$ $h_s \ is \ the \ clear \ storey \ height$ $b_w \ the \ thickness \ of \ the \ confined \ parts \ of \ the \ wall \ section$ $(boundary \ elements)$	Structural walls

Canadian Code requires a minimum thickness of $l_u/10$ to prevent instability of the compression zone, but may decrease to $l_u/14$ if the compression zone is relatively small or if a flange, having a minimum width of $l_u/5$ is provided.

The European standard has thickness limitations for the structural walls in both web and boundary regions. The boundary region thickness shall be equal or greater than 200 mm. A further limitation on this thickness depends on the length of the boundary region (confinement length). For the confinement length equal or smaller than max ($2 \times panel \ thickness, 0.2 \times wall \ length$), the boundary region thickness needs to be equal or

greater than $1/15 \times clear\ storey\ height$, otherwise $1/10 \times clear\ storey\ height$. The web thickness shall be equal or greater than max ($150\ mm, 1/20 \times clear\ storey\ height$).

The Japanese design guidelines for RC buildings specify that the cross sectional shape of a structural wall, as a general rule, shall be of I-shape with the boundary zones protruding from the wall surface. The panel region thickness shall be equal to or greater than max ($150\ mm, 1/20 \times clear\ storey\ height$). The use of rectangular wall section would be allowed if the thickness is equal to or greater than 400 mm.

2.4.1 SUMMARY

Different seismic design standards have specified different provisions for addressing the instability failure of walls. This variety can be attributed to the fact that the mechanism of out-of-plane instability failure is not clearly understood so far, and consequently the relevant design provisions are not backed up by strong research.

2.5 REFERENCES

Aaleti, S. R. (2009). Behavior of rectangular concrete walls subjected to simulated seismic loading, Iowa State University. PhD**,** 249.

Ali, A. and J. K. Wight (1990). "Reinforced concrete structural walls with staggered opening configurations under reversed cyclic loading."

Almeida, J., O. Prodan, A. Rosso and K. Beyer (2017). "Tests on Thin Reinforced Concrete Walls Subjected to In-plane and Out-of-plane Cyclic Loading." *Earthquake Spectra* 33(1), 323-345.

Beyer, K., A. Dazio and M. Priestley (2008). "Quasi-static cyclic tests of two U-shaped reinforced concrete walls." *Journal of earthquake engineering* 12(7), 1023-1053.

Birely, A. C. (2013). Seismic Performance of Slender Reinforced Concrete Structural Walls, University of Washington. PhD**,** 983.

Brueggen, B. L. (2009). Performance of T-shaped reinforced concrete structural walls under multi-directional loading. PhD**,** 498.

Cardenas, A. E. and D. D. Magura (1972). "Strength of high-rise shear walls-rectangular cross section." *ACI Special Publication* 36.

CERC (2012). "Canterbury Earthquakes Royal Commission Reports." *http://canterbury.royalcommission.govt.nz/Final-Report-Volume-Two-Contents*.

Chai, Y. H. and D. T. Elayer (1999). "Lateral stability of reinforced concrete columns under axial reversed cyclic tension and compression." *ACI Structural Journal* 96(5), 780-789.

Chrysanidis, T. and I. Tegos (2012). "The influence of tension strain of wall ends to their resistance against lateral instability for low-reinforced concrete walls." *15 WCEE*.

Creagh, A., C. Acevedo, J. Moehle, W. Hassan and A. C. Tanyeri (2010). "Seismic performance of concrete special boundary element." *University of Texas at Austin and University of California Berkley, Austin, Berkley*.

Dazio, A., K. Beyer and H. Bachmann (2009). "Quasi-static cyclic tests and plastic hinge analysis of RC structural walls." *Engineering Structures* 31(7), 1556-1571.

Deshmukh, K., G. Thiagarajan and T. Heausler (2006). Numerical Modeling of Seven Story Reinforced Concrete Model Using Sap. Workshop on Analytical Modeling of Reinforced Concrete Walls. NEES/UCSD. San Diego.

EERI (2011). "The M 6.3 Christchurch, New Zealand, Earthquake of February 22, 2011." *EERI Special Earthquake Report*.

Elwood, K. J. (2013). "Performance of concrete buildings in the 22 February 2011 Christchurch earthquake and implications for Canadian codes 1." *Canadian Journal of Civil Engineering* 40(3), 1-18.

fib-Bulletin-69 (2013). Critical comparison of major seismic codes for buildings, The International Federation for Structural Concrete.

Fischinger, M., K. Rejec and T. Isaković (2012). Modeling inelastic shear response of RC walls. Proceedings, 15th World Conference on Earthquake Engineering.

Ghorbani-Renani, I., N. Velev, R. Tremblay, D. Palermo and B. Massicotte (2009). "Modeling and testing influence of scaling effects on inelastic response of shear walls." *ACI Structural Journal* 106(3).

Goodsir, W. J. (1985). The design of coupled frame-wall structures for seismic actions, University of Canterbury. PhD.

Grange, S., P. Kotronis and J. Mazars (2006). Seven-story building-slice earthquake blind prediction contest: a simplified modeling using multifiber Timoshenko beams. Workshop and Seminar on Analytical Modeling of Reinforced Concrete Walls for Earthquake Resistance, San Diego, USA-California, December 15.

Ile, N. and J. Reynouard (2005). "Behaviour of U-shaped walls subjected to uniaxial and biaxial cyclic lateral loading." *Journal of earthquake engineering* 9(01), 67-94.

Iliya, R. and V. V. Bertero (1980). Effects of amount and arrangement of wall-panel reinforcement on hysteretic behavior of reinforced concrete walls. Report no. UCB/EERC-80/04, Earthquake Engineering Research Center, University of California, Berkeley.

Johnson, B. (2010). Anchorage detailing effects on lateral deformation components of R/C shear walls, Master Thesis, University of Minnesota.

Kabeyasawa, T., H. Shiohara, S. Otani and H. Aoyama (1983). "Analysis of the full-scale seven-story reinforced concrete test structure." *Journal of the Faculty of Engineering, University of Tokyo* 37(2), 431-478.

Kam, W. Y., S. Pampanin and K. Elwood (2011). "Seismic performance of reinforced concrete buildings in the 22 February Christchurch (Lyttelton) earthquake." *Bulletin of the New Zealand Society for Earthquake Engineering* 44(4), 239-278.

Kelly, T. (2007). "A blind prediction test of nonlinear analysis procedures for reinforced concrete shear walls." *Bulletin of the New Zealand Society for Earthquake Engineering* 40(3), 142-159.

Khalil, A. and A. Ghobarah (2005). "Behaviour of rehabilitated structural walls." *Journal of earthquake engineering* 9(03), 371-391.

Kim, T.-W., D. A. Foutch and J. M. LaFAVE (2005). "A practical model for seismic analysis of reinforced concrete shear wall buildings." *Journal of earthquake engineering* 9(03), 393-417.

Kolozvari, K., K. Orakcal and J. W. Wallace (2015). Shear-Flexure Interaction Modeling for Reinforced Concrete Structural Walls and Columns under Reversed Cyclic Loading, Pacifi c Earthquake Engineering Research Center.

Lefas, I. D. and M. D. Kotsovos (1990). "Strength and deformation characteristics of reinforced concrete walls under load reversals." *ACI Structural Journal* 87(6).

Lefas, I. D., M. D. Kotsovos and N. N. Ambraseys (1990). "Behavior of reinforced concrete structural walls: strength, deformation characteristics, and failure mechanism." *ACI Structural Journal* 87(1), 23-31.

Linde, P. (1993). Numerical modelling and capacity design of earthquake-resistant reinforced concrete walls, Diss. Techn. Wiss. ETH Zürich, Nr. 10124, 1993. Ref.: Hugo Bachmann; Korref.: Edoardo Anderheggen.

Liu, H. (2004). Effect of concrete strength on the response of ductile shear walls, McGill University. MSc.

Martinelli, P. and F. C. Filippou (2009). "Simulation of the shaking table test of a seven-story shear wall building." *Earthquake Engineering & Structural Dynamics* 38(5), 587-607.

Massone, L. and J. Wallace (2011). "Lessons from Chile: Impacts of Earthquake Engineering of RC Buildings in the US." *EERI/NEES Webinar*.

Massone, L. M., K. Orakcal and J. W. Wallace (2009). "Modeling of squat structural walls controlled by shear." *ACI Structural Journal* 106(5).

Milev, J. (1996). "Two dimensional analytical model of reinforced concrete shear walls." *Proc. 11th of WCEE*.

Moaveni, B., X. He, J. P. Conte, J. I. Restrepo and M. Panagiotou (2010). "System identification study of a 7-story full-scale building slice tested on the UCSD-NEES shake table." *Journal of structural engineering* 137(6), 705-717.

Mobeen, S. S. (2002). Cyclic Tests of Shear Walls Confined with Double Head Studs, University of Alberta. MSc.

Morgan, B. J., W. G. Corley and H. Hiraishi (1986). US-Japan Quasi-Static Test of Isolated Wall Planar Reinforced Concrete Structure, The Laboratories.

NZS3101 (2006). Concrete Structures Standard, NZS 3101:2006 Parts 1&2 Standards New Zealand.

Oesterle, R. (1976). Earthquake Resistant Structural Walls: Tests of Isolated Walls, Research and Development Construction Technology Laboratories, Portland Cement Association.

Oesterle, R. (1979). Earthquake Resistant Structural Walls: Tests of Isolated Walls: Phase II, Construction Technology Laboratories, Portland Cement Association.

Oesterle, R. G. (1986). Inelastic analysis for in-plane strength of reinforced concrete shear walls, Northwestern University. PhD.

Oh, Y. H., S. W. Han and L. H. Lee (2002). "Effect of boundary element details on the seismic deformation capacity of structural walls." *Earthquake Engineering & Structural Dynamics* 31(8), 1583-1602.

Orakcal, K. and J. W. Wallace (2006). "Flexural modeling of reinforced concrete walls-experimental verification." *ACI Structural Journal* 103(2).

Orakcal, K., J. W. Wallace and J. P. Conte (2004). "Flexural modeling of reinforced concrete walls-model attributes." *ACI Structural Journal* 101(5), 688-698.

Palermo, D. (2002). Behaviour and analysis of reinforced concrete walls subjected to reversed cyclic loading, University of Toronto. PhD**,** 372.

Parra Torres, P. F. (2016). Stability of Reinforced Concrete Wall Boundaries, University of California, Berkeley. PhD**,** 219.

Paterson, J. and D. Mitchell (2003). "Seismic retrofit of shear walls with headed bars and carbon fiber wrap." *Journal of structural engineering* 129(5), 606-614.

Paulay, T. and M. Priestley (1992). Seismic design of reinforced concrete and masonry buildings, John Wiley and Sons, New York.

Paulay, T. and M. Priestley (1993). "Stability of ductile structural walls." *ACI Structural Journal* 90(4), 385-392.

Pilakoutas, K. and A. Elnashai (1995). "Cyclic behavior of reinforced concrete cantilever walls, Part I: Experimental results." *ACI Materials Journal* 92(3), 271-281.

Pilakoutas, K. and A. Elnashai (1995). "Cyclic behavior of reinforced concrete cantilever walls, Part II: discussions and theoretical comparisons." *ACI Structural Journal-American Concrete Institute* 92(4), 425-434.

Riva, P., A. Meda and E. Giuriani (2003). "Cyclic behaviour of a full scale RC structural wall." *Engineering Structures* 25(6), 835-845.

Rosso, A., J. Almeida and K. Beyer (2015). "Stability of thin reinforced concrete walls under cyclic loads: state-of-the-art and new experimental findings." *Bulletin of Earthquake Engineering*, 1-30. DOI: 10.1007/s10518-015-9827-x.

Rosso, A., J. P. Almeida and K. Beyer (2014). Short report on the experimental cyclic test of a thin RC wall (TW1) for blind prediction purposes, ÉCOLE POLYTECHNIQUE FÉDÉRALE DE LAUSANNE.

Shea, M., J. W. Wallace and C. Segura (2013). "Seismic performance of thin reinforced concrete shear wall boundaries."

Shiu, K.-N., J. Daniel, J. Aristizabal-Ochoa, A. Fiorato and W. Corley (1981). "Earthquake resistant structural walls: Test of walls with and without openings." *NASA STI/Recon Technical Report N* 82, 21451.

Sittipunt, C. and S. L. Wood (1993). Finite element analysis of reinforced concrete shear walls, Department of Civil Engineering, University of Illinois at Urbana-Champaign.

Su, R. and S. Wong (2007). "Seismic behaviour of slender reinforced concrete shear walls under high axial load ratio." *Engineering Structures* 29(8), 1957-1965.

Tasnimi, A. (2000). "Strength and deformation of mid-rise shear walls under load reversal." *Engineering Structures* 22(4), 311-322.

Telleen, K., J. Maffei, M. Willford, A. Aviram, Y. Huang, D. Kelly and P. Bonelli (2012b). Lessons for Concrete Wall design from the 2010 Maule Chile Earthquake.

Proceedings of the International Symposium on Engineering Lessons Learned from the 2011, Great East Japan Earthquake, March 1-4, 2012, Tokyo, Japan.

Thomsen IV, J. H. and J. W. Wallace (1995). Displacement-based design of reinforced concrete structural walls: An experimental investigation of walls with rectangular and T-shaped cross-sections. Report No. CU/CEE-95-06, Department of Civil and Environmental Engineering, Clarkson University, Potsdam, N.Y.

Thomsen IV, J. H. and J. W. Wallace (2004). "Displacement-based design of slender reinforced concrete structural walls-experimental verification." *Journal of structural engineering* 130(4), 618-630.

Tupper, B. (1999). Seismic response of reinforced concrete walls with steel boundary elements, McGill University.

Vallenas, J. M., V. V. Bertero and E. P. Popov (1979). Hysteretic behaviour of reinforced concrete structural walls. Report no. UCB/EERC-79/20, Earthquake Engineering Research Center, University of California, Berkeley.

Vulcano, A. and V. Bertero (1986). Nonlinear analysis of R/C structural walls. Proceedings of the 8th European Conference on Earthquake Engineering, Lisbon, Portugal, Laboratório Nacional de Engenharia Civil, European Association for Earthquake Engineering.

Vulcano, A., V. V. Bertero and V. Colotti (1988). Analytical modeling of R/C structural walls. Proceedings of the 9th world conference on earthquake engineering, Tokyo-Kyoto, Japan, Science Council of Japan.

Wallace, J. (2012). "Behavior, design, and modeling of structural walls and coupling beams — Lessons from recent laboratory tests and earthquakes." *International Journal of Concrete Structures and Materials* 6(1), 3-18. DOI: 10.1007/s40069-012-0001-4.

Wallace, J. W. (2011). February 27, 2010 Chile Earthquake: Preliminary Observations on Structural Performance and Implications for US Building Codes and Standards. ASCE Structures Congress, Las Vegas, ASCE.

Wang, T. I., V. V. Bertero and E. P. Popov (1975). Hysteretic behavior of R/C framed-walls. Report no. UCB/EERC-75/23, Earthquake Engineering Research Center, University of California, Berkeley.**,** 75-23.

Waugh, J. D. (2009). Nonlinear analysis of T-shaped concrete walls subjected to multi-directional displacements, Iowa State University. PhD**,** 295.

Wolschlag, C. J. (1993). Experimental investigation of the response of R/C structural walls subjected to static and dynamic loading, University of Illinois at Urbana-Champaign.

Wood, S. L. (1991). "Observed Behavior of Slender Reinforced Concrete Walls Subjected to Cyclic Loading." *ACI Special Publication* 127.

Zhang, Y. and Z. Wang (2000). "Seismic behavior of reinforced concrete shear walls subjected to high axial loading." *ACI Structural Journal* 97(5).

3 NUMERICAL MODELING OF RECTANGULAR REINFORCED CONCRETE STRUCTURAL WALLS

Dashti, F., R.P. Dhakal, S. Pampanin (2017) "Numerical Modeling of Rectangular Reinforced Concrete Structural Walls" *Journal of Structural Engineering*, 143(6), DOI: 10.1061/(ASCE)ST.1943-541X.0001729

Dashti, F., R.P. Dhakal , S. Pampanin (2014) "Numerical simulation of shear wall failure mechanisms" *The 2014 New Zealand Society for Earthquake Engineering Conference, NZSEE2014*, Auckland, New Zealand

The performance of RC structural walls in recent earthquakes has exposed some problems with the existing design of RC structural walls; leading to a call for the wall design procedures to be reviewed and improved. Before design guidelines can be improved, it is necessary to investigate the nonlinear seismic response of walls including the causes of different failure modes observed in the recent earthquakes. As repeated experimental investigation is too demanding, a more plausible way to scrutinize the failure mechanisms of different structural components against their expected performance is simulating their behaviour using efficient numerical models. In this study, a numerical model is proposed for prediction of out-of-plane instability in rectangular structural walls under in-plane loading. In this chapter, the modeling approach has been described and used to predict the nonlinear behaviour and different failure patterns of rectangular reinforced concrete structural walls. Efficiency of the model has been evaluated using experimental results of walls with different shear-span ratios which failed in different modes. The walls are modelled in the finite element analysis program DIANA9.4.4. Reinforced concrete sections of the walls are represented by curved shell elements along with embedded bar elements. The plane sections are not enforced to remain plane in this type of model, and the in-plane axial-flexure-shear interaction can be simulated without requiring any empirical

adjustment. The model is found to be able to reasonably capture the lateral load versus top displacement response of the specimens and predict most of the experimentally observed failure mechanisms of rectangular walls except bar buckling. The simulated failure patterns include shear, flexure, flexure-shear and flexure-out-of-plane modes, and the failure to predict bar buckling was expected due to inherent deficiencies of embedded bar elements and limitations of material models available in the program. Moreover, the strain profile and crack pattern captured by the model are found to be in good agreement with experimental observations indicating that in addition to the overall global response predictions, local behaviour of the wall models can also be predicted reasonably well.

3.1 PROPOSED MODEL DESCRIPTION

The numerical models proposed in literature for simulating seismic response of reinforced concrete walls are summarized in Chapter 2. The out-of-plane instability has been seldom predicted by numerical models and researchers have tried to simulate the out of plane instability by providing an initial imperfection (i.e. eccentricity). However, the outcome cannot be generic in such cases as the prediction greatly depends on the arbitrary value of the initial imperfection input into the model.

Given the merits and disadvantages of different modeling approaches discussed in Chapter 2, models composed of nonlinear shell-type finite elements are able to capture the nonlinear strain profile along the wall length and axial-flexure-shear interaction, thereby enabling them to reliably predict different failure mechanisms of walls. Furthermore, if the mesh density is sufficient and the large deflection formulation is used, overall wall buckling can also be captured by this modeling and analysis approach (NEHRP 2014). Also, considering the mechanism of out-of-plane instability under in-plane loading, i.e. the failure being controlled by the response of the longitudinal reinforcement during unloading from a peak displacement and reloading in the opposite direction (Paulay and Priestley 1993, Chai and Elayer 1999), a shell element with the capability of situating longitudinal bars in their accurate position as well as numerical integration along the thickness could simulate this mode of failure with energy-based solution algorithm. Therefore, micro finite element modeling approach using shell-type elements has been chosen in this study to predict the response of rectangular walls with different failure patterns including out-of-plane instability. The reinforcing bars are modelled using embedded steel model which is available in the program used herein.

3.1.1 ELEMENT TYPE

In this study, finite element analyses were carried out using DIANA9.4.4 (DIANA 2011). Different shell-type elements were investigated regarding their ability to accommodate the features required to simulate the important mechanisms of wall behaviour including majority of the failure modes. The curved shell elements in DIANA can be used to capture buckling and post-buckling response under concentric in-plane loading. These elements are based on isoparametric degenerated-solid approach and have integration points along the thickness unlike flat shell elements in which integration is performed in one plane only. These elements are consequently able to capture variation of strain along the thickness and simulate the deformation in the out-of-plane direction.

Two shell hypotheses are implemented in this approach (DIANA 2011): 1) Straight-normals: this hypothesis assumes that normals remain straight, but not necessarily normal to the reference surface. Transverse shear deformation is included according to the Mindlin-Reissner theory (Reissner 1945, Mindlin 1951). 2) Zero-normal-stress: it assumes that the normal stress component in the normal direction of a lamina basis is forced to zero.

Figure 3.1 displays characteristics of the curved shell elements. Three translations and two rotations are defined in every element node. The thickness 't' of these elements must be small in relation to the dimension 'b' in the plane of the element. Force 'F'(Figure 3.1a) may act in any direction between perpendicular to the surface and in the surface, and moment 'M' should act around an axis in the element face. The in-plane lamina strains ε_{xx}, ε_{yy} and γ_{xy} vary linearly in the thickness direction and the transverse shear strains γ_{xz} and γ_{yz} are forced to be constant in the thickness direction. Bar elements can be embedded in curved shell elements if they are positioned inside the thickness domain of the element and intersect one or two edges of the element (Figure 3.1b).

The Q20SH element, which is a four-node quadrilateral isoparametric curved shell element, is used in this study. The polynomials for the translations u and the rotations ϕ are expressed in Figure 3.2a. Three-point integration scheme is considered along the thickness in which the integration points are located in the reference plane and at the two extremes of wall thickness (Figure 3.2b).

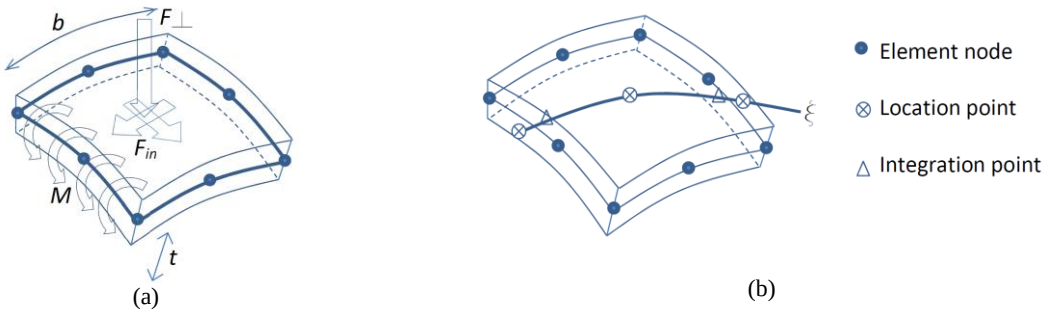

Figure 3.1: (a) Characteristics of a curved shell element (DIANA 2011); (b) bar embedded in a curved shell element

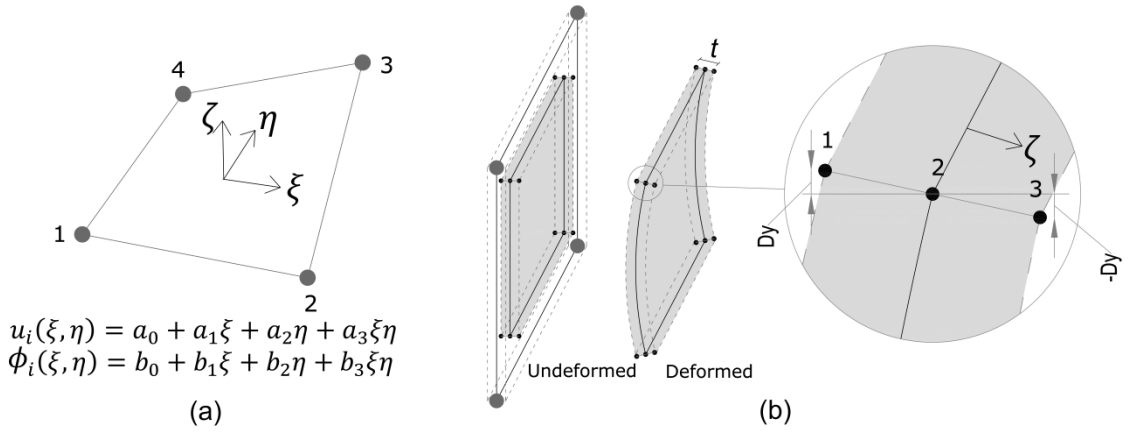

Figure 3.2: (a) Q20SH (Points 1-4 are element nodes); (b) integration scheme across the thickness (Points 1-3 are integration points)

Figure 3.3 shows a typical finite element model of a cantilever RC wall generated in DIANA. Figure 3.3b and Figure 3.3c display the mesh discretization using curved shell elements and the embedded bar elements along with wall boundary conditions, respectively. The size of the elements was determined based on a mesh sensitivity analysis. The numerical results were found not to be sensitive to the mesh size beyond a specific level of mesh refinement. On the other hand, the specimens with well-confined boundary regions were not very sensitive to fine mesh sizes.

The strain penetration effects that result in localized bond slip of the longitudinal reinforcement at the interface between wall and footing cannot be captured using this modeling approach. This phenomenon is well investigated by Zhao and Sritharan (2007) and Sritharan et al. (2000), and its representation requires application of interface elements with appropriate hysteretic rules. As the fully bonded embedded bar approach has been used for representation of the reinforcement, the strain penetration effects would not have been captured if the foundation had been simulated. Therefore, the footing is not simulated in this study.

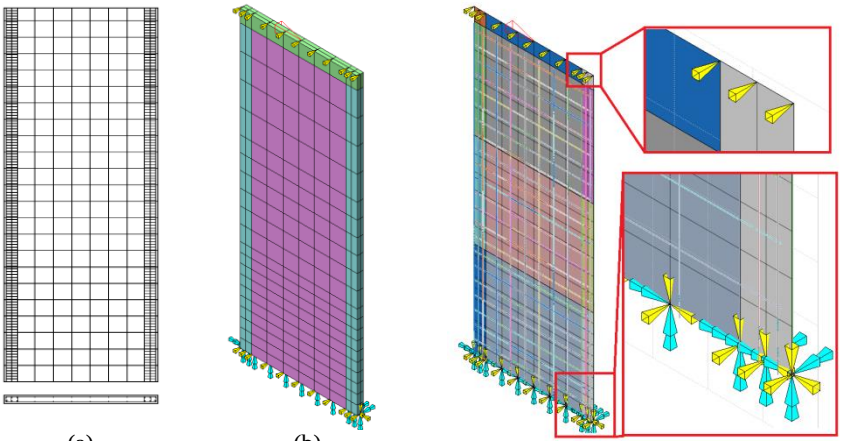

Figure 3.3: A typical finite element model: (a) wall geometry (b) mesh discretization; (c) embedded bar elements and boundary conditions

3.1.2 MATERIAL MODELS

The *Total Strain Crack Model* available in DIANA (DIANA 2011) is used in this study to represent the behaviour of the concrete elements. In the *Total Strain Crack Model*, constitutive relationship of concrete is developed along the lines of the Modified Compression Field Theory, originally proposed by Vecchio& Collins (1986). The total strain based crack models follow a smeared approach for the fracture energy. Two crack models are embedded in a total strain concept, the fixed orthogonal crack model in which the orientation of the crack is fixed during the entire computational process and the coaxial rotating crack model which allows the orientation of the crack to rotate with the axes of principal strains. These two classes of concepts have been compared comprehensively by Rots and Blaauwendraad (1989) and Feenstra et al. (1991). In the fixed smeared crack concept, the shear behavior is modeled explicitly with a relationship between the shear stress and the shear strain. Upon crack formation, the initial linear-elastic shear modulus is reduced via a factor called the shear retention factor β. Unlike the fixed crack model, the rotating crack model does not involve an independent shear retention factor, and the shear stiffness is associated with the rotation of the principal axes. Consequently, specification and validation of a shear retention factor is not required. However, the assumption that the principal stresses and strains remain coincident is considered a limitation for the rotating crack model although it has been extensively used in response prediction of reinforced concrete structures. Given the plus and minus points of both crack models, the rotating crack model is used in this study to represent nonlinear behaviour of concrete in web and boundary zones of the wall models.

One of the main advantages of the total strain crack model over the other concrete models in DIANA is that the stress-strain data describing the backbone curve of the confined and unconfined concrete can be input directly. In the current implementation in DIANA, the responses during loading and unloading are modelled with secant unloading, and the effects of cracking and crushing on deterioration of concrete are considered using internal damage variables. Figure 3.4 displays the origin-oriented secant type unloading behaviour of a single element subjected to tension and compression cycles, in which tension and compression constitutive models of concrete are defined using total strain crack model. It should be noted that the origin-oriented hysteretic rules have their limitations (e.g., gradual gap closure is not captured) which can understandably affect the amount of strain generated in the reinforcement. However, due to cyclic response of a reinforced concrete section, the concrete does not reach high values of compressive strains. Therefore, the concrete hysteresis in compression is close to the origin-oriented system, and the area of hysteretic energy neglected by the origin-oriented approach is not very considerable. On the tension side, although the strains reach considerably large numbers, as the values of tensile stresses are significantly small, the area neglected by using the origin-oriented model is not considerable. Thus, although the accuracy of the model would be affected by this approach, the effect would not be considerable. More sophisticated material models are available that describe the cyclic behavior of concrete more accurately.

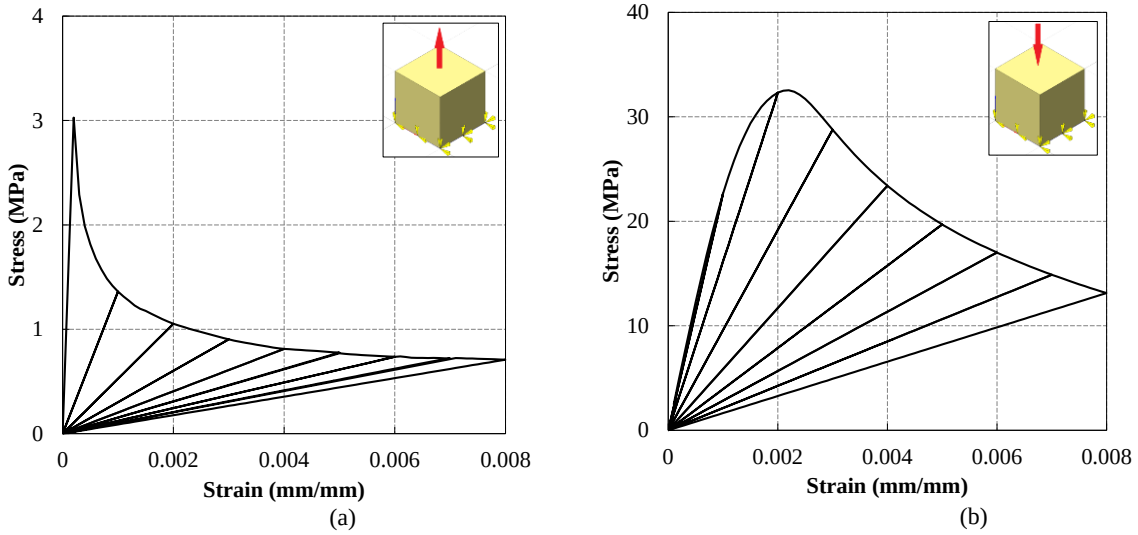

Figure 3.4: Total strain crack model: loading and unloading paths: (a) tension; (b) compression

The Popovics/Mander`s constitutive model (Mander et al. 1988) (Figure 3.5a) was implemented in the Total Strain Rotating Crack model to incorporate the confined concrete properties in the boundary elements and behavior of the unconfined portion was modeled

using the axial stress-strain relationship of unconfined concrete. The tensile behaviour of concrete has been defined using the relations proposed by Belarbi and Hsu (1994).

A single layer of shell elements was used for the numerical simulation in this study. Therefore, mesh discretization could not be done along the wall thickness and consequently the concrete properties along the thickness were considered to be identical, i.e. the entire thickness of the boundary zones was considered to have the confined concrete properties of the core region and the cover concrete was not assigned the unconfined concrete properties.

The stress-strain curve of the reinforcing steel is defined using Menegotto and Pinto (1973) model (Figure 3.5b). Bar buckling is not included in this constitutive model, hence the effect of bar buckling is neglected in the analysis conducted in this paper. Nevertheless, cyclic constitutive models of reinforcing bars including the effect of buckling are available in literature (e.g. Dhakal and Maekawa 2002a,b,c). Should these models be implemented in DIANA, the effect of bar buckling can also be captured in the prediction.

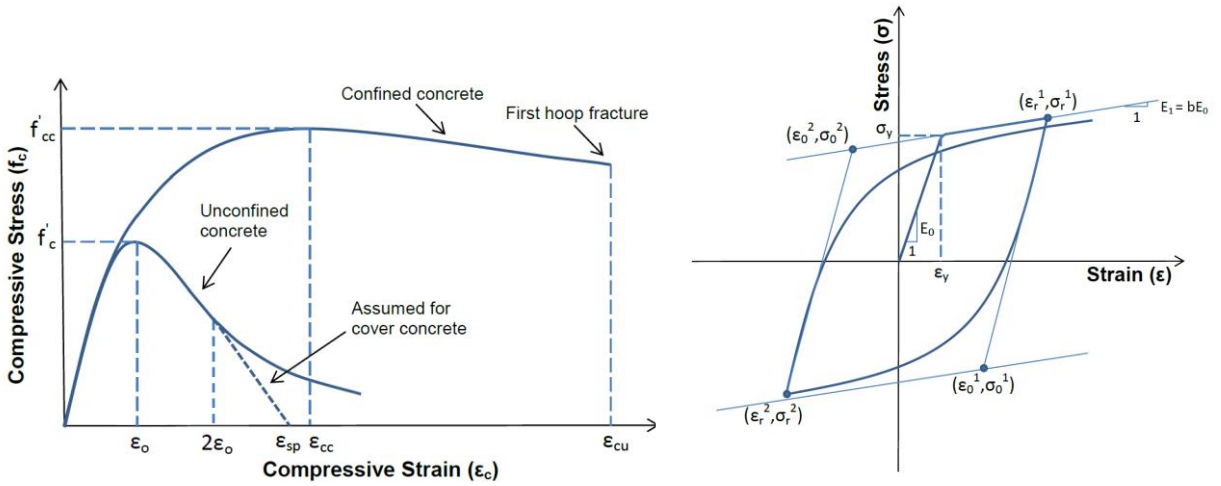

(a) Concrete (Mander et al. 1988)

(b) Steel (Menegotto and Pinto 1973, Orakcal et al. 2006)

Figure 3.5: Constitutive models of materials

3.1.3 ANALYSIS SETUP

The axial and lateral loads are applied using different analysis steps. The axial load has been applied at multiple nodes using the force-controlled regime, and the lateral load has been applied at a single node using the displacement-controlled regime. Secant iterative method has been adopted with Energy and Force as convergence norms. The convergence tolerance has been chosen after several trials so as to generate smooth curves within the minimum analysis time possible. Geometric nonlinearity has been accounted for in the analysis.

3.2 VERIFICATION OF THE NUMERICAL MODEL; DIFFERENT FAILURE PATTERNS

A number of wall specimens with different shear-span ratios and with various failure mechanisms have been simulated using the numerical model. The properties of the specimens are given in Table 3.1. Efficiency and versatility of the analysis model in predicting different failure modes is evaluated via comparing model predictions with experimental observations of specimens that exhibited a diversity of failure mechanisms during testing. Geometry and reinforcement details of the specimens are shown in Figure 3.7.

Specimens SW11 and SW12 were subjected to monotonic loading, whereas specimen S5 was subjected to the cyclic displacement history shown in Figure 3.6. Similarly, specimens PW4, R2 and RW2 were subjected to reversed cyclic loading with gradually increasing drift cycles with each drift level repeated thrice in PW4 and R2 and twice in RW2.

Table 3.1: Test specimens used for model verification

Specimen	Length, L_w, mm	Height, H_w, mm	Thickness, t_w, mm	Cross-Sectional Aspect Ratio, L_w/t_w	Aspect Ratio, H_w/t_w	Shear-span Ratio, $M/(VL_w)$	Axial Load, kN[$(\nu = N/(f'_cA_c)$]	Failure mechanism
SW11 (Lefas et al. 1990)	750	750	70	10.7	10.7	1.0	0 [0.0]	Shear
SW12 (Lefas et al. 1990)	750	750	70	10.7	10.7	1.0	230 [0.1]	Shear
S5 (Vallenas et al. 1979)	2412	3009	114	21.2	26.4	1.6	598 [0.06]	Flexure - Shear
PW4 (Birely 2013)	3048	3658	152.4	20.0	24.0	2.0	1601 [0.12]	Flexure - Bar buckling
R2 (Oesterle 1976)	1905	4572	101.6	18.8	45.0	2.4	0 [0]	Flexure - Out of plane instability
RW2 (Thomsen IV and Wallace 1995)	1219	3660	102	12.0	35.9	3.0	533 [0.1]	Flexure

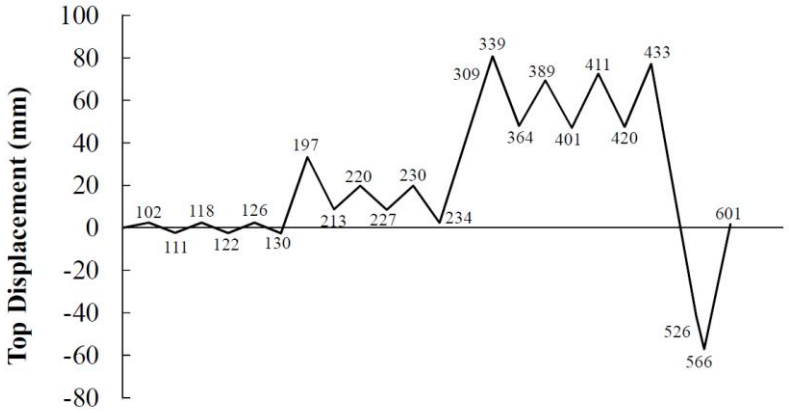

Figure 3.6: Load program for Specimen S5 (Vallenas et al. 1979)

Figure 3.8 compares the base shear-top displacement responses of the specimens with the corresponding test results. Only one cycle (the first cycle) per drift is displayed in the comparison for clarity. Points A-G refer to: A: first cracking, B: initiation of inclined cracking, C: first yielding of tension reinforcement, D: tension yielding of all boundary element reinforcement, E: concrete reaching compressive strength at the base, F: concrete degradation throughout the boundary region, G: out-of-plane deformation. The lateral load and drift values corresponding to Points A-F are compared with test results in Table 3.2 and Table 3.3.

Specimen S5 exhibited a combination of different failure mechanisms during testing; therefore, the loading points corresponding to key stages of the wall response are displayed in Figure 3.8c to compare with the sequence of events predicted by the model. These load points (referred to as LP in the text) are identified in Figure 3.6, which shows the displacement history applied to the specimen.

Figure 3.9 displays the principal tensile strain and compressive stress distribution and failure pattern of the specimens. These contours correspond to 2.5% drift for all the specimens except for Specimen PW4, which failed with considerable out-of-plane deformation at zero displacement while reversing from the maximum top drift of 1.5%. The principal tensile strain contours display the crack-induced extent of damage at different parts of the models and the principal compressive stress contours show the stress flow pattern in concrete elements and consequently compressive damage zones of the models.

Table 3.2: Lateral loads corresponding to the key milestones (kN)

Specimen	A		B		C		D		E		F	
	Test	Analysis	Test	Analysis	Test	Analysis	Test	Analysis	Test	Analysis	Test	Analysis
SW11	35	30.5	100	73.1	170	171.3	-----	209	-----	138	260	232.6
SW12	45	65	130	108	210	241	-----	277	-----	167	340	309
SW5	110	138	250	342	709	533	788	890	840	890	916	903.3
PW4	320	206	380	270	628	575	870	894	870	969	-----	-----
R2	66.7	51.2	-----	94.2	164.6	121	186	132	215	189.8	-----	-----
RW2	74	55	127	97	127	89.7	-----	107.5	138	143	-----	-----

Table 3.3: Drift values corresponding to the key milestones (%)

Specimen	A		B		C		D		E		F	
	Test	Analysis	Test	Analysis	Test	Analysis	Test	Analysis	Test	Analysis	Test	Analysis
SW11	0.05	0.01	0.24	0.09	0.48	0.45	-----	0.60	-----	0.36	1.1	0.71
SW12	0.03	0.03	0.17	0.08	0.39	0.45	-----	0.68	-----	0.21	1.18	0.93
SW5	0.07	0.04	0.15	0.08	0.39	0.23	0.42	0.48	0.49	0.48	2.45	1.22
PW4	0.06	0.02	0.07	0.04	0.21	0.18	0.35	0.40	0.5	0.52	-----	-----
R2	0.06	0.03	-----	0.14	0.33	0.2	0.47	0.28	1.11	0.83	-----	-----
RW2	0.18	0.06	0.44	0.2	0.44	0.16	-----	0.27	0.8	0.6	-----	-----

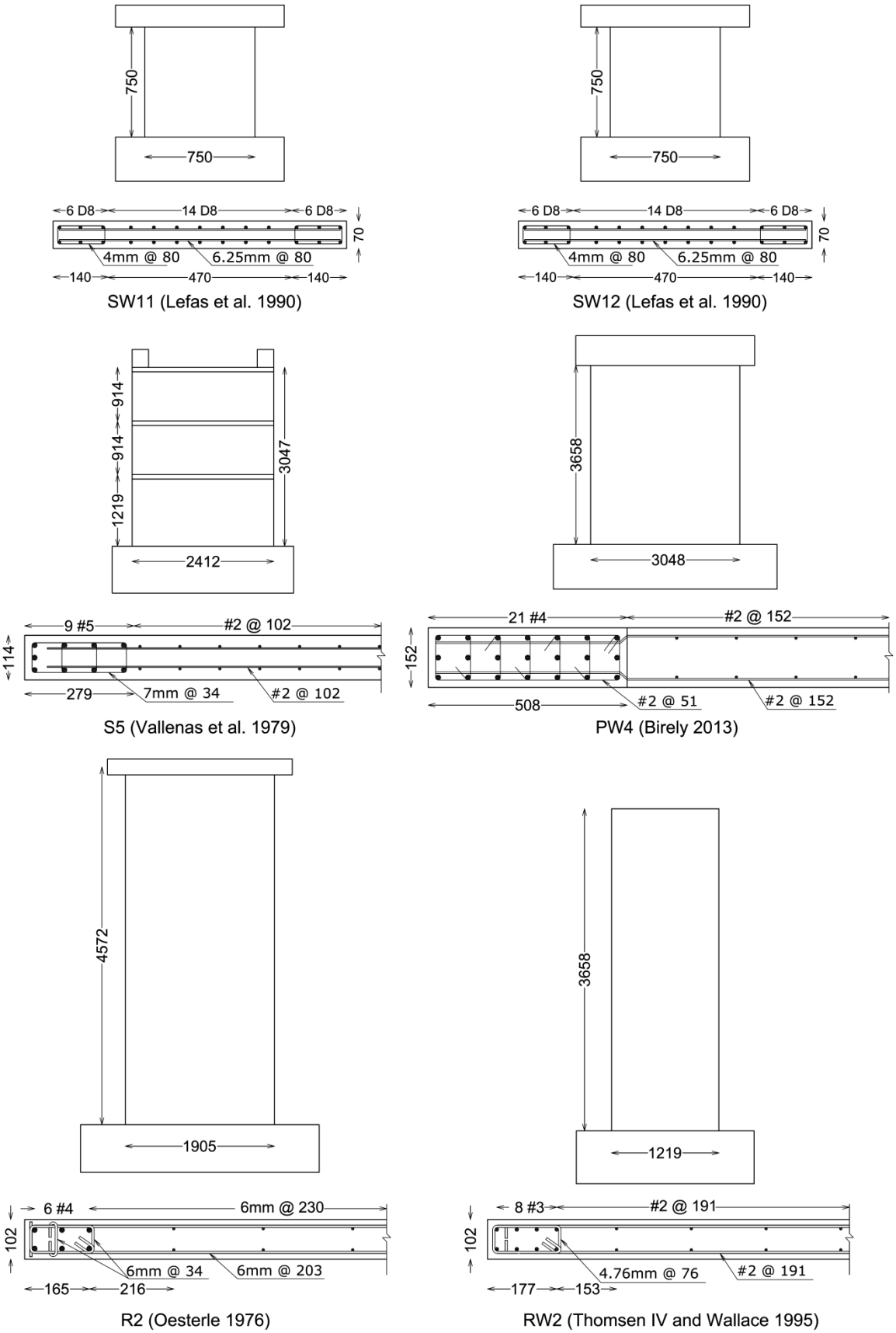

Figure 3.7: Geometry and reinforcement details of the specimens (dimensions in [mm])

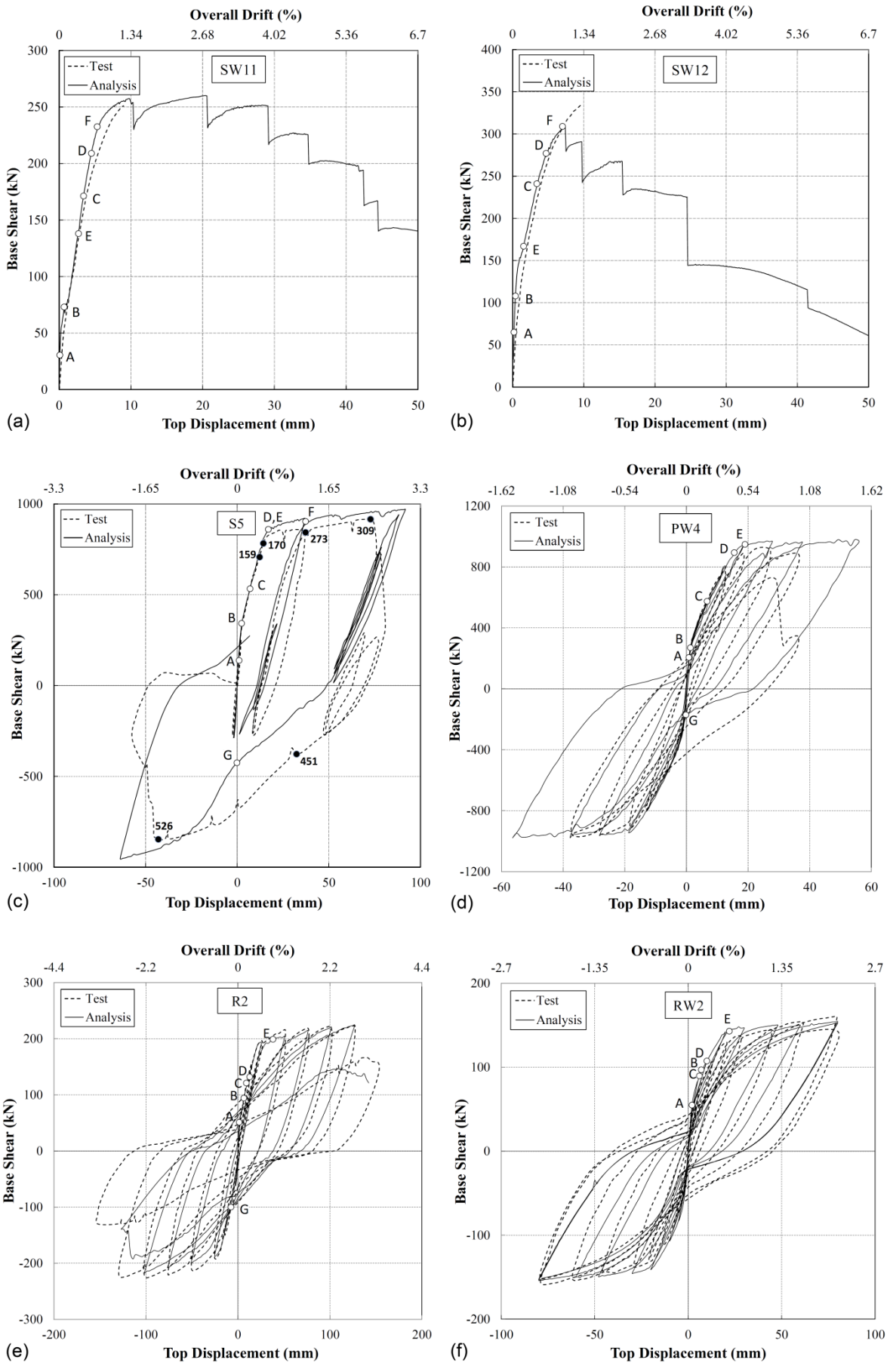

Figure 3.8: Base shear-top displacement response of the specimens

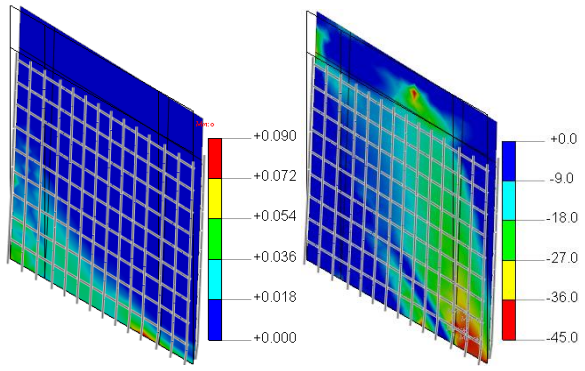

Principal Tensile Strain, E1 (mm/mm) Principal Compressive Stress, S3 (MPa)

(a) SW11

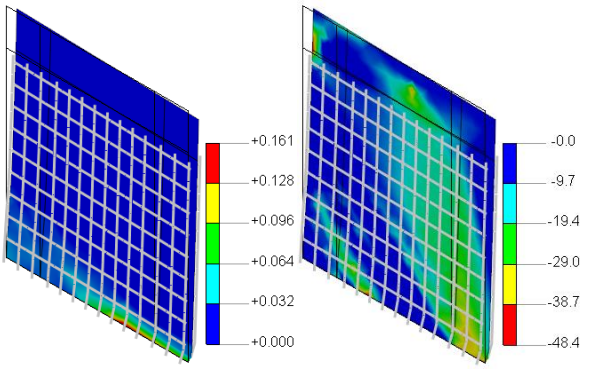

Principal Tensile Strain, E1 (mm/mm) Principal Compressive Stress, S3 (MPa)

(b) SW12

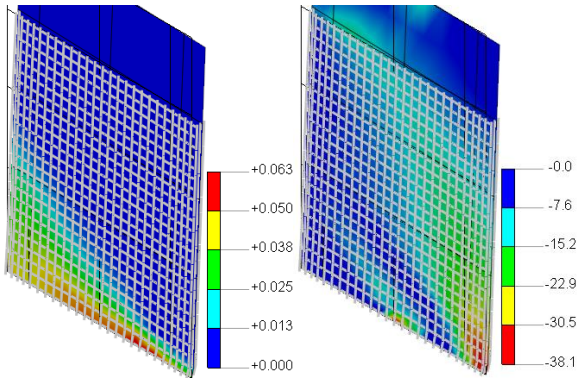

Principal Tensile Strain, E1 (mm/mm) Principal Compressive Stress, S3 (MPa)

(c) S5

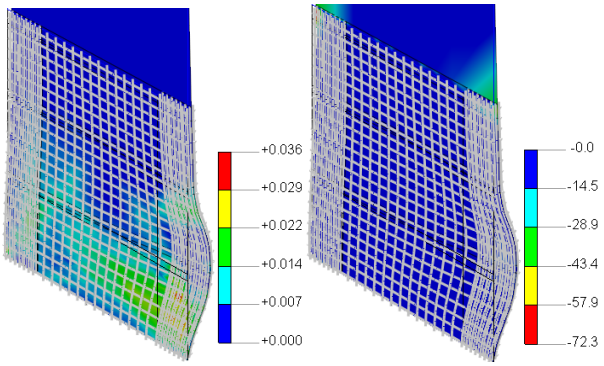

Principal Tensile Strain, E1 (mm/mm) Principal Compressive Stress, S3 (MPa)

(d) PW4

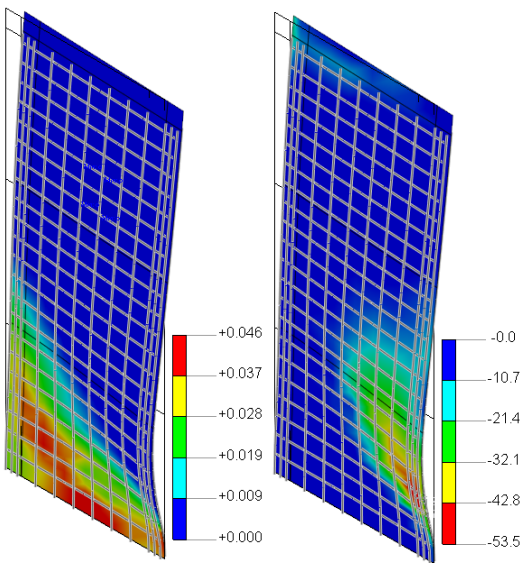

Principal Tensile Strain, E1 (mm/mm) Principal Compressive Stress, S3 (MPa)

(e) R2

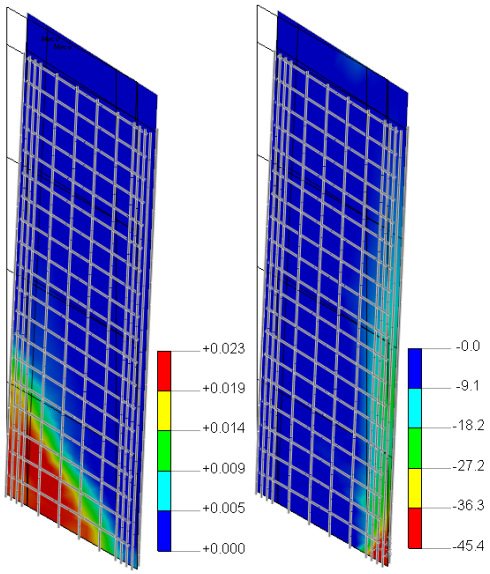

Principal Tensile Strain, E1 (mm/mm) Principal Compressive Stress, S3 (MPa)

(f) RW2

Figure 3.9: Principal tensile strain and compressive stress distribution and failure pattern of the specimens (at 2.5% drift except PW4 at 0.0% during unloading from 1.5% cycle)

3.2.1 SPECIMENS SW11 & SW12 (LEFAS ET AL. 1990)

Specimens SW11 and SW12 were tested under monotonic loading by Lefas et al. (1990). These specimens were squat walls (h/l = 1) and were different only in terms of the applied axial load ratio (Table 3.1). Because of their small shear-span ratios, response of these two specimens was shear-dominated. Figure 3.8a and Figure 3.8b display the regular abrupt strength drops due to shear failure of different elements occurring one after another resulting in brittle response of the specimens. This phenomenon is exacerbated by the axial load applied to Specimen SW12. The experimental measurements are reported up to 1.07% and 1.18% drift for SW11 and SW12, respectively. The numerical predictions show a reasonable match with the test results in both specimens. According to Figure 3.8a and Figure 3.8b, Point E which corresponds to the first concrete element reaching maximum strength at the base precedes reinforcement yielding resulting in brittle response of the walls.

Principal stress distribution of Specimens SW11 and SW12, shown in Figure 3.9, displays the diagonal strut action developed in these squat walls indicating shear-dominated failure of the specimens. In Figure 3.9a and Figure 3.9b, the stress values in light coloured region along the diagonal are around ten times greater than the ones in the dark coloured areas indicating that the main load carrying capacity of these walls comes from the diagonal strut action. The principal tensile strain plots show considerable tensile damage and crack openings for both specimens. The extent of tensile damage is significantly larger for Specimen SW12 and is concentrated mainly at the base, indicating substantial shear deterioration of this specimen.

3.2.2 SPECIMEN S5 (VALLENAS ET AL. 1979)

Specimen S5 was a three-story wall specimen tested by Vallenas et al. (1979) and was intended to idealize the three lower stories of a rectangular wall designed for a seven-story prototype building. The specimen was subjected to a monotonic loading protocol with several small cycles at different stages of loading as shown in Figure 3.6. It should be noted that the specimen was tested in a horizontal position; therefore the wall weight could have acted as a minor out-of-plane load which could affect the wall symmetry and result in a progressive eccentricity, particularly when the wall goes beyond cracking and reinforcement yielding. In order to consider this effect in the analysis, the model was subjected to an out-of-plane pressure equivalent to the wall weight. The experimental load

points corresponding to significant stages of wall response identified in Figure 3.6 are also shown in Figure 3.8c to facilitate comparison between the numerical and experimental results.

According to the test report (Vallenas et al. 1979), the outermost tensile bar reached yield strain at Load Point (LP) 159 according to the Load sequence of Figure 3.6, and all the tensile column reinforcement yielded at LP 170, resulting in overall yielding of the specimen. Initial concrete crushing at the base of the compression column was observed immediately after yielding of the specimen. The column in compression initiated spalling at LP 273, and the compression region panel showed initial crushing. The spalling was not symmetric around the column, and was concentrated on only one surface causing some eccentricity in the cross section. At LP 309 a lateral confinement hoop ruptured. The load dropped to 742 kN, and when the loading sequence was continued, buckling of the longitudinal bars at the base of the compressive column was observed leading to further drop in the load to 296 kN. Some hairline cracks appeared in the panel, indicating out-of-plane deformations. The specimen was subjected to a series of service load cycles and was loaded in the reverse direction introducing compression in the column that had a large number of residual open tensile cracks. At LP 451, a small out-of-plane deformation of the panel and compression column was observed. At LP 526, a flexural shear crack initiated at the buckled region of the tension column and the zone of crushed concrete propagated all the way through the specimen causing significant strength degradation and the load drop to -251 kN.

As shown in Figure 3.8c, the numerical results are in good agreement with the experimental measurements except that the sudden drop before reaching the maximum top displacements of 80.9 mm (2.67% drift) and -57.3 mm (-1.89% drift) was not captured by the analysis. Point E corresponds to the first concrete element reaching compressive strength at the base which happened at the same time as tension yielding of all boundary element reinforcement (Point D).

The pressure applied in the out-of-plane direction to represent the effect of the wall weight resulted in minor uniform out-of-plane displacements throughout the whole model, which became relatively large at the tensile boundary zone as all reinforcement in this region yielded (Point E). Thereafter, the out-of-plane displacement almost remained constant until the load was reversed producing compressive stresses in the previously tensile boundary region. At Point F, all concrete elements within the compression boundary region were in

the degradation zone of the confined concrete stress-strain curve. The significant strength degradation at LP 309 due to hoop rupture and bar buckling was not captured as bar buckling was not included in the model. When the model was loaded in the reverse direction, the compression boundary element, which was previously subjected to large tensile strains, exhibited an increased out-of-plane deformation which peaked at Point G. This out-of-plane deformation completely recovered in the compression boundary region when the model reached the peak displacement in the reverse direction, when out-of-plane deformation developed in the tensile boundary element as the reinforcement yielded throughout this region. The experimentally observed strength degradation observed at LP 526 was due to the flexure-shear cracks originating from the boundary zone that was under compression in the previous load peak and had exhibited bar buckling. This strength degradation was not captured by the model.

The stress and strain distribution shown in Figure 10c indicates the contribution of web and compression boundary element in lateral load resistance of the specimen. The principal tensile strain distribution displays relatively large shear crack openings at the base. Response of this specimen is governed by both flexure and shear and obviously the shear-flexure interaction as its shear-span ratio is greater than 1 (Table 3.1). Concrete reached compressive strength at the base (Point E) as soon as all the reinforcement in the tension boundary element yielded (Point D), which can be attributed to the shear-flexure interaction effect causing initiation of shear response soon after the overall yielding of the specimen.

3.2.3 SPECIMEN PW4 (BIRELY 2013)

Specimen PW4 was tested by Birely (2013) to address the seismic performance of slender reinforced concrete structural walls. Throughout the test, the ratio of the lateral force to the overturning moment applied to the top was held constant such that the base reactions (base shear and base moment measured at the wall-foundation interface) were equivalent to those of a 10-story wall with a uniform lateral load distribution. According to Figure 3.8d, the cyclic response of the specimen was well captured by the analysis. The considerable drop of strength observed in the experimental response during the second cycle of 1.0% drift is due to extensive bar buckling and core concrete crushing as well as out-of-plane deformation in the east (right) boundary element at the toe of the wall. Since bar buckling was not taken into account in the analysis the numerical model did not lose the load carrying capacity. Therefore, 1 more cycle of 1.5% drift was applied to the model to

investigate the likelihood of out-of-plane instability, which was observed as the model reached zero displacement while unloading from +1.5% drift.

As the shear-span ratio of this specimen (Table 3.1) is low, shear mode may contribute to the wall response to some extent. According to the test results, concrete reached compressive strength at the base (Point E) together with tensile yielding of all boundary element reinforcement (Point D). In the numerical prediction too, these two milestones occurred very close to each other. The model does not include bar buckling, so expectedly it could not capture the main failure pattern of the specimen which was characterized by bar buckling. However, it could capture the out-of-plane deformation of the specimen but to a greater extent than what was observed in the test before bar buckling, which may have perhaps been suppressed by the bar buckling. The considerable out-of-plane deformation of the model occurred after the stage corresponding to observation of bar buckling in the test, i.e., if the model was able to capture bar buckling, it would have been the predicted failure mode. Figure 3.9d displays the out-of-plane deformation pattern of the numerical model. The principal tensile strain distribution shows significant residual strain of the specimen at 0.0% drift level, which is known as one of the main parameters controlling out-of-plane deformation of rectangular walls (Paulay and Priestley 1993, Chai and Elayer 1999, Dashti et al. 2015).

3.2.4 SPECIMEN R2 (OESTERLE 1976)

Specimen R2 was tested by Oesterle (1976) at Portland Cement Association Laboratories. According to the test report, during Cycle 28, a 1 in. (25.4 mm) deflection cycle after the 3in. (76.2 mm) cycles, out-of-plane deformation of the compression end was observed. The compression boundary element was 0.25 in. (6.4 mm) out-of-plane at a point 3.5 ft (1.1 m) above the base. Although this bowing progressed further with each cycle, the load carrying capacity of the wall remained stable. The test was continued and considerable out-of-plane deformation was observed during the 5 in. (127 mm) deflection cycles, which progressed further until the severe strength drop in the 6 in. (152.4 mm) deflection cycle.

In the analysis, considerable out-of-plane deformation was observed at 41/3 ft (1.3 m) above the base during the 4 in. (101.6 mm) displacement cycle while reversing from the +4in peak and approaching towards the -4in peak. The analysis continued until reaching +5.6 in. (142 mm) displacement in the +6in. (152.4 mm) cycle. At this level the out-of-plane deformation was big enough to stop the analysis.

The analysis could reasonably predict the base shear-top displacement response of the specimen until the model became unstable due to out-of-plane deformation at the compression boundary element (Figure 3.8e). With a shear-span ratio of 2.4 (Table 3.1), response of this specimen was flexure-dominated with out-of-plane instability (Figure 3.9e). The out-of-plane deformation resulted in different stress and strain contours for different integration layers along the thickness of curved shell elements, and the principal stress and strain contours indicated in Figure 10e correspond to the inner surface of the out-of-plane deformation profile where larger compressive stresses due to this deformation pattern are developed.

Figure 3.10 displays the steel strain measurements of the specimen at the base in comparison with the model predictions at the positive peak of some drift cycles. It should be noted that the strain values at the base of the model are highly influenced by local effects of the boundary conditions as well as the inability of the model in capturing the strain penetration effects. Therefore, the strain values of the model at one mesh (150 mm) above the base are compared with the test measurements at the base. Due to a gauge malfunction in the test, the measurements were available up to 0.56% drift in some parts and 1.1% drift at the tension boundary element. The nonlinear strain gradient along the length of the wall, which is usually neglected in simplified analysis methods, is predicted by the analysis with a relatively good agreement with the measured steel strain profile. Since the reinforcement elements are fully bonded in the analysis, the predicted strain profiles are identical for concrete and reinforcement. As shown in Figure 3.10, the predicted strain profile of the wall section is in good agreement with the measured strain of the reinforcement in the test. The strain profile at 1.1% drift level follows the same trend as the one at 0.56% drift level, but understandably with considerably greater strain values. The predicted neutral axis position matched well with test results as well.

3.2.5 SPECIMEN RW2 (Thomsen IV and Wallace 1995)

Specimen RW2 was tested by Thomsen IV and Wallace (1995). This specimen was subjected to an axial load of $0.07A_g f'_c$ and a lateral cyclic displacement history. This specimen had a shear-span ratio of 3 and consequently had a flexure-dominated behaviour with bar buckling at 2.5% drift. The numerical prediction and experimental measurement of the lateral load-top displacement curve match reasonably well (Figure 3.8f).

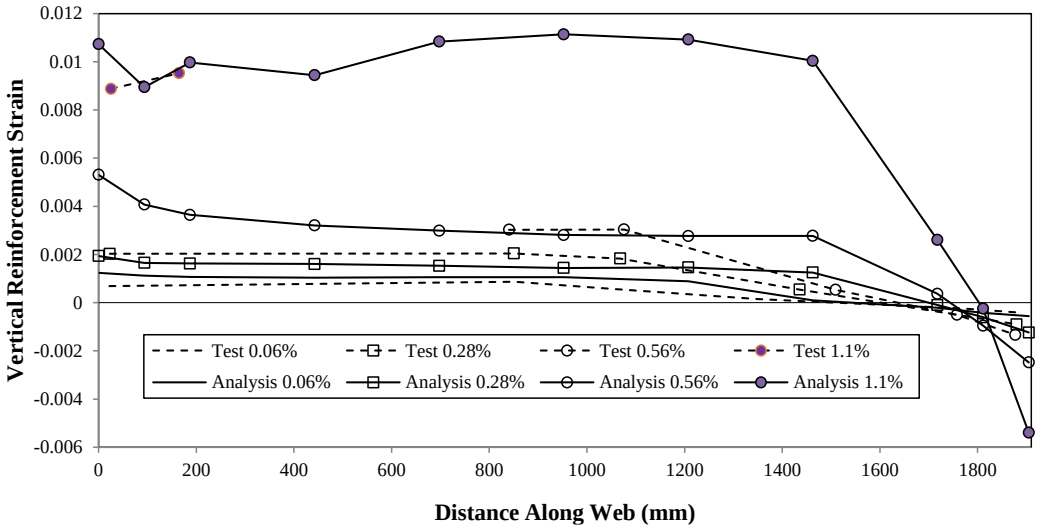

Figure 3.10: Wall strain gradient, Specimen R2

The compressive stress distribution, shown in Figure 3.9f, shows that the main contribution to the lateral load resistance of the wall comes from the compression grown in boundary concrete elements acting along with the tension developed in the reinforcement (which is not shown in Figure 3.9f). Flexure is dominant in this specimen as the stress values in the compression boundary element are significantly larger than the stress values in the panel. The tensile strain contour shows uniform increase of crack openings towards the boundary region indicating flexure as the main contributor to overall displacement of the specimen.

Figure 3.11displays the concrete strain measurements of Specimen RW2 at the base in comparison with the model predictions at the positive peak of some selected drift cycles applied during testing. The average concrete strains were measured by seven LVDTs over a 229 mm gage length at the base of the wall. The average concrete strain of two consecutive meshes (100x100 mm) at the base is used for comparison. As shown in Figure 3.11, the analysis and test results are relatively close at different drift levels. At 2.0% drift level, the difference between the test and analysis is relatively more although the strain profiles follow similar pattern. This difference can be attributed to the bond-slip effect which becomes more influential at higher displacement levels and is not considered in the analysis. Also, the neutral axis position, which is one of the main factors in calculating confinement length, is well predicted by the analysis.

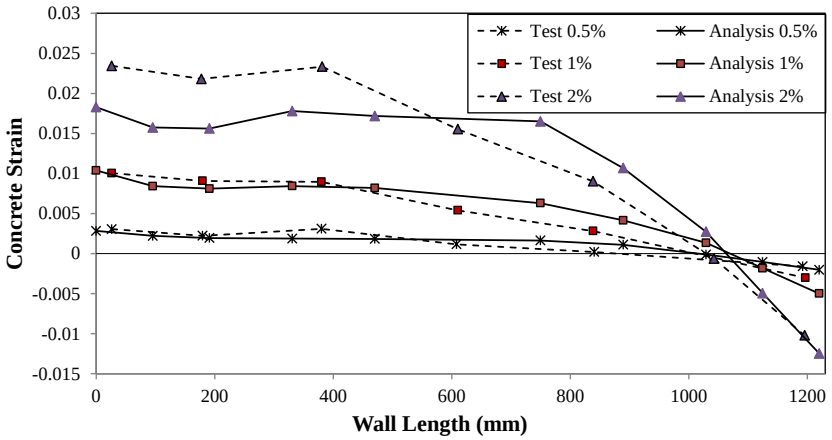

Figure 3.11: Wall strain gradient, Specimen RW2

3.2.6 CRACK PATTERNS

Figure 3.12 displays the predicted crack pattern to compare with the experimental observations. For each specimen, figures of crack patterns available in the corresponding test report are compared with the model predictions. As the first two specimens (SW11 and SW12) had similar cracking pattern, only one is included in the figure. Similarly, a clear crack pattern for Specimen RW2 was not available in the literature, so it could also be not included in the comparison.

It is worth noting that the smeared crack approach is used in the numerical prediction which calculates strains and shows cracks at all integration points of an element (if the cracking strain criteria is met); hence resulting in a denser crack representation when compared to test observations. The predicted results are filtered to show the major cracks for each specimen at the corresponding stage with the minimum crack strain set to be 1.8e-3 for all the specimens. Therefore, any minor cracks and the orthogonal cracks formed in the previous reverse loading, which have smaller crack strains due to crack closure, are not shown. The crack strain distribution is also indicated in Figure 16 for each specimen using the equivalent crack sum values at nodes. The colour contours, which are scaled differently for different specimens, clearly show concentration of the crack strain at the given drift levels of the specimens.

Specimen (Drift)	Test Observation	Predicted Crack Pattern	Predicted Crack Strains
SW11 (0.7%)	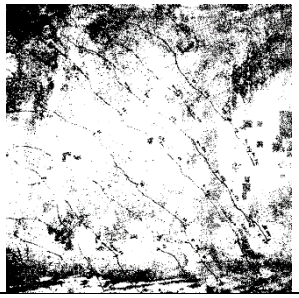	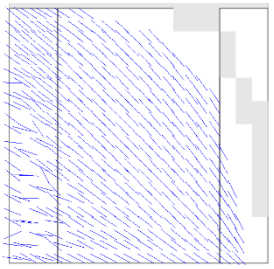	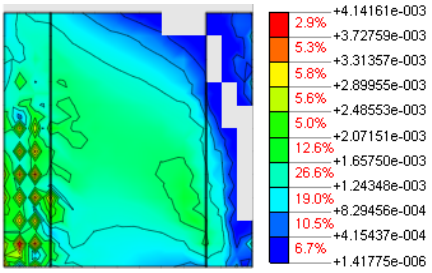
S5 (0.3%)	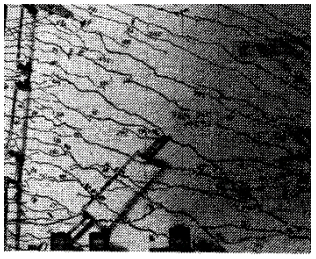	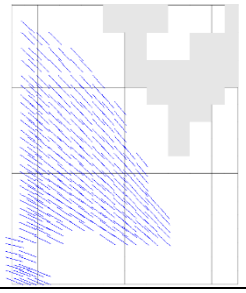	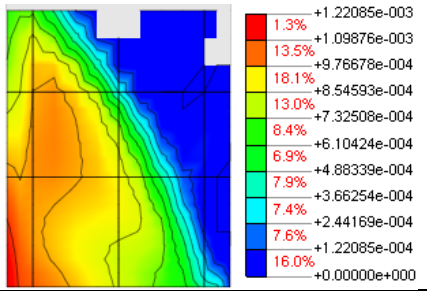
S5 (-1.3%)	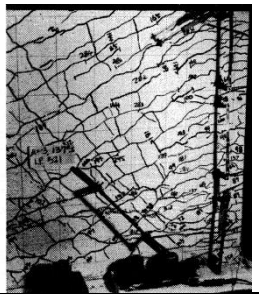	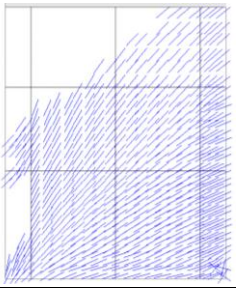	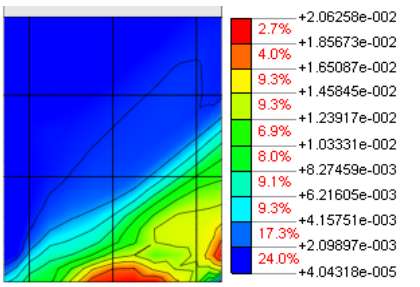
PW4 (1.0%)	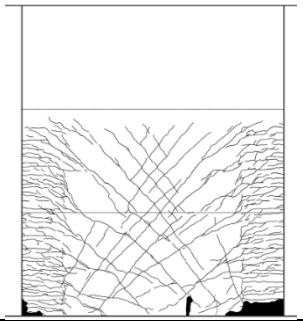	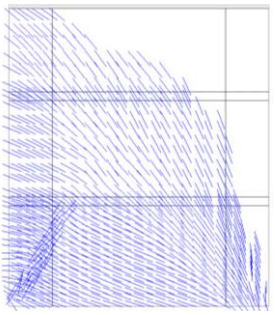	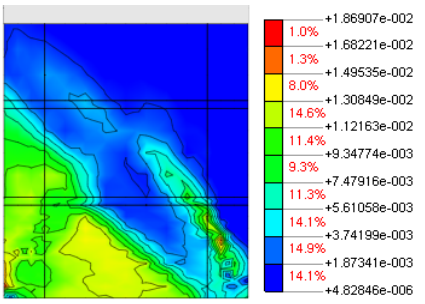
R2 (1.7%)	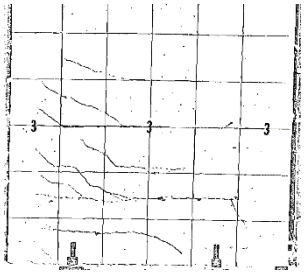	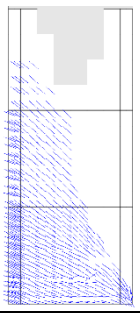	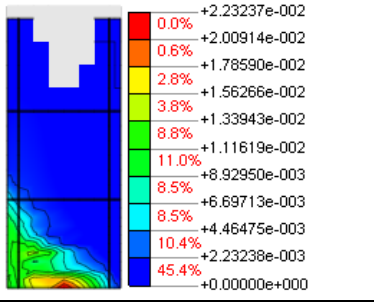

Figure 3.12: Crack patterns-experimental observations vs numerical predictions (Crack Strains: Sum of strains in all cracks in Gausspoint)

Figure 3.12 indicates a 45 degree inclined crack pattern for the shear-dominated specimen (SW11) at 0.7% drift with the crack strain concentrated mostly in the web. Variation of

crack strain is not considerable for this specimen. Specimen SW5 with a shear-flexure response exhibited horizontal cracks at the base of the tension boundary region as well as the inclined web cracks at 0.3% drift. At this stage, reinforcement yielding had started in the boundary region (Figure 3.8), and the contributions of shear and flexural deformations to the overall displacement of the specimen are similar (Vallenas et al. 1979). The crack strains are bigger at the base of the tension boundary region and at about mid-height region of the web (Figure 3.12) indicating the shear-flexure response of the specimen. The crack pattern of this specimen is displayed at -1.3% drift level as well which shows variation of the crack angle and redistribution of the crack strain due to further loading of the specimen. The crack orientation is more horizontal along majority of the base suggesting that the reinforcement may have yielded along this region as the neutral axis position must be closer to the compression end at this stage. The crack strain concentration at this region further verifies the reinforcement yielding.

The crack pattern for Specimen PW4 at 1.0% drift shows horizontal cracks in the tension boundary region. The web cracks are inclined towards horizontal orientation along the one-third height and have 45 degree orientation along the rest of the wall height. The compression boundary region shows some vertically oriented cracks and relatively large crack strains indicating a considerably large compression in this region. This stress concentration could have triggered bar buckling in this region at this loading stage which was observed in the test but expectedly was not predicted by the model. The crack strains are mainly concentrated in the lower two-third of the wall height with the biggest strains within one-third height from the base.

Specimen R2 was flexure-dominated and exhibited a considerable crack concentration at one-third height of the specimen. The crack pattern shows a horizontal orientation for the base cracks up to the neutral axis position which is located within the compression boundary region at this loading stage (Figure 3.10).

3.2.7 SUMMARY AND DISCUSSION OF THE NUMERICAL-EXPERIMENTAL COMPARISON

The sequence of events observed during the tests and predicted by the analysis showed initiation of concrete spalling before initiation of reinforcement yielding for squat walls which had brittle shear failure and very close-by occurrence of concrete crushing and overall yielding for specimens with shear-flexure failure.

Specimen SW11 was a squat wall and was shear-dominated. Specimen SW12 had the same properties as SW11 except that an axial load ratio of 0.1 was applied to the specimen. The axial load affected the base shear-top displacement curve resulting in a more brittle response.

Specimen SW5 had a flexure-shear failure pattern as its shear-span ratio was such that both flexure and shear contributed to the wall response. As the specimen was tested in a horizontal position the wall weight acted in the out-of-plane direction, when this out-of-plane force was accounted for, the analysis could predict the out-of-plane deformation which was also observed during the test. However, the considerable strength degradation of the specimen due to hoop rupture and bar buckling was not predicted by the model since bar buckling is not included in the model.

Specimen PW4 with a flexure-shear response had out-of-plane deformation during the test and failed due to extensive bar buckling and core crushing. The model could predict the out-of-plane deformation but was not able to capture bar buckling, and therefore, the abrupt strength degradation was not simulated. However, the predicted out-of-plane deformation occurred one drift cycle after the stage corresponding to the experimentally observed bar buckling, showing that the sequence of events could have been predicted if the model was able to capture bar buckling.

Out-of-plane deformation was observed during the test of Specimen R2, and it was well captured by the model. This specimen was a slender rectangular wall with a flexure-dominated response. Also, the nonlinear strain profile at different stages of loading was reasonably captured by the model.

Specimen RW2 had the greatest shear-span ratio among the selected specimens resulting in the response being flexure-dominated. The model predictions matched well with the experimental measurements for this specimen in terms of lateral load-top displacement response as well as the strain gradient at the base indicating that in addition to the overall global response predictions, local behaviour of the wall models can also be predicted reasonably well by the adopted modeling and analysis approach.

The crack pattern predicted by the smeared crack approach used in the model was qualitatively in agreement with the experimental observations. The predicted crack pattern showed dependency of the crack angle on the relative contribution of shear and flexure modes in the overall response of the specimen; for example, yielding of vertical

reinforcement, representing a flexural behaviour, made the cracks more horizontally oriented. The effect of response mode was observed in the distribution of crack strain throughout the web and boundary region as well. In other words, reinforcement yielding in ductile walls resulted in redistribution of crack strain, and consequently the width of the cracks, which were found to concentrate in the vicinity of the yielded reinforcement. Horizontal cracks observed in the test at the base of Specimen R2 suggest that the neutral axis was located within the compression boundary region, which was in line with the strain profile predicted by the model (Figure 3.10) as well as the nonlinear strain profile indicated by the crack orientation in tension and compression regions.

3.3 CONCLUSIONS

A generic finite element modeling and analysis approach is proposed in this study for the numerical prediction of cyclic behaviour of RC walls under combined effects of axial, shear and bending actions. The approach uses curved shell elements with embedded bar elements available in a commercial FE analysis program DIANA to simulate concrete and reinforcing bars in RC walls. Concrete in the curved shell elements is modelled by *Total Strain Crack Model* using smeared rotating crack approach whereas the reinforcing bars are assumed fully embedded inside (and controlled by) the curved shell elements. Response of concrete and reinforcing bars are computed using fully path-dependent cyclic constitutive relationships including loading-unloading-reloading paths which are based on the *Mander model* for confined concrete and *Menegotto-Pinto model* for reinforcing bars. Validity of the adopted models and tool was evaluated using test results of six wall specimens with different shear-span ratios and failure patterns. The model predictions were in reasonably good agreement with the experimental measurements for all specimens.

The FEM modeling approach adopted in this study could simulate the nonlinear response and failure pattern of specimens with different failure modes. In particular, the ability of the analysis to capture the out-of-plane deformation in the compression boundary zone despite being subjected to pure in-plane action is very encouraging and can be deemed as a plus point for this modeling approach over other wall modeling techniques available in literature. However as of now bar buckling is not accounted for in the model, and the prediction understandably could not capture bar buckling and its effects observed in some tests. Installing a reinforcing bar constitutive model that includes compression softening due to bar buckling in the analysis tool will help overcome this limitation in future. Also,

the bond-slip effects coming from the strain penetration of the longitudinal reinforcement in the footing cannot be captured by this modeling approach.

3.4 REFERENCES

Belarbi, A. and T. T. Hsu (1994). "Constitutive laws of concrete in tension and reinforcing bars stiffened by concrete." *ACI Structural Journal* 91(4).

Birely, A. C. (2013). Seismic Performance of Slender Reinforced Concrete Structural Walls, University of Washington. PhD**,** 983.

Chai, Y. H. and D. T. Elayer (1999). "Lateral stability of reinforced concrete columns under axial reversed cyclic tension and compression." *ACI Structural Journal* 96(5), 780-789.

Dashti, F., R. Dhakal and S. Pampanin (2015). Development of out-of-plane instability in rectangular RC structural walls 2015 NZSEE Conference, Rotorua, New Zealand, New Zealand Society for Earthquake Engineering.

Dhakal, R. and K. Maekawa (2002a). "Modeling for Postyield Buckling of Reinforcement." *Journal of structural engineering* 128(9), 1139-1147. DOI: doi:10.1061/(ASCE)0733-9445(2002)128:9(1139).

Dhakal, R. P. and K. Maekawa (2002b). "Reinforcement stability and fracture of cover concrete in reinforced concrete members." *Journal of structural engineering* 128(10), 1253-1262.

Dhakal, R. P. and K. Maekawa (2002c). "Path-dependent cyclic stress–strain relationship of reinforcing bar including buckling." *Engineering Structures* 24(11), 1383-1396. DOI: http://dx.doi.org/10.1016/S0141-0296(02)00080-9.

DIANA, T. (2011). Finite Element Analysis User's Manual - Release 9.4.4, TNO DIANA.

Feenstra, P., R. De Borst and J. Rots (1991). A comparison of different crack models applied to plain and reinforced concrete. Proceedings of the International RILEM/ESIS Conference" Fracture Processes in Concrete, Rock and Ceramics", Noordwijk, The Nehterlands, E. & F.N. Spon.

Jalali, A. and F. Dashti (2010). "Nonlinear behavior of reinforced concrete shear walls using macroscopic and microscopic models." *Engineering Structures* 32(9), 2959-2968. DOI: http://dx.doi.org/10.1016/j.engstruct.2010.05.015.

Lefas, I. D., M. D. Kotsovos and N. N. Ambraseys (1990). "Behavior of reinforced concrete structural walls: strength, deformation characteristics, and failure mechanism." *ACI Structural Journal* 87(1), 23-31.

Mander, J., M. N. Priestley and R. Park (1988). "Theoretical stress-strain model for confined concrete." *Journal of structural engineering* 114(8), 1804-1826.

Menegotto, M. and P. Pinto (1973). Method of Analysis for Cyclically Loaded Reinforced Concrete Plane Frames Including Changes in Geometry and Non-elastic Behavior of Elements Under Combined Normal Force and Bending. IABSE Symposium on the Resistance and Ultimate Deformability of Structures Acted on by Well-Defined Repeated Loads, Lisbon, Association internationale des ponts et charpentes.

Mindlin, R. D. (1951). "Influence of rotary inertia and shear on flexural motions of isotropic, elastic plates." *J. of Appl. Mech.* 18, 31-38.

Oesterle, R. (1976). Earthquake Resistant Structural Walls: Tests of Isolated Walls, Research and Development Construction Technology Laboratories, Portland Cement Association.

Orakcal, K., L. M. Massone and J. W. Wallace (2006). Analytical modeling of reinforced concrete walls for predicting flexural and coupled-shear-flexural responses, Pacific Earthquake Engineering Research Center, College of Engineering, University of California, Berkeley.

Paulay, T. and M. Priestley (1993). "Stability of ductile structural walls." *ACI Structural Journal* 90(4), 385-392.

Reissner, E. (1945). "The effect of transverse shear deformation on the bending of elastic plates." *Journal of applied Mechanics* 12, 69-77.

Rots, J. G. and J. Blaauwendraad (1989). "Crack models for concrete, discrete or smeared? Fixed, multi-directional or rotating?" *HERON, 34 (1), 1989*, 1-59.

Sritharan, S., M. J. Nigel Priestley and F. Seible (2000). "Nonlinear finite element analyses of concrete bridge joint systems subjected to seismic actions." *Finite Elements in Analysis and Design* 36(3–4), 215-233. DOI: http://dx.doi.org/10.1016/S0168-874X(00)00034-2.

Thomsen IV, J. H. and J. W. Wallace (1995). Displacement-based design of reinforced concrete structural walls: An experimental investigation of walls with rectangular and T-shaped cross-sections. Report No. CU/CEE-95-06, Department of Civil and Environmental Engineering, Clarkson University, Potsdam, N.Y.

Vallenas, J. M., V. V. Bertero and E. P. Popov (1979). Hysteretic behaviour of reinforced concrete structural walls. Report no. UCB/EERC-79/20, Earthquake Engineering Research Center, University of California, Berkeley.

Vecchio, F. J. and M. P. Collins (1986). "The modified compression-field theory for reinforced concrete elements subjected to shear." *ACI Journal Proceedings.* 83(2), 219-231.

Zhao, J. and S. Sritharan (2007). "Modeling of strain penetration effects in fiber-based analysis of reinforced concrete structures." *ACI Structural Journal* 104(2), 133-141.

4 NUMERICAL PREDICTION OF OUT-OF-PLANE DEFORMATIONS IN RECTANGULAR RC WALLS SUBJECT TO IN-PLANE LOADING

Dashti, F., R.P. Dhakal, S. Pampanin (2016) "Validation of a Numerical Model for Prediction of Out-of-plane Instability in Ductile Structural Walls under Concentric In-plane Cyclic Loading" *Journal of Structural Engineering*, Ms. No. STENG-5314R2 (Under Review)

Dashti, F., R.P. Dhakal, S. Pampanin (2015) "Development of Out-of-plane Instability in Rectangular RC Structural Walls" *The 2015 New Zealand Society for Earthquake Engineering Conference, NZSEE2015*, Rotorua, New Zealand

Dashti, F., R.P. Dhakal, S. Pampanin (2014) "Simulation of Out-of-plane Instability in Rectangular RC Structural Walls" *Second European Conference on Earthquake Engineering and Seismology, 2ECESS, August, 2014*, Istanbul, Turkey

The numerical model proposed and verified in Chapter 3 using experimental results of rectangular wall specimens with different failure patterns is verified in this chapter for its capability in capturing different aspects of the out-of-plane instability failure in rectangular walls under in-plane loading. For this purpose, experimental results of cantilever wall specimens which failed in out-of-plane mode are used. The model is found to be capable of predicting the trend of initiation, increase and recovery of out-of-plane deformation as well as formation of out-of-plane instability that was observed during the tests. Development of the out-of-plane deformation in different regions of a wall section is scrutinized in this chapter using detailed response of the reinforcement and concrete elements positioned along the wall thickness at different stages of the failure mode. Based on this detailed study,

the parameters controlling this mode of failure have been identified and sensitivity of the model to these parameters is evaluated.

A detailed description on different aspects of the modeling and analysis approach can be found in Chapter 3 (Section 3.1).

4.1 EXPERIMENTAL VERIFICATION

In this study, multiple wall tests reported in literature in which out-of-plane deformation was found to dominate the inelastic response are used for verification of the model capability in capturing out-of-plane instability.

4.1.1 SPECIMEN R2 (OESTERLE 1976)

The first test used for the experimental verification is one of the cantilever wall specimens (R2) tested by Oesterle (1976). This 1/3-scale specimen was a rectangular shaped wall with 4.0% vertical reinforcement concentrated within a distance of 190.5 mm (7.5 in.) from each end. The boundary element had confinement reinforcement in the lower 1.83 m (6 ft) of the boundary elements. Dimensions and reinforcement layout, loading history as well as the finite element model of the specimen are shown in Figure 4.1.

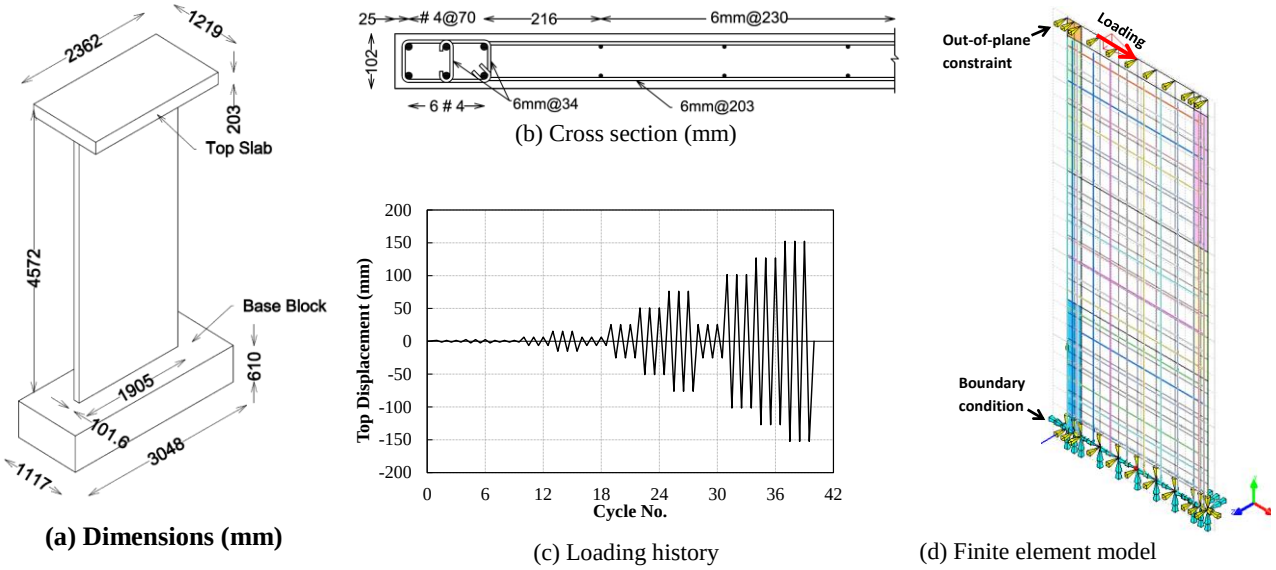

(a) Dimensions (mm)

(b) Cross section (mm)

(c) Loading history

(d) Finite element model

Figure 4.1: Wall specimen R2 (Oesterle 1976)

The cantilever specimen was subjected to 39 displacement cycles at the top level as per the loading history shown in Figure 4.1c, and no axial load was applied. According to the test report (Oesterle 1976), the specimen had a flexure-dominated response and its failure was accompanied by a large out-of-plane displacement of the compression zone within the

lower 1.07 m (3 ft 6 in.) height as well as bar fracture and considerable crushing and loss of concrete. The wall was subjected to in-plane loading only and the out-of-plane deformation was not triggered by any transverse loading. The top nodes were constrained against translation in the out-of-plane direction (Figure 4.1d). Figure 4.2a compares the lateral load vs top displacement response of the model with the experimental measurements. The key milestones of the analytical response are also indicated in this figure. The magnified part of the figure shows the comparison for initial cycles where concrete cracking and reinforcement yielding initiate. As can be seen in this figure, the model could reasonably capture the specimen response in terms of elastic and inelastic behaviour, loading and unloading stiffness, peak strength, and cyclic degradation. Also, the analytical milestones of the wall response such as cracking and yielding points match well with the ones observed during the test. In particular, the analysis could capture the out-of-plane deformation in the compression boundary zone of the wall despite being subjected to pure in-plane action (Figure 4.2b). The Out-of-plane deformation initiated at Point F in the analysis and progressively increased during the following cycles.

Figure 4.3a displays the steel strain measurements of the specimen at wall base in comparison with the model predictions at the positive peak of selected drift cycles. Due to a gage malfunction the measurements were taken up to 0.56% drift in some parts and 1.1% drift at the tension boundary element. The nonlinear strain gradient along the length of the wall, which is usually neglected in simplified analysis methods, is predicted by the analysis with a relatively good agreement with the measured steel strain profile. Since the reinforcement elements are fully bonded in the analysis, the predicted strain profiles are identical for concrete and reinforcement. As shown in Figure 4.3a, although the bond-slip effect is not considered in the analysis, the agreement between the predicted strain profile of the wall section and strain measurements of the reinforcement in the test is reasonable. The strain profile at 1.1% drift level follows the same trend as the one at 0.56% drift level, but understandably with considerably greater strain values. The predicted neutral axis position matched well with test results as well. Figure 4.3b shows the vertical displacement of the mid-length node at the top level of the wall indicating the wall elongation due to the residual strain developed in the reinforcement. Figure 4.4 displays the maximum out-of-plane displacement vs top displacement of the wall at both boundary zones.

The instability of the wall at different stages of loading due to out-of-plane deformation is further indicated in Figure 4.3b. As can be seen in this figure, Point F (initiation of out-of-

plane deformation) corresponds to a sudden considerable drop in the elongation curve. The degradation reaches its maximum level as the out-of-plane deformation reaches its peak between Points F and G1 (Figure 4.4a). The wall moved up thereafter as the out-of-plane deformation recovered. This recovery was helped by the compressive stress sustained through the concrete elements located on the compression side of the buckled section. A similar trend is observed in the following cycles and with a considerable degradation and failure of the model at Point H (ultimate point). The degradation and failure of the model was due to the compressive stresses reaching the maximum strength of the confined concrete at the base and at the section with out-of-plane deformation. Initiation and development of out-of-plane deformation is described in more detail in the following sections.

According to the test report, the first significant flexural cracking occurred in Cycle 4 (0.06% drift) at a load of 66.7 kN (15 kips). First yielding occurred in Cycle 19 (0.6% drift) at a load of 164.6 kN (37.0 kips). Minor spalling and flaking were first noted along horizontal web cracks in the lower 0.91 m (3 ft) in Cycle 19. In the first 76.2 mm (3 in., 1.7% drift) deflection, Cycle 25, it was noted that the cracks in the compression zone remained open 0.076 mm (0.003 in.). First indication of crushing of the outer shell at the base of the wall was noted in Cycle 22. A significant increase in spalling and flaking along the horizontal cracks was observed during the 76.2 mm (3 in., 1.7% drift) cycles. During Cycle 28, at 25.4 mm (1 in., 0.6% drift) deflection cycle after the 76.2 mm (3 in., 1.7% drift) cycles, bowing of the compression side of the wall was observed. The compression boundary element moved 6.4 mm (0.25 in.) out-of-plane at a point 1.1 m (3.5 ft) above the base. Although this bowing progressed further during subsequent cycles, the load carrying capacity of the wall remained stable. An omni-direction ball caster was placed against the face of each boundary element at 1.1 m (3.5 ft) above the base. This simulated lateral support at approximately the first story height. The test was continued with the 101.6 mm (4 in., 2.2% drift) deflection cycle. Considerable out-of-plane deformation was observed during the 127 mm (5 in., 2.8% drift) deflection cycles, which progressed further until the strength dropped severely in the 6 in. deflection cycle.

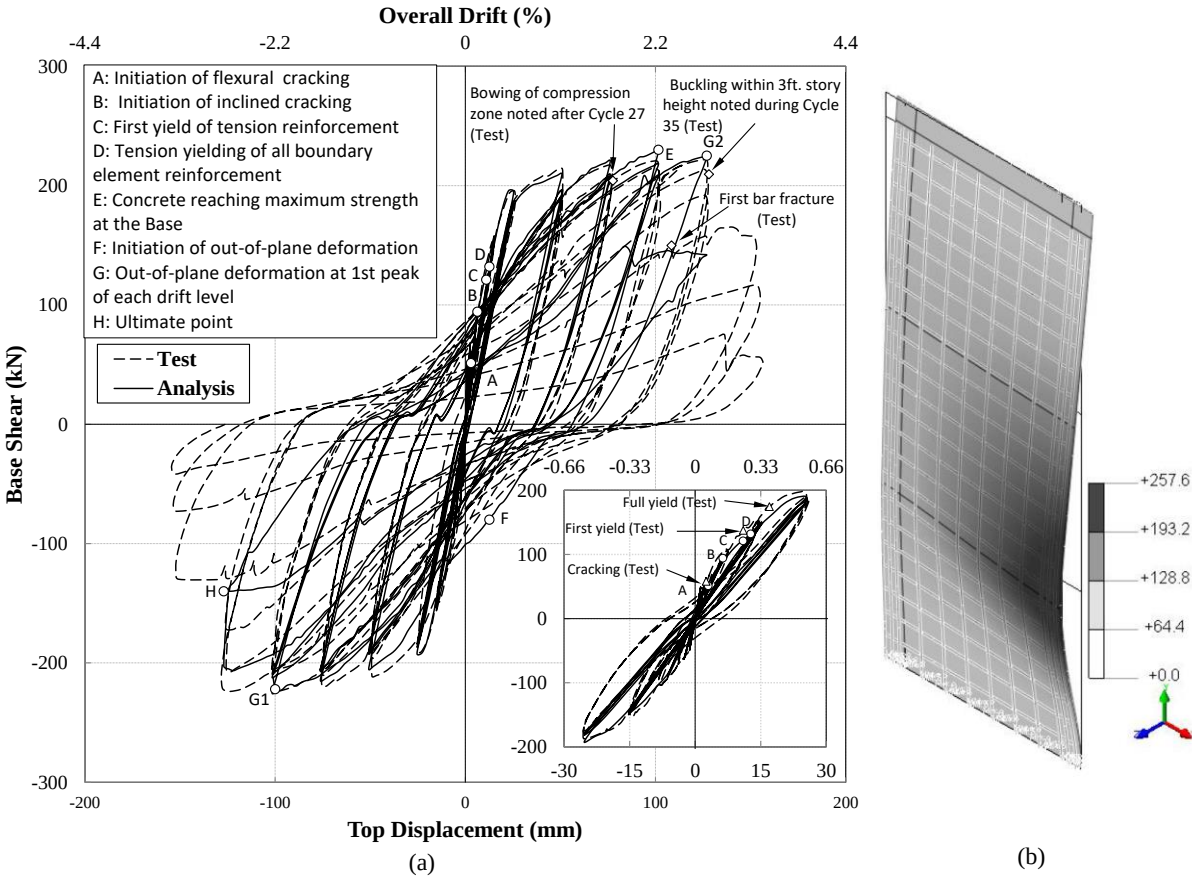

Figure 4.2: Response of the model for Specimen R2: (a) lateral load vs top displacement response; (b) out-of-plane deformation corresponding to Point G2, mm

In the analysis, flexural cracking initiated at 0.03% drift at a load of 51 kN and inclined cracks were observed at 0.14% drift at a load of 94 kN (Figure 4.2a, Points A&B). First yield of tension reinforcement occurred at 0.2% drift at a load of 121 kN and all the tension boundary element reinforcement yielded at 0.28% drift and a load of 132 kN (Figure 4.2a, Points C&D). The strain profile of the specimen at 0.28% drift (Figure 4.3) shows the neutral axis position is very close to the right end of the wall; thereby indicating that the unconfined concrete elements did not sustain much compression and most of the compressive stress was resisted by the confined boundary zone. The concrete in the right boundary zone reached the maximum strength at the end of 2.22% drift cycle (Figure 4.2a, Point E). While reversing from the positive peak drift, the compression boundary zone of the wall started to deform along the out-of-plane direction at a point 1.3 m (4.3 ft) above the base despite being subjected to pure in-plane action (Figure 4.2a, Point F). The height at which the out-of-plane deformation initiated in the analysis (1.3 m) is reasonably close to the one observed in the test (1.1 m). This deformation increased as the drift reached -2.2%, and this phenomenon repeated during the subsequent drift cycles in both directions (Figure

4.2a, Points G1 and G2). It should be noted that at Points F, G1 and G2 which correspond to the initiation and development of out-of-plane instability, there is no degradation in the lateral load-top displacement response of the specimen as shown in Figure 4.2a while Figure 4.3b displays noticeable degradations corresponding to the initiation and development of out-of-plane deformation. This can be attributed to the fact that out of plane deformation resulted in earlier closure of the cracks in compression part of the section, contributing to load carrying capacity of the wall via redistributing the compression stresses. In other words, as a result of the out-of-plane deformation, a considerable portion of the compression previously concentrated at the base (Point E) was transformed to the compression side of the section exhibiting out-of-plane deformation. At point H, due to the compressive stresses reaching the maximum strength of the confined concrete at the base and at the section with out-of-plane deformation, the wall became unstable.

As can be seen in Figure 4.4, the maximum out-of-plane deformation occurred alternately at the right and left boundary zones, whichever was under compression, and increased drastically after the 101.6 mm (4 in., 2.2% drift) cycle. The first 101.6 mm (4 in., 2.2% drift) cycle shows considerable recovery of the out-of-plane deformation along with the top displacement reaching the peak value of the cycle (Figure 4.4a, Point G1). The out-of-plane deformation increased along with the top displacement in the second and third cycles. Finally, the out-of-plane deformation became considerably larger during the first and second cycles of 127 mm (5 in. 2.8% drift) cycle resulting in instability of the model at Point H.

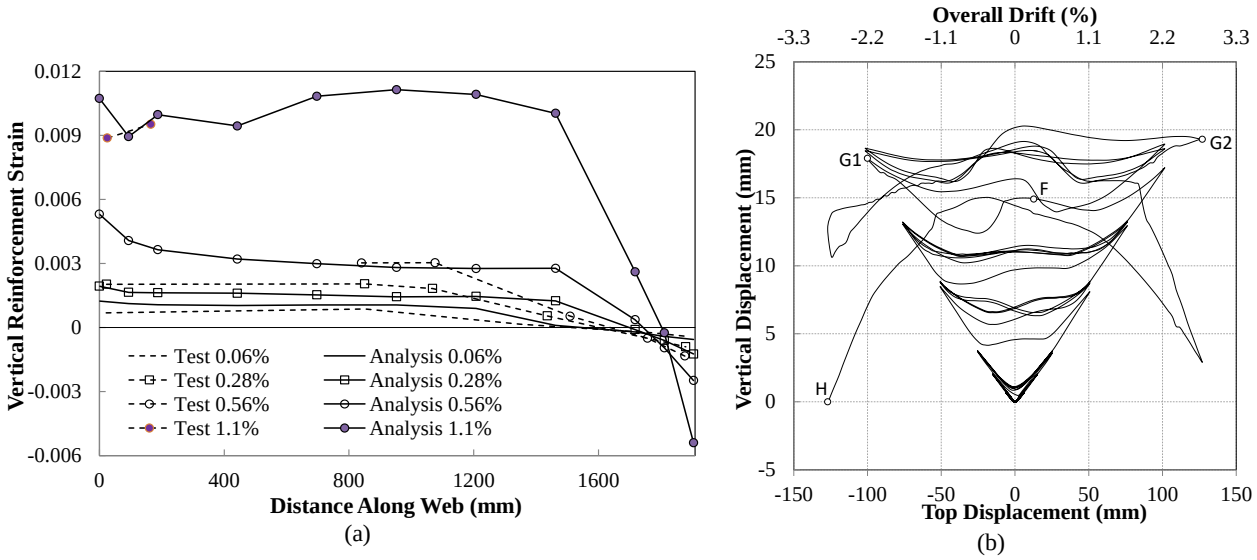

Figure 4.3: Numerical model predictions for Specimen R2: (a) variation of the vertical reinforcement strain along the wall length; (b) vertical displacement (uplifting due to plastic hinge elongation) at mid-length of the specimen

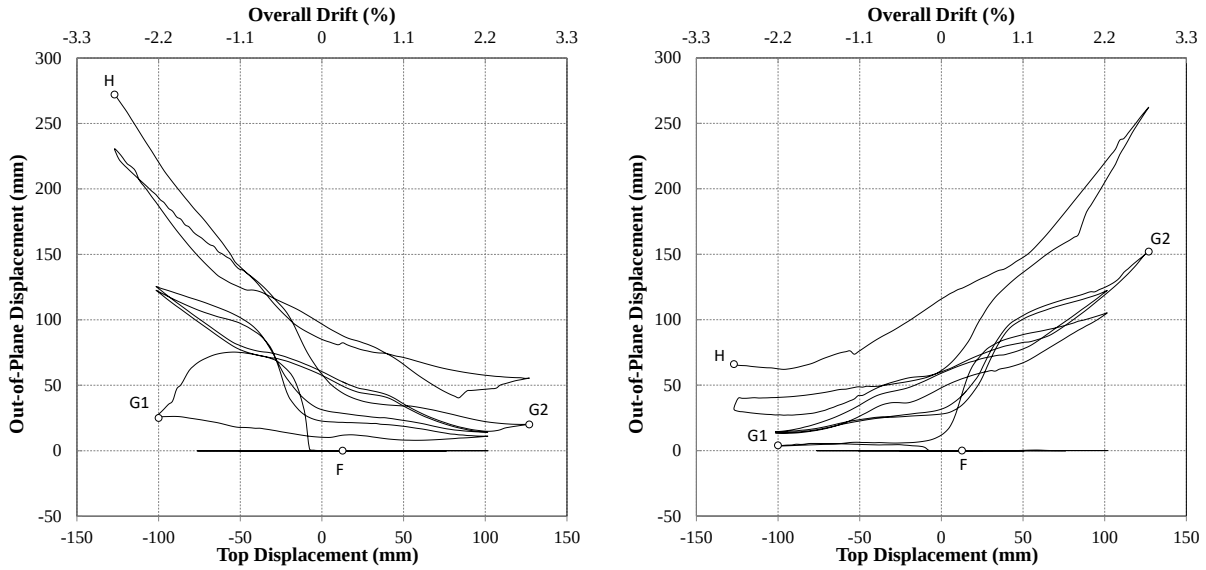

Figure 4.4: Numerical prediction of maximum out-of-plane displacement for Specimen R2: (a) left boundary zone; (b) right boundary zone

The element used in the model (curved shell element) has integration points along the thickness unlike flat shell elements in which the integration is done at one plane only. This element can easily capture bifurcation induced failure patterns. Some examples are provided by the program developers in documentation of DIANA (DIANA 2011) which use this element for capturing buckling failures. During unloading and reloading of a cracked wall section, the compression is taken by the reinforcement only until the crack closes and concrete restarts contributing to the load carrying capacity. This phenomenon is mainly controlled by residual strain of the reinforcement. At this stage, the wall section is more likely to deform in a pattern that requires less energy. In this method there is no need to introduce an artificial eccentricity that introduces a secondary bending moment, and out-of-plane deformation can be captured even under perfectly concentric in-plane loading.

4.1.2 SPECIMEN 3 (BEATTIE 2004)

Development of out-of-plane deformation has been verified using experimental results of a singly reinforced slender wall tested by BRANZ research company (Beattie 2004), as well, for which the history of out-of-plane displacement was measured during the test. Figure 4.5 shows the cross section and reinforcement layout of this specimen. The simulated response is compared with the experimental measurements in Figure 4.6.

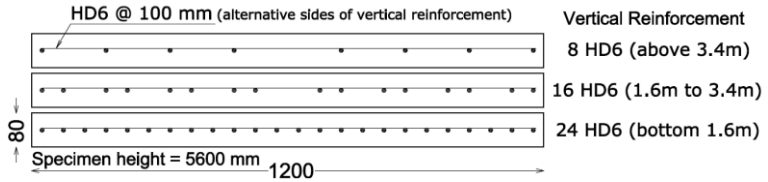

Figure 4.5: Cross section and reinforcement layout of Specimen 3 (Beattie 2004)

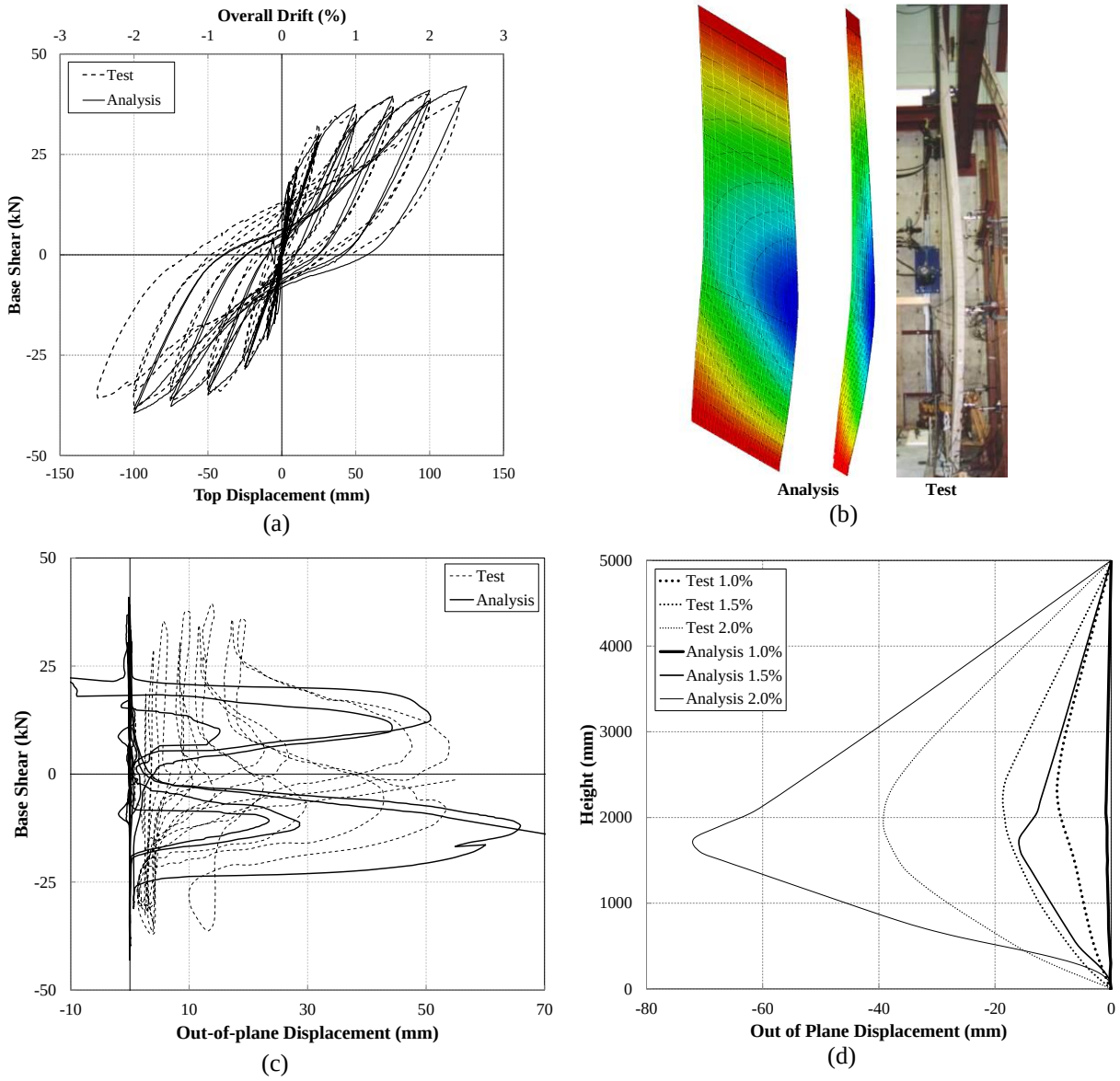

Figure 4.6: Simulation of out-of-plane instability in Specimen 3 (Beattie 2004): (a) lateral load vs top displacement response; (b) simulated vs experimental out-of-plane deformation; (c) out-of-plane displacement vs base shear at 2.5m above the base; (d) out-of-plane displacement profile along the height of the wall at different drift levels

The lateral load-top displacement response is reasonably predicted (Figure 4.6a) and the out-of-plane deformation pattern of the numerical model complies with the test observations (Figure 4.6b). The development of out-of-plane deformation at 2.5 m above the floor at one end of the panel and the out-of-plane displacement profile of the model are

compared with the test results in Figure 4.6c and Figure 4.6d, respectively, which indicate the fast growth of out-of-plane deformation in the numerical model in comparison with the test results. As can be seen in Figure 4.6d, the out-of-plane displacement predicted by the numerical model is quite small during 1.0% drift level, which increases considerably during the subsequent drift levels leading to an out-of-plane displacement value that is 70% higher than the test measurements during 2.0% drift level. The increase in out-of-plane displacement made the model unstable and resulted in termination of the analysis before reaching -2.5% drift level (Figure 4.6a).

4.1.3 SPECIMEN RWN (JOHNSON 2010)

Next, the test results of Specimen RWN (Johnson 2010) are used for further verification of the model. Figure 4.7 shows the cross section and reinforcement layout of this specimen. Figure 4.8 compares the numerical simulation with the experimental observations. The lateral load-top displacement response has been predicted quite reasonably except for the peak negative strength which is overestimated by the model. However, this discrepancy has been observed in some other numerical simulations of Specimen RWN such as Aaleti (2009) and Encina and Henry (2015). Figure 4.8b compares the out-of-plane displacement profile of the model with the test measurements at 2.0% drift level, and the deformation pattern of the model is compared with the one observed during testing in Figure 4.8c. It should be noted that development of the out-of-plane displacement was considerably fast in this specimen when compared to the test measurements.

The model could reasonably predict the load-deflection response and the out-of-plane deformation which increased up to a certain level and recovered considerably at the peak displacement of the corresponding cycle. This trend seems to indicate a reasonable correlation with the level of residual tensile strain reached by the reinforcement in the previous cycles as the maximum out-of-plane deformation happens when the compression is carried by the reinforcement only. This issue is currently under investigation by the authors and complies with the postulation given by Paulay and Priestley (1993) as well as experimental investigations of idealized columns typifying wall boundary regions (Chai and Elayer 1999).

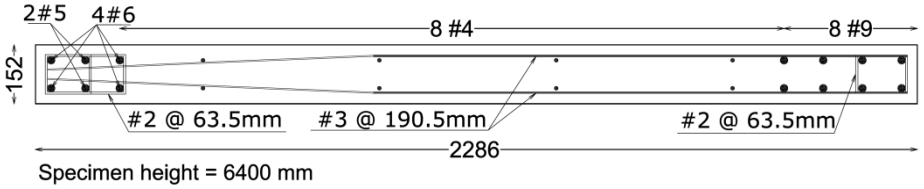

Figure 4.7: Cross section and reinforcement layout of RWN (Johnson 2010)

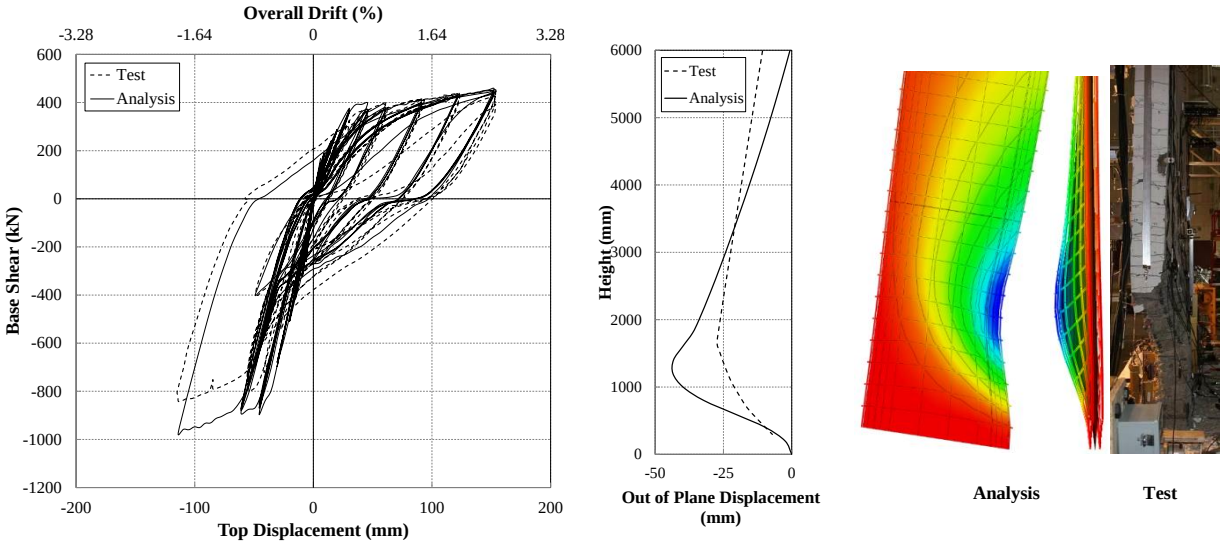

(a) (b) (c)

Figure 4.8: Simulation of out-of-plane instability in Specimen RWN (Johnson 2010): (a) lateral load vs top displacement response; (b) out-of-plane displacement profile along the height of the wall following 2.5% drift level; (c) simulated vs experimental out-of-plane deformation

4.1.4 EFFECT OF BAR BUCKLING: SPECIMEN PW4 (BIRELY 2013)

Inclusion of bar buckling in nonlinear response prediction of a wall would require either of the following approaches:

1- Using solid elements for both concrete and reinforcement to be able to mesh the cross section of a bar such that the strain variation along its cross section along with geometric nonlinearity can simulate bar buckling. This approach would immensely add analytical computational effort.

2- Using strain-based buckling models (e.g., Dhakal and Maekawa 2002) into the Menegotto-Pinto steel model. However, in the current modeling approach it is possible to track the strain-state of the main bars in the analysis and check if the strain corresponding to buckling-induced degradation of the material constitutive model (as per Dhakal and Maekawa model) has reached.

In order to address the effect of bar buckling on response of the model, a slender RC wall specimen PW4 tested by Birely (2013) was simulated as well. Figure 4.9 shows the

geometry and reinforcement configuration of the specimen as well as its numerical vs experimental lateral load-top displacement response. According to Figure 4.9b, the cyclic response of the specimen was well captured by the analysis. The considerable drop of strength observed in the experimental response during the second cycle of 1.0% drift is due to extensive bar buckling and core concrete crushing as well as out-of-plane deformation in the east (right) boundary element at the toe of the wall. Since bar buckling was not taken into account in the analysis, the numerical model did not predict the loss of load carrying capacity. Therefore, 1 more cycle of 1.5% drift was applied to the model to investigate the likelihood of out-of-plane instability, which did initiate as the model reached zero displacement while unloading from +1.5% drift.

The model expectedly could not capture the main failure pattern of the specimen which was characterized by bar buckling. However, it could capture the out-of-plane deformation of the specimen but to a greater extent than what was observed in the test before bar buckling, which may have perhaps been suppressed by the bar buckling. Figure 4.10a and Figure 4.10b show the experimental observations of the specimen corresponding to the failure stage and Figure 4.10c displays the out-of-plane deformation pattern of the numerical model. The principal tensile strain distribution shows significant residual strain in the specimen at 0.0% drift level, which is known as one of the main parameters controlling out-of-plane deformation of rectangular walls.

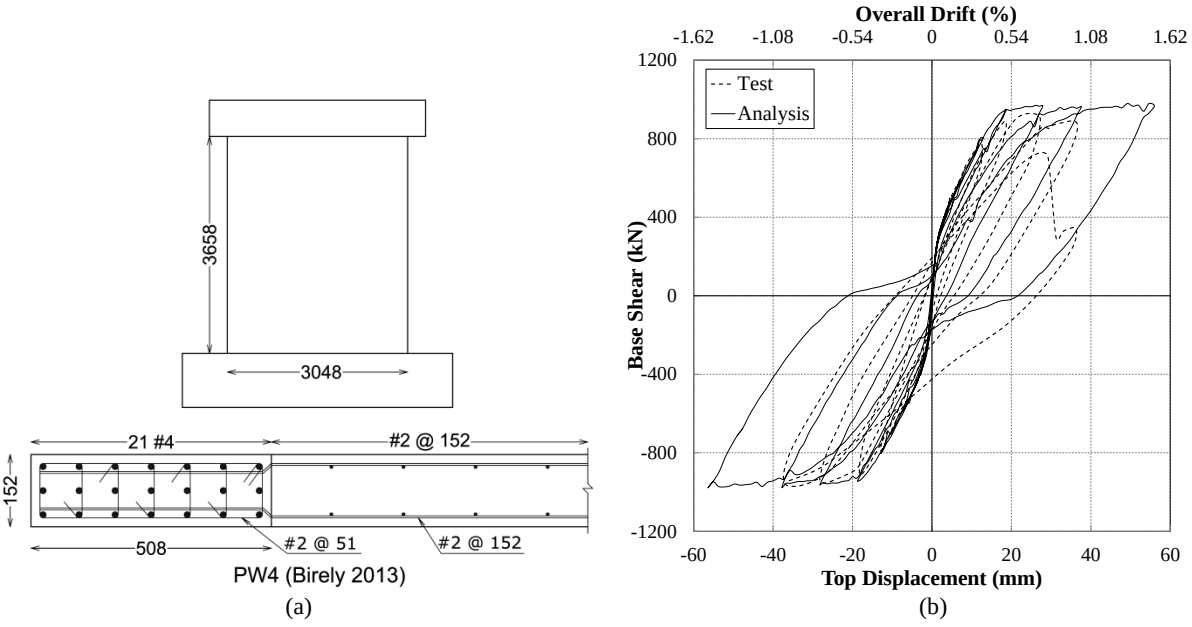

Figure 4.9: Specimen PW4: (a) geometry and reinforcement configuration; (b) lateral load-top displacement response

The stress-strain curve of the reinforcing steel is captured for the extreme end longitudinal bars, and its propensity to buckling is scrutinized by using the strain-based buckling model proposed by Dhakal and Maekawa (2002a, b). This buckling model accounts for the effect of the axial stiffness of the transverse reinforcement in calculation of the buckling length. According to the detailing of the transverse reinforcement shown in Figure 4.9a, the extreme end longitudinal bars were restrained by transverse hoops of #2 located at 51 mm spacing which surrounded all the boundary zone bars. These hoops, extending over the whole length of the boundary zone, provided a very low amount of stiffness against buckling of the three extreme end bars, and according to the buckling model mentioned above, would result in a buckling length equal to four times the spacing of the transverse reinforcement. These bars would have a buckling length to bar diameter greater than 15, and the aforementioned buckling model results in considerable degradation of these bars' average compressive strength after yielding with 20% loss of compressive strength at a strain value of around -0.012. Figure 4.10a shows the buckling length extending over at least three confinement hoops. As can be seen in this figure, bar buckling had resulted in opening of the confining hoops leading to the loss of the confinement at the base of the boundary region and an abrupt strength degradation due to bar buckling and concrete crushing of the compression boundary region.

The strain history of the extreme end bars of the numerical model showed that the strain value reached -0.0017 at initial stages of loading and, due to the accumulation of residual strain under cyclic loading, did not go below zero at higher drift levels even when the stress reached relatively high in compression. However, the stress-strain plot of the extreme end bars captured from the numerical model showed that the strain changed from +0.011 (at zero stress during unloading) to +0.001 (when the bar stress was maximum in compression) during the 1.0% drift cycle. In other words, the bar strains, despite being positive throuout the 1.0% drift cycle, decreased by about 0.01 mm/mm when the bar stress increased from zero to its maximum value in compression. As stated earlier, this amount of strain variation would result in the bars losing more than 20% of their compressive stress according to the Dhakal and Maekawa (2002b) buckling model. This is in line with the experimental response which shows an abrupt reduction of the wall strength after the buckling of bars.

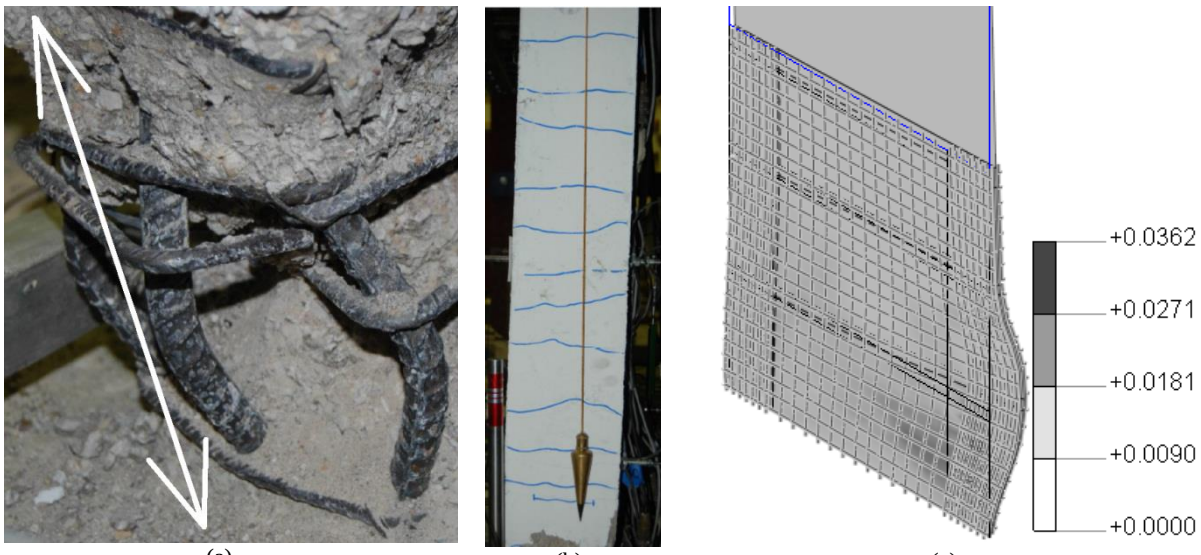

(a) (b) (c)

Figure 4.10: Numerical vs experimental failure of Specimen PW4: (a) bar buckling of the specimen (Birely 2013); (b) out-of-plane displacement of the specimen observed at 1.0% drift (Birely 2013); (c) principal tensile strain prediction of the numerical model, E1 (mm/mm) at 0.0% drift reversing from 1.5% drift

4.2 DEVELOPMENT OF OUT-OF-PLANE DEFORMATION AND THE CONTROLLING PARAMETERS

In order to scrutinize the development of out-of-plane deformation in rectangular walls, the numerical model of Specimen R2 was subjected to only one cycle at each drift level. Some points in the 101.6 mm (4 in., 2.2% drift) cycle are further investigated in Figure 4.11a, and the maximum out-of-plane deformation at boundary zones of the model at these points is indicated in Figure 4.11b. Deformation pattern of the wall at different stages is illustrated using vertical and horizontal section cuts in Figure 4.12. The vertical strain and stress gradients of the reinforcement and concrete elements at Section 2-2, where the out-of-plane deformation initiated, and corresponding to the points noted above are shown in Figures 4.18-4.23. Wall faces as well as the loading direction are also displayed in these figures. The deformation pattern along the wall thickness and at both ends of the wall is shown graphically in Part a of each figure to further clarify the consistency of stress and strain gradients with the out-of-plane deformation. C and T stand for the compressive and tensile stresses applied to the reinforcement, respectively. The schematic crack opening is compatible with the strain gradient displayed in Part b of each figure. With reference to Figures 18-25, the development of out-of-plane instability in the wall specimen can be described using the stress and strain variations in reinforcement and concrete elements along the section undergoing out-of-plane deformation. The value of reinforcement strain corresponding to different stages of this type of wall response indicates the effect of

residual strain of reinforcement on recovery of out-of-plane displacements or its increase and formation of out-of-plane instability. The trend of material behaviour at different stages of out-of-plane deformation is in line with the postulations well described by Paulay and Priestley (1993), and results of the experiments conducted by Chai and Elayer (1999) on some column specimens representing boundary regions of rectangular walls.

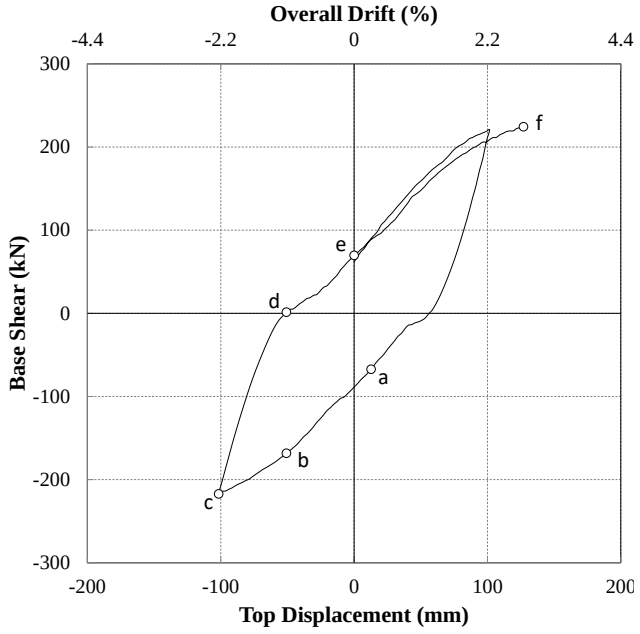

(a)

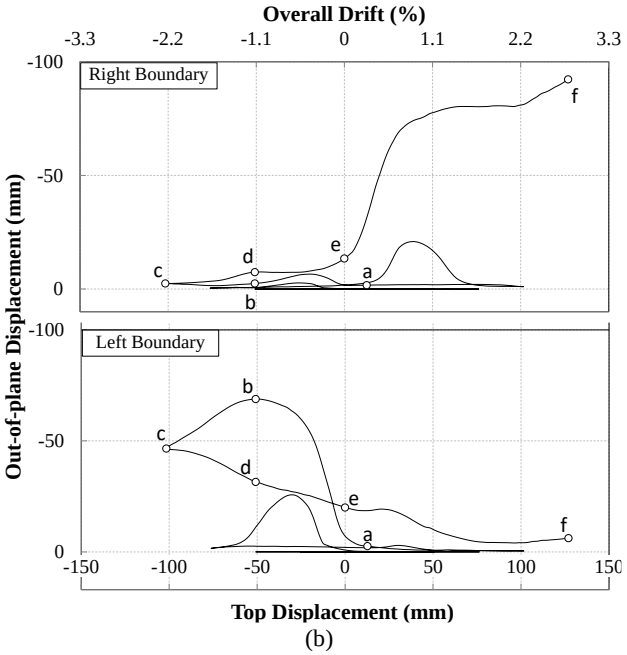

(b)

Figure 4.11: Points corresponding to occurrence of the out-of-plane instability in 101.6mm (4in) cycle: (a) base shear vs top displacement; (b) maximum out-of-plane displacement at boundary zones

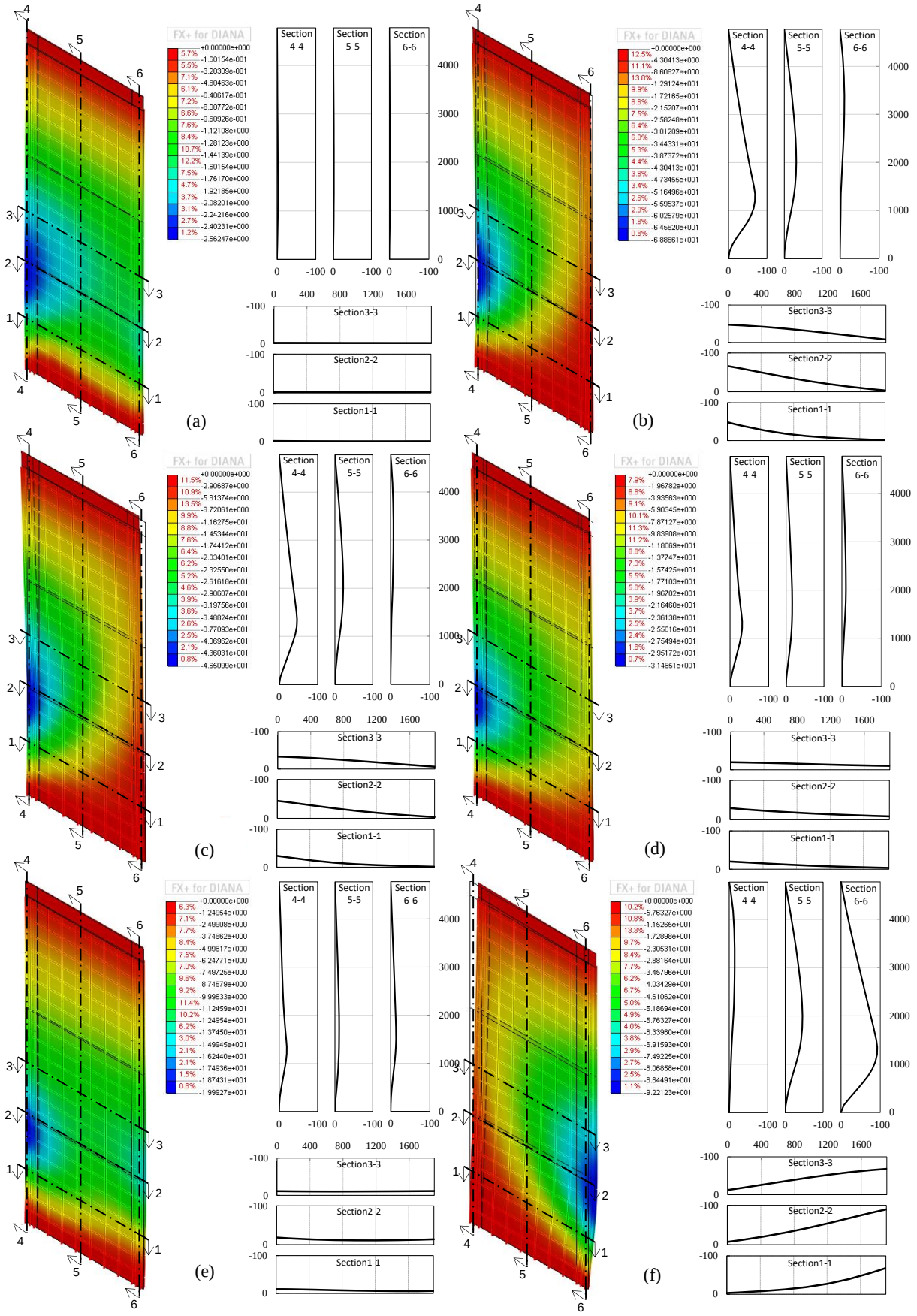

Figure 4.12: Out-of-plane deformation of the specimen (all dimensions in [mm]); Figures (a)-(f) correspond respectively to points (a)-(f) in Figure 4.11

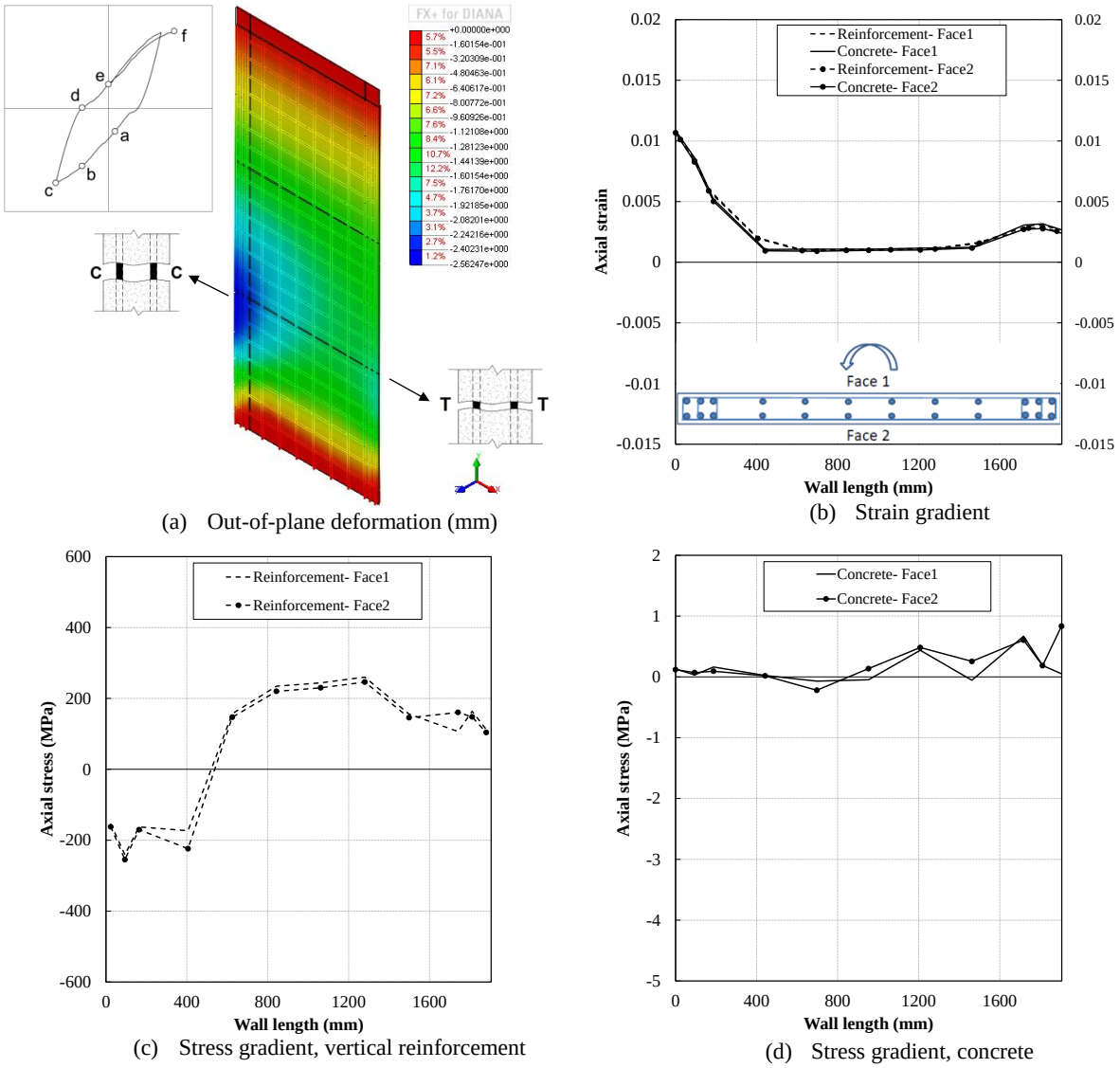

(a) Out-of-plane deformation (mm)

(b) Strain gradient

(c) Stress gradient, vertical reinforcement

(d) Stress gradient, concrete

Figure 4.13: Response of the wall model, Point a

Point a corresponds to initiation of the out-of-plane deformation (-2.6 mm, Figure 4.12a). At this point, the model has already been unloaded from the top displacement of +101.6 mm (4 in., 2.2% drift), reversing towards -101.6 mm (4 in., 2.2% drift) and is sustaining the top displacement of 12.7 mm (0.3% drift). Figure 4.13b displays the considerable residual strain of the reinforcement and concrete elements remaining from the previous peak displacement. The previous tension side is under compressive stress at this point but the residual strain is large enough not to let the compression side experience a compressive strain. Figure 4.13c shows the compressive stress developed in vertical reinforcement elements at the compressive side of the wall while the corresponding concrete elements undergo a very small tensile stress which can be attributed to the fact that the cracks have not closed at this stage. Consequently, only the reinforcement elements carry the axial compression.

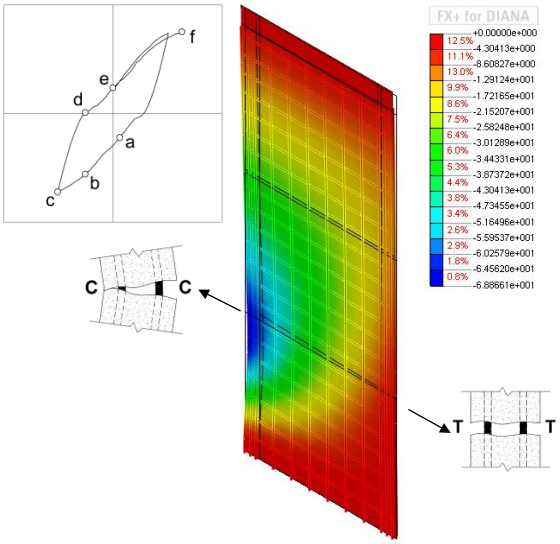

(a) Out-of-plane deformation (mm)

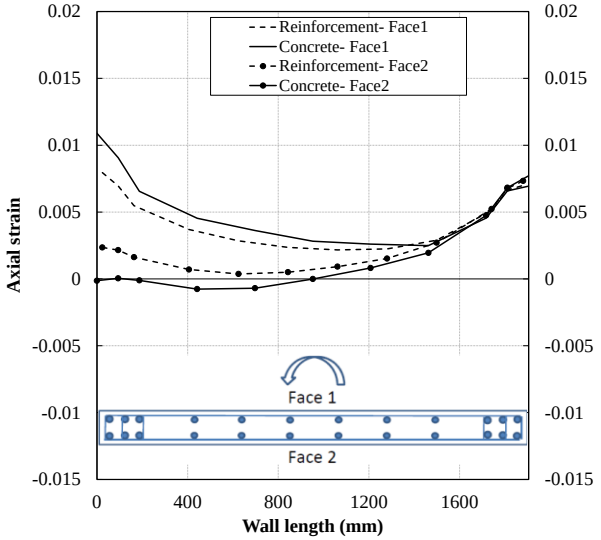

(b) Strain gradient

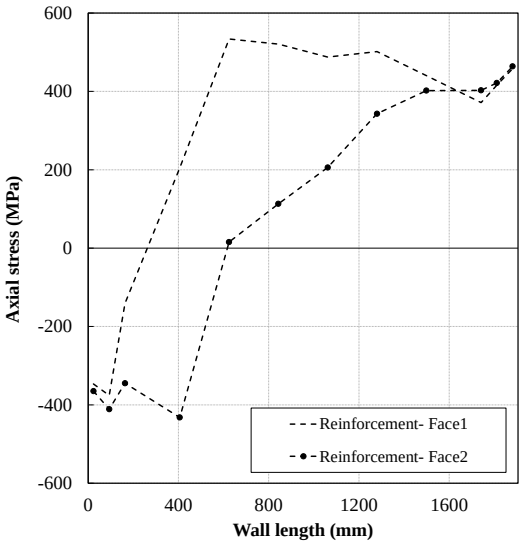

(c) Stress gradient, vertical reinforcement

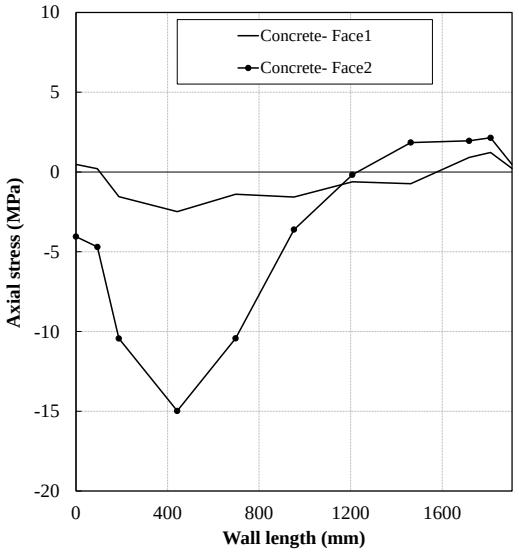

(d) Stress gradient, concrete

Figure 4.14: Response of the wall model, Point b

As shown in Figure 4.11, the out-of-plane deformation increases at the left boundary with increase of the top displacement until reaching Point b (-1.1% drift) and gradually decreases as the wall approaches Point c (-2.2% drift). The maximum out-of-plane displacement at Point b is 69 mm (Figure 4.12a) which is about 27 times greater than the one at Point a (Figure 4.12b). As shown in Figure 4.14, due to the out-of-plane deformation, strain profiles of the concrete and reinforcement elements depend on their position along the wall thickness with the outer layers (concrete layers) experiencing the extreme values. Also, the stress gradients of the reinforcement and concrete elements show greater compressive stresses for the elements located at Face 2. The out-of-plane deformation apparently closes the cracks at Face 2, as shown in Figure 4.14a, resulting in greater compressive stresses at this face. This crack closure can be considered as the main

reason why the lateral load-top displacement curve of the specimen does not show any strength degradation after initiation of out-of-plane deformation at Point F despite causing a sudden drop in the vertical displacement (elongation curve) in Figure 4.3b.

Point c corresponds to -4in (-2.2% drift) top displacement. The maximum out-of-plane displacement at this point is 47 mm which is about 40% less than the one at Point b (Figure 4.12c). As shown in Figure 4.15, the main difference of this stage with Point b (Figure 4.14) is the strain profiles and the maximum stress sustained by concrete and reinforcement elements is almost identical. The strain sustained by tensile elements has increased considerably and accordingly the strain in the compression part has decreased. Also, the difference between strain profiles of Face1 and Face2 has decreased along with decrease of the out-of-plane deformation. The stress gradients do not show a significant change in maximum stresses of concrete and reinforcement elements, but the compression stress seems to transfer towards the left boundary zone showing more crack closure in that region due to higher drift level.

At Point d (zero base shear and -1.1% drift, Figure 4.11) the maximum displacement of the model in the out-of-plane direction is still considerable (31 mm, Figure 4.12d). At this point, the out-of-plane deformation has started to develop in the other boundary zone (Figure 4.12d, Section 6-6). Separation of the strain profiles of concrete and reinforcing at the right boundary of the wall (Figure 4.16b) shows the initiation of out-of-plane deformation in that side of the wall as well. The compressive stress of concrete elements in Face 2 is much smaller than that in Point c as a result of unloading. The reinforcement elements at the right side which are subjected to a considerable residual tensile strain undergo a maximum compressive stress of 100 MPa while the concrete elements are still under tension (Figure 4.16).

Further recovery of the previously formed out-of-plane deformation (Figure 4.12e, Section 4-4) is observed at Point e. At this point the top displacement applied to the wall is zero and the base shear is 70 kN. Strain gradient across the wall thickness (indicating out-of-plane deformations) exists throughout the length. The reinforcement elements on the left part of the wall which were earlier subjected to compression are now under tensile stresses and the ones on the right are compressed more. The concrete elements on the left side of the wall sustain compressive stresses at both faces, whereas the ones on the right side has begun to take compressive stresses at Face 2 which indicates the initiation of out-of-plane deformation in this region.

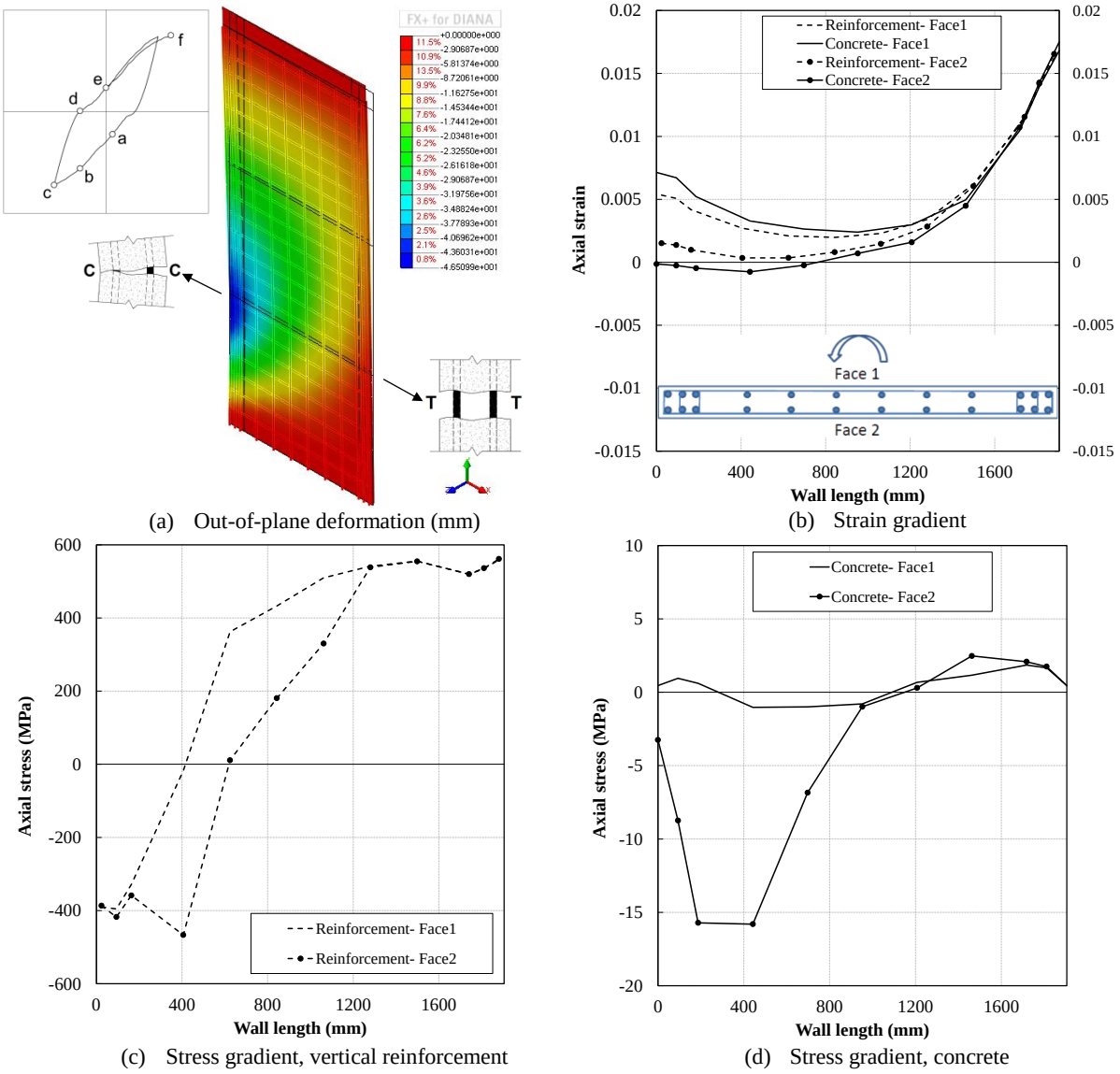

(a) Out-of-plane deformation (mm)

(b) Strain gradient

(c) Stress gradient, vertical reinforcement

(d) Stress gradient, concrete

Figure 4.15: Response of the wall model, Point c

After Point e, the out-of-plane deformation increases rapidly (Figure 4.11b) at the right boundary zone, but the rate of increase of out-of-plane deformation reduces while reaching around 0.7% drift level and remains almost constant between 1.4% and 2.2% drift levels and increases again while approaching Point f corresponding to 2.8% drift. The out-of-plane deformation is shifted to the right side (Figure 4.12f). The maximum out-of-plane deformation at this stage is almost 30% greater than the one observed in the previous cycle (Point b). At this stage, substantial out-of-plane gradient (Figure 4.18a) exists in the compression zone of the wall.

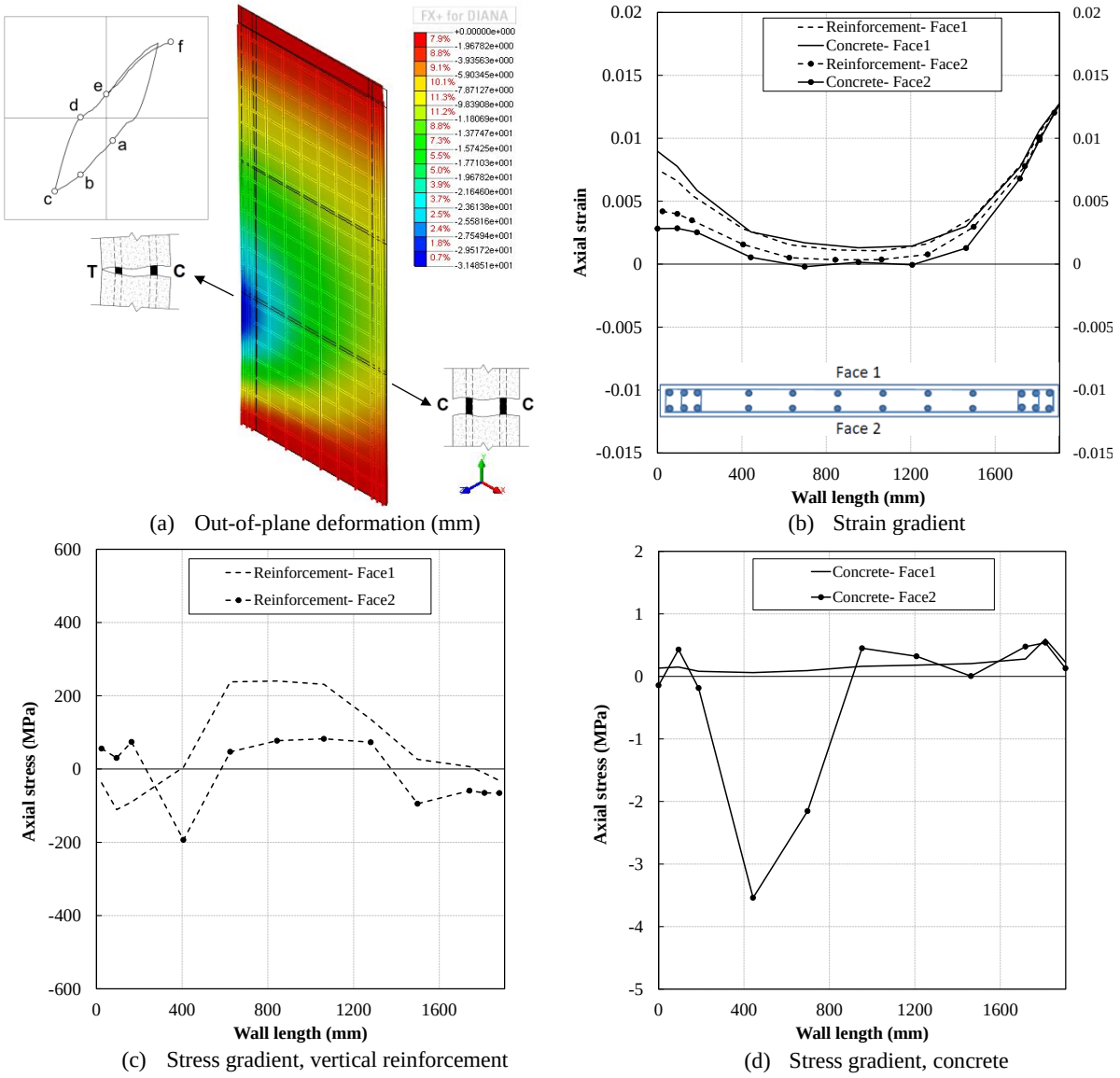

(a) Out-of-plane deformation (mm)

(b) Strain gradient

(c) Stress gradient, vertical reinforcement

(d) Stress gradient, concrete

Figure 4.16: Response of the wall model, Point d

Due to the out-of-plane deformation, more reinforcement elements are under compression in Face 2 when compared to Face 1, and concrete elements located in Face 2 undergo big compressive stresses while the ones in Face 1 change from compression to tension which is consistent with the deformation pattern of the wall at this point (Figure 4.12f). This stress distribution along the wall width can describe the reason the wall is still stable at this stage. In other word, the compressive stress in Face 2 contributes to load carrying capacity of the wall and prevents the wall instability.

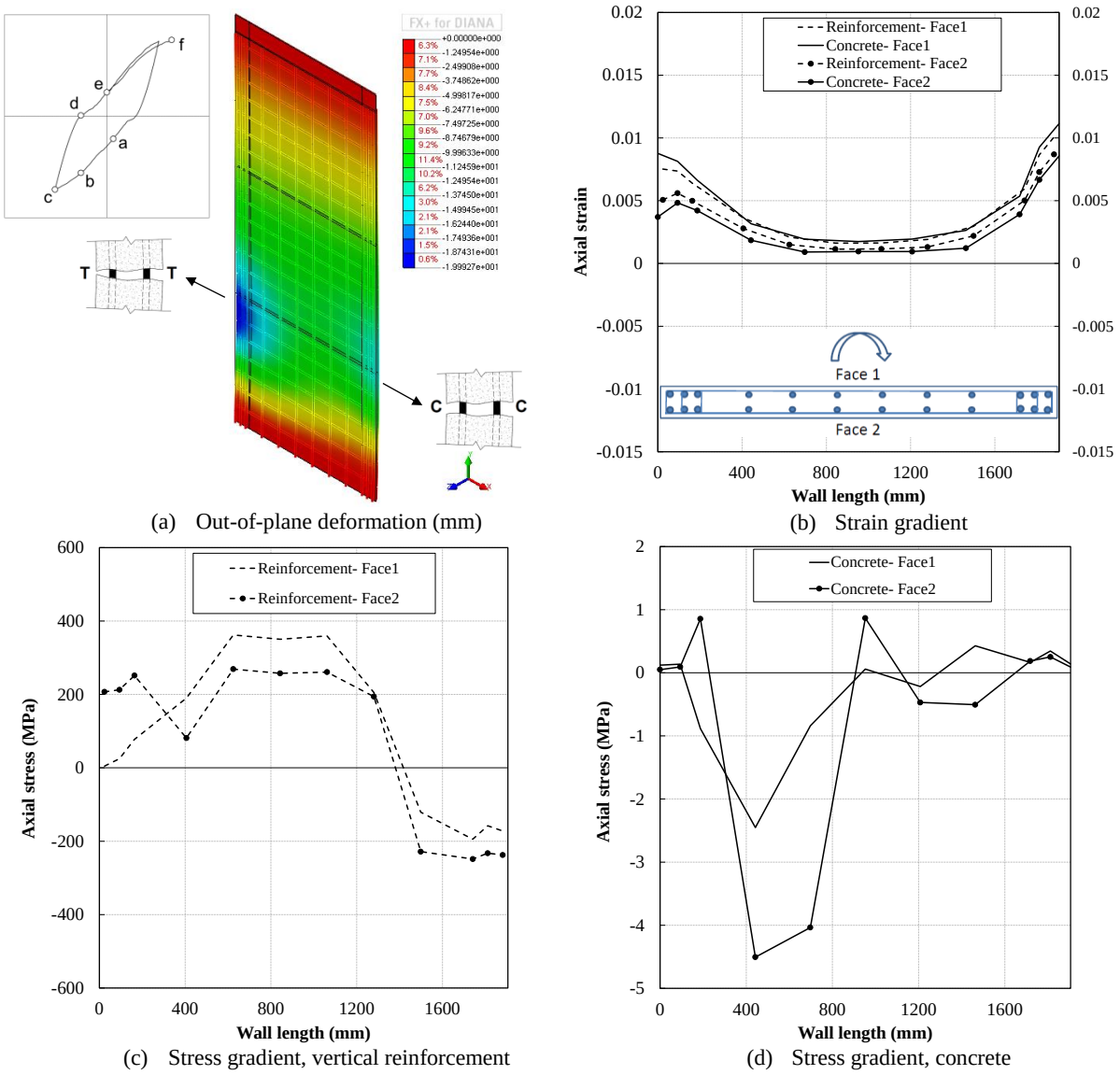

(a) Out-of-plane deformation (mm)

(b) Strain gradient

(c) Stress gradient, vertical reinforcement

(d) Stress gradient, concrete

Figure 4.17: Response of the wall model, Point e

The stress and strain gradients indicated in Figure 4.13 to Figure 4.18 clearly illustrate the combination of material response in a cracked wall section at different stages of loading resulting in development of out-of-plane instability. The key role of reinforcement strain which is controlling the crack closure at load reversal stages is quite obvious. Larger tensile strains can readily lead to development of larger compressive stresses in the reinforcement prior to crack closure and trigger earlier initiation of reinforcement yielding in compression and consequently earlier deformation of the wall in the out-of-plane direction which is apparently the direction requiring less energy for model deformation. Also, these figures show the variations of strain along the wall thickness which is the crucial capability of the curved shell element enabling it to simulate the out-of-plane deformations of walls under in-plane loading. This combination of material response describes the reason why the out-

of-plane deformation tends to start when a considerable amount of compressive stress is developed in the material resulting in its compressive yielding before crack closure and contribution of the concrete to load carrying capacity of the wall.

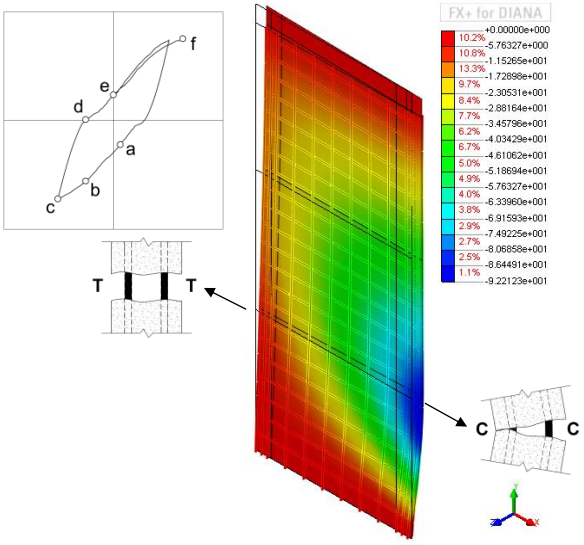

(a) Out-of-plane deformation (mm)

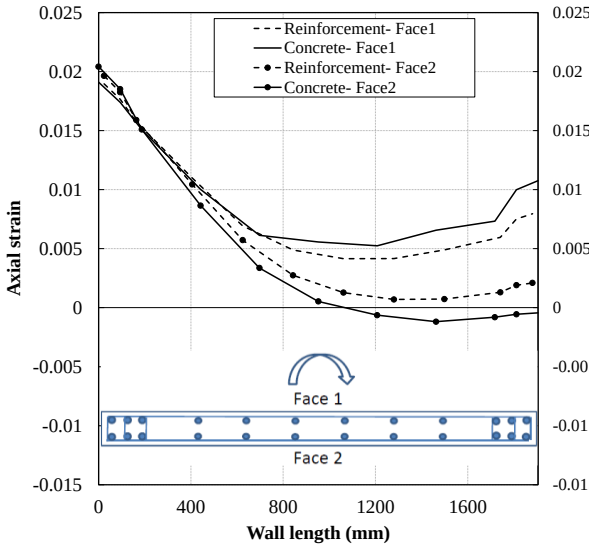

(b) Strain gradient

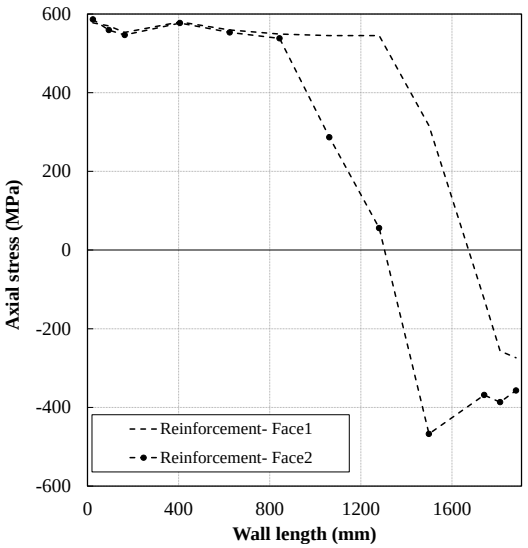

(c) Stress gradient, vertical reinforcement

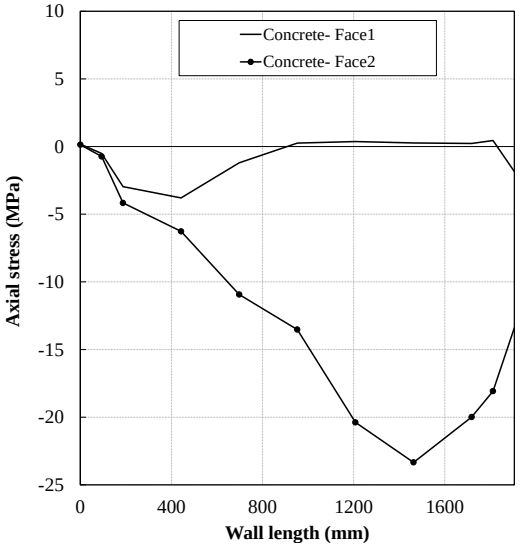

(d) Stress gradient, concrete

Figure 4.18: Response of the wall model, Point f

4.2.1 RESIDUAL STRAIN OF BOUNDARY REGION REINFORCEMENT

According to Paulay and Priestley (1993), at large curvature ductilities, large tensile strains may be developed in the vertical bars situated close to the extreme tension edge of a wall section. At this stage wide, near-horizontal cracks across the width of the section will develop over the extent of plasticity. During unloading of the wall, tensile stresses in these bars reduce to zero, while the crack width remains large, as a result of plastic tensile strains that developed in the bars, and a change in direction of the lateral load will produce compression stresses in the bars which must resist the internal compression force within the wall section until the cracks close.

The effect of reinforcement strain on development of out-of-plane deformation can be investigated using single cycles of loading, unloading, and reloading in the opposite direction (Dashti et al. 2015). The numerical model of Specimen R2 was subjected to a relatively large lateral displacement which could generate a considerable tensile strain in the boundary region reinforcement. The wall was then unloaded and reloaded up to a significant drift level in the opposite direction. Checking this process on different initial loading amplitudes, the reinforcement strain corresponding to initiation of out-of-plane deformation was derived. Figure 4.19a displays the top displacement history corresponding to initiation of out-of-plane deformation, and Figure 4.19b shows the maximum out-of-plane displacement of the left boundary zone versus top displacement of the model. Figure 4.20 displays the axial strain versus out-of-plane displacement response of the boundary region reinforcement for both layers of reinforcement at the section where the out-of-plane displacement was the greatest. The deformation pattern along the wall thickness is shown graphically to further clarify the sequence of events (C and T stand for the compressive and tensile stresses applied to the reinforcement, respectively). The same trend as observed in the idealized column specimens tested by Chai and Elayer (1999), shown in Figure 2.10, can be observed in this figure, and Points *a-d* correspond to the stages defined in Figure 2.10 and Table 2.1. However, Point *e* does not correspond to concrete crushing. Although the model was subjected to -6.0% drift level, the axial strain at Point *e*, as shown in Figure 4.20, is only -0.0004 which is far away from the axial strain capacity of the boundary zone confined concrete. In other words, the crack closure starting from Point *d* is completed after the wall has been subjected to a considerably large drift, and the main load carrying capacity of the cracked section was provided by the reinforcement only until the magnitude of axial strain reached zero. Also, the out-of-plane displacement predicted by the numerical

model initiated at Point *c* (corresponding to a considerable loss of stiffness, i.e. compression yielding, at both layers of reinforcement), while the development trend of out-of-plane displacement proposed by Chai and Elayer (1999), shown in Figure 2.10, displays a gradual initiation of out-of-plane displacement due to the inherent eccentricity of the axial force, followed by compression yielding of the reinforcement closer to the applied axial force. The out-of-plane displacement would increase due to reduction of the transverse stiffness caused by this reinforcement yielding and would grow rapidly if a further increase in the axial compression results in compression yielding in the second layer of the reinforcement, as indicated by the near horizontal Path *c-d* (Figure 2.10).

No eccentricities are accounted for in the numerical model as the outcome would greatly depend on the arbitrary value of the initial imperfections. The eccentricities could be associated with material properties (e.g., yield strain of reinforcement), positioning of the longitudinal bars and axial load along the wall thickness. The out-of-plane deformation predicted by the numerical model is mainly governed by compression yielding in the bars that are the main load carrying elements in a cracked wall section under compressive actions. The considerably abrupt increase of out-of-plane deformation in the numerical model can be attributed to the sudden reduction of the transverse stiffness caused by this phenomenon.

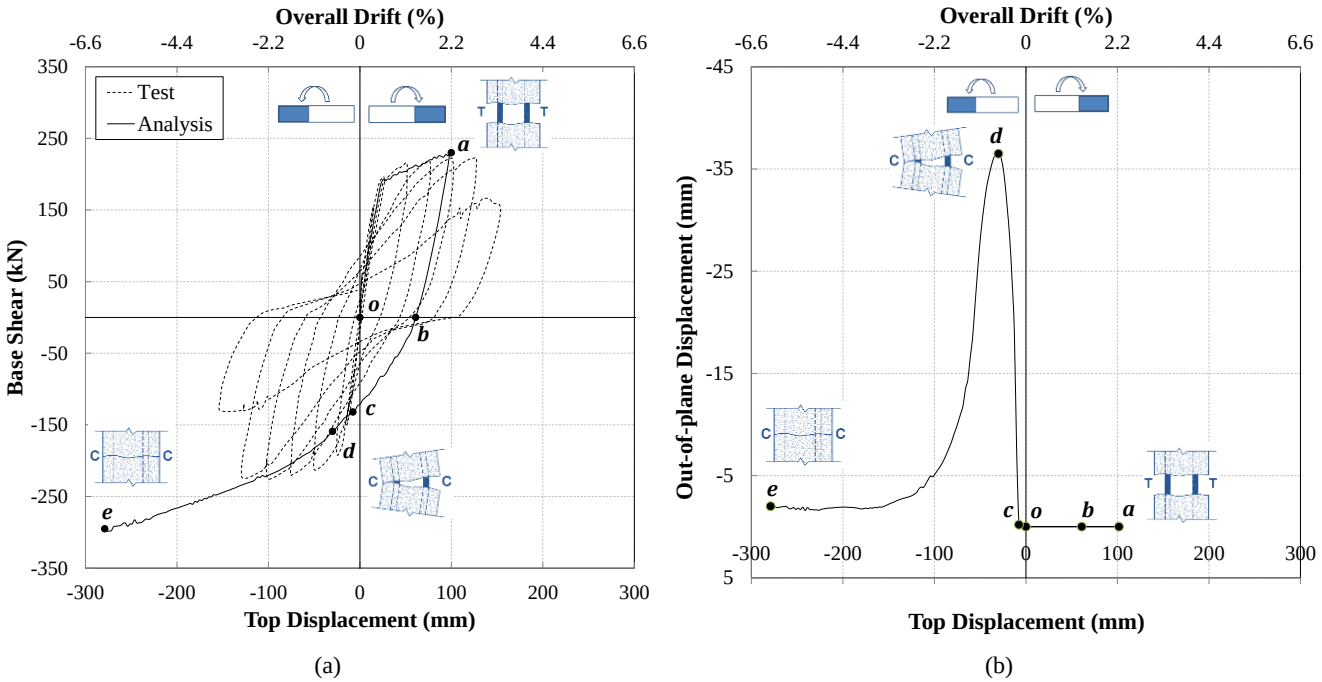

Figure 4.19: Response of the model: (a) lateral load vs top displacement response and comparison with experimental results; (b) maximum out-of-plane displacement

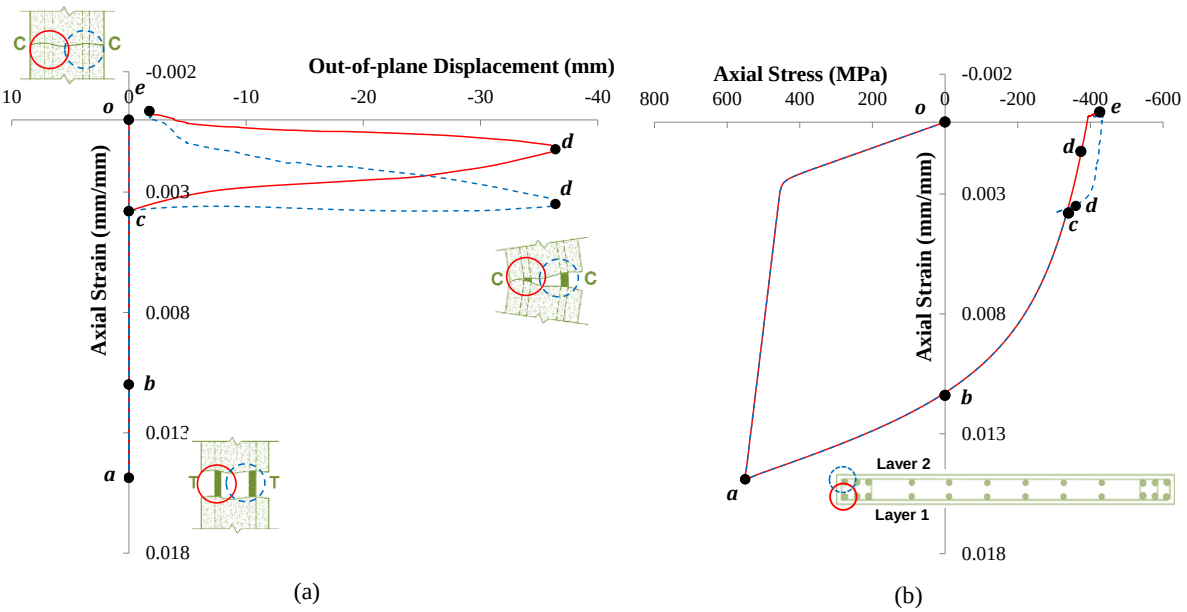

Figure 4.20: Axial reversed cyclic response of boundary region reinforcement: (a) axial strain versus out-of-plane displacement; and (b) axial strain versus axial stress

The wall was loaded up to Point *a* (Figure 4.19a), which resulted in development of a tensile strain of 0.015 (equivalent to about $6\varepsilon_y$) in the extreme end longitudinal reinforcement (Figure 4.20) at the section where the out-of-plane displacement was the greatest. The wall was then subjected to a loading reversal, as shown in Figure 4.19a. Figure 4.20a shows a significant amount of residual strain developed in the extreme end reinforcement at Point *b*, where the reloading in the opposite direction starts and the axial stresses change sign (tension to compression). The strain at this stage is equal to 0.011 ($4.4\varepsilon_y$). The reinforcing bar undergoing compressive stresses with this amount of residual tensile strain can easily experience considerable yielding in compression before the tensile strain reaches zero and cracks close. This compressive yielding, if developed along a sufficient height and length of the wall can provide ideal circumstances for deformation of the portion of the wall section under compressive actions in the direction that requires less energy, i.e., out-of-plane direction, until the cracks start closing in inner face of the out-of-plane displacement profile.

During Paths *o-a* and *a-b* (which correspond to loading and unloading stages, Figure 4.19a), the strain is identical in the two layers of reinforcement (Figure 4.20). As the out-of-plane deformation initiates at Point *c*, the reinforcement positioned in the inner face of the deformed section (referred to as Layer 1, Figure 4.20) undergoes a relatively bigger reloading in compression (recovering to smaller values of strain) for a given out-of-plane deformation when compared to the one in the outer face (referred to as Layer 2, Figure

4.20). The increase in out-of-plane displacement resulted in crack closure in the inner face at Point *d*, which in turn decreased the out-of-plane displacement during Path *d-e*, gradually reducing the difference between the axial strain values of the two layers of reinforcement. At Point *e*, the strain values at both layers of reinforcement are almost identical and are negative showing that the crack closure is almost complete with a rather minimal value of out-of-plane displacement.

Larger initial tensile strains were generated in the boundary region by applying a larger positive displacement in the model. Figure 4.21 displays the effect of this loading pattern on the response of the model. As can be seen in Figure 4.21a, the loading reversal after the model has been subjected to a larger displacement than the previous model resulted in considerable degradation starting from about -2.75% drift. This degradation was due to a continued increase in the out-of-plane displacement and eventual instability of the wall as the initial tensile strain was excessive and the subsequent compression did not result in the closure of the cracks and recovery of the out-of-plane displacement. This phenomenon is clearly shown in Figure 4.22. As shown in this figure, unlike in Figure 4.20, the response follows Path *d-f*, which is in line with the trend proposed by Chai and Elayer (1999) (Figure 2.10, Table 2.1). The initial tensile strain was equivalent to about $7.5\varepsilon_y$ in this case and the residual strain (Point *b*, Figure 4.22) was equivalent to about $5.7\varepsilon_y$.

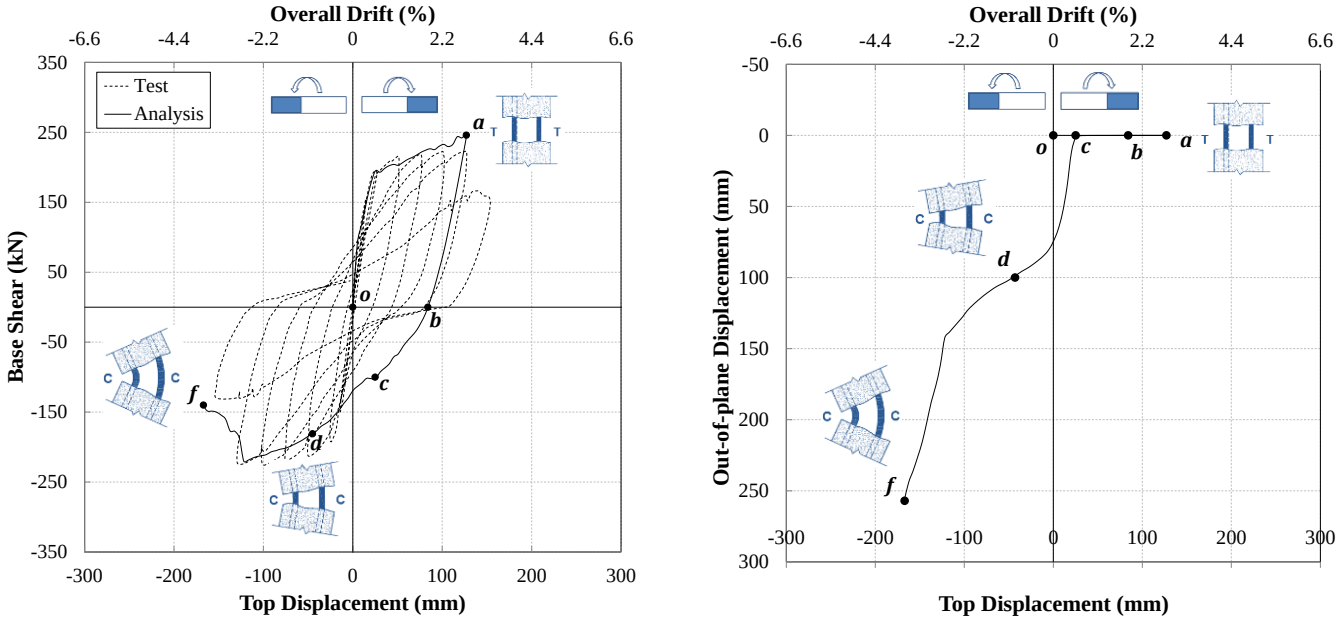

(a) (b)

Figure 4.21: Response of the model: (a) lateral load vs top displacement response; (b) maximum out-of-plane displacement

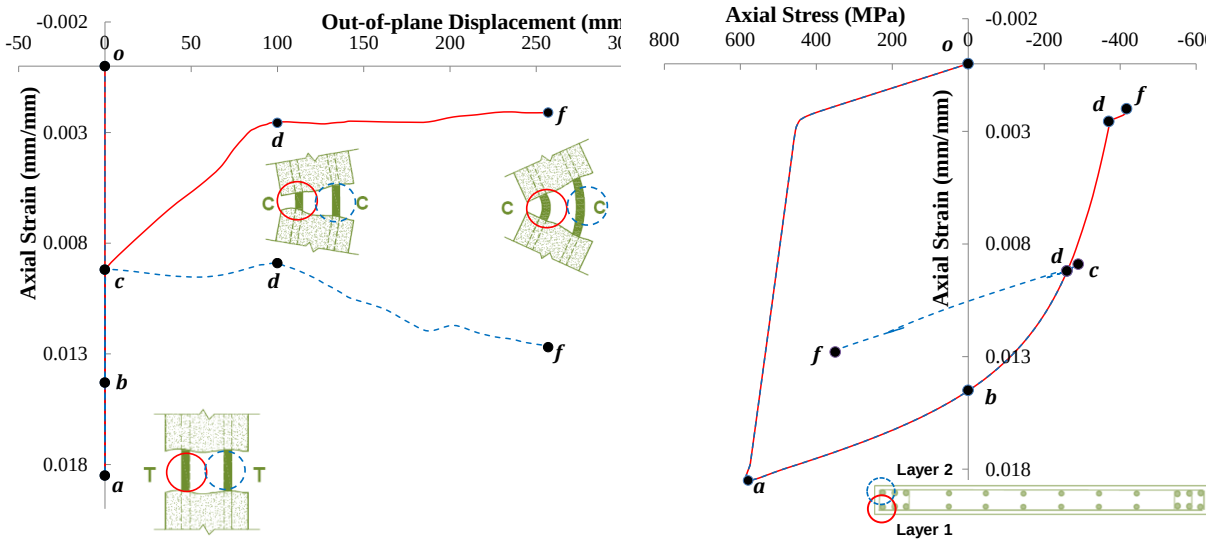

(a) (b)

Figure 4.22: Axial reversed cyclic response of boundary region reinforcement: (a) axial strain versus out-of-plane displacement; (b) axial strain versus axial stress

The reinforcement response in these two cases (Figure 4.20 and Figure 4.22) indicates that the out-of-plane deformation tends to start when a considerable amount of compressive stress is developed in the reinforcing bars resulting in their compressive yielding before the crack closes and concrete restarts contributing to the wall's load carrying capacity. Larger tensile strains (Figure 4.20 compared with Figure 4.22) can readily lead to development of larger compressive stresses in the reinforcement prior to crack closure and trigger earlier initiation of reinforcement yielding in compression and consequently earlier deformation of the wall in the out-of-plane direction (Figure 4.21b compared with Figure 4.19b).

Figure 4.23 displays the strain history of the extreme end reinforcement of Specimen R2 subjected to the test load. This strain history is derived at 1.3 m above the base, where the maximum out-of-plane deformation was observed, versus top displacement of the model. The points corresponding to initiation and development of out-of-plane deformation are shown in this figure. Figure 4.23a shows the level of strain reached by an extreme end reinforcement (ε_{sm}= 0.0177) before initiation of out-of-plane deformation at Point F which is about seven times the yield strain and did not even reach the yield strain in compression when the wall was unloaded and reloaded in the opposite direction (Figure 4.23a, Point G1) while the strain corresponding to lower drift levels reached below zero at this stage. This strain is pretty close to the tensile strain of the reinforcement when the model was subjected to a single cycle and exhibited the first out-of-plane deformation (ε_{sm}= 0.015, Point *a*,

Figure 4.20). The difference can be attributed to the effect of number of cycles in the test load which understandably increases the reinforcement strain.

The maximum out-of-plane displacements corresponding to these two cases are also consistent with the reinforcement strain in each case; i.e., 36 mm for ε_{sm}= 0.015 (Figure 4.19b and Figure 4.20) and 75mm for ε_{sm}=0.0177 (Figure 4.4a and Figure 4.23a). This phenomenon proves the fact that the initiation of out-of-plane displacement has a relationship with the level of residual strain developed in the boundary region reinforcement such that the exceedance of the residual strain above a specific level may result in the delay or prevention of crack closure when the same boundary region undergoes compression, and result in any out-of-plane deformations due to the load being resisted by the reinforcement only. It should be noted that the effect of other parameters such as axial load ratio and wall thickness cannot be neglected as these parameters can significantly influence the crack closure for a given level of residual strain developed in the reinforcement.

The effect of residual strain of reinforcement on development of out-of-plane deformations is well discussed by Chai and Elayer (1999), and the response of the numerical model in this regard is quite in agreement with the findings of their experiments. Figure 4.23 shows the effect of out-of-plane deformation on strain distribution along the wall thickness, as well. The bar elements located at two different layers of reinforcement undergo different strain histories after initiation of out-of-plane deformation at Point F, i.e., more compression in one layer (Figure 4.23a) rather than the other (Figure 4.23b). However, as also noted above, the reinforcement strain did not reach the yield strain after initiation of out-of-plane deformation even in the face undergoing more compression (Figure 4.23a, Point G1) until very large out-of-plane deformations corresponding to 2.8% drift level and failure at Point H.

4.2.2 PARAMETRIC STUDY

4.2.2.1 MESH SENSITIVITY

Localization in finite element analysis has been thoroughly studied by Bažant and Oh (1983), Bazant and Planas (1997) and De Borst (1997), and the concrete post-peak tensile stress-strain response model as well as concrete compressive response are generally regularized to limit mesh sensitivity. Figure 4.24 displays the effect of the mesh size on response of the model.

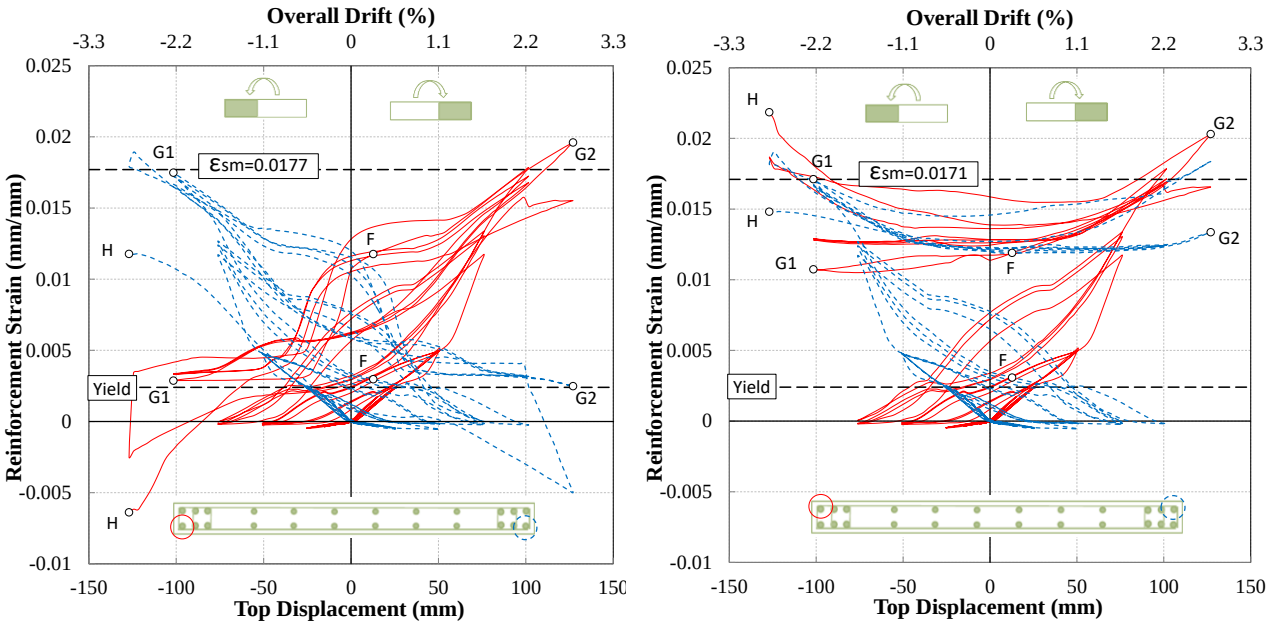

Figure 4.23: Strain history of the reinforcement at 1.3 m above the base.

The change of mesh size from coarse to fine results in a consistent change, although not considerable, in the level of peak strength reached at each drift level (Figure 4.24a). However, response of the model with medium mesh size indicates a significant degradation at positive and negative peaks of 2.8% drift level. This level of degradation can be attributed to the increased level of out-of-plane deformations corresponding to the mesh size at 2.8% drift level when compared to the other mesh sizes (Figure 4.24b and Figure 4.24c).

As can be seen in Figure 4.24b and Figure 4.24c, the medium mesh size results in an out-of-plane deformation that generally lies between the coarse and fine mesh sizes with a decreasing trend as the mesh becomes finer. However, at large drift levels, the model with medium mesh size has larger out-of-plane displacements particularly at peak levels resulting in a significant degradation observed in Figure 4.24a. The value of out-of-plane deformation at each drift level seems to depend on the geometric configuration of the mesh elements, and apart from the degradation due to out-of-plane deformations, the mesh sensitivity analysis indicates a small difference in the model response. Therefore, as the localization does not seem to have a considerable effect on the model response, the material model regularization has not been addressed in this study.

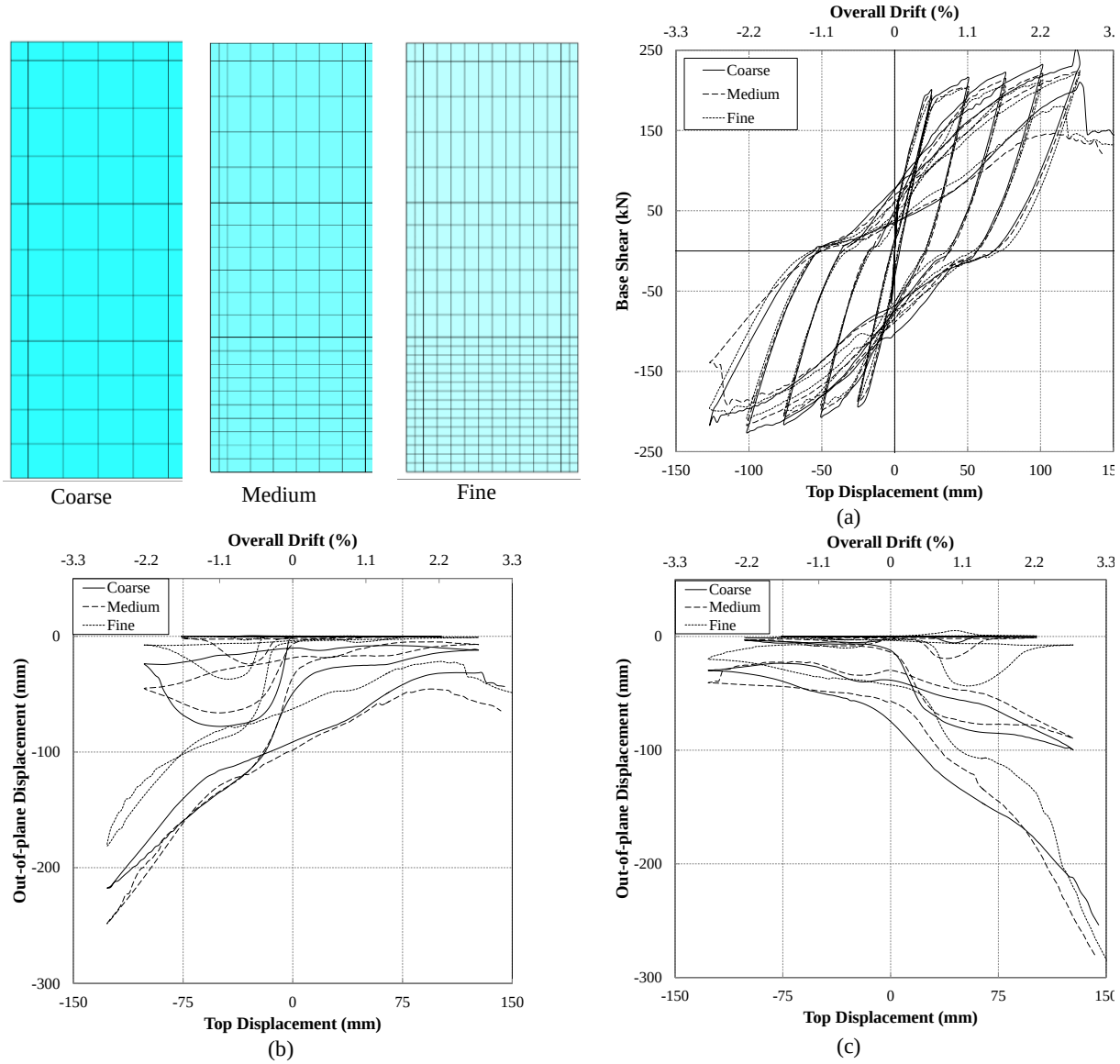

Figure 4.24: Mesh sensitivity of the model: (a) lateral load-top displacement response; (b) maximum out-of-plane displacement in the left boundary region; (c) maximum out-of-plane displacement in the right boundary region

4.2.2.2 DESIGN PARAMETERS

As noted above, the evolution of out-of-plane deformation is highly dependent on timely crack closure of a cracked wall during its reloading in the opposite direction. This crack closure is obviously controlled by the amount of tensile strain developed in the longitudinal reinforcement, as well as the wall thickness. Figure 4.25 displays a schematic representation of these parameters. As can be seen in this figure, there needs to be a critical value of tensile strain for a given wall thickness (t=b, Figure 4.25a) to provide ideal circumstances for development of out-of-plane instability. To prevent this, either the wall thickness should be increased (Figure 4.25b), to cause timely crack closure on one side of

the wall and trigger contribution of concrete to load-carrying capacity of the section, or the tensile strain developed in the reinforcement should be prevented from reaching the critical value (Figure 4.25c). Consequently, wall thickness as well as all the parameters that can govern the maximum tensile strains developed in the boundary regions of walls (e.g. axial load, wall length, etc.) could be considered as the key parameters controlling out-of-plane instability of rectangular walls.

The effect of wall thickness and axial load on out-of-plane response of Specimen R2 has been investigated to study the sensitivity of the numerical model to the parameters that would logically influence the development of out-of-plane instability in rectangular walls.

4.2.2.2.1 Effect of Wall Thickness

In order to study the effect of wall thickness on the model response, the model is analysed with different values for the wall thickness, as well. Figure 4.26a, and Figure 4.26b display the lateral load-top displacement response and the maximum out-of-plane displacement at left boundary regions of the walls with increased thickness values, respectively. The thickness values are 1.5 times and 2.0 times the thickness of the test specimen.

As can be seen in Figure 4.26b, the increase in wall thickness considerably reduces the out-of-plane displacement of the wall. Also, the out-of-plane displacement recovers completely in the wall models with increased thickness when the wall reaches the peak displacement of each drift level. The effect of this parameter can be seen in Figure 4.26a, in which, unlike the test specimen, the walls with increased thickness do not exhibit any degradation.

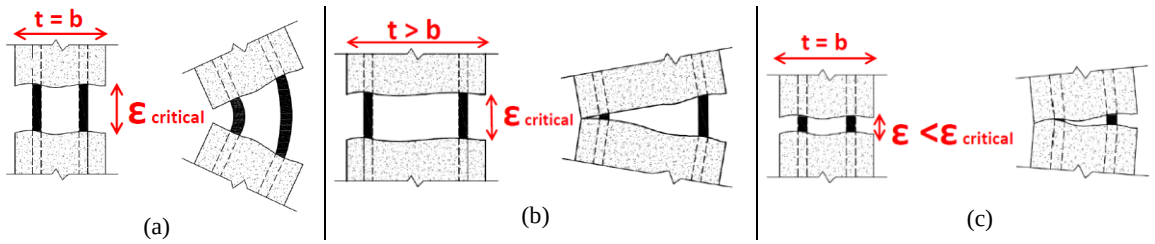

Figure 4.25: Parameters governing development of out-of-plane deformation in rectangular walls

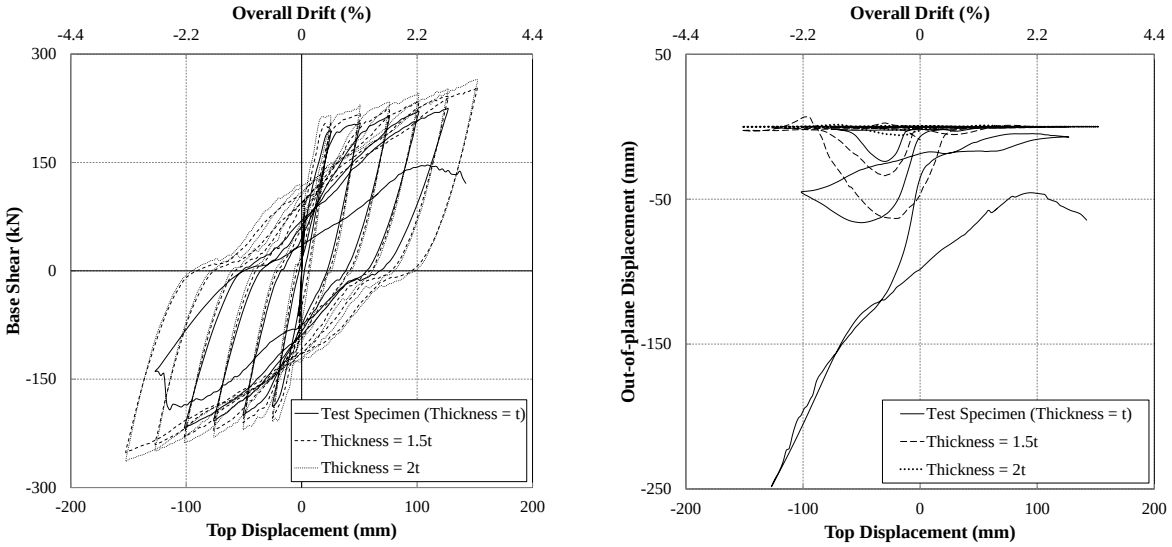

Figure 4.26: Effect of wall thickness on the model response: (a) lateral load-top displacement response; (b) maximum out-of-plane displacement in the left boundary region

4.2.2.2.2 Effect of Axial Load

The wall model has been subjected to different levels of axial load, as well. Figure 4.27a and Figure 4.27b display the lateral load-top displacement response and the maximum out-of-plane displacement at right boundary regions of the walls with increased axial load ratios, respectively. Response of the models with axial load ratios (n = N/(f'cAc)) of 0.05 and 0.1 are compared with the one of the test specimen (axial load ratio = 0.0). The increase of axial load ratio to 0.05 has resulted in a considerable delay in initiation of out-of-plane deformation and consequently, a stable cyclic response without any degradation. Also, the out-of-plane deformations recovered completely at peak displacement levels of each drift level. However, the axial load ratio resulted in fast increase of the out-of-plane displacement when the specimen was unloaded from -2.8% drift. This fast increase in out-of-plane displacement of the right boundary region resulted in instability of the model and termination of the analysis.

The model with axial load ratio of 0.1 did not exhibit any out-of-plane deformation (Figure 4.27b), which can be due to the fact that the axial load prevents the bars from reaching the critical value of residual strain to trigger the out-of-plane deformation. The response of an extreme end bar under axial load ratio of 0.1 was compared with the one under zero axial load ratio. Although the axial load ratio of 0.1 had a negligible effect in the linear elastic stage of the reinforcement, the initially experienced axial strain at loading stage of the model that was subjected to the axial load was about 15% smaller than the one without

axial load. The axial strain decrease resulting from the applied axial load along the compression reloading path can obviously affect the crack closure and prevent the out-of-plane displacements as the resulting crack opening is smaller than in the case without axial load. It should be noted that the effects of axial load ratio on reinforced concrete structures are complex as it can easily change the failure mode (e.g. from flexure to shear or flexure-out of plane to flexure-concrete crushing), and highly depends on other parameters like shear-span ratio. The strength degradation in the model with axial load ratio of 0.1 (Figure 4.27a) was due to concrete crushing under the applied moment and the increased axial load.

Therefore, The axial load can result in further increase of the out-of-plane displacement if cannot prevent the initial tensile strain from reaching the critical value and the out-of-plane deformation mode initiates, due to the fact that the out-of-plane deformation can readily increase eccentricity of the axial load, producing additional P-Delta effects.

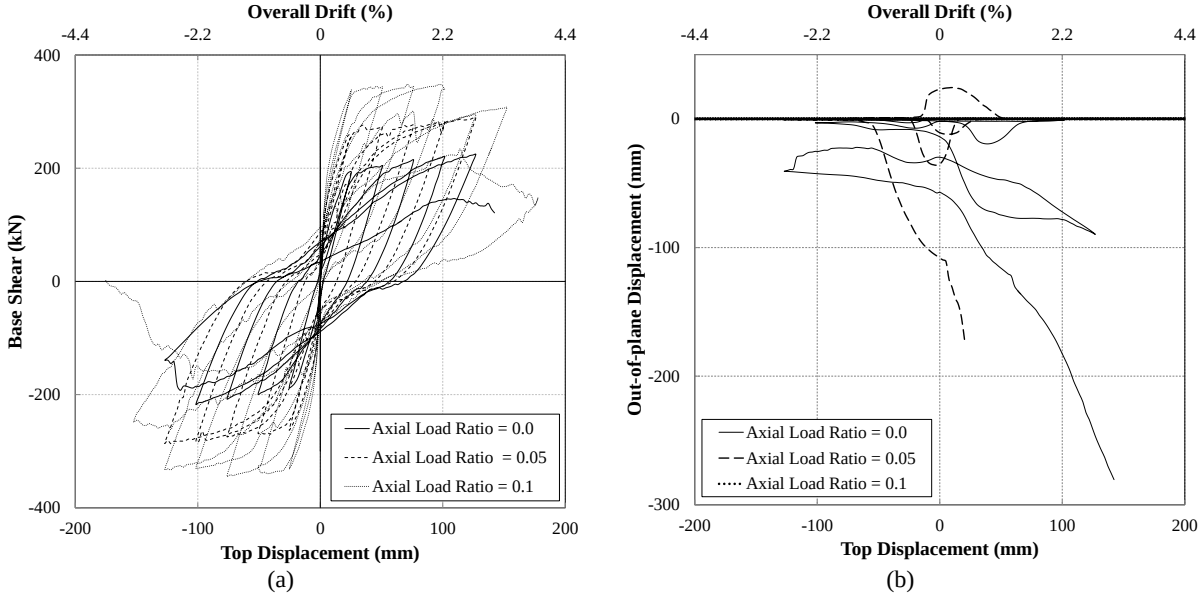

Figure 4.27: Effect of axial load ratio on the model response: (a) lateral load-top displacement response; (b) maximum out-of-plane displacement in the right boundary region

4.3 CONCLUSIONS

The capability of the model to predict failure of walls due to out-of-plane instability under in-plane loading (without any eccentricity) has been presented and experimentally verified in this study.

On scrutiny of the numerical simulation, it could be confirmed that the triggering of out-of-plane deformation is governed by the maximum strain reached by reinforcement elements in the previous cycles, which depends on the loading protocol. Larger residual tensile strains can readily lead to development of larger compressive stresses in the reinforcement

prior to crack closure during the load reversal. Once the reinforcing bars yield in compression while the cracks are still open, deformation of the wall in the out-of-plane direction is inevitable. Depending on the level of residual strain in the reinforcement, the out-of-plane deformation may recover to a great extent or steadily increase and turn into out-of-plane instability.

The strain gradients along the wall length and wall thickness clearly indicated the contributions of concrete and reinforcement elements to the load carrying capacity of the wall at different stages of loading and proved the key role of reinforcement in a cracked wall section. Depending on other parameters such as wall thickness and axial load ratio, this combination of material response in the cracked wall section imposes a substantial compression on the reinforcement that has developed a large residual strain, which provides the ideal circumstances for the wall to deform in out-of-plane direction as this mode of deformation requires less energy than for the rapid in-plane axial shortening of the wall. This effect is further supported by the postulations provided by other researchers which are based on experimental observations.

A parametric analysis was conducted to understand the effect of different parameters on the out-of-plane deformation of rectangular walls. It was found that an increase in wall thickness reduces the maximum amount of out-of-plane deformations without significantly affecting the point of start of out-of-plane deformation. As out-of-plane deformation helps the cracks to close in thicker walls, an increase in wall thickness helps the walls to recover (i.e. straighten) even after experiencing a substantial residual tensile strain, which understandably results in more stable response of the wall.

Axial load has different (and contradictory) effects on the out-of-plane deformation of rectangular walls. An increase in axial load can delay the onset of out-of-plane deformations (can even completely prevent it if the axial load is large enough) by decreasing the residual tensile strain developed in the reinforcement. However, as out-of-plane deformation invariably increases the eccentricity of an axial load, it can produce additional destabilizing P-Delta moment on the out-of-plane direction which accelerates the subsequent instability. Hence, if the axial load is not high enough to prevent the bars from reaching the critical tensile strain and to prevent the out-of-plane deformation mode, it can result in further increase of the out-of-plane deformation, making the wall more prone to out-of-plane failure.

4.4 REFERENCES

Aaleti, S. R. (2009). Behavior of rectangular concrete walls subjected to simulated seismic loading, Iowa State University. PhD**,** 249.

Bažant, Z. P. and B. H. Oh (1983). "Crack band theory for fracture of concrete." *Matériaux et construction* 16(3), 155-177.

Bazant, Z. P. and J. Planas (1997). Fracture and size effect in concrete and other quasibrittle materials, CRC press.

Beattie, G. J. (2004). Design of Slender Precast Concrete Wall Panels – Experimental Testing. BRANZ Study Report SR 129, BRANZ Ltd, Judgeford, New Zealand.

Birely, A. C. (2013). Seismic Performance of Slender Reinforced Concrete Structural Walls, University of Washington. PhD**,** 983.

Chai, Y. and D. Elayer (1999). "Lateral stability of reinforced concrete columns under axial reversed cyclic tension and compression." *ACI Structural Journal* 96(5).

Dashti, F., R. Dhakal and S. Pampanin (2014a). Numerical simulation of shear wall failure mechanisms. 2014 NZSEE Conference, Auckland, New Zealand, New Zealand Society for Earthquake Engineering.

De Borst, R. (1997). "Some recent developments in computational modelling of concrete fracture." *International journal of fracture* 86(1-2), 5-36.

Dhakal, R. and K. Maekawa (2002a). "Modeling for Postyield Buckling of Reinforcement." *Journal of structural engineering* 128(9), 1139-1147.

Dhakal, R. P. and K. Maekawa (2002b). "Reinforcement stability and fracture of cover concrete in reinforced concrete members." *Journal of structural engineering* 128(10), 1253-1262.

Dhakal, R. P. and K. Maekawa (2002c). "Path-dependent cyclic stress–strain relationship of reinforcing bar including buckling." *Engineering Structures* 24(11), 1383-1396.

DIANA, T. (2011). Finite Element Analysis User's Manual - Release 9.4.4, TNO DIANA.

Elwood, K. J. (2013). "Performance of concrete buildings in the 22 February 2011 Christchurch earthquake and implications for Canadian codes 1." *Canadian Journal of Civil Engineering* 40(3), 1-18.

Encina, E. and R. Henry (2015). Preliminary investigation of elongation in RC walls. 2015 NZSEE Conference. Rotorua, New Zealand, New Zealand Society for Earthquake Engineering.

Feenstra, P., R. De Borst and J. Rots (1991). A comparison of different crack models applied to plain and reinforced concrete. Proceedings of the International RILEM/ESIS Conference" Fracture Processes in Concrete, Rock and Ceramics", Noordwijk, The Nehterlands, 19-21 June 1991.

Goodsir, W. J. (1985). The design of coupled frame-wall structures for seismic actions, University of Canterbury. PhD.

Johnson, B. (2010). Anchorage detailing effects on lateral deformation components of R/C shear walls, Master Thesis, University of Minnesota.

Mander, J., M. N. Priestley and R. Park (1988). "Theoretical stress-strain model for confined concrete." *Journal of structural engineering* 114(8), 1804-1826.

Menegotto, M. and P. Pinto (1973). Method of Analysis for Cyclically Loaded Reinforced Concrete Plane Frames Including Changes in Geometry and Non-elastic Behavior of Elements Under Combined Normal Force and Bending. IABSE Symposium on the Resistance and Ultimate Deformability of Structures Acted on by Well-Defined Repeated Loads, Lisbon.

Mindlin, R. D. (1951). "Influence of rotary inertia and shear on flexural motions of isotropic, elastic plates." *J. of Appl. Mech.* 18, 31-38.

Oesterle, R. (1976). Earthquake Resistant Structural Walls: Tests of Isolated Walls, Research and Development Construction Technology Laboratories, Portland Cement Association.

Oesterle, R. (1979). Earthquake Resistant Structural Walls: Tests of Isolated Walls: Phase II, Construction Technology Laboratories, Portland Cement Association.

Orakcal, K., L. M. Massone and J. W. Wallace (2006). Analytical modeling of reinforced concrete walls for predicting flexural and coupled-shear-flexural responses, Pacific Earthquake Engineering Research Center, College of Engineering, University of California, Berkeley.

Paulay, T. and M. Priestley (1993). "Stability of ductile structural walls." *ACI Structural Journal* 90(4).

Reissner, E. (1945). "The effect of transverse shear deformation on the bending of elastic plates." *Journal of applied Mechanics* 12, 69-77.

Rots, J. G. and J. Blaauwendraad (1989). "Crack models for concrete, discrete or smeared? Fixed, multi-directional or rotating?" *HERON, 34 (1), 1989.*

Telleen, K., J. Maffei, J. Heintz and J. Dragovich (2012a). Practical Lessons for Concrete Wall Design, Based on Studies of the 2010 Chile Earthquake. 15th World Conference on Earthquake Engineering, 24-28 September 2012, Lisbon, Portugal.

Thomsen IV, J. H. and J. W. Wallace (2004). "Displacement-based design of slender reinforced concrete structural walls-experimental verification." *Journal of structural engineering* 130(4), 618-630.

Vallenas, J. M., V. V. Bertero and E. P. Popov (1979). Hysteretic behaviour of reinforced concrete structural walls. Report no. UCB/EERC-79/20, Earthquake Engineering Research Center, University of California, Berkeley.

Vecchio, F. J. and M. P. Collins (1986). "The modified compression-field theory for reinforced concrete elements subjected to shear." *ACI J.* 83(2), 219-231.

Wallace, J. (2012). "Behavior, design, and modeling of structural walls and coupling beams — Lessons from recent laboratory tests and earthquakes." *International Journal of Concrete Structures and Materials* 6(1), 3-18.

5 BLIND PREDICTION OF OUT-OF-PLANE INSTABILITY IN A SINGLY REINFORCED CONCRETE FLANGED WALL

Dashti, F., R.P. Dhakal, S. Pampanin (2016) "Blind Prediction of In-plane and Out-of-plane Responses for a Thin Singly Reinforced Concrete Flanged Wall Specimen" *Bulletin of Earthquake Engineering*, DOI 10.1007/s10518-017-0211-x

The validity of a finite element modeling approach in capturing different failure mechanisms of rectangular walls, with particular focus on out-of-plane instability is investigated in Chapters 3 and 4. As a further verification, this modeling approach was used for blind prediction of a singly reinforced wall panel tested at the Structural Laboratory of the *École Polytechnique Fédérale de Lausanne* (EPFL) (Rosso et al. 2014). A blind prediction report was submitted to the researchers in December 2014 prior to release of test results (Dashti et al. 2014). This chapter presents the numerical simulation as presented in the blind prediction report as well as the comparison between the numerical and experimental results recently released and published in literature (Rosso et al. 2015).

The specimen was a singly reinforced T-shaped wall panel with a shear-span ratio of 3.7 and was tested under uni-directional (in-plane) quasi-static reverse cyclic loading. The numerical model predicted a flexure-dominated response for the specimen accompanied by considerable out-of-plane deformations. The blind prediction report, submitted in advance to the principal investigator of the experimental campaign, included lateral load-top displacement response of the specimen, maximum out-of-plane deformation corresponding to each drift level, evolution of out-of-plane displacements throughout in-plane loading, response of the longitudinal reinforcement at the section exhibiting the maximum out-of-plane deformation, and von Mises as well as reinforcement stress distribution at some key points of the wall response. Furthermore, a parametric study was carried out addressing the

effects of shear-span ratio, reinforcement eccentricity and axial load ratio on the wall response.

Results of the numerical simulation that had been included in the blind prediction report have been compared with the experimental measurements indicating that the evolution of the out-of-plane deformation was well captured by the model.

5.1 REPRESENTATION OF THE EXPERIMENTAL PROGRAM IN THE NUMERICAL MODEL

Dimensions and reinforcement layout of the test specimen are shown in Figure 5.1. The specimen was tested at full scale and the dimensions and reinforcement details followed current design practices for low- to mid-rise construction of residential buildings in Colombia representing a shear-span ratio of 3.7. The specimen was 80 mm thick, 2700 mm long and 2000 mm tall. Height of the wall in the actual building was 2200, but due to laboratory space constraints, the specimen height was reduced to 2000 mm. The specimen had a shear span of 10m and represented a portion of a multi-storey wall. This shear span was provided by the loading pattern. The specimen had a flange at the north end that was 80 mm thick and 440 mm long to replicate the effect of a perpendicular wall on member stability. According to the CAD file provided by the experimenters, the longitudinal reinforcement was positioned with an eccentricity with respect to the section centreline as shown in Figure 5.2. The effect of this eccentricity on the predicted results will be discussed afterwards.

According to the test report, the wall was subjected to lateral displacement cycles in accordance with the drift history shown in Figure 5.3.Two vertical actuators were used to apply an axial load ratio$v=N/(f'_cA_c) =0.05$ as well as the bending moment corresponding to the shear span of 10 m (shear-span ratio of 3.7). In order to ensure that the shear span of 10 m was maintained during the analysis, the displacement was applied at a higher elevation through an elastic extension so that the total effective height of the wall could be 10 m. As the displacement was measured at the height of the actuator (2.2 m from the base) in the test, the ratio between the analytically applied displacement at the elevation of 10m to the displacement at the actuator elevation was captured at different stages of wall nonlinear response using a monotonic push-over analysis.

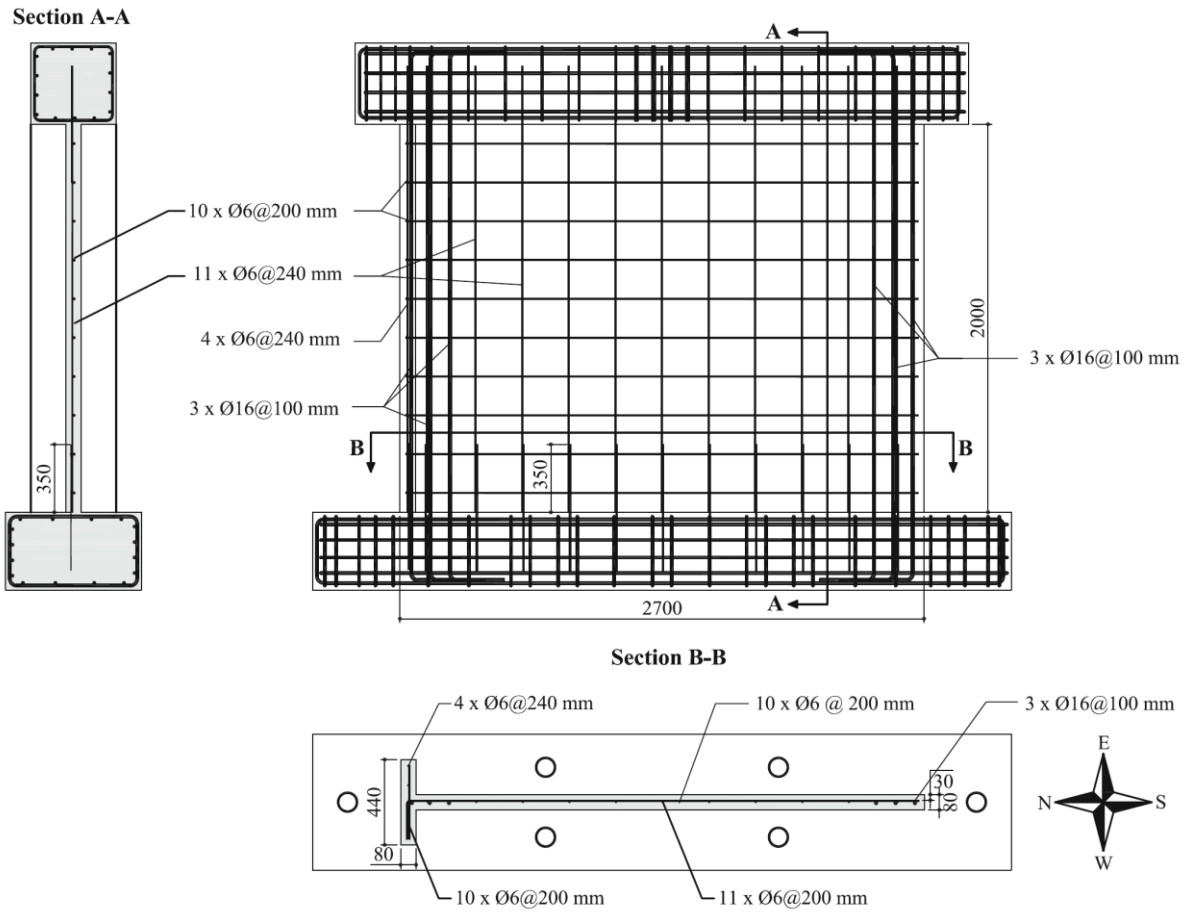

Figure 5.1: Dimensions and reinforcement layout of the test specimen (Rosso et al. 2015)

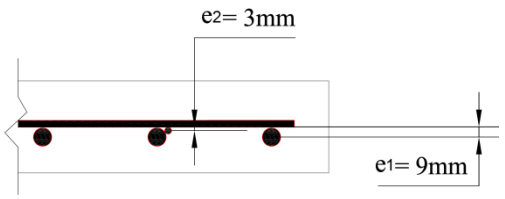

Figure 5.2: Eccentricities of the longitudinal reinforcement

Figure 5.4 shows a schematic view of the finite element model with loading and boundary conditions. The specimen was restrained against out-of-plane displacements at the storey height using steel tubes to prevent the top RC beam from moving sideways. The constraint system adopted in the experiment to restrain the out-of-plane displacement at the cap beam level and its representation in the numerical model is shown in Figure 5.4b. The wall section was modelled using the curved shell element, with a larger thickness in the flange part. The difference in shell thickness is shown using the extruded view (Figure 5.4c). Mesh sensitivity analysis was not carried out and a relatively fine mesh was adopted to capture a better prediction of the wall height undergoing the maximum out-of-plane displacements.

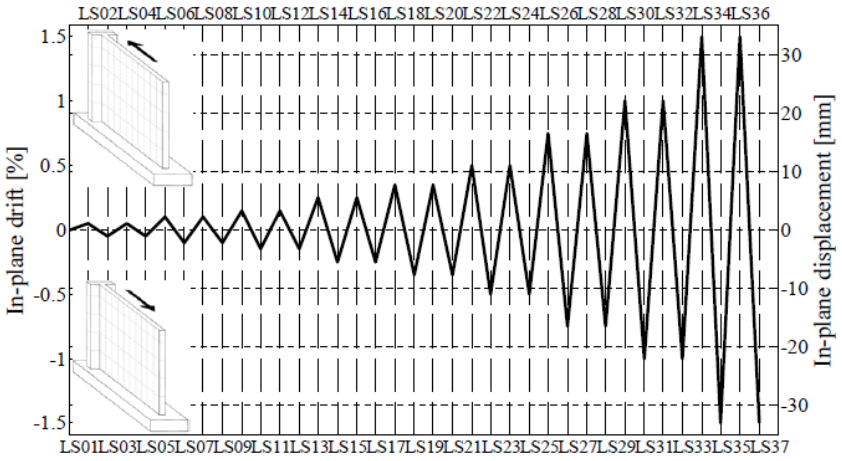

Figure 5.3: Applied drift history (Rosso et al. 2014)

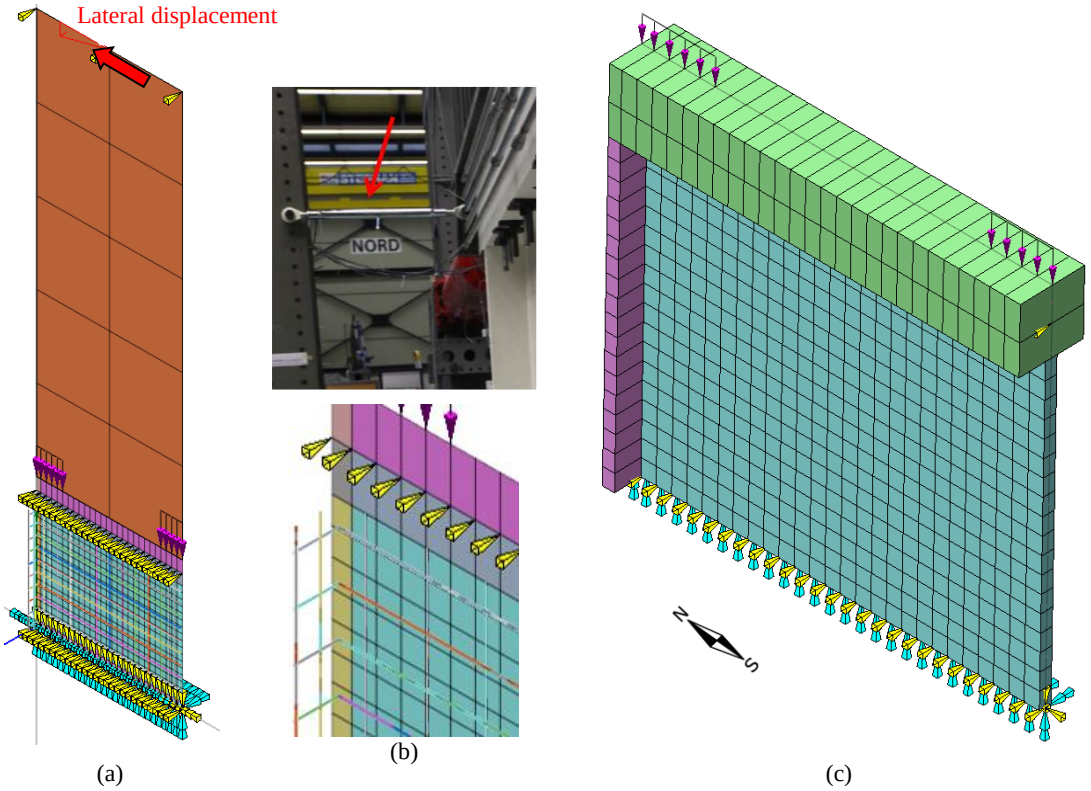

Figure 5.4: Finite element model: (a) increased height of the lateral load to generate the shear span of 10m; (b) experimental vs numerical model restraint against out-of-plane displacement at cap beam level, photo courtesy of Rosso et al. (2014); (c) extruded 3-D view of the model

Several parameters are known to influence the out-of-plane instability of rectangular walls, such as wall thickness, axial load ratio, etc. The effects of some of these parameters are investigated in this study. Table 5.1 displays the set of wall models analyzed in this study with the parameters changing in each model. Models TW1-A to TW1-D comply with the

test shear-span ratio. Eccentricity and axial load ratio are the parameters changing in this set of models. As noted above, the specimen had an eccentricity in positioning of the longitudinal reinforcement. As a part of parametric investigation, this eccentricity was neglected in some models and the axial load ratio of 0.05 applied in the test was also dropped to 0.0 in some models.

In order to evaluate the relationship between out-of-plane deformations and the shear-span ratio, which determines whether the wall response will be flexure or shear-dominated, the models TW1-A to TW1-D were subjected to a loading corresponding to a very low shear-span ratio of 0.8, compared to the axial load ratio of 3.7 that was adopted in the test .

These cases are denoted as TW1-a to TW1-d, respectively (Table 5.1). For this purpose, the lateral displacement was applied at the same elevation as the test actuator so that the effect of additional moment applied through vertical actuators would be eliminated. This loading condition, shown in Figure 5.5, represents a shear-span ratio of 0.8 which is considerably smaller than that of the benchmark test TW1-A, and can significantly change the wall response.

Table 5.1: Cases considered for sensitivity analysis

	Model	Shear-span ratio	Eccentricity	Axial load ratio
1	TW1- A (Test Specimen)	3.7	Yes	0.05
2	TW1- B	3.7	Yes	0.00
3	TW1- C	3.7	No	0.05
4	TW1- D	3.7	No	0.00
5	TW1- a	0.8	Yes	0.05
6	TW1- b	0.8	Yes	0.00
7	TW1- c	0.8	No	0.05
8	TW1- d	0.8	No	0.00

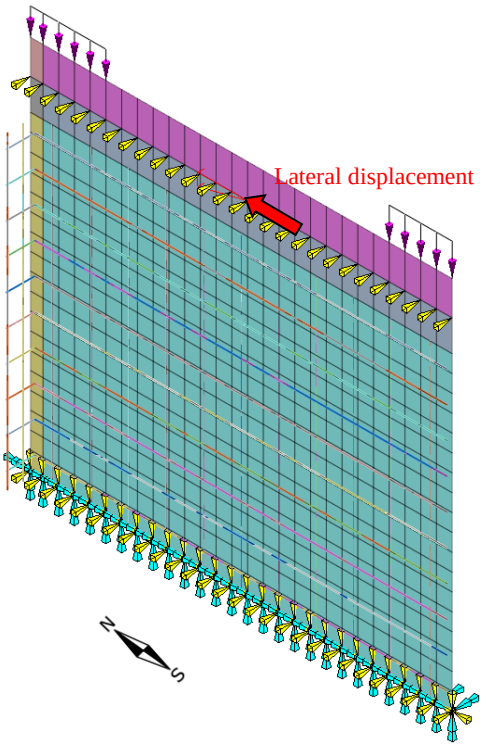

Figure 5.5: Model with a low shear-span ratio

5.2 NUMERICAL PREDICTIONS

5.2.1 TW1-A (TEST SPECIMEN)

The longitudinal reinforcement eccentricity was considered in this model, and the axial load was applied according to the test program. The predicted response of this specimen was governed by flexural deformations and was accompanied by out-of-plane deformations in the south boundary zone. The flange part of the wall section, as expected, did not exhibit out-of-plane deformations. Figure 5.6 displays the lateral load versus top displacement response of the specimen as well as the maximum out-of-plane displacement at each drift level. The key points corresponding to degradation of the model are displayed in this figure. At Point a, the maximum compression strength in the concrete was achieved at the base section in the flange. Figure 5.7 displays the von Mises stress distribution of the model at this point showing the concentration of stress at the compression toe. As there was no confinement provided along the wall section, the compressive stress carrying capacity of the concrete dropped considerably at this point resulting in the degradation of the lateral load observed at Point a. At Point b, as shown in Figure 5.8, the longitudinal reinforcement in the compression zone has gone through considerable yielding. At this point, the wall had elongated due to residual strain of the reinforcement, which prevented the cracked concrete

from closing fully and the majority of the load carrying capacity was provided by the reinforcement in compression. At Point c, a very significant degradation coming from the out-of-plane instability of the south (i.e. opposite to the flange) boundary zone is observed. As shown in Figure 5.6b, the out-of-plane deformation starts during the 0.5% drift cycle, gradually increases at the 0.75% and 1% drift cycles, and results in a sudden out-of-plane instability at 1.5% drift level. Figure 5.6a shows the considerable degradation of the model at Point c when reversing from +1.5% drift to -1.5% drift. At this point, the south boundary zone, which had experienced a large tensile strain at +1.5% drift, is gradually subjected to compressive stress; thereby, causing a considerable out-of-plane deformation.

Figure 5.9a indicates the maximum out-of-plane deformation of the model during 1.5% drift level and Figure 5.9b displays the maximum out-of-plane displacement at the south boundary zone at different stages of loading. As shown in this figure, at 0.5%, 0.75% and 1.0% drift levels, the out-of-plane deformation increases when reversing from peak positive drifts, and decreases when reaching the peak negative drifts, which is the general trend of this mode of deformation (Chai and Elayer 1999, Beattie 2004) before it results in the wall instability. After reaching the 1.5% drift cycle, the out-of-plane deformation does not recover during the drift reversals and results in response degradation of the model.

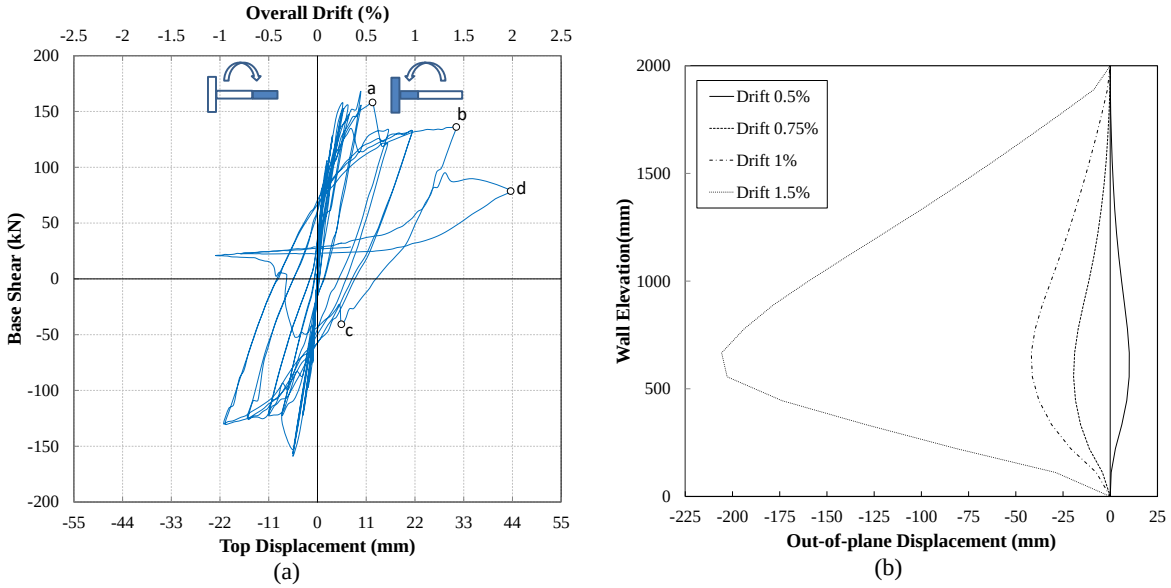

Figure 5.6: Model response, TW1- A: (a) lateral load vs top displacement response; (b) maximum out-of-plane deformation corresponding to each drift level

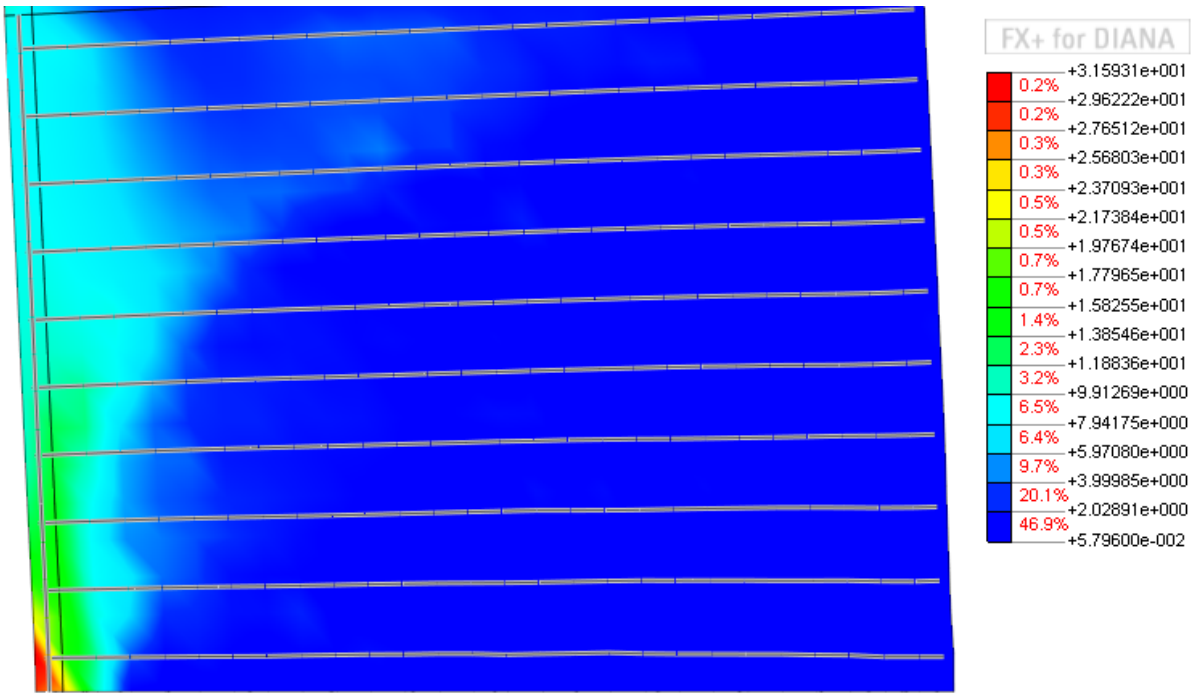

Figure 5.7: Von Mises stress distribution, TW1-A, Point a

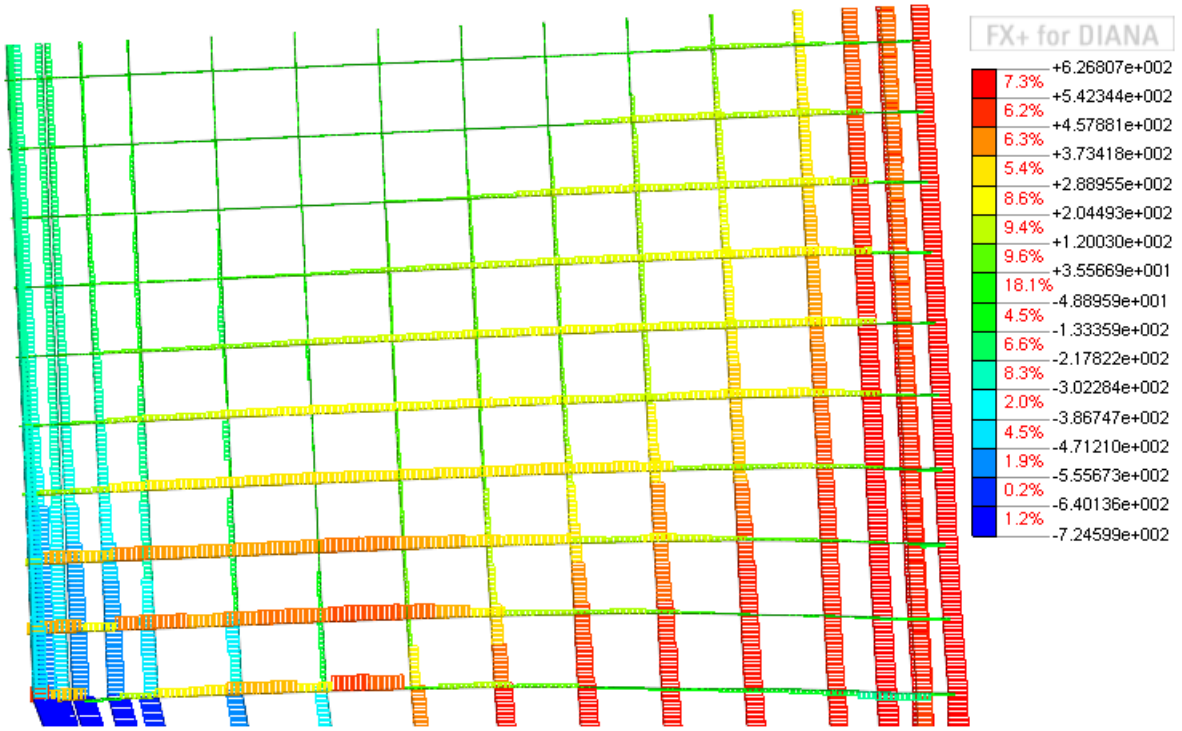

Figure 5.8: Reinforcement stress, TW1-A, Point b

It is worth noting that the displacement in the numerical simulation was controlled at the top of the 10 m high model (Figure 5.4a) whereas in the experiment the displacement was

applied at the actuator level located at 2.2 m height. As a result, at different levels of material nonlinearity, the displacement at the top of the numerical model was amplified when compared to the corresponding target displacement at the actuator level. However, due to the out-of-plane instability, the displacement at the top of the model increased significantly and reached the predefined target before the displacement at the actuator level would reach the desired drift level. Therefore, the displacement at the actuator level, which is indicated as "Top Displacement" in the figures, could not reach the experimentally applied -1.5% drift.

At Point d, the shear resistance of concrete is degraded, the von Mises stress distribution (Figure 5.10) and the reinforcement stress (Figure 5.11) show that the concrete is mostly unable to sustain more than 6 MPa of stress throughout the wall length, and the three lowest layers of horizontal reinforcement elements have crossed their yield limit. Interesting to note that this effect was not observed in the monotonic pushover curve, compared in Figure 5.12 with the cyclic hysteretic response; this difference is expected as the shear resistance of concrete is known to degrade during cyclic loading with increasing ductility demands (Krolicki et al. 2011). The out-of-plane deformation is typically localised within the end regions of the wall (as shown in Figure 5.9a) where vertical tensile and compressive strains from the in-plane cyclic actions are greatest, and the considerable residual strain of the reinforcement does not allow for crack closure before the reinforcement yielding in compression results in out-of-plane instability of the wall (Paulay and Priestley 1993, Chai and Elayer 1999).

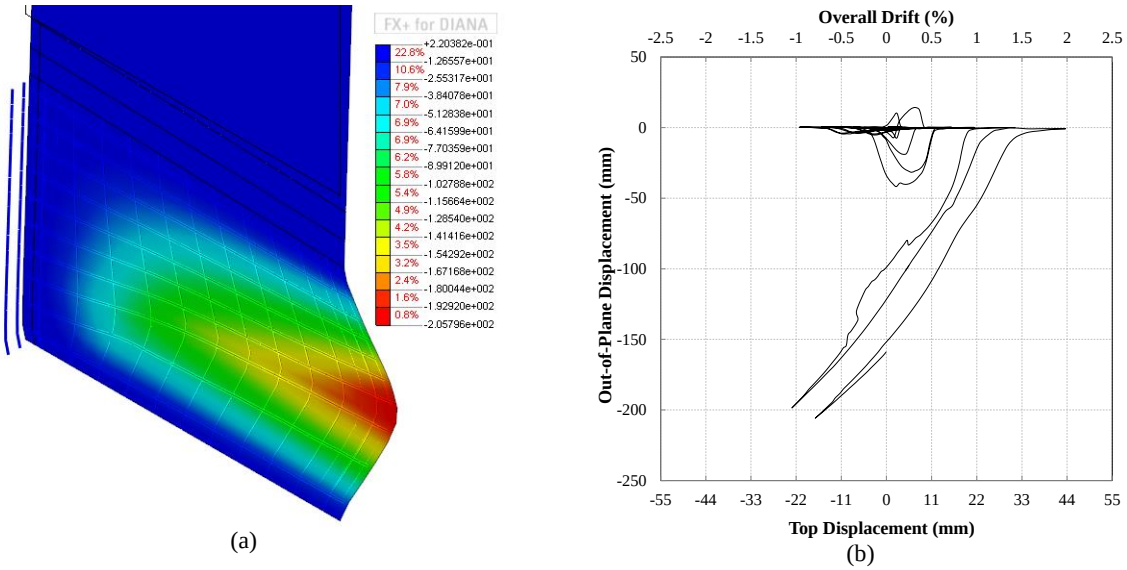

(a) (b)

Figure 5.9: Out-of-plane deformation-TW1-A: (a) deformation pattern at 1.5% drift cycle; (b) maximum out-of-plane displacement throughout the loading

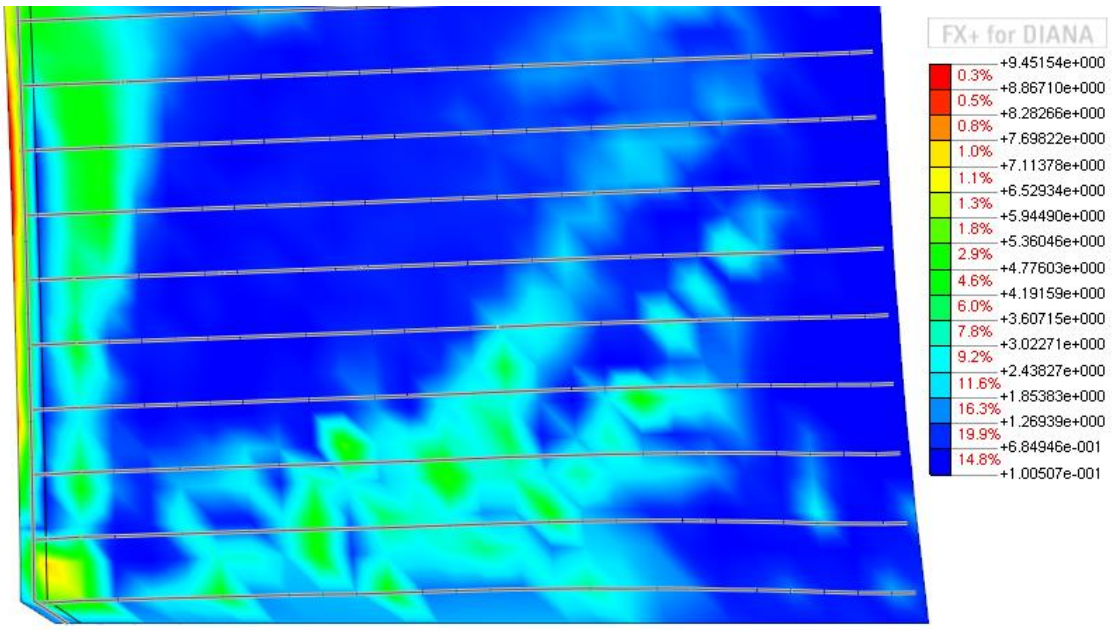

Figure 5.10: Von Mises stress distribution, TW1-A, Point d

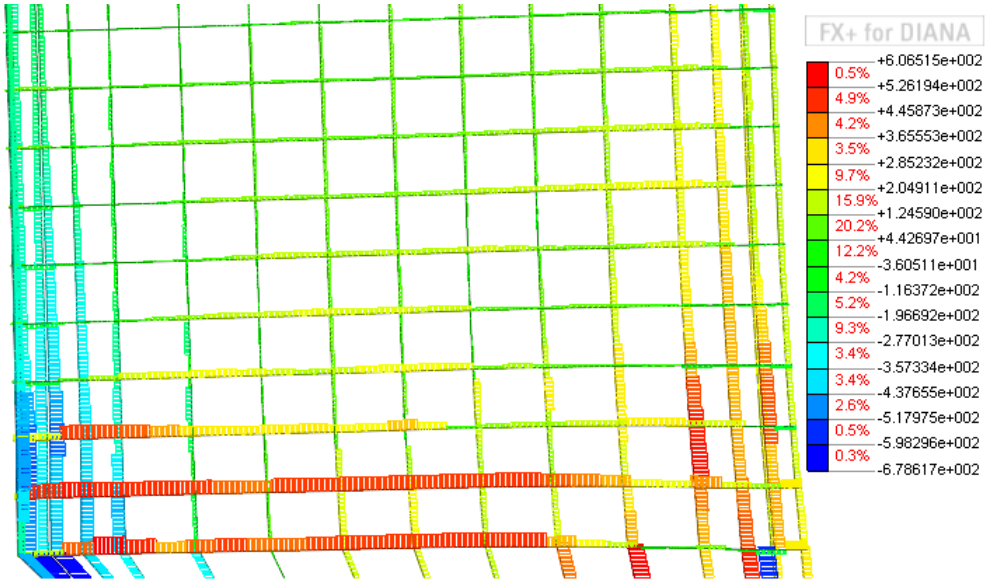

Figure 5.11: Reinforcement stress, TW1-A, Point d

The strain history of the reinforcement at the end region of the wall corresponding to the section exhibiting the maximum out-of-plane deformation is plotted in Figure 5.13.As can be noted, the reinforcement strain increases along with the increase of the top lateral displacement and the residual strain accumulates as a result of cyclic loading. Figure 5.13a shows that the maximum strain reached by the reinforcement prior to the abrupt increase of the out of plane deformation was ε_{sm}= 0.0204. The level of tensile strain reached by the end region reinforcement at each cycle is in fact acknowledged to be one of the most significant

parameters governing the probability of out-of-plane instability when this reinforcement is subjected to compression (Paulay and Priestley 1993, Chai and Elayer 1999, Moyer and Kowalsky 2003). Figure 5.13a and Figure 5.13b display the residual strain and wall elongation developed throughout the loading history. It can be noted that even under axial load ratio of 0.05, the strain at this region of the wall is mostly tensile throughout the loading, confirming that the axial load carrying capacity at this region is provided by the reinforcement only. In such conditions, small levels of eccentricity of the longitudinal reinforcement can easily trigger the out-of-plane instability of the wall.

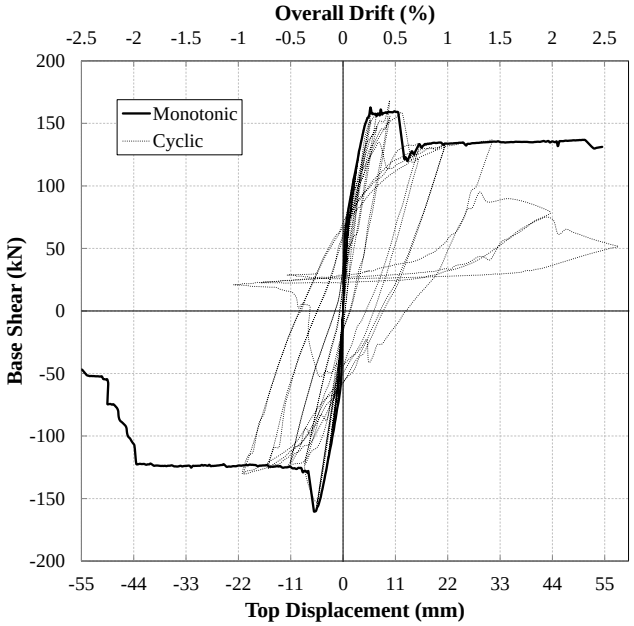

Figure 5.12: Comparison of monotonic and cyclic response of TW1-A

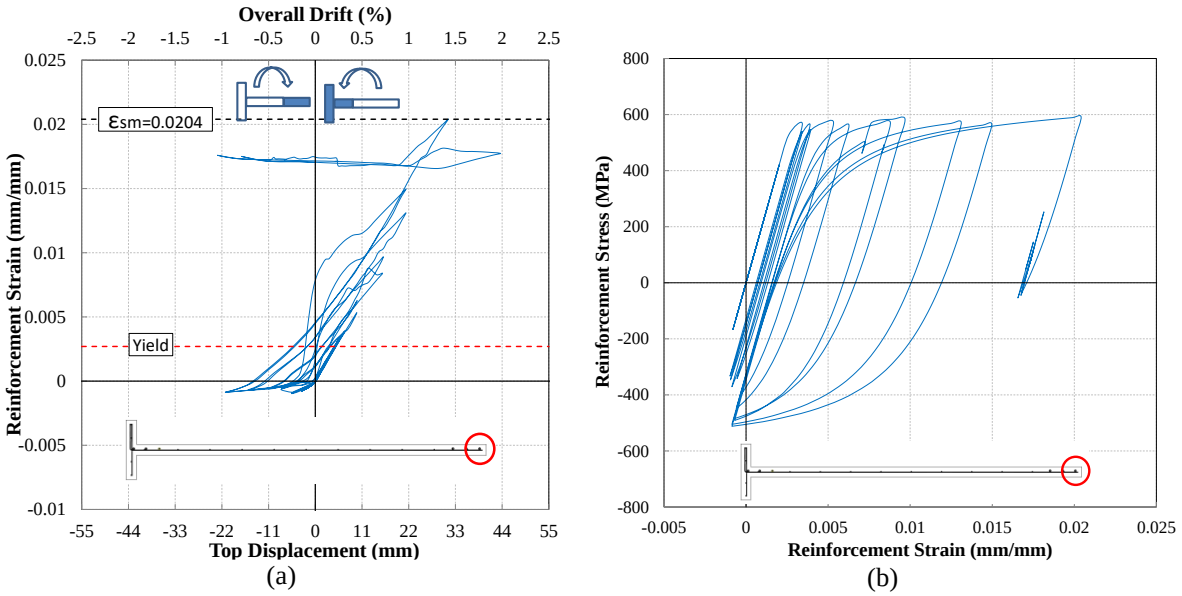

Figure 5.13: Response of the longitudinal reinforcement at the section exhibiting maximum out-of-plane deformation, TW1- A: (a) strain history; (b) stress-strain curve

5.2.2 PARAMETRIC STUDY

5.2.2.1 TW1- B

In order to investigate the effect of axial load ratio on the response of the wall, the previous model was analysed without any axial load. The numerical model response (Figure 5.14) shows that although this model did not exhibit the strength degradations observed at Points a, b and d in TW1-A (see Figure 5.6), the removal of the axial load did not prevent the out-of-plane deformation of the south boundary zone which started at the same drift level as in TW1-A. In fact the out-of-plane displacement in this model at 1% drift is considerably larger than that in TW1-A. Figure 5.14a displays the considerable degradation associated with the out-of-plane instability of the model. The development of the out-of-plane displacement at different stages of loading (Figure 5.15) shows the same trend as TW1-A. Figure 5.16 shows the strain history of the longitudinal reinforcement at the section exhibiting maximum out-of-plane deformation. The comparison between this figure and Figure 5.13 helps understanding the effect of axial load on the residual tensile strain developed in the reinforcement, which in turns results in the elongation of the wall. The removal of the axial load resulted in out-of-plan instability of the model at 1% drift when the end reinforcement had already experienced a strain of ε_{sm}= 0.0169. The reinforcement strain at this drift level was 0.015 in TW1-A.

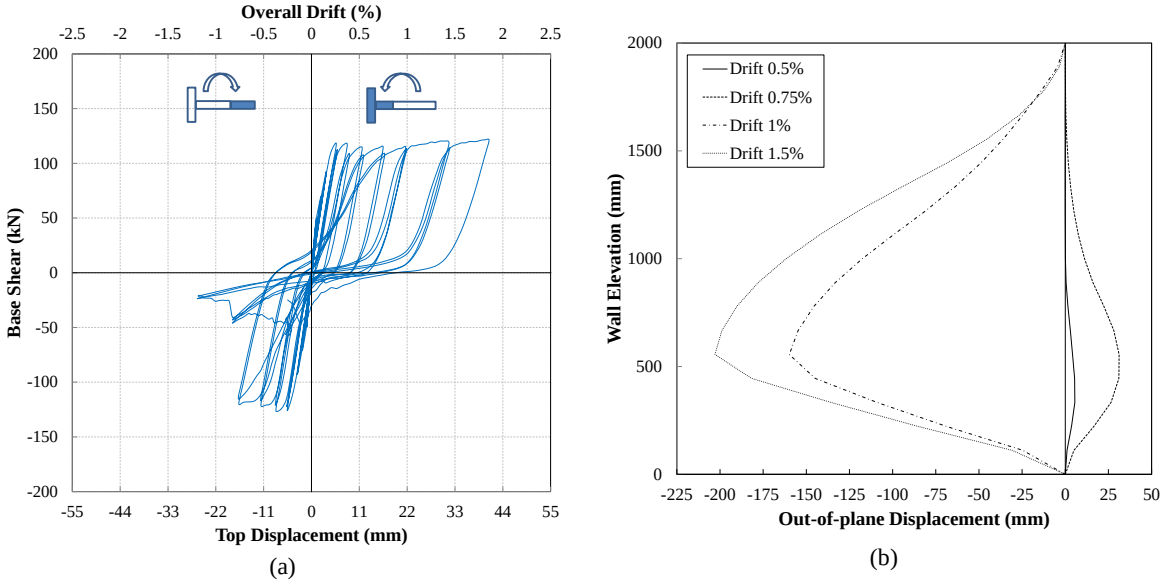

Figure 5.14: Model response, TW1- B: (a) lateral load vs top displacement response; (b) maximum out-of-plane deformation corresponding to each drift level

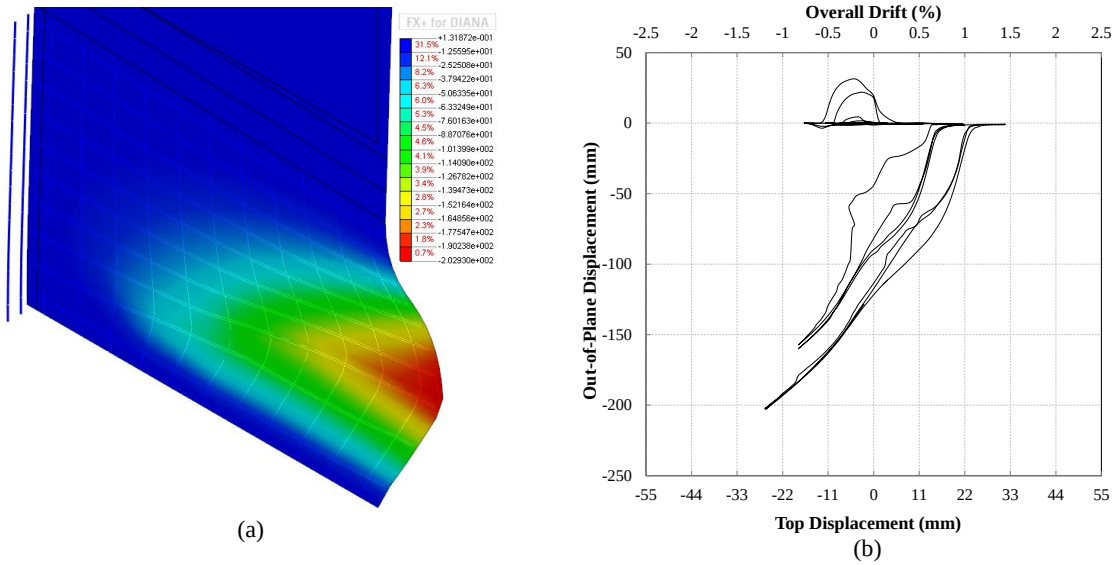

(a) (b)

Figure 5.15: Out-of-plane deformation-TW1-B: (a) deformation pattern at 1.5% drift cycle; (b) maximum out-of-plane displacement throughout the loading

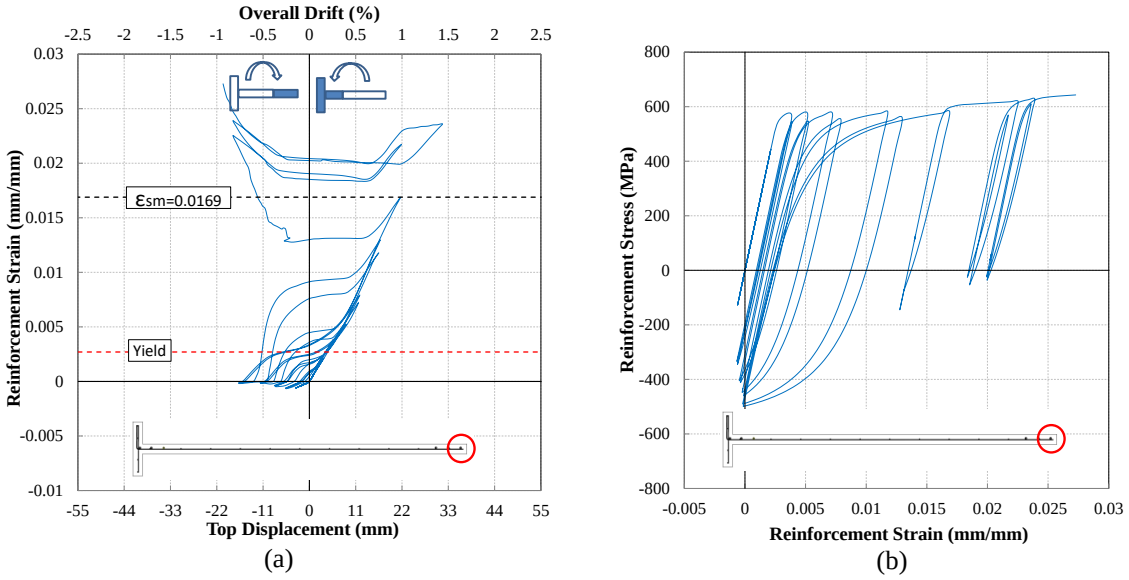

(a) (b)

Figure 5.16: Response of the longitudinal reinforcement at the section exhibiting maximum out-of-plane deformation, TW1- B: (a) strain history; (b) stress-strain curve

5.2.2.2 TW1- C

In this section, the effect of reinforcement eccentricity on development of the out-of-plane deformation is evaluated. For this purpose, the longitudinal and horizontal reinforcement elements are positioned at the section centreline with no eccentricity. The results shown in Figure 5.17 to Figure 5.19 show that the eccentricity does not play a significant role in preventing or triggering the out-of-plane instability of this model as the difference between the results of the model with eccentricity (TW1-A) and the model without eccentricity (TW1-C) is negligible. It should be noted that the analysis results for the benchmark model

with eccentricity showed very small out-of-plane deformations starting from the loading initiation, whereas the out-of-plane deformation of the model without eccentricity was zero up to a certain level (0.75% drift level). However, the initiation of the out-of-plane instability of this model seems to be independent of the eccentricity of the longitudinal reinforcement.

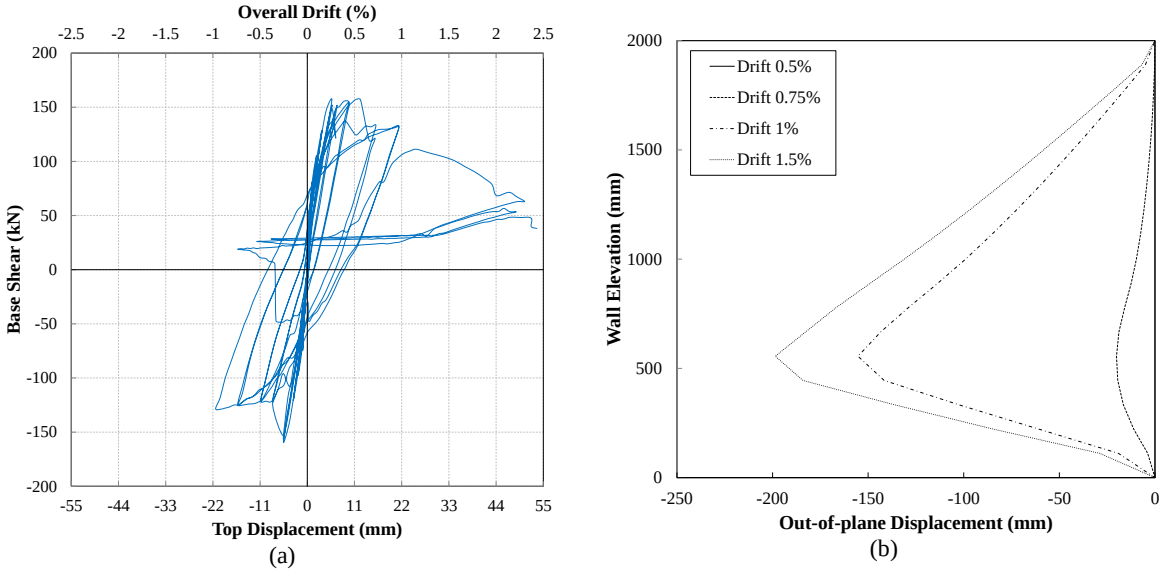

Figure 5.17: Model response, TW1- C: (a) lateral load vs top displacement response; (b) maximum out-of-plane deformation corresponding to each drift level

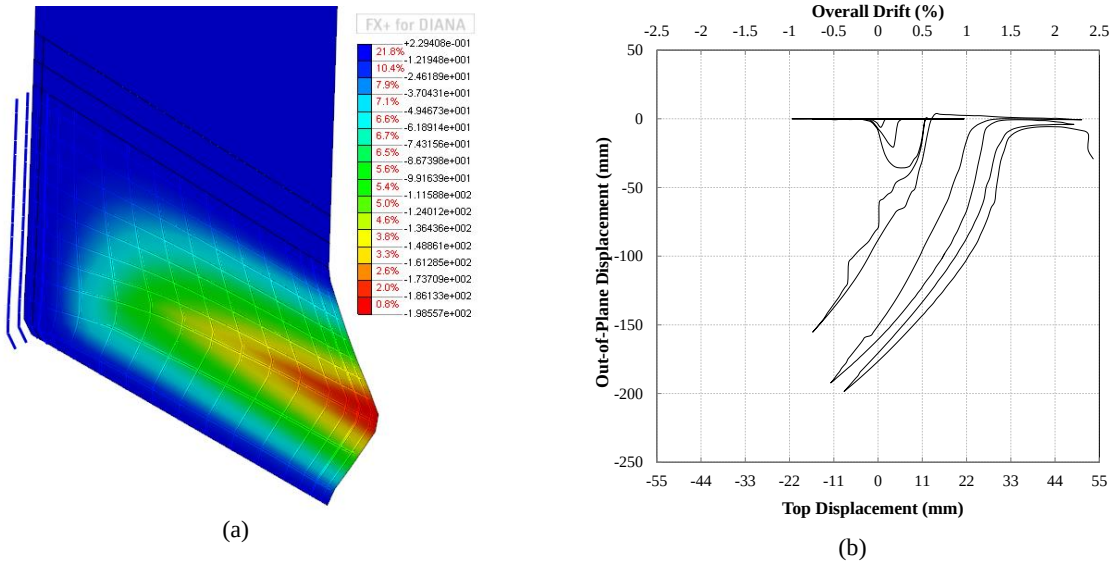

Figure 5.18: Out-of-plane deformation-TW1-C: (a) deformation pattern at 1.5% drift cycle; (b) maximum out-of-plane displacement throughout the loading

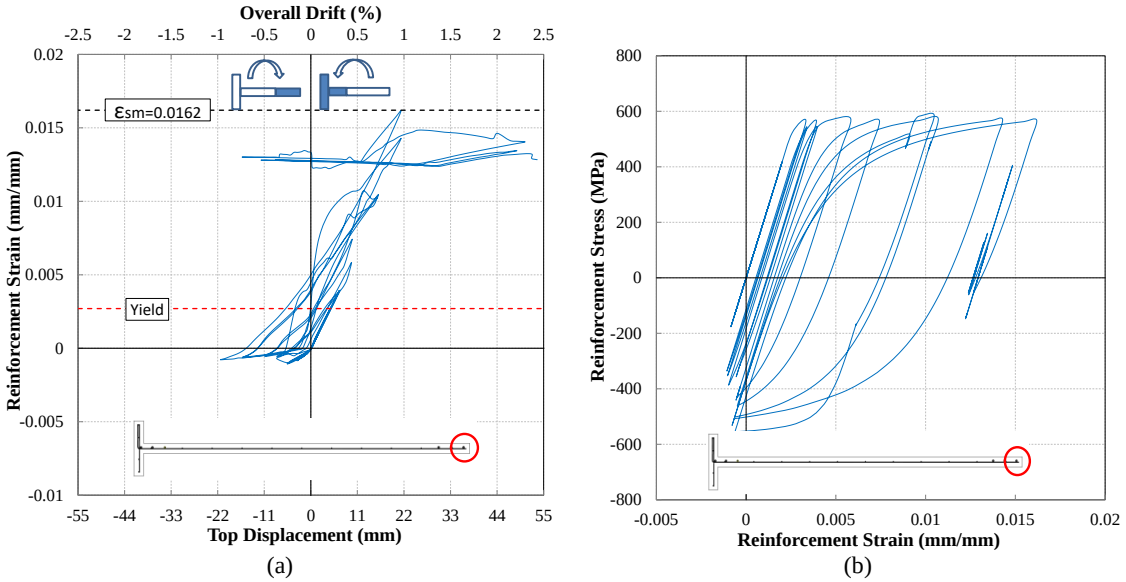

Figure 5.19: Response of the longitudinal reinforcement at the section exhibiting maximum out-of-plane deformation, TW1- C: (a) strain history; (b) stress-strain curve

5.2.2.3 TW1- D

The model without eccentricity is analyzed with also zero axial load ratio to evaluate the effect of axial load ratio on response of the concentrically loaded wall. The results of this model TW1-D (Figure 5.20 to Figure 5.22) do not indicate a considerable difference with respect to the model with eccentricity and no axial load (TW1-B).

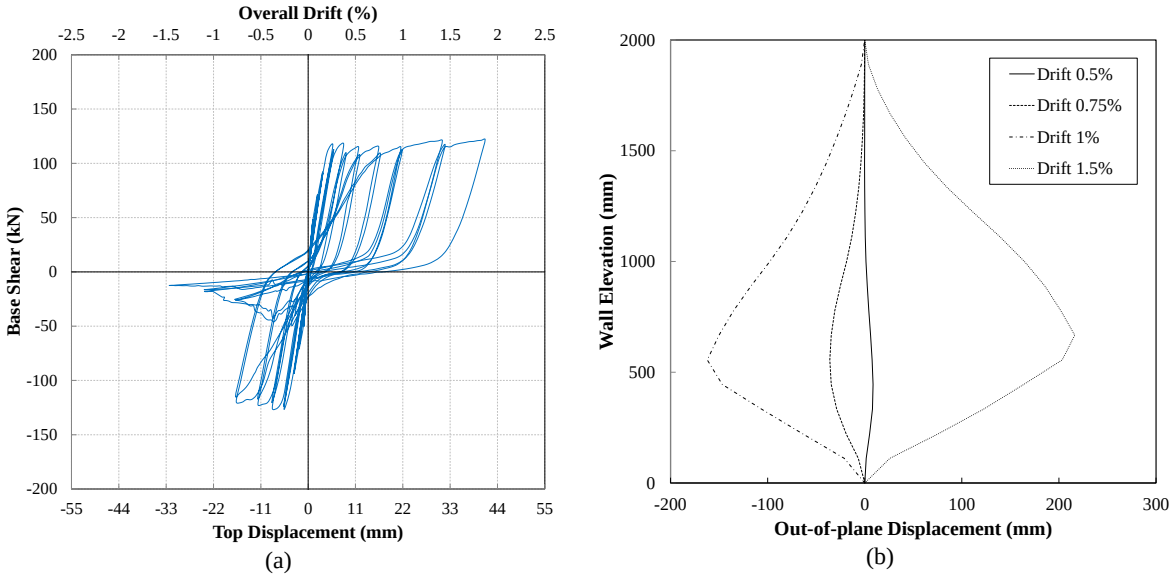

Figure 5.20: Model response, TW1- D: (a) lateral load vs top displacement response; (b) maximum out-of-plane deformation corresponding to each drift level

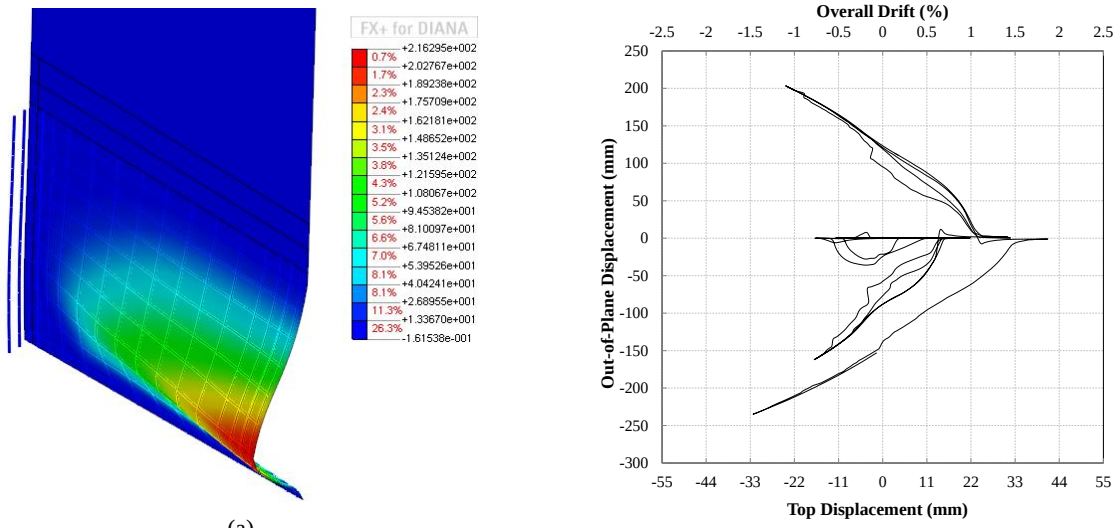

(a) (b)

Figure 5.21: Out-of-plane deformation-TW1-D: (a) deformation pattern at 1.5% drift cycle; (b) maximum out-of-plane displacement throughout the loading

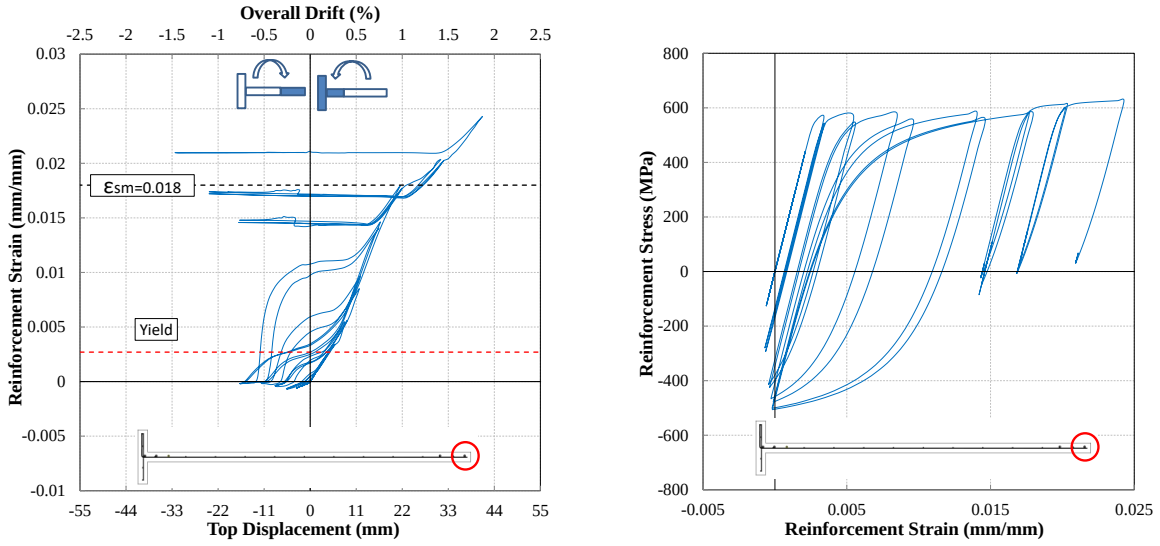

(a) (b)

Figure 5.22: Response of the longitudinal reinforcement at the section exhibiting maximum out-of-plane deformation, TW1- D: (a) strain history; (b) stress-strain curve

5.2.2.4 TW1-a

In the model TW1-a the reinforcement eccentricity was considered, and the axial load was applied according to the test program. The model differs from the benchmark test specimen TW1-A only for the shear span ration, reduced from 3.7 to 0.8 to investigate the effect of shear-dominated response to the development of out-plane mechanism. The response of this specimen was, as expected, governed by shear deformations and was accompanied by a limited out-of-plane deformation at the south boundary zone. The flange part of the wall

section, as expected, did not exhibit out-of-plane deformation. Figure 5.23 displays the lateral load versus top displacement response of the specimen as well as the maximum out-of-plane displacement at each drift level. As shown in Figure 5.23a, combination of the axial load and the wall geometry (i.e. squat wall) resulted in the shear-dominated response of the wall. Figure 5.6b shows development of the out-of-plane displacement starting from 0.5% drift level and increasing considerably at 1% and 1.5% drift levels. The out-of-plane displacement is minor in this case, only about 5% of that observed in TW1-A (e.g. max of 6 mm at 1.5% drift in TW1-a compared to 200 mm at 1.5% drift in TW1-A).

Figure 5.24a indicates the von Mises stress distribution of the model at 1.5% drift level when the out-of-plane displacement is developed at the south boundary zone, as shown in Figure 5.24b. The von Mises stress distribution shows development of the diagonal strut action with some partial vertical compression struts (mainly due to the axial load), and the dark blue region shows the area damaged considerably. As no load is carried by this area, the von Mises stress is understandably close to zero. The vertical strut at the boundary region is in fact not developed in the outer face of the section undergoing out-of-plane deformation, which has a von Mises stress value close to zero. On the other hand, the inner face of the section undergoing out-of-plane deformation (not presented herein), being under further compression, forms a strut and transfers the axial force to the base.

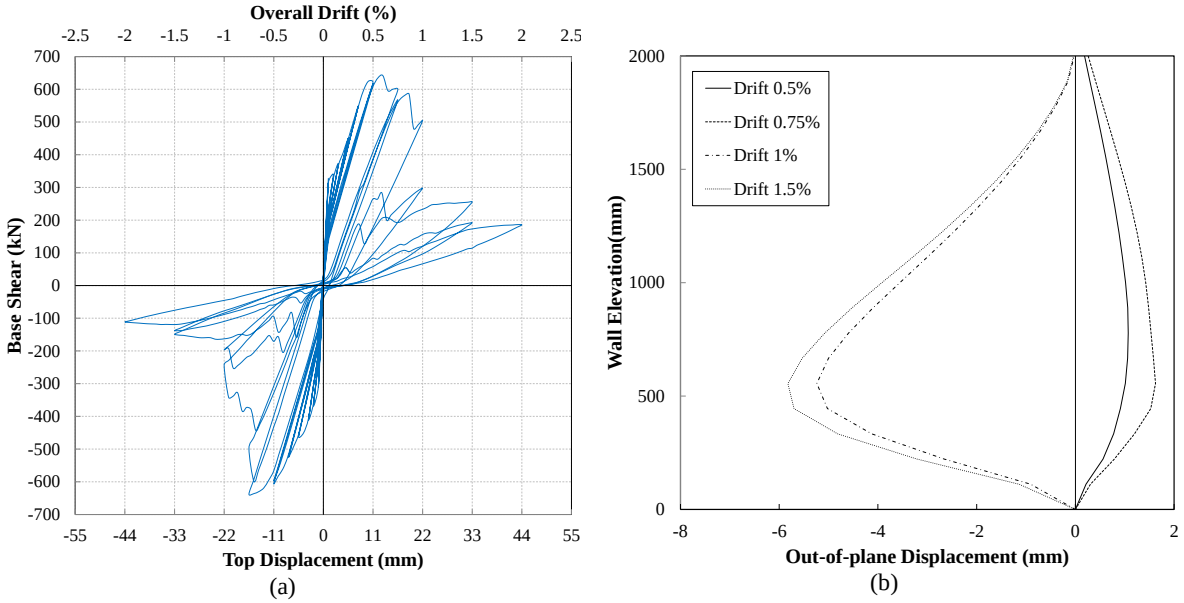

Figure 5.23: Model response, TW1-a: (a) lateral load vs top displacement response; (b) maximum out-of-plane deformation corresponding to each drift level

The strain history of the reinforcement at the end region of the wall corresponding to the section exhibiting the maximum out-of-plane deformation is plotted in Figure 5.25. It can be noted that up to 1% drift, there is an increase in the reinforcement strain along with increase of the top displacement and accumulation of residual strain as a result of cyclic loading. After that level of drift, there is a considerable decrease in the reinforcement strain which can be attributed to the shear failure of the model as a result of wall geometry and axial load ratio. The difference in this regard between this case and the corresponding model with high shear-span ratio (TW1-A, Figure 5.13a) is quite noticeable.

Figure 5.25a and Figure 5.25b display the residual strain and wall elongation developed throughout loading history. It can be observed that even under axial load ratio of 0.05, except for initial minor compressive strains, the strain at this region of the wall is tensile throughout the loading, confirming that the axial load carrying capacity at this region is provided by the reinforcement only.

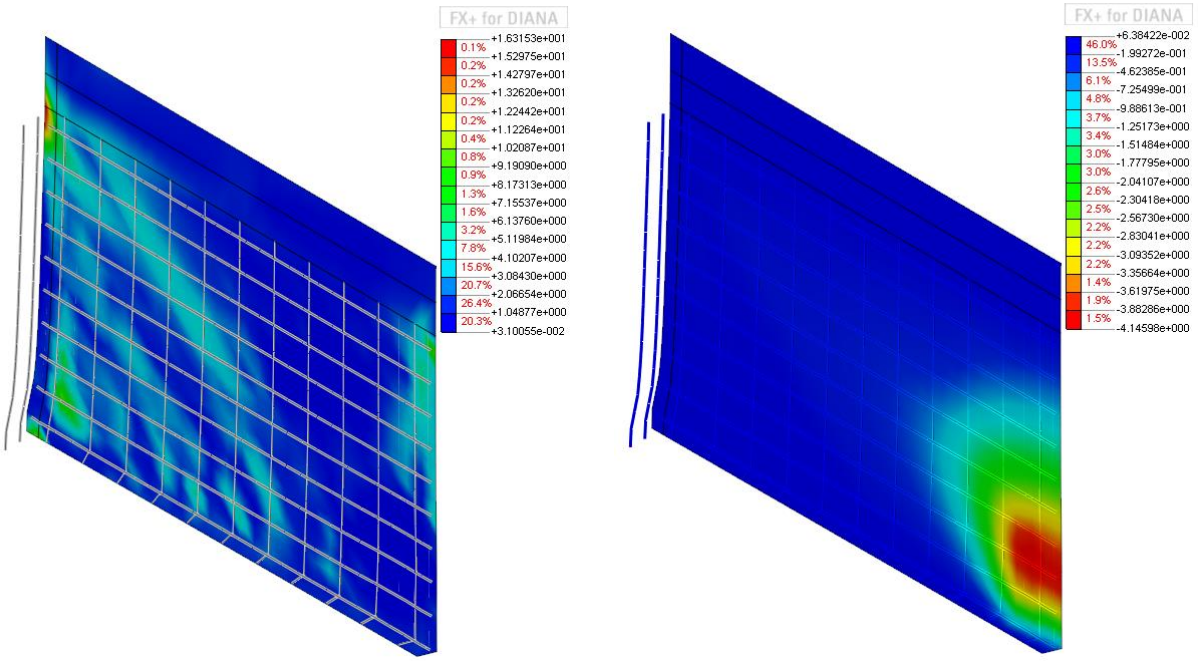

(a) (b)

Figure 5.24: Model response at -1.5% drift, TW1-a: (a) von Mises stress distribution; (b) out-of-plane deformation

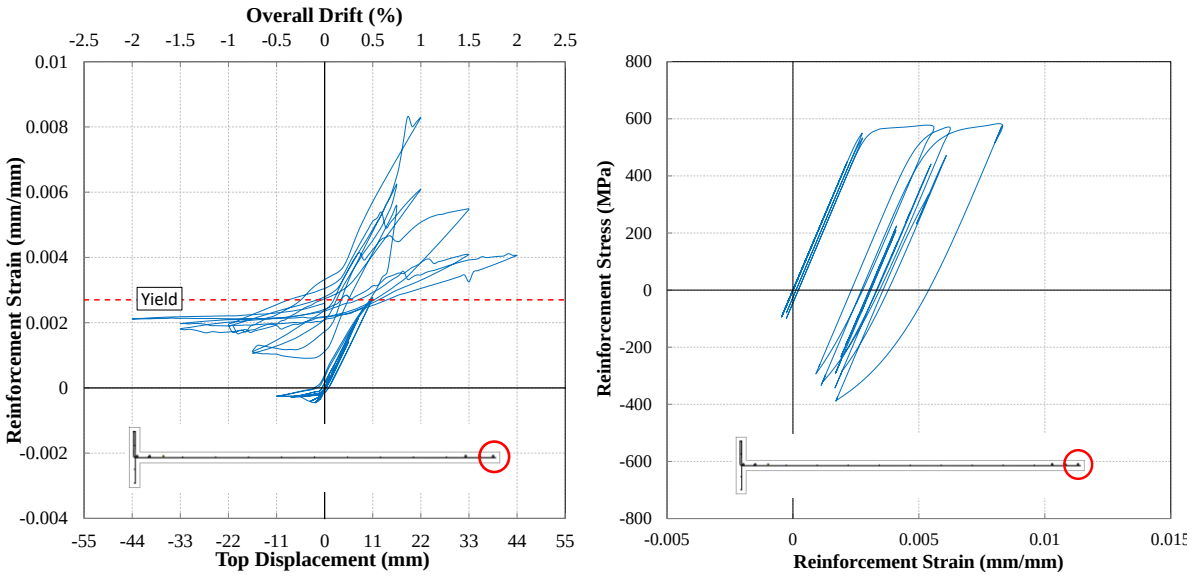

Figure 5.25: Response of the longitudinal reinforcement at the section exhibiting maximum out-of-plane deformation, TW1-a: (a) strain history; (b) stress-strain curve

5.2.2.5 TW1-b

In order to investigate the effect of axial load ratio on response of the wall, even in the case of lower shear span ratio 0.8, this model was analysed with no axial load. Being a squat wall, the model had considerable shear deformations. However, the lateral load-top displacement response (Figure 5.26a) does not show considerable degradation due to shear failure pattern which was observed in TW1-a. Instability of this model was due to the considerable out-of-plane deformation at the south boundary region as shown in Figure 5.26b. The out-of-plane deformation increased by five times between 1.0 and 1.5% drift levels showing instability of the model. The out-of-plane displacement of this model is about ten times that of TW1-a, showing the effect of axial load ratio on response of the wall. The von Mises stress distribution (Figure 5.27a) shows a diagonal strut as the only load carrying path since there is no axial load applied to the model. Figure 5.27b displays a considerable out-of-plane deformation of the model, almost two times the lateral displacement at the corresponding drift level (1.5% drift). Figure 5.28a shows the strain history of the south end region reinforcement at the section undergoing the maximum out-of-plane deformation. As can be seen in the figure, a significant residual tensile strain (about 0.0045) developed in the reinforcement during the 0.75% drift cycles, and consequently the cracks remained wide open forcing the bars to resist all vertical stresses, thereby resulting in considerable increase of the out-of-plane deformations. This residual strain increased significantly in the subsequent cycles and reached 0.01 during the 1.5%

cycle before abrupt increase of the out of plane deformation and instability of the wall. Figure 5.28a shows the maximum strain reached by the reinforcement at this drift level was ε_{sm}= 0.0136.

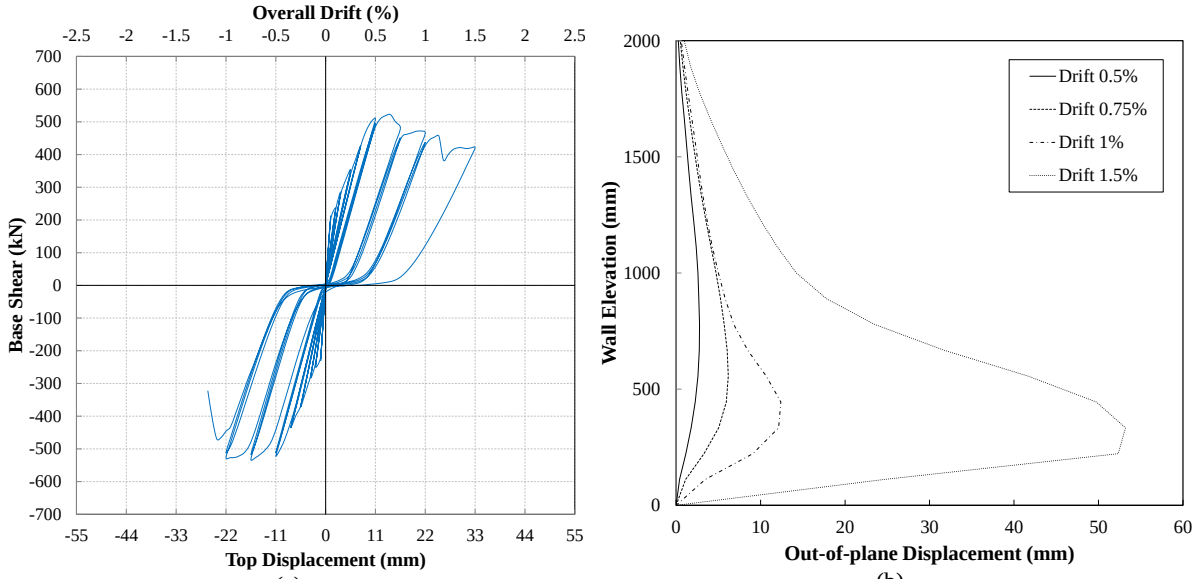

Figure 5.26: Model response, TW1-b: (a) lateral load vs top displacement response; (b) maximum out-of-plane deformation corresponding to each drift level

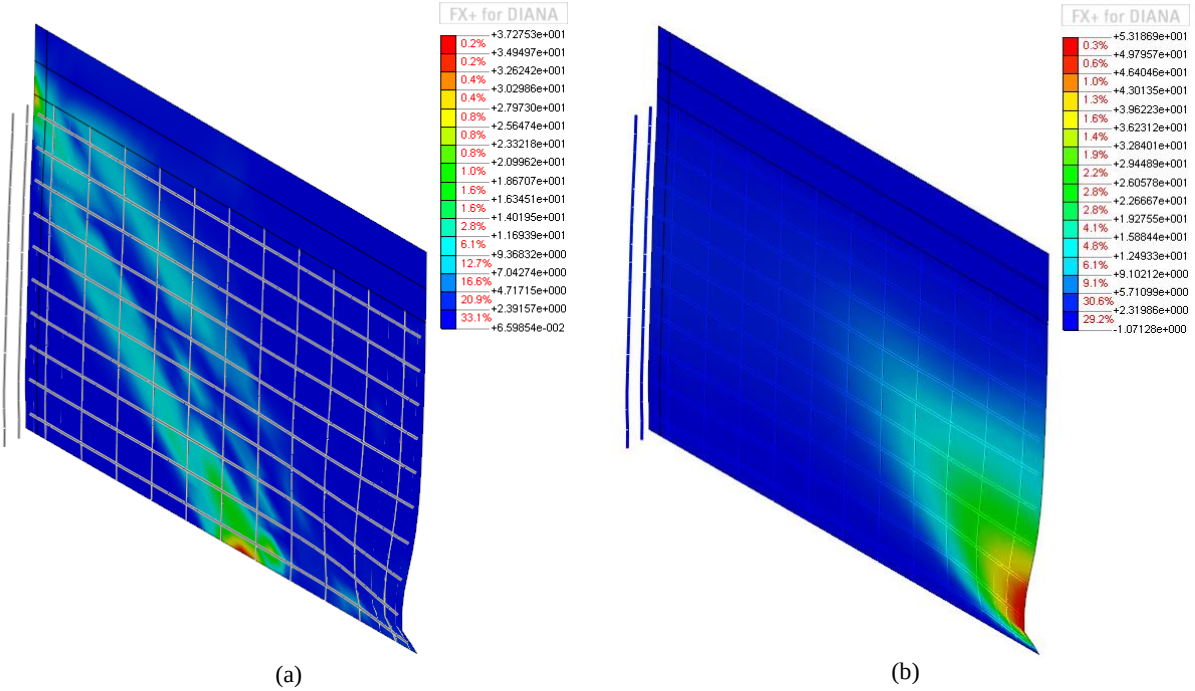

(a) (b)

Figure 5.27: Model response at -1.5% drift, TW1-b: (a) von Mises stress distribution (MPa); (b) out-of-plane deformation (mm)

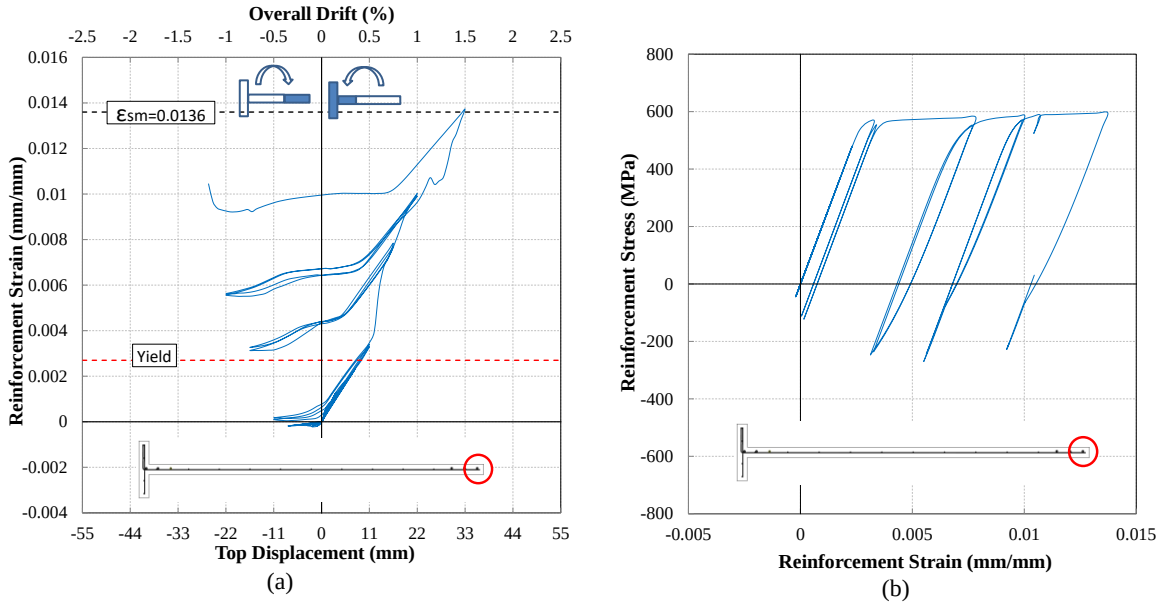

Figure 5.28: Response of the longitudinal reinforcement at the section exhibiting maximum out-of-plane deformation, TW1-b: (a) strain history; (b) stress-strain curve

5.2.2.6 TW1-c

In this section, the effect of reinforcement eccentricity on development of the out-of-plane deformation of the squat wall model is evaluated. For this purpose, the longitudinal and horizontal reinforcement elements are positioned at the section centreline, to represent the ideal condition of no eccentricity.

Significant shear degradation is observed in this model, as well (Figure 5.29a). The out of plane mechanism is still triggered but the out-of-plane deformations are decreased by almost 35% when compared to the equivalent model with eccentricity (i.e. TW1-a). The other response features (Figure 5.30 and Figure 5.31) resemble the ones of TW1-a, and are not hence described in this section.

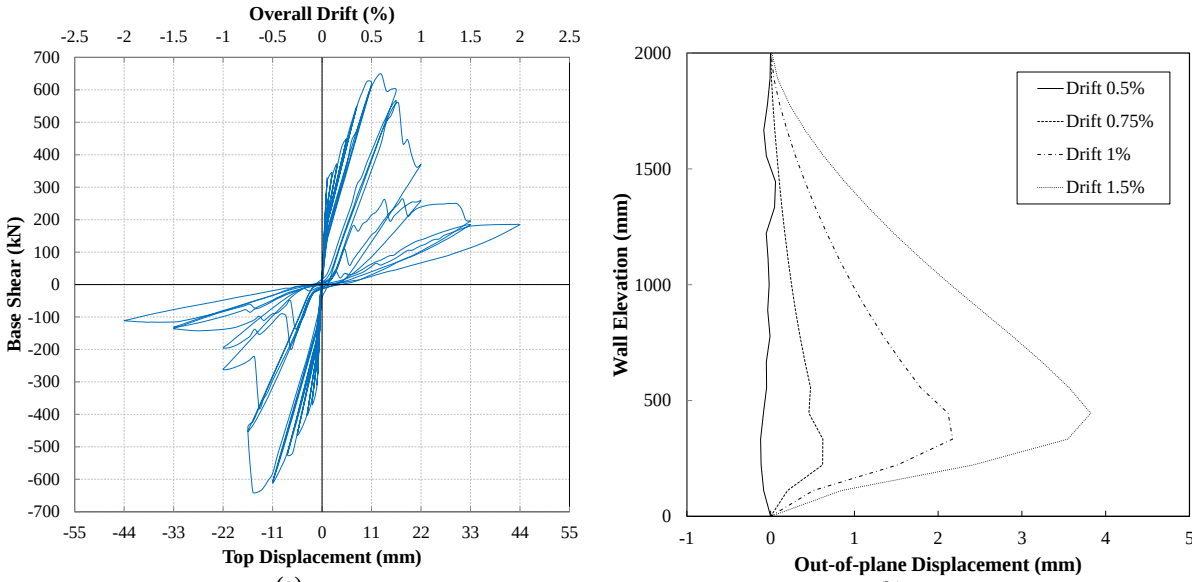

Figure 5.29: Model response, TW1-c: (a) lateral load vs top displacement response; (b) maximum out-of-plane deformation corresponding to each drift level

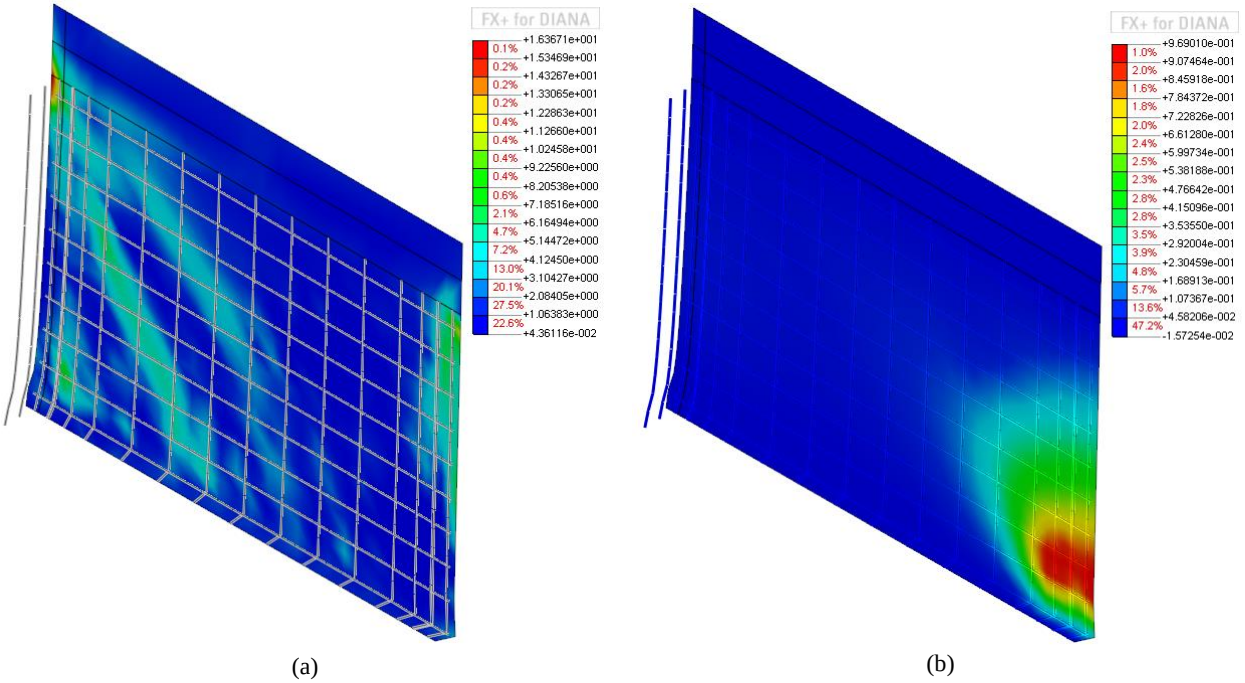

Figure 5.30: Model response at -1.5% drift, TW1-c: (a) von Mises stress distribution; (b) out-of-plane deformation

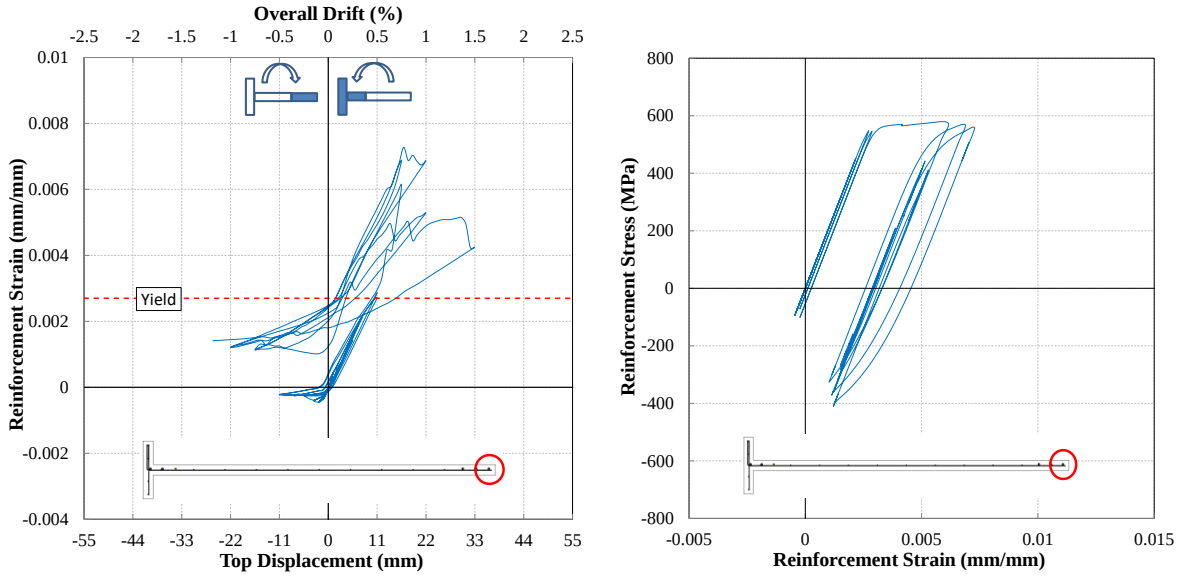

Figure 5.31: Response of the longitudinal reinforcement at the section exhibiting maximum out-of-plane deformation, TW1-c: (a) strain history; (b) stress-strain curve

5.2.2.7 TW1-d

The squat wall model with no eccentricity is analyzed without axial load in this section. The lateral load versus top displacement response of the wall shows a considerable degradation during the 1.5% drift cycle (Figure 5.32). However, despite having no eccentricity, the out-of-plane deformation is considerably large when compared to TW1-c, showing that the reduction of axial load ratio influences the response of this wall more than the eccentricity. The out-of-plane displacement of this model at 1.5% drift level is about 60% of that of TW1-b, showing that even a minor eccentricity, inevitable in construction particularly in singly reinforced walls, can significantly amplify out-of-plane deformations leading to instability and wall failure, as was observed in TW1-b. Figure 5.34a shows the level of strain reached by the end region reinforcement of TW1-d before development of a considerable out-of-plane deformation. The level of this strain is almost identical to the one in TW1-balthough the out-of-plane displacement is considerably lower at 1.5% drift level (33 mm compared to 53 mm) as no eccentricity was introduced in this case.

Figure 5.35 displays the maximum out-of-plane displacement of TW1-b and TW1-d throughout the loading. As can be seen in this figure, out-of-plane displacement of TW1-d recovered completely at lower drift levels until the 1.5% drift cycles, after which the out-of-plane displacement increased steadily and recovered only slightly. However, in the model with reinforcement eccentricity (i.e. TW1-b), the out-of-plane displacement did not recover during unloading from the 0.75% and 1.0% drift cycles, but its value was not large enough

to make the wall unstable. During the 1.5% drift cycle, the out-of-plane displacement of TW1-b increased quite significantly resulting in wall instability.

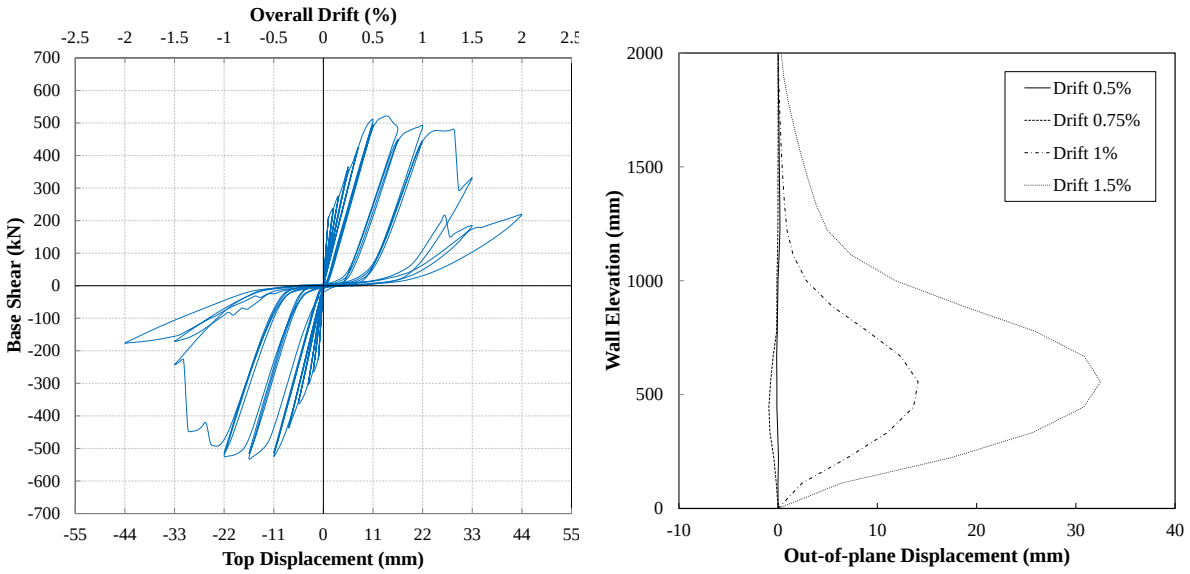

Figure 5.32: Model response, TW1-d: (a) lateral load vs top displacement response; (b) maximum out-of-plane deformation corresponding to each drift level

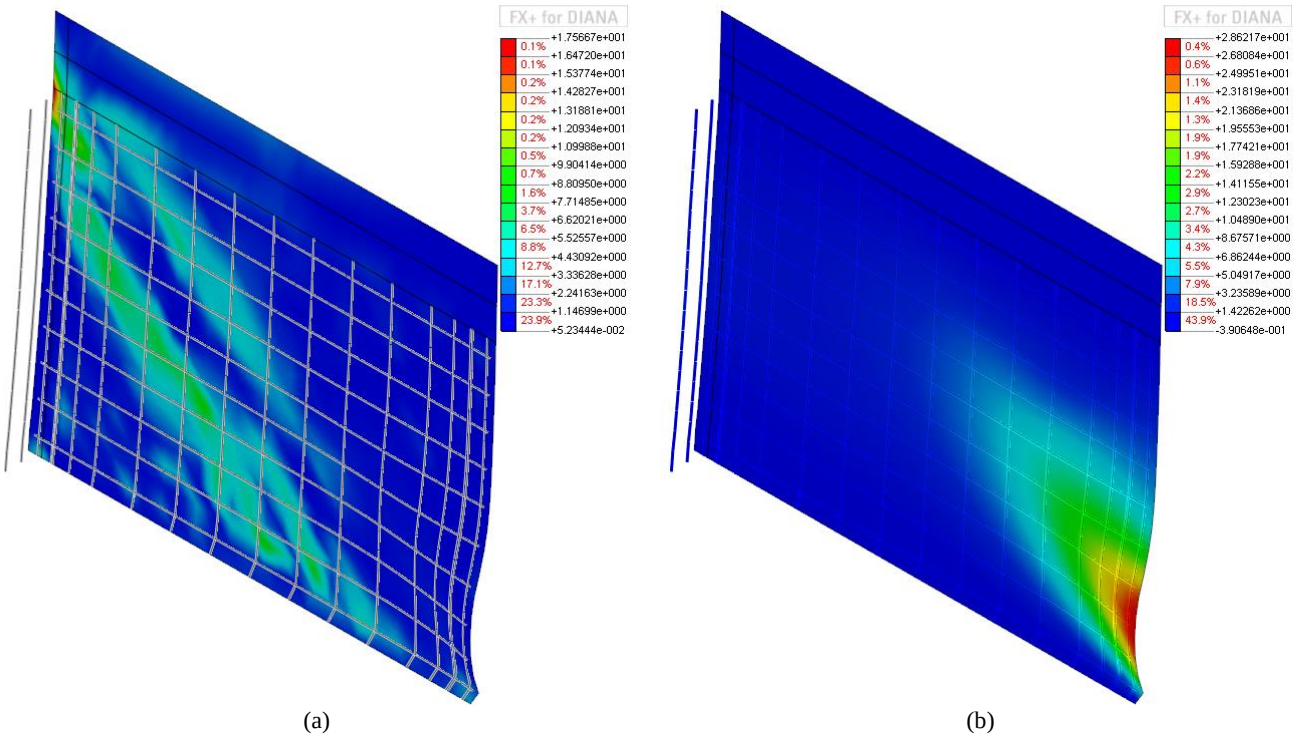

Figure 5.33: Model response at -1.5% drift, TW1-d: (a) von Mises stress distribution; (b) out-of-plane deformation

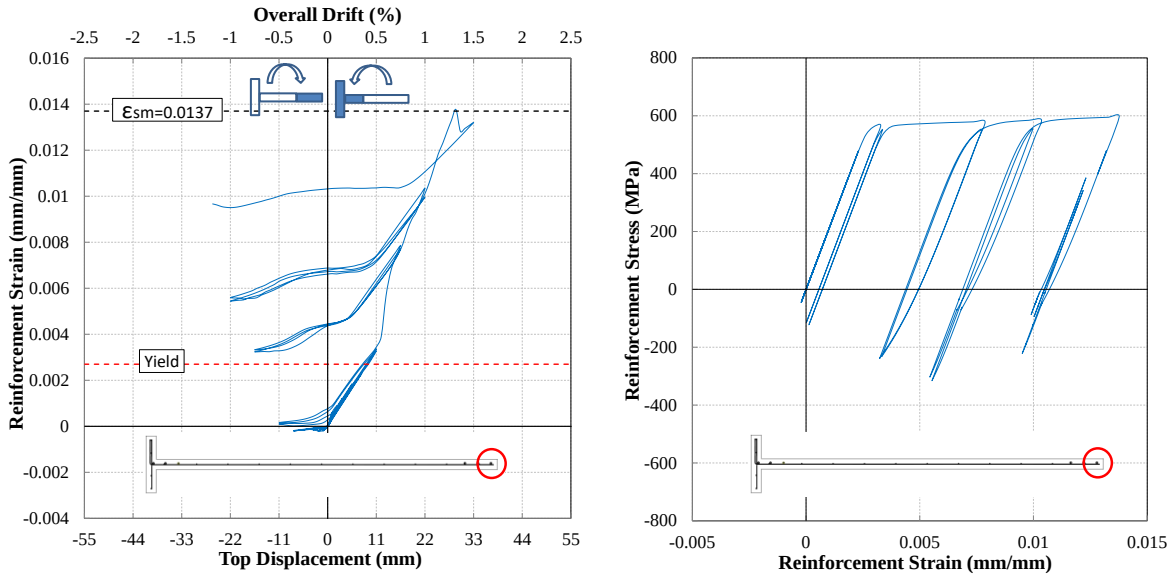

Figure 5.34: Response of the longitudinal reinforcement at the section exhibiting maximum out-of-plane deformation, TW1-d: (a) strain history; (b) stress-strain curve

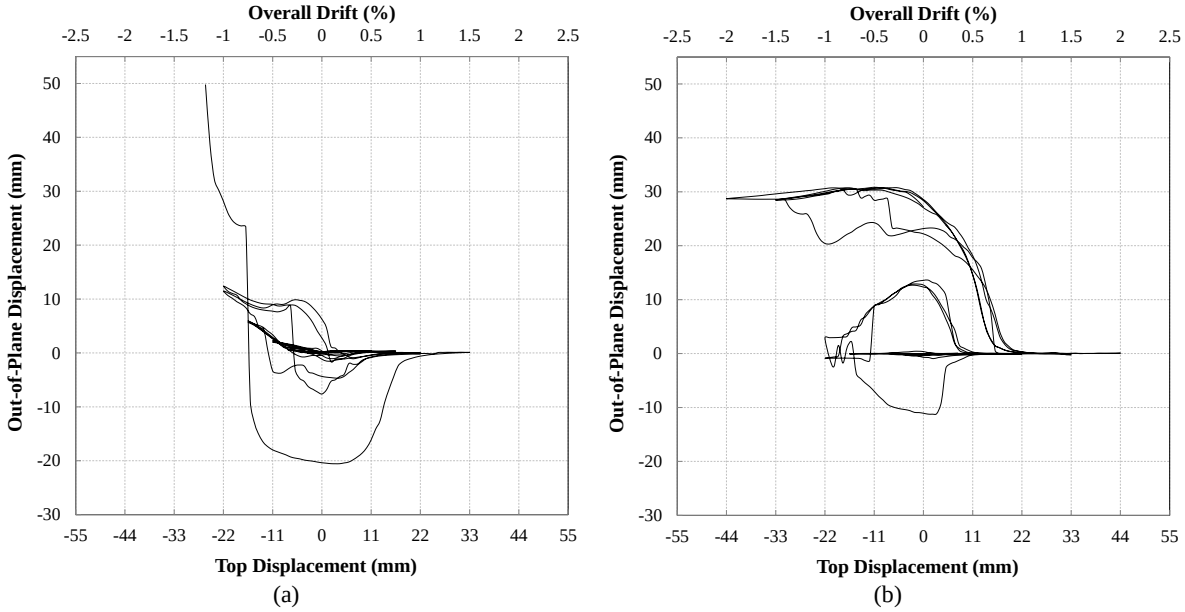

Figure 5.35: Out-of-plane displacement history at 450mm from the base: (a) TW1-b; (b) TW1-d

5.2.3 DISCUSSION

The numerical investigation presented in this study attempted to predict the failure patterns of a thin RC wall (TW1) tested in École Polytechnique Fédérale De Lausanne, Switzerland. Despite a short height of the specimen, the loading pattern was designed to represent a shear span of 10. For this purpose, in addition to the lateral displacement and axial load, a moment was also applied at the top of the specimen. Being a singly reinforced wall, the eccentricity of longitudinal reinforcement with respect to the loading plane could influence

the out-of-plane deformation pattern. The model was analyzed considering this effect as well as the effect of axial load which can also substantially affect the wall response. Another set of analysis was carried out by assuming a considerably lower shear-span ratio to investigate the effect of the same parameters in shear-dominated walls.

Figure 5.36 shows the effect of axial load ratio on the slender test model (shear-span ratio = 3.7) and the squat wall loading configuration (shear-span ratio = 0.8). Comparison between Figure 5.36a and Figure 5.36b displays the rather significant shear degradation of the squat wall. The slender model had out-of-plane instability as a governing failure pattern as shown by the degradation in negative displacement zone of the cyclic response curve (Figure 5.36a). According to Figure 5.36b, although the lack of the axial load reduced the brittleness of the shear failure of the model, the out-of-plane deformation increased significantly, leading to an abrupt instability to the numerical model and preventing it from reaching -1.5% drift level. The larger out-of-plane displacements of the wall with no axial load are due to the development of large residual tensile strains in the longitudinal reinforcement at the end region which delays or prevents the closing of the crack requiring compressive load (due to bending) to be transferred only to the steel reinforcement in the cracked section. Out-of-plane instability of the slender as well as the squat model indicated that, regardless of the shear-span ratio, geometric configuration of wall sections such as its thickness could also render the wall prone to out-of-plane instability.

The effect of reinforcement eccentricity on the slender wall was negligible although the eccentricity resulted in minor out-of-plane displacement at initial stages of loading. However, for the squat wall with no axial load the eccentricity resulted in earlier out-of-plane instability (Figure 5.37). Development of out-of-plane displacement in these models (Figure 5.14b and Figure 5.20b) indicate that, up to 1.0% drift level, the out-of-plane displacement of both models is almost identical. However, the reinforcement eccentricity of TW1-A resulted in faster increase of the out-of-plane displacement, leading to instability of the model (Figure 5.37). This instability happened before compression crushing along the diagonal strut or yielding of shear reinforcement could result in a considerable strength degradation. Only the reinforcement "design" eccentricity based on the CAD drawings provided by the experimenters are considered in this study. However, in real construction practice, there can be additional sources of eccentricities depending on the construction accuracy such as eccentricity in wall thickness along the height or even concrete homogeneity along the height or thickness depending on the casting type, i.e. horizontal or

vertical, which can significantly affect the wall response and generate bigger out-of-plane displacements at lower drift levels.

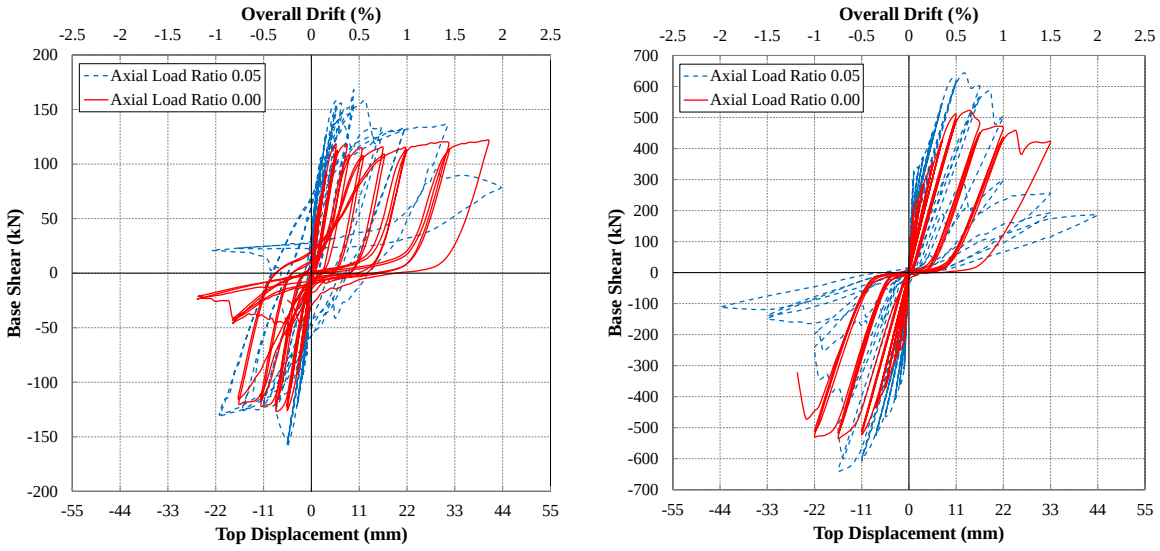

Figure 5.36: Effect of axial load ratio: (a) shear-span ratio = 3.7; (b) shear-span ratio = 0.8

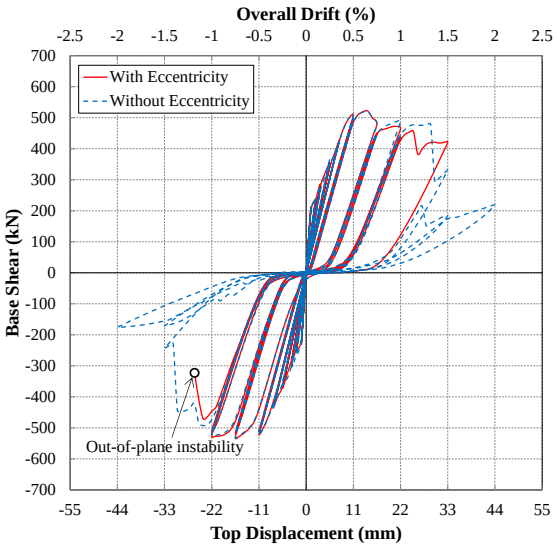

Figure 5.37: Effect of reinforcement eccentricity

Table 5.2 compares the maximum tensile strain of extreme end reinforcement prior to initiation of out-of-plane deformation and initiation of out-of-plane instability as well as the corresponding drift cycles for different models. Initiation of out-of-plane deformation corresponds to the phase when the first out-of-plane deformation started and fully recovered. Initiation of out-of-plane instability refers to the phase when the out-of-plane deformation reached a considerably large value (generally greater than half of the wall

thickness) and did not recover and increased steadily leading to instability of the wall model.

As can be seen in Table 5.2, TW1-A exhibited the initial out-of-plane deformation during the 0.50% drift cycle with the maximum reinforcement strain of 0.0053 ($2.0\varepsilon_y$) and became unstable during the 1.5% drift cycle with the maximum reinforcement strain of $\varepsilon_{sm} = 0.0204$ ($7.6\varepsilon_y$). When the axial load was removed from the same model (TW1-B), the initial out-of-plane deformation occurred during the 0.50% drift cycle when the reinforcement strain reached 0.0072 ($2.7\varepsilon_y$) and the out-of-plane instability happened during the 1.0% drift cycle when the maximum reinforcement strain was 0.0169 ($6.3\varepsilon_y$). TW1-A had a lower reinforcement strain (0.015) at the same (1.0%) drift level which prevented the instability during this cycle. However, the end region reinforcement had to reach a significantly higher level of strain in the next drift level (0.0204 at 1.5% drift) which exceeded the critical value and provoked the wall instability.

The initial out-of-plane displacement of TW1-B (during the 0.50% drift) was about half of the corresponding value in TW1-A. However, the removal of axial load resulted in significantly faster growth of out-of-plane displacement in TW1-B compared to TW1-A, and caused a maximum out-of-plane displacement of about four times greater during the 1.0% drift cycle. The comparison between Figure 5.13 and Figure 5.16 indicates the effect of axial load on the strain history of the end bar. Although removal of axial load resulted in higher values of strain at peak drift levels, its effect on the values of strain during unloading/reloading phase and at around 0.0% drift level was greater. The difference in strain histories during the 0.75% and 1.0% drift cycles of TW1-A (Figure 5.13) with the corresponding cycles of TW1-B (Figure 5.16) is a good case in point. The zone around 0.0% drift level during unloading/reloading phase corresponds to development of the maximum out-of-plane deformation, and any variation in the residual tensile strain at this stage would considerably affect the possibility of timely crack closure and consequently out-of-plane response of the wall.

When eccentricity of the longitudinal reinforcement was removed from the model, i.e. TW1-C and TW1-D, the value of maximum strain in TW1-C and TW1-D at 1.0% drift increased to 0.0162 and 0.018, respectively. Both models became unstable at this drift level indicating that the critical strain value for this model could be around 0.016. The axial load ratio of TW1-D was 0.0 and understandably had a larger reinforcement strain compared to TW1-C. Also, the initial out-of-plane deformation happened at a later stage in TW1-C

(ε_{sm}=0.01 during the 0.75% drift cycle) compared to TW1-A, and occurred at the same drift cycle in TW1-D as TW1-B.

The effect of eccentricity in position of the longitudinal reinforcement with respect to the loading plane was observed in the models with low shear-span ratios, as well. As can be seen in Table 5.2, removal of this eccentricity resulted in a delay in initiation of out-of-plane deformation and consequently caused the corresponding values of reinforcement strain to be higher by more than two times. Among the models with low shear-span ratios, only TW1-b and TW1-d that had no axial loads exhibited out-of-plane instabilities. The values of ε_{sm} and drift levels corresponding to instability phase were identical for these models but TW1-b was eccentrically reinforced and, as discussed above, exhibited faster increase of out-of-plane displacement.

Table 5.2: Reinforcement strain and drift levels prior to initiation of out-of-plane instability

Model	Shear-Span Ratio	Eccentricity	Axial Load Ratio	OOP Deformation		OOP Instability	
				ε_{sm}	Drift	ε_{sm}	Drift
TW1- A	3.7	Yes	0.05	0.0053(2.0ε_y)	0.50%	0.0204(7.6ε_y)	1.5%*
TW1- B	3.7	Yes	0.00	0.0072(2.7ε_y)	0.50%	0.0169(6.3ε_y)	1.0%
TW1- C	3.7	No	0.05	0.01(3.7ε_y)	0.75%	0.0162(6.0ε_y)	1.0%
TW1- D	3.7	No	0.00	0.008(3.0ε_y)	0.50%	0.018(6.7ε_y)	1.0%
TW1- a	0.8	Yes	0.05	0.0027(1.0ε_y)	0.50%	NA	NA
TW1- b	0.8	Yes	0.00	0.0033(1.2ε_y)	0.50%	0.0136(5.0ε_y)	1.5%
TW1- c	0.8	No	0.05	0.006(2.2ε_y)	0.75%	NA	NA
TW1- d	0.8	No	0.00	0.008(3.0ε_y)	0.75%	0.0137(5.0ε_y)	1.5%

Note: ε_{sm} = Maximum tensile strain of extreme end reinforcement prior to initiation of out-of-plane deformation/instability; Drift = maximum in-plane drift level of the specimen prior to initiation of out-of-plane deformation/instability.
*At 1.0% drift level, the maximum tensile strain of extreme end reinforcement in TW1-A was 0.015 (arguably just below the critical strain ~ 0.016).

5.3 NUMERICAL PREDICTIONS VS EXPERIMENTAL OBSERVATIONS

Figure 5.38 compares the numerical model predictions with the experimental observations (Rosso et al. 2015). As can be seen in Figure 5.6, the model was loaded up to 2% drift level before being terminated due to numerical instability. For the sake of better comparison between experimental and predicted load-displacement curves, Figure 5.38a does not display the numerical model results beyond the 1.5% drift cycle. During this cycle and upon unloading of the model, a significantly large out-of-plane displacement occurred (Point c, Figure 5.6), which increased steadily up to reloading in the reverse direction (Figure 5.9b).

The in-plane load-displacement response of the tested specimen (shown in Figure 5.38a) displays a reasonable agreement with the analytically predicted response. However, the

drop of strength does not seem to be well captured by the model. According to the parametric studies described in the previous sections, this abrupt drop of strength were predicted in other wall models that were subjected to axial load ratio of 0.05.

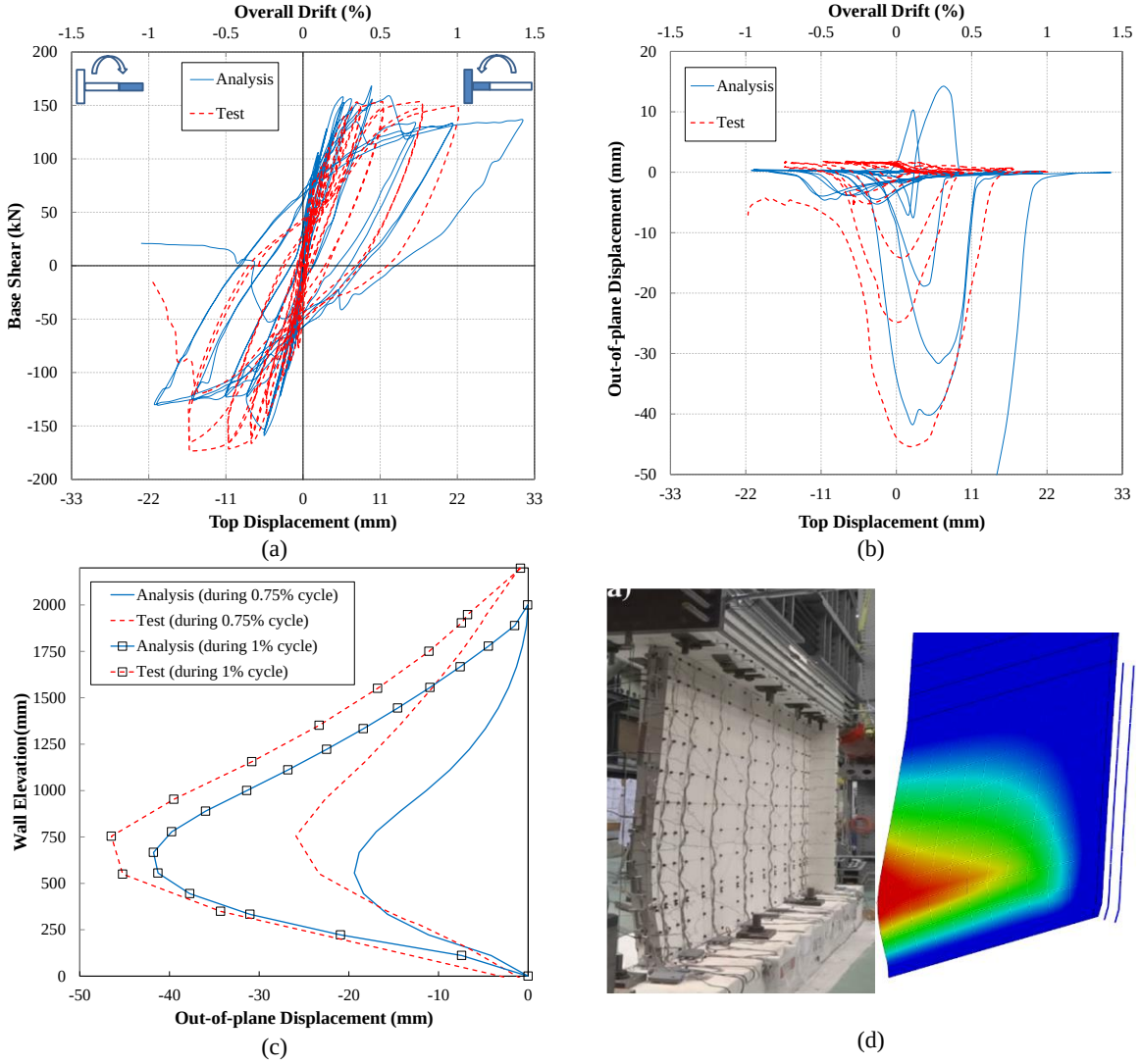

Figure 5.38: Verification of the blind prediction: (a) in-plane load-displacement response of the wall; (b) in-plane vs out-of-plane displacement response of the wall; (c) out-of-plane displacement profile along the wall height; (d) experimental observation vs numerical simulation of out-of-plane deformation, photo courtesy of Rosso et al. (2015)

As a mesh sensitivity analysis was not carried out and a relatively fine mesh was adopted to capture a better prediction of the out-of-plane displacement pattern along the wall height, localization of deformations was inevitable. In order to further investigate this effect, the tested wall is modelled and analyzed here again (as a controlled modification to the blind predictions) with medium and coarse mesh configurations. Figure 5.39 displays the effect of mesh size on the monotonic response of the model. As can be seen in this figure, the increase in mesh size has resulted in delay of the strength drop. Localization in finite element analysis has been thoroughly studied by Bažant and Oh (1983), Bazant and Planas

(1997) and De Borst (1997), and the concrete post-peak tensile stress-strain response model as well as concrete compressive response are generally regularized to limit mesh sensitivity. In this prediction, the material model regularization was not addressed.

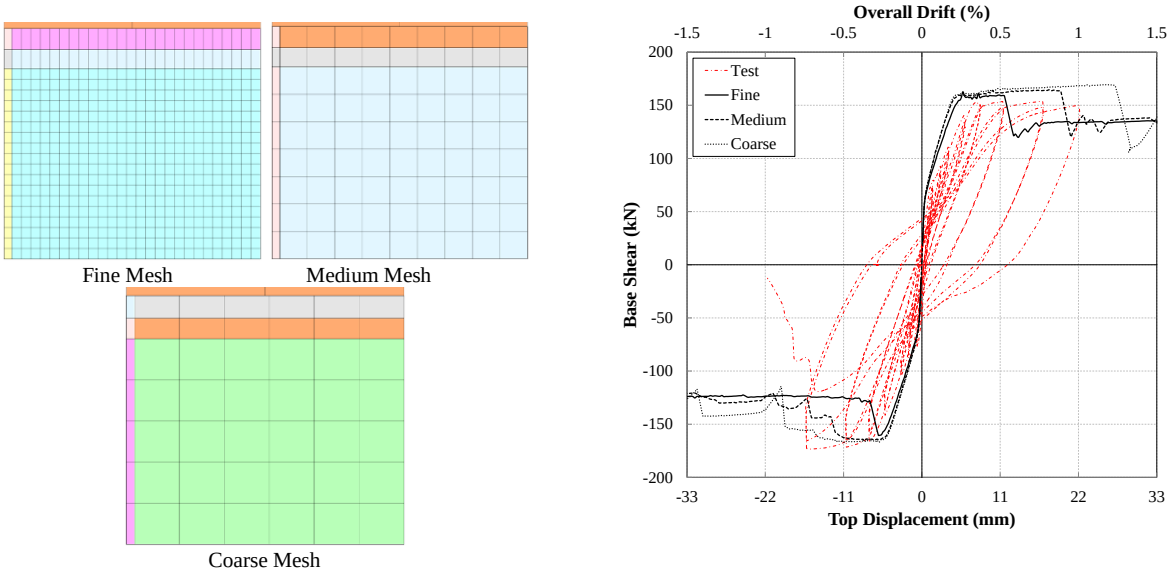

Figure 5.39: Sensitivity of the model to mesh size

Figure 5.38b displays the maximum out-of-plane displacement of the wall at different stages of loading. As can be seen in this figure, the numerical model could reasonably predict the development of the out-of-plane deformation. In both numerical prediction and test results, the out-of-plane displacement initiated at small drift levels, and increased along with increase of the drift level. At every cycle, out-of-plane displacement initiated and increased when unloading from the peak displacement of the cycle and recovered when reloading in the reverse direction. This phenomenon well describes dependency of the out-of-plane deformation of a wall section on the residual strain of the reinforcement and the crack opening corresponding to the peak in-plane displacement of a specific cycle. The numerical model could reasonably predict the milestones of the out-of-plane displacement; particularly the points corresponding to the maximum out-of-plane displacement.

As noted above, based on the numerical model predictions and the parametric studies, the critical value of strain for this wall could be around 0.016, above which the out-of-plane deformation could not recover and would increase steadily. However, the test was stopped when a considerable amount of residual out-of-plane deformation was developed in the south end of the specimen during the 1.0% drift cycle (Figure 5.38b) and the out-of-plane displacement had started to increase after its recovery by almost 90%. This increase in out-of-plane displacement could be attributed to concrete crushing at inner face of the out-of-

plane deformation profile and is well described by Chai and Elayer (1999) (Section 2.2.3). The maximum strain reached during this cycle was about 0.013. Had the loading continued with some more cycles at the same drift level or a higher drift level (i.e. 1.5% drift), the maximum strain might have exceeded the critical value, and could have prevented recovery of the out-of-plane displacement at around 0.0% drift during unloading/reloading from the peak positive top displacement. This could result in the steady increase of out-of-plane displacement and out-of-plane instability of the section.

Figure 5.38c shows the maximum out-of-plane displacement profile along the wall height predicted by the model in comparison with the experimental observations. The wall height corresponding to the maximum out-of-plane displacement was reasonably predicted by the model. However, due to the representation of the cap beam and the extended height of the model (Figure 5.4) using linear elastic material properties (to simulate the shear-span ratio experimentally adopted in the loading regime) the value of the out-of-plane displacement is zero above the 2000mm elevation of the wall, while the test measurements display non-zero values for this zone. Figure 5.38d compares the out-of-plane deformation pattern of the specimen with the numerical simulation.

5.4 CONCLUSIONS

The capability of the numerical model to simulate the out-of-plane displacement of rectangular structural walls subjected to in-plane loading was further verified through blind prediction of the response of a wall specimen tested in École Polytechnique Fédérale de Lausanne (EPFL). The specimen was a singly reinforced T-shaped wall panel with a shear-span ratio of 3.7 and subjected to uni-directional (in-plane) quasi-static reversed cyclic loading regime. The numerical model exhibited a flexure-dominated response accompanied by out-of-plane deformations. A parametric analysis was carried out addressing the effects of axial load ratio, shear-span ratio, and eccentricity of the longitudinal bars on response of the specimen.

The numerical model could predict the lateral load-top displacement response of the specimen reasonably well. The out-of-plane displacement of the specimen was well captured by the model at different drift levels. Furthermore, the model could simulate the out-of-plane instability of the specimen, which was characterized by an abrupt degradation of the cyclic load displacement curves.

The axial load proved to affect the development of out-of-plane deformation in rectangular walls by controlling the values of strain developed in the longitudinal reinforcement at different stages of a specific cycle. This effect was significantly large during unloading/reloading phase and at around 0.0% drift level in a loading cycle, which is the stage corresponding to the maximum values of out-of-plane displacement.

Out-of-plane deformation of the slender models as well as the squat models indicated that, regardless of the shear-span ratio, geometric configuration of wall sections such as its thickness could also render the wall prone to out-of-plane instability. The maximum tensile strain corresponding to initiation of out-of-plane deformation and out-of-plane instability was lower in squat wall models when compared to the slender ones.

Being a singly reinforced wall, the eccentricity of longitudinal reinforcement with respect to the loading plane influenced the out-of-plane response and resulted in its earlier initiation. However, its effect during the final stages of wall response and formation of out-of-plane instability was not very significant.

Since accumulation of residual tensile strain in bars under cyclic loading leads to a significant delay in crack closure and all compression is taken by the bars at this stage, the wall is prone to undergo out-of-plane deformations in the compression boundary region if yielding in compression occurs before crack closure can happen. Therefore, depending on the initial tensile strain developed in the longitudinal reinforcement, different scenarios can happen. If this strain is less than a critical value, timely crack closure can activate contribution of concrete to the load-carrying capacity of the section and lead to recovery of the out-of-plane deformation. Otherwise, the out-of-plane deformation can increase steadily and lead to out-of-plane instability of the wall. Based on the numerical model predictions and the parametric studies, this critical value of strain for could be around six times the yield strain for the tested specimen.

Use of a single layer of reinforcement makes structural walls more susceptible to out-of-plane instability failure. This is because following development of large tensile residual strains in the longitudinal reinforcement, a single layer of vertical reinforcement lacks a mechanism to restore stability when development of yielding in compression occurs in the reinforcement before crack closure can activate contribution of concrete to the load-carrying capacity of the section. In doubly reinforced sections, this instability can be delayed as both layers of longitudinal reinforcement would not undergo identical amounts of tensile and compressive strains due to the inherent eccentricities of the wall section along

its thickness, and the second layer of longitudinal reinforcement would restore stability of the section if only one of the layers yielded in compression.

5.5 REFERENCES

Almeida, J., O. Prodan, A. Rosso and K. Beyer (2017). "Tests on Thin Reinforced Concrete Walls Subjected to In-plane and Out-of-plane Cyclic Loading." *Earthquake Spectra* 33(1), 323-345.

Bažant, Z. P. and B. H. Oh (1983). "Crack band theory for fracture of concrete." *Matériaux et construction* 16(3), 155-177.

Bazant, Z. P. and J. Planas (1997). Fracture and size effect in concrete and other quasibrittle materials, CRC press.

Beattie, G. J. (2004). Design of Slender Precast Concrete Wall Panels – Experimental Testing. BRANZ Study Report SR 129, BRANZ Ltd, Judgeford, New Zealand.

Chai, Y. H. and D. T. Elayer (1999). "Lateral stability of reinforced concrete columns under axial reversed cyclic tension and compression." *ACI Structural Journal* 96(5), 780-789.

Dashti, F., R. Dhakal and S. Pampanin (2015). Development of out-of-plane instability in rectangular RC structural walls 2015 NZSEE Conference, Rotorua, New Zealand, New Zealand Society for Earthquake Engineering.

De Borst, R. (1997). "Some recent developments in computational modelling of concrete fracture." *International journal of fracture* 86(1-2), 5-36.

Krolicki, J., J. Maffei and G. Calvi (2011). "Shear strength of reinforced concrete walls subjected to cyclic loading." *Journal of earthquake engineering* 15(S1), 30-71.

Moyer, M. J. and M. J. Kowalsky (2003). "Influence of tension strain on buckling of reinforcement in concrete columns." *ACI Structural Journal* 100(1).

Paulay, T. and M. Priestley (1993). "Stability of ductile structural walls." *ACI Structural Journal* 90(4), 385-392.

Rosso, A., J. Almeida and K. Beyer (2015). "Stability of thin reinforced concrete walls under cyclic loads: state-of-the-art and new experimental findings." *Bulletin of Earthquake Engineering*, 1-30. DOI: 10.1007/s10518-015-9827-x.

Rosso, A., J. P. Almeida and K. Beyer (2014). Short report on the experimental cyclic test of a thin RC wall (TW1) for blind prediction purposes, ÉCOLE POLYTECHNIQUE FÉDÉRALE DE LAUSANNE.

6 A PARAMETRIC STUDY ON OUT-OF-PLANE DEFORMATIONS OF RECTANGULAR STRUCTURAL WALLS SUBJECT TO IN-PLANE LOADING; EXPERIMENTAL INVESTIGATION

Dashti, F., R.P. Dhakal, S. Pampanin (2017) “Tests on Slender Ductile Structural Walls Designed According to New Zealand Standard” *Bulletin of the New Zealand Society for Earthquake Engineering*

Dashti, F., R.P. Dhakal, S. Pampanin (2017) "An Experimental Study on Out-of-plane Deformations of Rectangular Structural Walls Subject to In-plane Loading" *16th world conference on earthquake engineering, 16WCEE, January, 2017,* Santiago, Chile.

As also mentioned in Chapter 1, although the out-of-plane instability was observed in several wall tests, scrutinizing the failure mechanism and the governing parameters had not been the main objective of these researches. Therefore, the test setups did not include restraints at story levels to represent the unsupported height in a real building which is a crucial parameter for investigation of out-of-plane instability. Also, the measurements were not done to capture the initiation of out-of-plane deformation and its relationship with the local response of materials. This mode of failure has generally been investigated by testing concrete columns representing boundary zones of rectangular walls under axial cyclic loading. However, some assumptions regarding the boundary conditions and extent of the wall height and length involved in formation of the buckling failure need to be made in this approach. Almeida et al. (2017) investigated the out-of-plane failure mode of walls by analyzing the response of two singly reinforced T-shaped walls tested under cyclic loading. The specimens were identical but were subjected to two different in-plane and bi-directional loading patterns. However, no tests have been conducted on doubly reinforced

walls to address the mechanism of out-of-plane instability failure in rectangular walls and the governing parameters. Therefore, the out-of-plane instability of slender rectangular walls subject to in-plane loading is investigated in this study by testing three rectangular wall specimens subject to cyclic quasi-static loading. This chapter describes the test matrix, the specimen design, the configuration of the test setup, the loading, and the instrumentation scheme used in this experimental study. The specimens were half-scale, representing a shear span of 6.0 m and were designed according to NZS3101:2006, with different thicknesses and lengths to investigate the effects of these parameters on the onset and extent of out-of-plane displacement. Response of the specimens was predicted using the numerical model validated in Chapters 3, 4 and 5 using test results of several wall specimens available in literature that had exhibited different failure patterns including out-of-plane instability. This numerical prediction is discussed in Chapter 7 and the experimental results are presented in this chapter with focus on the significant stages of wall response observed during the test and the effects of the above-mentioned parameters on the sequence of these stages.

6.1 TEST MATRIX

In order to identify the parameters affecting the initiation and development of out-of-plane deformation in rectangular walls, a detailed investigation of the wall response at the material level and at different stages of development of the out-of-plane deformation was carried out using a numerical model that had been verified for its capability to simulate different failure modes of rectangular walls (Section 4.4.1 and Section 4.4.2). Also, the formation of out-of-plane deformation in the numerical model was scrutinized with reference to the postulations and experimental observations of other researchers. Wall thickness as well as the parameters that affect the development of tensile strain in the reinforcement, such as wall length and axial load, was identified as the main parameters controlling this mode of deformation in rectangular walls. Wall thickness, wall length and axial load were selected as the parameters of the experimental study. A four-specimen test matrix was hence designed (Table 6.1) to investigate the effect of these parameters. However, due to the structural laboratory decanting and refurbishment process, the last specimen could not be tested, i.e. the effect of axial load could not be investigated. The specimens were all designed according to the latest version of the New Zealand Concrete Standard (NZS3101 2006). Response of the specimens was predicted using the numerical

model. The numerical model predictions are compared with the experimental observations in Chapter 7.

Table 6.1: Test specimens

Parameter	Specimen
	RWB (Benchmark specimen)
Wall thickness, t_w	RWT (Thickness increase)
Wall length, l_w	RWL (Length decrease)
Axial load	RWA (Axial load increase)

Specimen RWB was considered the benchmark specimen. All other specimens differed from the benchmark specimen in just one of the above-mentioned three parameters, while satisfying roughly identical moment capacities as the benchmark specimen. Specimen RWT differed from Specimen RWB in its thickness (8% increase). Specimen RWL was shorter when compared to Specimen RWB (20% decrease), and consequently had larger longitudinal reinforcement ratio in the boundary region to compensate for the reduction of the moment capacity coming from the reduction of the flexural lever arm of the section. Specimen RWA was identical in geometry and reinforcement characteristics to Specimen RWB and was supposed to be subjected to a higher axial load ratio.

6.1.1 DIMENSIONS

The specimen dimensions were determined based on an iterative approach to satisfy the laboratory limitations (i.e. length, height and loading restrictions), the specified shear-span ratio, and a thickness slightly higher than the corresponding minimum thickness requirement of the standard. A shear-span ratio of 3.0 was considered for the benchmark specimen. As the main objective of the experimental study was to investigate the out-of-plane response of walls, the out-of-plane restraint provided by the floor slab was taken into account. For this purpose, the scale factor of the specimens was chosen such that the specimens could represent the first storey of a multi-storey high wall. The unsupported height of the specimens was considered to be 2.0 m, and the maximum wall length that could be accommodated in the laboratory was 2.0 m. Therefore, the test specimens could be considered as half-scale models of a prototype wall.

With shear-span ratio of 3.0, if a linear (triangular) equivalent lateral load distribution acting at an effective height of $0.75h_4$ was considered, where h_4 is the height of the multi-storey wall, the specimens could represent the first story of a four-storey high wall. Figure 6.1 displays the dimensions of the possible prototype wall and the specimens as well as the loadings applied on the specimen. To safeguard against premature out-of-plane buckling in

the potential plastic hinge region of the walls, the dimension limitations of Section 11.4.2 of the New Zealand Concrete Standard (NZS3101 2006) were checked. For walls with axial force levels greater than $0.05f_c'A_g$ and for ductile or limited ductile plastic region a minimum thickness shall be provided in the boundary region of the wall section, extending over the lesser of the plastic hinge length or the full height of the first storey. The specified thickness of the specimens was slightly higher than this minimum thickness although the axial force level of all the test specimens except RWA was about $0.05f_c'A_g$. Specimen RWL was 400 mm (20%) shorter in length compared to the benchmark specimen (RWB), and thickness of Specimen RWT was 10 mm (8.0%) larger than the one of Specimen RWB.

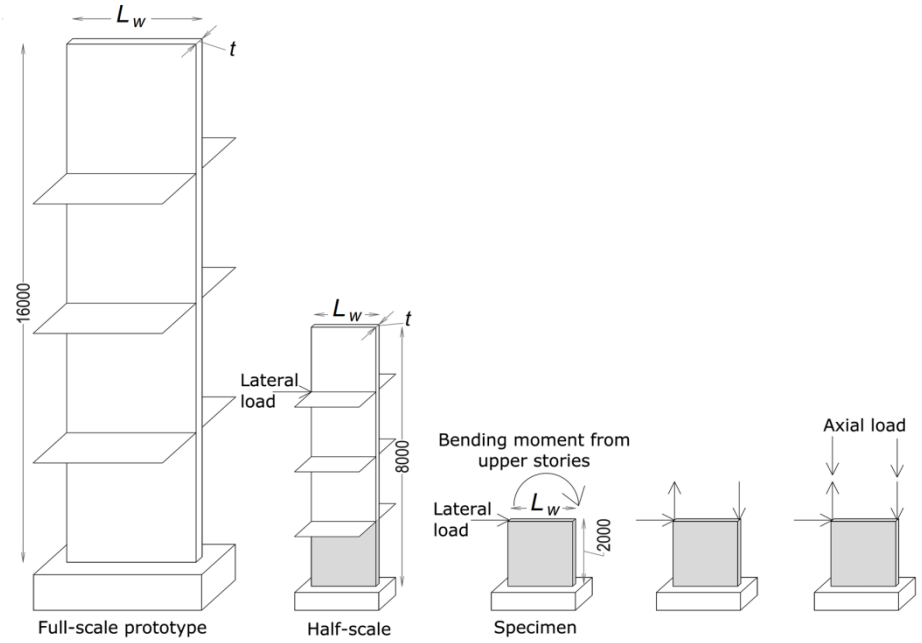

Figure 6.1: Specimen scaling and loading pattern (units in [mm])

6.1.2 SPECIMEN DESIGN

The detailed design of the specimens is provided in Appendix A, while this section summarizes the main steps of the design process. Figure 6.2 displays the geometry and reinforcement configuration of the specimens, and Table 6.2 lists general characteristics of the specimens.

In order to comply with the capacity design approach, the specimens were designed such that after considerations of the over-strength factors, their response would be flexure-dominated. The shear demand corresponding to the flexural capacity of the designed sections with considerations of all the possible over-strength factors were used for the shear design of the walls as well as the test setup design. The specimens were designed assuming

a concrete compressive strength of 35 MPa and reinforcing steel with yield strength of 300 MPa. Considering the wall geometry and design material properties, the nominal shear strength, V_n, was estimated as 1405 kN for the prototype wall, and 351 kN for the specimen. The shear demand, $V_u = \phi V_n$ (ϕ=0.75 for shear), was calculated as 1053 kN and 263 kN for the prototype and Specimen RWB sections, respectively. This shear demand was 211 kN for Specimen RWL which was shorter in length.

The longitudinal reinforcement was designed such that the over-strength moment capacity of the wall sections would meet the shear demand corresponding to Specimen RWL (i.e., for a moment resulting from the minimum shear demand among all the specimens and the effective height of the wall) to ensure the flexure-dominated response of all the specimens. The reinforcement layout was established using an iterative approach to achieve the nominal moment strength while all code requirements (i.e., confinement requirements, etc.) are met. The transverse reinforcement provided at the boundary regions complied with the lateral restraint provisions of Clause 11.4.6.3.

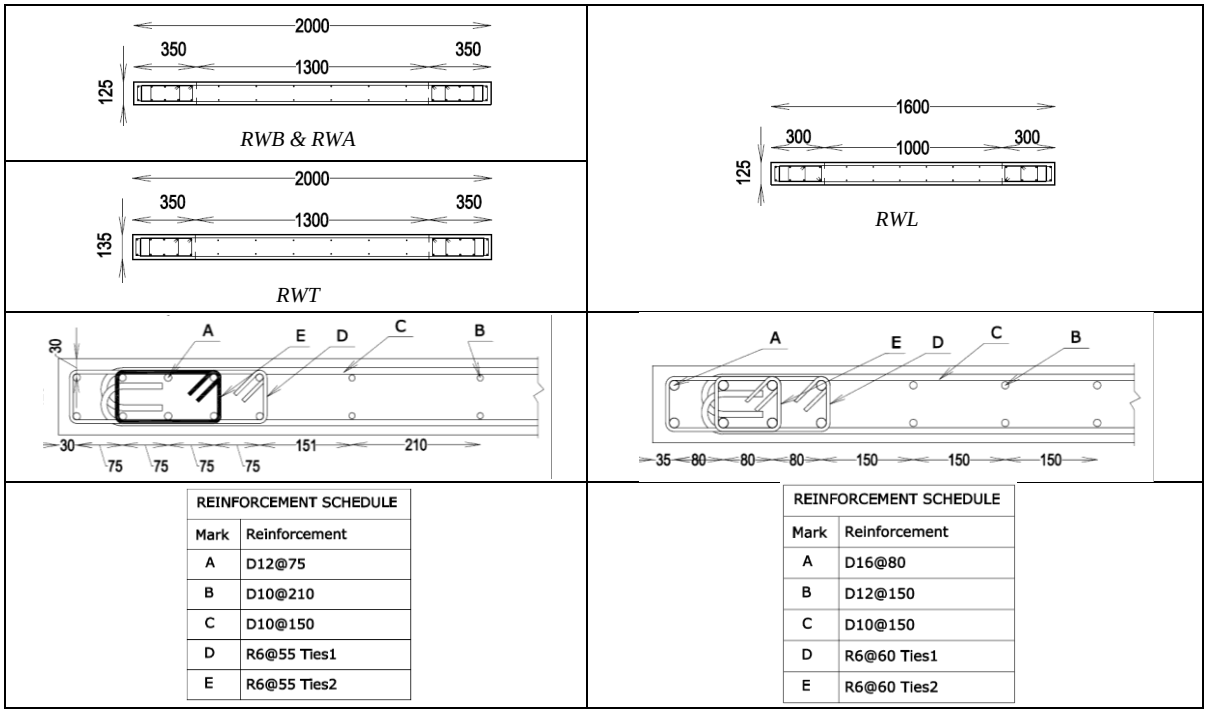

REINFORCEMENT SCHEDULE	
Mark	Reinforcement
A	D12@75
B	D10@210
C	D10@150
D	R6@55 Ties1
E	R6@55 Ties2

REINFORCEMENT SCHEDULE	
Mark	Reinforcement
A	D16@80
B	D12@150
C	D10@150
D	R6@60 Ties1
E	R6@60 Ties2

Figure 6.2: Geometry and reinforcement configuration of the four specimens (D refers to deformed bars, R to plain round bars)

Table 6.2: General characteristics of the specimens

Parameter	Specimen	Length, l_w, mm	Thickness, t_w, mm	Shear-span ratio	Length of boundary elements, l_C, mm	Axial load, kN	Axial load ratio, N/f'_cA_g	Longitudinal reinforcement ratio, $\rho = A_S/A_C$	
								Boundary region	Web
Benchmark	RWB	2000	125	3.0	350	438	0.042	0.026	0.0059
Thickness	RWT	2000	135	3.0	350	438	0.047	0.024	0.0055
Length	RWL	1600	125	3.75	300	438	0.063	0.043	0.012
Axial load	RWA	2000	125	3.0	350	657	0.07*	0.026	0.0059

*Calculated based on f`c=38 MPa (28th day strength) as this specimen has not been tested.

6.2 MATERIAL PROPERTIES

The concrete compressive strength, f'_c, was determined from 100x200 mm cylinder tests conducted on the first day of testing. Three cylinders were tested for each specimen and the maximum compressive strengths were averaged (Table 6.3). Stress-strain curves for the rebar used in each specimen were determined from standard tension tests (Figure 6.3 to Figure 6.6), and the general properties of the reinforcing steel are provided in Table 6.4.

Table 6.3: Compressive strength of concrete

Specimen	$f'_c(MPa)$
RWB	41.3
RWT	34.5
RWL	34.8
RWA*	38.0

*28th day strength as this specimen has not been tested.

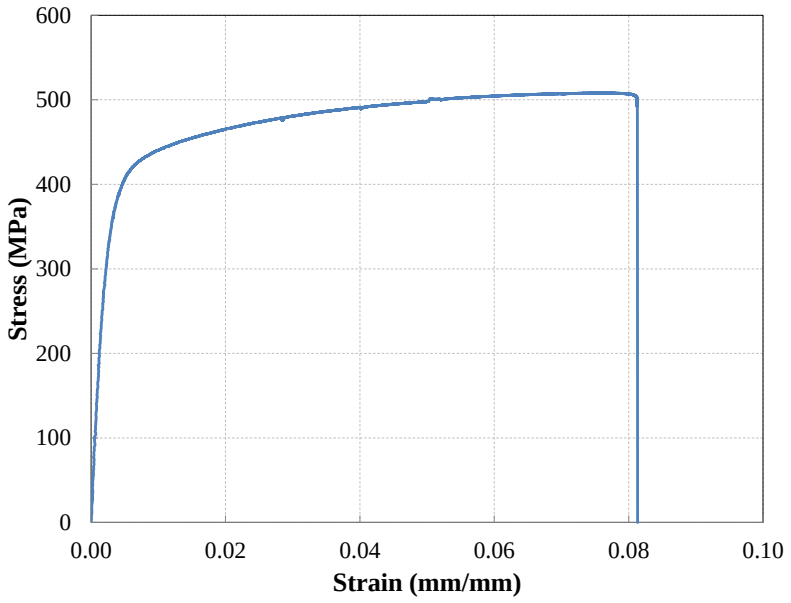

Figure 6.3: Reinforcement stress-strain response; R6

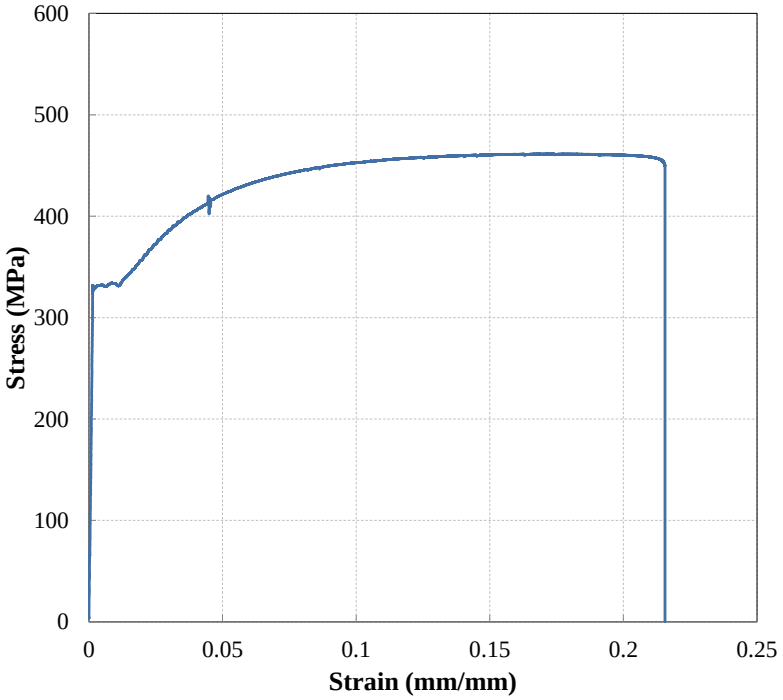

Figure 6.4: Reinforcement stress-strain response; D10

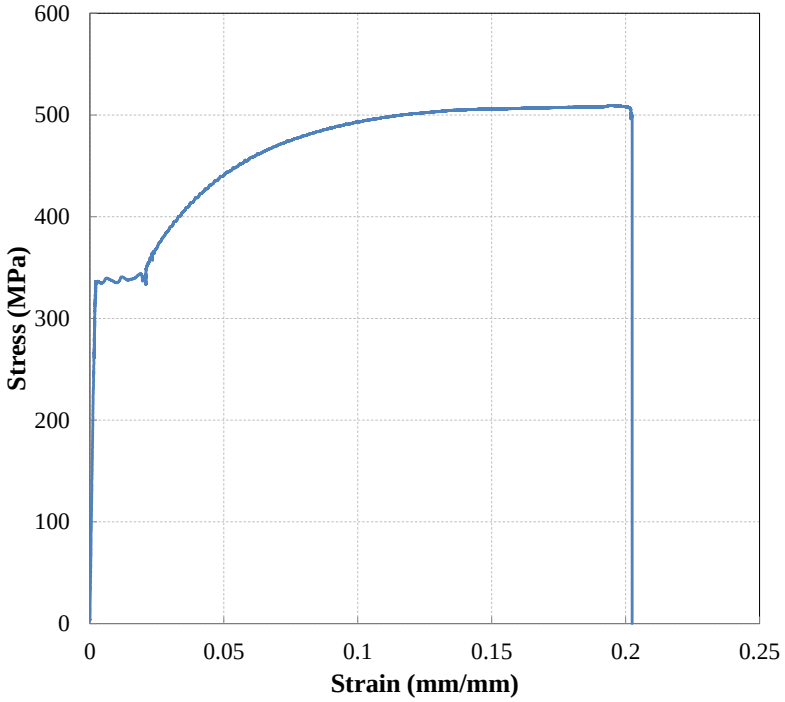

Figure 6.5: Reinforcement stress-strain response; D12

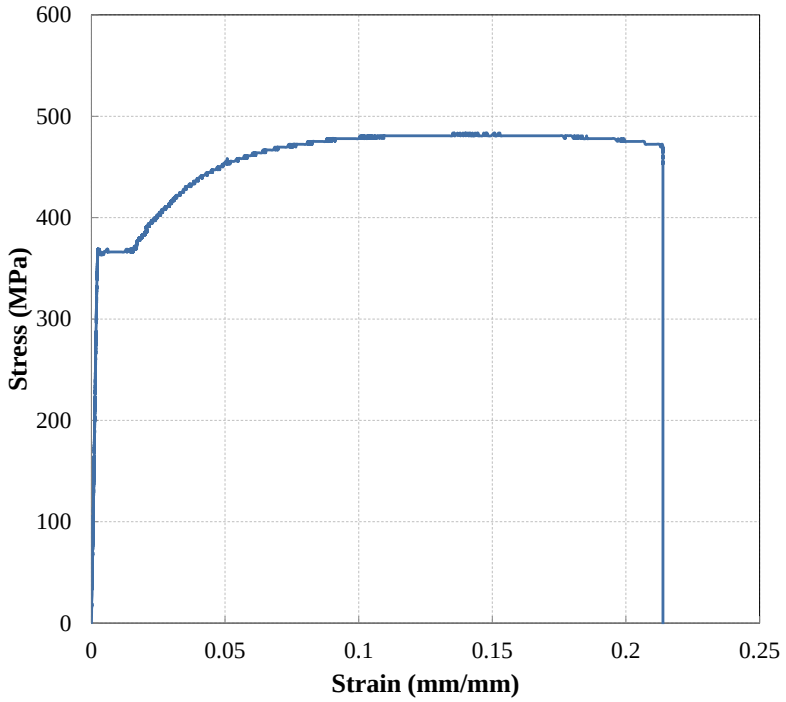

Figure 6.6: Reinforcement stress-strain response; D16

Table 6.4: Properties of reinforcing steel

Bar	R6	D10	D12	D16
E (MPa)	166000	228560	170235	168210
f_y (MPa)	411	330	334	366
f_{sh} (MPa)	-	332	340	369
f_u (MPa)	506	460	509	478
ε_y	0.0025	0.0014	0.0021	0.0023
ε_{sh}	-	0.011	0.019	0.0157
ε_u	0.08	0.2	0.19	0.185

(D refers to deformed bars, R to plain round bars)

6.3 SPECIMEN CONSTRUCTION

The wall specimens were constructed by Bradfords Precast Ltd. To connect the wall specimens to the laboratory strong floor, a foundation block was designed to ensure appropriate dimensions and strength. The rebar cage was assembled for the whole unit including the foundation block and the wall panel, and the concrete was cast for the whole unit in a horizontal position. The construction sequence of the specimens is represented in Appendix B.

6.4 EXPERIMENTAL TEST SETUP

To apply the loading pattern shown in Figure 6.1, the test setup was designed to apply the lateral load as well as the bending moment coming from the upper stories. Figure 6.7

displays the configuration of horizontal and vertical actuators producing this loading pattern.

As the movements of the horizontal and vertical actuators were interdependent, a control program was designed to balance the actuators at each step through an iterative approach so that they comply with the above mentioned loading conditions and satisfy the design shear-span ratio. A safety frame was designed against any instability issues of the loading frame in the event of a sudden wall failure. Figure 6.8 displays the details of the test setup assembly and Specimen RWB connected to the strong floor and the loading beam. The specimen was connected to the loading beam by two angle profiles bolted to the wall panel through embedded threaded rods and to the loading beam by high strength bolts. The out-of-plane deformation of the specimen was restricted at loading level using two roller supports at each side of the loading beam. These roller supports were positioned at different elevations of the loading beam to restrain the rotation of the loading beam and consequently of the top of the specimen, representing the fixity at the story level of a structural wall connected to the floor system in a building. Figure 6.9 shows the details of the wall-beam connection and the out-of-plane constraint. As it can be seen in this figure, a load cell was attached to the roller to measure the variations of the out-of-plane load at different stages of loading. See Appendix B for more details on the test setup preparation.

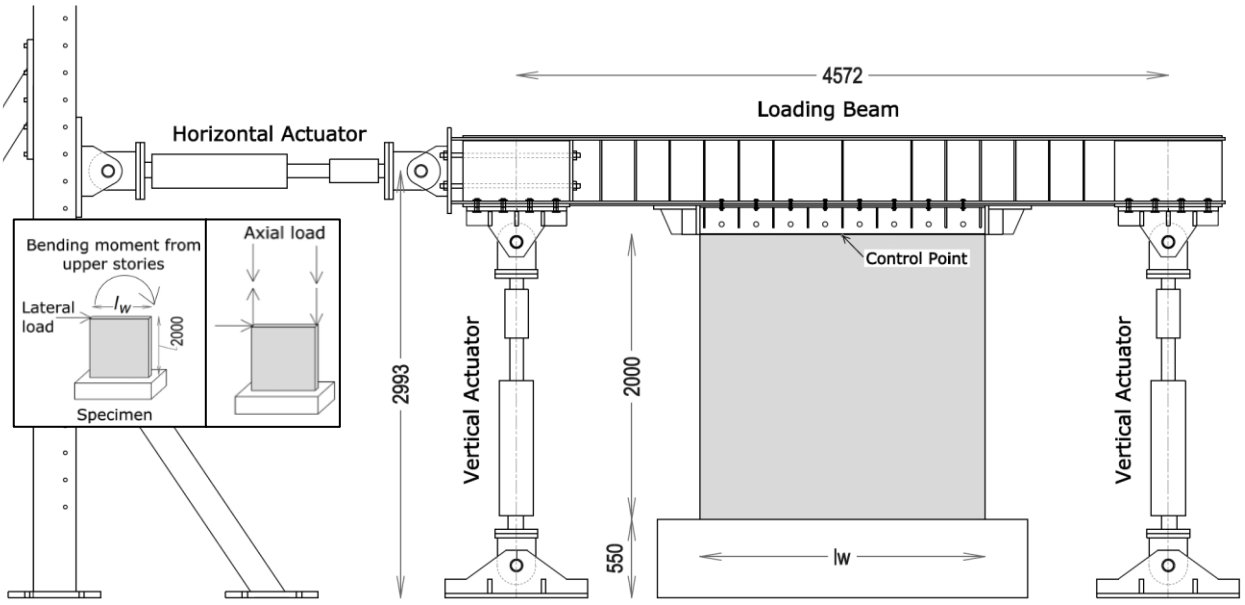

Figure 6.7: Test set up: configuration of actuators (units in [mm])

Figure 6.8: Test setup

Figure 6.9: Out-of-plane support and connection details of the loading beam

6.5 INSTRUMENTATION

The instrumentation of the specimens was prepared to capture as much information as possible regarding the initiation and development of the out-of-plane deformation. For this purpose, 36 linear potentiometers (30 mm stroke potentiometers) were attached to the boundary zones at both faces of the wall to measure the vertical displacements of the wall boundary regions at different positions along the wall height. This information could be used to capture the variation of vertical displacements along the wall thickness and identify the loading stage corresponding to the initiation of out-of-plane displacements. Figure 6.10a and Figure 6.10b indicate these linear potentiometers at north and south faces of the specimen, respectively. As it can be seen in Figure 6.10b, in addition to the potentiometers attached to the boundary regions, three potentiometers were also used along the wall panel at the base, to capture the variation of vertical displacements along 300 mm distance from

the base, and allow to analytically derive the nonlinear strain profile along the wall length and locate the neutral axis position at different stages of loading.

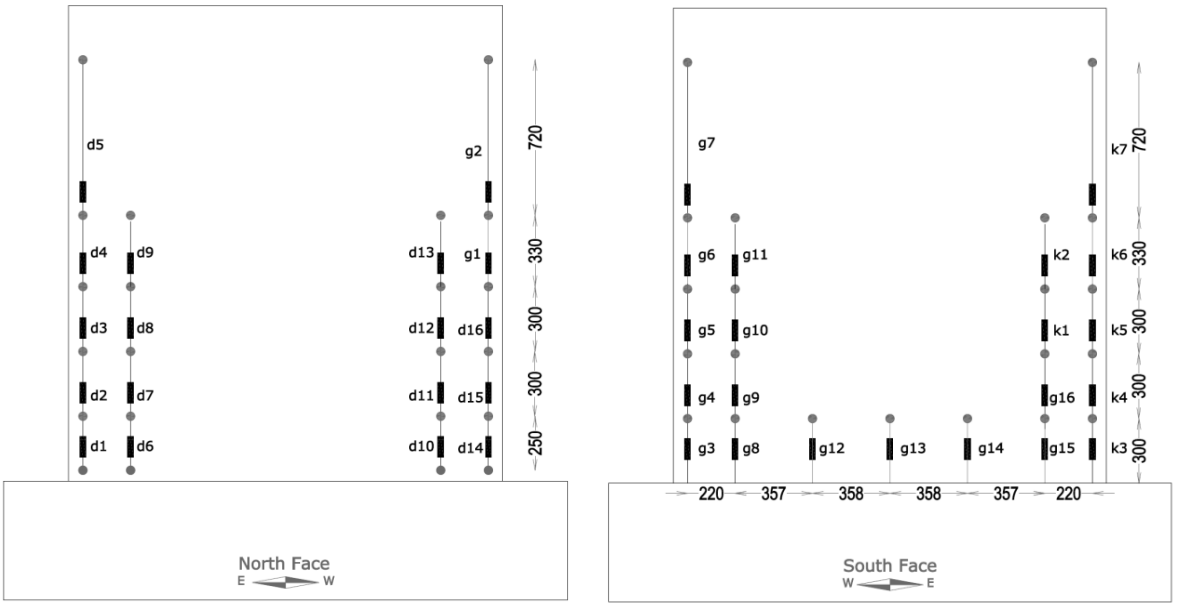

(a) North face (b) South face

Figure 6.10: Linear potentiometers for measurement of vertical displacement (units in [mm])

The shear deformation of the wall panel was measured using the diagonal potentiometers shown in Figure 6.11, and rotary potentiometers were used to measure the lateral displacement of the wall at different elevations along the wall height.

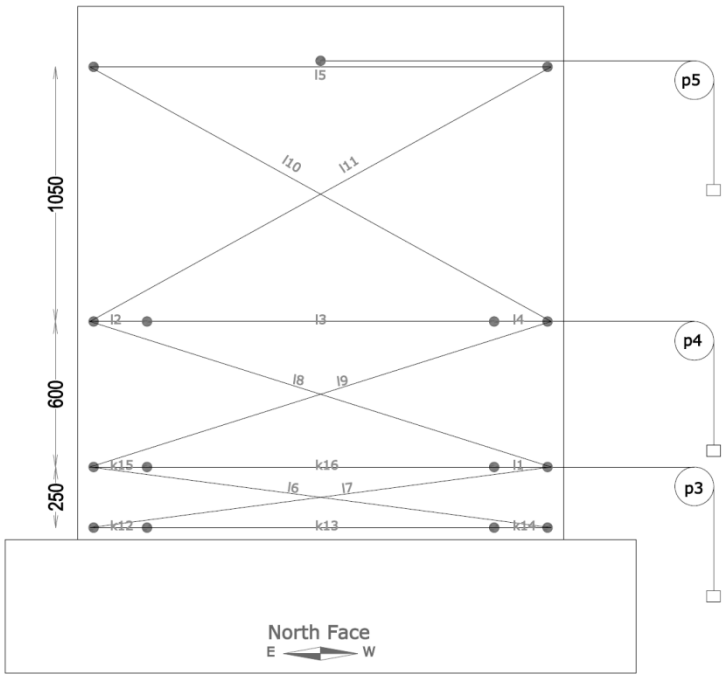

Figure 6.11: Linear and rotary potentiometers for measurement of shear and lateral displacements (units in [mm])

String potentiometers were mounted on fixed supports in order to measure the out-of-plane displacements along about half of the height of the boundary zones. Figure 6.12 indicates the points of out-of-plane displacement reading and Figure 6.13 displays the connection of the string pots to the support frame and the wall. As can be seen in this figure, the support frame used for this instrumentation is separated from the other frames to avoid any possible noises coming from vibration of the loading or safety frames.

Lateral constraint was provided to prevent any movement of the footing. Spring potentiometers were installed at different parts of the foundation to measure the horizontal and vertical displacements of the foundations (Figure 6.15).

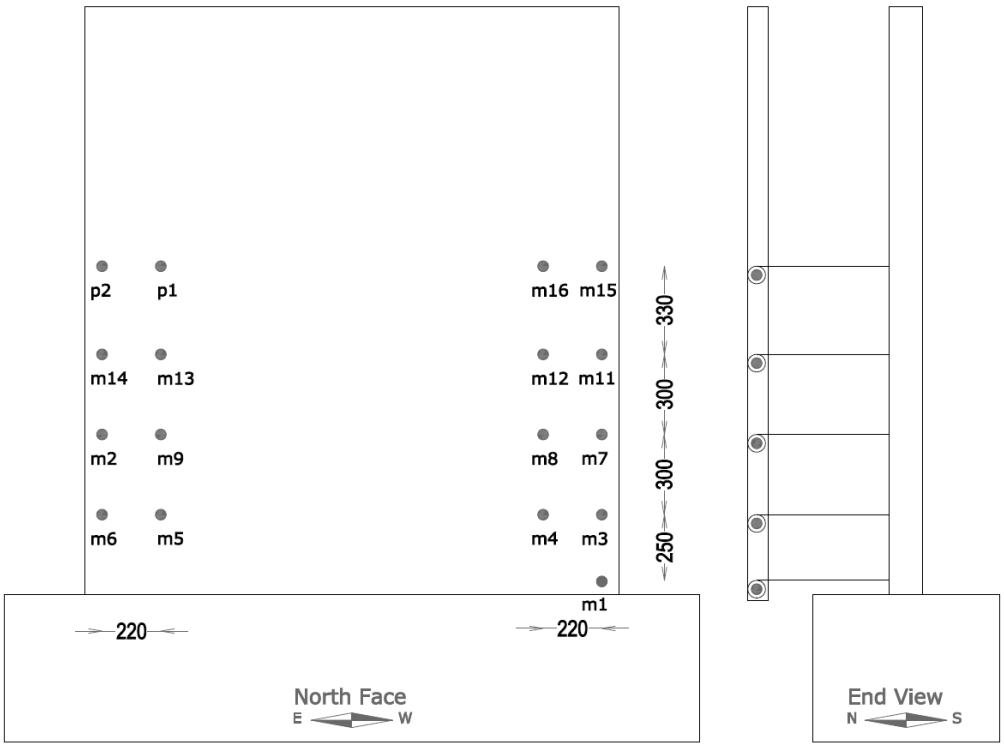

Figure 6.12: String potentiometers for measurement of out-of-plane deformation

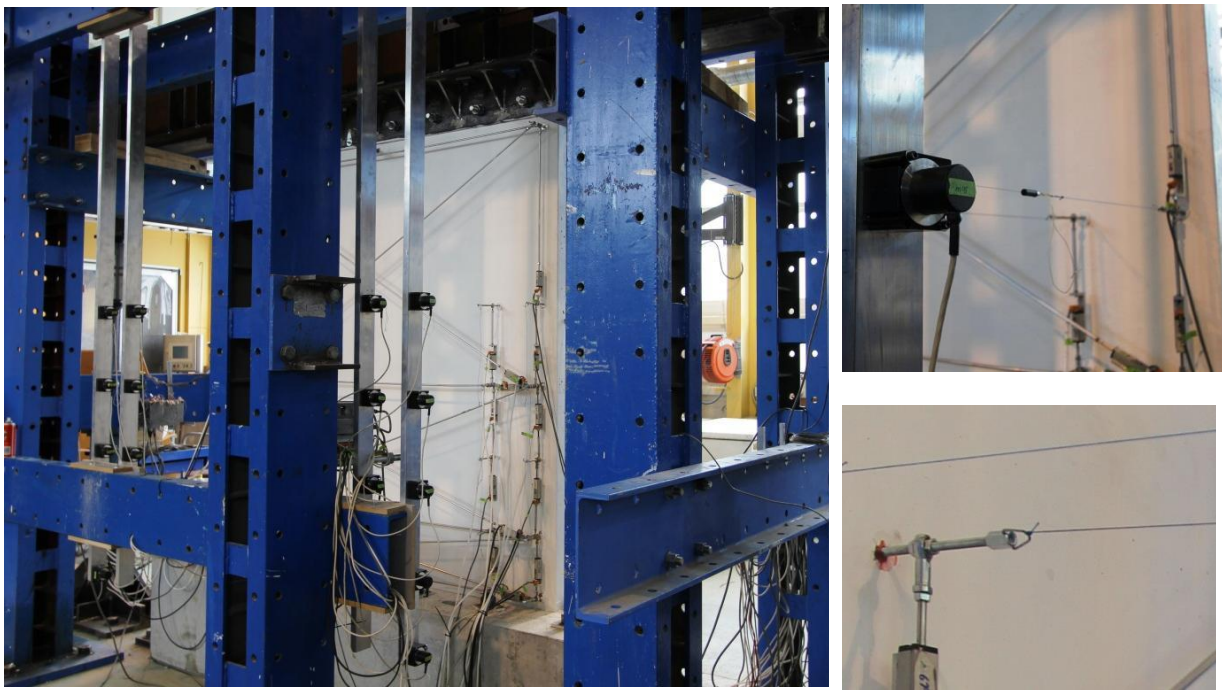

Figure 6.13: Connection of the string pots to the support frame and the specimen

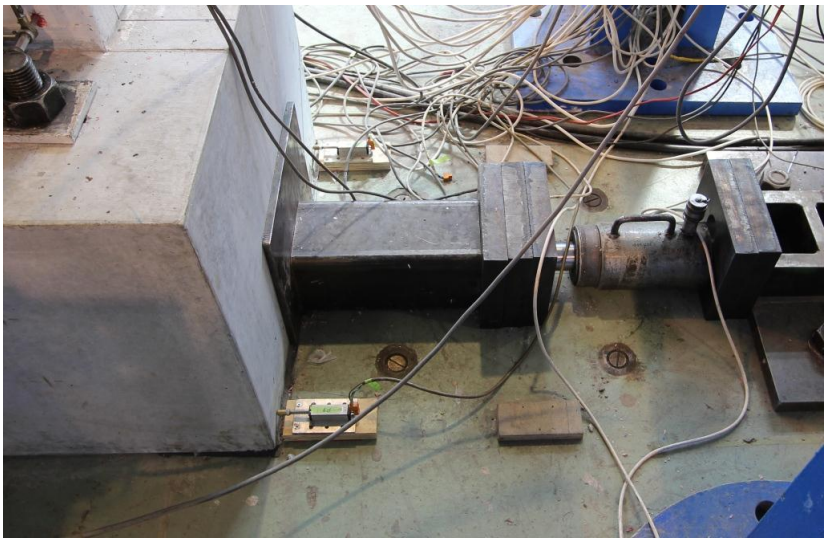

Figure 6.14: Lateral constraint of the wall foundation

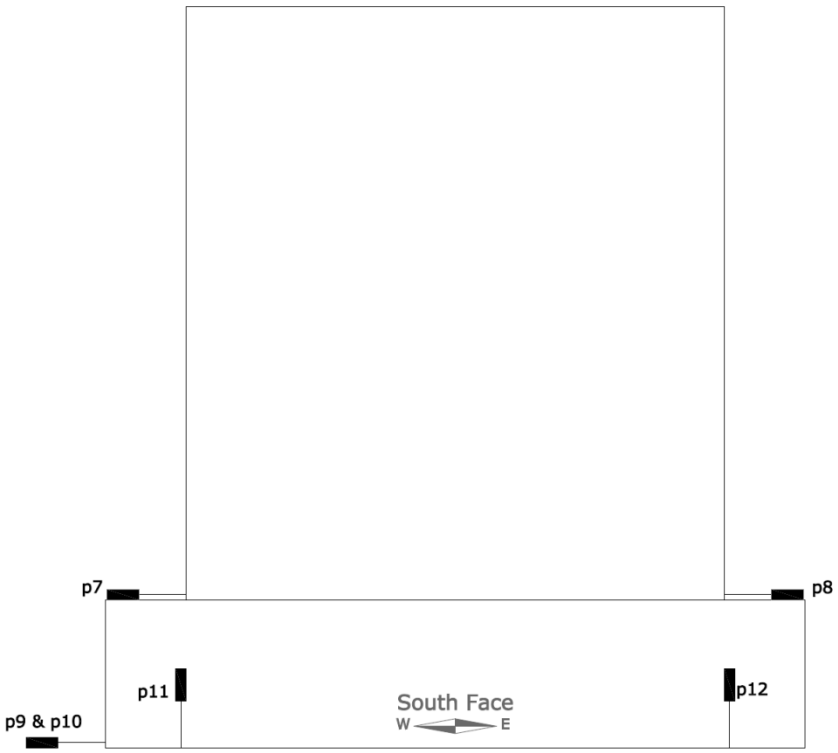

Figure 6.15: Spring potentiometers for measurement of foundation displacements

Also, grid lines were drawn on the specimens, as shown in Figure 6.16, to visualize the crack and deformation patterns at different positions of the wall using a digital still camera which was connected to the lateral displacement controller and captured a photo at each step of loading (Figure 6.17).

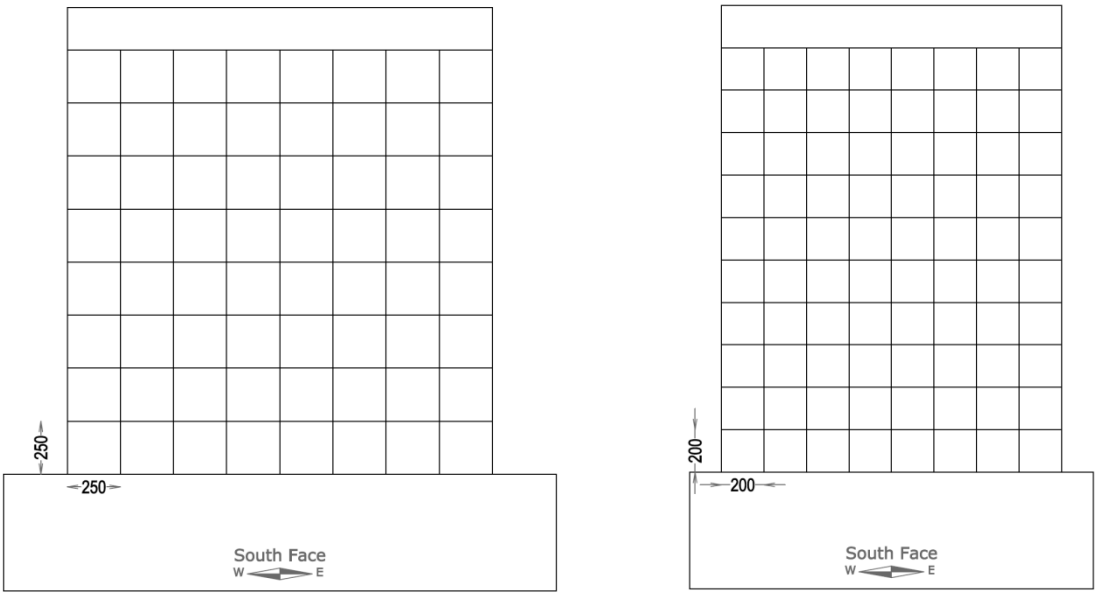

(a) RWB & RWT (b) RWL

Figure 6.16: Grid lines plotted on the specimens

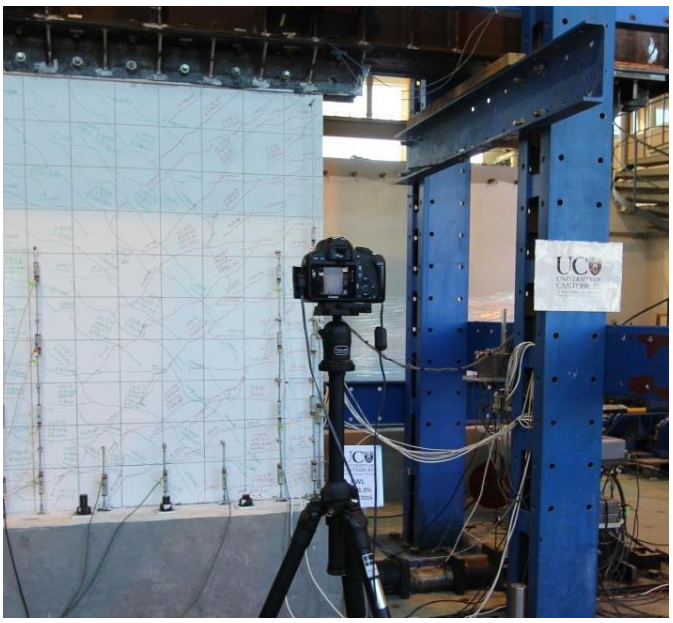

Figure 6.17: Digital still camera used for tracking crack pattern

Reinforcement strain at different stages of loading, unloading and reloading has been identified as one of the main parameters controlling out-of-plane deformation of rectangular walls. In order to investigate the effect of this parameter, in addition to 70 strain gauges attached to the reinforcement along the half-height of the wall, couplers were welded to the longitudinal reinforcement at each extreme to capture the average reinforcement strain along the distance between two couplers (400-550 mm). Figure 6.18 displays the strain gauges installed on Specimen RWL. The strain gauges were attached to both layers of reinforcement layers at about 345 mm and 570 mm from the wall base to monitor any variation of strain between the two layers of reinforcement due to the initiation of out-of-plane deformation. Figure 6.19 indicates one of the couplers welded to the end region rebar for attachment of linear potentiometers and Figure 6.20 displays the positioning of these potentiometers.

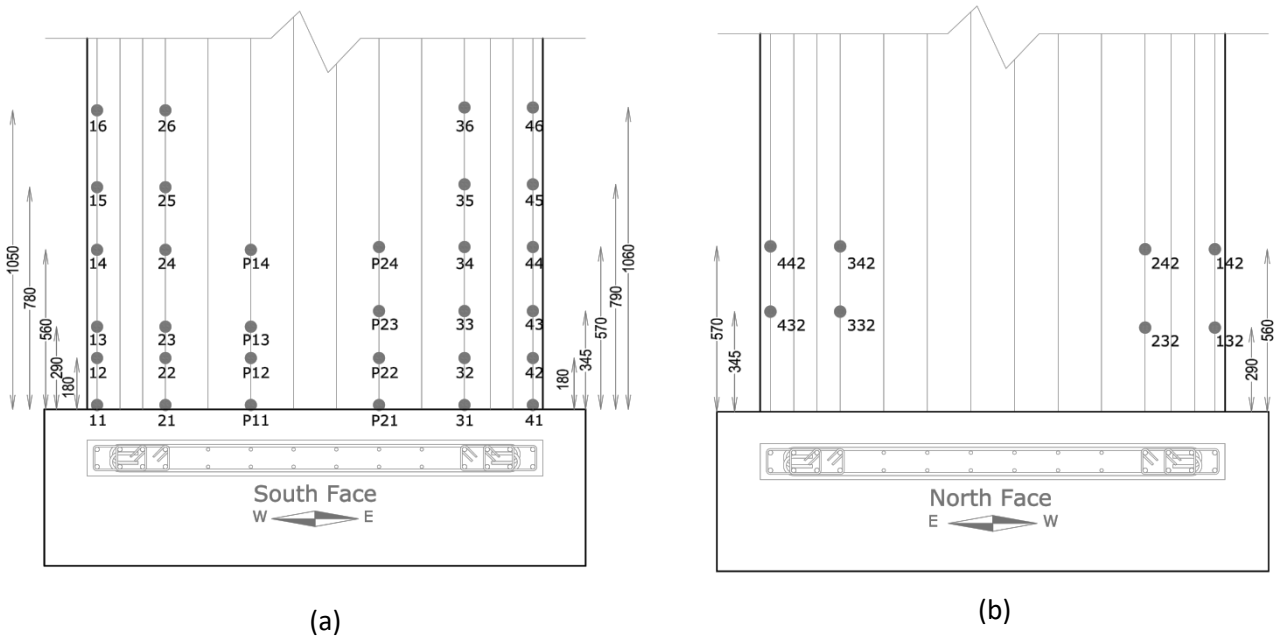

Figure 6.18: Location of Strain gauges on the longitudinal reinforcement, Specimen RWL: (a) south face; (b) north face

Figure 6.19: Strain gauges and welded couplers

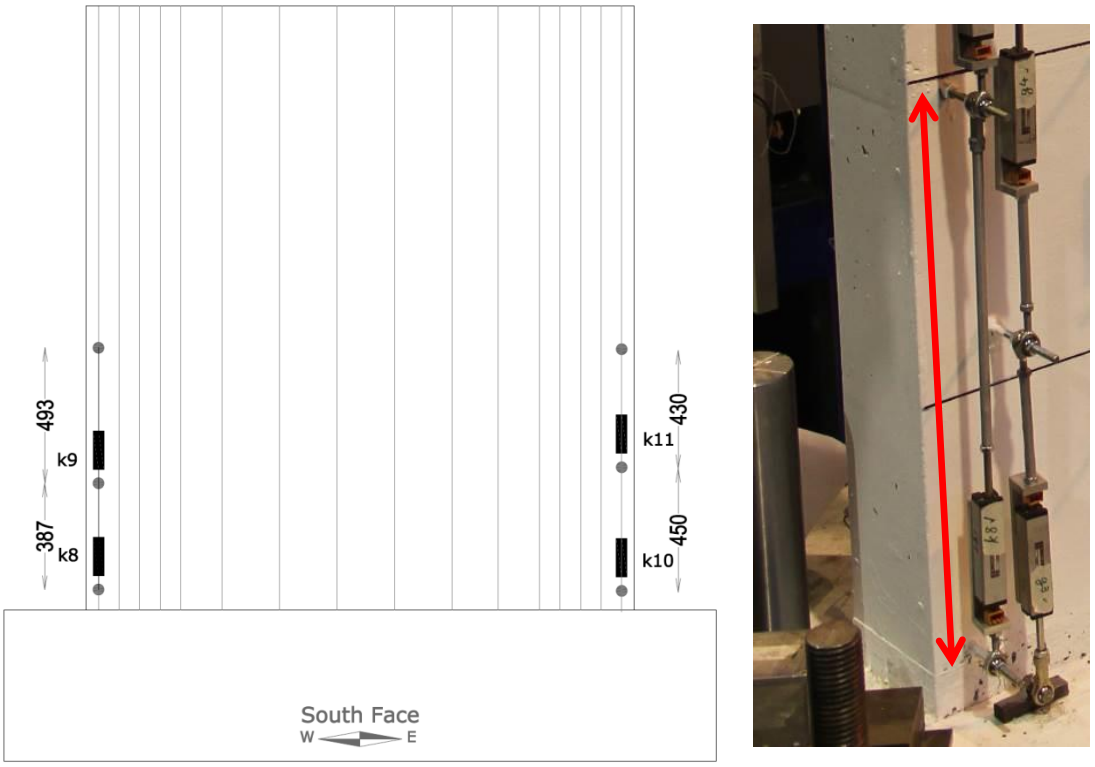

Figure 6.20: Linear potentiometer attached to the end rebars using welded couplers to measure the average reinforcement strain

6.6 LOADING

The specimens were subjected to an in-plane quasi-static cyclic loading regime with three cycles at each drift level. Figure 6.21 displays the displacement history of the control point, located at elevation of 2.0 m from the wall base (Figure 6.7), which was used to control the horizontal actuator. As the inter-storey drift (not the overall building/wall drift) is considered as a performance limit/target by the New Zealand standard for structural design actions (NZS1170.5 2004), the horizontal displacement within the bottom storey was used to control the loading program. The loading applied by the vertical actuators consisted of the axial load and the bending moment corresponding to every increment of the lateral displacement. As the specimens were considered to be different alternatives for a specific loading condition, the value of axial load was kept constant for Specimens RWB, RWT, and RWL; i.e. the axial load ratio, as given in Table 6.2, had to vary due to the variations of the cross-section geometry in addition to the unavoidable differences in concrete strength.

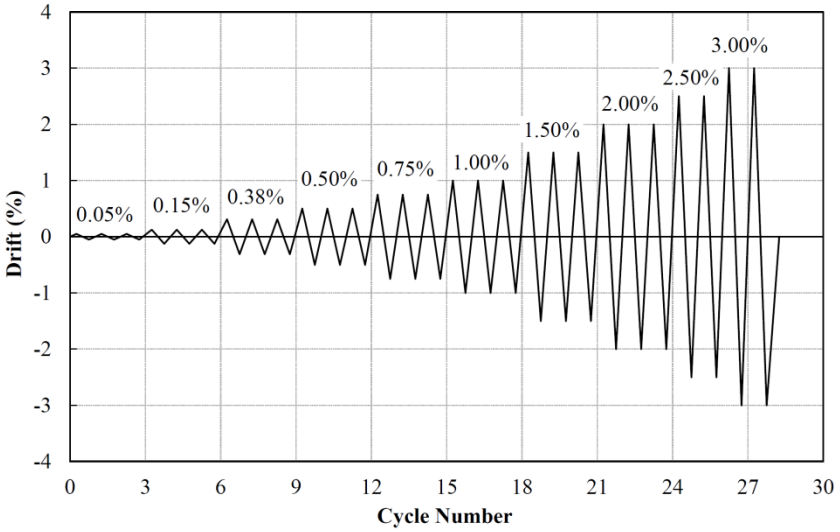

Figure 6.21: Applied displacement history

6.7 RESPONSE OF THE SPECIMENS

6.7.1 SPECIMEN RWB

Specimen RWB was the benchmark specimen. Figure 6.22 and Figure 6.23 show the cross section and elevation of this specimen, respectively. It should be noted that the unsupported height of the specimens was 2000 mm, and a 200 mm extension was used to connect the specimens to the loading beam using embedded rods and steel angle beams clamping the specimens at both faces (see Figure 6.10). Therefore, the elevation of 2000 mm could represent the storey level as the loading beam was restrained against out-of-plane deformations. Figure 6.24 shows the lateral load versus top displacement response of Specimen RWB, and Figure 6.25 illustrates the maximum out-of-plane displacement measured at the boundary zones of the specimen. The sequence of events resulting in the failure of the specimen is indicated in Figure 6.24. Figure 6.26 displays the crack pattern of Specimen RWB at different drift levels, and Figure 6.27 displays some of the observations at ultimate stages of wall response for Specimen RWB.

Initial cracking occurred at 0.05% drift level. As it can be seen in Figure 6.26, the cracks at this stage are all horizontal flexural cracks mostly located in the boundary zones. At 0.15% drift level, these horizontal cracks extended more with a diagonal orientation at the central region, and more cracks developed up to 1750 mm along the height of the specimen. The maximum crack width at this stage was 0.25 mm and the cracks were more distributed in the boundary regions merging into a wider crack in the central panel region.

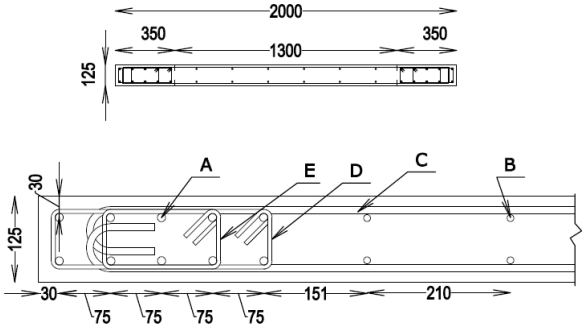

REINFORCEMENT SCHEDULE	
Mark	Reinforcement
A	D12@75
B	D10@210
C	D10@150
D	R6@55 Ties1
E	R6@55 Ties2

Figure 6.22: Specimen RWB cross-section

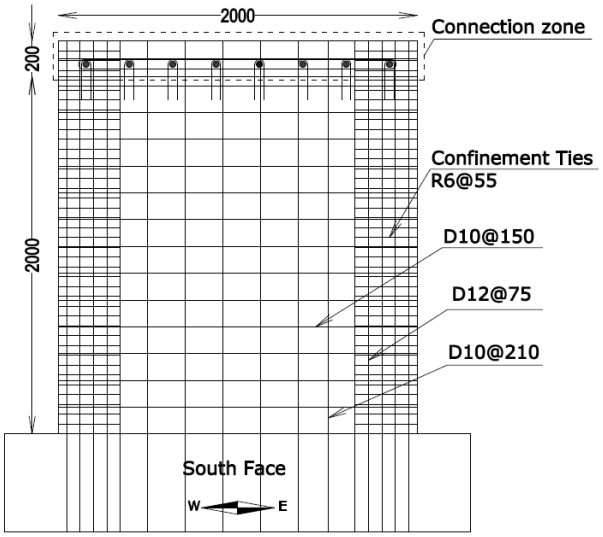

Figure 6.23: Specimen RWB elevation

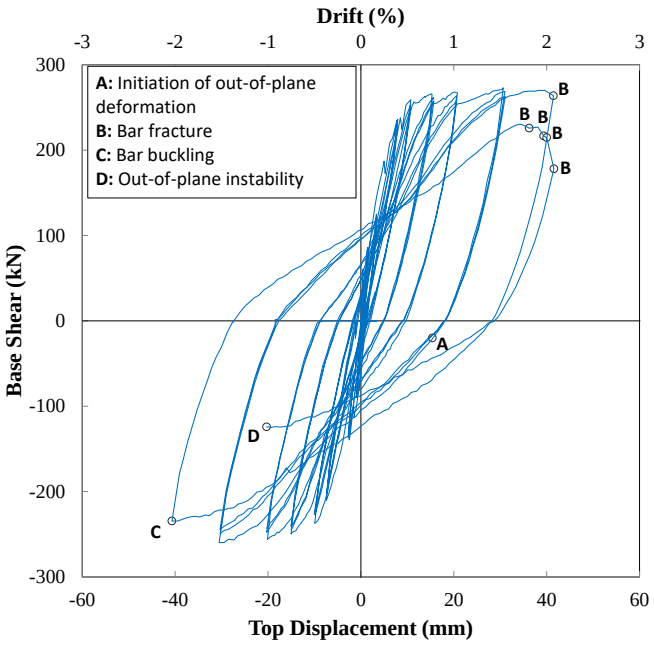

Figure 6.24: Lateral load-top displacement response of Specimen RWB

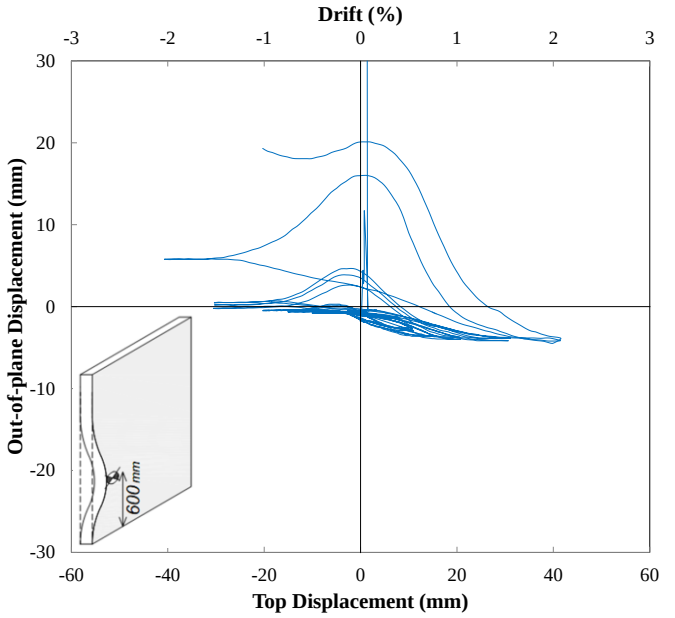

(a)

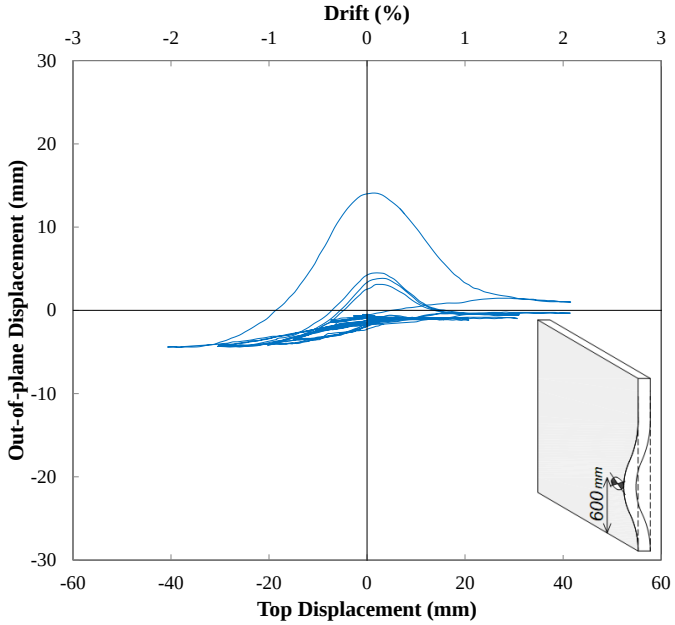

(b)

Figure 6.25: Top displacement vs maximum out-of-plane displacement of Specimen RWB: (a) west boundary; (b) east boundary

At 0.38% drift level, the cracks increased further both in terms of number and length. The previously formed cracks grew slightly wider. The cracks extended up to 1500 mm out of the whole length of 2000 mm, which shows the considerable movement of the neutral axis position along the wall length. Cracks became wider at 0.5% drift level, especially the diagonal ones, and the ones developed at the base. At this stage, the specimen reached the yield point (Figure 6.24).

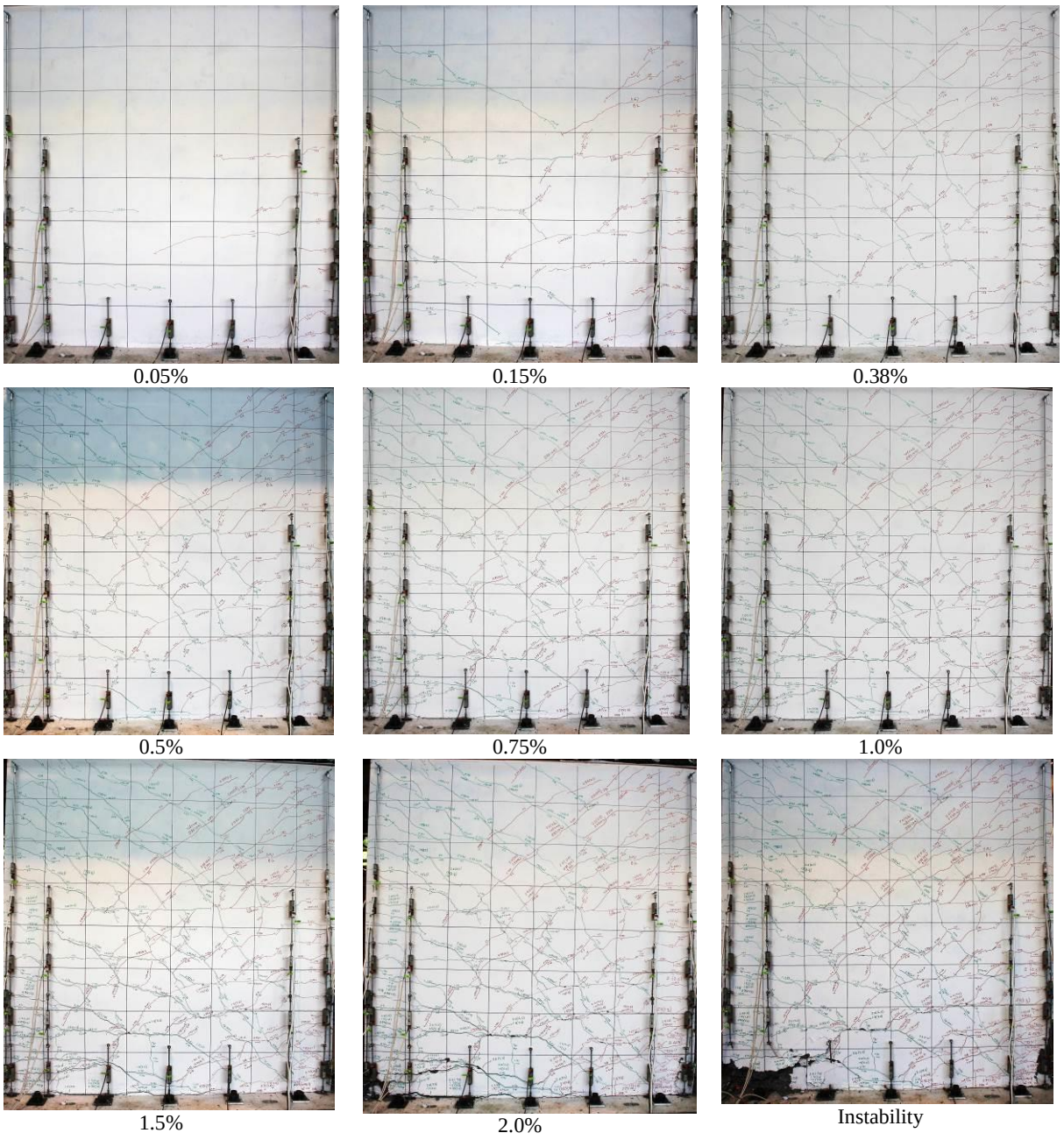

Figure 6.26: Crack pattern of Specimen RWB at different drift levels

During the 0.75% drift cycle, the cracks did not increase further in number and the former cracks became wider and extended up to 1750 mm of the wall length. Large crack opening (1.3 mm) was observed at the base. During the 3rd cycle of 0.75% drift, cover spalling started on one face of the wall. The cracks widened further during 1.0% and 1.5% drift levels. At 1.5% drift level, the base line crack width was 5.0 mm along 500 mm from the extreme tension fiber and gradually decreased to 3.0 mm and 0.0 mm at the 1250 and 1750 mm distance from the tension extreme end, respectively. The cracks within the bottom 375 mm of the wall height had a similar trend. This trend is obviously due to the nonlinear strain profile along the wall length. These cracks were considerably wider when compared

to the rest of the wall area. When the specimen was being unloaded and reloaded in the opposite direction, the crack width decreased by about 20-30% when the load reached zero (static residual crack) and by about 50% when the wall displacement reached zero. At this stage, as the load carrying capacity of the wall was provided by the reinforcement that had already undergone a large tensile strain, the specimen started to deform in the out-of-plane direction (Figure 6.25). These wide cracks did not close until about 1.0% drift level in the opposite direction which is the stage when the out-of-plane deformation of the specimen had recovered (Figure 6.25). This phenomenon was repeated in both boundary regions at the subsequent cycles of 1.5% drift level with larger out-of-plane deformations, which was obviously due to increase of the longitudinal reinforcement strain with the number of cycles.

While reaching the peak displacement of the first 2.0% drift cycle, a bar in the extreme tension region snapped at the base. The cracks became wider mostly at the base and within 600 mm from the base and the base crack width reached 7.0 mm. When the load was applied in the opposite direction, the out-of-plane deformations increased in the west boundary region and reached the maximum value of 17 mm at about zero displacement (Figure 6.25). This out-of-plane deformation did not recover completely at the peak displacement of -2.0% drift level and the following cycle started with about 6 mm residual out-of-plane deformation in the west boundary zone. At this stage bar buckling was observed at the base of the compression boundary region (Point C, Figure 6.24). During the second cycle of 2.0% drift level, more bar fractures happened at the base of the west boundary region, and the specimen exhibited higher out-of-plane deformations when the load was reversed. As it can be seen in Figure 6.25, the out-of-plane deformation increased until 0.1% drift level and decreased slightly afterwards but unlike the previous cycle, started to increase. At this stage, a strength degradation of about 50% was observed (Figure 6.24) and the test was stopped.

(a) (b) (c) (d) (e)

Figure 6.27: (a) Wide cracks at 2.0% drift level; (b) out-of-plane deformation; (c) bar fracture; (d) bar buckling ; (e) instability

6.7.2 SPECIMEN RWT

Specimen RWT was the specimen in which the thickness was slightly increased to investigate the effect of thickness on the initiation and development of out-of-plane deformations. Due to the limitations of the test setup, the thickness increase in the scaled specimen was only 10 mm (8.0%), corresponding to an increase of the prototype wall's

thickness from 250 mm to 270 mm. The numerical model predicted this increase in wall thickness to result in about 60% and 10% decrease in out-of-plane displacement of the specimen during the first cycle and second cycle of the 2.0% drift, respectively. Figure 6.28 and Figure 6.29 display the cross section and elevation of this specimen, respectively.

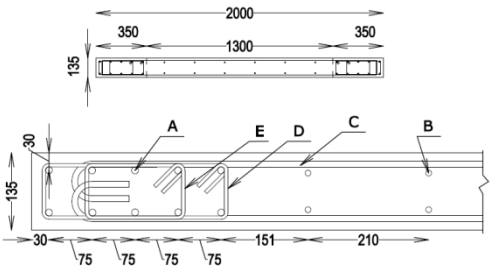

REINFORCEMENT SCHEDULE	
Mark	Reinforcement
A	D12@75
B	D10@210
C	D10@150
D	R6@55 Ties1
E	R6@55 Ties2

Figure 6.28: Specimen RWT cross-section

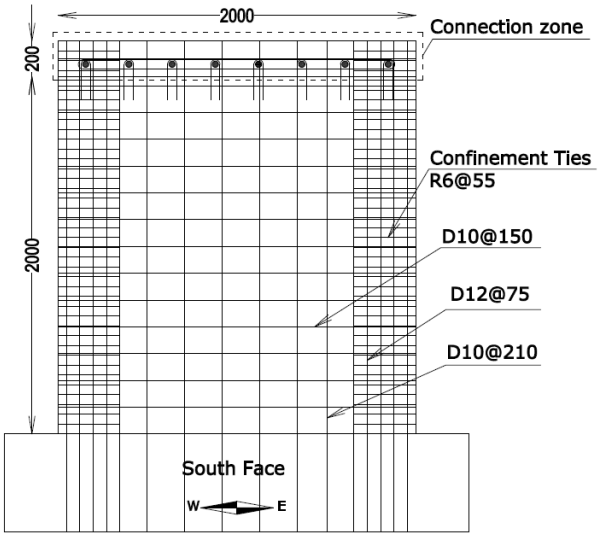

Figure 6.29: Specimen RWT elevation

Figure 6.30 displays the lateral load versus top displacement response of Specimen RWT, and Figure 6.31 indicates the maximum out-of-plane displacement measured at both boundary zones of the specimen. The sequence of events resulting in the failure of the specimen is indicated in Figure 6.30.

The crack pattern on this specimen was similar to the one observed for the benchmark Specimen RWB. Therefore, the crack patterns for this specimen are not shown again and the sequence of events leading to instability of the specimen is summarized in the text below.

The cracking first initiated at 0.05% drift level up to the height of about 1.0 m from the base. The cracks extended up to the whole height of the specimen with wide horizontal cracks at the base (0.3 mm crack width) as well as some wide diagonal cracks (0.2-0.3 mm

crack width). During the 0.5% drift cycles, the cracks became wider and rarely new cracks happened in the specimen. Therefore, a stable crack pattern was formed at 0.38% drift which is corresponding to 125% of bar yielding. Thereafter, increase in crack width was mostly at the base. Some more cracks emerged along the height at 0.75% drift level and the crack width reached 1.5 mm at the base. The crack width grew at 1.0% drift level.

The crack width further increased during 1.5% drift cycles. At this drift level, out-of-plane deformations started at the west boundary region during the first cycle when the specimen was unloaded from the peak positive displacement and was being reloaded in the opposite direction. The maximum value of out-of-plane displacement was 3 mm at this boundary region. A relatively wide crack at the base (with 5.0 mm crack width), which remained wide open during unloading and even reloading in the opposite direction, was a sign of larger tensile strains at the base of the specimen. Out-of-plane deformations initiated at the east boundary zone, as well, during the first cycle of 1.5% drift level with maximum out-of-plane displacement of 6 mm. At this drift level, cover spalling was observed in both boundary zones. A buckled bar was observed in the east boundary zone during the third cycle of this drift level (Point B, Figure 6.30).

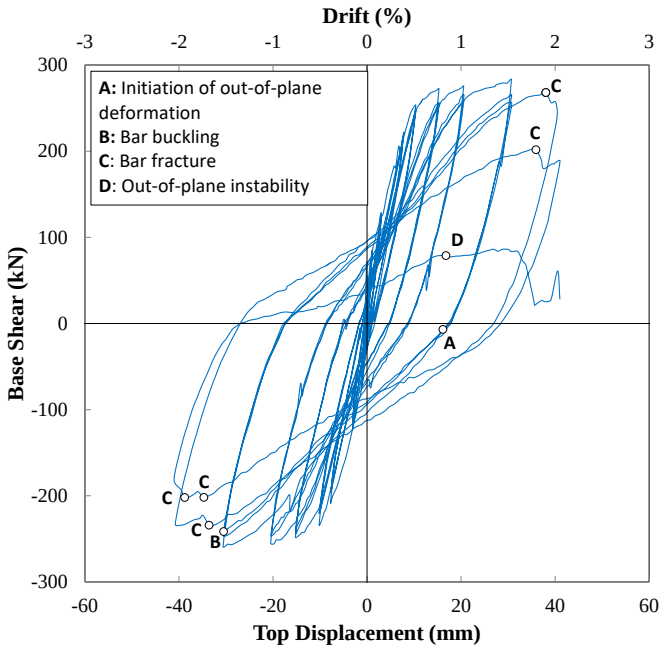

Figure 6.30: Lateral load-top displacement response of Specimen RWT

While reaching the peak displacement in the 1st cycle of 2.0% drift level, one bar fractured in the west boundary zone accompanied by a degradation observed in the load-displacement curve. The buckled bar in the east boundary straightened during the load reversal at -1.55% drift level. One bar also buckled in the west boundary zone, and one bar

fractured in the east boundary at -1.8% drift, which resulted in another abrupt drop in the load-displacement curve. The fractured bar is the same bar that had buckled in the previous peak. Different instances of bar fracture are denoted as "C" in Figure 6.30, whereas only the initial bar buckling is shown in this figure (Point B) as bar fracture was generally accompanied by bar buckling in the opposite boundary zone.

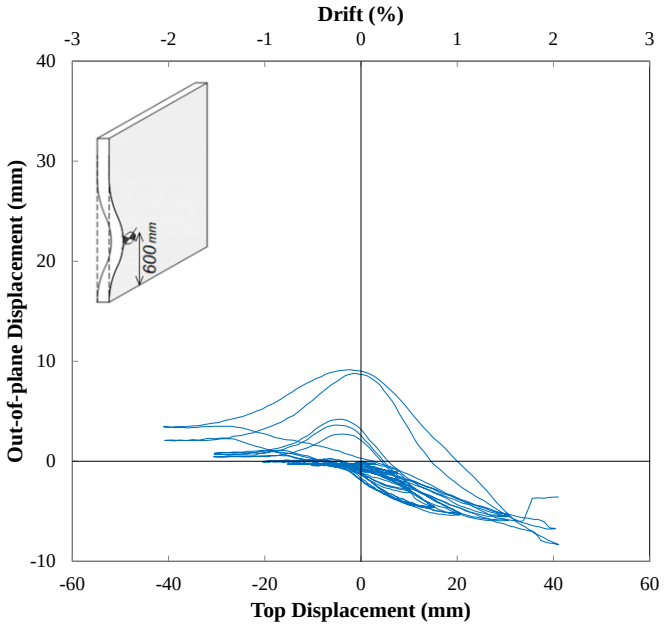

(a)

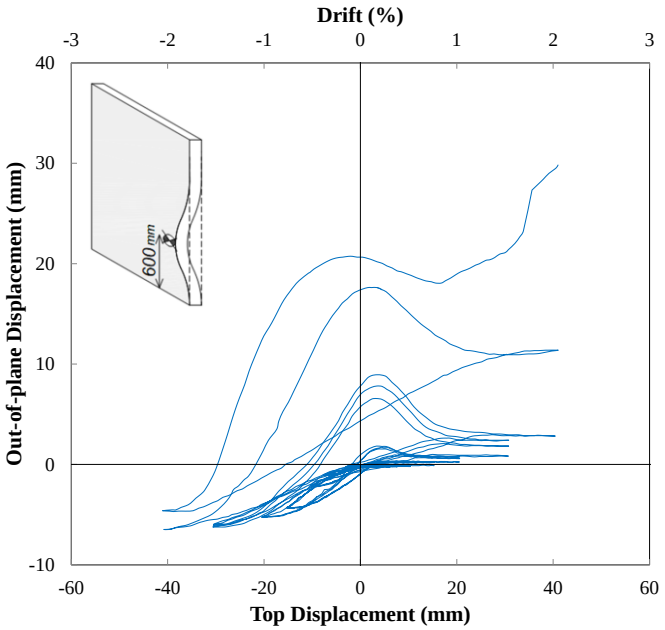

(b)

Figure 6.31: Top displacement vs maximum out-of-plane displacement Specimen RWT: (a) west boundary; (b) east boundary

The maximum out-of-plane displacement increased to about 16 mm at around zero drift level. Two more bars fractured in the west boundary region when the specimen was at

1.85% drift level. This successive occurrence of bar fracture and bar buckling exacerbated the resistance of the severely cracked wall section against out-of-plane deformations and the specimen became unstable when reloading toward +2.0% drift level after unloading from -2.0% drift level. Response of Specimen RWT was very similar to the one of Specimen RWB, and its failure initiated with out-of-plane deformation and included bar fracture and bar buckling at later stages of loading. However, the values of out-of-plane displacement were smaller in Specimen RWT compared to Specimen RWB when bar fracture had not come into effect in both specimens, which could be due to the slight increase in the wall thickness. Figure 6.32 and Figure 6.33 display the cracking, cover spalling, bar buckling and bar fracture observations and Figure 6.34 shows the instability of this specimen.

Figure 6.32: Wide cracks at +2.0% drift level - Specimen RWT

(a) (b) (c)

Figure 6.33: (a) Cover spalling; (b) bar buckling; (c) bar fracture - Specimen RWT

Figure 6.34: Instability of Specimen RWT (see Appendix C for more figures)

6.7.3 SPECIMEN RWL

Specimen RWL had a 20% reduction in length when compared to the benchmark RWB to investigate the effect of wall length on initiation and development of out-of-plane deformations. Therefore, this specimen had larger reinforcement ratios in the boundary regions and in the web to provide a flexural capacity close to the other specimens. The over-strength moment capacity of Specimens RWB and RWT was calculated to be 1522 kN.m and the one of Specimen RWL to be 1485 kN.m. Figure 6.35 and Figure 6.36 display the cross section and elevation of this specimen, respectively.

Figure 6.37 displays the lateral load-top displacement response of the specimen. The failure pattern of the specimen was pure out-of-plane instability and neither bar fracture nor bar buckling was observed in the test. The out-of-plane deformation initiated at Point A when the specimen was unloaded from 1.5% drift and was starting to reload in the opposite direction. Figure 6.38 indicates the maximum out-of-plane displacement measurement of the specimen at different stages of loading. As it can be seen in this figure, the out-of-plane deformation recovered completely as the specimen was reloaded in the opposite direction. This out-of-plane displacement recovery happened at early stages of loading. During 2.5% drift cycles, the out-of-plane deformation did not recover completely, and the specimen started to exhibit residual out-of-plane displacement. The residual out-of-plane

displacement increased with the number of cycles and the specimen became unstable at Point B where the abrupt strength degradation was observed.

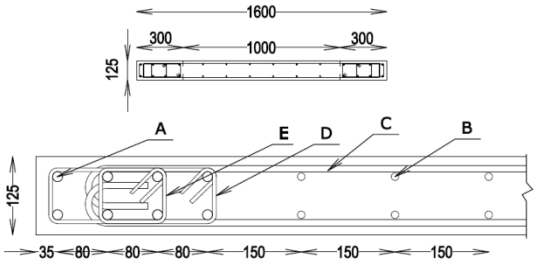

REINFORCEMENT SCHEDULE	
Mark	Reinforcement
A	D16@80
B	D12@150
C	D10@150
D	R6@60 Ties1
E	R6@60 Ties2

Figure 6.35: Specimen RWL cross-section

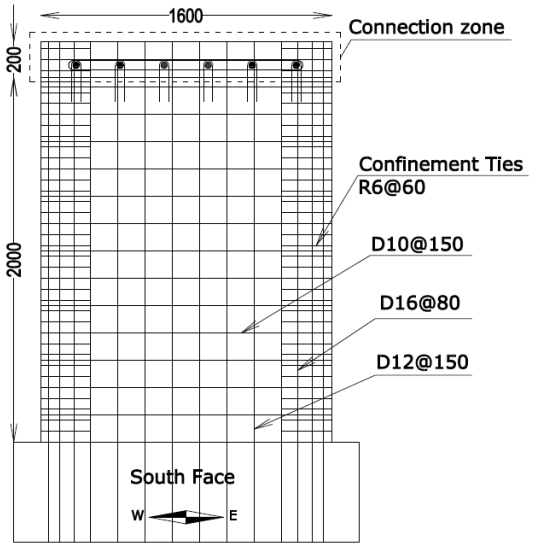

Figure 6.36: Specimen RWL elevation

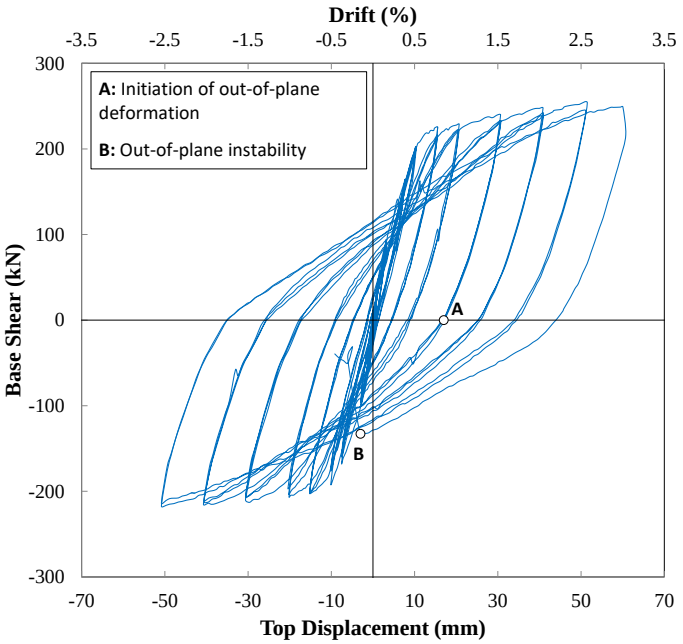

Figure 6.37: Lateral load-top displacement response of Specimen RWL

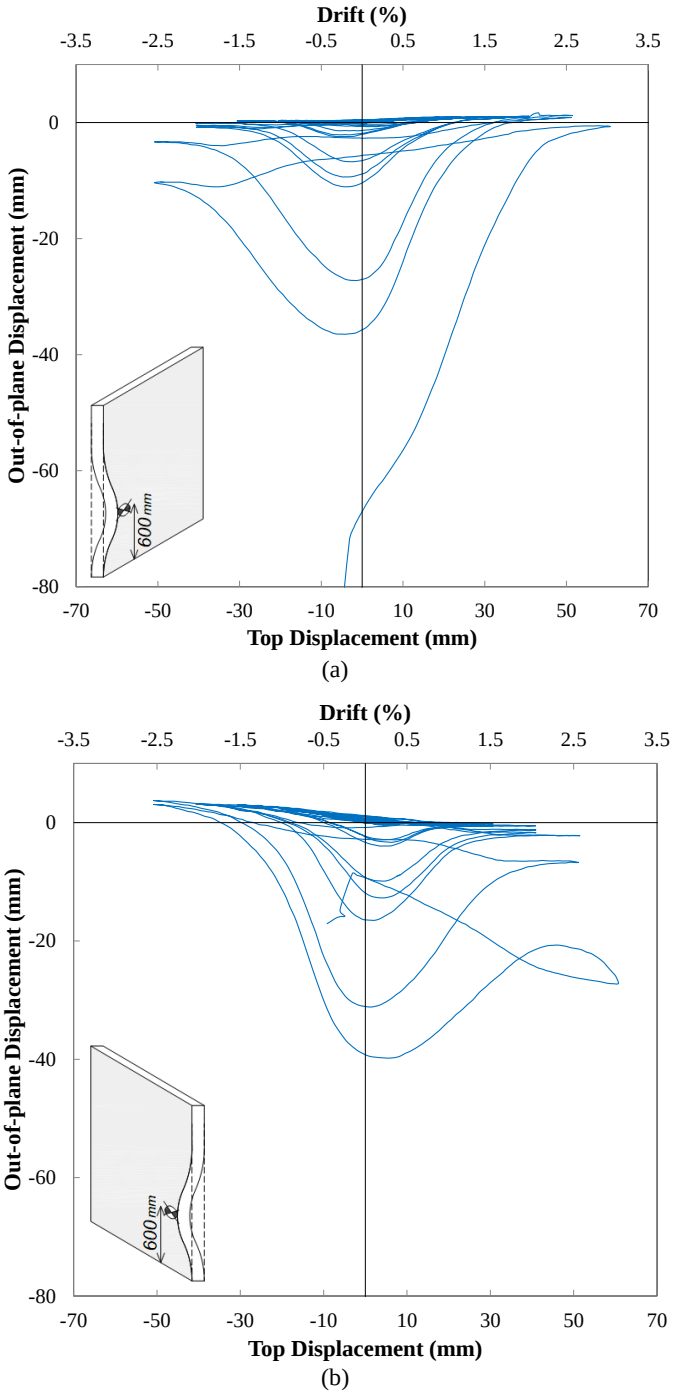

Figure 6.38: Top displacement vs maximum out-of-plane displacement Specimen RWL: (a) west boundary; (b) east boundary

Figure 6.39 displays the crack pattern of the specimen at different stages of loading. The grid size was 200x200 mm for this specimen. The specimen did not exhibit any cracking at 0.05% drift cycle and the first cracking happened at 0.06% drift and at about 550mm from the base during the 0.15% drift cycle. As it can be seen in Figure 6.39, the flexural cracks were distributed along the whole height of the specimen during the 0.15% drift cycle. The crack width was almost equal throughout the wall at this stage and was about 0.04 mm. The

number of horizontal cracks increased significantly at 0.38% drift level. These cracks were observed mostly along the boundary regions. A considerable number of diagonal cracks were observed throughout the panel at this drift level, as well. The distribution of crack width was almost uniform all over the specimen which can be attributed to the fact that the specimen represented the plastic hinge region of a four-storey wall. The cracks became wider and increased in number at 0.5% drift level. During the first cycle of 0.75% drift, a wide crack (1 mm) happened at the base and extended up to 1150 mm along the wall length (70% of the wall length). Another wide crack was observed at about 200 mm from the base in the boundary region which did not extend more than 600 mm along the wall length. According to the lateral load-top displacement response of the specimen, this is the stage where overall yielding of the specimen happened. During the 1.0% drift cycles, the width of horizontal cracks in the boundary region increased considerably within 600 mm from the base and the width of diagonal central region cracks increased within 1000 mm from the base. Cover spalling was observed at the extreme compression end of the specimen during the 1st cycle of 1.0% drift.

At the peak of the 1.5% drift cycle, new horizontal cracks had formed in the boundary regions between former cracks which merged into wide diagonal cracks in the central region. This can be attributed to the different bar sizes in the boundary and central regions. At this stage, wide boundary cracks were uniformly distributed within 700 mm from the base and had an average crack width of 1.3 mm. These cracks merged in the panel region and resulted in diagonal cracks that had an average crack width of 1.7 mm. Unlike the benchmark specimen, the crack width was uniformly high within 35% of the wall height from the base and was not significant at the base only. The initial out-of-plane displacement (1 mm) happened during the 1st cycle of 1.5% drift in the west boundary, and it increased in the subsequent cycles.

Quite a number of small cracks occurred during the 2.0% drift cycle, merging together and forming wide cracks in the panel region. The wide cracks had extended up to 50% of the wall height at this stage. Unlike Specimens RWB and RWT, no bar fracture or bar buckling happened during 2.0% drift cycles, and the out-of-plane displacement increased to about 7mm and 10mm in the 1st and 3rd cycles of 2.0% drift level, respectively.

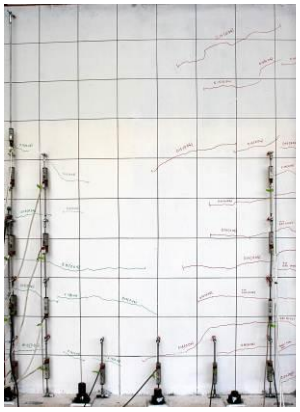

0.15%

0.38%

0.5%

0.75%

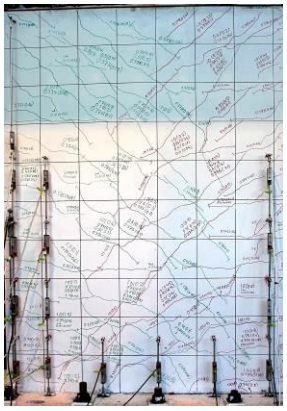

1.0%

1.5%

2.0%

2.5%

3.0%

Instability

Figure 6.39: Crack pattern of the specimen RWL at different drift levels

The crack pattern at 2.5% drift level was similar to the one at 2.0% drift level, and the crack width had increased, particularly the diagonal cracks. The wide cracks in the tension boundary region extended up to 1350 mm from the base with a uniform distribution of crack width. When the load was reversed from the peak of 2.5% drift cycle, the cracks in the tension region were wide open, and were still wide when the specimen was being reloaded in the opposite direction. Being spaced at an average distance of 120 mm, these residual cracks had an average crack width of 0.7 mm. At this stage, the out-of-plane

deformation increased significantly in the compression boundary region and was clearly visible. The out-of-plane deformation did not recover completely at this stage since the compressive stresses increased in the inner face of the out-of-plane displacement profile (where the crack closure initiated) along with reloading in the opposite direction and resulted in concrete crushing in one face of the wall. The out-of-plane deformation increased in the right boundary element as well when the specimen was being unloaded and reloaded towards the positive peak of the 3.0% drift cycle. Following the same trend as the previous cycles, the out-of-plane deformation increased up to the state where the cracks started closing in one face of the wall resulting in an increase of compressive stresses in this face and recovery of the out-of-plane deformation.

During unloading from +3.0% drift level and reloading towards -3.0% drift level, the out-of-plane deformation increased in the left boundary region. However, as the cracks generated in this boundary region during the +3.0% drift were wider than the previous cycle at 2.5% drift level, the crack did not close and the out-of-plane deformation increased considerably leading to out-of-plane instability of the wall. Figure 6.40 indicates out-of-plane instability failure of this specimen.

The sequence of events resulting in out-of-plane instability of the specimen is comprehensively described in the following chapter.

Appendix C compares the crack pattern and instability pattern of Specimens RWB and RWL at different drift levels.

6.8 OUT-OF-PLANE DISPLACEMENT PROFILE OF THE SPECIMENS

In order to compare the effect of the investigated parameters on out-of-plane deformation of rectangular walls, the out-of-plane deformation of the test specimens is compared herein. Figure 6.41 indicates the out-of-plane displacement profile of the specimens along the wall height in the boundary zones that did not exhibit considerable deterioration due to bar fracture and bar buckling. Since the benchmark Specimen RWB became unstable during the second cycle of 2.0% drift level, all the out-of-plane displacement profiles are provided up to this level only, for better comparison of the effects of different parameters on this mode of deformation. Although the slight (8%) increase in wall thickness (Specimen RWT as compared to Specimen RWB) did not significantly affect the out-of-plane deformation values at 1.5% drift level, it resulted in about 37% decrease of this type of deformation at

2.0% drift level. Specimen RWL was 20% shorter than Specimen RWB and had a maximum out-of-plane deformation of about 6.7 mm during the first cycle of 2.0% drift level which is about 53% reduction compared to 14.1 mm out-of-plane deformation of Specimen RWB.

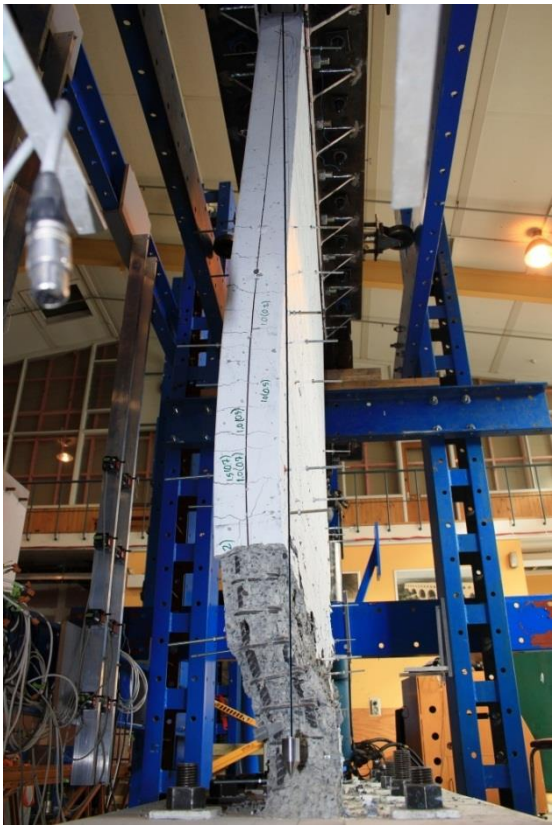

Figure 6.40: Out-of-plane instability of Specimen RWL

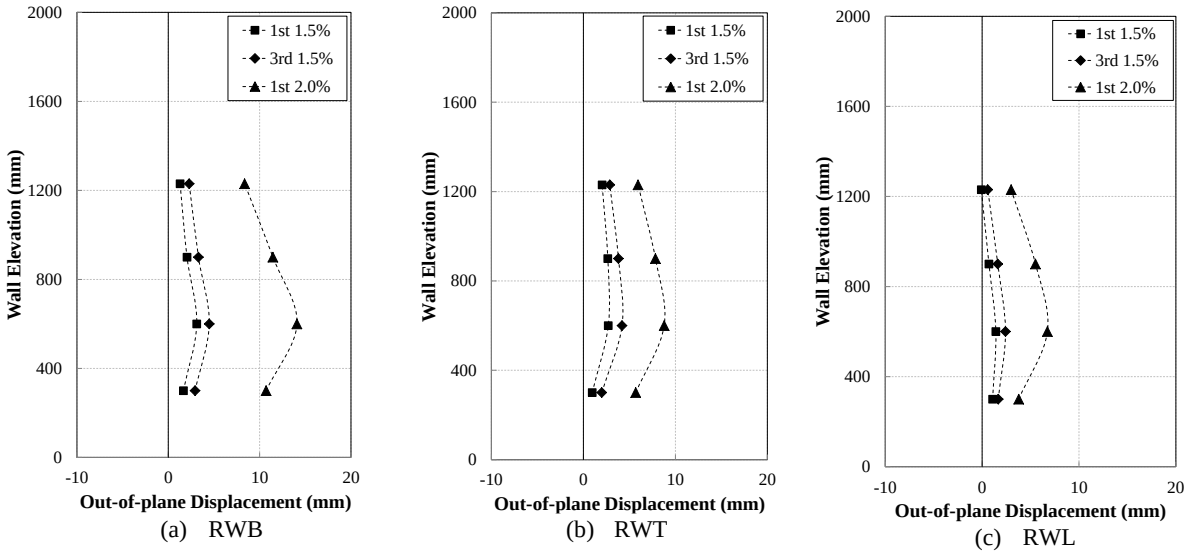

(a) RWB (b) RWT (c) RWL

Figure 6.41: Maximum Out-of-plane displacement profile of the specimens during 1.5% and 2.0% drift cycles

6.9 LOCAL RESPONSE OF THE SPECIMENS

One of the parameters commonly used in evaluation of local response of reinforced concrete structural components is the crack propagation at different stages of loading. This parameter is directly linked with the level of strains developed at different parts of the structure. In flexure-dominated structures, the strain aligned with direction of the longitudinal reinforcement will indicate the crack propagation as well as the level of flexural plasticity developed at different stages of loading. In this section, the variation of average vertical strain along the length of the wall (measured using potentiometers within a gauge length of 300 mm) and along the height of the boundary zones (measured using potentiometers within a gauge length of 250-720 mm) are used for response evaluation of the tested specimens. The average strain of the end rebars, measured using potentiometers that were connected to the reinforcement using welded couplers are also used in this investigation. Also, the reinforcement strain measurements captured along the wall length using strain gauges are compared with the average strain profile calculated using potentiometer readings to explore the reinforcement response associated with the corresponding average strain. Figure 6.10 and Figure 6.20 display the positioning and gauge length of these potentiometers at both faces of the Specimen RWB. The same configuration was used for the other specimens, except that the horizontal spacing between the potentiometers was less in Specimen RWL as the length of this specimen was 400mm less than Specimens RWB and RWT.

6.9.1 SPECIMEN RWB

Figure 6.42 and Figure 6.43 indicate the average vertical strain profile along the length of Specimen RWB within 300 mm from the base at peak positive drift levels, and at zero displacement during unloading from the positive peak, respectively. The average strain profiles are not compared with the reinforcement strain gauge readings as the wiring for a considerable number of strain gauges, particularly the ones at the end regions of the specimen, was obviously damaged inside the specimen. This comparison is done for Specimen RWT, which was identical to Specimen RWB in all features except for a slightly (10 mm) higher thickness.

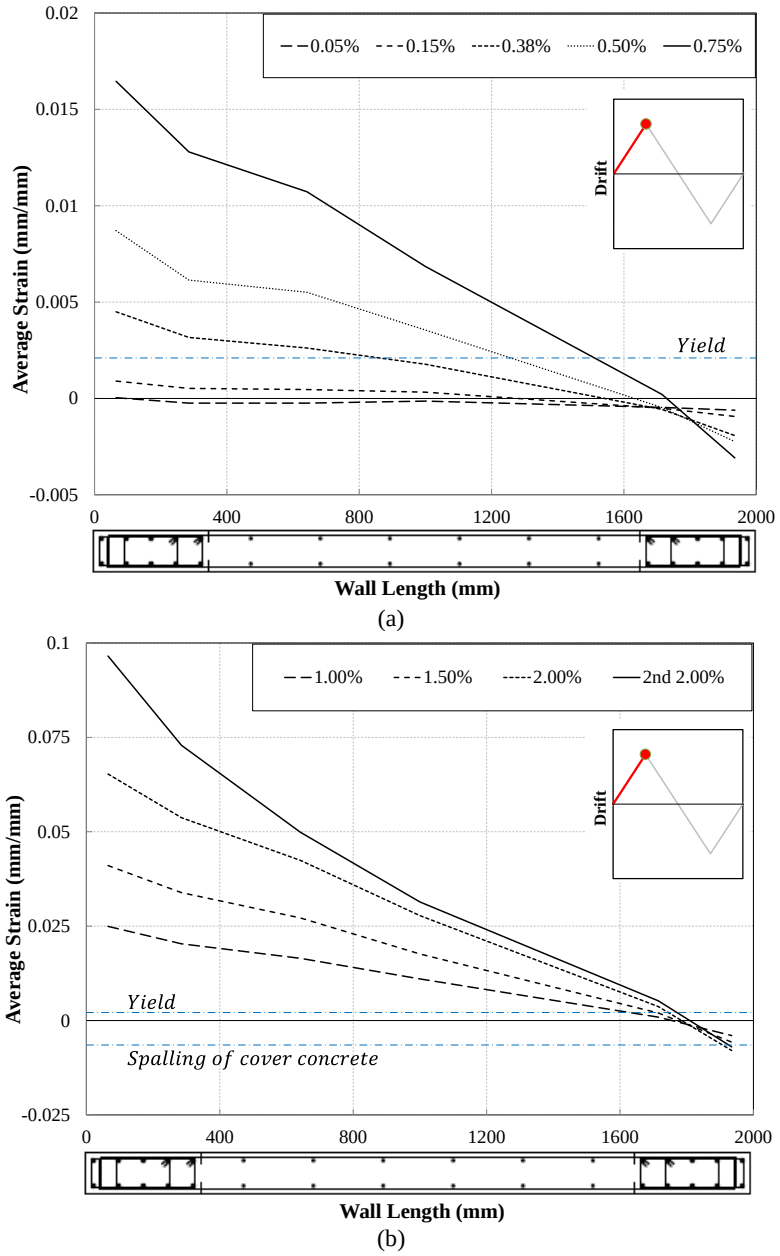

Figure 6.42: Average strain profile along the length of Specimen RWB, peak positive drift levels

Increase of the average tensile strain as well as migration of the neutral axis position along with the rise in the applied drift level can be observed in Figure 6.42. At 0.05% drift level, the strain values were negative for almost the whole length of the wall due to the applied axial load. From 0.05% to 0.15% drift levels, the increase in tensile strain was not very considerable. This stage corresponds to initial propagation of cracking along the length and height of the wall (Figure 6.26). However, at 0.38% drift level, the strain level in the west boundary region had exceeded the yield strain of the reinforcement (0.0021), resulting in a considerable movement of the neutral axis position. As the average tensile strain exceeded the yield strain, the rate of increase in tensile strain with respect to increase in the drift level

grew considerably. This trend is more sensible between 0.50% and 0.75% drift levels. According to the lateral load-top displacement response of the specimen (Figure 6.24), the overall yielding of the specimen can be recognized as happening at 0.50% drift level. Figure 6.42 displays that the average strain along more than half of the wall length has exceeded the yield strain at this stage. The nonlinearity of strain profile can be observed at yielding and post-yielding stages of the specimen (Figure 6.42a). This nonlinearity seems to depend on the variation of the reinforcement ratio along the wall length. The increase in tensile strain at peak positive displacement of the 2.0% drift level resulted in a bar fracture at the extreme end of the west boundary region.

Figure 6.43 indicates the stage where the specimen has reached the zero displacement after being unloaded from a peak positive displacement and while being reloaded in the opposite direction. As it can be seen in this figure, the amount of tensile residual strain developed in the specimen at this stage was minimal until 0.50% drift level, which corresponds to overall yielding of the specimen. It should be noted that, depending on the level of maximum tensile strains at positive peak displacement levels, the previously tensile rebars started to undergo compressive stresses at the onset of reloading in the opposite direction. The residual strain, increasing with the rise of the drift level, indicates the fact that wide cracks had developed in the tension side of the wall during this reloading, while the previously formed cracks in the opposite side were still wide open. As it can be seen in Figure 6.43, the level of residual strain developed in the specimen during the 0.75% and succeeding drift cycles would require the reinforcement to undergo considerable strains (and yield) in compression before any crack closure occurs. If this situation (compressive yielding of reinforcement before crack closure) exists at an adequately high elevation from the base, out-of-plane deformation may initiate in the compression boundary zone. In other words, Figure 6.43 indicates the stage where the flexural cracks are wide open in both tension and compression sides of the specimen.

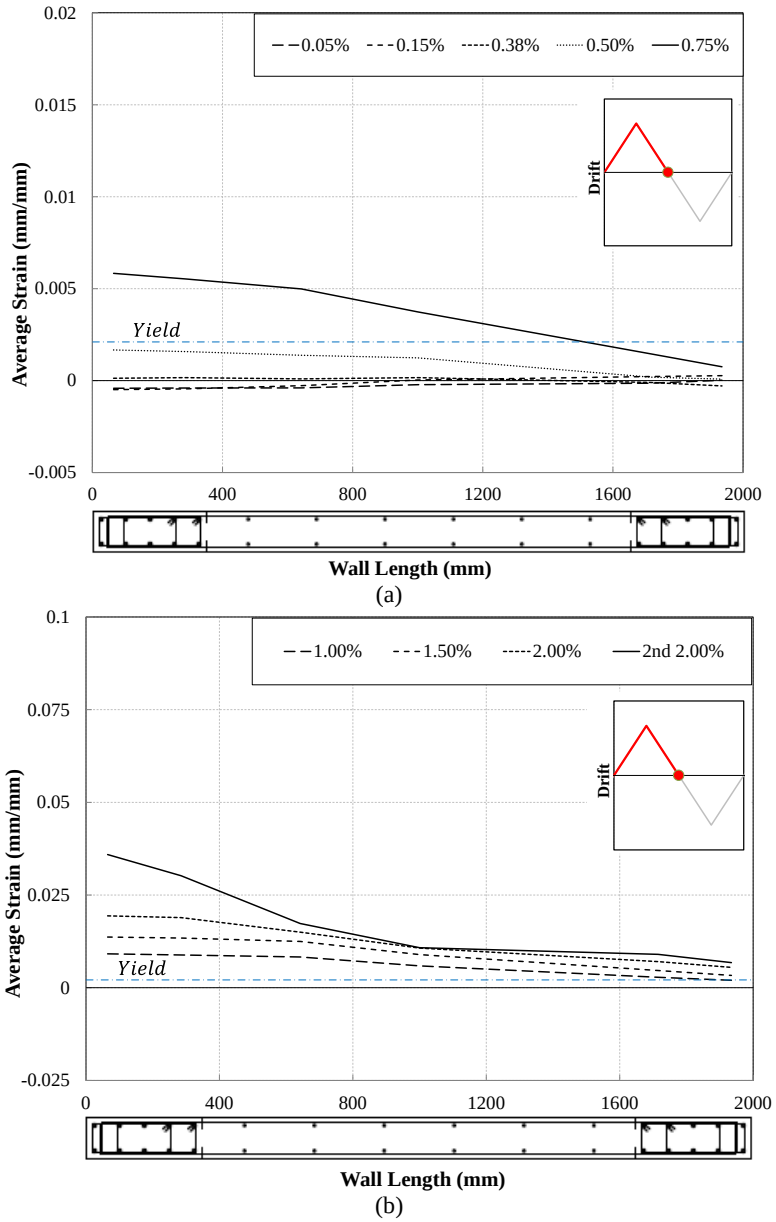

Figure 6.43: Average strain profile along the length of Specimen RWB, zero drift levels

In order to scrutinize the development of strain along the height of Specimen RWB, the average strains are calculated using measurements of the potentiometers shown in Figure 6.10 and Figure 6.20. These average strains, calculated for both faces of the east boundary zone using measurements of the extreme end potentiometers (d1 to d5 and k3 to k7, Figure 6.10) and normalized by the yield strain, are plotted at the peak negative displacement stages of each drift cycle, when this boundary zone was subjected to its maximum tension. The drift levels are categorized into pre-yielding (Figure 6.44), yielding (Figure 6.45), post-yielding (Figure 6.46) and ultimate (Figure 6.47) stages of the wall response. The average reinforcement strain measured using the potentiometers connected to the extreme end bar located on south face of the east boundary (k10 and k11, Figure 6.20) is plotted in these

figures, as well, to be compared with the average strain measurements of the south face (using potentiometers k3 to k7, Figure 6.10b).

At 0.05% drift level, the flexural cracking initiated within 1250 mm from the base, and at 0.15% drift level, the cracking distributed throughout the wall height (Figure 6.26). The maximum average strain at 0.05% drift level (crack initiation) is about ($0.4\varepsilon_y$= 0.0008 mm/mm). As it can be seen in Figure 6.44, the average strain measurements are not symmetric along the wall thickness in the pre-yielding stages indicating asymmetric crack initiation along the wall thickness.

Bar yielding started at 0.38% drift level along the height of approximately 1200 mm from the base and further developed at 0.50% drift level, mainly within 600 mm from the base (Figure 6.45b). This drift level, as noted based on the average strain profile along the wall length and load-displacement curve (Figure 6.24), corresponds to overall yielding of the specimen. The average strain measurement of the south face end bar has reasonable match with average strain of the south face. However, the average strain measurements along the wall thickness have become more asymmetric at this stage.

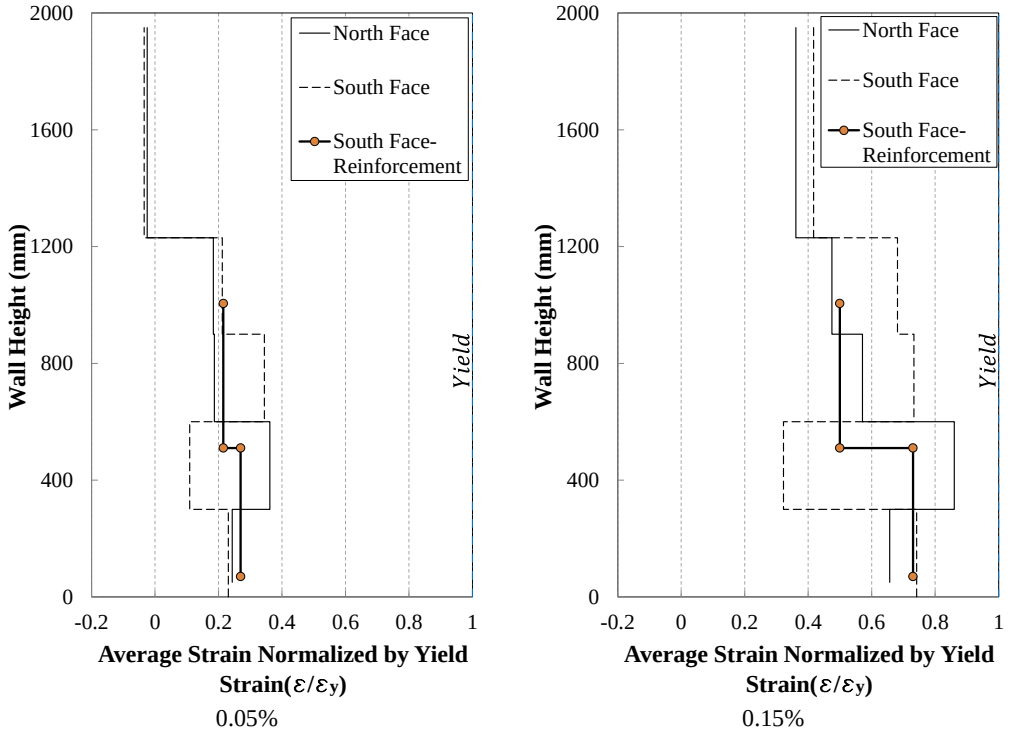

Figure 6.44: Average tensile strain profile along the height of the east boundary region corresponding to 0.05% and 0.15% drift levels (before yielding stage) - Specimen RWB

Figure 6.46 displays the strain state after the overall yielding of the specimen. Compared to 0.50% drift level, the amount of yielding at 0.75% drift level within 600 mm distance from the base almost doubled. This increase was not very significant above this level in height. A similar trend can be observed between 1.00% and 0.75% drift levels.

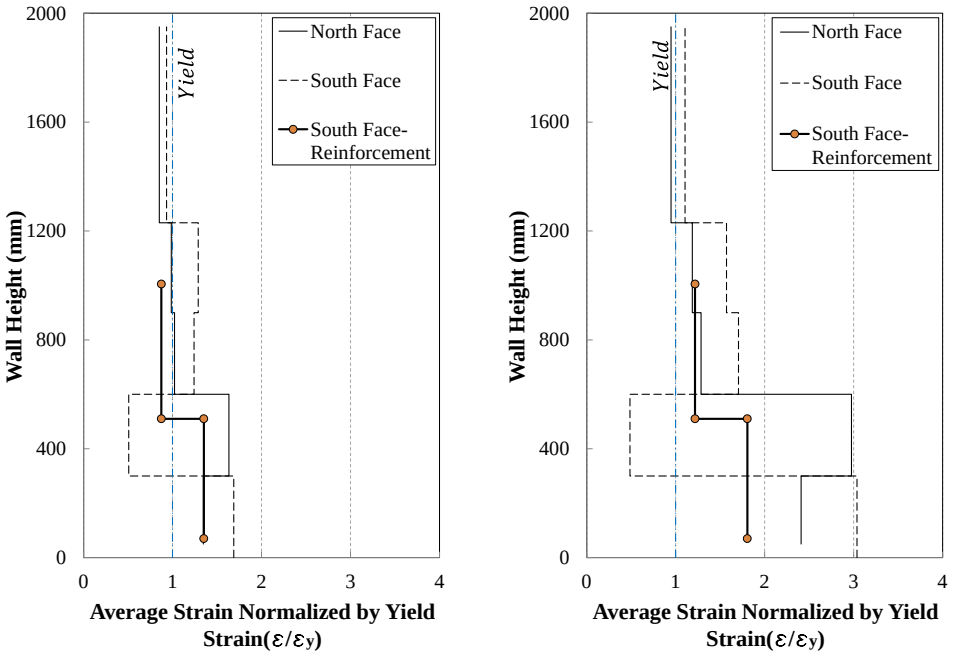

(a) 0.38% (b) 0.5%

Figure 6.45: Average tensile strain profile along the height of the east boundary region corresponding to 0.38% and 0.5% drift levels (at yielding stage) - Specimen RWB

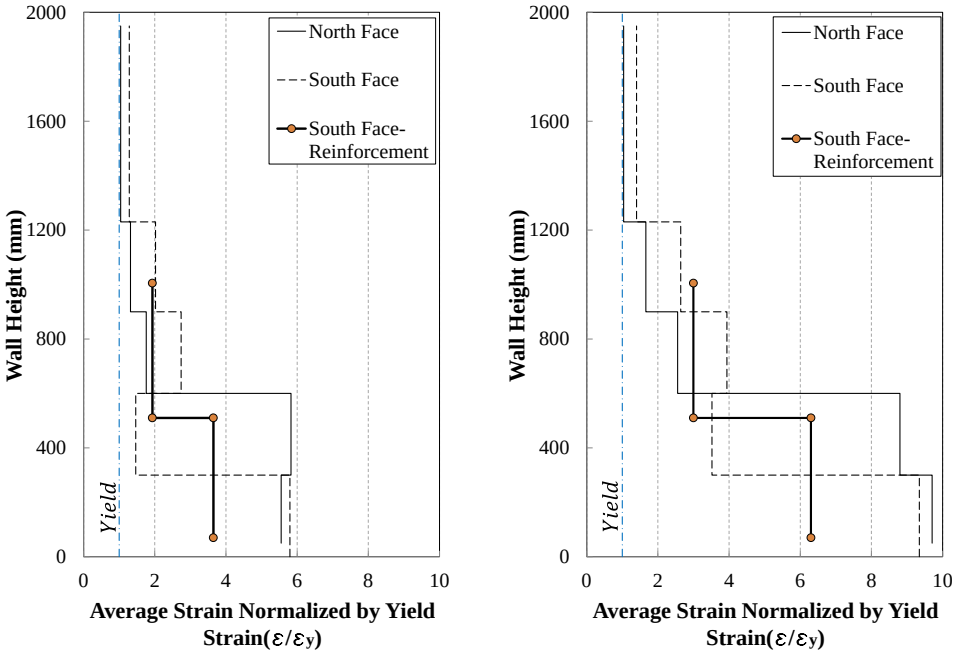

(a) 0.75% (b) 1.00%

Figure 6.46: Average tensile strain profile along the height of the east boundary region corresponding to 0.75% and 1.0% drift levels (after yielding stage) - Specimen RWB

The increase of average strain at 1.50% drift level is also considerable, and the increase is mainly within 600 mm from the base. When the specimen was unloaded from this peak displacement level, and was being reloaded in the opposite direction, the out-of-plane deformation initiated in this boundary region. The out-of-plane displacement profile of the specimen (Figure 6.41a) shows that the length of the wall involved in formation of out-of-plane deformation is around 1200 mm from the base. The strain status shown in Figure 6.47a indicates that at this drift level (1.50%), the average strain on both faces of the boundary zone and within 1200 mm from the base are above $2\varepsilon_y$. This is actually the first stage when the average strain has exceeded $2\varepsilon_y$. During elastic unloading, a strain recovery equal to ε_y is expected to happen, leaving a residual strain of above ε_y. This level of residual strain would require the reinforcement to undergo compression yielding before any crack closure can occur. If this (compressive yielding of reinforcement before crack closure) happens at an adequately high elevation from the base, the out-of-plane deformation is likely to initiate in the compression boundary zone. This out-of-plane deformation increased with the number of cycles at 1.50% drift level. At 2.00% drift level, the average strain increased considerably within 600 mm from the base.

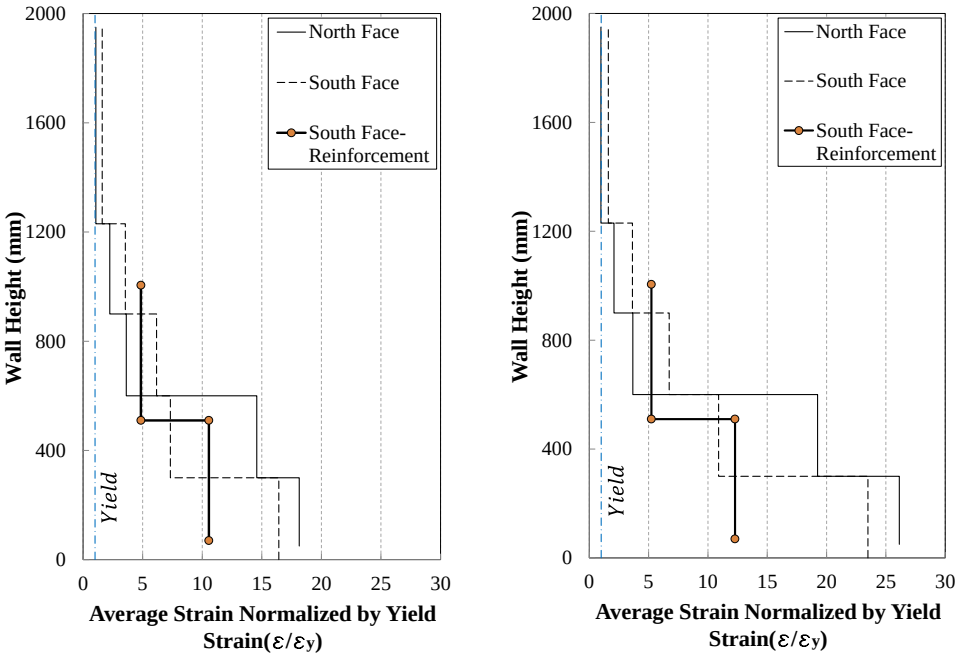

Figure 6.47: Average tensile strain profile along the height of the east boundary region corresponding to 1.5% and 2.0% drift levels (ultimate stages) - Specimen RWB

The average strain profile along the height of north and south faces of the boundary regions indicated that different faces of boundary regions were subjected to different values of maximum tensile strain at a specific height from the base. This variation of maximum tensile strain along the thickness proved to be consistent at different stages of cracking, yielding and post-yielding, indicating that a cracked wall section will not necessarily undergo equal amount of compression plasticity before the cracks close. This can be one of the main sources of eccentricity that can trigger initiation of out-of-plane deformation in rectangular walls. This effect is further studied by comparison of the strain gauge measurements along the wall thickness.

6.9.2 SPECIMEN RWT

Specimen RWB and RWT were identical except that Specimen RWT had a slightly (8%) larger thickness compared to Specimen RWB. Therefore, the variation of strain along the wall length and height was understandably similar. However, more reinforcement strain gauges were functional in this specimen at the onset of testing. The variation of strain profile for Specimen RWT is thus investigated by the average strain profiles captured using measurements of the potentiometers positioned within 300 mm from the base and along the wall length as well as the reinforcement strain gauge readings at 50mm from the base. Figure 6.48 and Figure 6.49 indicate these measurements for the peak positive and zero displacement stages of the applied drift cycles. The functionality of the reinforcement strain gauges was limited to a maximum strain reading of 0.02. Therefore, the strain gauge measurements are not plotted for the cycles above 1.00% drift level as the strains exceeded 0.02 in the higher cycles.

As it can be seen in Figure 6.48, prior to 0.50% drift level (which is the overall yielding stage of Specimen RWT, as well, see Figure 6.30), the reinforcement strain at the base is lower than the average strain within 300 mm from the base, except for the 0.38% drift level where yielding had happened in the west boundary at the base. The reinforcement strain profiles at 0.50%, 0.75% and 1.00% drift levels are fairly close to the average strain measurements. The reinforcement strain profile plotted for the 0.50% drift level indicates development of tensile yielding along more than half of the wall length.

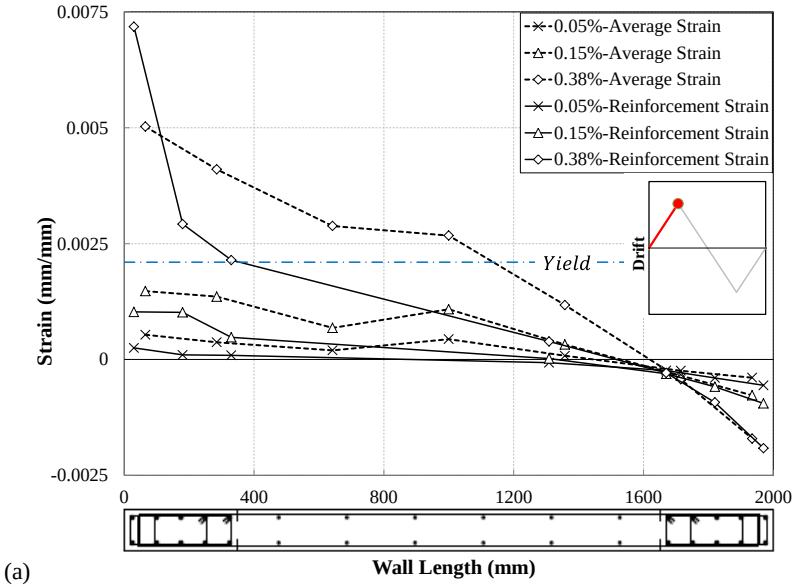

(a)

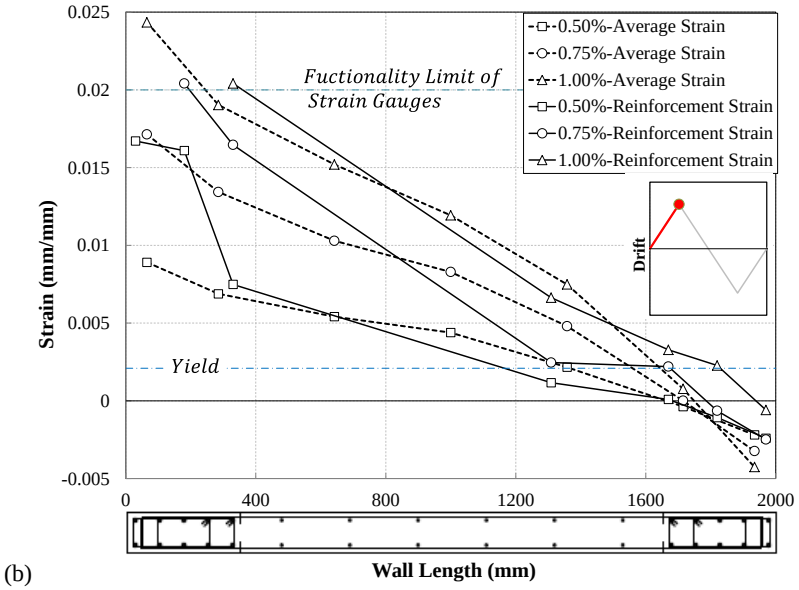

(b)

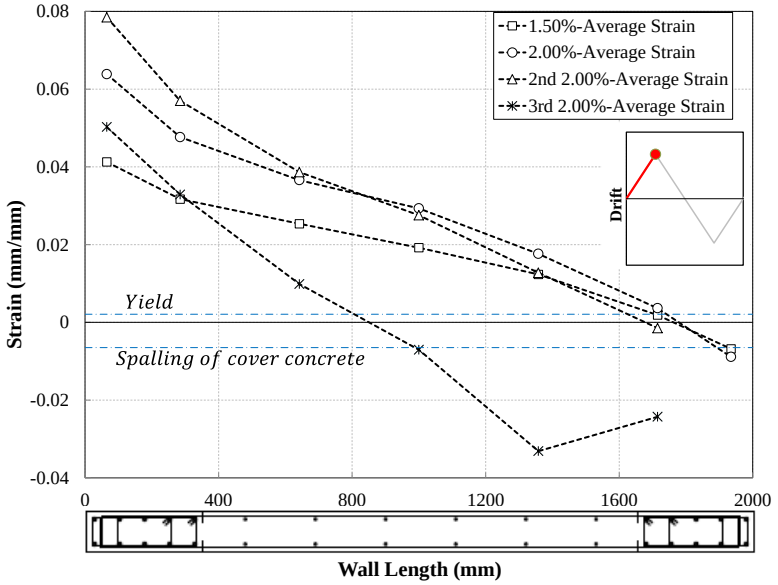

(c)

Figure 6.48: Average strain vs reinforcement strain profile along the length of Specimen RWT, peak positive drift levels

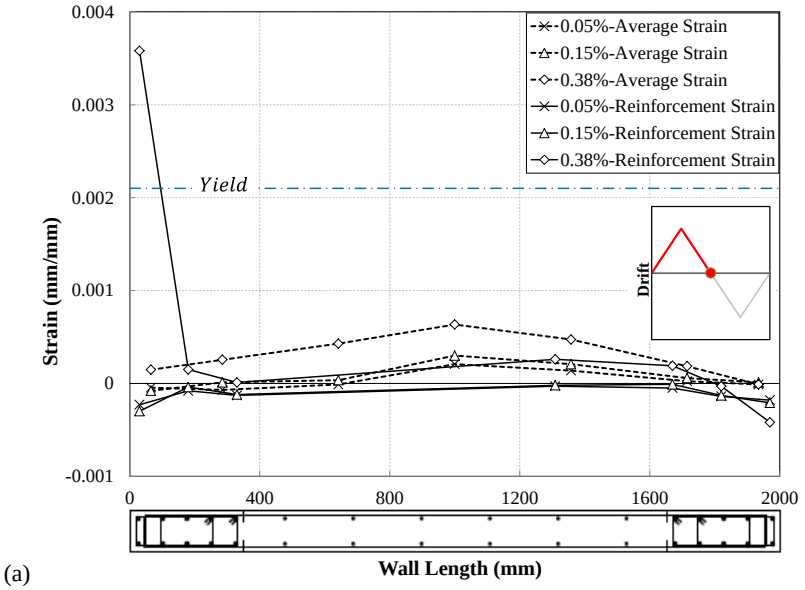

(a)

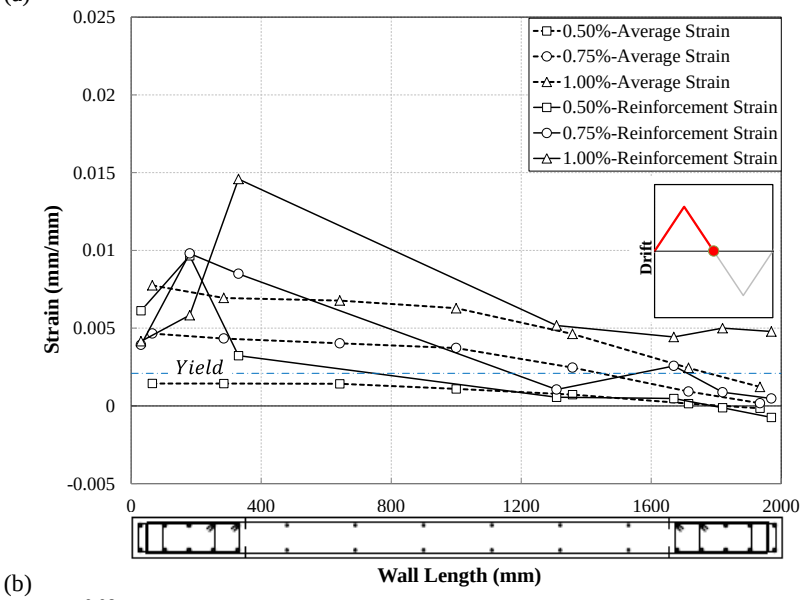

(b)

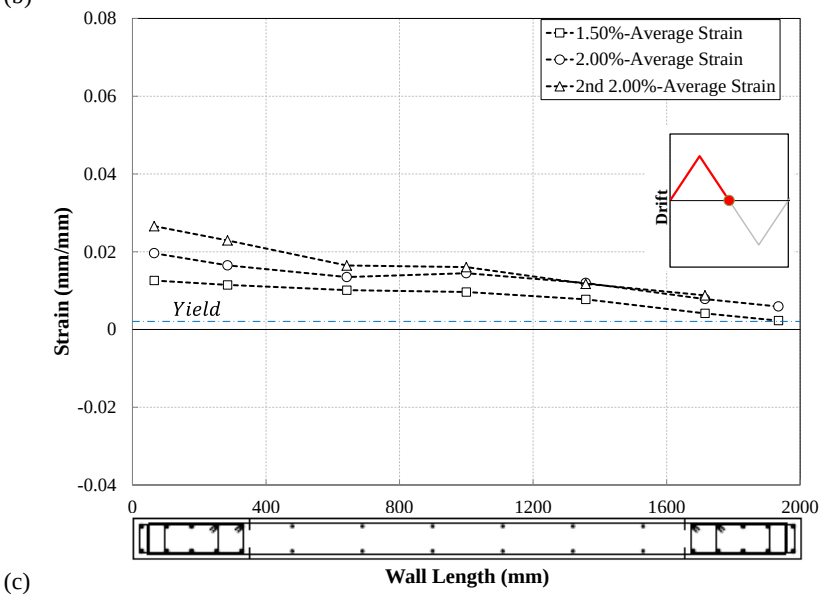

(c)

Figure 6.49: Average strain vs reinforcement strain profile along the length of Specimen RWT, zero drift levels

The movement of the neutral axis position can also be interpreted from the plots at different drift levels. The higher drift levels involve further yielding in the tension side requiring smaller area of compression to satisfy equilibrium of the section. The out-of-plane deformation started at 1.50% drift level and bar fracture occurred at 2.00% drift level in the bars that exceeded the tensile strain of 0.06. It should be noted that this premature bar fracture could be attributed to the effect of low-cycle fatigue on tensile strain capacity of the bars. Bar buckling, first observed during the 3rd cycle of 1.50% drift, continued to occur during the succeeding drift cycles. The combination of the three failure patterns of out-of-plane deformation, bar fracture, and bar buckling resulted in overall instability of the specimen during the 3rd cycle of 2.00% drift level (Figure 6.34), creating an average strain profile shown in Figure 6.48.

Figure 6.49 displays the amount of tensile residual strain at zero displacement in the tension side of the wall section from the peak positive displacement stage (Figure 6.48). At lower drift levels (0.05% and 0.15%), the strain in the reinforcement was back to the initial stage where the applied axial load had resulted in negative strains. However, the average strain was slightly higher, which can be attributed to the fact that the cracked section had not returned to the original situation. Development of residual strain started from the 0.38% drift level, where a portion of the reinforcement had yielded in the peak positive displacement stage, and became significant at 0.50% drift level as the amount of tensile yielding experienced in the previous stage was considerable. During unloading from the peak positive displacement stage, the tensile strain in the reinforcement had decreased by an amount equal to the yield strain (0.0021) following which the reinforcement had started to undergo compression despite having a noticeable amount of tensile strain remaining (residual strain).

Depending on the value of the maximum tensile strain developed in the peak displacement stage, the bars may undergo a significant amount of compression plasticity before the initially developed tensile strain reaches zero and the crack closure happens. Figure 6.49b and Figure 6.49c display the increase of residual strain at zero displacement stage with the increase in the applied drift level. Particularly, the strain profile at 1.50% drift level and above (Figure 6.49c) represents a situation where the strain is above the yield strain along the whole length of the wall, although the stress varies from tension at the east boundary zone to compression at the west boundary zone. This amount of crack opening along the whole length in addition to bar yielding at both end regions (one in tension and the other in

compression) can provide ideal situations for flexibility of the wall section against any out-of-plane deformations arising from the compression side and dissipating towards the tension side. Although the maximum out-of-plane deformation usually occurs at a height above the base, the strain status and section equilibrium would follow a similar trend with smaller values of strain depending on the distance from the base.

6.9.3 SPECIMEN RWL

In this section, only the average strain profiles along the length of the wall are investigated for Specimen RWL and the strain variation along the wall height is discussed in the following section in comparison with measurements of Specimen RWB. Figure 6.50 and Figure 6.51 display the average strain plots for Specimen RWL. Being a shorter specimen compared to RWB and RWT, the maximum strain reached at a given drift level is understandably smaller in this specimen. Therefore, the milestones of the wall response controlled by strain values, such as yielding, happened slightly later in terms of drift level in this specimen. The overall yielding of Specimen RWL happened at 0.75% drift level (Figure 6.37) which corresponds to development of average tensile strain higher than the yield strain along more than half of the wall length (Figure 6.50a). The residual strain corresponding to this drift cycle at zero displacement stage is also considerably high compared to the preceding drift levels (Figure 6.51a). It is interesting to note that as soon as bar yielding initiated in this specimen, the average strain profile followed a nonlinear pattern along the wall length with the nonlinearity increasing further with the drift level. This level of nonlinearity was not observed in the other specimens and can be attributed to the considerable difference between reinforcement ratios of the boundary zone and the panel in Specimen RWL, putting restrictions on development of high tensile strains in the extreme end regions as well as better bond characteristics due to larger bar diameter in this specimen compared to the other specimens. As this specimen had no bar fracture or bar buckling failure patterns, the neutral axis position migrated steadily towards the extreme end of the east boundary zone resulting in compression strains of the confined boundary zone to exceed the ultimate strain capacity at 3.0% drift level. This ultimate strain capacity of the confined concrete zone was calculated using the equation proposed by Priestley et al. (2007).

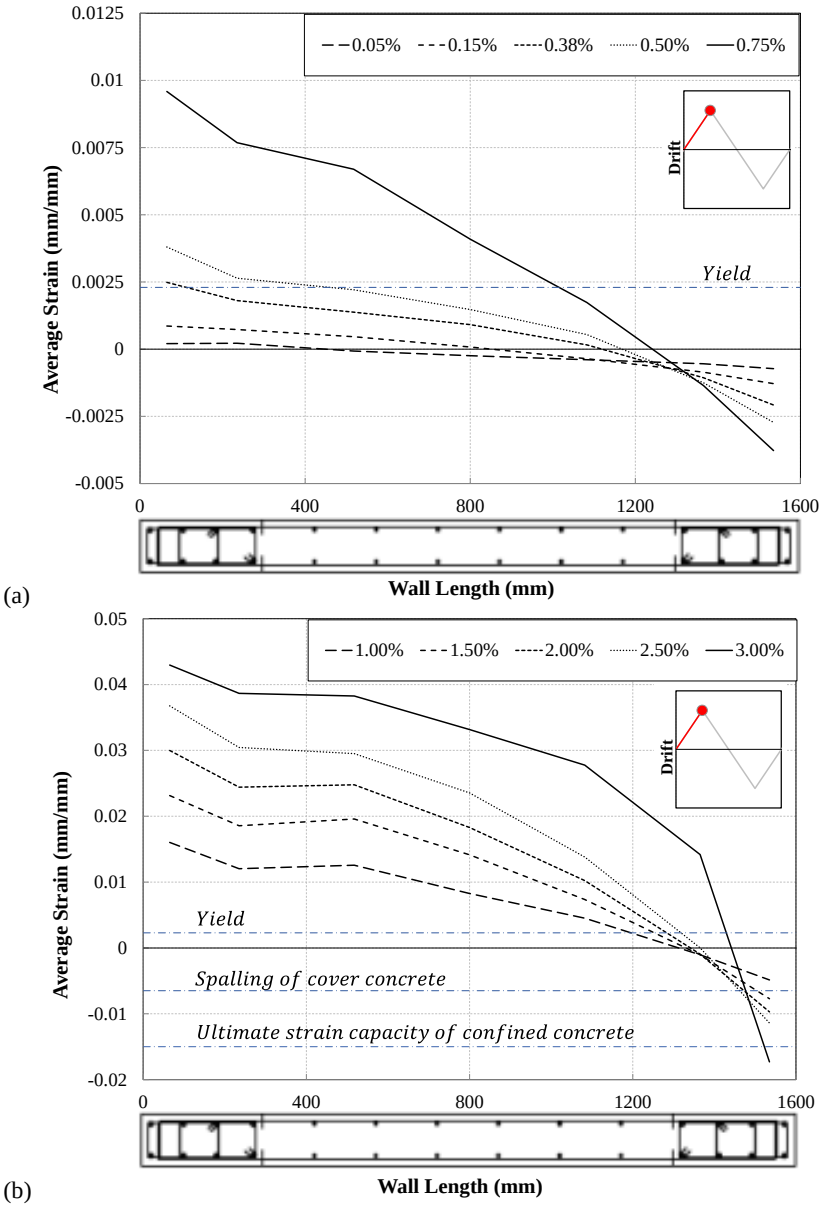

Figure 6.50: Average strain profile along the length of Specimen RWL, peak positive displacement levels

The residual strain profiles at the zero displacement stage in higher drift cycles (1.00% to 2.50%) are shown in Figure 6.51b. As it can be seen in this figure, the average strain profiles follow a trend similar to the ones at peak positive displacement levels (Figure 6.50b), except for the 2.50% drift profile which is obviously affected by the considerable out-of-plane deformation of the west boundary zone at this stage. The specimen became unstable at about zero displacement stage after experiencing the peak positive displacement of 3.00% drift cycle. The corresponding average strain profile is not plotted in this figure since it was significantly influenced by the wall instability.

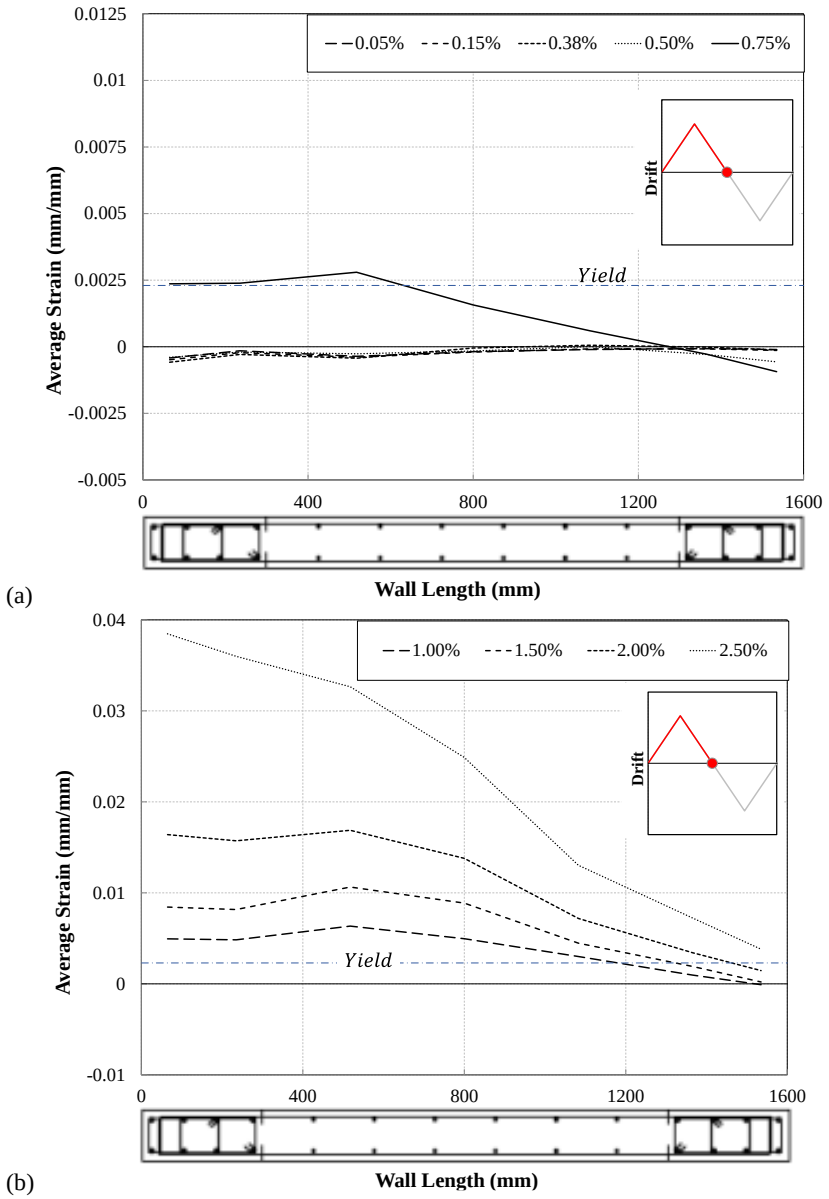

Figure 6.51: Average strain profile along the length of Specimen RWL, zero displacement levels

It is quite obvious that the cyclic behavior of reinforcing bars is one of the main parameters controlling the cyclic response of a reinforced concrete wall unit. The maximum tensile and compressive strains developed in the reinforcement at peak displacement levels of a specific loading cycle determines its response during different stages of unloading and reloading (i.e., the amount of residual strain) controlling the crack closure and consequently contribution of the compression capacity of concrete to the load bearing capacity of the specimen. Figure 6.52 shows the strain history of the west boundary end bar measured using strain gauges located at 15 mm and 180 mm from the base. The functionality limit of the strain gauges is 0.02 and the data above this level (1.50% drift) was not valid and is not shown in this figure. The strain gauge history clearly shows the increase in amount of

residual strain as a result of increase in the drift level as well as the increase in the number of cycles per drift level.

The strain gauge readings at different drift levels compare reasonably well with the average strain measurements at the extreme end region of the west boundary zone at both peak positive displacement and zero displacement stages of the applied drift cycle shown in Figure 6.50 and Figure 6.51, respectively.

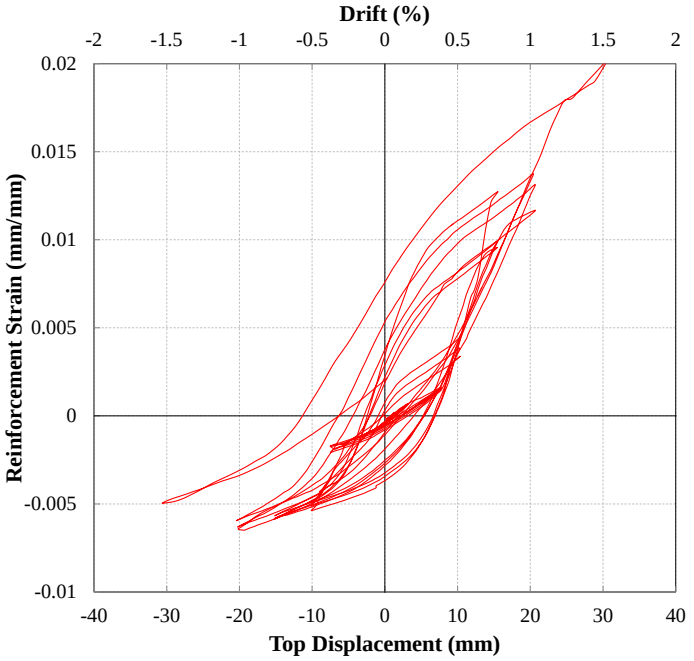

(a)

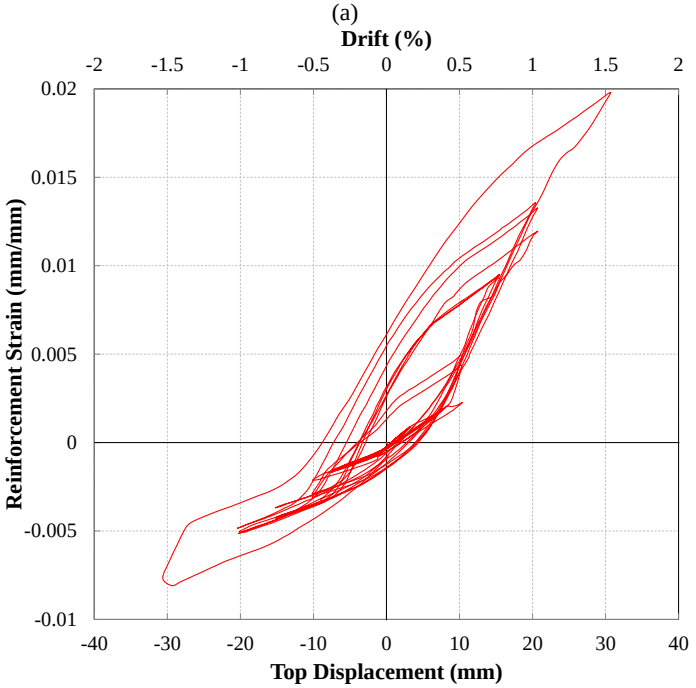

(b)

Figure 6.52: Strain history of the west boundary end bar: (a) 15 mm from the base; (b) 180 mm from the base

6.9.4 COMPARISON

As discussed in Section 6.8, although the specimens having different geometrical characteristics exhibited different values of out-of-plane deformation, the initiation of out-of-plane deformation happened at 1.50% drift in all the three specimens. Therefore, the average strain developments along the length and height of the specimens at one drift level before 1.50% drift level (1.00% drift level), at 1.50% drift level, and at one drift level after 1.50% drift level (2.00% drift level) are compared in this section.

Figure 6.53 and Figure 6.54 compare the average strain measurements of Specimen RWB with the ones of Specimen RWT and Specimen RWL, respectively. As it can be seen in Figure 6.53, as Specimens RWB and RWT were different in thickness (8%) only, the average strain profiles are almost identical. However, the 400 mm (20%) decrease in wall length resulted in lower tensile strain values at extreme end regions of wall for a given drift level. However, since Specimen RWL was designed to have a flexural capacity close to the one of Specimen RWB, the reinforcement ratio was higher at the boundary zones and the panel area. The increase in reinforcement content would require less tensile strain to be developed in the reinforcement to equate with the compression force and generate the same flexural capacity as a longer wall with lower reinforcement ratio.

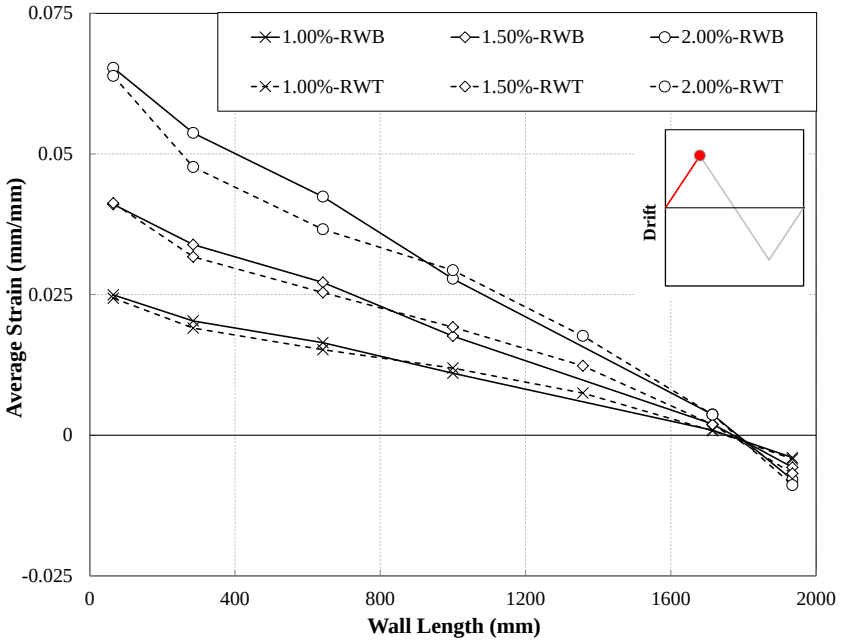

Figure 6.53: Average strain profile along the wall length, Specimen RWB vs Specimen RWT

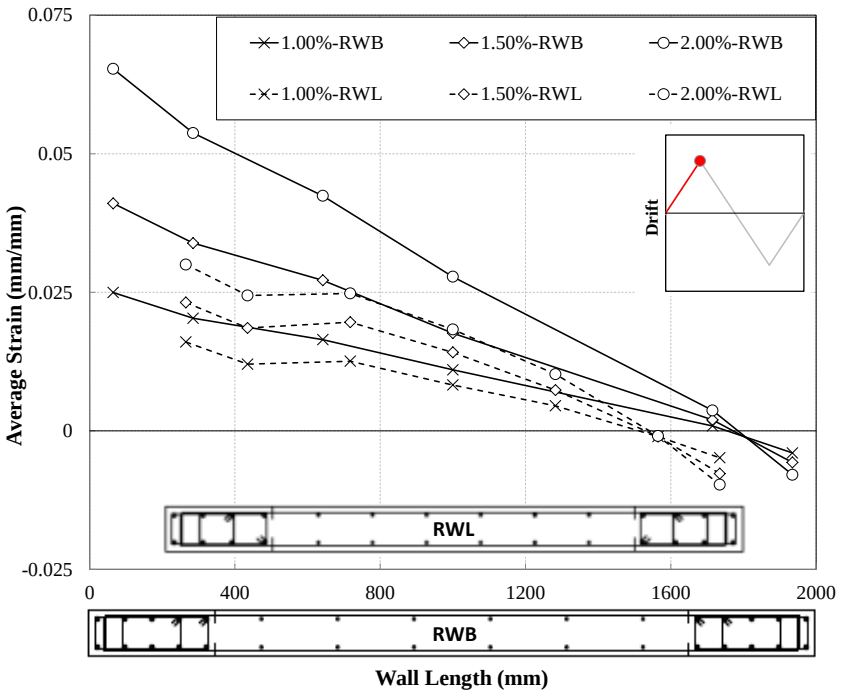

Figure 6.54: Average strain profile along the wall length, Specimen RWB vs Specimen RWL

In order to investigate the effect of this change in wall length and reinforcement configuration on distribution of strain along the height of the wall, the average strain measurements of the potentiometers attached to the end bars are compared in Figure 6.55 and Figure 6.56. The location and the coverage length of these instruments are shown in Figure 6.20 for Specimen RWB. The gauge lengths are slightly different for Specimen RWL. Although the average reinforcement strain within about 500 mm from the base is higher in Specimen RWB (Figure 6.55a) when compared to the strain values at corresponding drift levels in Specimen RWL (Figure 6.55b), these values are higher in Specimen RWL (Figure 6.56b) within the distance between 500 and 1000 mm from the base in comparison with Specimen RWB (Figure 6.56a).

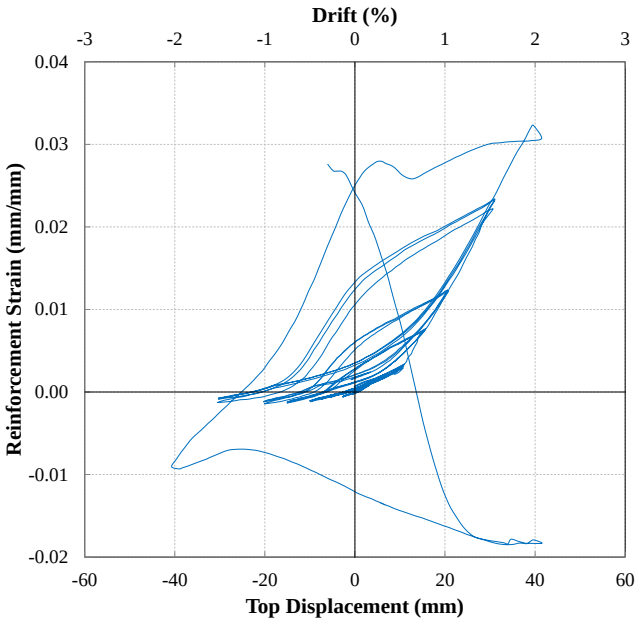

(a)

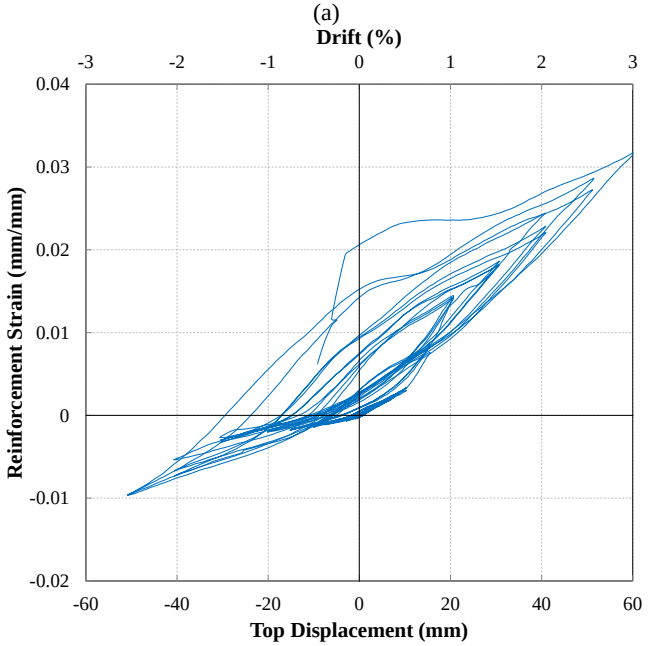

(b)

Figure 6.55: Average strain history of the west boundary end bar: (a) RWB, within 75-522 mm from the base; (b) RWL, within 75-462 mm from the base

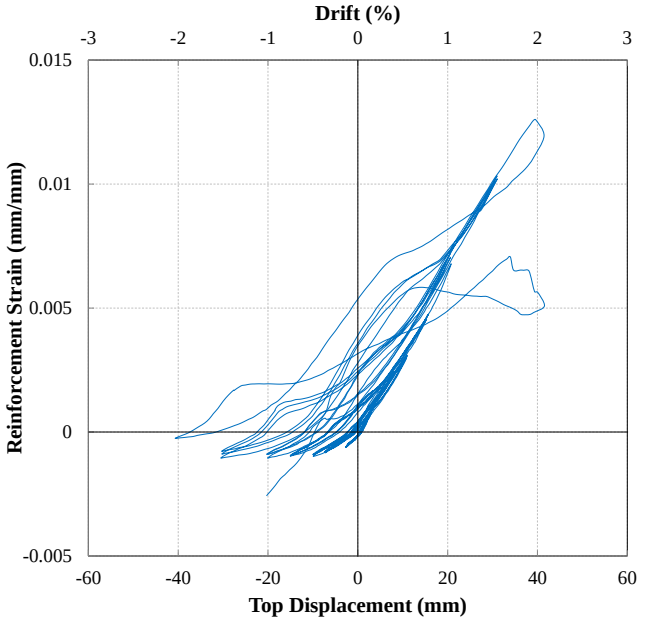

(a)

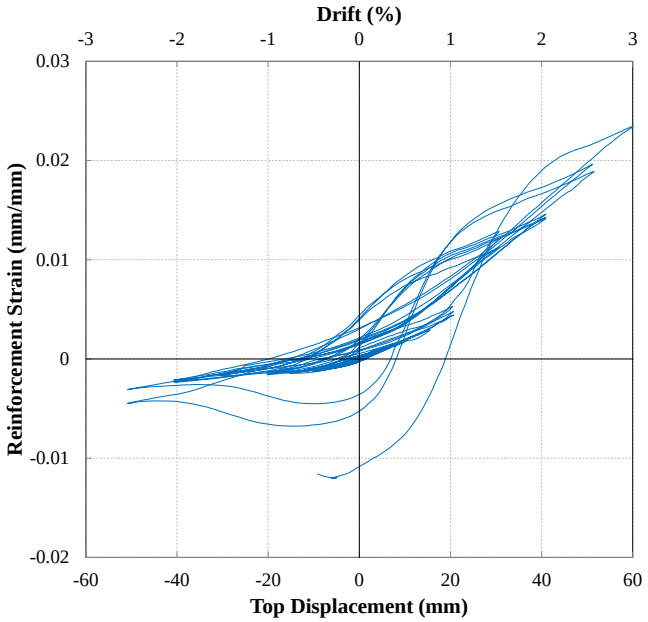

(b)

Figure 6.56: Average strain history of the west boundary end bar: (a) RWB, within 522-1017 mm from the base; (b) RWL, within 462-955 mm from the base

The variation of average strain along the height of Specimen RWB is compared with the measurements of Specimen RWL at both boundary regions (Figure 6.57 and Figure 6.58). As noted above, the comparison is done at 1.00%, 1.50% and 2.00% drift cycles at the stages where the boundary zones are under tension; i.e., positive peak displacements for west boundary and negative peak displacements for east boundary. The strain values are normalized by yield strain as the yield strains were almost identical (0.0023 and 0.0021 for boundary zone bars of Specimen RWL and Specimen RWB, respectively).

As it can be seen in Figure 6.57 and Figure 6.58, with increase of the drift level, the average strain of Specimen RWB at both boundary zones increases more rapidly within 600 mm from the base compared to the strain values within 600-1200 mm from the base. In other words, with increase of the applied drift level the plasticity gets more concentrated at the 600 mm distance from the base in Specimen RWB. However, plasticity distribution of Specimen RWL is almost linear along the 1200 mm from the base in the west boundary region (Figure 6.57) at different drift levels. Regarding the east boundary region of Specimen RWL (Figure 6.58), the increase from 1.00% to 1.50% generated more plasticity within 600-900 mm from the base, and the increase from 1.50% to 2.00% drift level resulted in more plasticity within the distance between 900 and 1200 mm elevations. The development of strain profile along the length of Specimen RWL and its relationship with the formation of out-of-plane deformation is discussed in more detail in the following chapter as failure pattern of this specimen was pure out-of-plane instability.

Reducing the length of Specimen RWB and making use of higher reinforcement ratio to provide a similar flexural capacity affected the strain profile along both length and height of the specimen. With reduction of maximum tensile strain at the base, bar fracture and bar buckling failure patterns were suppressed. Variation of strain along the height of Specimen RWB was extremely nonlinear, with considerably large plasticity developed along a specific height from the base. However, the strain variation became relatively linear in specimen RWL, distributing the plasticity (that was less than the one of Specimen RWB due to a smaller length and larger reinforcement ratio) along a larger portion of the wall height. Figure 6.58c shows distribution of an average plastic strain of about $7\varepsilon_y$ along the height of 1200 mm in Specimen RWL compared to formation of an average plastic strain of about $20\varepsilon_y$ within 600 mm from the base of Specimen RWB which is about ten times higher than the average plastic strain within the 600-1200 mm height.

As also mentioned in the previous sections, a maximum tensile strain of higher than $2\varepsilon_y$ can induce compression yielding in the reinforcement before any crack closure can happen. This compression yielding, if developed along an adequate height, can potentially lead to formation of out-of-plane deformations as a result of the inherent eccentricities in material response along the thickness of a thin wall section. Therefore, although a reduction in wall length would result in smaller values of tensile strain at the extreme end region, it is less likely to have a considerable effect on the formation of out-of-plane deformation if its

reinforcement configuration can still develop a specific amount of plasticity over a height that is vulnerable to exhibit out-of-plane deformations.

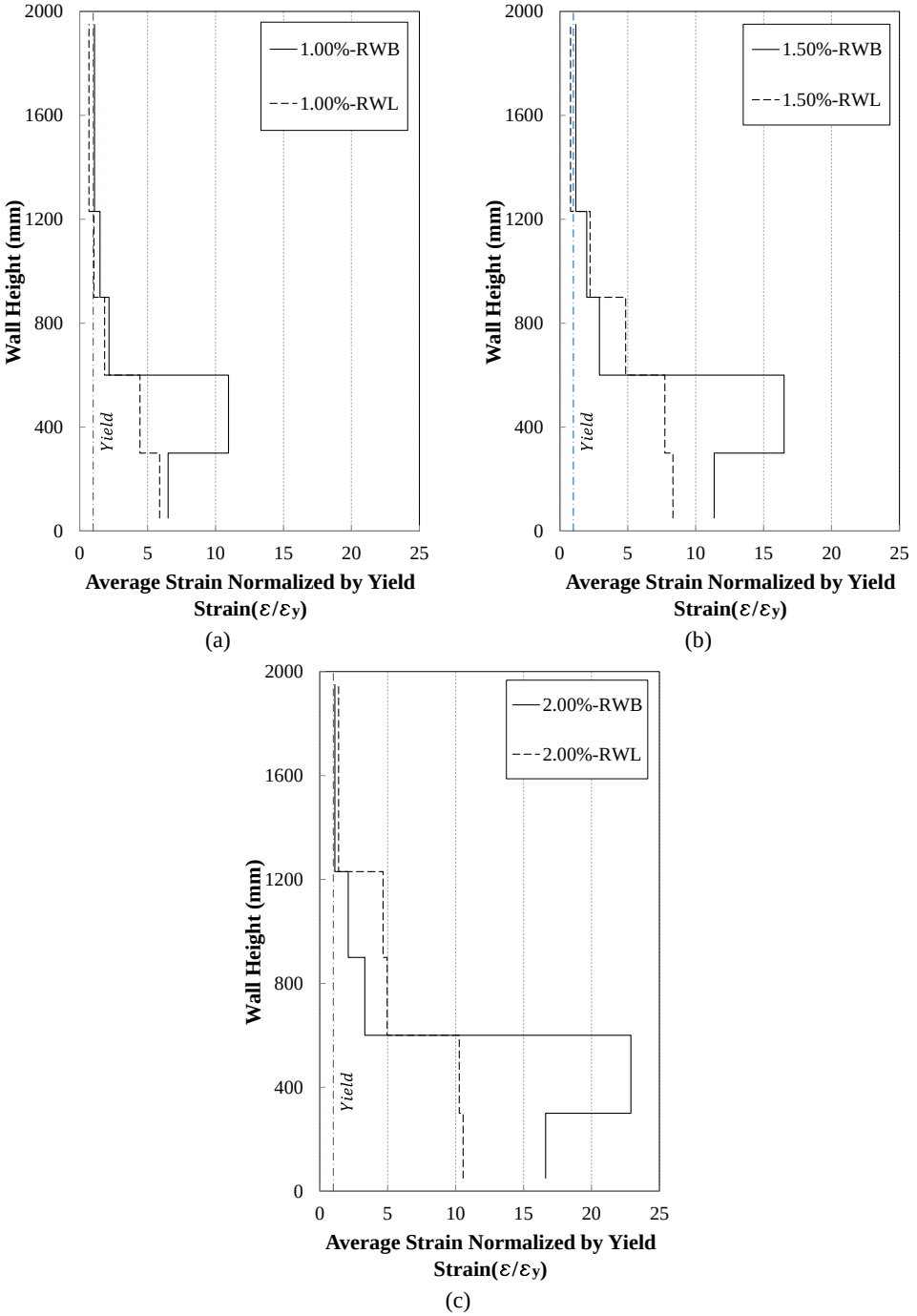

Figure 6.57: Average tensile strain profiles along the west boudary region, Specimen RWB vs Specimen RWL

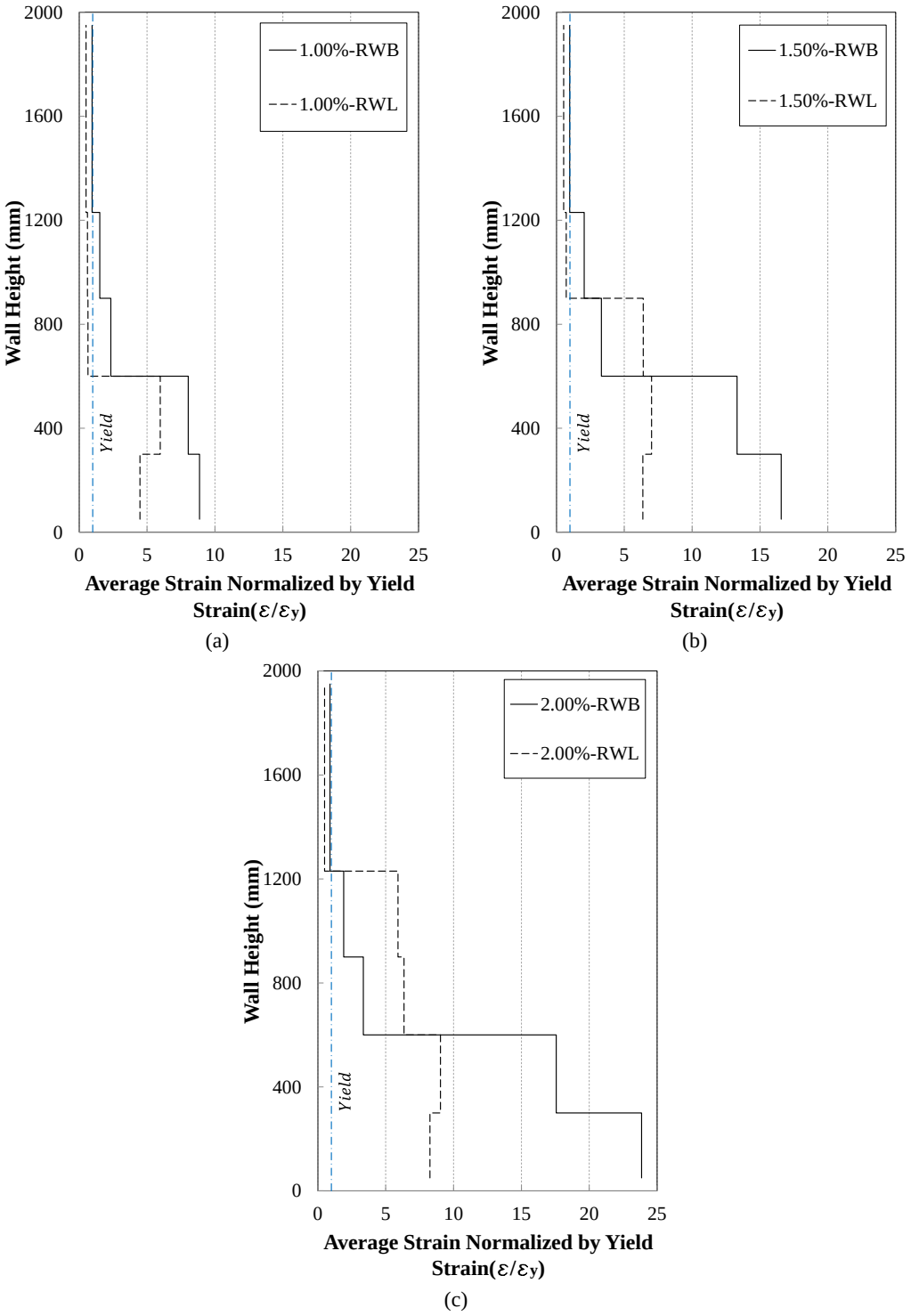

Figure 6.58: Average tensile strain profiles along the east boundary region, Specimen RWB vs Specimen RWL

The difference between plasticity rates of Specimen RWB and Specimen RWL can be clearly observed in the crack distribution along the height of boundary zones. Figure 6.59 and Figure 6.60 display the crack pattern of Specimen RWB and Specimen RWL at 2.00% drift level, respectively (Appendix C presents crack pattern of these specimens at different drift levels). The grid line spacing is 250x250 mm for Specimen RWB and 200x200 mm

for Specimen RWL. Distribution of wide cracks along the height of 1250 mm (5 cells of grid line, Figure 6.59a) indicates the amount of plasticity (wide cracks) developed along about 600 mm from the base (Figure 6.59b) compared to the one along the 600-1250 mm zone. The crack pattern of Specimen RWL along the height of 1200 mm (6 cells of the grid line, Figure 6.60a) displays a relatively uniform distribution of crack width along this height with more cracks within 600 mm height from the base (Figure 6.60b).

The difference in crack pattern of Specimen RWB and Specimen RWL can be attributed to the difference in the reinforcement ratio, resulting in less bond stress along the bars with larger diameters and formation of numerous uniformly spaced cracks in Specimen RWL compared to several wide cracks at the base of Specimen RWB.

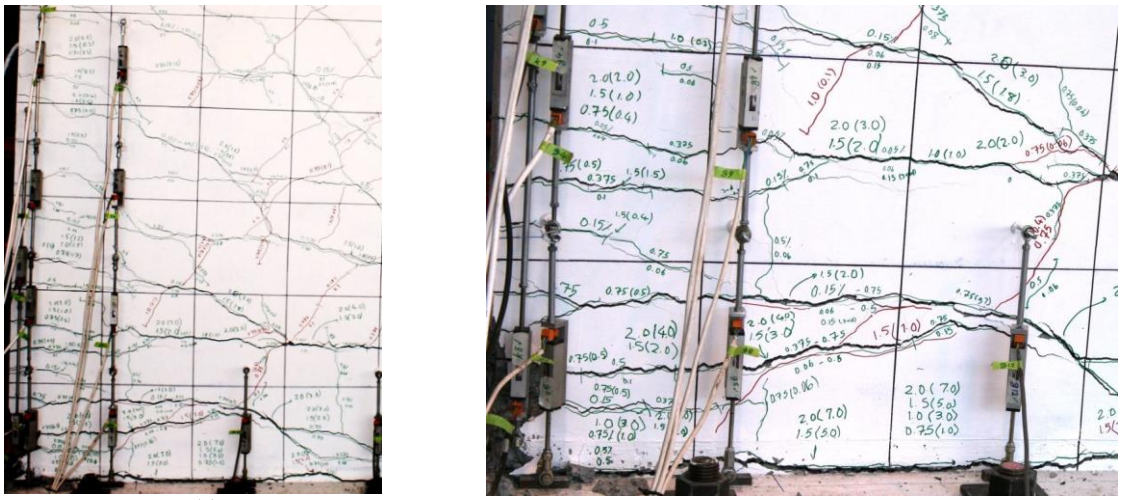

(a) (b)

Figure 6.59: Crack pattern of Specimen RWB at 2.00% drift level

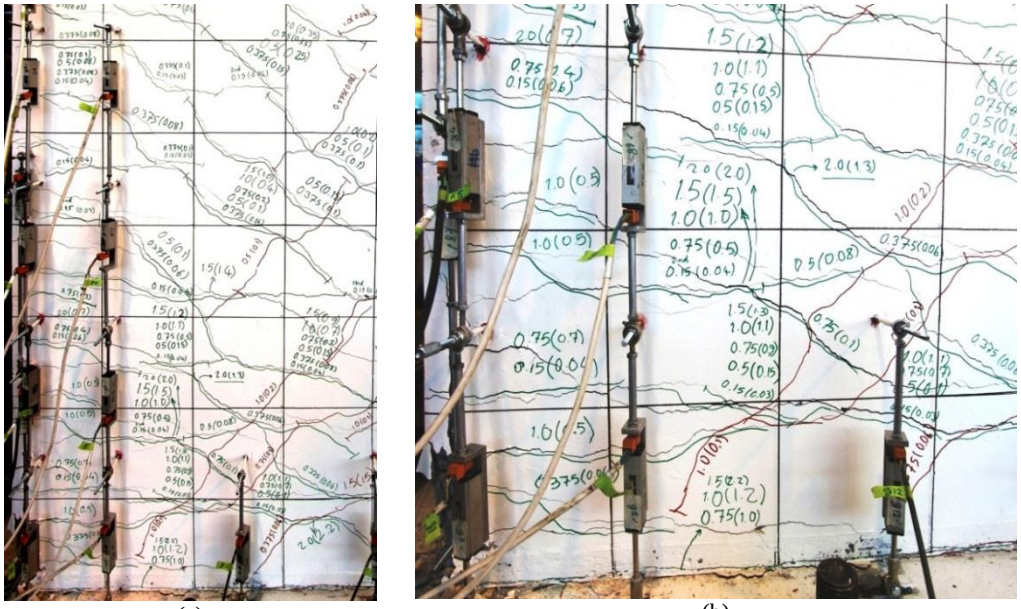

(a) (b)

Figure 6.60: Crack pattern of Specimen RWL at 2.00% drift level

6.10 KEY STAGES OF WALL RESPONSE AND OBSERVED FAILURE MODES

All three specimens exhibited flexural cracks along the boundary regions and within about half of the wall height at initial stages of the loading. On further loading, these cracks developed along the whole height of the storey level and diagonal cracks appeared in the panel region of the specimens. The number of cracks increased in Specimens RWB and RWT up to the overall yielding of the specimen, after which the width of the existing cracks increased. As for Specimen RWL, the number of cracks continued increasing along with the gradual increase of crack width throughout the loading of the specimen. Average values of crack width and the number of cracks within 300mm elevation from the base of Specimens RWB, RWT and RWL corresponding to different drift levels are given in Table 6.5. As can be seen in this table, the crack width of all the specimens increased considerably after overall yielding (0.5% drift). The ratio of this increase was significantly higher in Specimens RWB and RWT while the crack width of Specimen RWL increased rather linearly. After 0.75% drift, the number of cracks within 300 mm spacing from the base did not increase in Specimens RWB and RWT, while the number of cracks increased steadily in Specimen RWL.

As the tensile strain distribution of the boundary region reinforcement reached a critical value along a sufficient height of the wall, all three specimens exhibited out-of-plane deformations during the 1.5% drift cycles. During unloading and reloading in this cycle, the maximum out-of-plane deformation was measured at about 600 mm (30% of the wall height) from the wall base. This out-of-plane deformation is in line with numerical model predictions and is believed to evolve as a result of large tensile strains developed in the boundary region longitudinal reinforcement which prevent crack closure under compressive forces during loading in the opposite direction. The extent of this out-of-plane deformation was different in different specimens due to the difference in length and thickness.

Table 6.5: Average crack width and number of cracks in the boundary regions within 300 mm from the base at different drift levels

Specimen	0.05%		0.15%		0.38%		0.5%		0.75%		1.0%		1.5%		2.0%		2.5%		3.0%	
	CW	NoC	CW	NoC	CW	NoC	CW	NoC	CW	NoC	CW	NoC	CW	NoC	CW	NoC	CW	NoC	CW	NoC
RWB & RWT	0.06	1	0.06	2	0.06	3	0.15	3	0.7	4	2.0	4	3.5	4	5.0	4	_	_	_	_
RWL	_	_	0.04	1	0.08	2	0.08	3	0.6	3	0.8	5	1.3	6	1.5	6	1.8	7	2.0	7

Note: CW= Crack Width (mm); NoC= Number of Cracks

Further concentration of tensile strains at the wall base in the subsequent cycles (2.0% drift) was observed in Specimens RWB and RWT, resulting in a significant increase in crack width within the base region. The excessive amount of tensile strain at the base as well as the effects of cyclic loading caused a premature bar fracture in this region. The bar fractured when the specimen reached the maximum displacement during the first 2.0% drift cycle. At this stage, the average tensile strain within 300mm from the wall base exceeded 0.06.

In addition to bar fracture, bar buckling was also observed during the 2.0% drift cycles in Specimens RWB and RWT although buckling resistance provisions of NZS3101:2006 were satisfied. The bar buckling mode of these specimens, shown in Figure 6.27d and Figure 6.33b, indicates that the effective buckling length is higher than the transverse reinforcement spacing. Therefore, the assumption of buckling length being limited to the distance between two adjacent hoops or ties is not necessarily true in practice. The lateral anti-buckling stiffness, which depends on the diameter and configuration of the transverse reinforcement, would understandably affect the effective buckling length of the longitudinal reinforcement and should be taken into account. The buckling model proposed by Dhakal and Maekawa (2002b) accounts for the effect of the axial stiffness of the transverse reinforcement in calculation of the buckling length. The effect of cyclic loading which induces large compressive stresses on the bars with large residual strains until crack closure should not be neglected.

The bar fracture and bar buckling would rapidly transfer the compressive stresses to concrete resulting in fast development of concrete crushing at the base, which in turn leads to a laterally unstable cross section. Therefore, the considerable change in strain distribution along the height of the wall, triggering bar fracture and bar buckling at the wall base (during 2.0% drift cycles), is believed to have interfered with progression of the out-of-plane deformation that had initiated during the previous drift cycle (1.5% drift cycle) and have generated a localized out-of-plane instability. This local instability is different from the global instability of the specimen that could have occurred if the progression of out-of-plane deformation was not interrupted by other failure patterns. This type of out-of-plane instability can be classified as a secondary failure mode (Parra and Moehle 2014), triggered by concrete crushing in the compression boundary zone, with the maximum out-of-plane deformation observed within a limited height from the wall base where the initial failure modes (e.g. bar fracture, bar buckling and concrete crushing) had occurred.

Unlike Specimens RWB and RWT, the tensile strain increased uniformly along the height of boundary region in Specimen RWL and resulted in closely spaced cracks with almost identical crack width. This phenomenon can be attributed to better bond properties provided by larger bar diameters in this specimen. Also, as the length of Specimen RWL was smaller than the other two specimens, the maximum tensile strain developed in the reinforcement was smaller for the same drift level. Therefore, strain localization and consequently bar fracture and bar buckling was not observed in the base region. As a consequence, the out-of-plane deformation, which had initiated during 1.5% drift cycle, progressed steadily in this specimen and was not obstructed by other failure modes. As the maximum out-of-plane deformation exceeded a stability criterion, the specimen failed in the out-of-plane instability mode during the 3.0% drift cycle. This out-of-plane instability is different from the local instability observed in Specimens RWB and RWT and is purely originated from the excessive tensile strains developed over a specific height of the wall. Upon loading in the opposite direction, these large tensile strains would result in development of compression yielding in the reinforcement before crack closure can activate contribution of concrete to the load carrying capacity of the wall section. This can trigger out-of-plane instability over a considerable height of the wall from the base. Table 6.6 summarises the sequence of events observed in the tested specimens and the corresponding drift levels.

Table 6.6: Drift levels corresponding to key stages of wall response

	Crack initiation	Yielding	Cover Spalling	Initiation of out-of-plane deformation	Bar fracture	Bar buckling	Concrete crushing	Out-of-plane instability	
								Global (main failure)	Local (secondary failure)
RWB	0.05% (1st cycle)	0.5% (1st cycle)	1.0% (1st cycle)	1.5% (1st cycle)	2.0% (1st and 2nd cycles)	2.0% (1st and 2nd cycles)	2.0% (2nd cycle)	–	2.0% (2nd cycle)
RWT	0.05% (1st cycle)	0.5% (1st cycle)	1.0% (1st cycle)	1.5% (1st cycle)	2.0% (1st, 2nd and 3rd cycles)	2.0% (1st, 2nd and 3rd cycles)	2.0% (3rd cycle)	–	2.0% (3rd cycle)
RWL	0.15% (1st cycle)	0.5% (1st cycle)	1.0% (3rd cycle)	1.5% (1st cycle)	–	–	–	3.0% (1st cycle)	–

6.11 CONCLUSIONS

This chapter experimentally investigated the effects of wall thickness and length on out-of-plane deformation of rectangular structural walls.

The slight increase in wall thickness (about 8% from 125 mm to 135 mm in the half-scaled specimen) and the 20% reduction in wall length (from 2000 mm to 1600 mm in the half-

scaled specimen) did not change the drift level corresponding to initiation of out-of-plane deformation, but the initial out-of-plane deformation values were slightly less in both the thicker and the shorter walls.

The increase in wall thickness and the reduction in wall length resulted in about 37% and 53% decrease of out-of-plane deformation at 2.0% drift level, respectively.

All three specimens were designed to be flexure-dominated by resisting the brittle shear failure patterns using the capacity design approach and by meeting all design and detailing provisions of the code.

However, it can be argued that the design objective was not met in two of the specimens as they failed before reaching the 2.5% drift level. The following failure mechanisms were observed in the specimens:

- Development of out-of-plane deformation, during 1.5% drift cycles: Although the minimum thickness requirements of the code were satisfied, a considerable amount of out-of-plane deformation was observed in both specimens (albeit with different values) that could have resulted in out-of-plane instability of the specimens if the following failure modes had not supressed its progression.
- Bar fracture in the boundary regions, during 2.0% drift cycles as the maximum tensile strain at the base exceeded 0.06 in the boundary region: This phenomenon was controlled by the strain localization at the wall base following a considerable bond deterioration along the height of the wall. This issue is not acknowledged by the code as a reason of bar fracture.
- Bar buckling in the boundary regions, during 2.0% drift cycles: Although the anti-buckling provisions of the code were satisfied, the bar buckling failure was not prevented/delayed until reaching 2.5% drift level.
- Concrete crushing in the boundary regions, during 2.0% drift cycles: Although the confinement requirements of the code were satisfied, development of bar fracture and bar buckling in the boundary zones resulted in excessive compression on concrete and triggered crushing along the whole length of the compression boundary zone and a portion of the panel.
- Local out-of-plane instability at the base, following concrete crushing of the boundary region: This type of out-of-plane instability is a secondary failure mode as is triggered by other mechanisms

The third specimen was shorter in length and provided a flexural capacity close to the other two specimens with lower strain demands at the base. Out-of-plane deformation initiated in this specimen at 1.5% drift and all the other failure patterns mentioned above were suppressed. However, a global type of out-of-plane instability progressed in this specimen and resulted in its abrupt strength degradation during 3.0% drift cycle. This type of out-of-plane instability has a completely different mechanism compared to the one preceded by other failure modes and is bound to lead to sudden collapse of slender ductile walls which are designed to resist other failure modes. Observation of this mode of failure in some well-confined walls in the past earthquakes is a case in point.

The average strain profile along the height of north and south faces of the boundary regions indicated that different faces of boundary regions were subjected to different values of maximum tensile strain at a specific height from the base. This variation of maximum tensile strain along the thickness proved to be consistent at different stages of cracking, yielding and post-yielding, indicating that a cracked wall section will not necessarily undergo equal amount of compression plasticity before crack closure occurs.

Although a reduction in wall length would result in smaller values of tensile strain at the extreme end region, it is less likely to have a considerable effect on the formation of out-of-plane deformation if its reinforcement configuration can still develop a specific amount of plasticity over a height that is vulnerable to exhibit out-of-plane deformations.

6.12 REFERENCES

Almeida, J., O. Prodan, A. Rosso and K. Beyer (2017). "Tests on Thin Reinforced Concrete Walls Subjected to In-plane and Out-of-plane Cyclic Loading." *Earthquake Spectra* 33(1), 323-345.

Dhakal, R. P. and K. Maekawa (2002b). "Reinforcement stability and fracture of cover concrete in reinforced concrete members." *Journal of structural engineering* 128(10), 1253-1262.

NZS3101 (2006). Concrete Structures Standard, NZS 3101:2006 Parts 1&2 Standards New Zealand.

Parra, P. and J. Moehle (2014). Lateral buckling in reinforced concrete walls. Tenth US Natl Conf Earthq Eng, Anchorage, Alaska.

Priestley, M., G. Calvi and M. Kowalsky (2007). Displacement-Based Seismic Design of Structures, IUSS Press, Pavia, Italy.

7 A PARAMETRIC STUDY ON OUT-OF-PLANE DEFORMATIONS OF RECTANGULAR STRUCTURAL WALLS SUBJECT TO IN-PLANE LOADING; NUMERICAL PREDICTIONS

This chapter presents numerical modeling and response prediction of the rectangular walls tested in this study with an aim to identify the parameters affecting out-of-plane deformations. The experimental program and the test observations are discussed in Chapter 6, and the key features of the modeling approach, such as element type and material models, along with extensive validations are presented in Chapters 3, 4 and 5. This chapter provides a comparison between the numerical predictions and the experimental observations. The comparisons are carried out at both global and local levels to scrutinize the capability of the model in capturing the global failure pattern and its relationship with the local material behavior, e.g. local strain levels.

7.1 SPECIMEN RWB

Out-of-plane deformation response of a cantilever wall under in-plane loading is known to be controlled by the unsupported height of the specimen. Figure 7.1 shows the elevation of Specimen RWB where the wall is connected to the loading beam using steel angles clamping the specimen at both sides. This height is half of the story height determined in the design phase of the prototype wall. The loading beam was restrained against out-of-plane displacement using roller supports, as shown in Figure 7.2. These roller supports were positioned at different elevations of the loading beam to restrain the rotation of the loading beam and consequently of the top of the specimen, representing the fixity at the story level of a structural wall connected to the floor system in a building.

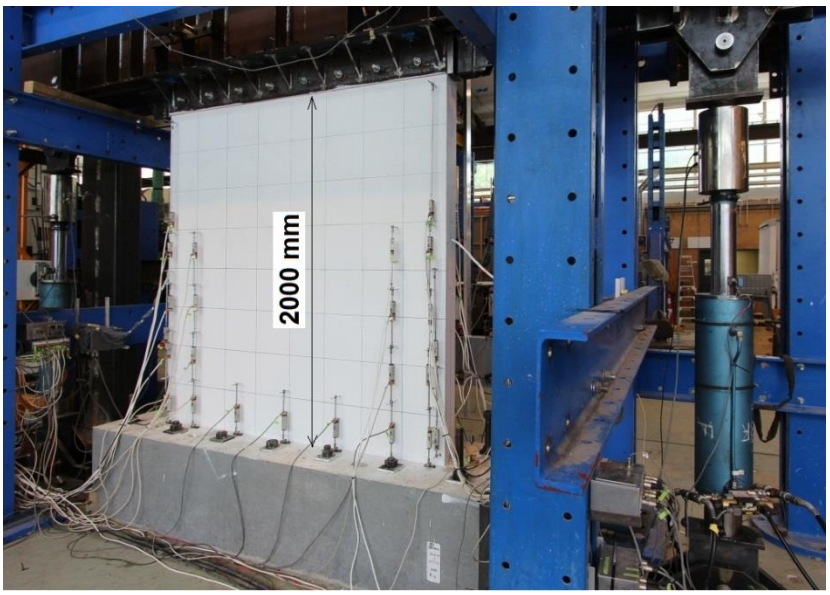

Figure 7.1: Specimen RWB

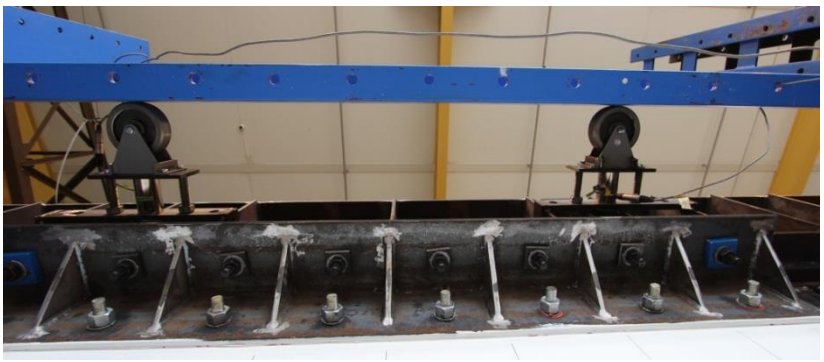

Figure 7.2: Out-of-plane support of the loading beam

Figure 7.3 shows boundary conditions, loading and mesh discretization used in the numerical modeling of the benchmark Specimen RWB. In order to represent the experimentally-applied shear-span ratio in the numerical model, the concept of equivalent height is used by an elastic lever arm at top of the wall model. The in-plane lateral displacement is applied at the top of the elastic part, and the axial load is applied at top of the wall specimen. The wall model is restrained against out-of-plane deformations both at the top of the elastic part as well as the top of the specimen. This configuration of out-of-plane constraints results in restrain against out-of-plane rotation at the top of the specimen, representing a boundary condition similar to the one generated in the test setup. More details on the numerical model can be found in Chapter 3.

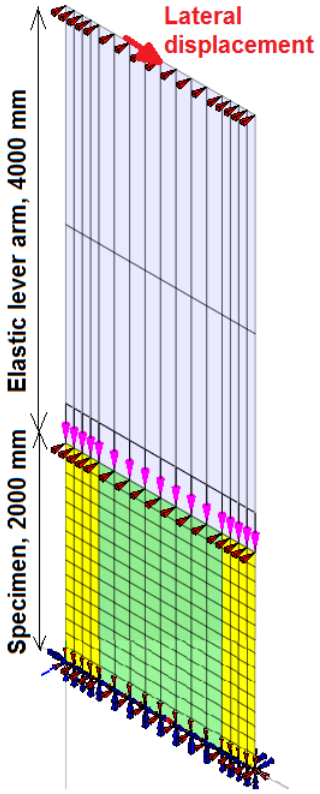

Figure 7.3: Boundary conditions, loading and mesh discretization used for the numerical model of Specimen RWB

Figure 7.4 displays the lateral load-top displacement prediction of the numerical model compared with the test results. The model results are generally in good agreement with the test measurements. As discussed in Chapter 7, the specimen exhibited out-of-plane deformations during the 1.5% drift cycle and became unstable after bar fracture and bar buckling occurred in the boundary regions of the wall. The strength degradation observed in the experimental load-displacement curve was due to these bar fracture and bar buckling failures. Neither bar fracture nor bar buckling could be captured by the numerical model; therefore, the strength degradation observed in the experimental load-displacement curve was not predicted. Also, the initial stiffness of the numerical model is not matching well with the test results. This can be attributed to the iterative method of load application. Since the horizontal and vertical actuators were connected to the loading beam, their movements were quite interdependent, and an iterative approach was used to balance the actuators at each step using a tolerance factor of 5.0 kN. The data was recorded when a balance was reached and the next step was initiated. Figure 7.5 shows the initial stages of loading and the predicted load-displacement curve. As can be seen in Figure 7.5a, the very first part of the loading is considerably affected by this experimental limitation. For instance, when the axial load was applied at the beginning, the vertical movement of the vertical actuators

resulted in movement of the horizontal actuator producing lateral load in the horizontal load cell and in the wall. This initial condition shifted the initiation point of the load-displacement cycles. Similar to the axial load application, the application of bending moment through the vertical actuators at each step after the target displacement was reached by the horizontal actuator, imposed additional movement to the horizontal actuator. Therefore, the data was recorded when a balance was reached at each step through an iterative approach with a fixed tolerance. Before this balance happens, the actuators, particularly the horizontal one, were subjected to higher displacements and consequently higher loads which were not recorded by the data logger, and the recorded data correspond to the states where the loads were balanced after iteration. With this iterative loading system, the cracking developed in the specimen before reaching the balance state would result in a reduction in stiffness of the wall. The gradual change of stiffness related to this phenomenon can be observed in Figure 7.5. As can be seen in Figure 7.5b, the second cycle of the numerical model at 0.38% drift level matches well with the corresponding cycle of the test results.

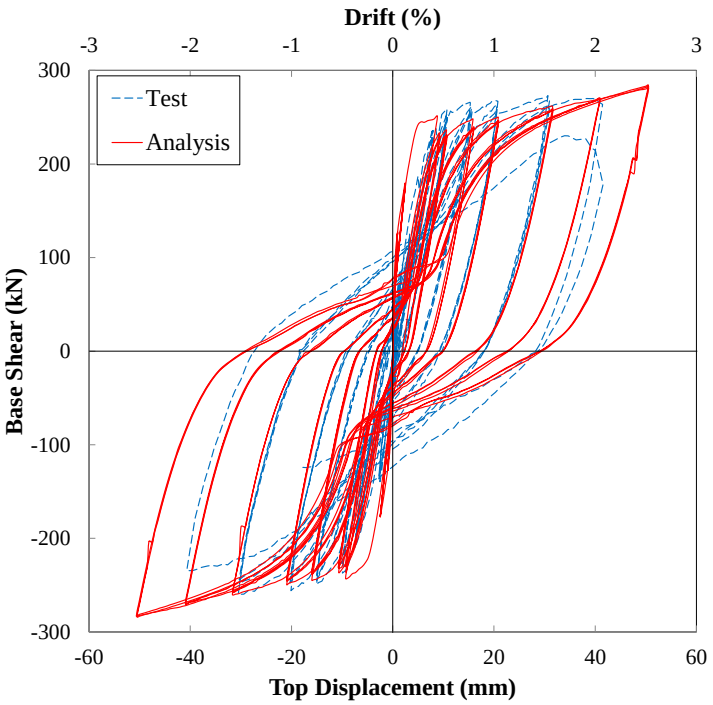

Figure 7.4: Base shear-top displacement response of Specimen RWB - Numerical vs. experimental comparison

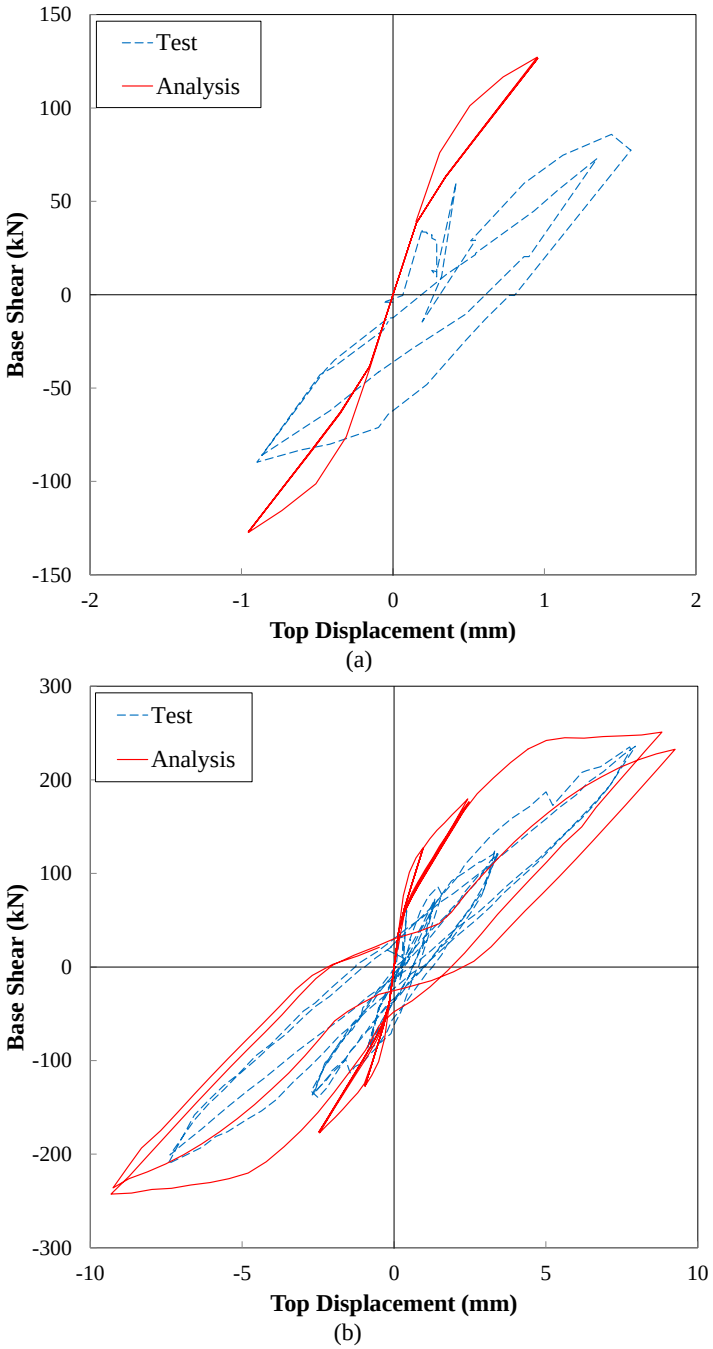

Figure 7.5: Initial stages of load-displacement response, Specimen RWB: (a) 0.05% drift level; (b) up to 0.38% drift level - Numerical vs. experimental comparison

Figure 7.6 and Figure 7.7 compare the numerical prediction and the experimental measurements of maximum out-of-plane displacement at different stages of loading for the west and east boundary regions, respectively. The out-of-plane displacement measurement of the instrument positioned at 600 mm from the base provided the maximum measurement for both boundary regions and was compared with the maximum out-of-plane displacement prediction of the numerical model, which occurred at 667 mm from the base.

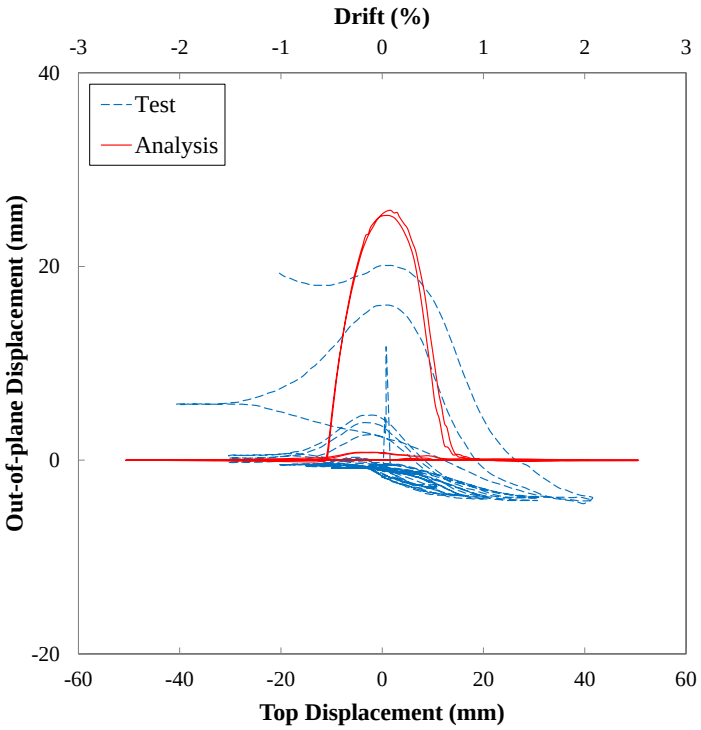

Figure 7.6: Top displacement vs maximum out-of-plane displacement at west boundary region, Specimen RWB - Numerical vs. experimental comparison

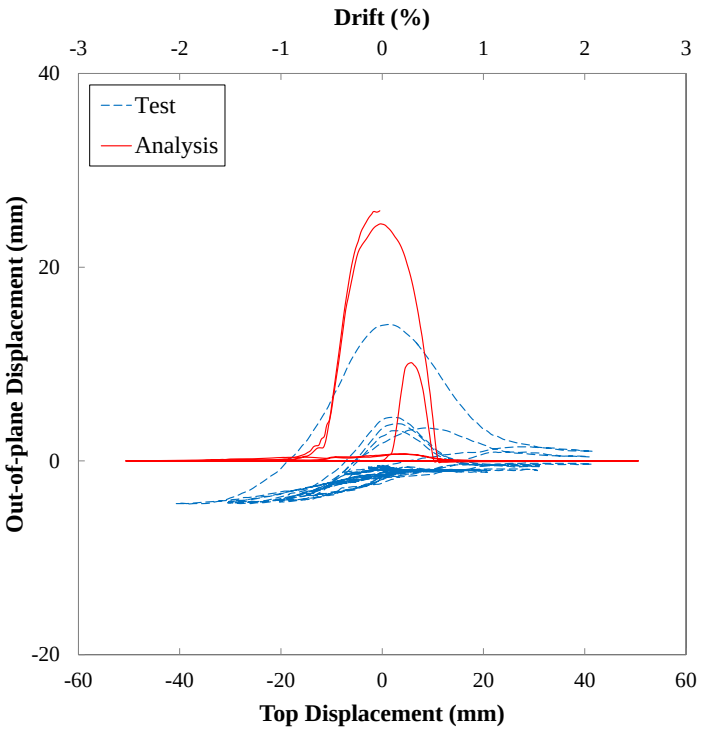

Figure 7.7: Top displacement vs maximum out-of-plane displacement at east boundary region, Specimen RWB - Numerical vs. experimental comparison

The out-of-plane displacement initiated during the 1.5% drift cycles in both boundary zones and increased with the number of cycles and with the drift level. At 2.0% drift, a significant number of bars fractured in the west boundary region, considerably influencing the out-of-

plane displacement during the 2.0% drift cycles. This fast growth of out-of-plane displacement in the west boundary region due to the effects of bar fracture resulted in repositioning of the wall centerline in the west boundary region and instability of the specimen. No bar fracture was observed in the east boundary region and only one bar buckled in this boundary at the negative peak of the 2.0% drift cycle, which did not coincide with the peak out-of-plane displacement happening at around zero displacement levels. Therefore, the out-of-plane displacement of the east boundary region was not affected by any other failure patterns.

However, the bar fracture and bar buckling failure patterns were due to high localized strains in the extreme end regions of the wall base which prevented distribution of strains along the height of the plastic hinge region. Therefore, development of out-of-plane deformation, which initiated during the 1.5% drift cycles, was influenced by the localization of tensile strains and occurrence of bar fracture and bar buckling during the 2.0% drift cycles.

The numerical model had predicted the initiation of out-of-plane displacement during the first cycle of the 2.5% drift, and its considerable increase during the second and the third cycles in both boundary zones. Therefore, there was a delay in initiation of the out-of-plane deformation in the numerical model when compared to the test observations. This delay could be attributed to the effects of inherent eccentricities in construction, loading and material properties across the wall thickness that had not been included in the numerical model due to the uncertainties involved in their amount and location. However, the numerical model had predicted the same trend for evolution and recovery of the out-of-plane deformation as the experimental observations, with the maximum value of out-of-plane displacement happening around 0.0% drift level in a specific cycle.

As also discussed in Chapter 4, the out-of-plane deformation of the numerical model starts when compression yielding develops in both layers of the boundary zone longitudinal reinforcement, before crack closure can activate contribution of concrete to load carrying capacity of a cracked wall section under compressive stresses. Therefore, the numerical model had predicted a faster increase in the out-of-plane displacement after its initiation, while the imperfections noted above would result in a more gradual trend for initiation and evolution of the out-of-plane deformation after development of compression yielding in one layer of the boundary region reinforcement. Also, the effects of bar fracture, bar buckling

and the subsequent concrete crushing observed at the base of this specimen during the 2.0% drift cycles on the progression of out-of-plane displacement should not be neglected.

The out-of-plane displacement profile along the height of the east boundary region, where bar fracture was not observed, is compared with the numerical prediction in Figure 7.8. The height of the wall involved in formation of out-of-plane displacement as well as the elevation corresponding to the maximum out-of-plane displacement is well predicted by the analysis. However, the elevation corresponding to the maximum out-of-plane deformation predicted by the numerical model during the third 2.5% drift cycle is higher than the experimental measurement, which can be attributed to the change of strain distribution along the height of the boundary region and further localization of strains at the wall base at this drift level.

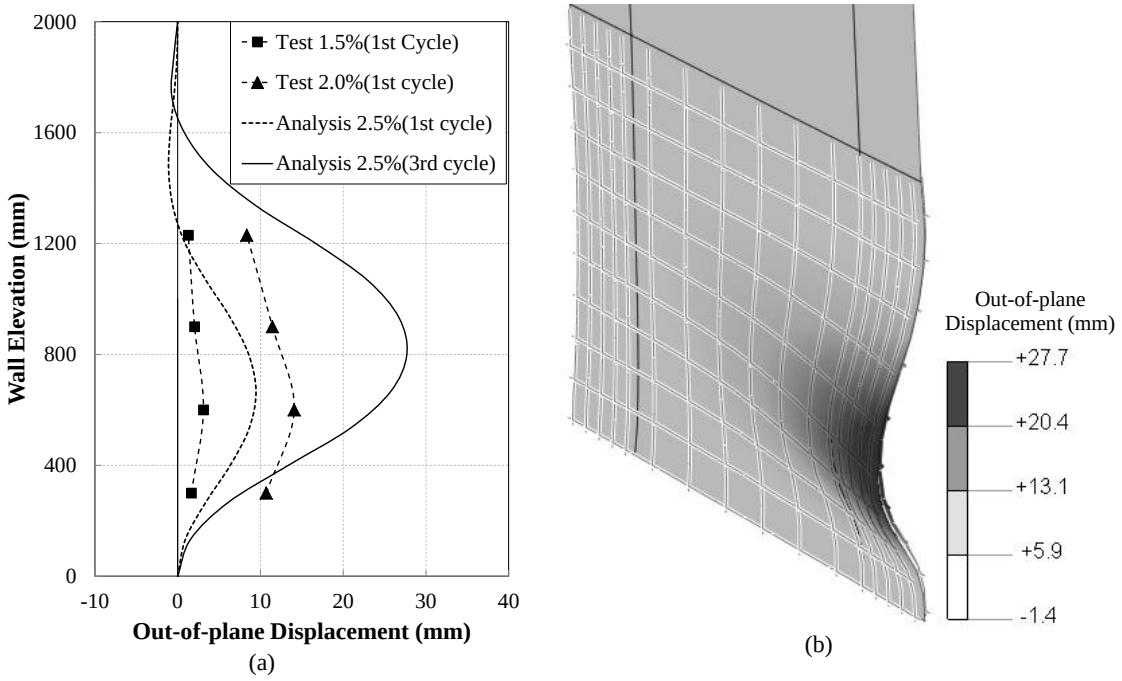

Figure 7.8: Out-of-plane displacement profile along the height of east boundary region of Specimen RWB: (a) numerical vs experimental; (b) numerical model at 2.5% drift cycle

7.1.1 STRAIN GRADIENTS

Figure 7.9 compares the experimental and numerical average strain profiles at the peak of different cycles along the length of Specimen RWB. The test measurement was made within a gauge length of 300 mm from the base, whereas the numerical result used is the average vertical strain values of two rows of elements at the base of the numerical model with an overall height of 267 mm. As can be seen in Figure 7.9a, the numerical results are

in good agreement with the test measurements up to 0.38% drift cycles, after which the numerically predicted strain values become considerably smaller in the boundary region and higher in the panel region when compared to the test results. This difference can be attributed to the phenomenon of bond-slip, which is not considered in the analysis as the bars are modelled using embedded bar approach and are fully bonded. Due to the significant bond deterioration along a specific height of the reinforcing bars where considerable plasticity has been developed, the tensile strain is more localized at the base of the specimen during its post-yield stage. This phenomenon can be clearly observed in distribution of crack width along the height of the boundary zones after overall yielding of the specimen. At this stage, the cracks have widened mainly at the base region and the rate of increase in crack width throughout the other parts of the boundary regions is negligible compared to a limited area at the base. Bond deterioration along the length of a reinforcing bar in a reinforced concrete member, and the influence of yielding of reinforcement on reduction of the bond stress are well described by Shima et al. (1987), and fib Model Code for Concrete Structures (International Federation for Structural Concrete 2013).

Moreover, the strain penetration effect is not captured by the analysis, while the average strains were measured in the test using potentiometers that were connected to the foundation in one end. Hence, the experimental measurement included the strain penetration at the wall base. According to the test observations, the cracks were considerably wider at the base of the specimen, showing concentration of strain at the base that is apparently due to the bond-slip effects. Figure 7.9b indicates a considerable difference between numerical predictions and experimental measurements of strain at higher drift levels, where the bond-slip effects are greater. Therefore, the premature bar fracture coming from the strain localization at the base of the specimen was not captured by the model.

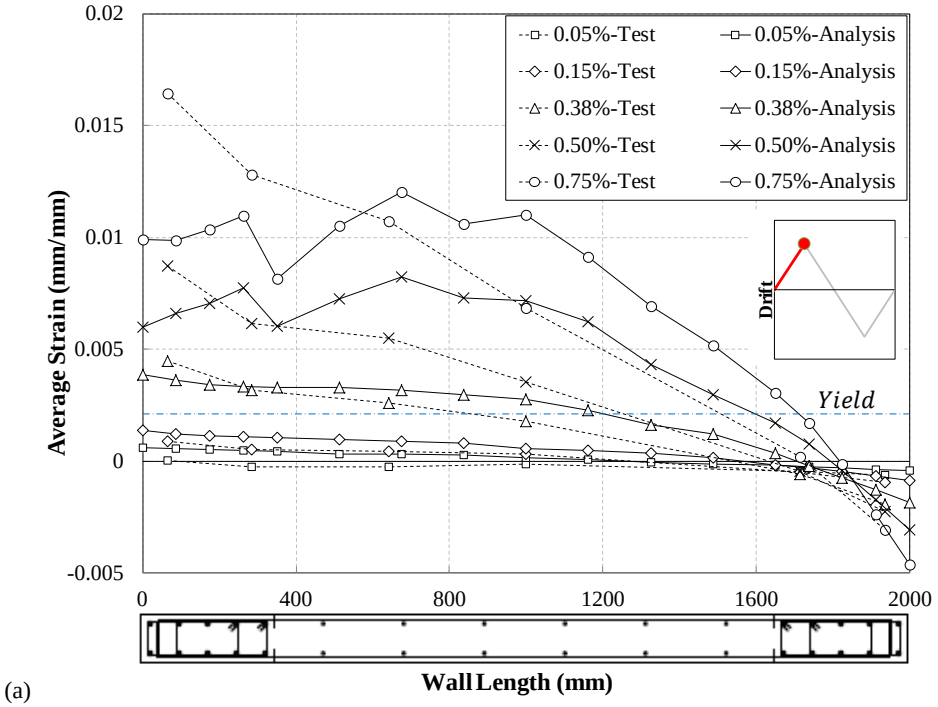

(a)

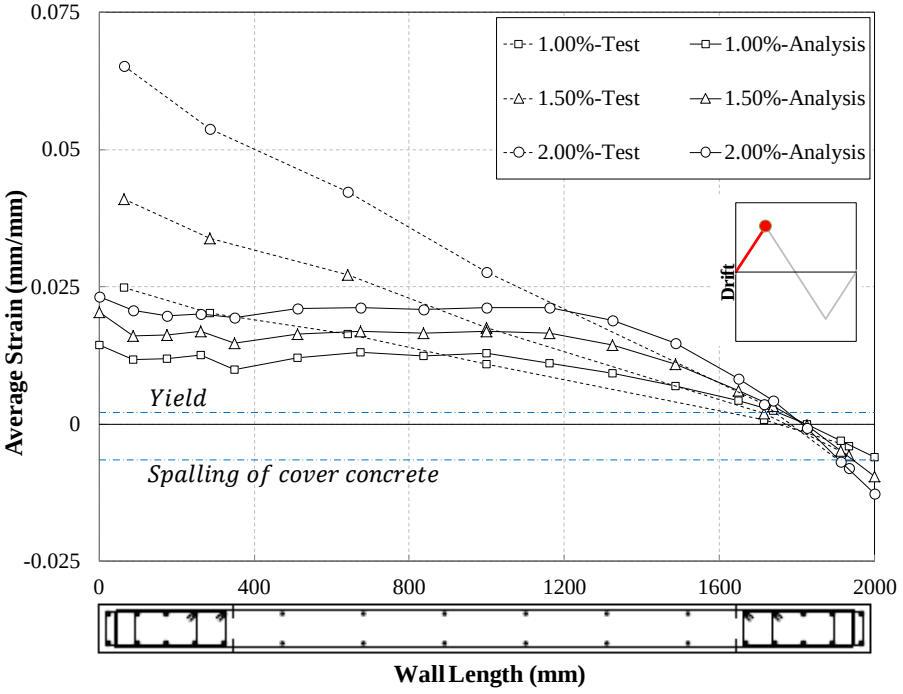

(b)

Figure 7.9: Average strain profile along the length of Specimen RWB, peak positive drift levels, Specimen RWB - Numerical vs. experimental comparison

With the extreme end bar reaching a significantly high tensile strain (exceeding 0.06), the first bar fracture was observed at peak positive displacement of the 2.0% drift cycle, while the analysis did not predict this amount of tensile strain in the reinforcement. Prior to the development of bond-slip in the specimen (up to 0.38% drift level, Figure 7.9a), both the numerical and experimental strain profiles followed a similar trend of nonlinearity. It should be noted that, as mentioned in Section 7.1.1, the cracks increased in number until the

0.38% drift cycles, whereas these cracks got wider in the subsequent drift cycles, which is a further indication of bond between reinforcement and concrete being active up to this drift level.

Figure 7.10 to Figure 7.13 compare the strain profile along the height of the extreme end bar in the east boundary region with the test measurements at different stages of the wall response: i.e. before yielding, at yielding, after yielding and at ultimate stages. As can be seen in these figures, the strain values captured by the numerical model are in good agreement with the test measurements up to 0.38% drift level. After this stage, the tensile strains increase mostly at the base of the specimen in the test whereas in the numerical model the strains increase mainly within 1200 mm from the base at 0.5%, 0.75% and 1.0% drift levels. At 1.5% and 2.0% drift levels, the strain values of the numerical model become distributed along almost the whole height of the bar, while the test measurements show a considerable localization of strain at the base compared to the other parts of the specimen. As noted above, this difference between numerical and experimental strain values can be attributed to the bond-slip effect being neglected in the numerical model. Obviously, had the reinforcement configuration (bar diameter, etc.) been such that the effect of bond-slip be minimal (i.e. if plenty of closely spaced cracks with uniform crack width could be developed), it is believed that the numerical model predictions could have had a better agreement with test results. Due to this difference in response of the numerical model and the test specimen, the value of out-of-plane displacement was predicted to be steadily increasing with increase in the number of cycles and the applied drift levels. However, the occurrence of strain localization at the wall base prevented the out-of-plane displacements from reaching as high values in the experiment.

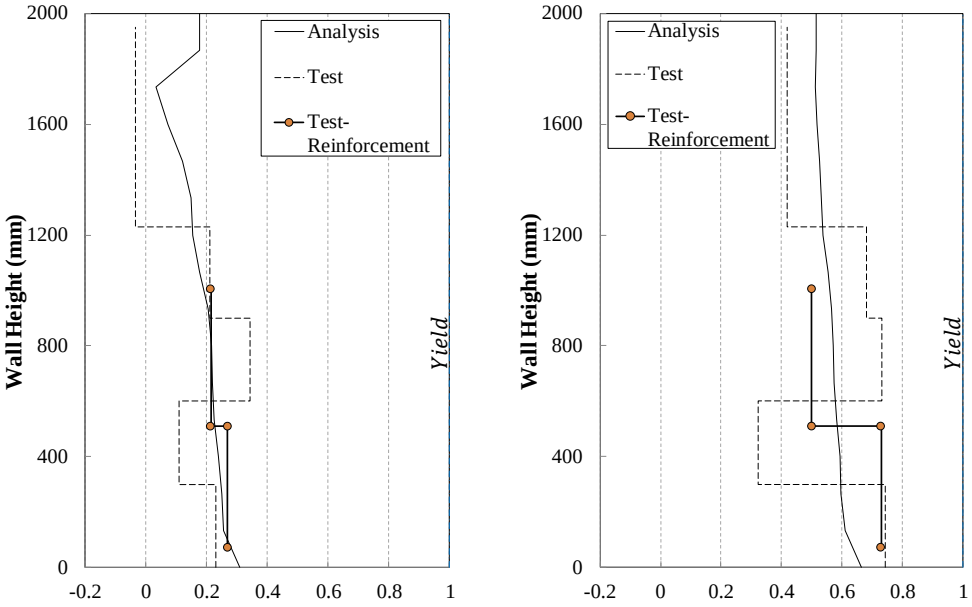

Figure 7.10: Average strain profile along the height of the east boundary region before yielding stage

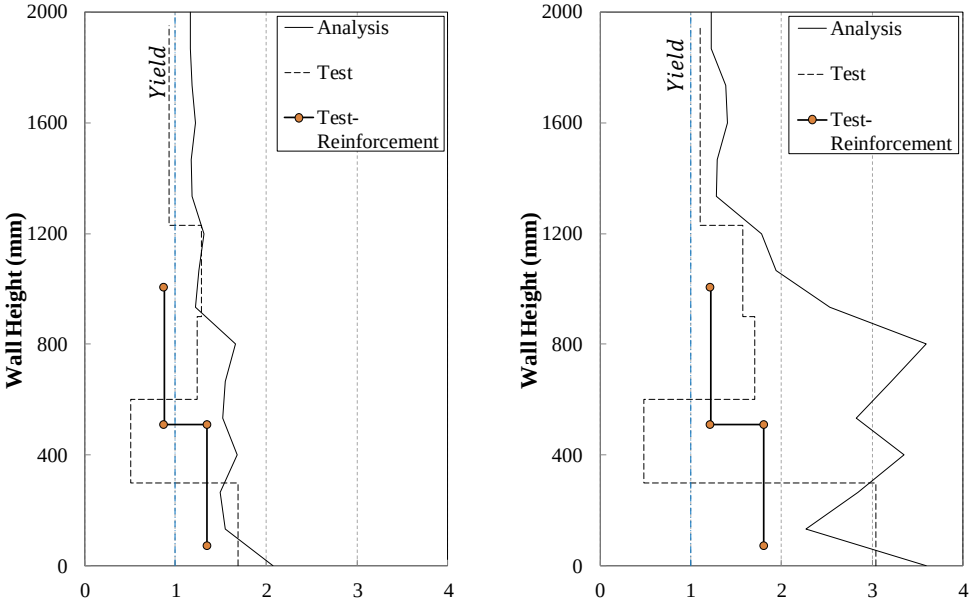

Figure 7.11: Average strain profile along the height of the east boundary region at yielding stage

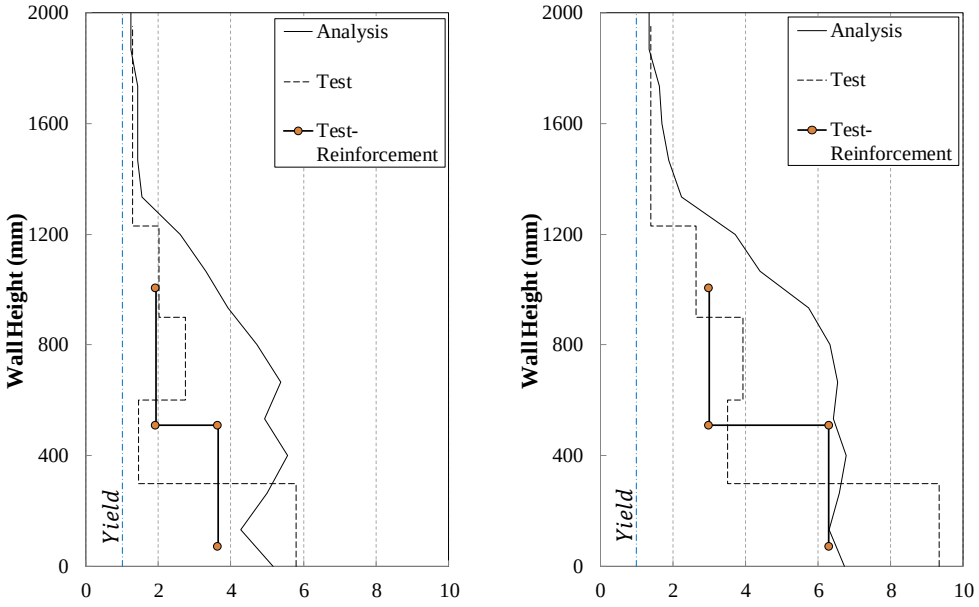

(a) 0.75% (b) 1.0%

Figure 7.12: Average strain profile along the height of the east boundary region after yielding stage

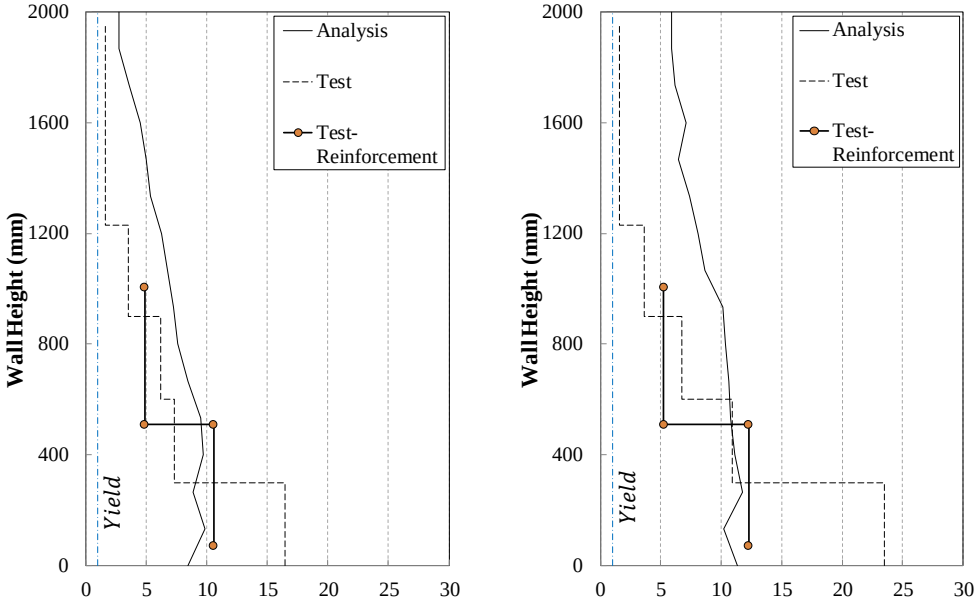

(a) 1.5% (b) 2.0%

Figure 7.13: Average strain profile along the height of the east boundary region at ultimate stages

7.2 SPECIMEN RWT

In order to investigate the effect of increase in wall thickness on response of the rectangular walls, Specimen RWT, which was 10 mm thicker than the benchmark specimen RWB, was subjected to the same loading history. Figure 7.14 shows the predicted lateral load versus top displacement response of the specimen in comparison with the experimental response,

and Figure 7.15 and Figure 7.16 compare the numerical predictions of the maximum out-of-plane displacement with the test measurements for the west and east boundary zones, respectively.

Specimen RWT exhibited a similar failure pattern as Specimen RWB. The out-of-plane deformation started at 1.5% drift level in this specimen. During the 2.0% drift cycle, some of the longitudinal bars fractured and buckled at the wall base and resulted in instability of the specimen. However, the out-of-plane displacements of this specimen were lower than the ones of Specimen RWB. The numerical model could predict the development of out-of-plane deformation in this specimen with a similar trend to Specimen RWB. The maximum out-of-plane displacements predicted by the numerical model for this specimen are slightly lower than the ones in Specimen RWB.

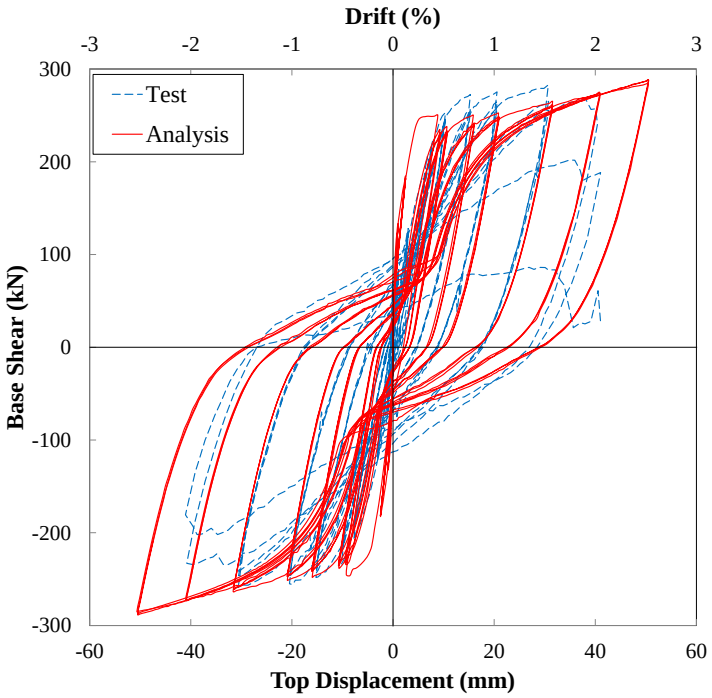

Figure 7.14: Base shear-top displacement response of Specimen RWT - Numerical vs. experimental comparison

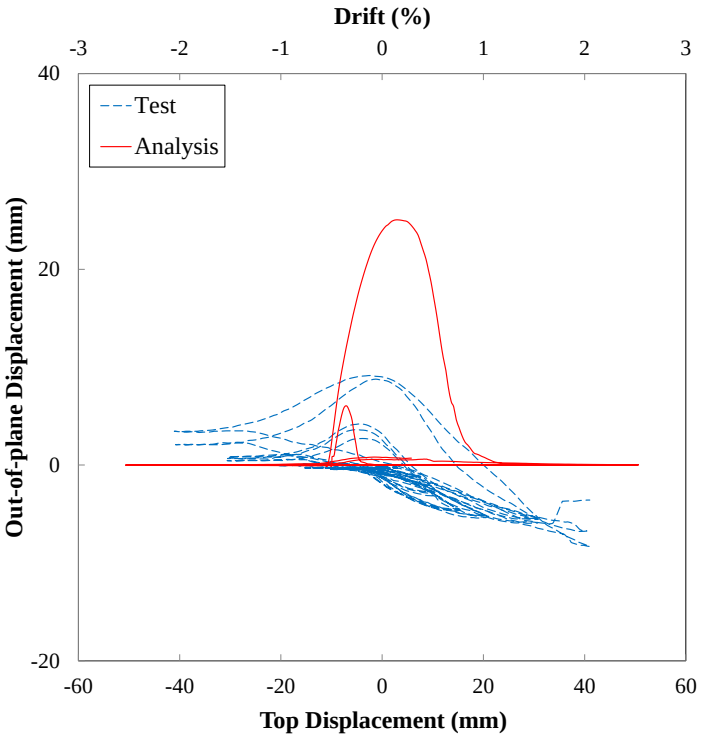

Figure 7.15: Top displacement vs maximum out-of-plane displacement at west boundary region, Specimen RWT- Numerical vs. experimental comparison

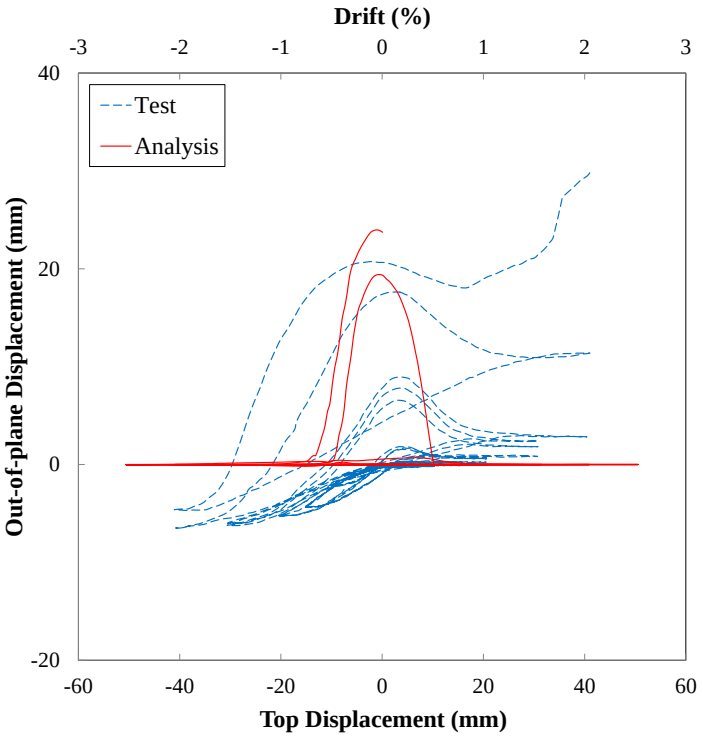

Figure 7.16: Top displacement vs maximum out-of-plane displacement at east boundary region, Specimen RWT - Numerical vs. experimental comparison

7.3 SPECIMEN RWL

Figure 7.17 shows the numerical prediction of the lateral load versus top displacement response of Specimen RWL in comparison with the experimental response, and Figure 7.18 and Figure 7.19 compare the numerical prediction of the maximum out-of-plane deformation with the test measurements for the west and east boundary regions, respectively. Unlike Specimen RWB and Specimen RWT, the failure of this specimen was purely due to its out-of-plane instability. The out-of-plane deformation of this specimen started during the 1.5% drift cycle and increased steadily with increase of the drift level and the number of cycles per drift level resulting in instability of the specimen during the 3.0% drift cycle. As can be seen in Figure 7.18 and Figure 7.19, the out-of-plane deformation of the numerical model started at 3.0% drift level in both boundary zones. The reason for this late initiation of out-of-plane deformation in analysis is explained below.

The development of out-of-plane deformation in this specimen has been comprehensively discussed in Chapter 8, and one of the main factors contributing to initiation of out-of-plane deformation was identified as the asymmetric behaviour of reinforcement along the wall thickness, particularly the difference in maximum tensile strain developed in the bars positioned in different layers along the wall thickness. Another source of eccentricity could be the accuracy of longitudinal reinforcement position along the wall thickness, which is somehow inevitable, especially if relatively larger bar diameters are used. However, no artificial eccentricity was considered in the analysis, and the out-of-plane deformation prediction of the numerical model was carried out through stability analysis of a cracked wall section subjected to compression. With wide crack openings and large residual strains of the longitudinal reinforcement, the compression yielding of reinforcement can occur before crack closure of the section and the wall may deform in a direction that requires less energy.

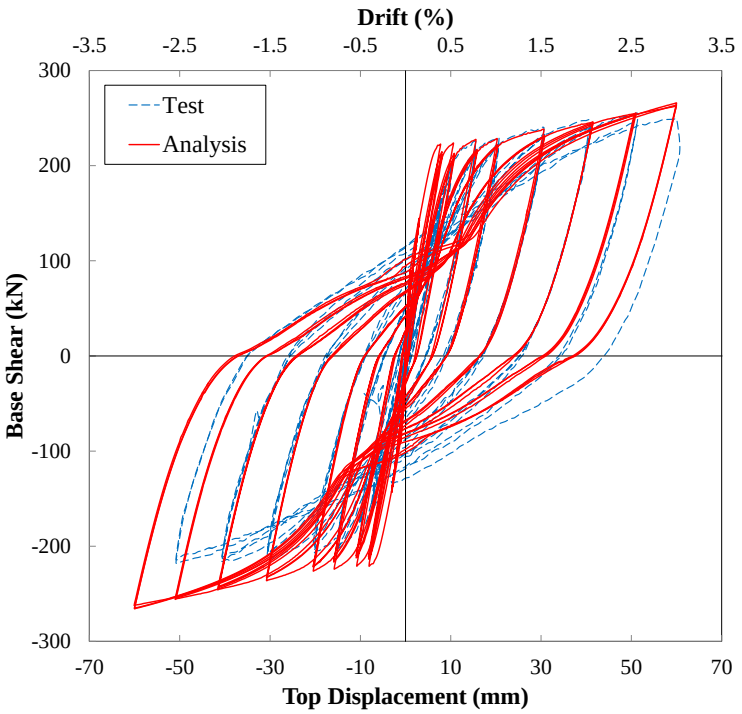

Figure 7.17: Base shear-top displacement response of Specimen RWL - Numerical vs. experimental comparison

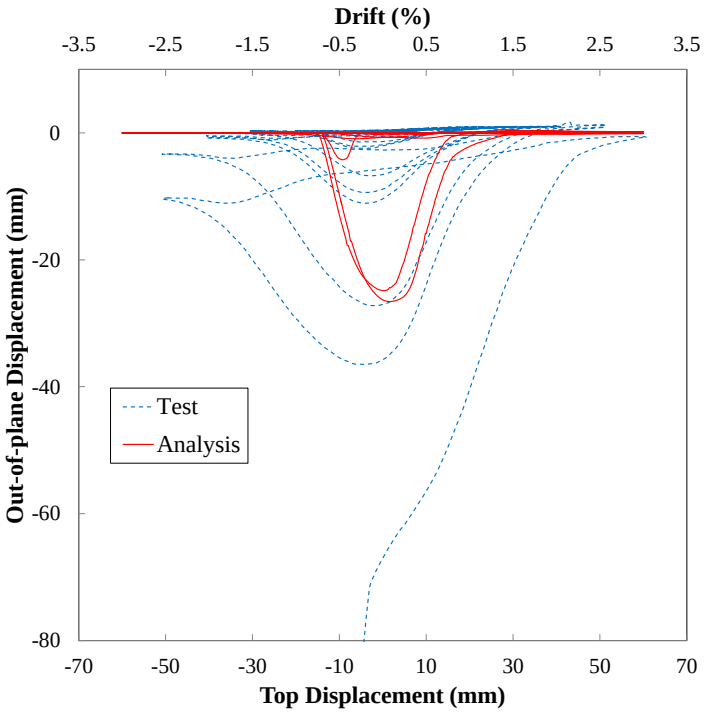

Figure 7.18: Top displacement vs maximum out-of-plane displacement at west boundary region, Specimen RWL - Numerical vs. experimental comparison

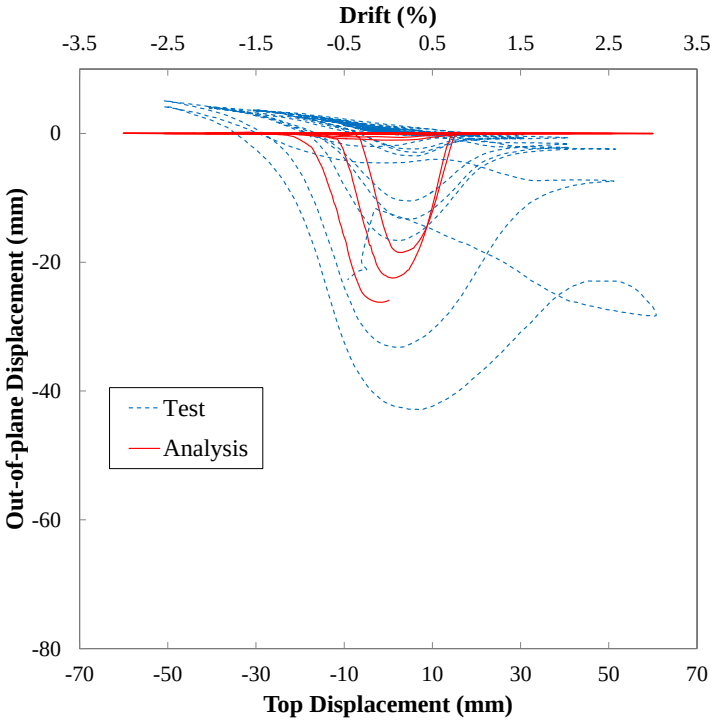

Figure 7.19: Top displacement vs maximum out-of-plane displacement at west boundary region, Specimen RWL - Numerical vs. experimental comparison

Figure 7.20 compares the out-of-plane displacement profile of the numerical model with the test measurements for the west boundary region, and Figure 7.21 shows the out-of-plane deformation prediction of the numerical model and the experimental observation at 3.0% drift cycle. Unlike in Specimen RWB (Figure 7.8a), the elevation corresponding to the maximum out-of-plane displacement increased with the increase in the drift level (except for the 3.0% drift cycle), and obviously with the increase in the number of cycles per drift level (the test results are plotted for the first cycle of each drift level only). The out-of-plane deformation did not recover during the 3.0% drift cycle and changed to out-of-plane instability failure which could be the reason it does not comply with this trend. The increase in the elevation corresponding to the maximum out-of-plane displacement with the increase in the number of cycles per drift level is captured by the numerical prediction, as well (Figure 7.20).

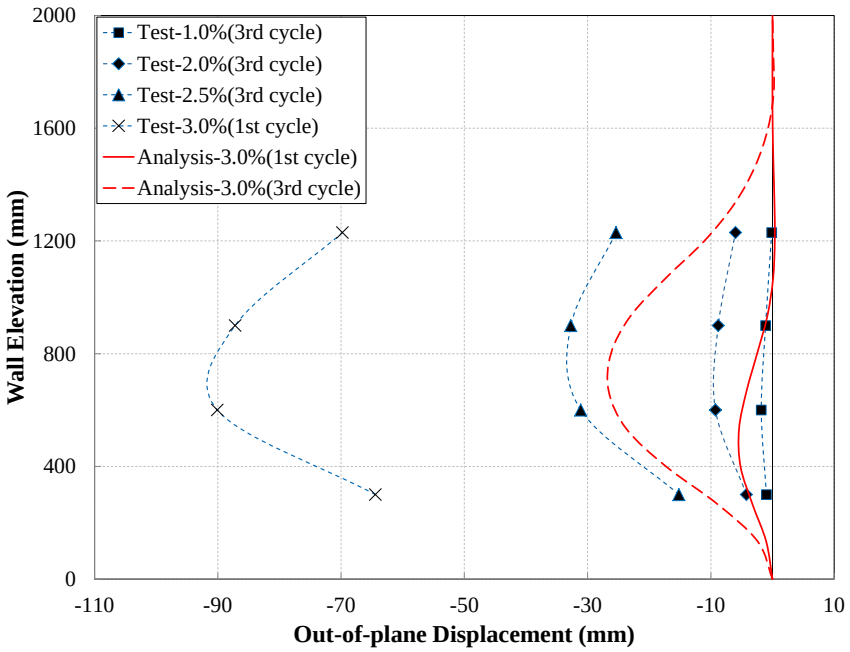

Figure 7.20: Out-of-plane displacement profile of west boundary, Specimen RWL - Numerical vs. experimental comparison

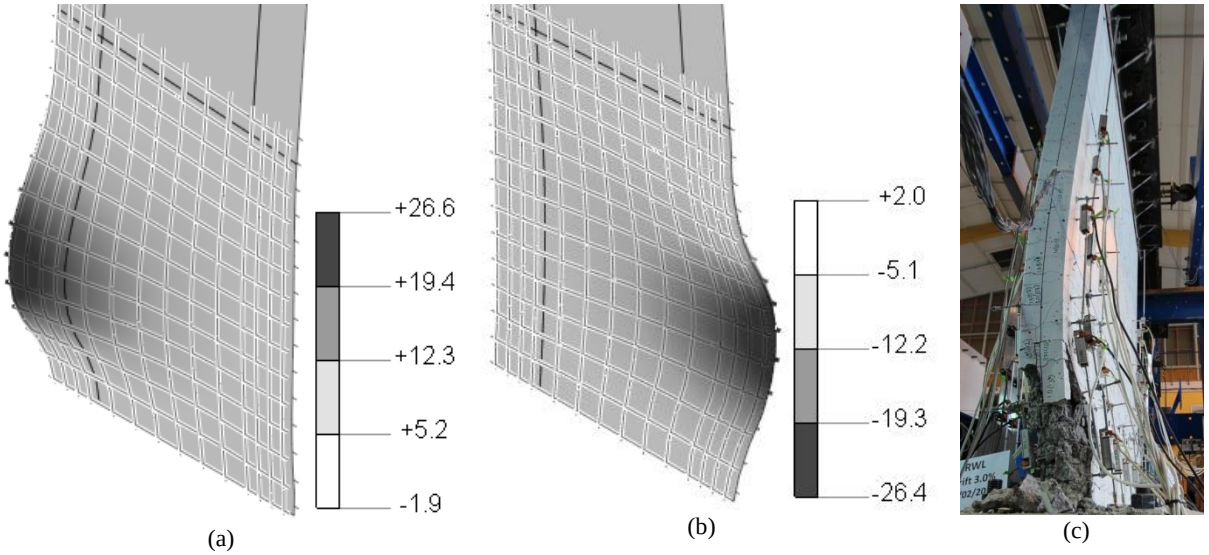

Figure 7.21: Out-of-plane deformation of Specimen RWL during 3.0% drift cycle: (a) west boundary; (b) east boundary; (c) experimental observation

7.3.1 STRAIN GRADIENTS

Figure 7.22 compares the variation of strain measured along the length of Specimen RWL with the predictions of the numerical model. As can be seen in this figure, unlike Specimen RWB, the numerical model prediction is in good agreement with the test measurements in terms of the nonlinearity of strain profile along the wall length, which can be attributed to the fact that the larger bar diameters of reinforcement in Specimen RWL provided better bond between concrete and reinforcement when compared to Specimen RWB. However, at

higher drift levels (Figure 7.22b) the measured strains are generally higher than the numerical predictions although the strain profiles follow a similar pattern.

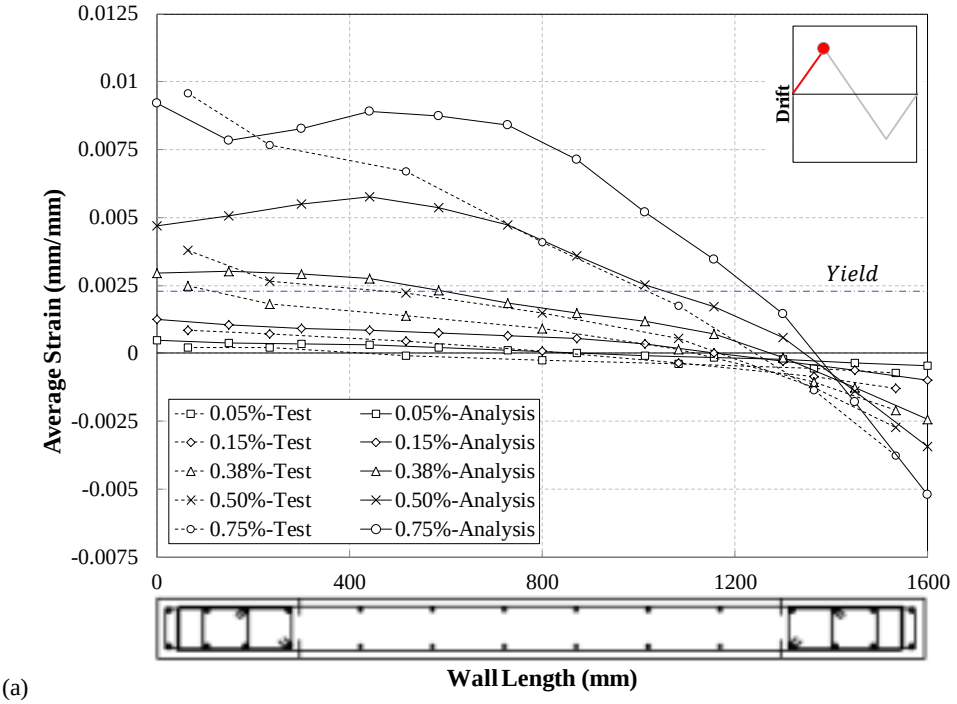

(a)

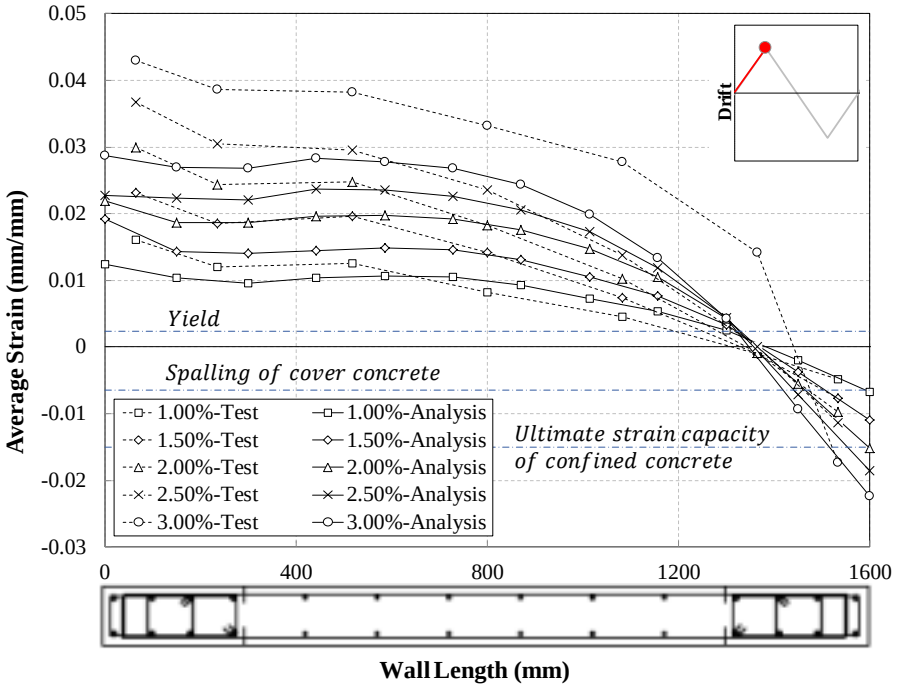

(b)

Figure 7.22: Average strain profile along the length of Specimen RWL, peak positive drift levels - Numerical vs. experimental comparison

The difference between the strain profiles along the wall height obtained from the numerical model and the test measurements is due to the difference in variation of strain profiles along the wall length (Figure 7.22). In other words, the total amount of strain in the numerical model is almost identical to the one generated in the real specimen at a specific

drift level. However, the distribution of strains is different along both the length and the height. As mentioned above, one of the main factors controlling the strain distribution is known to be the bond-slip which results in higher strains at the base of the specimen. As noted above, with the larger bar diameters, the bond-slip issue seems to be less pronounced in Specimen RWL when compared to Specimen RWB.

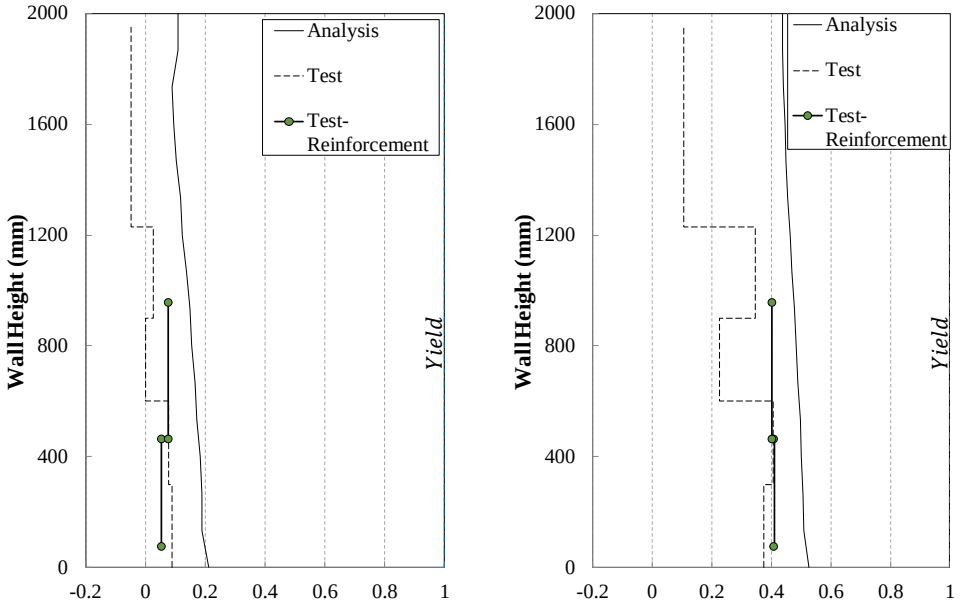

(a) 0.05% (b) 0.15%

Figure 7.23: Average strain profile along the height of the east boundary region before yielding stage - Numerical vs. experimental comparison

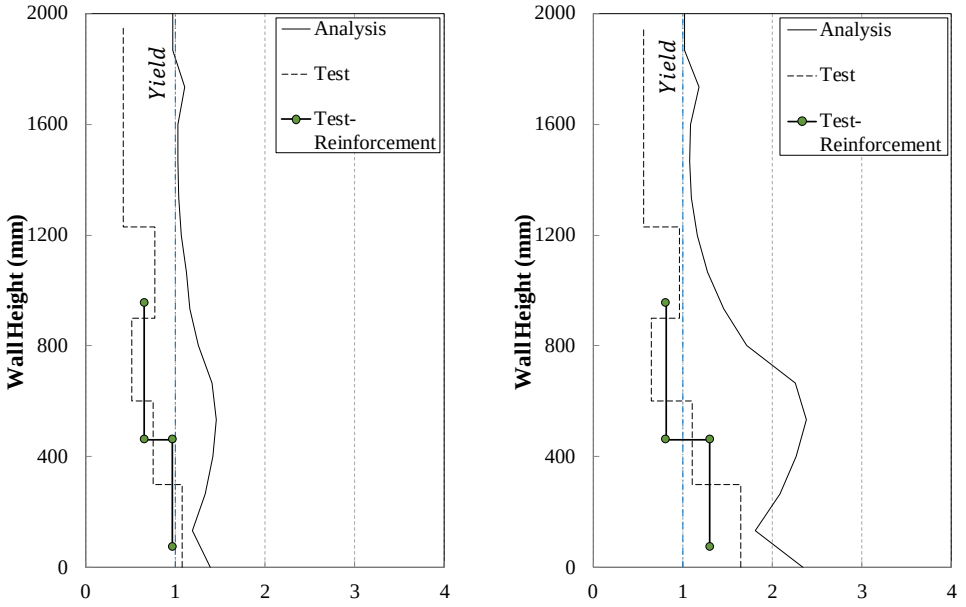

(a) 0.38% (b) 0.50%

Figure 7.24: Average strain profile along the height of the east boundary region at yielding stage - Numerical vs. experimental comparison

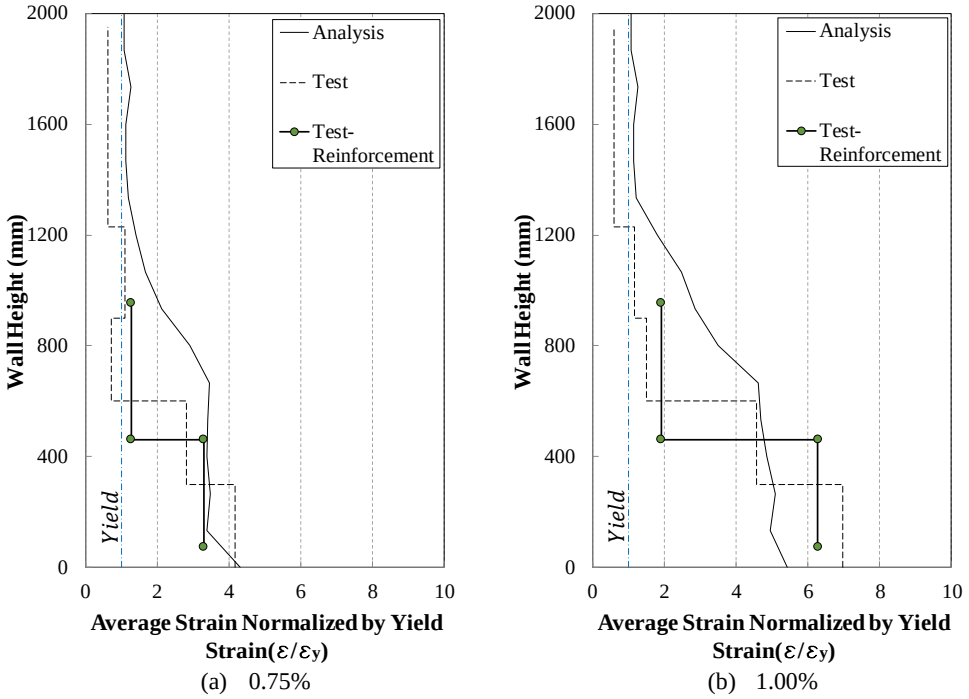

Figure 7.25: Average strain profile along the height of the east boundary region after yielding stage - Numerical vs. experimental comparison

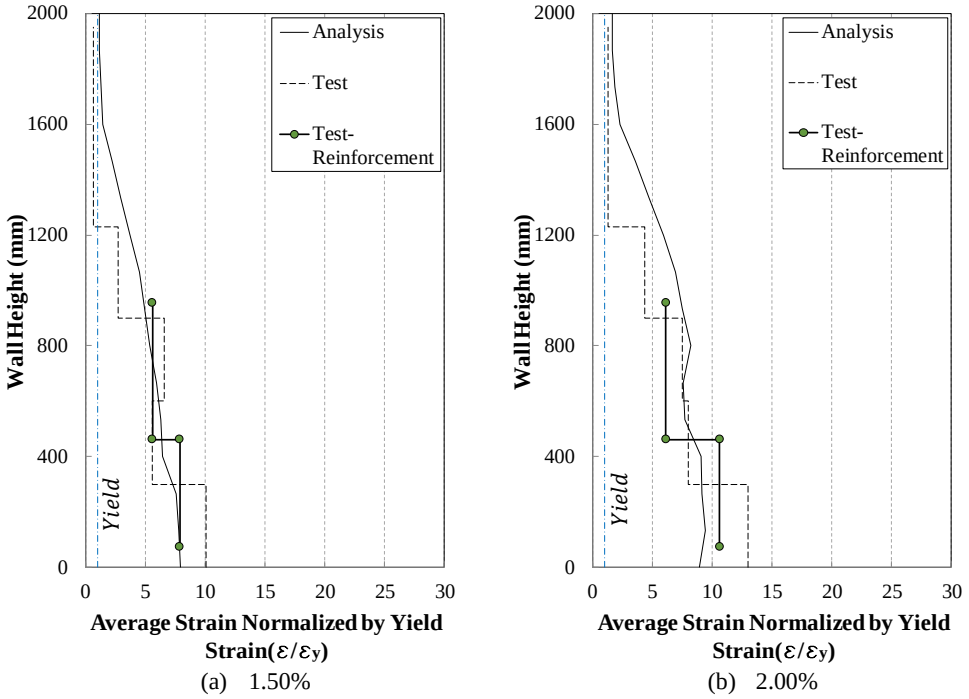

Figure 7.26: Average strain profile along the height of the east boundary region at initiation of out-of-plane deformation - Numerical vs. experimental comparison

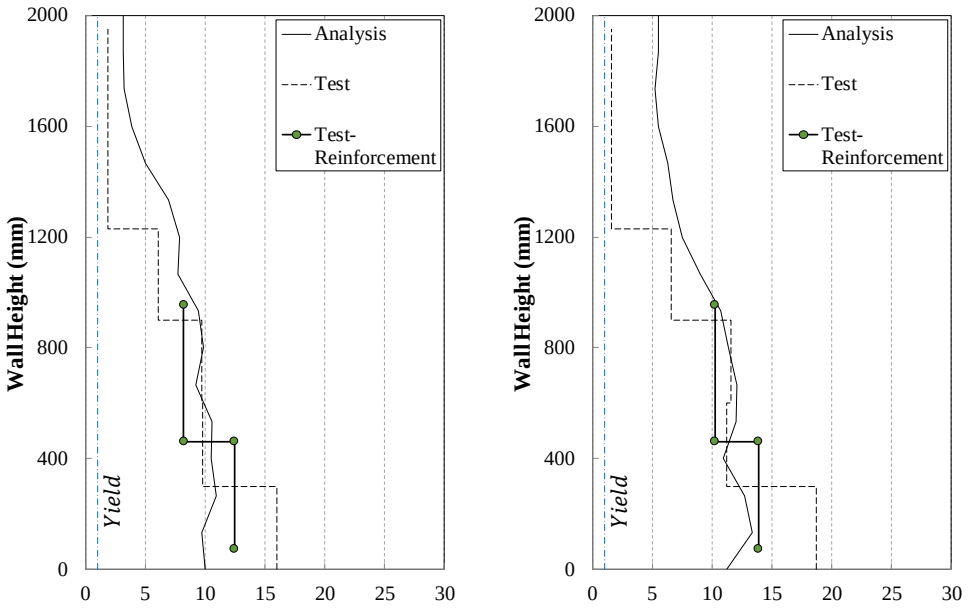

Figure 7.27: Average strain profile along the height of the east boundary region at ultimate stages - Numerical vs. experimental comparison

7.4 COMPARISON

Figure 7.28 compares the out-of-plane displacement prediction of Specimen RWB with the ones of Specimen RWT and Specimen RWL. As can be seen in this figure, an 8% increase in wall thickness (Specimen RWT) resulted in delay and decrease in out-of-plane displacement of the specimen. As for Specimen RWL, decreasing the length of the specimen by 20% resulted in a delay in the formation of out-of-plane deformation (from 2.5% to 3.0% drift level) in addition to decrease in the initial out-of-plane deformation. The values of out-of-plane displacement during the second and the third cycles of 2.5% drift in Specimen RWB are comparable to the ones of 3.0% drift in Specimen RWL. Figure 7.29 compares the experimental measurements of out-of-plane displacement profiles of Specimen RWB with the ones of Specimen RWT and Specimen RWL. According to this figure, the slight increase in wall thickness (about 8%) and the 20% reduction in wall length did not change the drift level corresponding to initiation of out-of-plane deformation, but the initial out-of-plane deformation values were slightly less in thicker and shorter walls. The increase in wall thickness and the reduction in wall length resulted in about 37% and 53% decrease of out-of-plane deformation at 2.0% drift level, respectively.

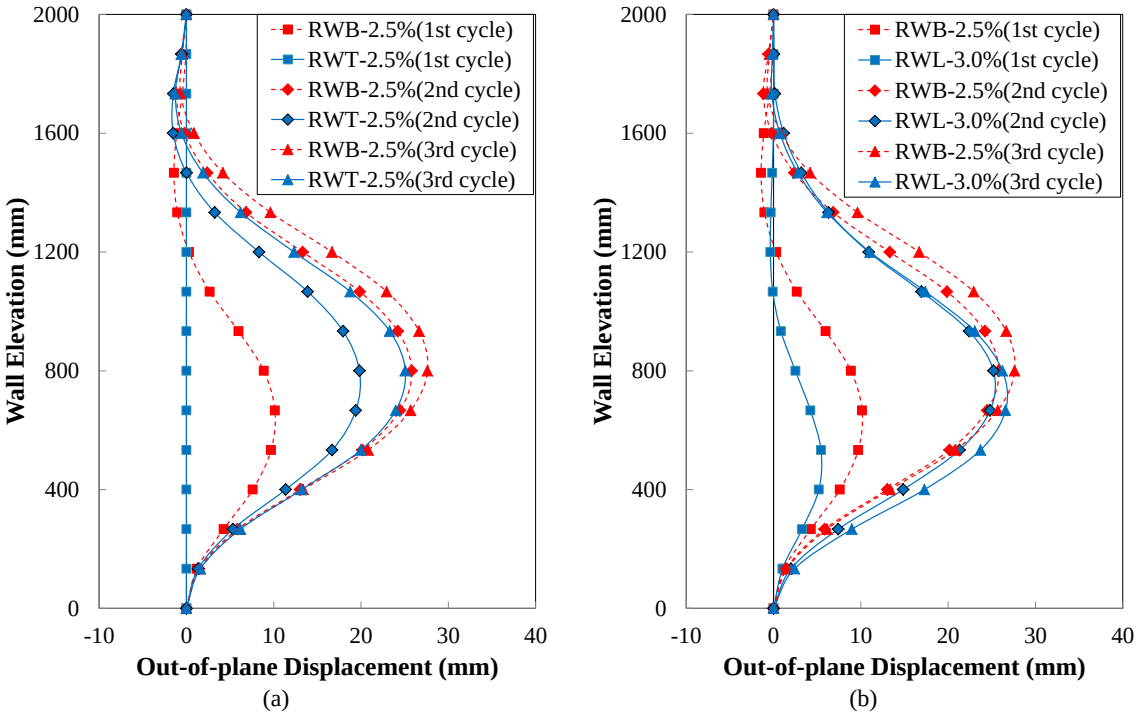

Figure 7.28: Comparison of numerical out-of-plane displacement profiles: (a) RWB vs RWT; (b) RWB vs RWL

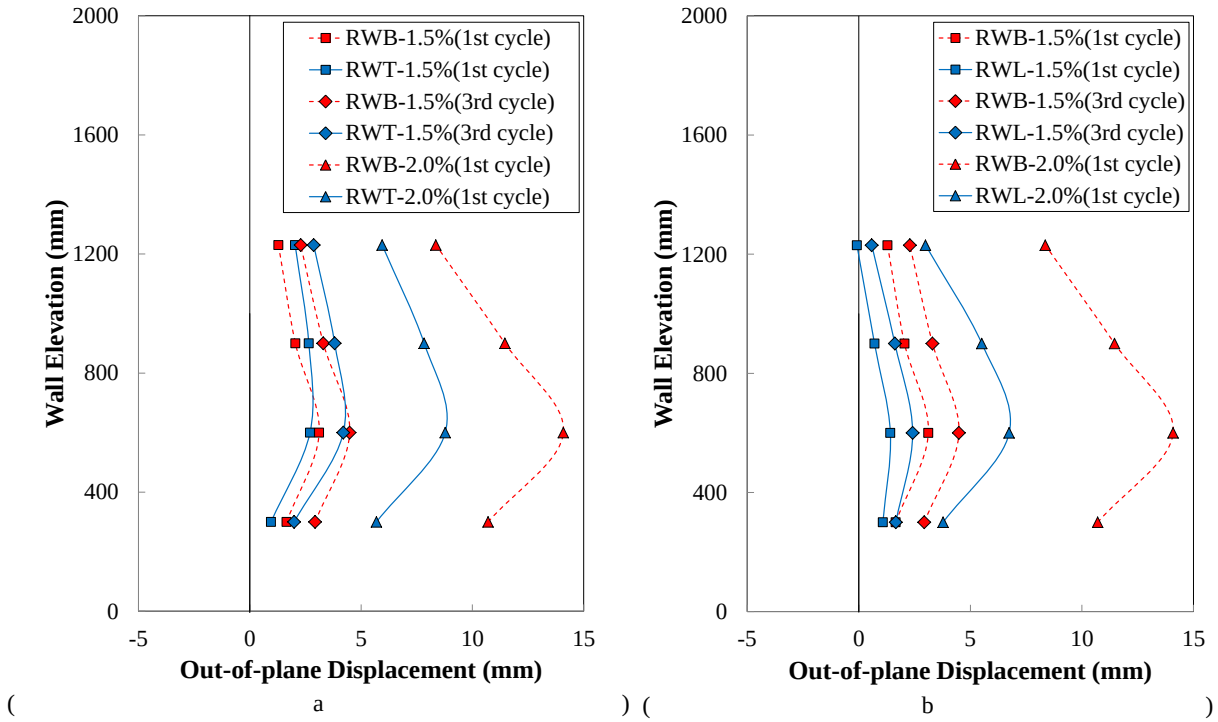

Figure 7.29: Comparison of experimental out-of-plane displacement profiles: (a) RWB vs RWT; (b) RWB vs RWL

In order to scrutinize the effect of reduction of wall length on distribution of strain along the length and height of the wall, Figure 7.30 compares the strain profile prediction of the numerical models along the length at the base of Specimens RWB and RWL and Figure

7.31 compares the variation of strain along the height of these specimens. Since the effect of bond-slip is neglected in the numerical models, any parameters affecting the bond behaviour would not influence the comparison. This is indeed the reason why, unlike the experimental measurements described in Section 7.3, the numerically predicted strain profiles for both specimens follow a similar nonlinear pattern along the length (Figure 7.30) and along the height (Figure 7.31).

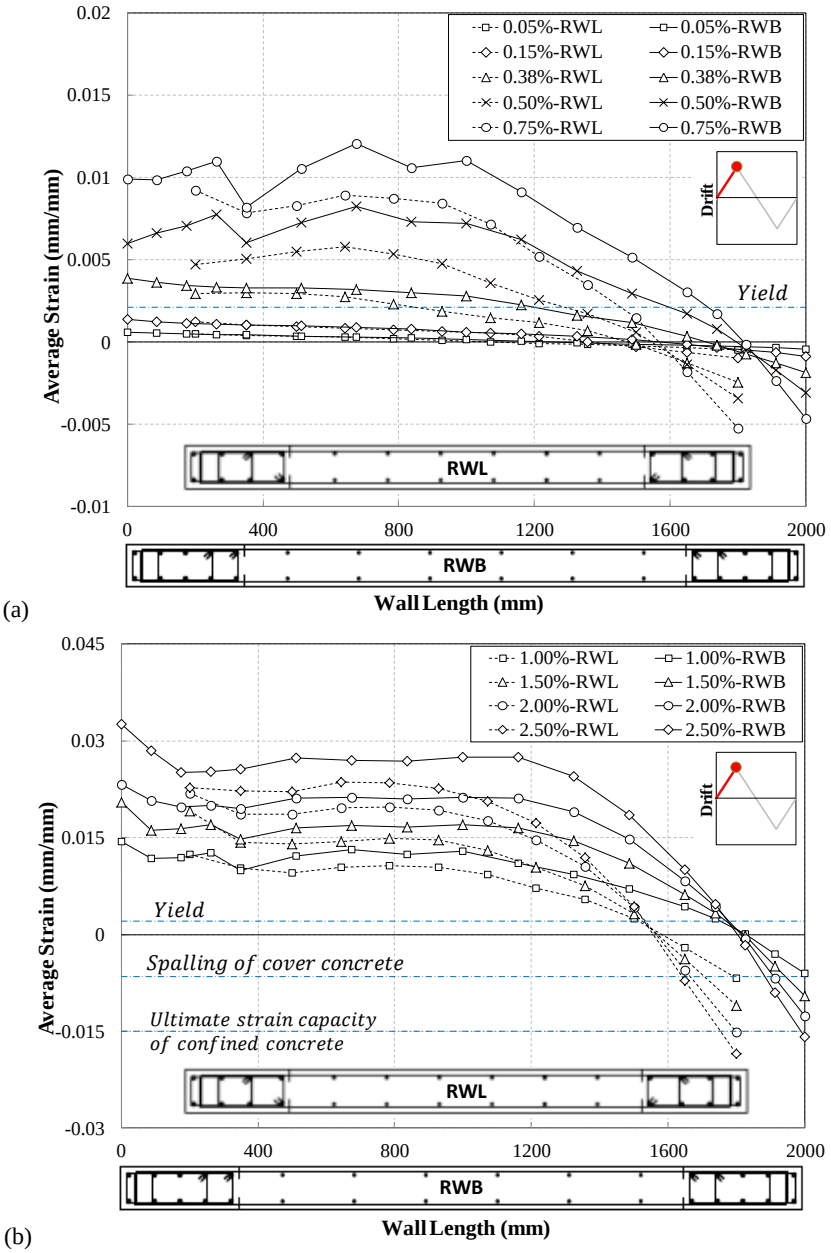

Figure 7.30: Strain variation along the length of numerical models of Specimen RWB and RWL at the base

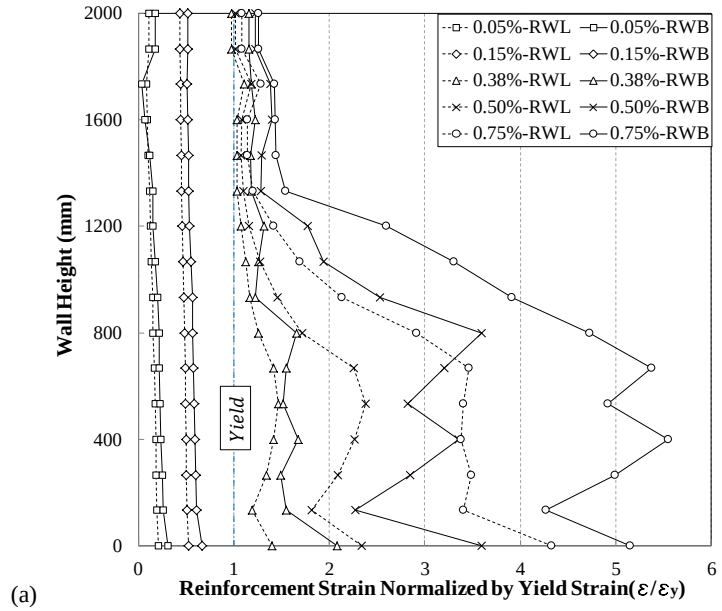

(a)

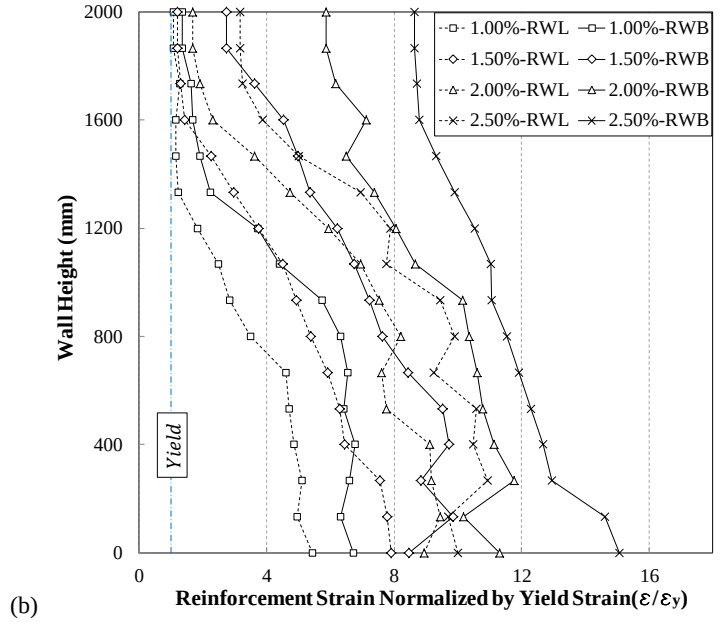

(b)

Figure 7.31: Strain variation along the height of numerical models of Specimen RWB and RWL

As can be seen in Figure 7.30, due to nonlinearity of the strain profile along the wall length, the reduction in wall length did not result in a considerable difference in the maximum tensile strain along the whole length of the base region. The strains along the height of the extreme end bar elements of the specimens (Figure 7.31) shows higher values for Specimen RWB compared to Specimen RWL, and the difference becomes larger with increasing drift level, ranging between $1\varepsilon_y$ to $3\varepsilon_y$ when the drift level increases from 0.50% to 2.50%. Knowing that the tensile strain of reinforcement is identified as a key parameter controlling the out-of-plane deformation of rectangular walls, Specimen RWB might have exhibited relatively higher values of out-of-plane deformation in the test if a decent bond behaviour had allowed the development of large tensile strains within a specific height. The strain

localization at the base of this specimen had prevented the development of large tensile strains at higher elevations. The distribution of large tensile strains along a higher elevation could induce a more uniform compression yielding along a given height. The development of this compression yielding along a critical height, and when the previously formed cracks are still wide open, would result in a buckling mode similar to the one of Specimen RWL.

7.5 EFFECT OF CONCRETE COVER

A single layer of shell elements was used for the numerical simulation in this study. Therefore, mesh discretization could not be done along the wall thickness and consequently the concrete properties along the thickness were considered to be identical, i.e. the entire thickness of the boundary zones was considered to have the confined concrete properties of the core region and the cover concrete was not assigned the unconfined concrete properties. In literature (Vallenas et al. 1979, Hilson et al. 2014), asymmetric spalling of concrete cover has been postulated to be one of the factors contributing to out-of-plane deformation of rectangular walls under cyclic loading. In this section, the effect of cover spalling on development of out-of-plane deformation is investigated.

Figure 7.32 and Figure 7.33 show the initiation and development of cover spalling observed in the east and west boundary regions of Specimen RWL, respectively. As can be seen in these figures, although these drift levels (1.5% and 2.0%) correspond to initiation and increase of out-of-plane deformations, the cover concrete had spalled off quite symmetrically at these stages. Also, considering the very limited area of spalled cover concrete compared to the length of boundary regions, its asymmetric spalling would not have a noticeable effect on initiation and development of out-of-plane deformation.

(a) (b)

Figure 7.32: Cover spalling of east boundary: (a) 1.5% drift; (b) 2.0% drift

(a) (b)

Figure 7.33: Cover spalling of west boundary: (a) 1.5% drift; (b) 2.0% drift

Also, Figure 7.34 and Figure 7.35 show the out-of-plane deformation of the wall boundary regions at 2.5% drift cycle. As can be seen in these figures, cover spalling is less likely to affect this phenomenon as the out-of-plane deformations usually start at a considerably higher elevation from the base while cover spalling due to in-plane loading happens at the base region.

Moreover, out-of-plane deformation develops when the cracks are wide open (and the compressive forces are taken by the reinforcement only) and reaches its maximum value at around zero displacement of each cycle, whereas cover spalling happens at the peak of the displacement cycles when one of the end regions is under high compression at the base. When the amount of out-of-plane deformation results in crack closure in one face of the wall, the out-of-plane deformation starts to recover as concrete starts to contribute to the load carrying capacity of the wall section. The recovery of out-of-plane deformation prevents the application of considerable compressive stresses to the face of the wall that has experienced this crack closure. Therefore, as cover spalling does not happen at this elevation it cannot affect this mode of deformation. However, at ultimate stages of loading, when the out-of-plane deformation does not fully recover at the peak displacement level, cover spalling may initiate at the elevation where the maximum out-of-plane deformation happens.

Given the reasons noted above, consideration of unconfined concrete properties for the cover in the numerical model is not vital for prediction of out-of-plane deformations under in-plane loading, but it may be effective for better simulation of the residual out-of-plane deformation.

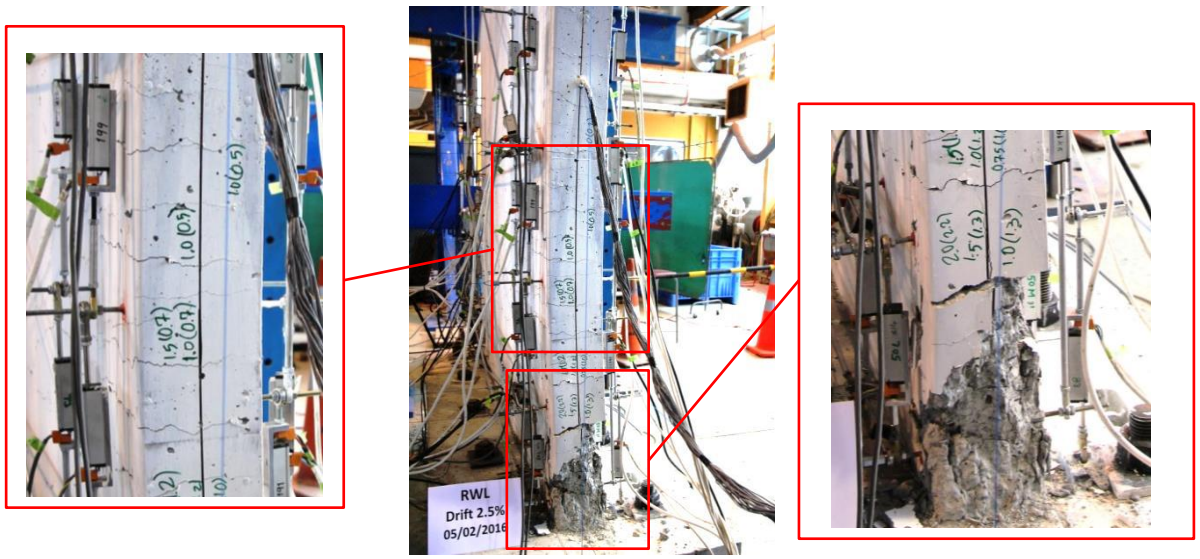

Figure 7.34: Crack pattern and cover spalling at maximum out-pf-plane deformation, west boundary at 2.5% drift cycle

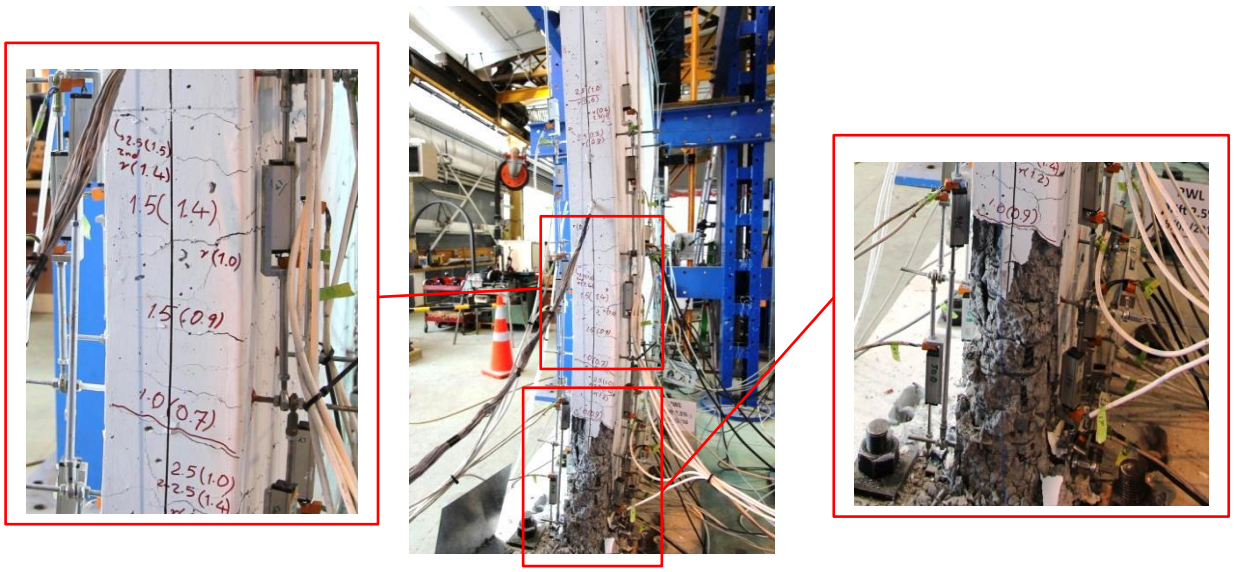

Figure 7.35: Crack pattern and cover spalling at maximum out-pf-plane deformation, east boundary at 2.5% drift cycle

7.6 CONCLUSIONS

Based on the results of a numerical study, an experimental program had been conducted to scrutinize the parameters that affect the out-of-plane deformation of rectangular walls. In this study, the numerical predictions were compared with the experimental observations in terms of global response (lateral load-top displacement curves and failure patterns) as well as the local behaviour (strain distribution along the length and height of the wall).

The numerical model had predicted a steady development of out-of-plane deformations in boundary regions of all the specimens, albeit with lower values of out-of-plane

displacement for the specimen that was slightly higher in thickness and the specimen that had a shorter length compared to the benchmark specimen. Due to inevitable construction eccentricities that had not been taken into account in the analysis; e.g., asymmetric positioning of reinforcement along the wall thickness, the specimens were expected to exhibit higher values of out-of-plane deformation in the experiment.

The experimental response of the benchmark specimen proved to be reasonably in line with the numerical predictions in terms of the lateral load-top displacement curve as well as evolution and recovery of out-of-plane displacement. However, the occurrence of bar fracture and bar buckling suppressed regular increase of out-of-plane deformation and resulted in a localized instability of the specimen. These failure modes were not predicted by the numerical model. A numerical versus experimental investigation of the strain profiles along the length of the wall base and along the height of the extreme end of the wall showed a considerably high localization of tensile strains at the base region of the wall specimen compared to the numerical prediction. This strain localization in the experiment, that was obvious from the crack patterns, could be attributed to the effect of bond-slip which was neglected in the numerical model as embedded bar elements were used for simulation of reinforcement. Due to this phenomenon, the strains at the base of the specimen were about two times higher than the expected values resulting in bar fracture and bar buckling failure patterns to suppress the steady development of out-of-plane deformation.

Response of the specimen with a slightly higher thickness was quite similar to the one of the benchmark specimen. However, as predicted by the numerical model, the out-of-plane deformations were slightly smaller in this specimen.

The specimen with a shorter length was predicted to have a delay in the formation of the out-of-plane deformation when compared to the benchmark specimen. However, the out-of-plane deformation of this specimen started at the same drift level as the other specimens, though with smaller out-of-plane displacements which increased steadily leading to instability of the specimen without any interference from other failure modes. This specimen was designed to have the same lateral load capacity as the benchmark specimen and understandably had higher reinforcement ratio at the boundary regions which was provided by larger bar diameters. These larger bar diameters contributed to development of stronger bond between concrete and reinforcement compared to the benchmark specimen. The closely spaced cracks with relatively small crack width, observed during the test, were

a further indication of this effect. The numerical versus experimental investigation of the strain profiles along the wall base and along the height of the tensile boundary region at different drift levels showed a reasonably good prediction of the strain profiles by the numerical model in which the bars were considered to be fully bonded. The earlier development of out-of-plane deformation in the experiment compared to the numerical model could be attributed to the asymmetric development of tensile strain along the wall thickness due to inevitable construction eccentricities which could be significantly large with larger bar diameters positioned in a relatively thin wall panel.

Comparison of the predicted strain profiles of the benchmark specimen and the specimen with shorter length showed higher strain values for the benchmark specimen along the height of the wall. If the bond behaviour of the benchmark specimen was good enough to allow development of large tensile strains at higher elevations, a buckling mode similar to the one of the short specimen could happen.

Cover spalling of the specimen that exhibited out-of-plane instability as the only failure mechanism happened quite symmetrically. Moreover, cover spalling and development of out-of-plane deformation happen at two different stages of loading and at two different positions along the wall height. Therefore, not representing the concrete cover in the numerical model would not have a great influence on prediction of out-of-plane deformation.

7.7 REFERENCES

Hilson, C., C. Segura and J. Wallace (2014). Experimental study of longitudinal reinforcement buckling in reinforced concrete structural wall boundary elements. Tenth U.S. National Conference on Earthquake Engineering (10NCEE). Anchorage, Alaska.

International Federation for Structural Concrete, f. (2013). fib Model Code for Concrete Structures 2010. Berlin, Germany.

Shima, H., L.-L. Chou and H. Okamura (1987). "Micro and macro models for bond in reinforced concrete." *Journal of the Faculty of Engineering* 39(2), 133-194.

Vallenas, J. M., V. V. Bertero and E. P. Popov (1979). Hysteretic behaviour of reinforced concrete structural walls. Report no. UCB/EERC-79/20, Earthquake Engineering Research Center, University of California, Berkeley.

8 MECHANISM OF OUT-OF-PLANE INSTABILITY FAILURE IN RECTANGULAR RC STRUCTURAL WALLS DUE TO IN-PLANE LOADS; EXPERIMENTAL OBSERVATIONS & ANALYTICAL PREDICTIONS

Dashti, F., R.P. Dhakal, S. Pampanin (2017) "Evolution of Out-of-plane Deformation and Subsequent Instability in Rectangular RC Walls under In-plane Cyclic Loading; Experimental Observation" *Earthquake Engineering & Structural Dynamics*, EQE-17-0078 (Under Review)

Dashti, F., R.P. Dhakal, S. Pampanin (2016) "Out-of-plane Instability of a Rectangular Wall Specimen Subject to In-plane Cyclic Loading" *New Zealand Concrete Industry Conference 2016*, Auckland, New Zealand

In this chapter, the development of out-of-plane instability in rectangular walls is investigated by analyzing the response of Specimen RWL. The failure pattern of this specimen was pure out-of-plane instability, and its response was not influenced by other failure patterns such as bar buckling. Therefore, the observations and measurements at different stages of loading are used to scrutinize the mechanism of out-of-plane instability and the controlling parameters.

The postulations and observations presented in some prior research on development of out-of-plane instability of concrete columns representing the boundary zones of rectangular walls are linked with the observations made in this experimental research. The effect of the residual strain of the reinforcement known to be the main parameter controlling this mode of wall failure is scrutinized by the strain measurements at different locations of the

specimen and throughout the test. The analytical models proposed in literature for prediction of out-of-plane instability failure as well as the relevant assumptions are compared with the test measurements.

8.1 RESPONSE OF THE SPECIMEN

Response of Specimen RWL is discussed and compared with the experimental behavior of Specimens RWB and RWT in Chapter 6. In this section, the observations related to development of out-of-plane instability in this specimen are presented and compared with the evolution of this failure mechanism reported by Chai and Elayer (1999). The development of out-of-plane instability presented by these researchers is based on the results of the experiments conducted on concrete columns representing boundary zones of rectangular walls and is comprehensively described in Chapter 2.

Figure 8.1a displays the lateral load-top displacement response of the specimen. The failure pattern of the specimen was pure out-of-plane instability and neither bar fracture nor bar buckling was observed in the test. The out-of-plane deformation initiated at Point A when the specimen was unloaded from the 1.5% drift cycle and was starting to reload in the opposite direction. Figure 8.1b indicates the maximum out-of-plane displacement measurement of the specimen at different stages of loading. As can be seen in this figure, the out-of-plane deformation recovered completely as the specimen was reloaded in the opposite direction. This out-of-plane displacement recovery occurred at early stages of loading. When the specimen was reloaded from the 2.5% drift level, the specimen started to exhibit residual out-of-plane displacement. The residual out-of-plane displacement increased with the number of cycles and the specimen became unstable at Point B where the abrupt strength degradation was observed.

Out-of-plane displacement (1 mm) was first noticed during the 1st cycle of 1.5% drift on the west boundary which experienced the 1st tension in each cycle, and increased with the number of cycles. A number of smaller cracks occurred in the tension boundary at 2.0% drift; these cracks merged together and formed wide cracks in the panel region. The wide cracks extended up to 50% of the wall height at this stage. The out-of-plane displacement increased to about 7 mm and 10 mm in the 1st and 3rd cycles of 2.0% drift level, respectively. The crack pattern at 2.5% drift level was similar to the one at 2.0% drift level, but the cracks were a bit wider, particularly the diagonal cracks. The wide cracks of the tension boundary region extended up to 1350 mm from the base with a uniform distribution

of crack width. When the load was reversed from the 2.5% drift level, the cracks in the tension region were wide open, and were still wide when the specimen was being reloaded in the opposite direction. Being spaced at an average distance of 120 mm, these residual cracks had an average crack width of 0.7 mm. At this stage, the out-of-plane deformation increased significantly in the compression boundary region and was clearly observable. Figure 8.2 displays the formation of out-of-plane deformation in the west boundary region during the second cycle of 2.5% drift level.

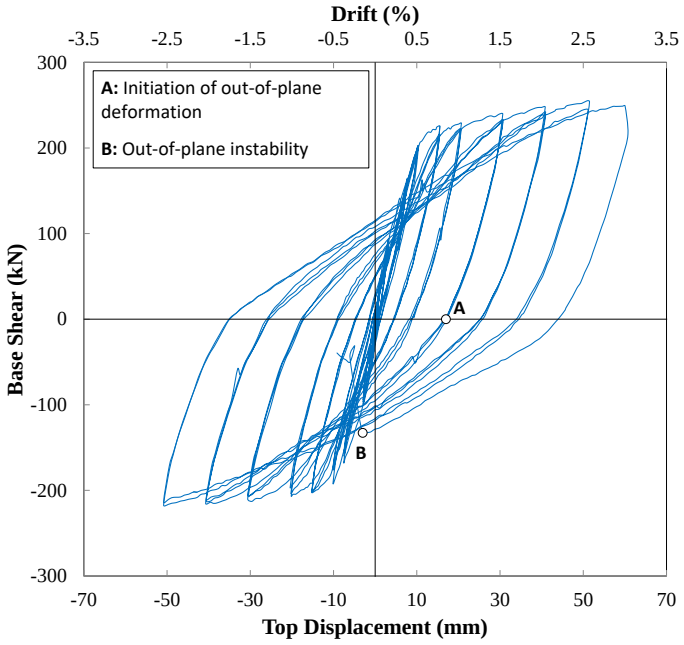

(a)

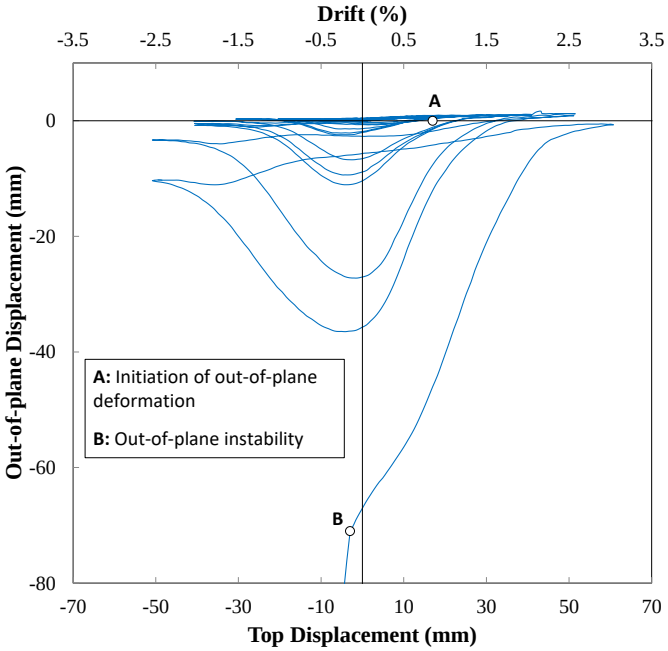

(b)

Figure 8.1: Response of the specimen: (a) lateral load vs top displacement response of the specimen; (b) maximum out-of-plane vs top displacement response of the west boundary region

Figure 8.2a indicates the wide cracks in the boundary region before initiation of out-of-plane displacement at 2.5% drift level. Figure 8.2b and Figure 8.2c display development of the out-of-plane deformation at this drift level. Figure 8.2c indicates the maximum out-of-plane deformation and initiation of crack closure in one face of the wall at this drift level. This crack closure resulted in decrease of the out-of-plane deformation in the following stages (Figure 8.2d and Figure 8.2e) and its recovery (Figure 8.2f). The out-of-plane deformation did not recover completely at this stage since the compressive stresses increased in inner face of the out-of-plane displacement profile (where the crack closure initiated) along with reloading in the opposite direction and resulted in concrete crushing in one face of the wall. The out-of-plane deformation increased in the east boundary element as well when the specimen was being unloaded and reloaded in the positive direction toward 3.0% drift level.

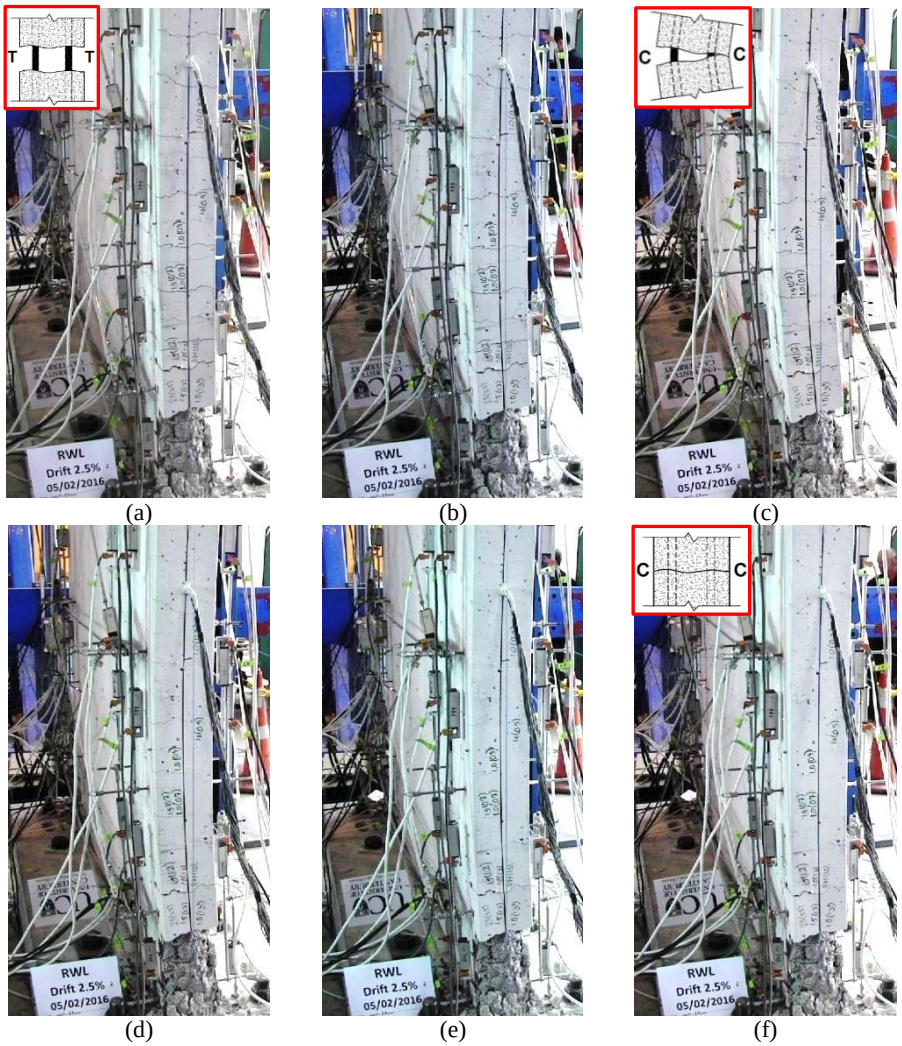

Figure 8.2: Formation and recovery of out-of-plane deformation in the west boundary region, 2.5% drift level: (a) formation of wide cracks; (b) initiation of out-of-plane displacement; (c) maximum out-of-plane displacement and initiation of crack closure; (d) &(e) decrease of out-of-plane displacement; (f) recovery of out-of-plane displacement

Following the same trend as in the previous cycles, the out-of-plane deformation increased up to the state where the cracks started closing in one face of the wall resulting in increase of compressive stresses in this face and recovery of the out-of-plane deformation. Figure 8.3 indicates the asymmetric response of concrete in the section undergoing out-of-plane deformation. Figure 8.3a displays the stage where the crack closure has initiated in one face of the wall and the out-of-plane deformation is recovering. Further recovery of the out-of-plane displacement can be observed in Figure 8.3b. As can be seen in this figure, due to the out-of-plane deformation of the wall, the cracks are still open in the south face of the compression boundary region while the cracks in the tension side of the wall have reopened. In other words, when the out-of-plane deformation increases in a boundary region that is under compression, the shear and flexural cracks of the inner face of the section with out-of-plane deformations close and the out-of-plane deformation starts to recover along with increase in top displacement applying further compression in the boundary region. At this stage, the cracks are still open in south face of the wall while the cracks in the tension side start to reopen (Figure 8.3b). At this stage, the inner face undergoes considerable compressive stresses due to the loading direction as well as the out-of-plane deformation of the boundary region. These increased compressive stresses can lead to cover spalling in the inner face of the wall at the location of the maximum out-of-plane deformation. Figure 8.3c indicates the colour flaking as an indication of cover spalling in the inner face of the out-of-plane deformation section which was observed when the specimen was being unloaded from 3.0% drift level and Figure 8.3d displays the extent of cover spalling in this section at the end of the test.

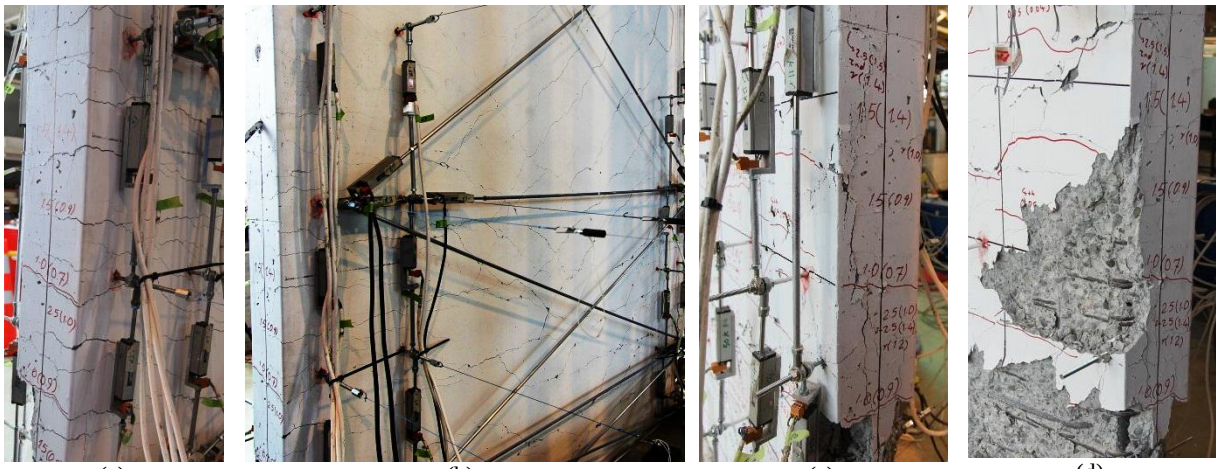

(a) (b) (c) (d)

Figure 8.3: Asymmetric response of concrete in the section with maximum out-of-plane deformation (east boundary region)

During unloading from +3.0% drift level and reloading towards -3.0% drift level, the out-of-plane deformation increased in the left boundary region. However, as the cracks generated in this boundary region during +3.0% loading were wider than the previous cycle at 2.5% drift level, the cracks did not fully close and the out-of-plane deformation increased considerably leading to out-of-plane instability of the wall. Figure 8.4 displays the formation of out-of-plane instability which can be compared with Figure 8.2, the stage where timely crack closure resulted in recovery of the out-of-plane deformation. As can be seen in Figure 8.4d, the crack closure in one face of the wall started when the specimen had undergone a considerable out-of-plane deformation (more than half of the wall thickness).

The above mentioned steps leading to formation of out-of-plane deformation and out-of-plane instability are in line with the postulations well described by Paulay and Priestley (1993), and results of the experiments conducted by Chai and Elayer (1999) (Figure 2.10, Table 2.1). As can be seen in Figure 2.10 and Table 2.1, the reloading in compression of the idealized column could be either Path *b-c-d-e* or Path *b-c-d-f*. Response of the specimen's west boundary region illustrated in Figure 8.2 represents Path *b-c-d-e*, where the maximum tensile strain of the boundary region developed when this boundary region was subjected to tension (corresponding to Path *o-a*, Figure 2.10) was large enough to result in development of out-of-plane deformations (Figure 8.2b). However, this strain was small enough to result in timely crack closure in one face of the wall (Figure 8.2c) before the out-of-plane deformation exceeds a critical limit. The recovery of out-of-plane deformation following this crack closure (Figure 8.2d-Figure 8.2f) corresponds to Path *d-e* (Figure 2.10, Table 2.1). Crushing of concrete in the inner face of the wall at the maximum out-of-plane deformation (Point *e*, Figure 2.10) was clearly observed in the right boundary zone at +3.0% drift level (Figure 8.3c and Figure 8.3d).

As the left boundary zone of the specimen was subjected to a larger tensile strain at +3.0% drift level, the crack closure did not happen before the out-of-plane deformation exceeded the critical value (Figure 8.4d), and the wall followed Path *d-f* (Figure 2.10, Table 2.1), and became unstable (Figure 8.4f).

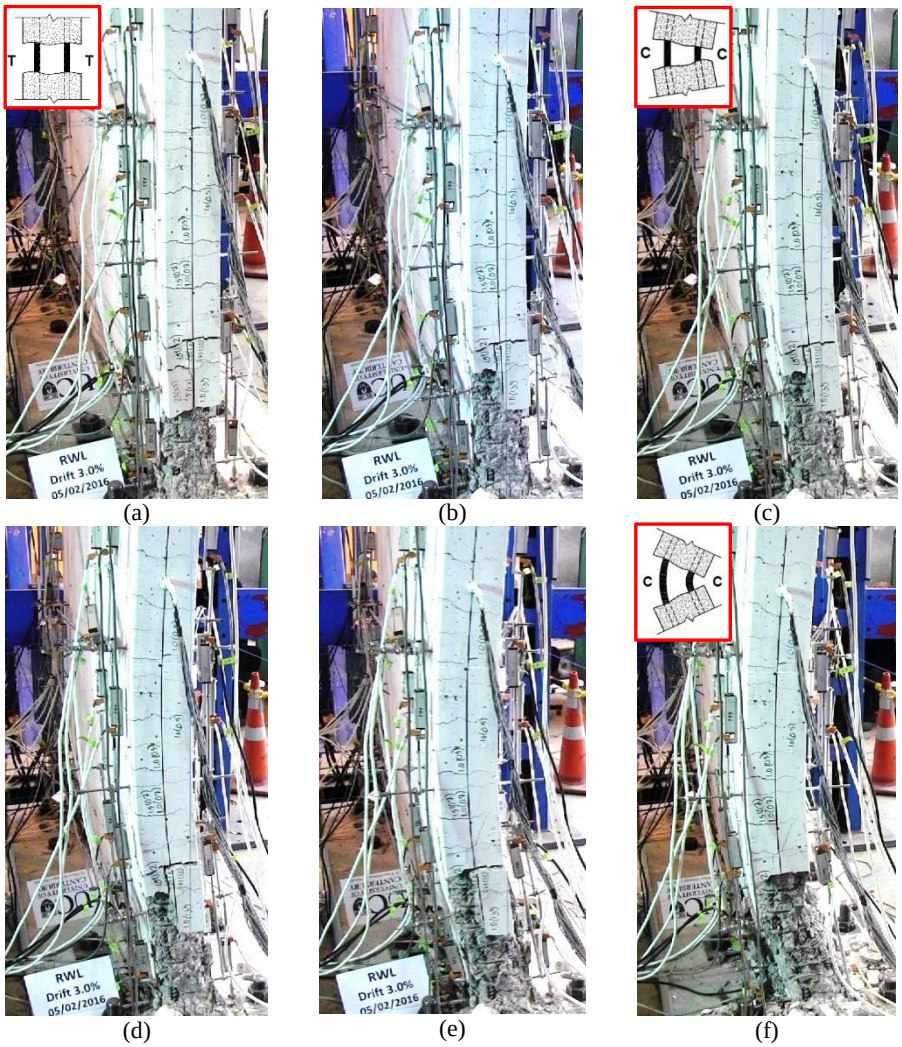

Figure 8.4: Formation of out-of-plane instability, 3.0% drift level: (a) formation of wide cracks; (b) initiation of out-of-plane displacement; (c), (d) & (e): steady increase of out-of-plane displacement; (f) out-of-plane instability

8.2 EFFECT OF REINFORCEMENT STRAIN ON DEVELOPMENT OF OUT-OF-PLANE DEFORMATION

Reinforcement strain at different stages of loading, unloading and reloading has been identified as one of the main parameters controlling out-of-plane deformations of rectangular walls. In order to capture the average strain of reinforcement along the area which was assumed to be more prone to out-of-plane deformations, linear potentiometers had been used in the test. Figure 8.5a displays the configurations of these linear potentiometers and Figure 8.5b indicates the positioning of the instruments used for capturing the out-of-plane deformations.

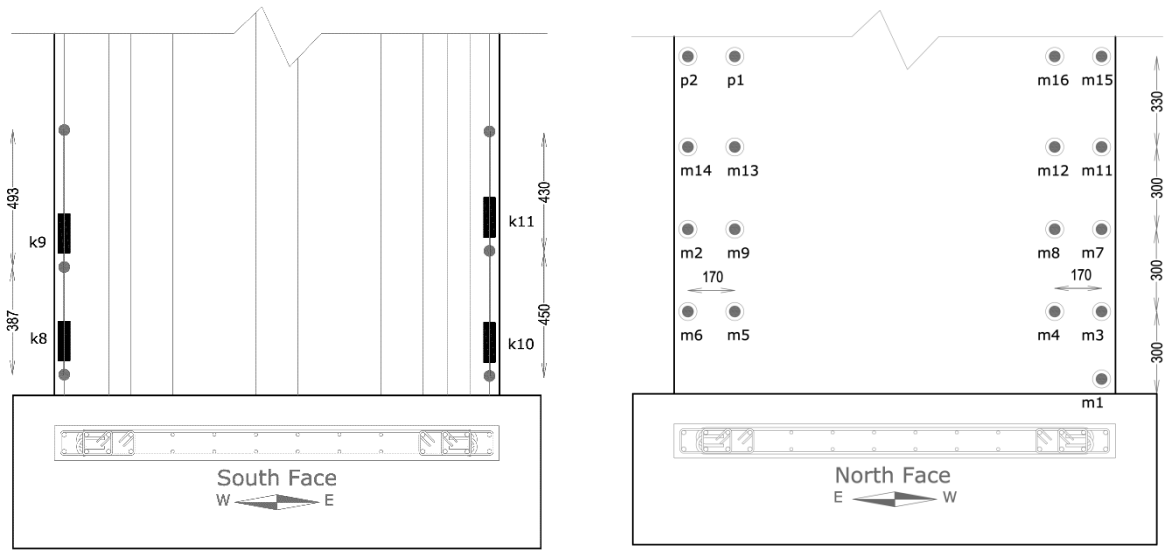

(a) (b)

Figure 8.5: Measurement of average strain and out-of-plane displacement: (a) configuration of the potentiometers attached to the extreme end reinforcement; (b) configuration of the string pots for measurement of out-of-plane deformation

Figure 8.6 indicates the out-of-plane displacement of the specimen along the height of both boundary regions. According to this figure, the maximum value of out-of-plane displacement occurred at the height of about 800 mm and 700 mm from the base in the east and west boundary regions, respectively.

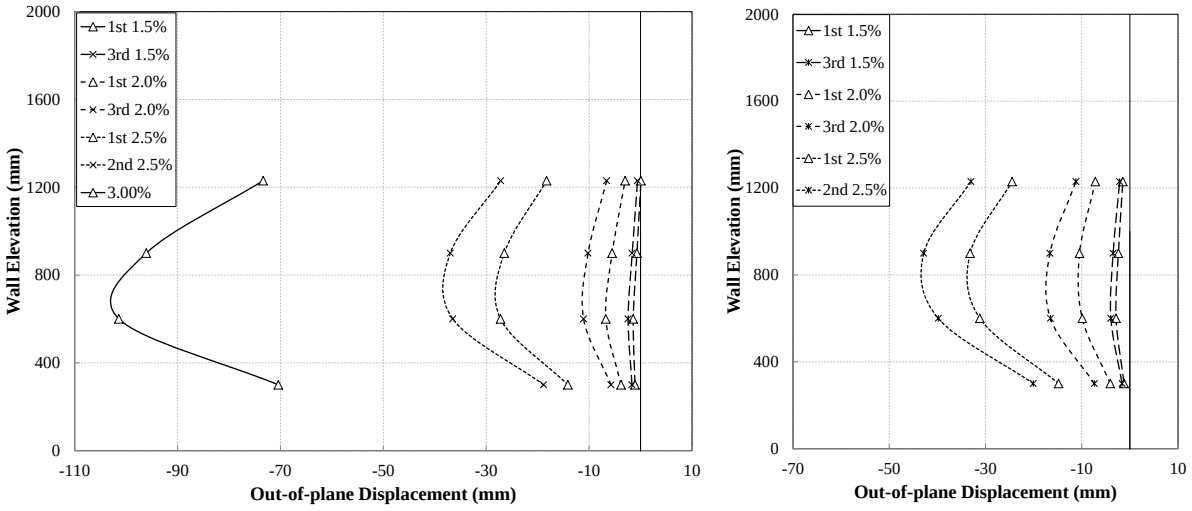

(a) (b)

Figure 8.6: Maximum out-of-plane displacement of the specimen corresponding to the applied drift levels: (a) west boundary region; (b) east boundary region

Figure 8.7 displays the measurement of the average strain by the potentiometers attached to the extreme end reinforcement of the west boundary region versus the top displacement of the specimen and Figure 8.8 indicates the average strain measures by these potentiometers versus the out-of-plane displacement measures by m7 (Figure 8.5) which is the maximum

out-of-plane displacement measurement of the west boundary region (Figure 8.6). Figure 8.7a and Figure 8.7b indicate the average strain history of the extreme end reinforcement within 70-457 mm and 457-950 mm from the base, respectively. Therefore, the values of strain are understandably less in Figure 8.7b when compared to Figure 8.7a for the corresponding drift levels. Also, the out-of-plane deformation pattern of the specimen resulted in big strain reductions in Figure 8.7b when the out-of-plane deformation reached a considerable value at 2.5% and 3.0% drift cycles. These figures show the gradual increase of tensile reinforcement strain with the level of drift level as well as the number of cycles at a specific drift level. Figure 8.7a indicates the considerable residual strain of the reinforcement particularly when the specimen unloads to 0.0% drift from post-yielding drift levels (0.75% and above) and while reloading in the opposite direction. The residual strain increases along with increase of the maximum strain in a specific cycle so that crack closure does not occur until a significant reloading in the opposite direction. This considerable gap between the drift levels corresponding to the maximum tensile strain and zero tensile strain in a specific cycle is the duration over which the cracks are still open and the reinforcement is the main load carrying element of the section which is under compression stresses. Therefore, any eccentricity in response of the reinforcement along the wall thickness can result in initiation of out-of-plane deformations.

The strain history of the reinforcement corresponding to 1.5% drift level is magnified in Figure 8.7a and Figure 8.7b. This is the drift level during which the out-of-plane displacement initiated. The strain versus out-of-displacement history of the specimen at this drift level is magnified in Figure 8.8a and Figure 8.8b. As can be seen in these figures, the average reinforcement strain within 70-457 mm and 457-950 mm levels is about 0.018 and 0.013, respectively, and the maximum out-of-plane deformation is less than 2.0 mm. The out-of-plane deformation increases with the drift levels and the number of cycles at a specific drift level along with the increase of reinforcement strain. However, this out-of-plane deformation recovers when the reinforcement strain decreases as the specimen is being reloaded in the opposite direction and the crack closure initiates at one face of the wall. During the initial stages of out-of-plane displacement, the recovery is almost complete, and the residual out-of-plane displacement increases with increase of the maximum out-of-plane displacement. This residual out-of-plane displacement increases considerably during the 2.5% drift cycles where the maximum out-of-plane displacement is more that 20% of the wall thickness. As the value of the maximum out-of-plane displacement exceeded a value equivalent to 50% of the wall thickness (Figure 8.8), the

wall became unstable. This threshold is the upper bound out-of-plane displacement limit proposed by the analytical models and is discussed in Section 8.5. The instability corresponds to the considerable change of slope in Figure 8.8a and Figure 8.8b when the specimen was unloaded from the first 3.0% drift level and was reloading in the opposite direction with the maximum strain of 0.032 and residual strain of 0.021 at 0.0% drift level (Figure 8.7a). The significant increase of out-of-plane displacement during this cycle can be observed in Figure 8.8.

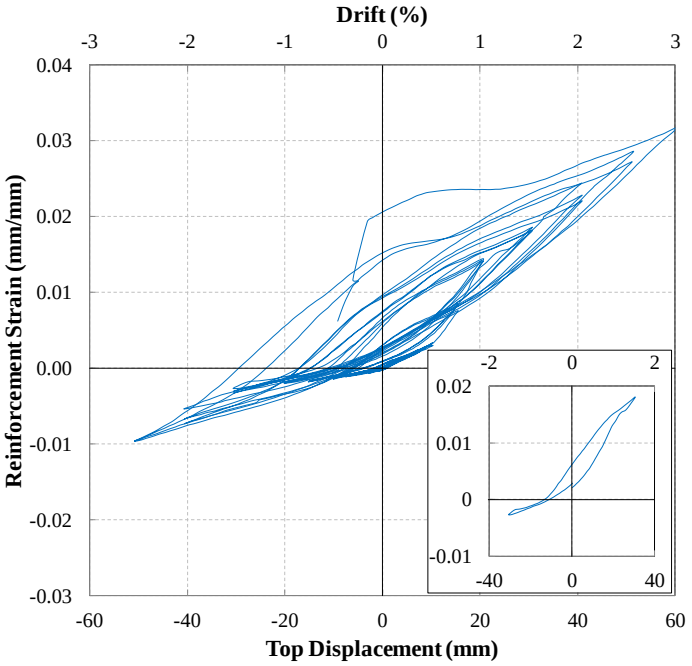

(a)

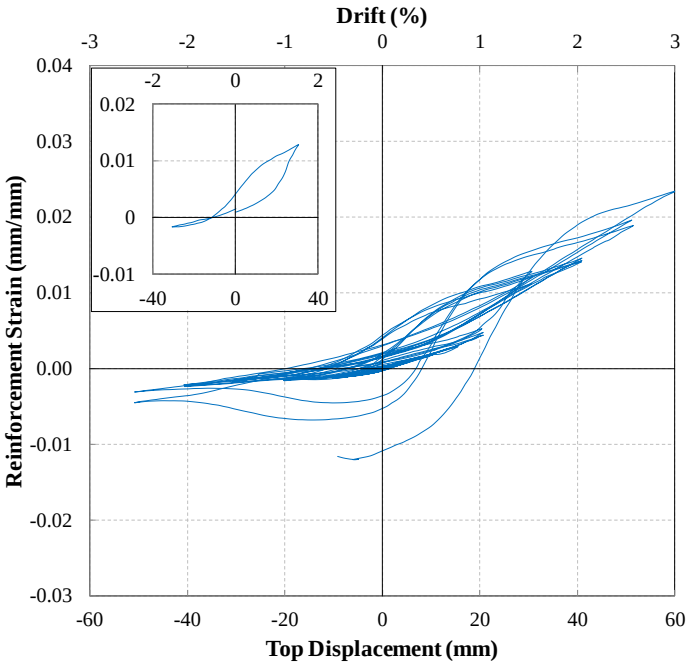

(b)

Figure 8.7: Average strain of the extreme end reinforcement vs top displacement of the specimen: (a) Potentiometer k8; (b) Potentiometer k9

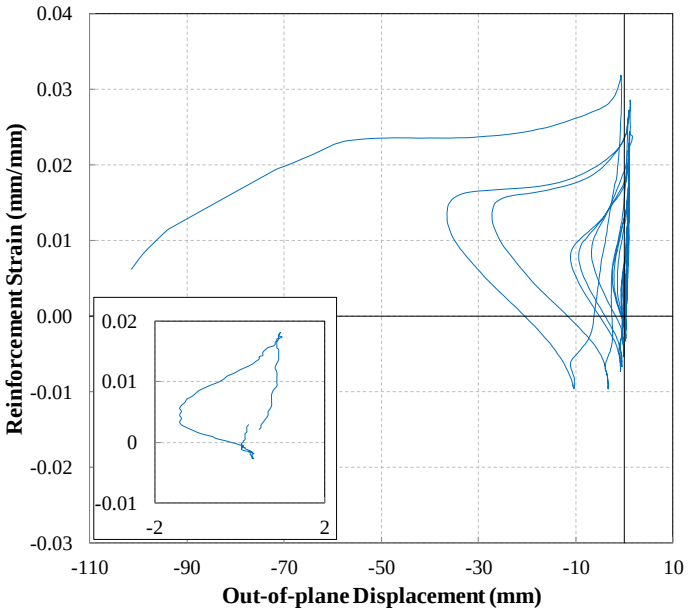

(a)

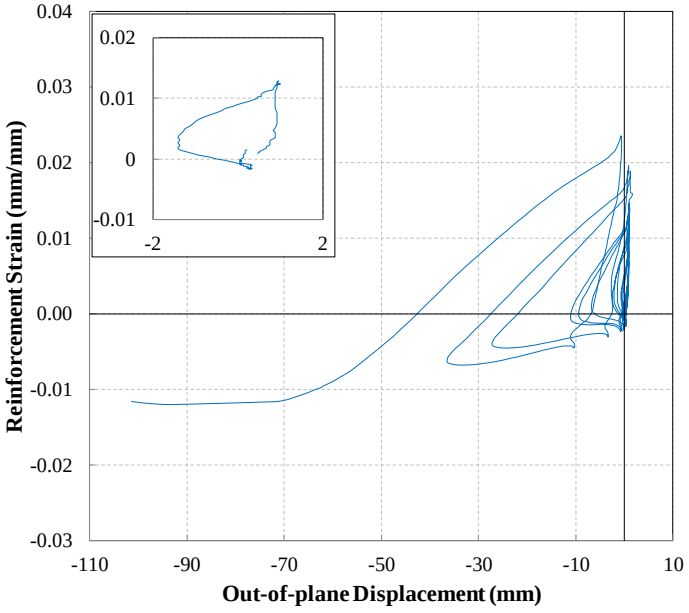

(b)

Figure 8.8: Average strain of the extreme end reinforcement vs the out-of-plane displacement of the specimen measurement of m7: (a) Potentiometer k8; (b) Potentiometer k9

In order to compare the test observations with the findings of Chai and Elayer (1999) on the relationship between the axial strain and out-of-plane buckling of the boundary region, the points described in Figure 2.10 and Table 2.1 are identified in the lateral load-top displacement curve of the specimen. The average strain response of the extreme end reinforcement at both boundary regions versus the corresponding maximum out-of-plane deformation is plotted in Figure 8.9 and Figure 8.10. Only the final stages of the wall response are shown in these figures.

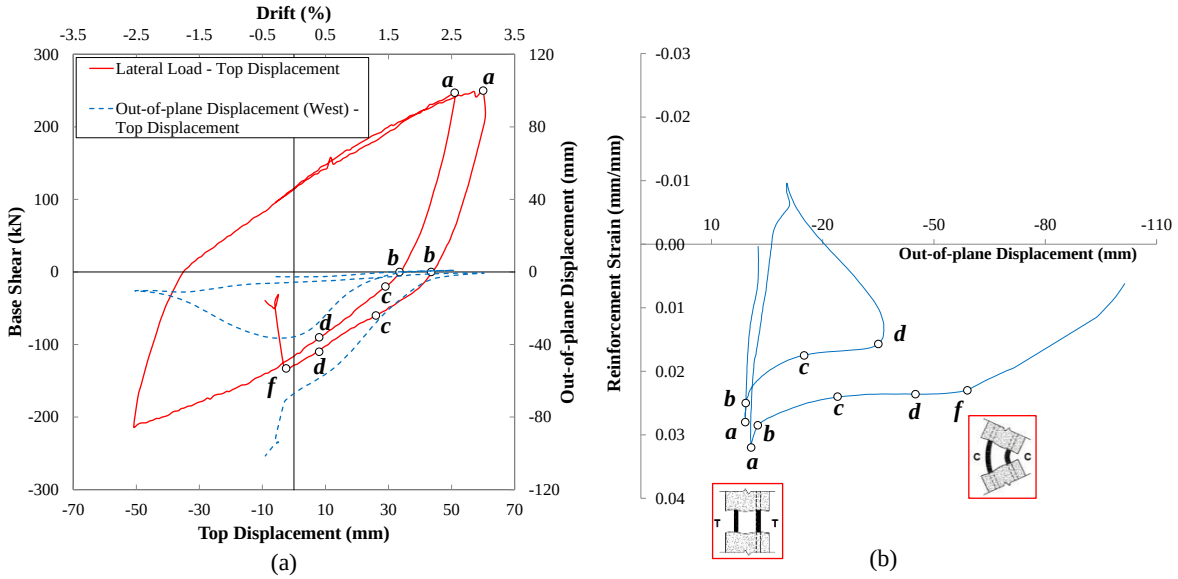

Figure 8.9: Comparison of the specimen reinforcement strain vs out-of-plane displacement with the findings of Chai and Elayer (1999), west boundary

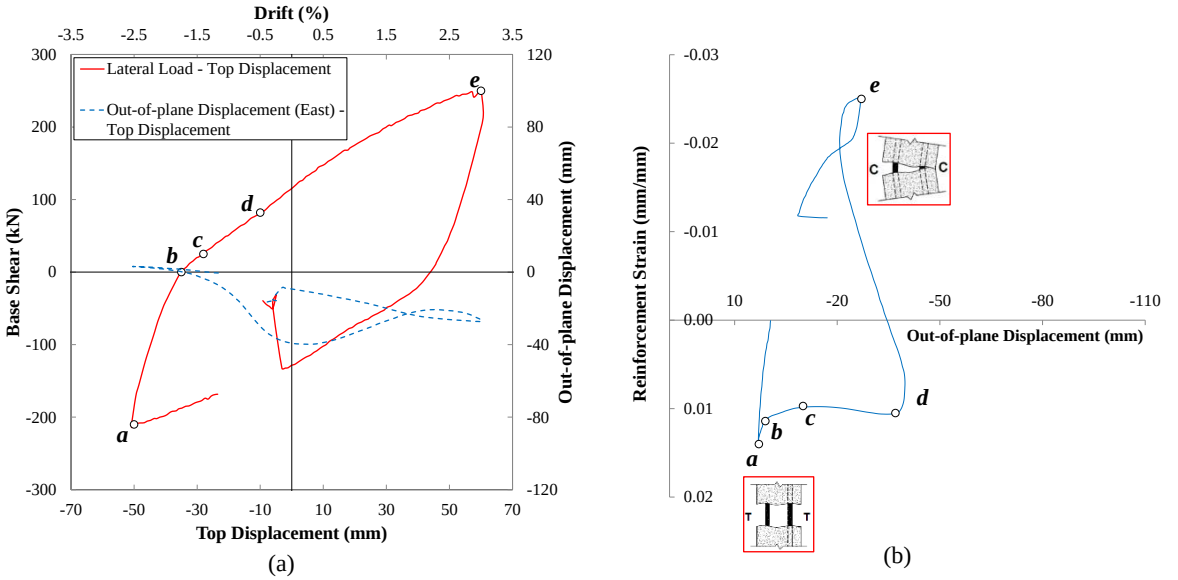

Figure 8.10: Comparison of the specimen reinforcement strain vs out-of-plane displacement with the findings of Chai and Elayer (1999), east boundary

Figure 8.9b displays the strain vs out-of-plane displacement response of the west boundary region where the instability happened, and Figure 8.10b indicates the one for the east boundary region where the loading towards 3.0% drift level resulted in concrete crushing in the inner face of the section that had undergone out-of-plane deformation. These graphs are plotted in the same style as Figure 2.10a and represent the response of a rectangular wall that had exhibited out-of-plane instability using the same method that was used by Chai and Elayer (1999) to discuss response of the wall boundary regions under axial cyclic loading.

As can be seen in Figure 8.9, as the specimen was loaded up to +2.5% drift level, a significant tensile strain developed in the extreme end reinforcement of the west boundary region. The elastic strain recovery occurred when the specimen was unloaded in Path *a*-*b*. The out-of-plane displacement initiated when the lateral load reached zero and the specimen was reloaded in the opposite direction, increased during Path *b*-*c*-*d* and started decreasing at the onset of crack closure at Point *d*. Almost two-third of the out-of-plane displacement recovered as the specimen was loaded further in this direction. The specimen was subjected to a higher drift level in the following cycle (3.0% drift), resulting in a higher reinforcement strain (Figure 8.9b). Similar paths were followed until Point *d*, where the high tensile strain of the reinforcement prevented the timely crack closure and, unlike in the previous cycle, the out-of-plane displacement increased considerably and when it exceeded 50% of the wall thickness at Point *f*, the specimen became unstable. In the east boundary region (Figure 8.10), the trend was quite similar to the one in the west boundary at 2.5% drift cycle except that the loading of the specimen towards +3.0% drift level after recovery of the out-of-plane displacement resulted in concrete crushing in the inner face at the section with maximum out-of-plane deformation, and the out-of-plane displacement increased at Point *e*. This concrete crushing was discussed in Section0 and was depicted in Figure 8.3.

In order to monitor the variations of strain throughout the wall panel and along the wall thickness at different stages of loading, in addition to the potentiometers that were welded to the reinforcement, reinforcement strain gauges and linear potentiometers attached to the concrete core were also used. The configuration of strain gauges attached to both layers of reinforcement and the linear potentiometers attached to both faces of the wall are indicated in Figure 8.11 and Figure 8.12, respectively.

The strain measurements captured using the instrumentation described above are compared in Figure 8.13 for the west boundary region and on the south face where a combination of all types of measurements was available. Figure 8.13a compares the reinforcement strain along the height of the west boundary extreme end reinforcement that was captured using strain gauges with the average strain obtained by the potentiometers that were attached to the reinforcement using welding (denoted as Pot). Figure 8.13b displays the average strain calculated by vertical displacement measurements of the potentiometers shown in Figure 8.12 for the west boundary (g3-g7). Due to limitations of the strain gauges, the strain captured by these instruments is limited to 0.02. As can be seen in Figure 8.13a, the strain

gauge measurements are in good agreement with the data captured by the potentiometers attached to the reinforcement for all drift levels indicating reliability of the measurements. The average strain captured by the potentiometers that were attached to the concrete core (Figure 8.13b) provides a good matching with the reinforcement strain measurements which is a sign of minimal bond-slip between concrete and reinforcement in this specimen until 3.0% drift level.

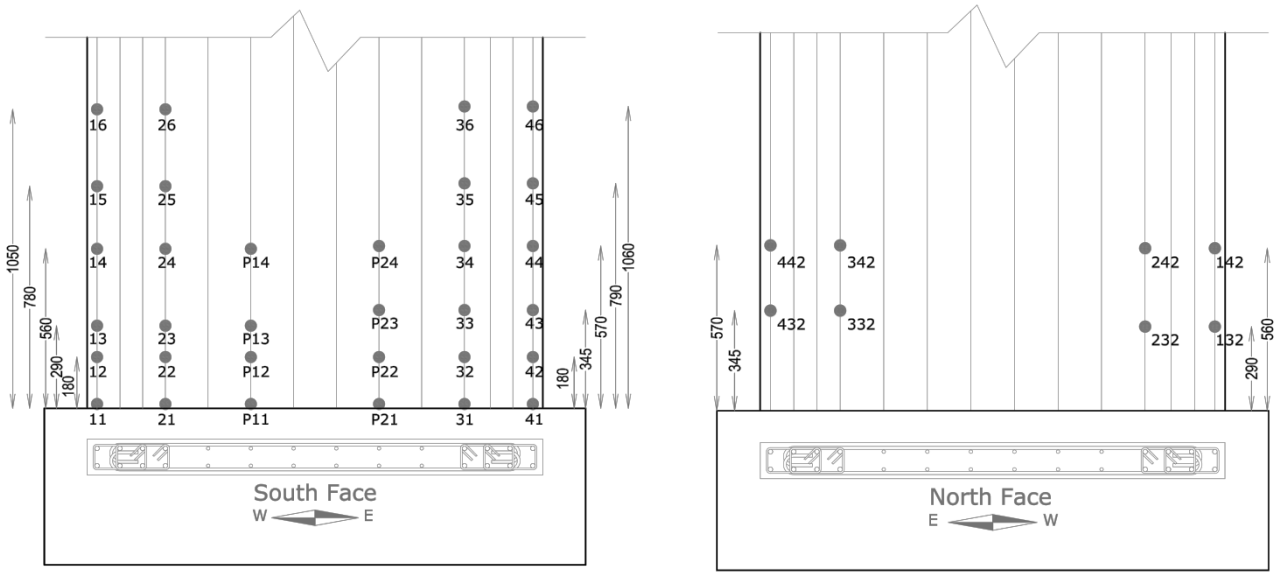

(a) (b)

Figure 8.11: Strain gauges of the longitudinal reinforcement: (a) south face; (b) north face

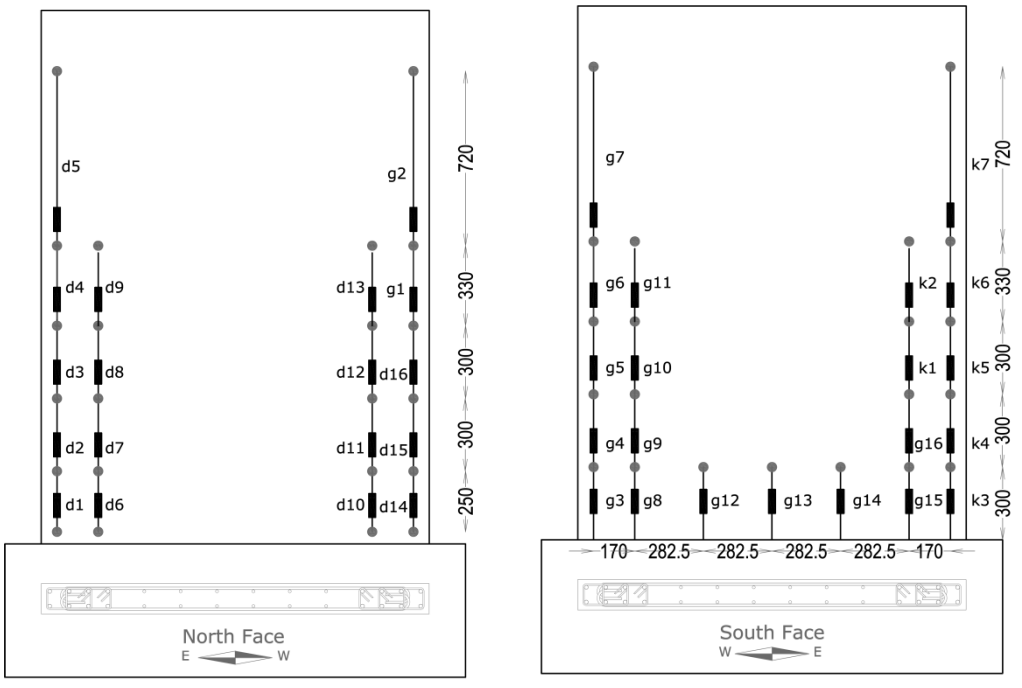

(a) (b)

Figure 8.12: Linear potentiometers used for average strain measurements: (a) north face; (b) south face

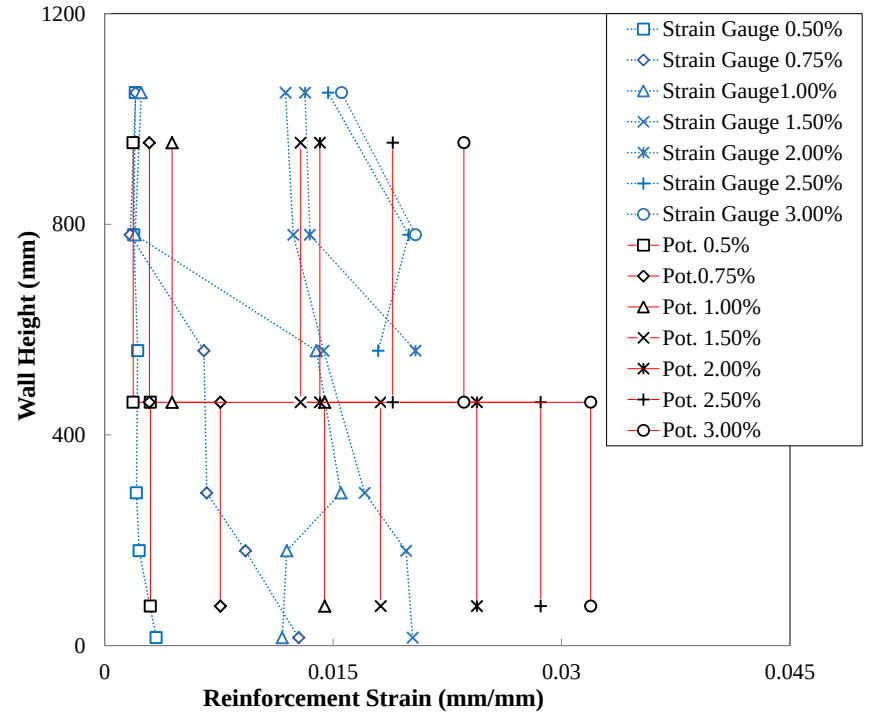

(a)

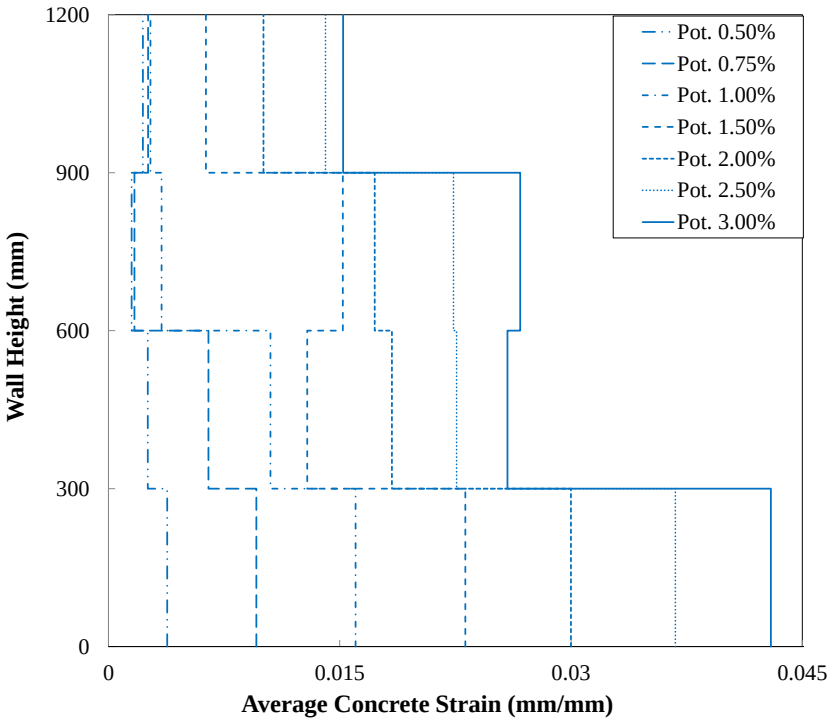

(b)

Figure 8.13: Strain profiles along the wall height, west boundary, south face: (a) reinforcement; (b) concrete

The strain measurements at both layers of the reinforcement, particularly at the section close to the elevation where the maximum out-of-plane displacement was recorded, can be used to scrutinize the initiation of this mode of wall response under in-plane concentric loading. Figure 8.14 indicates the strain history of the west boundary extreme end

reinforcement at both layers and at the elevation of 560 mm which is fairly close to the location of the maximum out-of-plane displacement (m7, Figure 8.5b). The development of the maximum out-of-plane displacement corresponding to each drift level is also plotted for better illustration of the relationship between reinforcement strain history and out-of-plane displacement. Prior to development of yielding in reinforcement at this elevation (0.5% drift, Figure 8.14a), the two strain gauges recorded almost identical measurements for both of the longitudinal bars. After the bars yielded at the elevation of the attached strain gauges (0.75% drift, Figure 8.14b), the bars located at the same location along the wall length and at two different layers along the wall thickness did not necessarily exhibit exactly alike strain histories as the bar yielding generated further sensitivity in the reinforcement to the unavoidable eccentricities across the wall thickness. From this drift level onwards, the points corresponding to the elastic strain recovery of the reinforcement are denoted as "*b*". The bars reached different levels of maximum strain at Point *a* and followed the unloading and reloading paths with different strain values. However, as the strains reached negative values (i.e. compression) soon after the elastic strain recovery, which is a sign of crack closure, the section recovered its stiffness and no out-of-plane displacement was recorded.

At 1.0% drift level (Figure 8.14c), the bars exhibited different maximum strain values at Point *a* but the difference became less in the unloading and reloading stages. Although the drift level had increased by only 0.25%, the maximum strains reached quite larger values when compared to 0.75% drift level and the residual strain at the point of elastic strain recovery was large enough to induce a slight out-of-plane displacement before the crack closure initiated. The larger tensile strains as well as different values of maximum strains of the bars located at two different positions along the thickness at 1.5% drift cycle resulted in a long distance between the elastic strain recovery and crack closure in terms of residual strain and caused initiation and development of a considerable value of out-of-plane displacement after Point *b*.

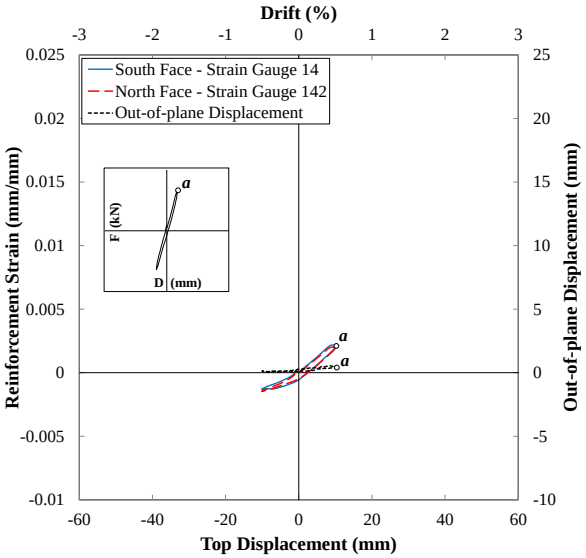

(a) 0.5% drift level

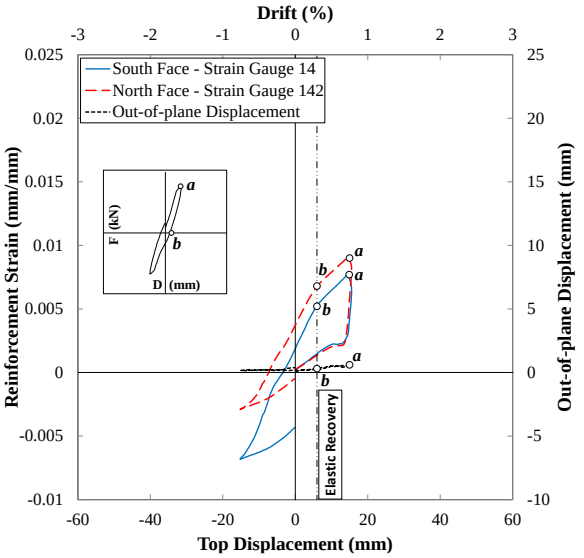

(b) 0.75% drift level

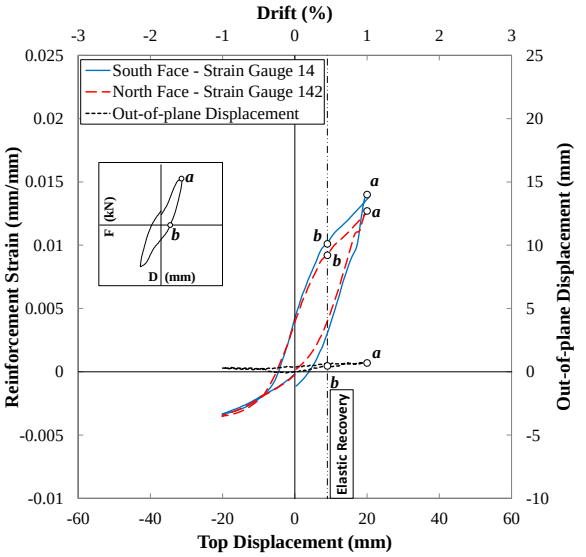

(c) 1.0% drift level

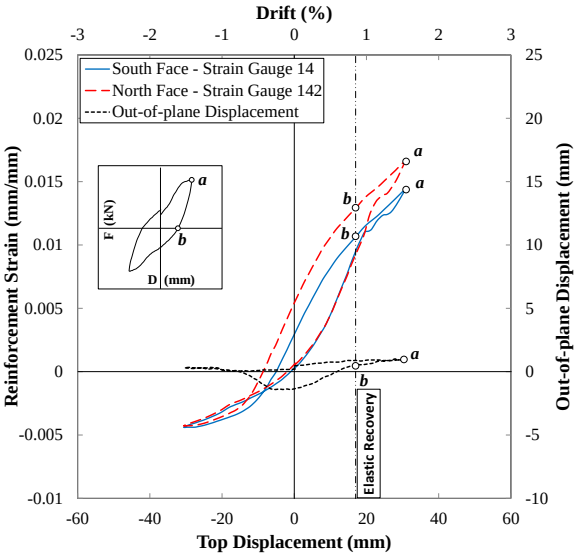

(d) 1.5% drift level

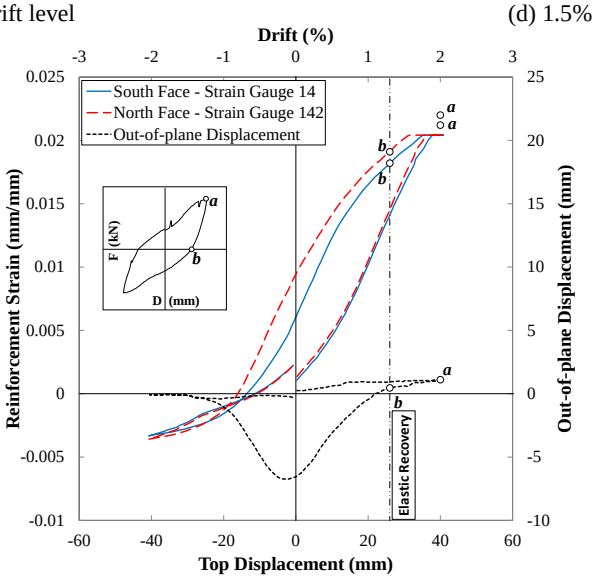

(e) 2.0% drift level

Figure 8.14: Response of the west boundary extreme end reinforcement at 560 mm from the base

A similar trend was observed at 2.0% drift level (Figure 8.14e). At this drift level, the maximum tensile strain was not recorded after reaching 0.02 which seems to be the maximum level of measurable strain by this type of strain gauges. However, the unloading and reloading paths were captured and the maximum tensile strains were estimated using the trend of the strain-top displacement curves. With higher reinforcement strains and consequently higher residual strains, the out-of-plane displacement reached a higher value at this drift level and recovered as the crack closure (compressive reinforcement strain) occurred and the two strain graphs representing the two different layers of reinforcement converged.

The measurements of the strain gauges were valid up to 2.0% drift level after which higher reinforcement strain caused them to fail to function properly. As can be seen in Figure 8.14, the out-of-plane displacement originated from higher tensile strains generated in the reinforcement as well as the difference in these strains across the wall thickness, particularly after the elastic strain recovery.

In order to scrutinize the variation of strain along the thickness of the boundary regions at different stages of loading, the average strain profiles along the height of the boundary regions and on both faces of the specimen are plotted in Figure 8.15 and Figure 8.16. These average strains have been calculated using the measurements of the potentiometers attached to both faces of the boundary regions as shown in Figure 8.12. These instruments were anchored deep enough into the concrete to measure the displacement values of concrete at the same position as the reinforcement along the thickness. However, they had to be positioned slightly far from the extreme end reinforcement along the wall length and may not represent the concrete response at the same level along the length as the extreme end reinforcement. The average strain measurements are plotted at mid-height of the corresponding instrument in Figure 8.15and Figure 8.16 with linear variation between two readings to facilitate illustration of the strain variations at different drift levels in a single figure. Since these potentiometers were installed at both faces of the specimen and covered a considerable area of the boundary regions, their measurements are used to investigate the relationship between development of out-of-plane deformation and the growth of vertical strain in the boundary regions. The strain values represented post-yielding stage (0.75% drift onwards) state of the specimen due to the variations of strains (as discussed above) that were observed in this state.

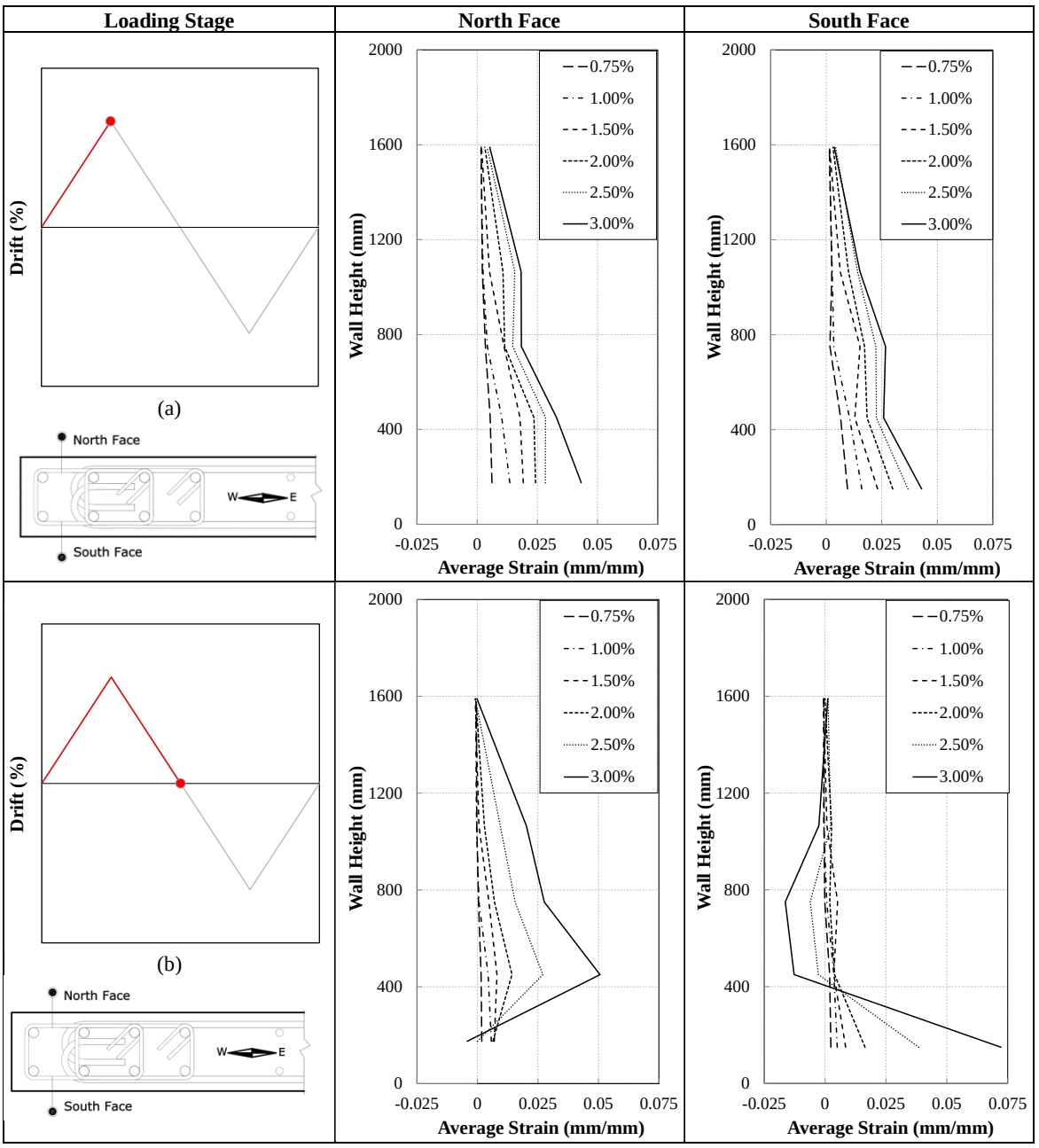

Figure 8.15: Average strain along the height and on both faces of the west boundary region: (a) peak positive drift levels; (b) zero drift levels following the peak positive drift levels

Figure 8.15a indicates development of tensile strain along the west boundary region at different drift levels of lateral loading in the positive (east) direction when the west boundary region is subject to tensile stresses and Figure 8.15b displays the strain values on both faces of the west boundary region when the loading direction has reversed and the specimen has reached the zero displacement. The maximum out-of-plane displacement in a specific boundary region (as shown in Figure 8.1b) increased when the specimen approached zero drift level after large tensile strains had developed at the peak drift levels. As can be seen in Figure 8.15a, the maximum tensile strains along the height of the north

and south faces of the west boundary region are different. This difference is very small at 0.75% drift level, grows with increase of the drift level and the number of cycles per drift level (not shown in the graphs) and is noticeable at 1.5% drift level. This asymmetric tensile vertical strain along the thickness at 1.5% could play its part on eccentricity of the wall section during unloading and reloading stages resulting in initiation of the out-of-plane deformation.

Figure 8.15b indicates the strain values when the specimen has reached zero displacement while unloading from the peak positive drift levels. The initiation and development of out-of-plane displacement at 1.5% and the subsequent drift levels resulted in great variations in strain values along the wall thickness, particularly at 2.5% and 3.0% drift levels, where the extent of out-of-plane displacement caused the strain values of the south face to become negative around the section with maximum out-of-plane displacement along the height. However, this negative strain cannot be a sign of crack closure as the instruments, being unavoidably positioned slightly far from the wall surface, measured larger tensile and compressive strains than the wall surface strains when the corresponding boundary region was exhibiting out-of-plane deformations.

The same trend was observed in the east boundary region when the specimen was loaded in the negative direction. There was a slight difference in maximum tensile strain profile between the two faces of the specimen in the east boundary region (Figure 8.16a) as well which could be a potential source of eccentricity particularly after the elastic strain recovery. The initiation and development of out-of-plane deformations resulted in significant variation of strain along the wall thickness at 0.0% drift level (Figure 8.16b).

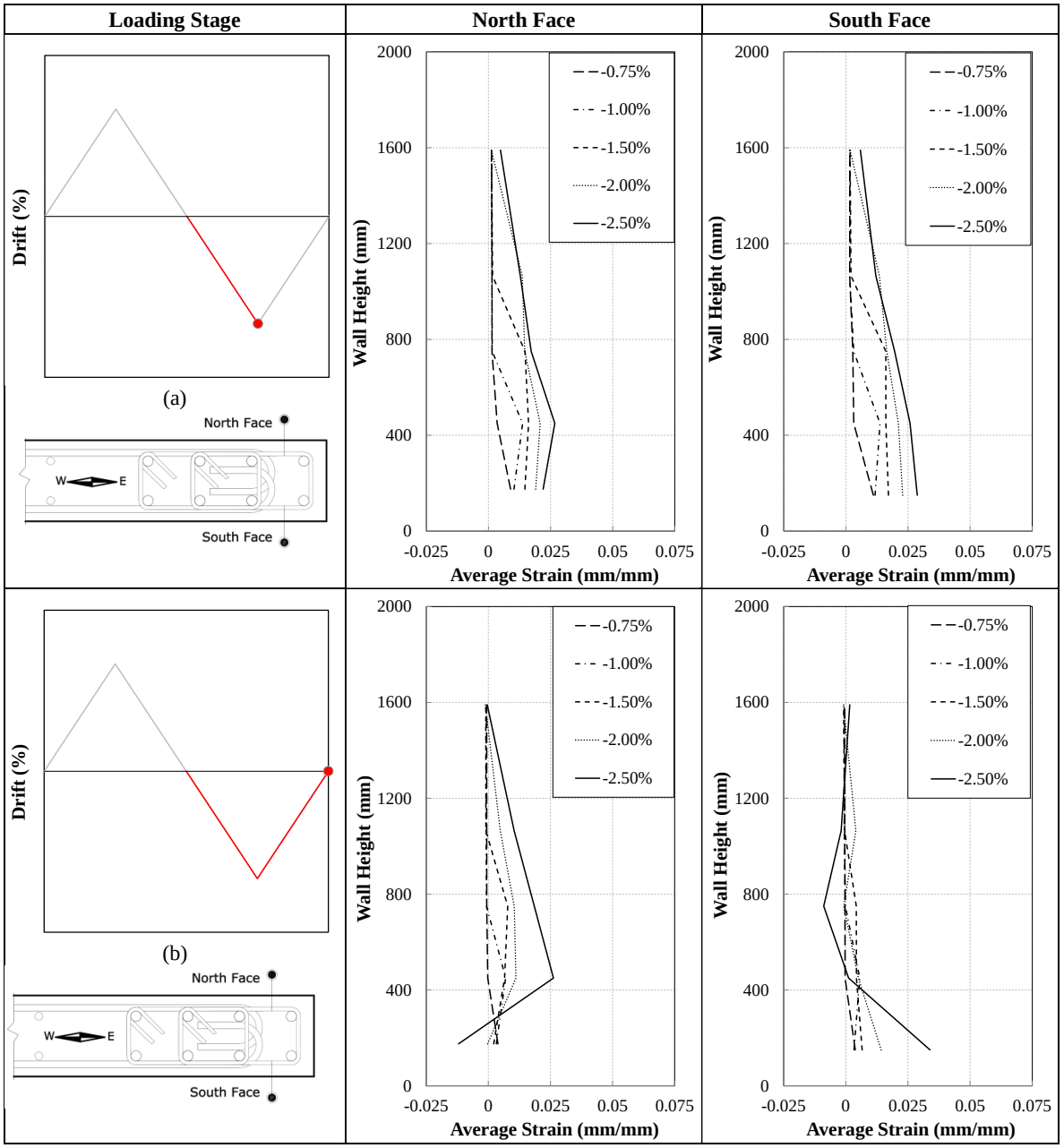

Figure 8.16: Average strain along the height and on both faces of the east boundary region: (a) peak positive drift levels; (b) zero drift levels following the peak positive drift levels

8.3 ANALYTICAL PREDICTIONS VS EXPERIMENTAL OBSERVATIONS

In this section, the analytical models proposed in the literature for predicting out-of-plane response of rectangular walls are verified against the experimental results presented in this study. These analytical models are described in Section 2.2.3.2.

Figure 8.17 and Figure 8.18 display the maximum out-of-plane displacement measured at boundary zones, as normalized by the wall thickness ($\xi = \delta/b$), versus the in-plane top displacement of the specimen. As can be seen in Figure 8.17, the out-of-plane deformation

in the west boundary region increased around 0.0% drift level at different cycles and recovered up to a certain level until 3.0% drift level, where instead of recovering, the out-of-plane deformation increased steadily after reaching the maximum value and resulted in instability of the specimen. The normalized out-of-plane displacement prior to instability of the specimen was measured as $\xi = -0.57$ which is slightly more than the upper bound limit of instability proposed by Paulay and Priestley (1993) which corresponds to $\xi = -0.5$ (when out-of-plane displacement is equal to half of the wall thickness).

Figure 8.18 shows the response of the east boundary region in terms of development of out-of-plane deformation at different stages of loading. This boundary region exhibited a similar trend for initiation, increase and recovery of out-of-plane deformation as the west boundary region, remaining residual out-of-plane deformations. This residual out-of-plane deformation was considerable at 2.5% drift cycles. When the specimen was being loaded towards 3.0% drift level after unloading from the second -2.5% drift level, the out-of-plane deformation reached a normalized value of $\xi = -0.35$, decreased to $\xi = -0.18$ (2.5% drift) following initiation of crack closure. However, unlike in the previous cycles and in the west boundary region, the out-of-plane deformation here increased again to $\xi = -0.23$ at 3.0% drift level. As also depicted in Figure 8.3c and Figure 8.3d, the concrete crushing was observed at the inner face of the section. Since concrete contributed to the load carrying capacity of the specimen after the crack closure at inner face, leading to recovery of the out-of-plane displacement, this concrete crushing resulted in changing the trend and increasing the out-of-plane deformation. This point corresponds to Point *e* in Figure 2.10, which was considered as the limit state for calculation of the out-of-plane displacement by Paulay and Priestley (1993) and Chai and Elayer (1999). As noted above, this limit state was assumed to be fairly close to the out-of-plane displacement at first crack closure. However, as the specimen was unloaded after reaching this point, the increased out-of-plane deformation due to the concrete crushing could not go beyond 66% of the out-of-plane displacement at first crack closure. Also, the concrete crushing started when the out-of-plane deformation (which can be denoted as the residual out-of-plane deformation) was about half of the maximum value of out-of-plane deformation at first crack closure. If the specimen had been loaded further in this direction, the concrete crushing would have resulted in steady increase of the out-of-plane deformation and instability of the specimen. Only about half of the residual out-of-plane displacement created in the east boundary

region recovered when the specimen was unloaded from 3.0% drift level and was being reloaded in the opposite direction before the global instability of the specimen occurred.

Using Equation 2.8, the stability criterion proposed by Paulay and Priestley (1993) and used by Chai and Elayer (1999) has been calculated for the specimen as $\xi = 0.15$ which is a conservative estimation of the maximum out-of-plane deformation when compared to the experimental observations at both boundary regions in Figure 8.17 and Figure 8.18. However, as shown in these figures, before reaching this criterion, the out-of-plane displacement could be recovered to a great extent, and the relatively considerable residual out-of-plane displacements were created when the maximum out-of-plane displacement exceeded this criterion that could have resulted in instability of the specimen if the loading direction had not changed when reaching the peak displacements. This residual out-of-plane displacement could have been created due to the initiation of concrete crushing in the concave face of the section exhibiting maximum out-of-plane deformation, which is the limit state used for derivation of the stability criterion.

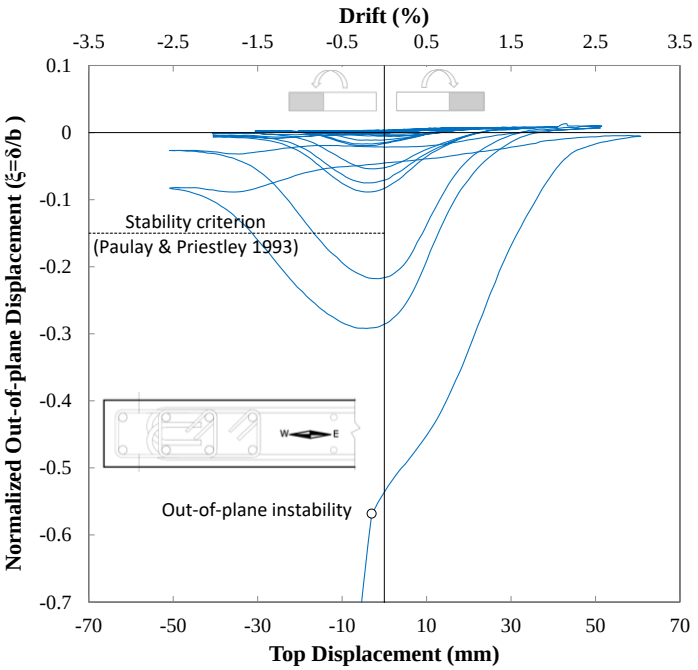

Figure 8.17: In-plane top displacement versus normalized maximum out-of-plane displacement of the west boundary region (instrument m7, Figure 8.5b)

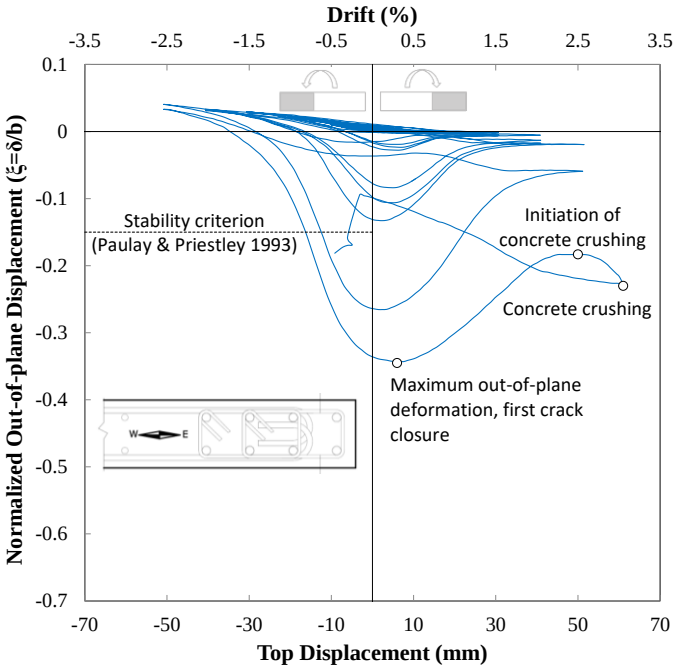

Figure 8.18: In-plane top displacement versus normalized maximum out-of-plane displacement of the east boundary region (instrument m14, Figure 8.5b)

Paulay and Priestley (1993) and Chai and Elayer (1999) proposed Equation 2.1 and Equation 2.13, respectively, as relationships between the maximum tensile strain ε_{sm} over l_o and the normalized out-of-plane displacement ξ. The plastic hinge length, l_p (given by Equation 8.1), was postulated to be a reasonable approximation of the potential length of the wall over which out-of-plane buckling may occur, l_o.

$$l_p = 0.2l_w + 0.044h_w \qquad \textbf{8.1}$$

Where

l_w= horizontal length of the wall section

h_w= full height of the cantilever wall

The plastic hinge length calculated for the specimen using Equation 8.1 is 584 mm resulting in $\varepsilon_{sm} = 0.042$, and $\varepsilon_{sm} = 0.041$ from Equation 2.1 and Equation 2.13, respectively. The two approaches give fairly close and considerably large values for the maximum tensile strain corresponding to the stability criterion calculated using Equation 2.8.

Using the experimental measurements, the relationship between the plastic response of the wall boundary region and the extent of the wall height effectively involved in formation of the out-of-plane instability can be investigated. This height is one of the parameters that is used for calculation of the maximum tensile strain of the reinforcement (Paulay and

Priestley 1993, Chai and Elayer 1999). For this purpose the strain gauge measurements and the average strain profiles of the boundary regions along the wall height are compared with the corresponding out-of-plane displacement profile at 1.5% drift level (Figure 8.19, Figure 8.20).

Figure 8.19a displays the out-of-plane displacement profile of the west boundary region. The elevation corresponding to the maximum out-of-plane deformation is denoted as "OOP max", and the height of the plastic hinge length calculated using Equation 8.1 as well as the visual buckling length of the wall are displayed as l_p and l_o, respectively. The strain gauge measurements along the height of this boundary region as well as the average concrete strain (measured using the instruments shown in Figure 8.12) are plotted for post-yielding drift levels and up to 1.5% drift level (Figure 8.19b and Figure 8.19c). During the 1.5% drift cycle, the initial out-of-plane deformation was observed at both boundary zones. As can be seen in Figure 8.19b, during 0.75% and 1.0% drift levels, the plasticity has developed along a distance from the base to 800 mm from the base. The 0.75% drift level is the stage where overall yielding of the specimen has just taken place. The strain variation at this stage indicates yielding up to the height of about 1100 mm from the base. During the following drift level (1.00%), yielding is measured up to the same elevation as the 0.75% drift level. However, the amount of plastic strain developed at the base is considerably larger and is about 6 times the yield strain.

At 1.5% drift level, the amount of yielding in tension is extended up to the height of 1230 mm from the base and the maximum strain at the base is about 10 times the yield strain. When the specimen was unloaded from this stage and was being reloaded in the opposite direction, the out-of-plane deformation started in the west boundary region as shown in Figure 8.19a. This figure shows that the height of the wall effectively involved in formation of the out-of-plane deformation is about 1200 mm from the base (denoted as l_o). It should be noted that this out-of-plane displacement profile is measured using 5 potentiometers uniformly spaced along the height of 1230 mm from the base and cannot represent the exact displacement pattern, particularly above this elevation. The amount of plastic strain developed in the extreme end reinforcement at the height corresponding to the maximum out-of-plane deformation (600 mm from the base) is slightly bigger than six times the yield strain of the reinforcement. The value of l_p, calculated using Equation 8.1, marked in Figure 8.19 is almost 50% of the height of the wall involved in initiation of out-of-plane deformation.

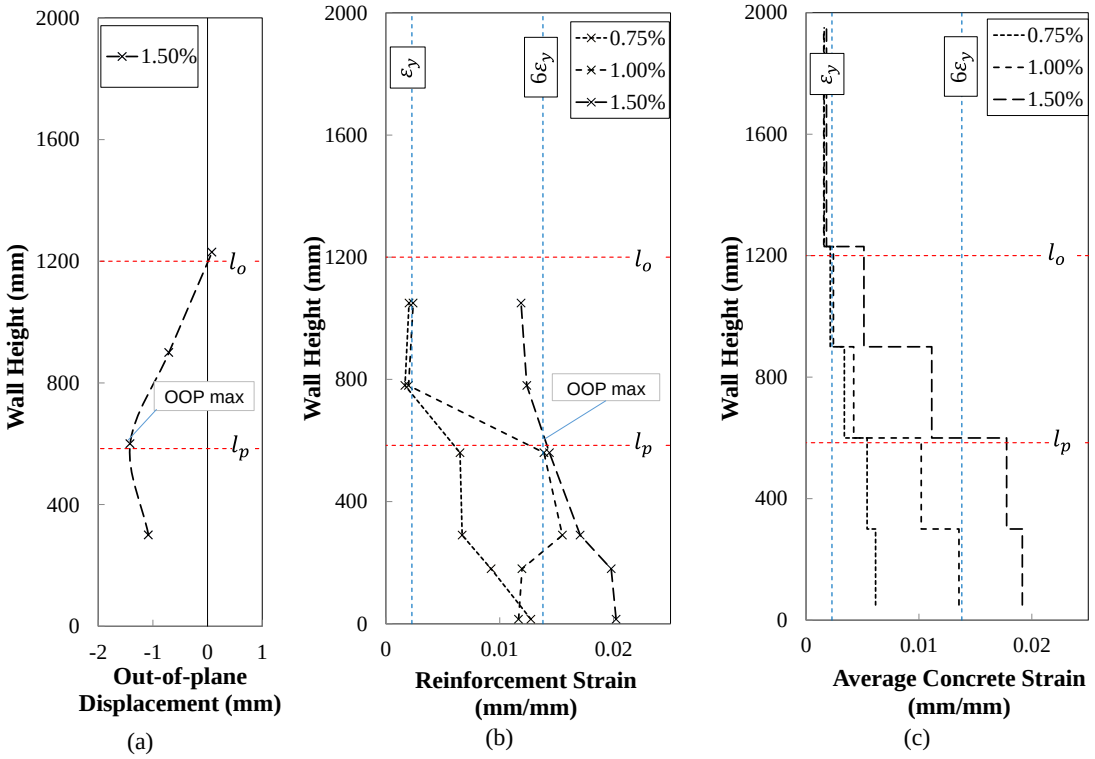

Figure 8.19: Initiation of out-of-plane displacement at the west boundary: (a) out-of-plane displacement profile; (b) reinforcement strain profile; (c) average concrete strain profile

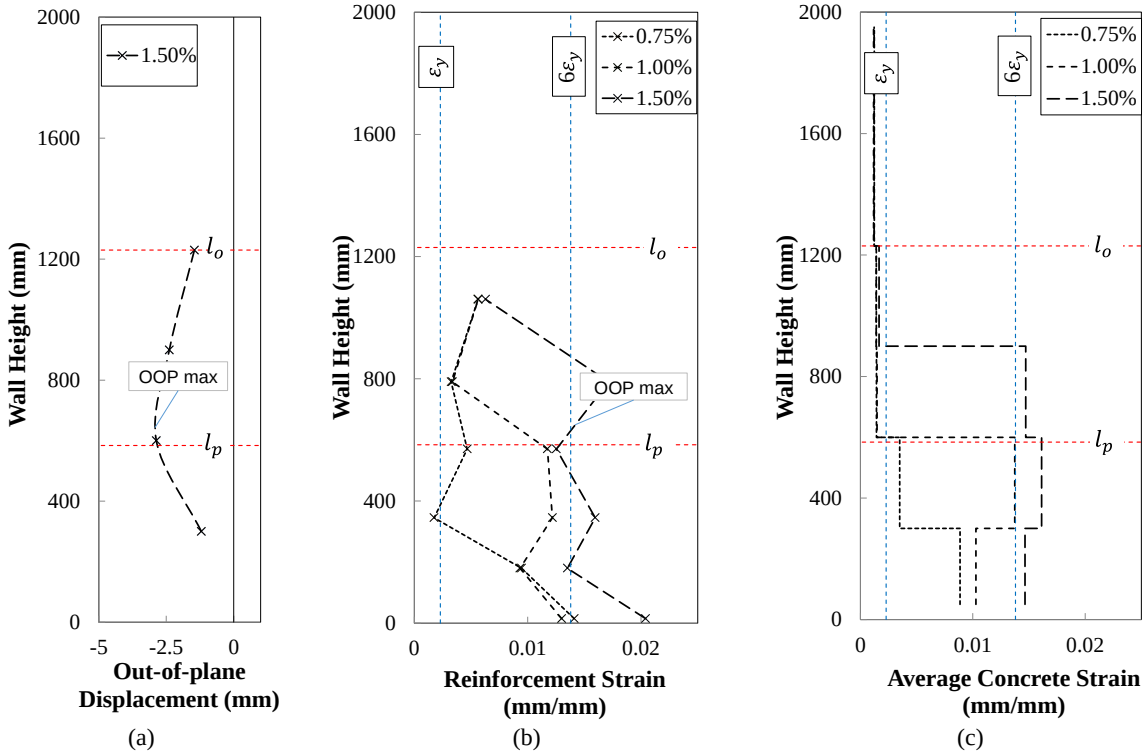

Figure 8.20: Initiation of out-of-plane displacement at the west boundary: (a) out-of-plane displacement profile; (b) reinforcement strain profile; (c) average concrete strain profile

The same measurements have been plotted for the east boundary region in Figure 8.20, which shows the maximum out-of-plane displacement at 650 mm from the base with the

extreme end reinforcement strain slightly higher than six times the yield strain. The buckling height (l_o) is not recognizable for this boundary zone as no instrument was used above the elevation of 1230mm.

Using the value of $l_o = 1200$, captured using the initial out-of-plane displacement profile, the maximum tensile strain is calculated as $\varepsilon_{sm} = 0.01$, and $\varepsilon_{sm} = 0.015$ from Equation 2.1 and Equation 2.13, respectively. According to Figure 8.19b and Figure 8.20b, the maximum tensile strain corresponding to 1.5% drift level and at the location of maximum out-of-plane deformation is 0.0143 which is fairly close to the value predicted by Equation 2.13 (Chai and Elayer 1999). However, these equations were developed for the state where first crack closure followed by concrete crushing, defined as the limit state, happens. The stability criterion derived using Equation 2.8 corresponds to this limit state. Figure 8.21a displays the variation of the normalized out-of-plane displacement along the height of the west boundary in company with this stability criterion. The value of the effective height involved in development of out-of-plane deformation seems to have increased from 1200mm (1.5% drift) to 1230 mm (2.0% drift). However, this length is not easily recognizable at 2.5% and 3.0% drift levels since the out-of-plane displacement was not measured above 1230 mm from the base. Therefore, this height was estimated using the crack formation along the wall height, as displayed in Figure 8.21b. This figure shows the stage where the crack closure at concave face of the out-of-plane deformation profile of the specimen resulted in initiation of out-of-plane deformation recovery at 2.5% drift level. The height of 1430 mm is corresponding to observation of a wide crack that does not follow the same trend as the cracks below this point. This height is approximately two times the height corresponding to the maximum out-of-plane displacement (700mm, Figure 8.21a).

Using the value of $l_o = 1430$, the maximum tensile strain is calculated as $\varepsilon_{sm} = 0.007$, and $\varepsilon_{sm} = 0.013$ from Equation 2.1 and Equation 2.13, respectively. To compare these estimations with the test measurements, the value of the normalized out-of-plane displacement at 2.5% drift level ($\xi = 0.22$, Figure 8.21a) is used as the stability criterion and the corresponding tensile strains are calculated as $\varepsilon_{sm} = 0.01$, and $\varepsilon_{sm} = 0.015$ from Equation 2.1 and Equation 2.13, respectively. These values are around 4.3 and 6.5 times the yield strain, respectively. Figure 8.22 displays the average strain measurements along the height of the west boundary normalized by the yield strain. The normalized strain at 2.5% drift level and at 700 mm from the base is about 7.4. The values predicted by Equation 2.1 and Equation 2.13 are conservative approximations of the maximum tensile strain

corresponding to the out-of-plane displacement at 2.5% drift level, which is fairly close to and slightly higher than the stability criterion developed by Paulay and Priestley (1993). The value of the buckling height at 2.5% drift level, $l_o = 1430$, is about 70% of the wall height.

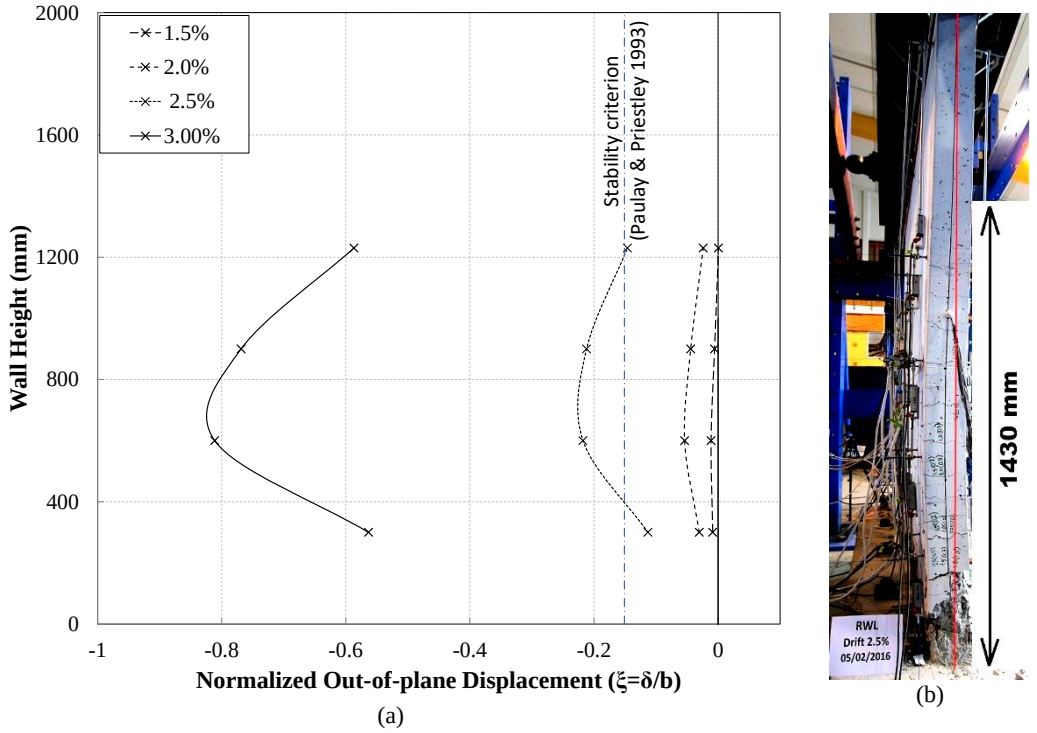

Figure 8.21: (a) Normalized out-of-plane displacement along the height of the west boundary at different drift levels; (b) height of the west boundary involved in formation of out-of-plane deformation at 2.5% drift level

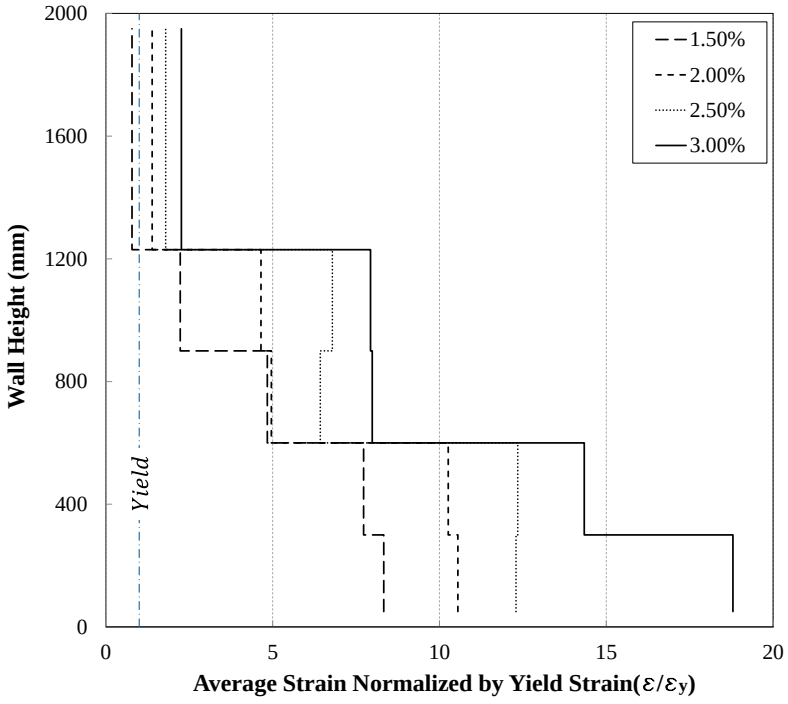

Figure 8.22: Average strain normalized by yield strain along the height of the west boundary

Figure 8.23 indicates the normalized out-of-plane displacement profile of the east boundary zone at all the drift levels at which out-of-plane deformation was observed (1.5, 2.0 and 2.5% drift levels) as well as the corresponding average strain (normalized by yield strain) developed along the height of this boundary zone. This figure shows an increasing trend in the height of the wall involved in formation of buckling with the drift level, as well. This trend seems to have a relationship with extension of the plasticity along the height of the boundary zone at different drift levels. With the maximum normalized out-of-plane displacement of $\xi = 0.27$, at 800 mm from the base, the buckling seems to have extended up to the height of 1600 mm. However, as also shown in Figure 8.23c, the point of inflection starts at about 200 mm from the base for this specimen, leaving an effective buckling height of $l_o = 1400$ mm. The normalized strain reached at the height corresponding to the maximum out-of-plane deformation (calculated by linear interpolation in Figure 8.23b) is about 7.2. The values of $\xi = 0.27$ and $l_o = 1400$ would result in $\varepsilon_{sm} = 0.013$ $(5.7\varepsilon_y)$, and $\varepsilon_{sm} = 0.017$ $(7.6\varepsilon_y)$ from Equation 2.1 and Equation 2.13, respectively.

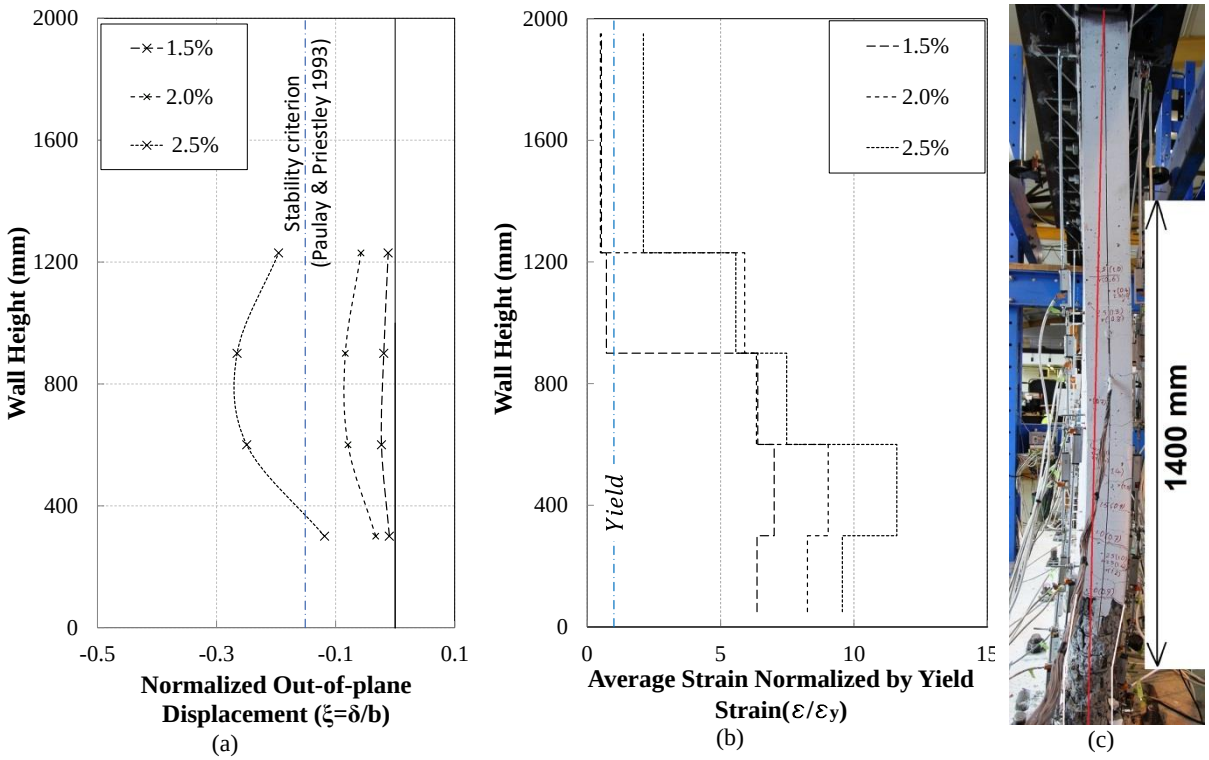

Figure 8.23: (a) Normalized out-of-plane displacement along the height of the east boundary at different drift levels; (b) average strain normalized by yield strain along the height of the east boundary at different drift levels; (c) height of the east boundary involved in formation of out-of-plane deformation at 2.5% drift level

In order to predict the possibility of out-of-plane deformations using the analytical models developed by Paulay and Priestley (1993) and Chai and Elayer (1999), the assumption of

$l_o = l_p$ (the extent of the wall height effectively involved in formation of the out-of-plane instability) needs to be revised. This parameter appears to correlate well with the profile of the maximum tensile strain developed along the height of the boundary zone at a specific drift level. At all drift levels, the averages train profile of the west boundary zone follows a regularly ascending value of strain towards the base of the boundary zone, where the out-of-plane deformation profile starts. However, the average strain profile of the east boundary zone has an increasing trend from the top to 400 mm from the base and decreases slightly at the base. This trend could be the reason for the out-of-plane deformation pattern of the east boundary to have an inflection point at a point slightly above (200 mm from) the base.

The maximum values for the average strain profiles in the west boundary are $8.3\varepsilon_y$, $10.6\varepsilon_y$ and $12.3\varepsilon_y$ for 1.5%, 2.0% and 2.5% drift levels, respectively. For the east boundary, these values are $7.0\varepsilon_y$, $9.0\varepsilon_y$ and $11.6\varepsilon_y$ for 1.5%, 2.0% and 2.5% drift levels, respectively. Also, the height corresponding to the maximum out-of-plane deformation experienced a maximum tensile strain of $6\varepsilon_y$ (1.5% drift) and $7.4\varepsilon_y$ (2.5% drift) at the west boundary and $6\varepsilon_y$ (1.5% drift) and $7.2\varepsilon_y$ (2.5% drift) at the east boundary.

The inconsistency between assumption of $l_o = l_p$ and the experimental measurements of l_o has been observed by Rosso et al. (2015) and Johnson (2010), as well. The value of l_o was identified as 75% of the wall unsupported height for two singly reinforced wall specimens tested by Rosso et al. (2015). Johnson (2010) evaluated the method proposed by Paulay and Priestley (1993) with the test data and observed that the critical buckling thickness calculated using this approach was smaller than the thickness of the tested specimens that had exhibited out-of-plane instability. However, more reasonable values were obtained when the height of first yield was considered as the buckling length instead of the length of plastic hinge. The height of the maximum out-of-plane displacement, let alone the entire length of out-of-plane deformation was more than two times the plastic hinge length calculated using Equation 8.1. It should be noted that the specimens were representing walls of a 6-story building and lateral supports were not provided at story levels against out-of-plane deformations. The values of buckling length observed in this study is about 70% of the unsupported height (story level) and is fairly close to the estimation of 75% of the unsupported height proposed by Rosso et al. (2015). Sensitivity of the equations proposed by Paulay and Priestley (1993) and Chai and Elayer (1999) to the value of the buckling length (l_o) is plotted in Figure 8.24 along with buckling length and corresponding maximum strain measurements of the specimen investigated herein. While

both equations provide a conservative estimation of the maximum tensile strain that could trigger out-of-plane instability of rectangular walls, the equation proposed by Chai and Elayer (1999) (Equation 2.13) gives better predictions for this specimen. In addition to consideration of a sinusoidal curvature distribution by Chai and Elayer (1999) compared to the circular shape idealization of Paulay and Priestley (1993), these two approaches are different in that the maximum tensile strain, ε_{sm}, proposed by Chai and Elayer (1999) (Equation 2.10) includes two more components as the elastic strain recovery, ε_e, and a reloading strain, ε_r, associated with compression yielding of the reinforcement.

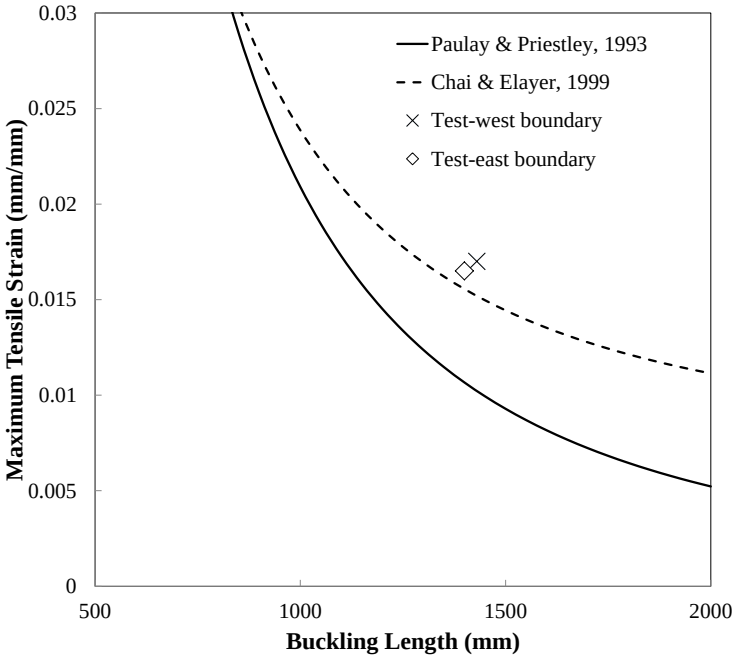

Figure 8.24: Effect of buckling length on prediction of the maximum tensile strain

8.4 CONCLUSIONS

In order to investigate the causes and evolution of out-of-plane deformation and subsequent out-of-plane instability, the experimental response of a rectangular wall specimen that failed in out-of-plane instability mode under concentric in-plane cyclic loading is dissected in great details in this paper. Out-of-plane instability was the main and only failure pattern that was observed in the test, and the wall response was not influenced by other failure patterns such as bar buckling. Therefore, the observations were used to scrutinize the mechanisms leading to out-of-plane instability. The experimental observations regarding initiation, development and recovery of out-of-plane deformations as well as the out-of-plane instability of the specimen were in line with the observations presented in the benchmark research on development of out-plane instability in concrete columns

representing the boundary zones of rectangular walls. The main findings from this study are summarized below:

- The triggering of out-of-plane deformation is governed by the maximum strain reached by the boundary zone reinforcing bars in the previous cycles, which depends on the loading protocol. Larger residual tensile strains can readily lead to development of larger compressive stresses in the reinforcement prior to crack closure during the load reversal. Once the reinforcing bars yield in compression while the cracks are still open, eccentricity is naturally created and deformation of the wall in the out-of-plane direction then becomes inevitable. This out-of-plane deformation may recover to a greater extent if the crack closure in the inner face of the out-of-plane displacement profile happens early enough so as to trigger contribution of concrete to the load carrying capacity of the section; otherwise, it may increase steadily and turn into out-of-plane instability. This phenomenon understandably depends on the level of residual strain in the reinforcement and the wall thickness. The value of out-of-plane deformation, being dependent on the value of reinforcement strain, increases with increase of the applied drift level and the number of cycles per drift level.
- The out-of-plane deformation response of rectangular walls under in-plane cyclic loading comprises of the following stages:
  1) Minimal or no out-of-plane deformation
  2) Development of out-of-plane deformation during unloading and reloading stages of a cyclic loading and its rather complete recovery at peak displacement level in the opposite direction, with negligible residual out-of-plane deformation. This stage is associated with development of an average strain of about $\varepsilon_{sm} = 0.014$ (about $6\varepsilon_y$ for the tested specimen) within a height equivalent to 60% of the unsupported height of the wall.
  3) Development of out-of-plane deformation during unloading and reloading stages of a cyclic loading and its partial recovery at peak displacement level in the opposite direction, resulting in considerable residual out-of-plane deformation. This stage corresponds to an out-of-plane deformation greater than the stability criterion proposed by the analytical models ($\xi > \xi_c$) and is associated with development of an average strain of about $\varepsilon_{sm} = 0.017$ (about $7.2\varepsilon_y$ for the tested specimen) within a height equivalent to 70% of the

unsupported height of the wall. This height (referred to as l_o) is expected to be involved in formation of out-of-plane deformation with the maximum value of out-of-plane deformation occurring roughly at $0.5l_o$. This stage is the limit state for OOP instability as the wall would eventually become unstable if continuously loaded in the same direction and the limits given in literature correspond to this limit.

4) Development of out-of-plane deformation during unloading and reloading stages of a cyclic loading and its steady increase resulting in out-of-plane instability of the wall. This stage corresponds to an out-of-plane deformation greater than the upper bound limit proposed by the analytical models, i.e., half of the wall thickness ($\xi > 0.5b$) and is associated with development of an average strain of about $\varepsilon_{sm} = 0.023$ (about $10\varepsilon_y$ for the tested specimen) within a height equivalent to 70% of the unsupported height of the wall.

- The assumptions made in the analytical models regarding the height of the wall effectively involved in formation of out-of-plane deformations (l_o) need to be revised. The test measurements indicate that the out-of-plane deformation profile, i.e., the elevation corresponding to the maximum out-of-plane deformation and the buckling height correlate well with profile of the plastic strain along the height of the wall. The elevation corresponding to the maximum out-of-plane deformation is approximately equal to the plastic hinge length proposed in literature, and the value of l_o is about twice this length.

8.5 REFERENCES

Chai, Y. and D. Elayer (1999). "Lateral stability of reinforced concrete columns under axial reversed cyclic tension and compression." *ACI Structural Journal* 96(5).

Dashti, F., R. Dhakal and S. Pampanin (2014a). Numerical simulation of shear wall failure mechanisms. 2014 NZSEE Conference, Auckland, New Zealand, New Zealand Society for Earthquake Engineering.

Dashti, F., R. Dhakal and S. Pampanin (2015). Development of out-of-plane instability in rectangular RC structural walls 2015 NZSEE Conference, Rotorua, New Zealand, New Zealand Society for Earthquake Engineering.

Goodsir, W. J. (1985). The design of coupled frame-wall structures for seismic actions, University of Canterbury. PhD.

Johnson, B. (2010). Anchorage detailing effects on lateral deformation components of R/C shear walls, Master Thesis, University of Minnesota.

Oesterle, R. (1976). Earthquake Resistant Structural Walls: Tests of Isolated Walls, Research and Development Construction Technology Laboratories, Portland Cement Association.

Paulay, T. and M. Priestley (1993). "Stability of ductile structural walls." *ACI Structural Journal* 90(4).

Rosso, A., J. Almeida and K. Beyer (2015). "Stability of thin reinforced concrete walls under cyclic loads: state-of-the-art and new experimental findings." *Bulletin of Earthquake Engineering*, 1-30.

Sritharan, S., K. Beyer, R. S. Henry, Y. Chai, M. Kowalsky and D. Bull (2014). "Understanding poor seismic performance of concrete walls and design implications." *Earthquake Spectra* 30(1), 307-334.

9 CONCLUSIONS AND RECOMMENDATIONS

The work presented in this dissertation is focused on enhancing the engineering community's i) ability to predict potential damage to slender reinforced concrete walls, particularly out-of-plane instability failure using a numerical modeling approach, ii) ability to understand the mechanism of out-of-plane instability failure in rectangular RC walls, iii) understanding of the effects of different parameters on out-of-plane instability failure of rectangular walls, iv) understanding of the effects of the assumptions made in the modeling approaches on predicting global and local aspects of wall behavior. Specifically, this included the following tasks:

1. A review of relevant literature to summarize i) observations of wall damage in the 2010 Chile and the 2011 New Zealand earthquakes ii) the modeling approaches used in prediction of wall response, iii) the parameters investigated in experimental studies of other researchers and the research gaps, iv) experimental and analytical investigations of out-of-plane instability failure
2. Validation of a numerical modeling approach using test results of wall specimens with different shear-span ratios and failure patterns.
3. Evaluating capability of the modeling approach in the prediction of out-of-plane instability failure using test results of wall specimens that exhibited this mode of failure, and identifying the governing parameters.
4. Blind prediction of the response of a singly reinforced wall that had exhibited out-of-plane instability failure.
5. Designing a test program for the parametric study of the out-of-plane deformation of rectangular walls using the numerical model.
6. An experimental study on the parameters affecting the out-of-plane deformation of rectangular walls, and comparison of the test observations with the strain variations along the length and height of the wall.
7. Comprehensive analysis of experimental data for the specimen that exhibited out-of-plane instability as the only failure pattern in terms of strain response of the boundary zones at both faces and at different stages of loading, and comparison of the test observations with the assumptions made in the analytical models proposed for prediction of this mode of failure.

8. Verification of the numerical model predictions with the test observations and scrutinizing the pros and cons of the numerical model in prediction of the wall failure patterns.

9.1 CONCLUSIONS

The conclusions resulted from different parts of this research are included at the end of each chapter, and the overall findings are presented herein accompanied by the corresponding objectives presented in Chapter 1.

***Objective 1**: Proposing a numerical model for seismic performance assessment of RC walls including in-plane high localized strains as well as out-of-plane instability of slender walls*

The procedures for numerical modeling of an RC shear wall are classified into two broad groups of microscopic and macroscopic models. Taking the computational efforts as well as the accuracy of global behavior into account, phenomenological macroscopic models which are based on capturing the overall behavior with reasonable accuracy are advantageous over the sophisticated microscopic models. However, macro models generally require plane sections to remain plane along the wall and are not able to capture the nonlinear strain profile which is needed to simulate failure patterns coming from high localized strains.

On the other hand, between the two options of two-dimensional and three-dimensional elements in microscopic modeling approach, use of solid elements requires larger computational effort as well as a better understanding of the behavior of concrete in a three-dimensional state of stress. Using this approach, the response of walls along the length and thickness under bi-directional lateral loads can be investigated. However, a large number of solid elements may be required to model concrete and reinforcement inside a wall accurately, which may require significant computational effort. Therefore, an alternative modeling approach would be a two-dimensional micro model which could incorporate some particular features of three-dimensional elements, particularly variation of strain along the thickness of the element. If the mesh density is sufficient and the large deflection formulation is used, overall wall buckling can be captured by this modeling and analysis approach.

A numerical model composed of nonlinear shell-type finite elements has been proposed and validated for seismic performance prediction and simulation of out-of-plane instability failure in rectangular walls. The plane sections are not enforced to remain plane in this type of model, and the in-plane axial-flexure-shear interaction can be simulated without

requiring any empirical adjustment. The element used in the model (curved shell element available in DIANA finite element analysis program) has integration points along the thickness, unlike flat shell elements in which integration is performed in one plane only. This element is consequently able to capture the variation of strain along the thickness and simulate the deformation in the out-of-plane direction. Also, the computational ability of the program allows performance of bifurcation analysis based on the energy consumed by different possible modes of deformation.

During unloading and reloading of a cracked wall section, the compression is taken by the reinforcement only until the existing cracks in concrete close and concrete contributes to the load carrying capacity. This phenomenon is mainly controlled by the residual strain of the longitudinal reinforcement and is easily captured by the program using its path-dependent cyclic constitutive models. At this stage, the wall section is more likely to deform in a pattern that requires less energy and will deform in the out-of-plane direction if the excessive compressive stress on the reinforcement results in its considerable stiffness reduction (i.e., the reinforcement yields in compression). In this method, there is no need to make use of an artificial eccentricity that introduces a secondary bending moment, and out-of-plane deformation can be captured under pure in-plane loading through numerical computations.

The numerical model could predict the trend of initiation, increase and recovery of out-of-plane deformation as well as the formation of out-of-plane instability that was observed in several wall specimens. Also, the dependency of initiation and amount of the out-of-plane deformation on the maximum tensile strain developed in the longitudinal reinforcement during a specific loading cycle was well confirmed by a set of parametric studies conducted on the models developed for some of these specimens, indicating the validity of the proposed numerical model.

***Objective 2**: Understanding the causes and consequences of out-of-plane instability failure mechanism of the RC structural walls under in-plane loading*

The mechanism of out-of-plane instability failure in rectangular structural walls under in-plane loading and the controlling parameters have been studied by scrutinizing the sequence of events resulting in this mode of failure and using the validated numerical model. On scrutiny of the numerical simulation, it could be confirmed that the triggering of out-of-plane deformation is governed by the maximum strain reached by reinforcement elements in the previous cycles, which depends on the loading protocol. Larger residual

tensile strains can readily lead to the development of larger compressive stresses in the reinforcement prior to crack closure during the load reversal. Once the reinforcing bars yield in compression while the cracks are still open, deformation of the wall in the out-of-plane direction is inevitable. This out-of-plane deformation may recover to a great extent if the crack closure in the inner face of the out-of-plane displacement profile happens early enough so as to trigger contribution of concrete to the load carrying capacity of the section; otherwise, it may increase steadily and turn into out-of-plane instability. This phenomenon understandably depends on the level of residual strain in the reinforcement and the wall thickness.

Based on these findings, the out-of-plane deformation response of rectangular walls under in-plane cyclic loading comprises of the following stages:

1) Minimal or no out-of-plane deformation
2) Development of out-of-plane deformation during unloading and reloading stages of a cyclic loading and its complete recovery at peak displacement level in the opposite direction
3) Development of out-of-plane deformation during unloading and reloading stages of a cyclic loading and its partial recovery at peak displacement level in the opposite direction, resulting in some residual out-of-plane deformation
4) Development of out-of-plane deformation during unloading and reloading stages of a cyclic loading and its steady increase resulting in out-of-plane instability of the wall

The progression of these stages depends on i) axial load, ii) wall length, and iii) cyclic loading protocol, which control the residual strain developed in the longitudinal reinforcing bars, as well as iv) wall thickness, which governs the possibility of timely crack closure in the inner face of the out-of-plane displacement profile (as noted above).

The effect of eccentricity of longitudinal reinforcement with respect to the loading plane on the out-of-plane response of singly reinforced walls was studied as part of a blind prediction practice used for further verification of the model. The eccentricity applied in the model complied with the construction drawings of the test specimen and resulted in the earlier initiation of out-of-plane deformation. However, its effect during the final stages of wall response and formation of out-of-plane instability was not very significant.

Use of a single layer of reinforcement makes structural walls more susceptible to out-of-plane instability failure. This is because, following the development of large tensile residual

strains in the longitudinal reinforcement, a single layer of vertical reinforcement lacks a mechanism to restore stability when the development of yielding in compression occurs in the reinforcement before crack closure can activate contribution of concrete to the load-carrying capacity of the section. In doubly reinforced sections, this instability can be delayed as both layers of longitudinal reinforcement would not undergo identical amounts of tensile and compressive strains due to the inherent eccentricities of the wall section along its thickness, and the second layer of longitudinal reinforcement would restore stability of the section if only one of the layers yielded in compression.

Objective 3: *Collection and generation of experimental data to qualitatively and quantitatively understand the parameters affecting out-of-plane instability failure of rectangular walls*

Although out-of-plane instability failure has been observed in several wall tests, scrutinizing the failure mechanism and the governing parameters has not been the main objective of these research programs. This failure pattern has generally been investigated by conducting experiments on concrete prisms representing boundary zones of rectangular walls. Hence, based on the results of a numerical study, an experimental program was conducted to generate more experimental data on the sequence of events that result in out-of-plane instability of rectangular walls and to investigate the effect of wall length and thickness on this mode of failure.

Although different failure modes were observed during these wall tests, out-of-plane deformation was observed in all the specimens after overall yielding stage and before commencement of the other failure modes. As predicted by the numerical model, the increase in wall thickness and the decrease in wall length resulted in the reduction of the out-of-plane displacement. The failure pattern of one of the specimens was pure out-of-plane instability, and its response was not influenced by other failure patterns such as bar buckling. Therefore, the observations and measurements at different stages of loading for this specimen are used to scrutinize the mechanism of out-of-plane instability, and the controlling parameters are investigated by comparing the test data obtained for all the specimens.

The merits and shortcomings of the proposed numerical model reflecting on its accuracy in predicting different aspects of the specimens' response, particularly the out-of-plane instability mechanism, have been investigated by comparing its predictions with the test observations. The experimental observations regarding initiation, increase, and recovery of

out-of-plane deformation, as well as the out-of-plane instability of the specimen, are in line with the mechanism predicted by the numerical model. However, the evolution of out-of-plane deformation was more gradual in the tests compared to the numerical simulations, which is believed to be due to the inherent construction, material and loading eccentricities that were not included in the model due to their uncertainties and to avoid dependency of the results on some arbitrary values. Also, consideration of cyclic bond deterioration along the length of the longitudinal reinforcement could have resulted in better predictions of the strain variations throughout the height as well as the length of the wall.

The numerical and experimental findings regarding the evolution of out-of-plane instability in rectangular structural walls are also compared with and proved to be in good agreement with observations presented in the benchmark research on the development of out-plane instability in concrete columns representing the boundary zones of rectangular walls.

Moreover, the assumptions made in the analytical models used for predicting this mode of failure were evaluated using observations of the experiments conducted in this research. According to the findings of this study, the height of the wall involved in the formation of the out-of-plane instability is considerably larger than the assumed plastic hinge length and needs to be revised.

The parameters identified to be influential on the out-of-plane instability failure of rectangular RC structural walls (noted in conclusions regarding Objective 2 of the research) need to be considered in the revision of codal provisions related to prevention of this failure pattern, and, qualitatively speaking, a combination of i) increase in wall thickness, ii) decrease of drift demand, and iii) reduction of wall length should be taken into account. It should be noted that axial load is found to have different (and contradictory) effects on the out-of-plane deformation of rectangular walls. An increase in axial load can delay or even prevent the onset of out-of-plane deformations by decreasing the residual tensile strain developed in the reinforcement. However, as out-of-plane deformation invariably increases the eccentricity of an axial load, it can produce additional destabilizing P-Delta moment in the out-of-plane direction which accelerates the subsequent instability. Therefore, further research should be done in this area before incorporation of axial load in the relevant design provisions.

9.2 RECOMMENDATIONS FOR FUTURE RESEARCH

1. The effect of bar buckling on the cyclic response of RC walls needs to be incorporated in the numerical modeling as can potentially suppress the development of out-of-plane deformation and significantly influence the prediction of this failure pattern.
2. The effect of bond-slip needs to be included in the numerical model so that the distribution of vertical strain along the height of the wall can be predicted more accurately.
3. The varying axial load due to restrictions of the floor slab or frame against vertical movement of the concrete walls in a real building should be investigated.
4. The effect of axial load is very crucial in the development of out-of-plane deformations in rectangular walls and needs to be experimentally investigated.
5. More specimens need to be tested to identify clear boundary for the minimum wall thickness preventing the formation of out-of-plane deformation and out-of-plane instability.
6. The effect of loading regime on the development of out-of-plane deformation needs to be investigated.
7. The effect of wall length needs to be further investigated by specimens that change in length only, with the other parameters such as the configuration of boundary region reinforcement being constant.
8. Reinforcement ratio can be considered as a parameter potentially affecting the development of out-of-plane deformation.
9. A comprehensive parametric study needs to be conducted to propose amendments to the current concrete design standards regarding the limitations that rectangular walls need to satisfy in order to be able to resist against out-of-plane instability failure.

APPENDIX A – SPECIMEN DESIGN

The specimen design was conducted according to the New Zealand concrete structures standard (NZS3101 2006) and using the following steps (list of symbols is provided in Table A- 2):

1- *Determine dimensions of prototype, choose a scaling ratio based on the laboratory restrictions and determine the specimen dimensions*

The specimen dimensions were determined based on an iterative approach to satisfy the laboratory limitations (i.e. length, height and loading restrictions), the specified shear-span ratio, and a thickness slightly higher than the corresponding minimum thickness requirement of the standard. A shear-span ratio of 3.0 was considered for the benchmark specimen. As the main objective of the experimental study was to investigate the out-of-plane response of walls, the out-of-plane restraint provided by the floor slab was taken into account. For this purpose, the scale factor of the specimens was chosen such that the specimens could represent the first storey of a multi-storey high wall. The unsupported height of the specimens was considered to be 2.0 m, and the maximum wall length that could be accommodated in the laboratory was 2.0 m. Therefore, the test specimens could be considered as half-scale models of a prototype wall.

With shear-span ratio of 3.0, if a linear (triangular) equivalent lateral load distribution acting at an effective height of $0.75h_4$ was considered, where h_4 is the height of the multi-storey wall, the specimens could represent the first story of a four-storey high wall. Figure A - 1 displays the dimensions of the prototype wall and the specimen as well as the loadings applied on the specimen.

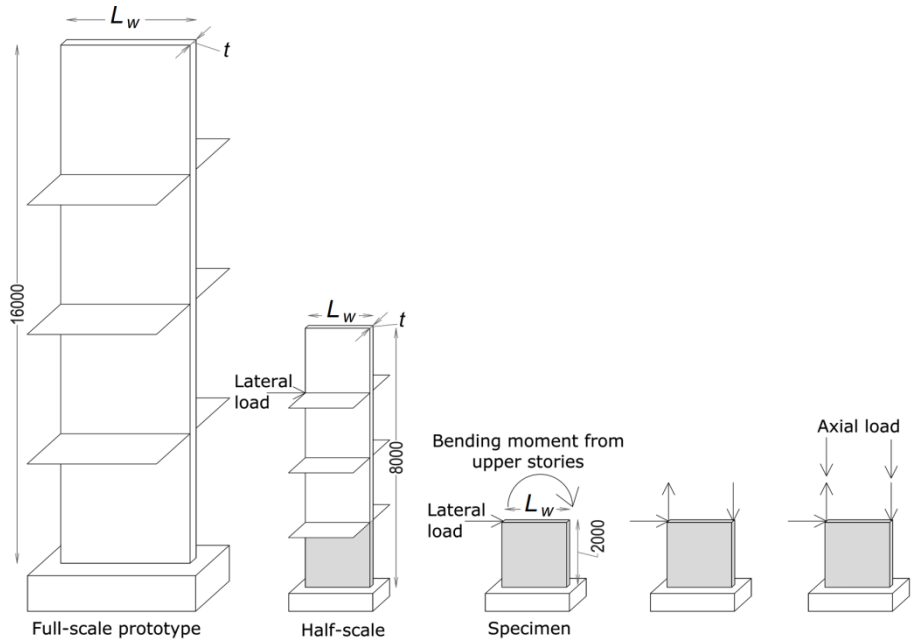

Figure A - 1: Specimen scaling and loading pattern (units in [mm])

A four-specimen test matrix was designed in this research. The benchmark specimen was designed for a given bending moment and all other specimens differed from the benchmark specimen in just one of the parameters of thickness, length and axial load, while satisfying roughly identical moment capacities as the benchmark specimen. Figure A - 2 shows the section specified for the benchmark specimen. The wall thickness was chosen following an iterative design approach such that the thickness is slightly above the minimum thickness requirement of Clause 11.4.2.2 for prevention of out-of-plane instability.

The specified compressive strength of concrete was 35 MPa and the specified yield strength of the reinforcement was 300 MPa. The wall axial load was considered as $0.05f_c'A_g$.

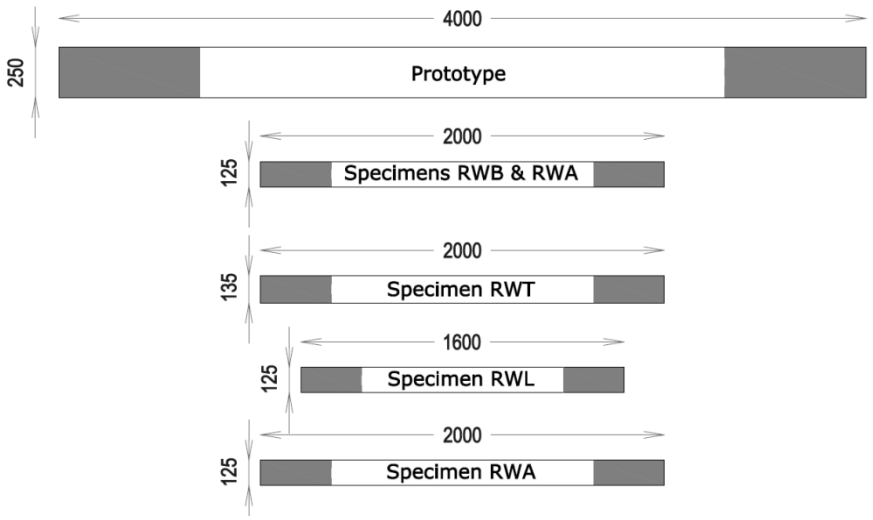

Figure A - 2: Cross section geometry of the prototype and the specimens

2- Determine nominal shear strength of the wall section, V_n, using a simplified method

The nominal shear strength of the wall section was determined according to Clause 11.3.10.3.4, and assuming 0.25% horizontal reinforcement.

$$V_n = A_{cv}(0.17\sqrt{f_c'} + \rho_t f_y)$$

Where, A_{cv} is the shear area, and ρ_t is the horizontal reinforcement ratio. Considering the wall geometry and design material properties, the nominal shear strength, V_n, was estimated as 1405 kN for the prototype wall, and 351 kN for the specimen.

3- Determine shear demand, V_u

The shear demand, $V_u = \phi V_n$ (ϕ=0.75 for shear), was calculated as 1053 kN and 263 kN for the prototype and Specimen RWB sections, respectively. This shear demand was 211 kN for Specimen RWL which was shorter in length.

4- Determine flexural demand, M_u

A linear (triangular) equivalent lateral load distribution acting at an effective height of $0.75h_4$ was considered, where h_4 is the height of the 4-story scaled specimen. The longitudinal reinforcement was designed such that the over-strength moment capacity of the wall sections would meet the shear demand corresponding to Specimen RWL (i.e., for a moment resulting from the minimum shear demand among all the specimens and the effective height of the wall) to ensure the flexure-dominated response of all the specimens.

The over-strength moment capacity of Specimens RWB and RWT was calculated to be 1522 kN.m and the one of Specimen RWL to be 1485 kN.m.

5- Design boundary region and panel longitudinal reinforcement

In order to design the longitudinal reinforcement layout of the walls, an iterative approach was used specifying different dimensions for the boundary regions and various reinforcement configurations to achieve $\phi_{flex} M_n > M_u$ by the section analysis.

6- *Calculate the over-strength bending moment and the corresponding neutral axis position*

The over-strength moment capacity of Specimens RWB and RWT was calculated to be 1522 kN.m and the one of Specimen RWL to be 1485 kN.m. The neutral axis position corresponding to the over-strength moment capacity was calculated by section analysis and

used to check the minimum confinement length requirement of Clause 11.4.6.5. The length of boundary region was consequently specified as 300 mm for Specimen RWL and 350 mm for the other specimens.

Minimum confinement length: $max\begin{Bmatrix} c - 0.7c_c \\ 0.5c \end{Bmatrix} = 210\ mm\ (RWB)$

c: neutral axis depth

$$c_c = \frac{0.1\phi_{ow}L_w}{\lambda} = 125\ mm\ (RWB)$$

$$\lambda = 2.0(DPR)$$

7- Control Dimensions to safeguard against out-of-plane buckling

The out-of-plane buckling of slender walls is addressed in Section 11.4.2 (Dimensional Limitations) of the New Zealand standard (NZS3101 2006). For walls with axial force levels greater than $0.05f_c'A_g$ and for ductile or limited ductile plastic region the thickness in the boundary region of the wall section, extending over the lesser of the plastic hinge length or the full height of the first storey, shall not be less than:

$$b_m = \frac{\alpha_r k_m \beta (A_r + 2)L_w}{1700\sqrt{\xi}} = 107\ mm\ (RWB)$$

where

α_r=1.0 for doubly reinforced walls and 1.25 for singly reinforced walls; and

β = 5 for limited ductile plastic regions

β = 7 for ductile plastic regions

k_m = 1.0, unless it can be shown that for long walls:

$$k_m = \frac{L_n}{(0.25 + 0.055A_r)L_w} < 1.0 = 2.3\ (RWB) \Rightarrow k_m = 1.0$$

and

$$\xi = 0.3 - \frac{\rho_l f_y}{2.5f_c'} > 0.1 = 0.21\ (RWB)$$

where

ρ_l= vertical reinforcement ratio of the boundary region

The minimum thickness, b_m, was calculated as 223 mm for the prototype wall, 107 mm for Specimen RWB (the benchmark specimen) and 99.6 mm for Specimen RWL. The minimum thickness of the prototype was rounded up to the nearest value that would be more appropriate in real practice. Therefore, the wall thickness was conservatively specified as 250 mm for the prototype wall and 125 mm for Specimens RWB, RWL and RWA. Please note that the specimen reinforcement detailing was not exactly equivalent to the scaled down values due to the limitations on bar diameters. Therefore, the minimum boundary region thickness calculated for the benchmark specimen was not exactly half of the one calculated for the prototype wall. All the design process was conducted for the prototype wall and the specimens.

8- Design shear (horizontal) reinforcement

The shear reinforcement was designed to satisfy a shear capacity higher than the shear demand corresponding to the over-strength bending moment capacity of the designed sections. It should be mentioned that the designed walls were analyzed using the numerical modeling approach investigated in this research (Chapters 3,4 and 5) and the effects of flexure-shear interaction were checked.

9- Design transverse reinforcement of the boundary regions

The boundary region transverse reinforcement was designed to satisfy the confinement requirements of Clause 11.4.6.5 as well as the provisions for buckling restraint of the longitudinal reinforcement (Clause 11.4.6.3).

Confinement reinforcement:

Where neutral axis depth > $c_c = 125\ (RWB)$

$\lambda = 2.0(DPR)$

$$A_{sh} = \alpha s_h h'' \frac{A_g^*}{A_c^*}\frac{f_c'}{f_{yh}}\left(\frac{c}{L_w} - 0.07\right) = 87\ mm^2 (RWB)$$

$\Rightarrow Use\ 4\ legs\ of\ R6@55mm = 112\ > 87\ mm^2 \Rightarrow OK$

$\alpha = 0.25(DPR)$

Maximum spacing of confinement reinforcement (DPR): $\min\{6d_b, 0.5t\} = 63\ mm\ (RWB)$

Anti-buckling reinforcement (Within the potential plastic hinge region):

Where $\rho_l > \frac{2}{f_y}$ (DPR), $\quad A_{te} = \frac{\sum A_b f_y}{96 f_{yt}}\frac{s}{d_b} = 22\ mm^2\ (RWB), R6(28\ mm^2) \Rightarrow OK$

$Spacing \leq 6d_b\ (DPR) = 72, s = 55(RWB) \Rightarrow OK$

Figure A - 3 displays the geometry and reinforcement configuration of the specimens, and Table A -1 lists general characteristics of the specimens.

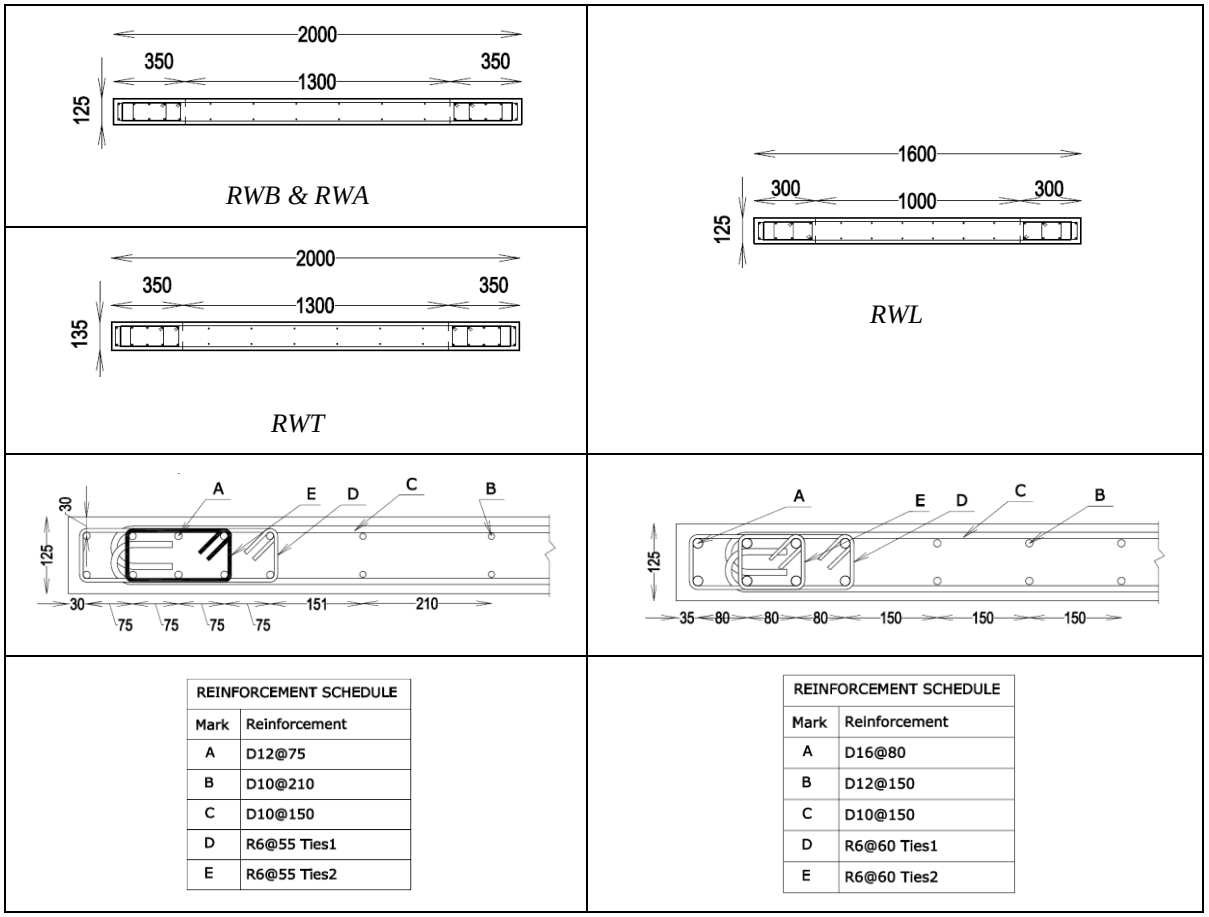

REINFORCEMENT SCHEDULE	
Mark	Reinforcement
A	D12@75
B	D10@210
C	D10@150
D	R6@55 Ties1
E	R6@55 Ties2

REINFORCEMENT SCHEDULE	
Mark	Reinforcement
A	D16@80
B	D12@150
C	D10@150
D	R6@60 Ties1
E	R6@60 Ties2

Figure A - 3: Geometry and reinforcement configuration of the four specimens (D refers to deformed bars, R to plain round bars)

Table A- 1: General characteristics of the specimens

Parameter	Specimen	Length, l_w, mm	Thickness, t_w, mm	Length of boundary elements, mm	Axial load, kN	Longitudinal reinforcement ratio (As/Ac)	
						Boundary region	Web
Benchmark	RWB	2000	125	350	438	0.026	0.0059
Thickness, t_w	RWT	2000	135	350	438	0.024	0.0055
Length, l_w	RWL	1600	125	300	438	0.043	0.012
Axial load	RWA	2000	125	350	657	0.026	0.0059

Table A- 2: List of symbols (NZS3101 2006)

N^*	Design axial load at the ultimate limit state
L_n	The clear vertical distance between floors or other effective horizontal lines of lateral support, or clear span
t , b	Wall thickness
k_e	Effective length factor for Euler buckling
k_{ft}	Effective length factor for flexural torsional buckling
L_w	Horizontal length of wall
b_m	Thickness of boundary region of wall at potential plastic hinge region
h_w	Total height of wall from base to top
A_r	Aspect ratio of wall (h_w/L_w)
f_y	Yield strength of non-prestressed reinforcement
f_{yh}	Yield strength of transverse reinforcement
f_{yt}	Yield strength of shear reinforcement
$\rho_n = \frac{A_t}{A_g}$	Ratio of vertical (longitudinal) wall reinforcement area to gross concrete area of horizontal section
$\rho_l = \frac{A_s}{ts_v}$	The ratio of vertical wall reinforcement area to unit area of horizontal gross concrete section
d_b	Diameter of longitudinal bar
s	Centre-to-centre spacing of shear reinforcement along member
c	Computed distance of neutral axis from the compression edge of the wall section
c_c	A limiting depth for calculation of the special transverse reinforcement
ϕ_{ow}	Over-strength factor
A_c^*	Area of concrete core
A_g^*	Gross area of concrete section
h''	Dimension of concrete core of rectangular section measured perpendicular to the direction of the hoop bars to outside of peripheral hoop
s_h	Centre-to-centre spacing of hoop sets
A_{cv}	Area used to calculate shear area
V_n	Total nominal shear strength
V^*	Design shear force
V_c	Concrete shear strength
V_s	Nominal shear strength provided by shear reinforcement
v_c	Shear stress provided by concrete
s_2	Centre-to-centre spacing of horizontal shear reinforcement

APPENDIX B – SPECIMEN CONSTRUCTION & TEST SETUP PREPARATION

Figure B - 1: Coupler welded to the extreme end bar for attaching LVDTS

Figure B - 2: Strain gauge attachment

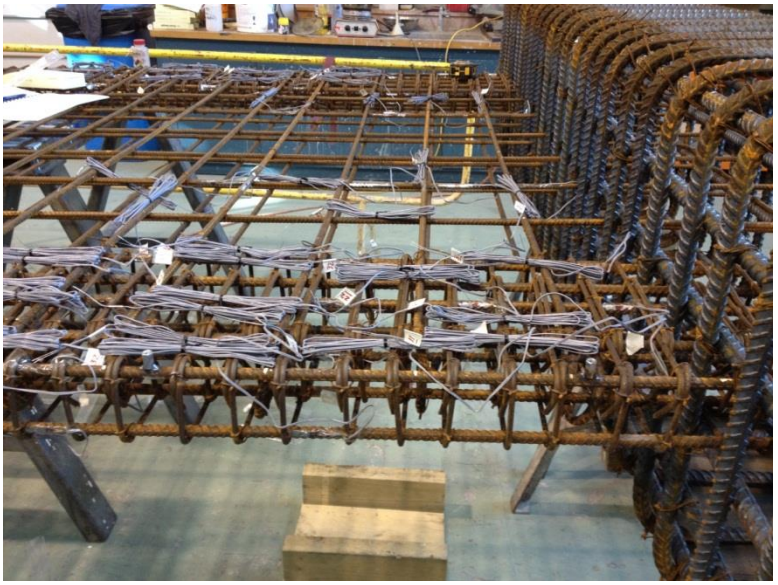

Figure B - 3: Strain gauge attachment

Figure B - 4: Strain gauge wiriing

Figure B - 5: Formwork preparation

Figure B - 6: Specimen caging

Figure B - 7: Concrete casting

Figure B - 8: Leveling the concrete surface

Figure B - 9: Specimen RWB after curing

Figure B - 10: Specimen RWB painted white

Figure B - 11: 6mm threaded rods installed using high-strength epoxy for instrumentation attachment

Figure B - 12: Preparation of connection pieces

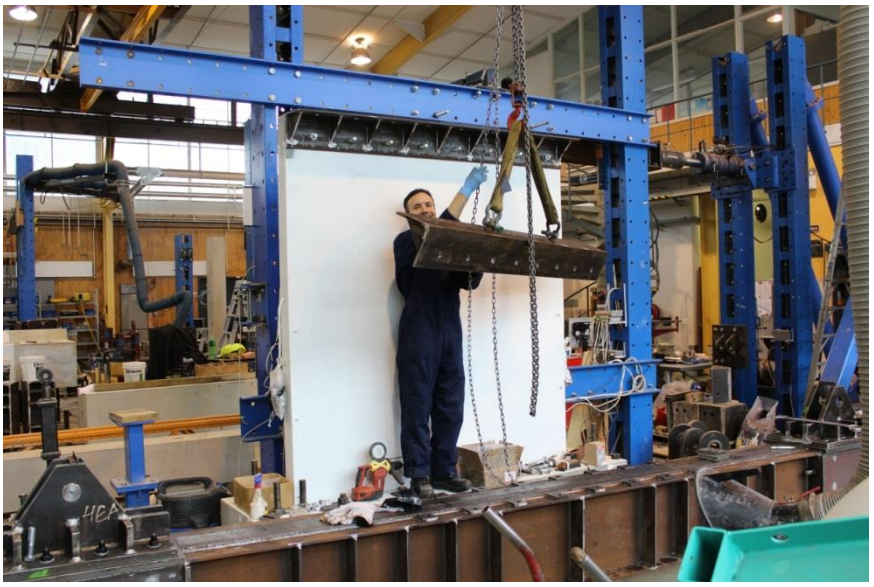

Figure B - 13: Connection assembly

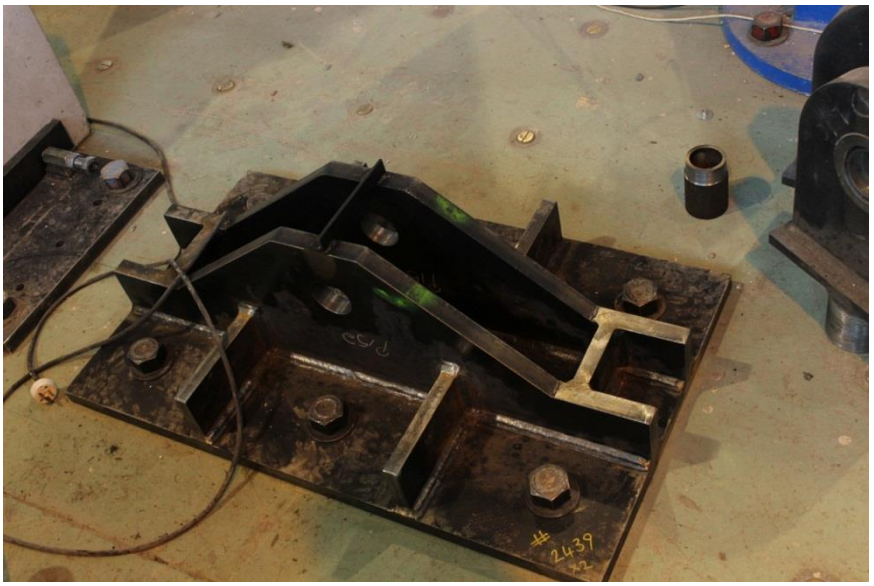

Figure B - 14: Floor fitting in place

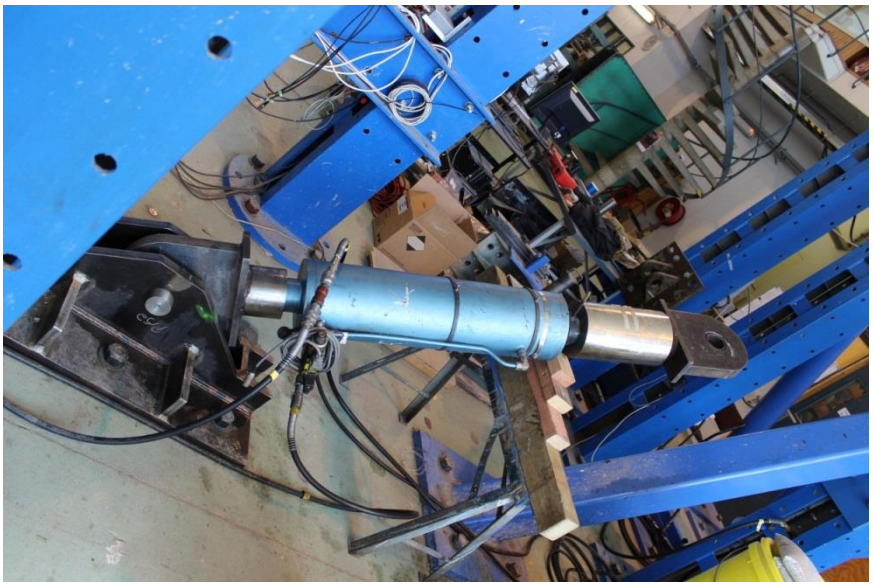

Figure B - 15: Actuator connected to the floor fitting

Figure B - 16: Assembling the loading beam

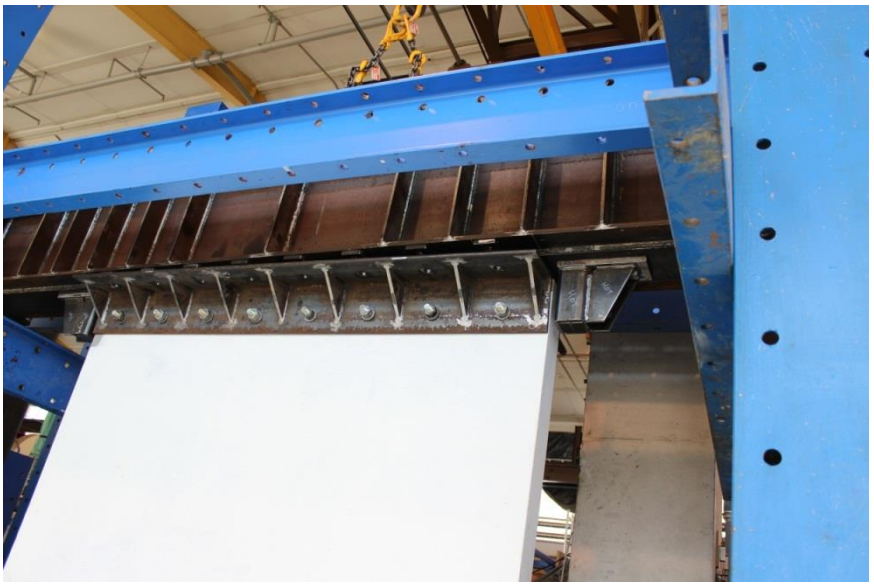

Figure B - 17: Assembling the loading beam

Figure B - 18: Loaing beam on the specimen

Figure B - 19: Filling the gaps with High-strength epoxy

Figure B - 20: Instrumentation attached

Figure B - 21: The actuators connected to the loading beam

APPENDIX C – VISUAL SUPPLEMENT FOR EXPERIMENTAL OBSERVATIONS

This appendix presents crack pattern and failure observations of the specimens. Figure C - 1 to Figure C - 8 compare the crack pattern of Specimens RWB and RWL at different drift levels and within 1230 mm distance from the wall base. Since Specimen RWB became unstable during the second cycle of the 2.00% drift level, the comparison is done up to this drift level. Figure C - 9 presents crack pattern of Specimen RWL at 2.50% and 3.00% drift levels.

Figure C - 10 and Figure C - 11 compare the instability of Specimen RWB with the one of Specimen RWL and Figure C - 12 displays the failure state of Specimen RWT.

CRACK PATTERNS

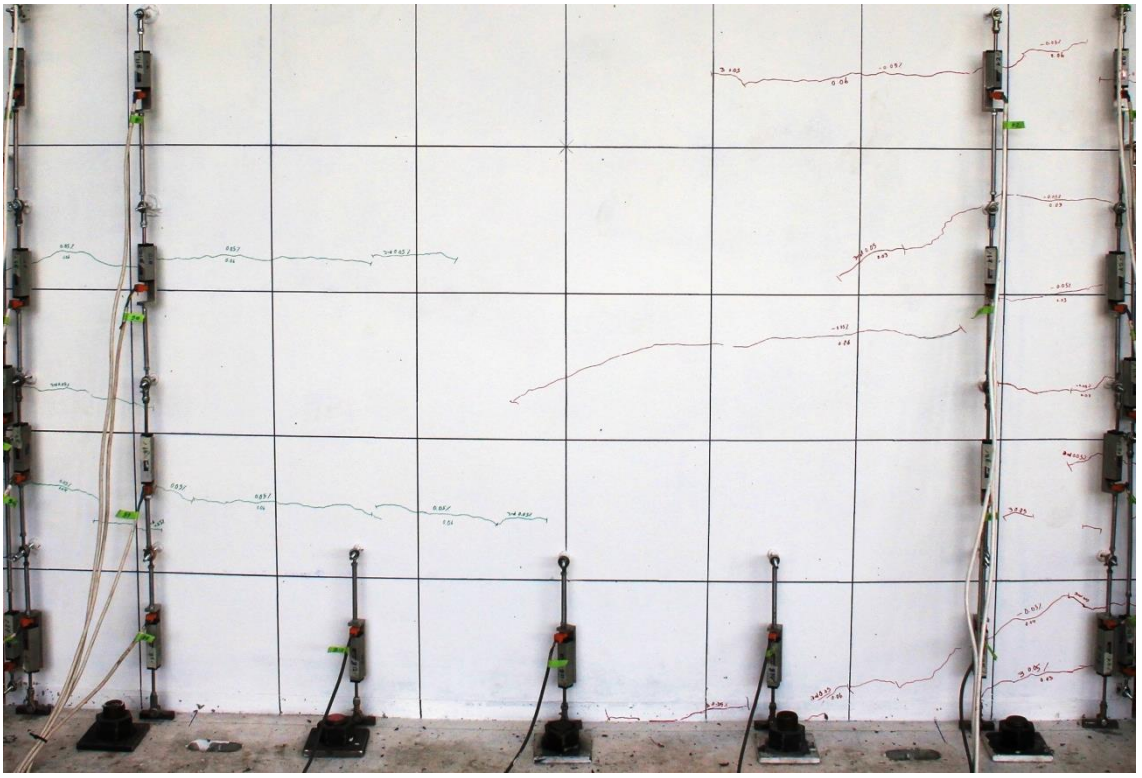

RWB - Grid size: 250x250 mm

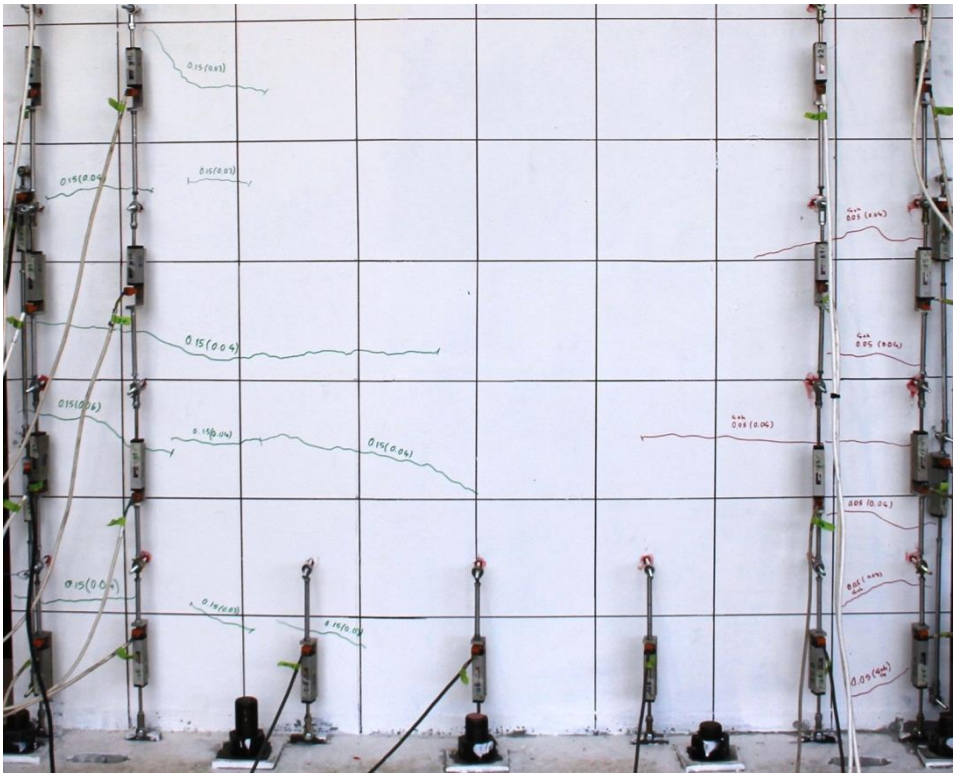

RWL - Grid size: 200x200 mm

Figure C - 1: Crack pattern at 0.05% drift level

RWB - Grid size: 250x250 mm

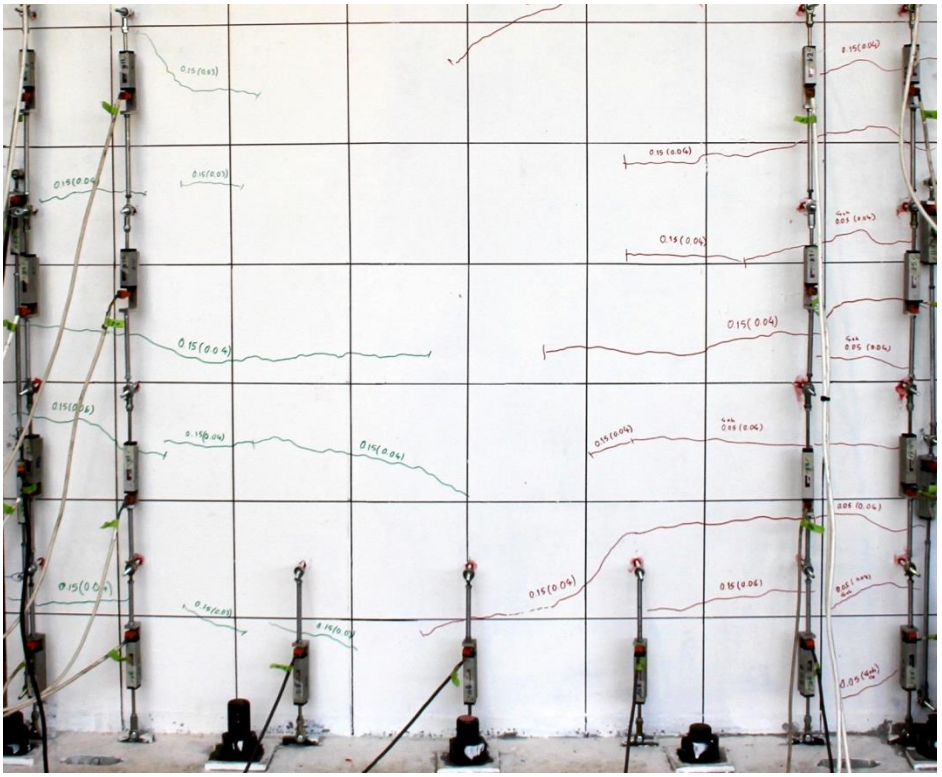

RWL - Grid size: 200x200 mm

Figure C - 2: Crack pattern at 0.15% drift level

RWB - Grid size: 250x250 mm

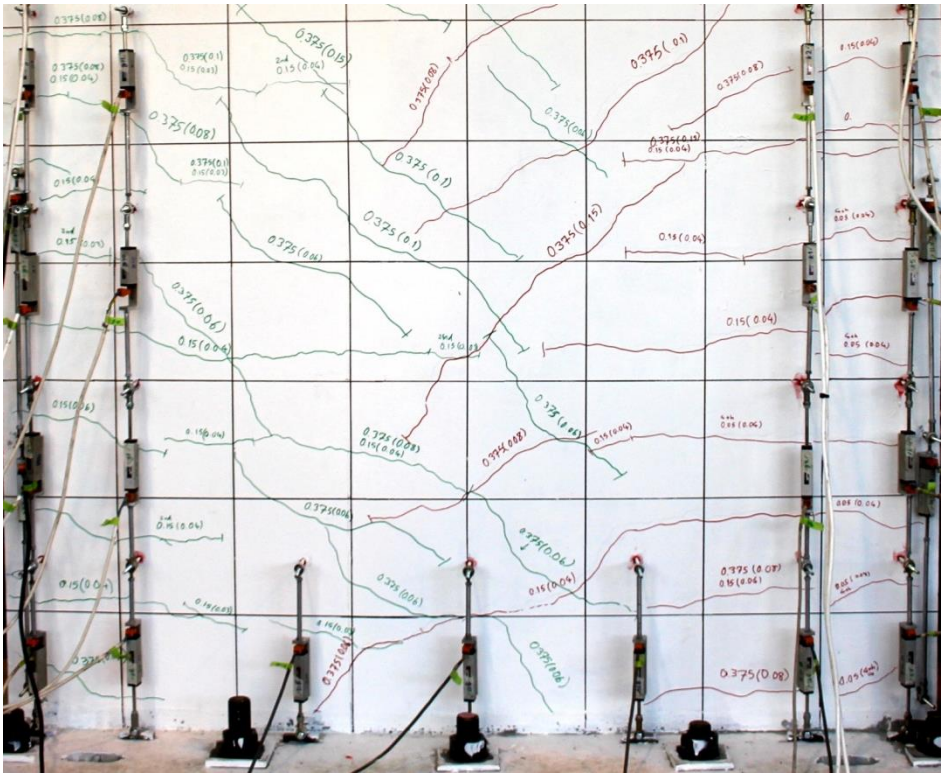

RWL - Grid size: 200x200 mm

Figure C - 3: Crack pattern at 0.38% drift level

RWB - Grid size: 250x250 mm

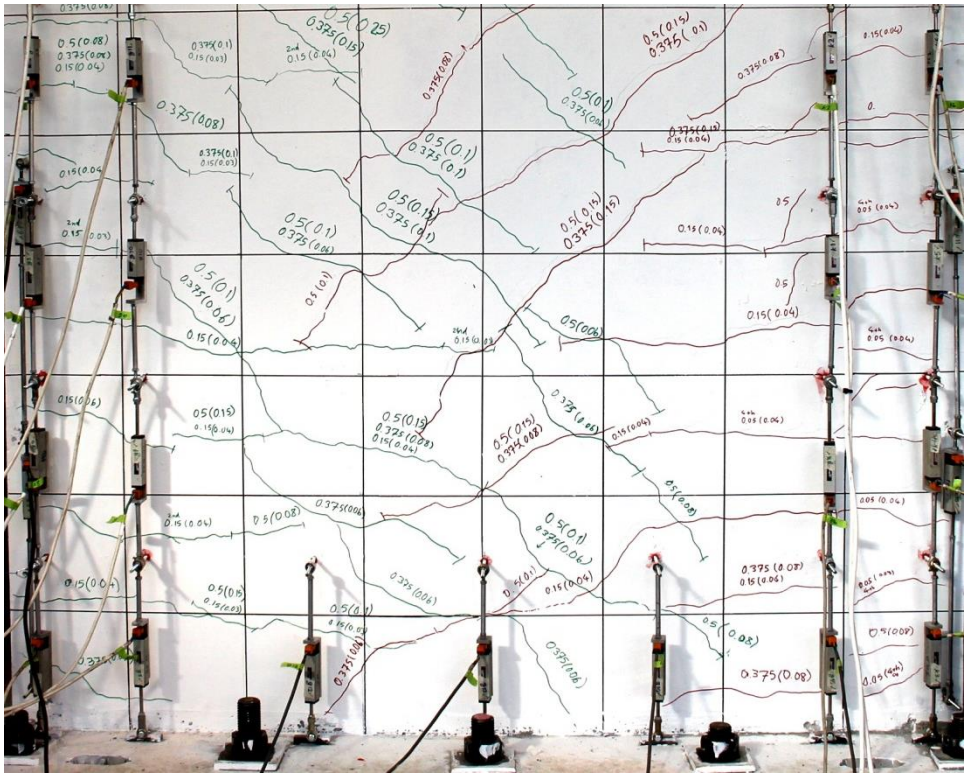

RWL - Grid size: 200x200 mm

Figure C - 4: Crack pattern at 0.50% drift level

RWB - Grid size: 250x250 mm

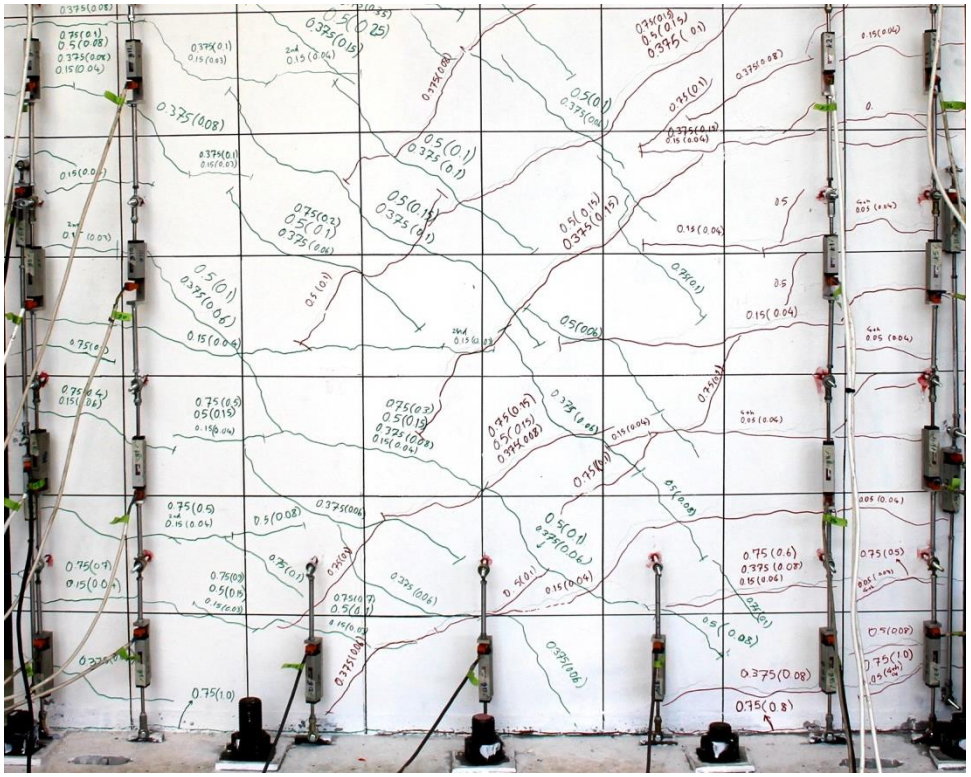

RWL - Grid size: 200x200 mm

Figure C - 5: Crack pattern at 0.75% drift level

RWB - Grid size: 250x250 mm

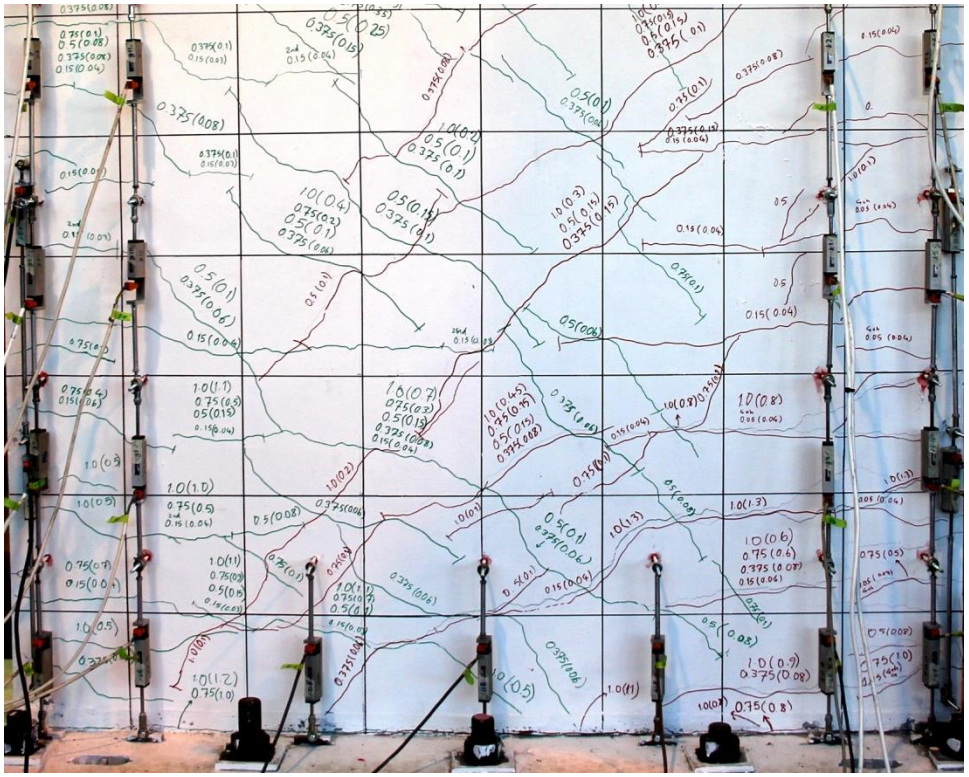

RWL - Grid size: 200x200 mm

Figure C - 6: Crack pattern at 1.00% drift level

RWB - Grid size: 250x250 mm

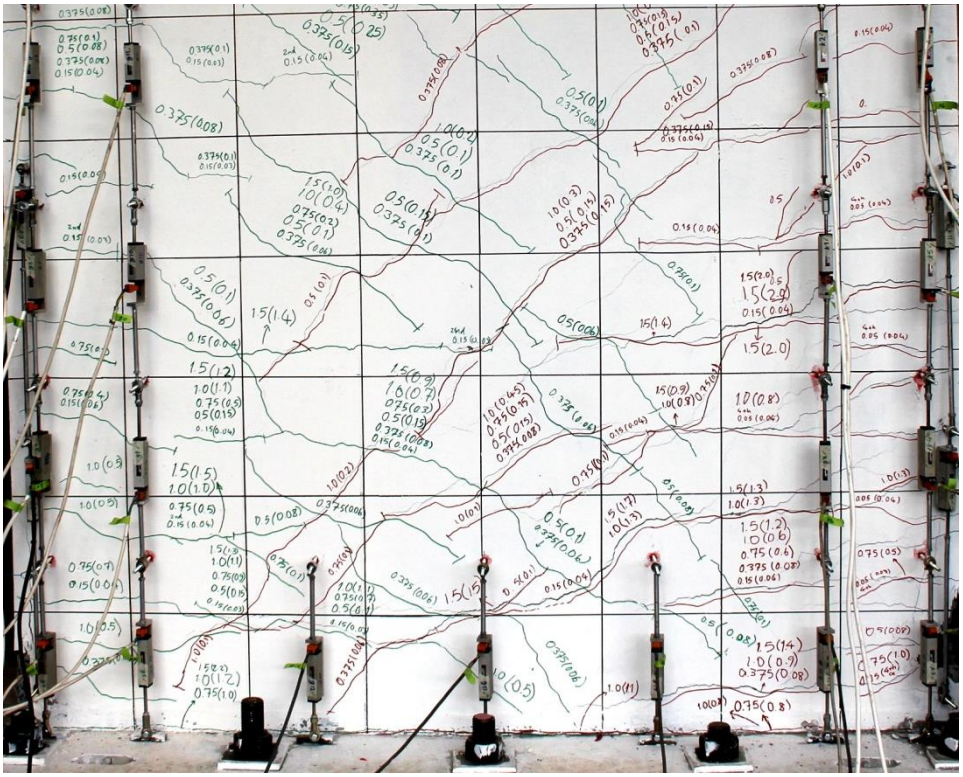

RWL - Grid size: 200x200 mm

Figure C - 7: Crack pattern at 1.5% drift level

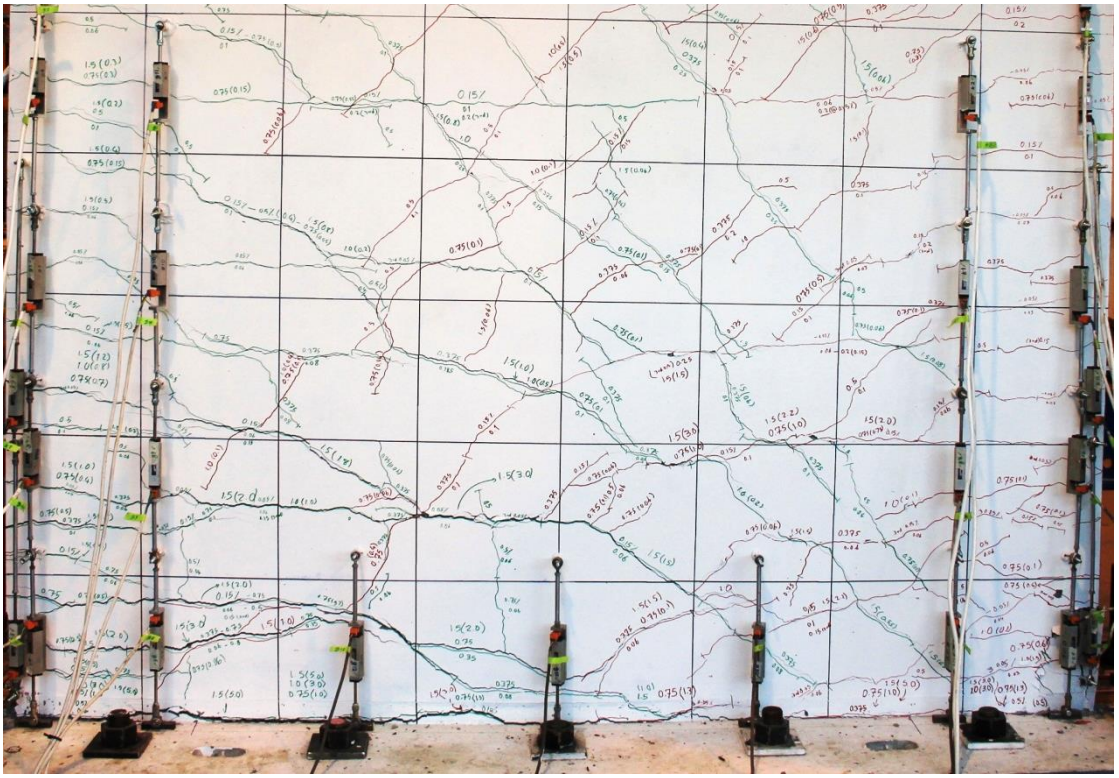

RWB - Grid size: 250x250 mm

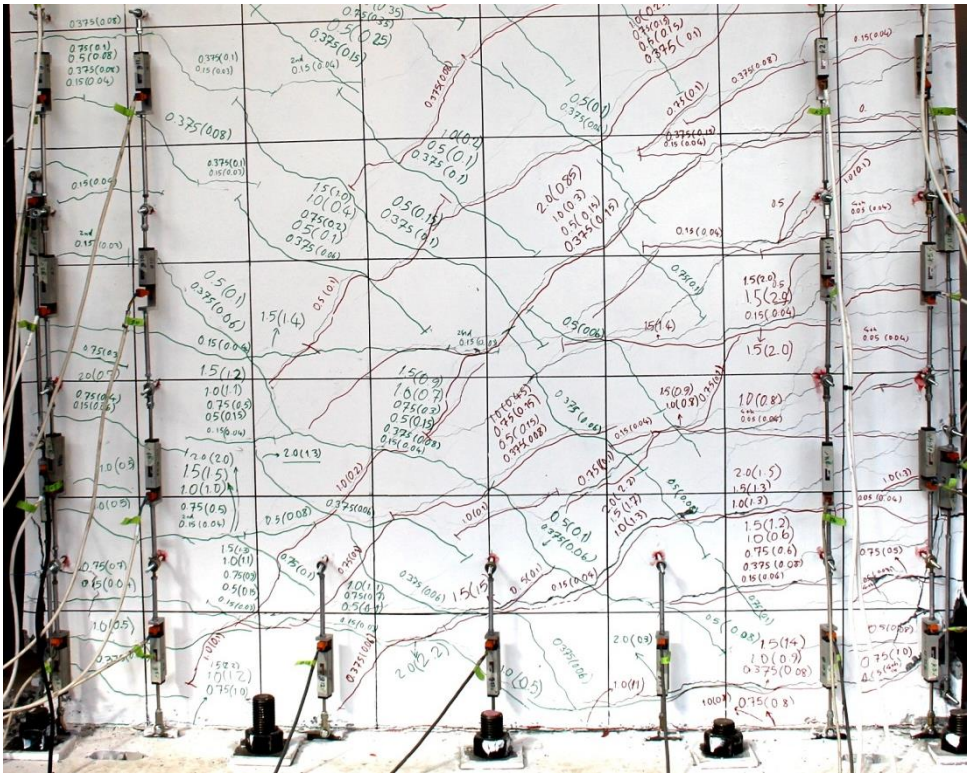

RWL - Grid size: 200x200 mm

Figure C - 8: Crack pattern at 2.00% drift level

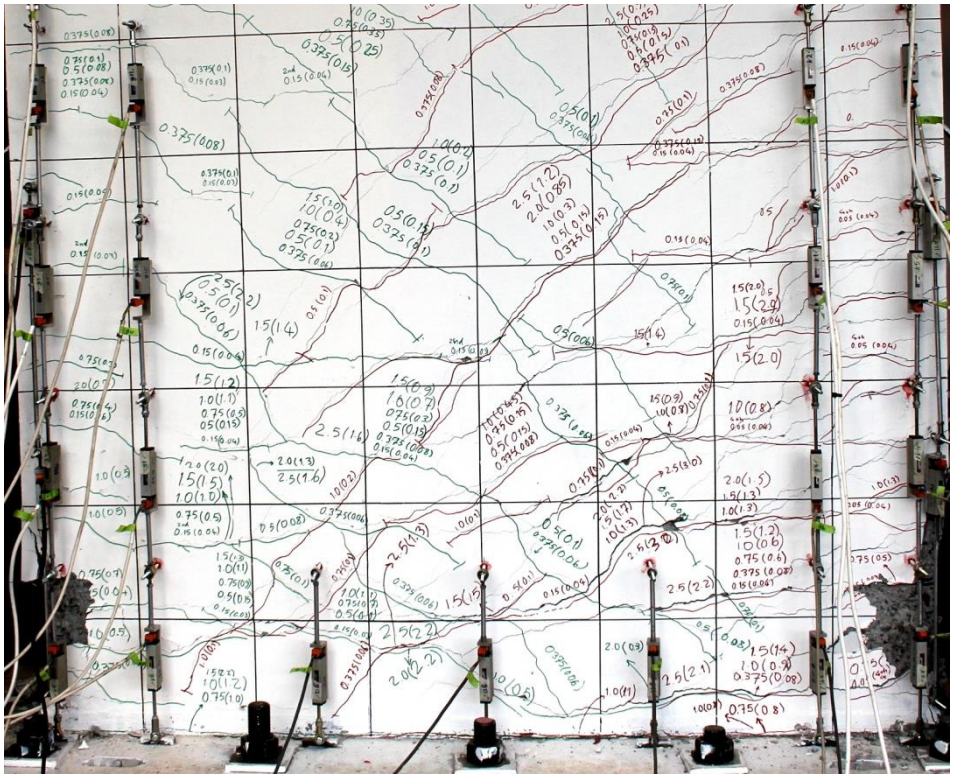

RWL – 2.50% drift

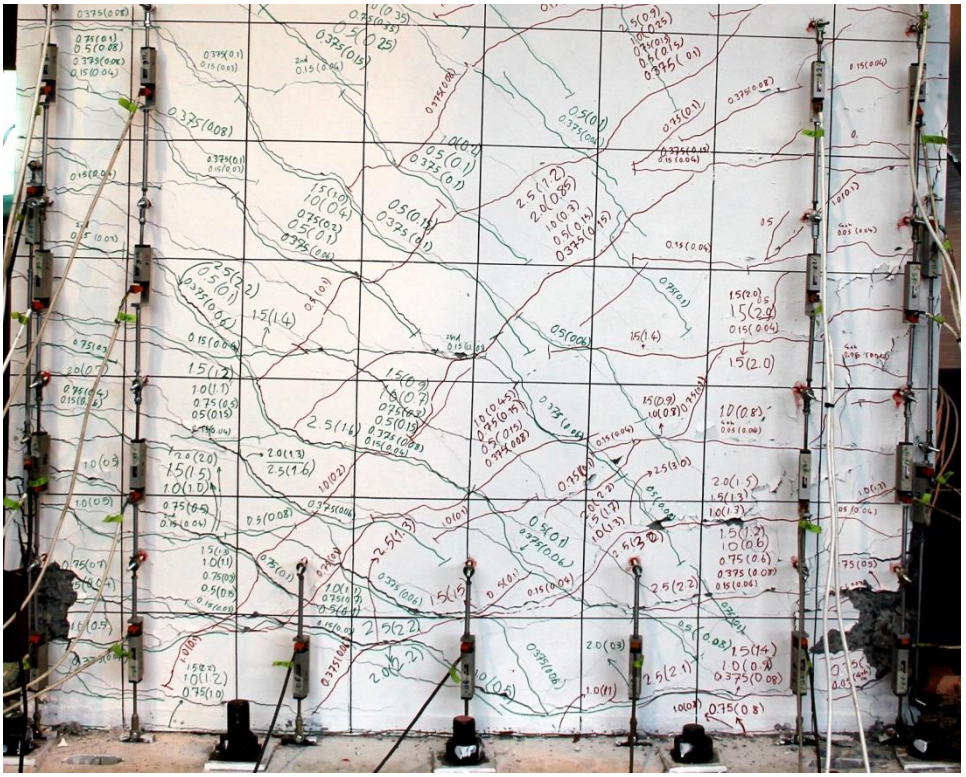

RWL – 3.00% drift

Figure C - 9: Crack pattern of Specimen RWL at 2.50% and 3.00% drift levels

INSTABILITY

RWB – During 2nd cycle of the 2.00% drift

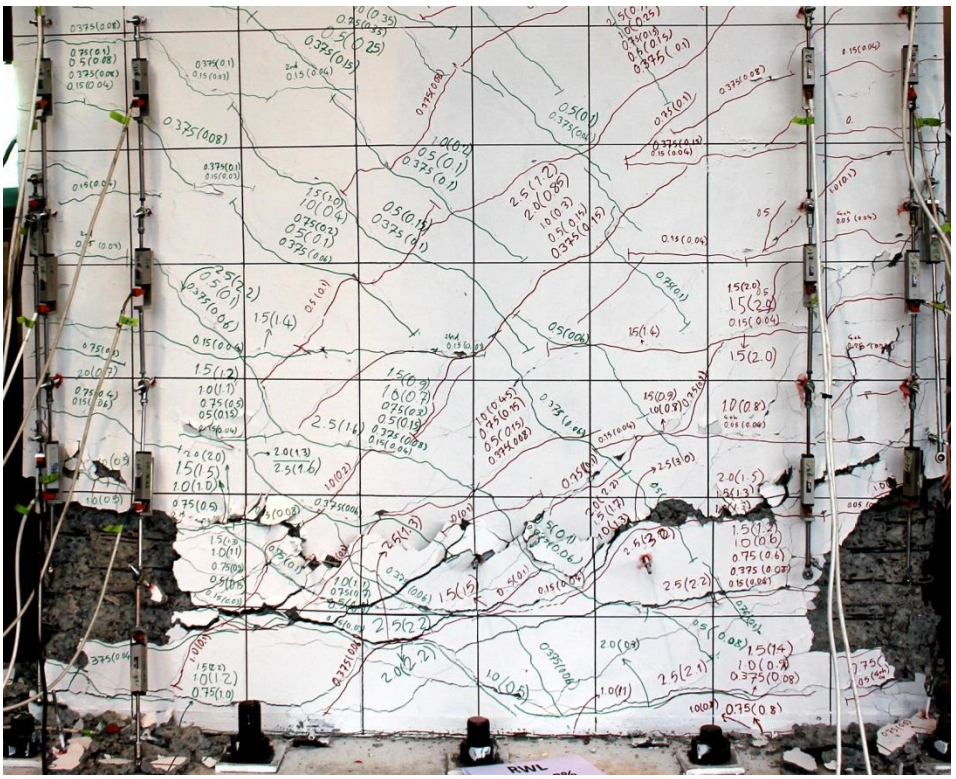

RWL - During 1st cycle of the 3.00% drift

Figure C - 10: Instability of the specimens

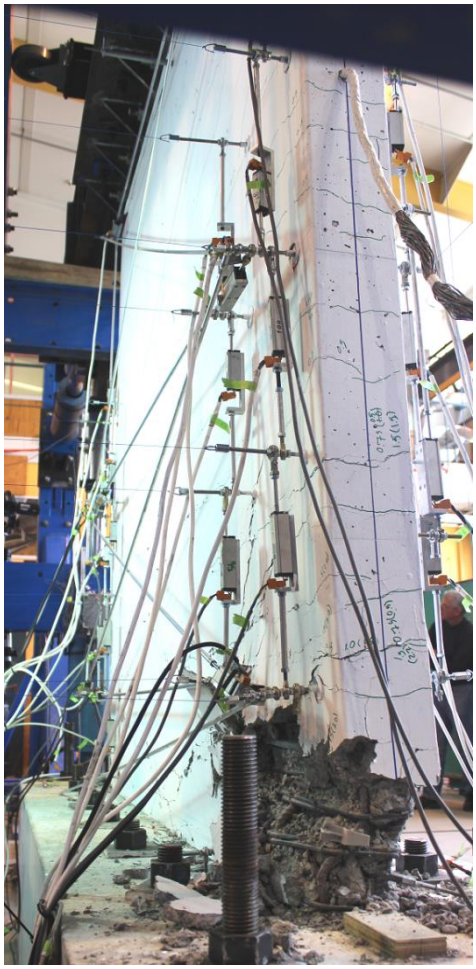

RWB – During 2nd cycle of the 2.00% drift

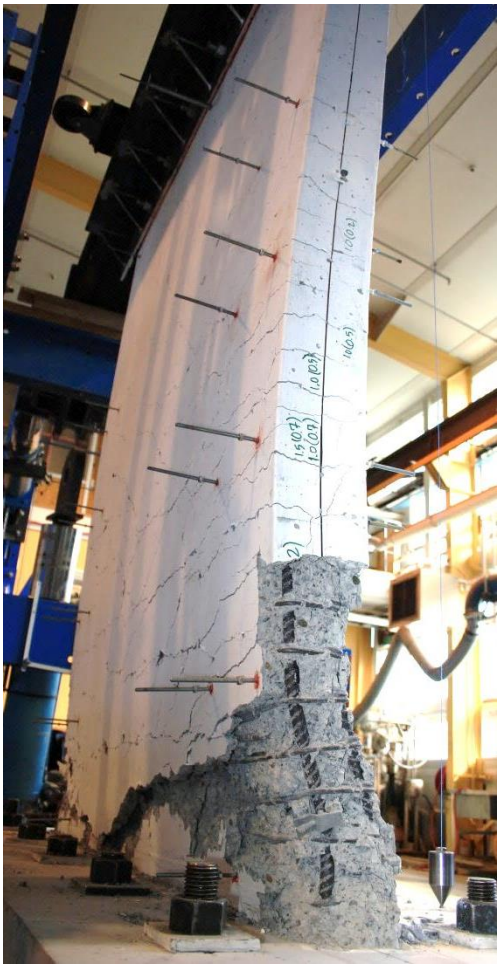

RWL - During 1st cycle of the 3.00% drift

Figure C - 11: Instability of Specimens RWB & RWL

(a) Movement of the specimen centerline

(b) Bar fracture

(c) Bar buckling (Boundary region)

(d) Bar buckling in the panel region

Figure C - 12: Instability of Specimen RWT